

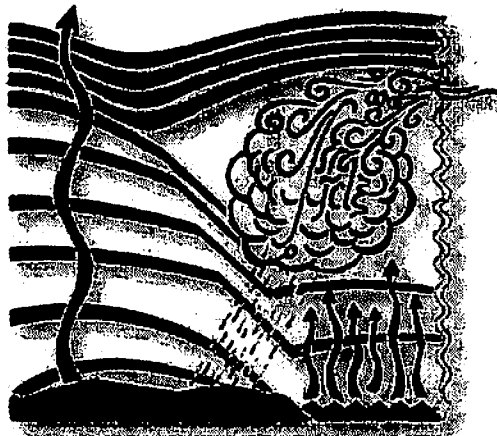
PENNSSTATE



Eighth International Symposium on Long-Range Sound Propagation

***September 9-11, 1998
The Pennsylvania State University
University Park, PA 16802***

***Sponsored by the
Applied Research Laboratory,
Department of Meteorology, and the Graduate Program in Acoustics***





Eighth International Symposium on Long-Range Sound Propagation

*September 9-11, 1998
The Pennsylvania State University
University Park, PA 16802*

*Sponsored by the
Applied Research Laboratory,
Department of Meteorology, and the Graduate Program in Acoustics*

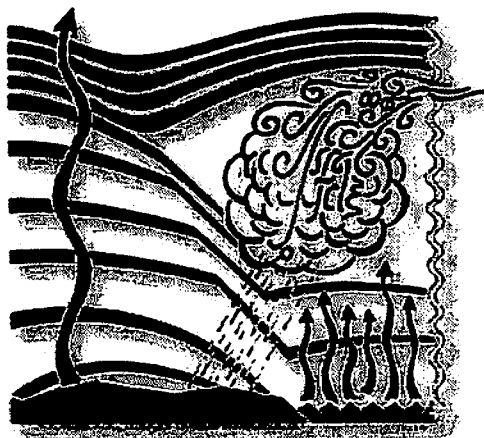


Table of Contents

Preface	iv
Attendees	v
<i>Signal propagation--relevant meteorology (Chair: D. Keith Wilson)</i>	1
Wave propagation engineering: Bringing in the Meteorology..... John C. Wyngaard	2
Mesoscale analysis and forecasting..... Nelson Seaman	13
<i>Field observations (Chair: Dennis W. Thomson)</i>	25
Environmental sensors for long range sound propagation measurements Karl Reichard, Jason Estep, and David Swanson	26
The influence of wind noise on the performance of helicopter detection and classification algorithms..... A.C. van Koersel	36
Acoustic propagation, prediction, validation, and training models for civilian applications..... D.C. Swanson, K.T. McClintic, M.P. Mahon, and K.M. Reichard	48
Comparison of seismic and acoustic signals from moving vehicles Roy J. Greenfield, Mark L. Moran, and Donald G. Albert	61
Review of models for ground effects over level terrain..... Keith Attenborough	70
<i>Interpretation of ground and terrain effects (Chair: Keith Attenborough)</i>	85
Measurement of ground impedance with the level difference method Mikael Ögren	86
Measurement of multipath outdoor sound propagation with spread-spectrum signals..... T. Douglas Mast, David C. Swanson, Mark P. Mahon, and David E. Norris	97
Sound propagation in a refracting medium above an uneven terrain..... Shahram Taherzadeh, Kai Ming Li, and Keith Attenborough	101
Blast noise propagation above a snow cover Donald G. Albert and Lars R. Hole	112
Theoretical analysis of pulse propagation above a curved surface which supports a surface wave..... Richard Raspet and Keith Attenborough, Kai Ming Li, and Qiang Wang	125

Survey of research of sound propagation in forests	131
Michelle Swearingen, David Swanson, and Karl Reichard	
Using a boundary element method for predicting noise barriers efficiency with meteorological effects	139
E. Premat and Y. Gabillet	
Scale model experiments on the insertion loss of wide and double barriers and barriers under turbulent conditions.....	153
James P. Chambers, Glenn J. Wadsworth, Mark Kelly, and Richard Raspet	
<i>Computational models and methods (Chair: D. Keith Wilson)</i>	168
Wave propagation in a 3-D turbulent atmosphere: Horizontal coherence	169
Xiao Di and Kenneth E. Gilbert	
A large vertical step parabolic equation (LVS-PE) for long range propagation in the atmosphere	181
M. West and R.A. Sack	
A wide angle parabolic equation for sound waves in moving media.....	194
L. Dallois, Ph. Blanc-Benon, D. Juvé, and V.E. Ostashev	
Numerical modeling of long range propagation from explosion sources (<i>Abstract</i>)	209
Rod Whitaker, James H. Hunter, and Kalpak Dighe	
Using modified mode-ray theory to understand counter-wind propagation effects from atmospheric explosions	210
D.O. ReVelle	
Impedance discontinuity and range dependent refraction profile: A numerical study.....	225
Benoit Gauvreau, Michel Berengier, Philippe Blanc-Benon, and Claude Depollier	
Lamb waves from small explosions: Boundary layer effects.....	241
D.O. ReVelle, R.W. Whitaker, and S.N. Kulichkov	
A propagation model based on Gaussian beams that accounts for wind and temperature inversions	254
R.L. Bronsdon and H. Forschner	
On the development of approximate models for outdoor sound propagation	263
Karsten Bo Rasmussen	
Modeling outdoor sound propagation with modeled weather data	276
Brian Magill and David Swanson	
Description of facilities for propagation and meteorological measurements at Rock Springs, with example datasets	283
David E. Norris, Dennis W. Thomson, and David C. Swanson	

<i>Some effects of atmospheric turbulence (Chair: John C. Wyngaard)</i>	295
On the application of turbulence spectral/correlation models to sound propagation in the atmosphere	296
D. Keith Wilson	
Interference of direct and ground reflected waves in a turbulent atmosphere	313
V.E. Ostashev and G.H. Goedecke	
The fluctuating field of a monopole source in a turbulent atmosphere above a ground surface. Time-averaged sound pressure level and statistical distributions	326
Erik M. Salomons	
Influence of atmospheric turbulence on sound reduction by a thin, hard screen: A parameter study using the sound scattering cross-section.....	352
Jens Forssén	
The effects of temperature and wind velocity stratification on sound scattering cross- section in a turbulent atmosphere.....	362
V.E. Ostashev, G.H. Goedecke, R.C. Wood, H. Auvermann, and S.F. Clifford	
Influences of the Doppler effect on the bandwidth of acoustical signals scattered from atmospheric turbulence.....	375
Harry J. Auvermann and George H. Goedecke	

PREFACE

This Symposium on Long-Range Sound Propagation is the eighth assembly since 1981 of a group of scientists who have specific interests in the observation, interpretation, understanding, and modeling of sound propagation over distances ranging from hundreds of meters to thousands of kilometers. The last, Seventh, Symposium was held on 24-26 July 1996 in Lyon, France at the Ecole Centrale de Lyon.

The present meeting was held on 9-11 September 1998 at The Pennsylvania State University, with sponsorship by the University's Applied Research Laboratory, Department of Meteorology and Graduate Program in Acoustics. Again, it has been organized to provide an opportunity for its participants to exchange ideas, to identify areas of research challenge and opportunity, and to foster collaboration in potential observational and computational programs. Most institutions having active research programs in various aspects of atmospheric sound propagation were represented. The papers selected for presentation were organized roughly into five sessions covering relevant meteorology, field observations, ground and terrain effects, computational models and methods, and effects of turbulence. The first session on meteorology relevant to acoustics was organized intentionally to depart somewhat from prior symposia. Penn State's Department of Meteorology is the oldest, largest and one of the finest in the world. Thus, a special effort was made to organize papers which would bring the symposia's attending acousticians up to date on acoustic propagation-relevant meteorological science and technology. During the last decade, in particular, enormous progress has been made in upgrading meteorological observational systems (e.g., the "modernization" program of the U.S. National Weather Service), and in developing and applying new analysis and forecast models for atmospheric phenomena ranging from turbulence and the boundary layer, to storm or mesoscales, and up to continental and hemispherical scales. All these scales are of interest to acousticians who must deal with problems ranging from the spatial and temporal variability of audible sounds to the very long range propagation of infrasound and blast noise.

Your hosts would like to express their appreciation to the participants for participating, and for sharing their enthusiasm and knowledge with their colleagues. We want also to especially thank Mrs. Dianne Taylor for the patient and outstanding support she contributed to organizing and conducting the meeting.

Kenneth E. Gilbert

Applied Research Laboratory and Graduate Program in Acoustics
Penn State University, University Park, PA

Dennis W. Thomson

Department of Meteorology and Graduate Program in Acoustics
Penn State University, University Park, PA

D. Keith Wilson

U.S. Army Research Laboratory, Adelphi, MD

Attendees

Don G. Albert
USA CRREL
Geophysical Science Branch
72 Lyme Road
Hanover, NH 03755-1290 USA
dalbert@crrel.usace.army.mil

W.T. Armstrong
EES - 8, MS - F659
LANL
Los Alamos, NM 87544 USA
wta@lanl.gov

Keith Attenborough
The Open University
Faculty of Technology
Milton Keynes MK7 6AA UK
k.attenborough@open.ac.uk

Harry J. Auvermann
U.S. Army Research Laboratory
2800 Powder Mill Road
Adelphi, MD 20783 USA
hauverma@arl.mil

Henry E. Bass
University of Mississippi
National Center for Physical Acoustics
University, MS 38677 USA
pabass@olemiss.edu

Philippe Blanc-Benon
Lab. de Mecanique des Fluides
et d'Acoustique de l'Ecole
Centrale de Lyon, UMR
CNRS 5509, BP 163, 69131
Ecully Cedex France
phbb@selene.mecaflu.ec-lyon.fr

Robert Bronsdon
Walt Disney Imagineering
1401 Flower Street
Glendale, CA 91221 USA
robert_bronsdon@wdi.disney.com

Patrice Boulanger
CRREL
72 Lyme Road
Hanover, NH 03755 USA
pboulanger@crrel.usace.army.mil

Jim Chambers, Ph.D.
National Center for Physical Acoustics
University of Mississippi
University, MS 38677 USA
chambers@olemiss.edu

Fred Campbell
DOD Army
Dir. AMSAS
392 Hopkins Blvd.
APG, MD 21005

Laurent Dallois
LMEA BP 163
Ecole Centrale de Lyon
69131 Ecully Cedex
France

Xiao Di
Graduate Programs in Acoustics
Applied Research Laboratory
The Pennsylvania State University
University Park, PA 16801 USA
di@seaair.acs.psu.edu

Jens Forssén
Chalmers University of Technology
Department of Applied Acoustics
S-41296 Gothenburg, Sweden
jf@ta.chalmers.se

Benoit Gauvreau
Laboratoire Central des Ponts et Chaussées
Centre de Nantes, BP 19
44340 Bouguenais, France
benoit.gauvreau@lcpc.fr

Kenneth E. Gilbert
The Pennsylvania State University
Applied Research Laboratory
P.O. Box 30
University Park, PA 16801 USA
gilbert@seaair.acs.psu.edu

Roy Greenfield
The Pennsylvania State University
Department of Geoscience
441 Deike Building
University Park, PA 16802 USA
roy@geosc.psu.edu

Logan E. Hargrove
Office of Naval Research, ONR 331
800 North Quincy Street
Arlington, VA 22217-5660 USA
hargrol@onr.navy.mil

Brian Magill
Graduate Programs in Acoustics
217 Applied Science Building
The Pennsylvania State University
University Park, PA 16802 USA
bem157@psu.edu

David Norris
GTE/BBN Technologies
1300 North 17th Street
Arlington, VA 22153 USA
dnorris@bbn.com

Mikael Ögren
SP Swedish National Testing and
Research Institute
Box 857 S-501 15 Boras, Sweden
mikael.ogren@sp.se

Vladimir Ostashev
New Mexico State University
Department of Physics
Box 30001/Dept. 3D
La Cruces, NM 88003 USA
vostashe@nmsu.edu

David Payne
DOD Army
AMSAA
392 Hopkins
APG, MD 21105 USA

Eric Premat
Ecole Nationale des Travaux Publics
De l'Etat
2 rue Maurice Audin
69518 Valx en Velin Cedex France
premat@entpe.fr

Kodali V. Rao
VASA Associates, Inc.
1814 Golf View Ct.
Reston, VA 20190 USA
kvrao@vasaa.com

Karsten Bo Rasmussen
Acoustics Laboratory
Technical University of Denmark
Building 352
DK-2800 Lyngby Denmark
kbr@dat.dtu.dk

Richard Rasket
Department of Physics and Astronomy
University of Mississippi
University, MS 38677 USA
rasket@next1.ncpa.olemiss.edu

Karl Reichard
Graduate Program in Acoustics
The Pennsylvania State University
University Park, PA 16802 USA
kmr5@psu.edu

Douglas O. Revelle
P.O. Box 1663
MS F659
Los Alamos National Lab., EES-8
Los Alamos, NM 87545 USA
dor@vega.lanl.gov

Erik M. Salomons
TNO Institute of Applied Physics
P.O. Box 155
2600 AD Delft, The Netherlands
salomons@tpd.tno.nl

Nelson Seaman
Department of Meteorology
503 Walker Building
The Pennsylvania State University
University Park, PA 16802 USA
seaman@ems.psu.edu

Ed Shallis
Countermeasure Branch AMSTA-RSC
Survivability Division
TACOM
Warren, MI 48090 USA
shalise@cc.tacom.army.mil

Louis C. Sutherland
27803 Longhill Drive
Rancho Palos Verdes, CA 90274 USA
lou-sutherland@juno.com

David Swanson
Applied Research Laboratory
The Pennsylvania State University
University Park, PA 16802 USA
dcs5@psu.edu

Michelle Swearingen
Graduate Programs in Acoustics
217 Applied Science Building
The Pennsylvania State University
University Park, PA 16802 USA
swear@sabine.acs.psu.edu

Shahram Taherzadeh
Engineering Mechanics Department
The Open University
Milton Keynes, MK7 6AA UK
S.TAHERZADEH@OPEN.AC.UK

Hassan Tavossi
Engineering Science and Mechanics
The Pennsylvania State University
University Park, PA 16802 USA
hmt111@psu.edu

Dennis Thomson
The Pennsylvania State University
Department of Meteorology
503 Walker Bldg.
University Park, PA 16802 USA
thomson@ems.psu.edu

A.C. van Koersel
TNO Physics and Electronics Laboratory
P.O. Box 96864
2509 JG The Hague,
The Netherlands
vankoersel@fel.tno.nl

Martin West
Department of Applied Acoustics
University of Salford
Salford M5 4WT UK
m.west@acoustics.salford.ac.uk

Rodney Whitaker
EES-5 MSF665
Los Alamos National Laboratory
Los Alamos, NM 87545 USA
rww@lanl.gov

Keith Wilson
U.S. Army Research Laboratory
ATTN: AMSRL-IS-EE
2800 Powder Mill Road
Adelphi, MD 20783-1197 USA
dkwilson@arl.mil

John C. Wyngaard
The Pennsylvania State University
Department of Meteorology
503 Walker Building
University Park, PA 16802 USA
wyngaard@ems.psu.edu

R.C. Wood
Dept. of Physics
New Mexico State University
Las Cruces, NM 88003-8001 USA

Signal Propagation--Relevant Meteorology

The propagation of radio waves is affected by the atmosphere in a number of ways. The most important factors are the refractive index, absorption, and scattering. The refractive index of the atmosphere is not constant and varies with altitude, temperature, and humidity. This variation causes the bending of radio waves, which is known as refraction. The bending of radio waves is most pronounced at low altitudes and is the cause of the "ducting" effect, which allows radio waves to travel beyond the horizon.

Another important factor is absorption. Radio waves are absorbed by the atmosphere, particularly by water vapor and oxygen. The amount of absorption depends on the frequency of the radio waves and the amount of water vapor and oxygen in the atmosphere. Absorption is most pronounced at high frequencies and in humid conditions. Scattering is also a factor, particularly at low frequencies and in the presence of ionospheric irregularities. Scattering occurs when radio waves are deflected by irregularities in the ionosphere, which can cause the waves to travel in unexpected directions.

The ionosphere is a layer of the atmosphere that contains free electrons and ions. It is formed by the ionization of atmospheric gases by solar radiation. The ionosphere is responsible for the reflection of radio waves, which allows them to travel long distances. The height and density of the ionosphere vary with time and location, and these variations affect the propagation of radio waves.

The atmosphere also affects the propagation of radio waves through the troposphere. The refractive index of the troposphere varies with altitude, temperature, and humidity, and these variations cause the bending of radio waves. The bending of radio waves is most pronounced at low altitudes and is the cause of the "ducting" effect, which allows radio waves to travel beyond the horizon.

The atmosphere also affects the propagation of radio waves through the stratosphere. The refractive index of the stratosphere varies with altitude, temperature, and humidity, and these variations cause the bending of radio waves. The bending of radio waves is most pronounced at high altitudes and is the cause of the "ducting" effect, which allows radio waves to travel beyond the horizon.

The atmosphere also affects the propagation of radio waves through the mesosphere. The refractive index of the mesosphere varies with altitude, temperature, and humidity, and these variations cause the bending of radio waves. The bending of radio waves is most pronounced at high altitudes and is the cause of the "ducting" effect, which allows radio waves to travel beyond the horizon.

The atmosphere also affects the propagation of radio waves through the thermosphere. The refractive index of the thermosphere varies with altitude, temperature, and humidity, and these variations cause the bending of radio waves. The bending of radio waves is most pronounced at high altitudes and is the cause of the "ducting" effect, which allows radio waves to travel beyond the horizon.

The atmosphere also affects the propagation of radio waves through the exosphere. The refractive index of the exosphere varies with altitude, temperature, and humidity, and these variations cause the bending of radio waves. The bending of radio waves is most pronounced at high altitudes and is the cause of the "ducting" effect, which allows radio waves to travel beyond the horizon.

Wave-propagation Engineering: Bringing in the Meteorology

John C. Wyngaard

Departments of Meteorology, Mechanical Engineering, and GeoEnvironmental Engineering
508 Walker, Penn State University, University Park, PA 16802
814-863-7714; Fax 865-3663; wyngaard@ems.psu.edu

I thank the organizers for this opportunity to contribute to this symposium. I will sketch out the broad aspects of what I call “wave-propagation engineering”. Since engineering is often underappreciated by scientists, I suppose that is bound to be an unpopular term. Nonetheless, three parallel developments over the past few decades now allow us, we believe, to develop a new type of propagation calculation tool, one that (in the words of a colleague) does not require you to invent your own atmosphere or ocean.

I will discuss the three developments in the context of electromagnetic (EM) propagation in the lower atmosphere, but I believe they will apply also to acoustics, and in the ocean. They are

- numerical prediction of atmospheric flows
- numerical simulation of turbulence
- parabolic-equation models of wave propagation

All three developments were made possible, of course, by the advent of large-scale, high-speed digital computers about thirty years ago.

The first development has led to the remarkable skill of today’s meteorological predictions on atmospheric scales of tens of km to 1000 km. Today this mesoscale modeling, as it is called, is the workhorse of regional meteorology. Its resolution in the continuously turbulent region called the boundary layer, while not sufficient to resolve the turbulence, is sufficient to resolve the key *forcing mechanisms* of the turbulence—e.g., the surface buoyancy flux, the surface stress, and the vertical variation of the horizontal pressure gradient. As we shall discuss, knowledge of such parameters allows us to make an approximate diagnosis of the refractive-index structure of the boundary layer.

At about this same time (ca 1970) came the second development, direct numerical solutions of the basic fluid equations for turbulent flows. Because this *direct numerical*

simulation, or DNS, resolves the entire eddy size range, and because the width of this range increases with the flow Reynolds number, only modest Reynolds-number flows can be calculated; they correspond roughly to those of turbulence in a teacup, say. But this was a no-excuses turbulence calculation, a breakthrough; finally we could actually study in detail the extraordinarily intricate, three-dimensional, time-dependent, chaotic, non-linear interactions that are turbulence.

A spinoff of DNS is a less pure form that today we call *large-eddy simulation* (LES). It solves approximately the spatially filtered governing equations in which turbulence scales smaller than the filter scale have been removed. As far as we can tell this gives extremely realistic turbulence fields. Figure 1 shows a "snapshot" of a vertical plane in the turbulent atmospheric boundary layer made visible through LES in a domain 2.5 km by 2.5 km in the horizontal by 1 km deep. This is from Martin Otte's Ph.D. work; he used about 200^3 grid points for this run. The tracer is the scalar product of turbulent vorticity and the gradient of turbulent water-vapor mixing ratio, a good marker of turbulence. It shows the instantaneously sharp but irregular top of the turbulent boundary layer and the completely turbulent nature of the fluid within it. This is a turbulence-simulation counterpart of the acoustic sounding that electrified the boundary-layer meteorology community in the early 1970s.

Numerical simulation has fundamentally changed the way we deal with turbulence. Until perhaps three decades ago we viewed turbulence primarily in the dim light of the ensemble average. The primacy of ensemble statistics generated through experiment and observation testifies to the impact 50 years ago of the Russian school that includes Kolmogorov. Today, for better and for worse, the turbulence community has become substantially if not predominantly simulation based.

However, we do not yet have a set of turbulence terms that refer specifically to instantaneous fields. Our turbulence language has not kept up with our changing perspective; essentially all our turbulence terms are everyday words appropriated and given special meaning in reference to turbulence statistics. As it becomes more accessible in applications, turbulence might for this reason be initially even more confusing. I can illustrate this with a contemporary example.

A review paper on parabolic equation EM propagation models contains the phrase *horizontally homogeneous refractive environments*. Since the refractive environment in the lower troposphere is usually turbulent, one meaning of the phrase might appear to be *turbulent refractivity of uniform composition in the horizontal*. But that is an oxy-

moron, for turbulence is by definition spatially irregular in all three directions. Turbulence *statistics* can be of uniform composition in the horizontal, however; in turbulence language that is called horizontally homogeneous turbulence. Thus, a second meaning could be *turbulent refractivity of statistically uniform composition in the horizontal*. Turbulence was not explicitly mentioned in the paper, however, so a third meaning could be *refractivity that is nonturbulent and of uniform composition in the horizontal*.

I wrote to the author. He intended the third meaning and did not think there would be confusion. There was, but to minimize future confusion we have a phrase at the ready: we call this the *plywood approximation* (Khanna et al., 1998).

The third development, parabolic-equation (PE) techniques, makes it possible to calculate wave propagation through a 2-D or 3-D field of refractive-index turbulence—through an individual realization rather than a large ensemble of them. Our hard-earned turbulence statistics are not obviously useful here, for the PE technique needs a random field, not statistics. It is tempting to generate a turbulence field through random modes with amplitudes chosen to fit the Kolmogorov (1941) spectrum. But this is apt to be unphysical, because it fails to account for the phasing of the Fourier modes that results in spatially coherent eddies. It fails also to connect turbulence with its forcing meteorology.

These three advances—mesoscale meteorological modeling, numerical simulation of turbulence, and the PE technique for calculating wave propagation—are the essential ingredients of a wave-propagation solver on the mesoscale. With Ken Gilbert, Xiaodi, Nelson Seaman, Dave Stauffer, Martin Otte, and Samir Khanna we are now using these tools for calculating EM propagation in the marine boundary layer for frequencies of hundreds of MHz to several GHz. The largest scales (5 km to 100s of km, say) of the refractivity field are calculated with a mesoscale model. Today one can run a mesoscale model for a specific region with actual initial conditions and predict the evolution of meteorological fields on a relatively fine grid for a few days into the future. Figure 2 shows a computer rendering of the 34-hour forecasted cloud-water field over North America on August 31, 1998, courtesy of Nelson Seaman. The forecast was made by the Penn State/NCAR mesoscale model (known as MM5) on a 36-km grid mesh. MM5 is a research model similar in many respects to the most advanced operational forecast models used by NOAA.

Figure 2 shows the early development of Hurricane Earl over the Gulf of Mexico, about one day before it turned eastward and headed inland over the Florida panhandle. The spiral cloud bands surrounding the eye of Earl are easily recognizable, and demon-

strate that today’s mesoscale models are indeed quite proficient.

Figure 3, top panel, shows the MM5-calculated water-vapor field on a 2.5 km-deep plane from an MM5 grid column with 12-km horizontal resolution. The calculated water-vapor field has only vertical structure within the grid column. We turn to large-eddy simulation for the missing, subgrid-scale water-vapor field. The mesoscale model gives the forcing conditions for the subgrid-scale fields within this grid column—the grid-averaged surface fluxes, wind speed, water-vapor gradient at the boundary-layer top, and the like.

The subgrid-scale water-vapor fields within the MM5 grid volume, which we calculate from archived LES, look like Figure 4, which is from Martin Otte’s Ph.D. thesis work. This case happens to show a 2.5-km grid in a convective boundary layer that is resolved down to about 20 m. We have developed a way to extend these turbulent water-vapor fields to scales of 1 m when necessary (Khanna et al., 1998).

Figure 5 shows the fluctuating part of the water-vapor field in Figure 4; the area mean has been removed. The highest-intensity fluctuations occur at the top of this entraining boundary layer, where they contribute strong “troposcatter” in non-ducted environments (Khanna et al., 1998).

Figure 6 shows the local refractive index structure-function parameter \tilde{C}_N^2 within a typical LES domain in a convective boundary layer. It shows a horizontal plane near the surface and a vertical plane as well. \tilde{C}_N^2 is a local generalization of the usual structure-function parameter (Peltier and Wyngaard, 1995), an ensemble-mean statistic that is proportional to the amplitude of the refractive-index spectrum in the inertial range of wavenumbers. The local parameter derives from the Kolmogorov (1962) and Obukhov (1962) revisions of the original Kolmogorov (1941) hypotheses about turbulence fine structure. Wilson et al. (1996) discuss an application of these revised notions about turbulence fine structure to atmospheric acoustics.

The superposability of EM refractive index allows us to combine numerical simulation of turbulence (on scales from 1 m to a few km) and mesoscale modeling (on scales of a few km to hundreds of km). In the EM problem the refractive-index fluctuations are caused by water vapor, which is governed by a linear transport equation. Thus, we can diagnose the forcing conditions for the water vapor and scale archived LES fields to produce the missing fine structure in the mesoscale refractive-index fields. The bottom panel of Figure 3 shows the resulting field. There is a good deal of boundary-layer meteorology involved in this superposition, but we believe it is all within the present state of

the art.

That is a quick review of our interdisciplinary approach to EM propagation. The acoustics problem is more complicated than the EM problem in that its refractive index depends in part on the velocity field. Velocity fields, being governed by a nonlinear equation, are technically not superposable. Nonetheless it ought to be possible to diagnose the SGS velocity field from local grid-scale conditions in a broadly similar way, while accommodating the constraints of nonlinearity. We stand ready to collaborate on such efforts.

References

Khanna, S., K. Gilbert, X. Di, M. Otte, and J. Wyngaard, 1998: Electromagnetic wave propagation through simulated atmospheric refractivity fields. Submitted to *Radio Science*.

Kolmogorov A. N., 1941: The local structure of turbulence in incompressible viscous fluid for very large Reynolds numbers. *C. R. Seances Acad. Sci.*, **30**, 301–305.

Kolmogorov A. N., 1962: A refinement of previous hypotheses concerning the local structure of turbulence in a viscous incompressible fluid at high Reynolds number. *J. Fluid Mech.*, **13**, 82–85.

Obukhov A. M., 1962: Some specific features of atmospheric turbulence. *J. Fluid Mech.*, **13**, 77–81.

Peltier, L. J., and J. C. Wyngaard, 1995: Structure-function parameters in the convective boundary layer from large-eddy simulation. *J. Atmos. Sci.*, **52**, 3641–3660.

Wilson, D. K., J. C. Wyngaard, and D. I. Havelock, 1996: The effect of turbulent intermittency on scattering into an acoustic shadow zone. *J. Acoust. Soc. Am.*, **99**, 3393–3400.

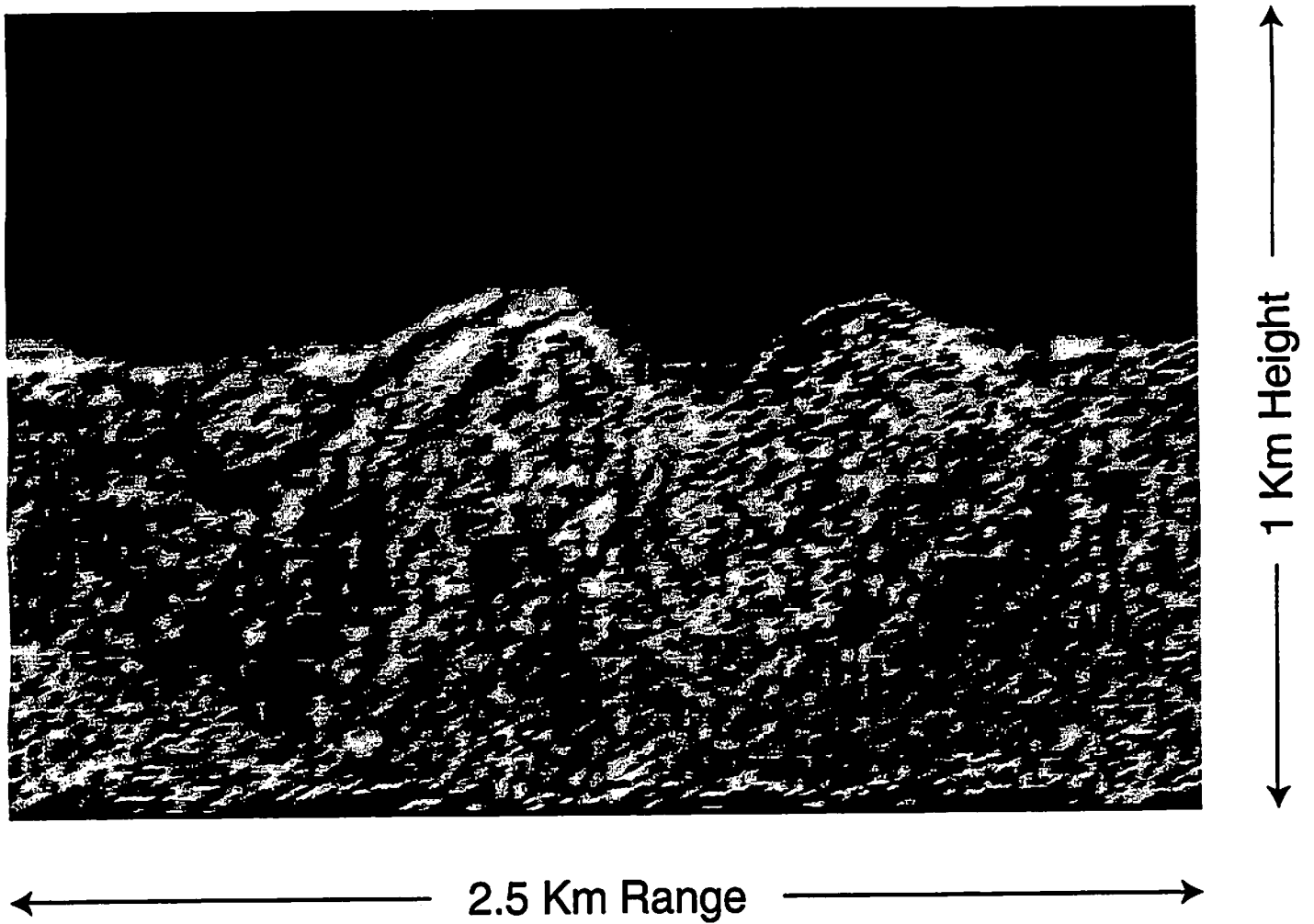


Figure 1. A “snapshot” of turbulence in a vertical plane of a convective atmospheric boundary layer calculated through large-eddy simulation. The tracer, the dot product of vorticity and the water-vapor gradient, is essentially zero in the non-turbulent fluid above the boundary layer. The instantaneous top of the boundary layer is quite sharp. Graphics courtesy Martin Otte.

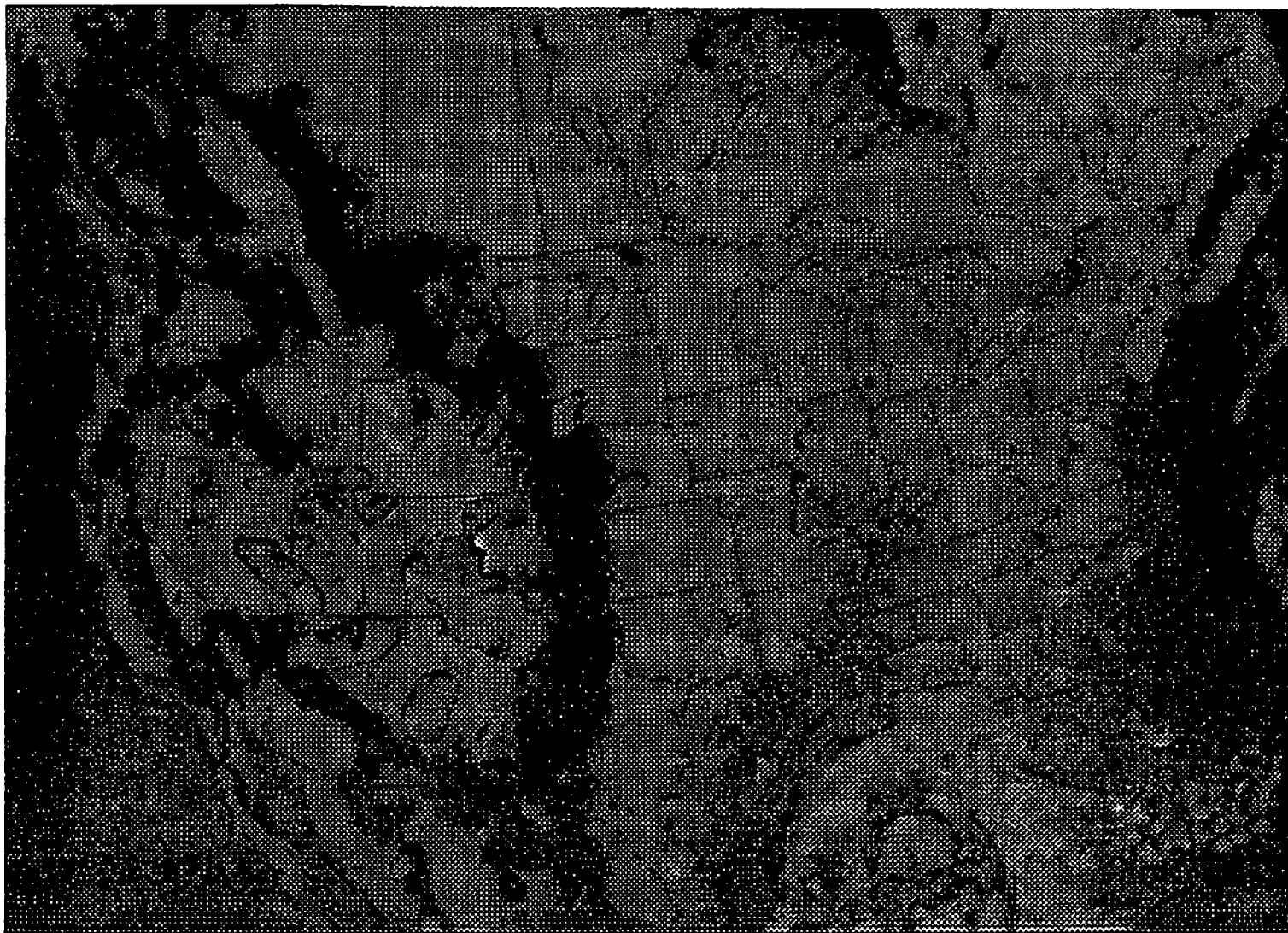
N
↑

Figure 2. A computer rendering of the 34-hour forecasted cloud-water field over North America on August 31, 1998, showing the early development of Hurricane Earl over the Gulf of Mexico. The forecast was made by the Penn State/NCAR mesoscale model MM5 on a 36-km grid mesh. Graphics courtesy of Nelson Seaman.

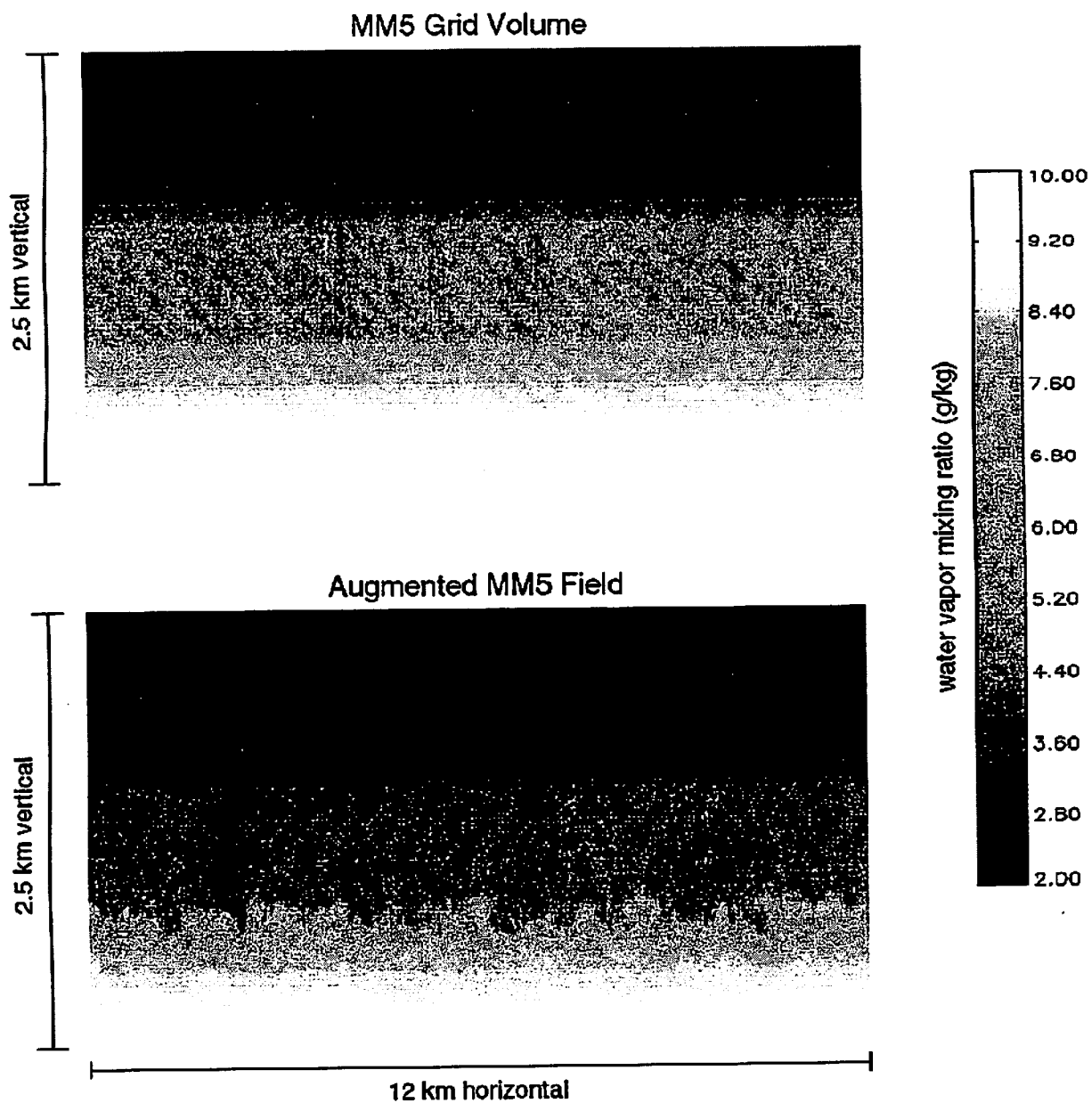


Figure 3. Top: The MM5-calculated water-vapor field on a 2.5 km-deep plane in a grid column with 12-km horizontal resolution. The calculated field has only vertical structure. Bottom: The water-vapor field after augmentation with the subgrid-scale field from LES.

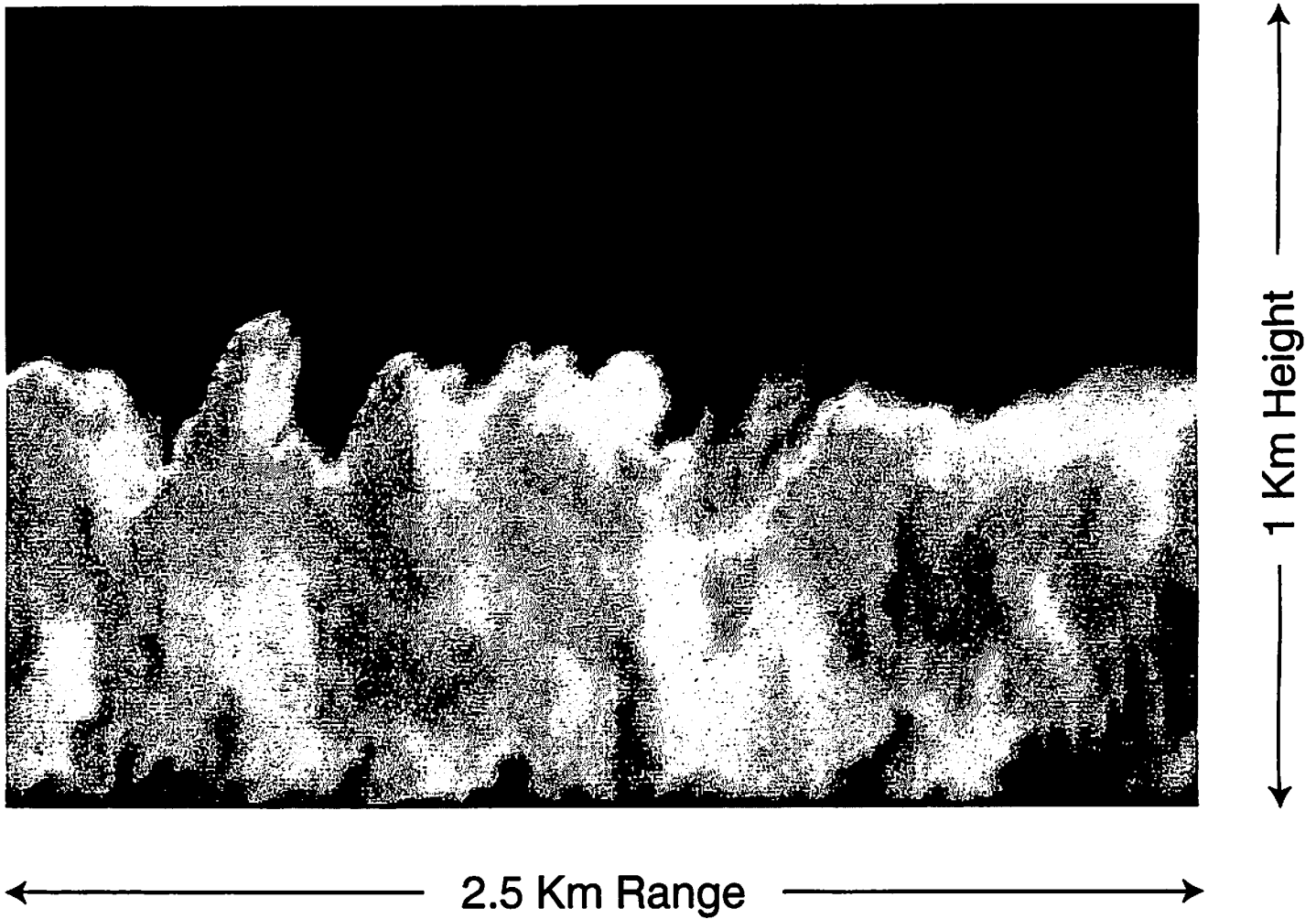


Figure 4. Detailed water-vapor fields calculated from LES for a 2.5-km domain and resolution of 20 m. Graphics courtesy Martin Otte.

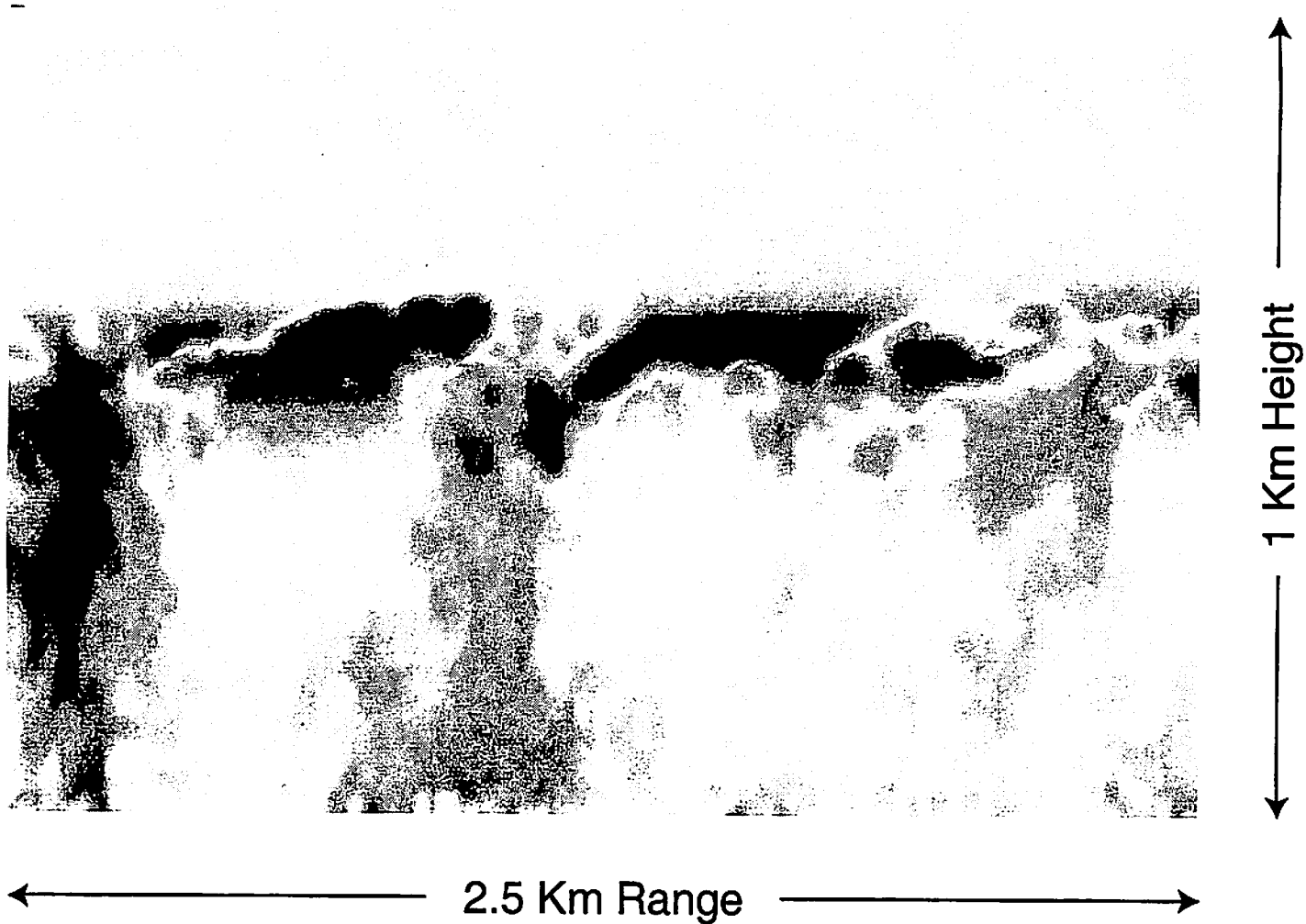


Figure 5. The fluctuating part of the water-vapor field in Figure 4; the area mean has been removed. The highest-intensity fluctuations occur at the top of this entraining boundary layer, where they contribute strong "troposcatter" in non-ducted environments. Graphics courtesy Martin Otte.

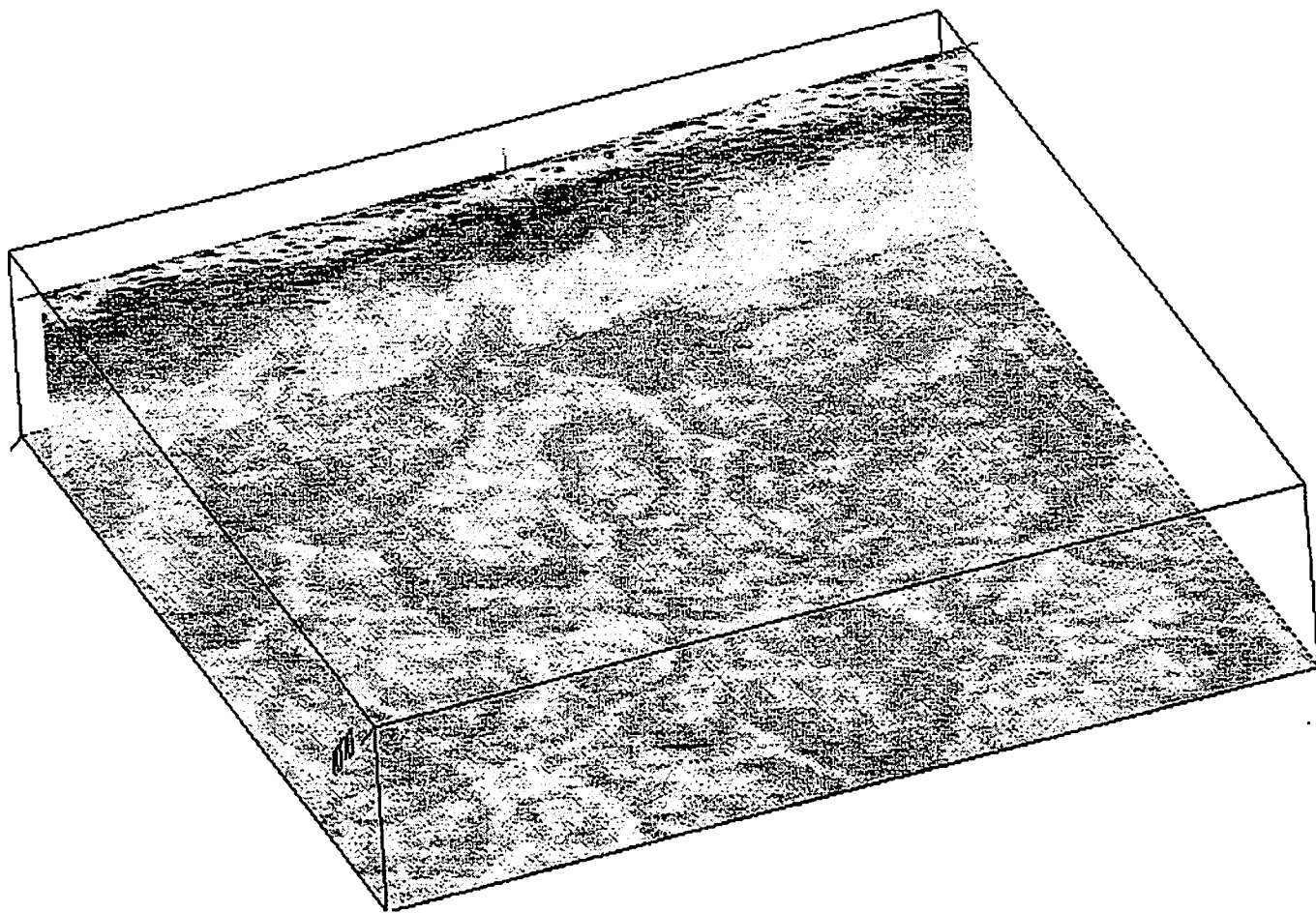


Figure 6. The local refractive index structure-function parameter \tilde{C}_N^2 within a typical LES domain in a convective boundary layer. Contours of \tilde{C}_N^2 are shown in a horizontal plane near the surface and on a vertical plane as well. Graphics courtesy Samir Khanna.

Mesoscale Analysis and Forecasting

Nelson L. Seaman
Department of Meteorology
The Pennsylvania State University
University Park, PA 16802
email: seaman@ems.psu.edu

Eighth International Symposium on Long-Range Sound Propagation
Penn State University
September 9-11, 1998

Refraction of wave energy in the atmosphere is primarily a function of the vertical structure of temperature, water vapor and pressure. For a standard lapse rate, horizontally emitted EM waves are bent upwards away from the earth's surface. However, in very stably stratified conditions, a *trapping layer* is formed, in which horizontally emitted EM waves are bent downward. If the base of the trapping layer is above the surface, so that waves below the layer can propagate upward, then the waves alternate between upward and downward propagation inside a wave *duct*. To simplify interpretation of the refractivity, a "modified refractivity", M , can be defined such that the effect of the earth's curvature is removed (Burk and Thompson 1997). That is, $dM/dz = 0$ describes the refractivity condition for which a horizontally emitted wave bends downward just enough to remain at the same altitude above a spherically curved earth. When M increases (decreases) with height, EM waves are bent upward (downward) relative to the earth.

Traditionally, estimates of refractivity conditions have been made using intermittent radiosondes, which are then assumed to represent horizontally homogeneous and steady-state propagation conditions over a range of up to 100 km. This approach has met with only limited success. Consequently, it is appropriate to consider data-assimilating mesoscale models as a means for analyzing and predicting the refractivity structure of the atmosphere such that variability in space and time is accounted for. To enable this modeling approach to succeed for the full range of conditions in which wave energy (electromagnetic [EM] or sound waves) can be detected near the surface at long range, a mesoscale model should be applied in conjunction with a turbulence model (large eddy simulations, or LESs).

In the present study, the Penn State/National Center for Atmospheric Research mesoscale model, MM5, was run for the week of 24-31 August 1993 during the VOCAR (Variability of Coastal Atmospheric Refractivity) experiment. The VOCAR study collected observations of EM refractivity along the coast of southern CA. During the period of interest, the summer climatology of the region, which is characterized by the synoptic-scale East Pacific Ridge, was interrupted for two days when a weak tropical storm moved north-northeastward from southern Baja California to the mouth of the Colorado River. The storm spread a deep layer of moist air through the mid-troposphere over study area, displacing the dry air normally found above the marine atmospheric boundary layer (MABL) in the coastal region. The *objectives* were (1) to evaluate model physics and data

assimilation techniques necessary for improved mesoscale predictions of the MABL and its capping inversion layer (which defines the trapping and ducting layers), and (2) to identify the importance of synoptic-scale and mesoscale processes which can contribute to the evolution of the MABL and ducting characteristics. This work is a preliminary step in the development of multi-scale model predictions covering the full range of scales controlling refractivity and EM propagation, from the mesoscale (2 - 2000 km) to the turbulence scales (0.01 - 2000 m).

The MM5 is a non-hydrostatic mesoscale model with a terrain-following vertical coordinate. A full description of the model equations and numerics is given by Grell et al. (1994). In this study, four nested grids were used, with mesh sizes of 108-km, 36-km, 12-km and 4-km, centered on the southern CA coast. The domains had 53 layers in the vertical direction, with layer thicknesses of 40 m from the surface to 600 m, and 24 layers below 1500 m AGL. The top of the model was at 100 mb. Initial and lateral boundary conditions were derived from standard surface and upper-air data obtained from NCEP (National Centers for Atmospheric Predictions).

Special data from the VOCAR study confirm that the MM5 model simulates the synoptic-scale and mesoscale variability in the depth of the MABL and the height and intensity of the trapping layer in the continuous seven-day simulation (Williams et al. 1998). Over time scales of several days, MABL characteristics were shown to be a function primarily of synoptic-scale subsidence in the East Pacific Ridge and surface heat and moisture fluxes from the ocean surface. At the mesoscale, diurnal variations in the vertical velocity field due to the mesoscale coastal sea-breeze were found to have a significant impact on the MABL depth, measured at San Nicolas Island (about 120 km offshore). Mid-tropospheric moisture flowing outward from the tropical storm was successfully simulated and produced a complex vertical moisture structure in the California Bight (Figure 1) that contributed to a strong surface-based ducting layer on August 26-27 (Figure 2). Finally, the MM5 developed gravity waves in the MABL as the regional flow encountered the coastal mountains of southern CA.

Burk, S.D. and W.T. Thompson, 1997: Mesoscale modeling of summertime refractive conditions in the Southern California Bight. *J. Appl. Meteor.*, **36**, 22-31.

Grell, G.A., J. Dudhia and D.R. Stauffer, 1994: A description of the fifth-generation Penn Stat/NCAR mesoscale model (MM5). NCAR Technical Note, NCAR/TN-398+STR, 122 pp.

Williams, R.T., N.L. Seaman, D.R. Stauffer and J.C. Wyngaard, 1998: Mesoscale simulation of electromagnetic refractivity in surface and elevated ducts during the VOCAR experiment. Proceedings of the 1997 Battlespace Atmospherics Conference, 2-4 Dec. 1997. SPAWAR-SCSD Tech. Doc. 2989. Anderson and Richter, Eds., 611-620.

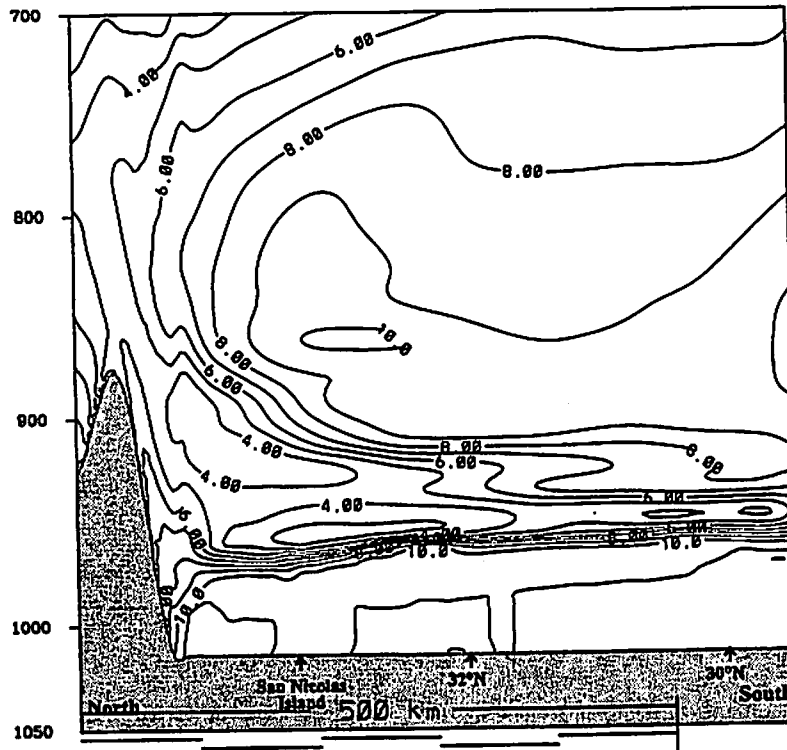


Figure 1. North-south vertical cross section of water vapor mixing ratio (g kg^{-1}) versus pressure (mb) simulated by MM5, at 0500 PDT (1200 GMT), 26 August 1993. Cross section follows 119.5 W from Santa Barbara through San Nicolas Is. southward to 29 N. Contour interval is 2 g kg^{-1} . MM5 results from 12-km domain.

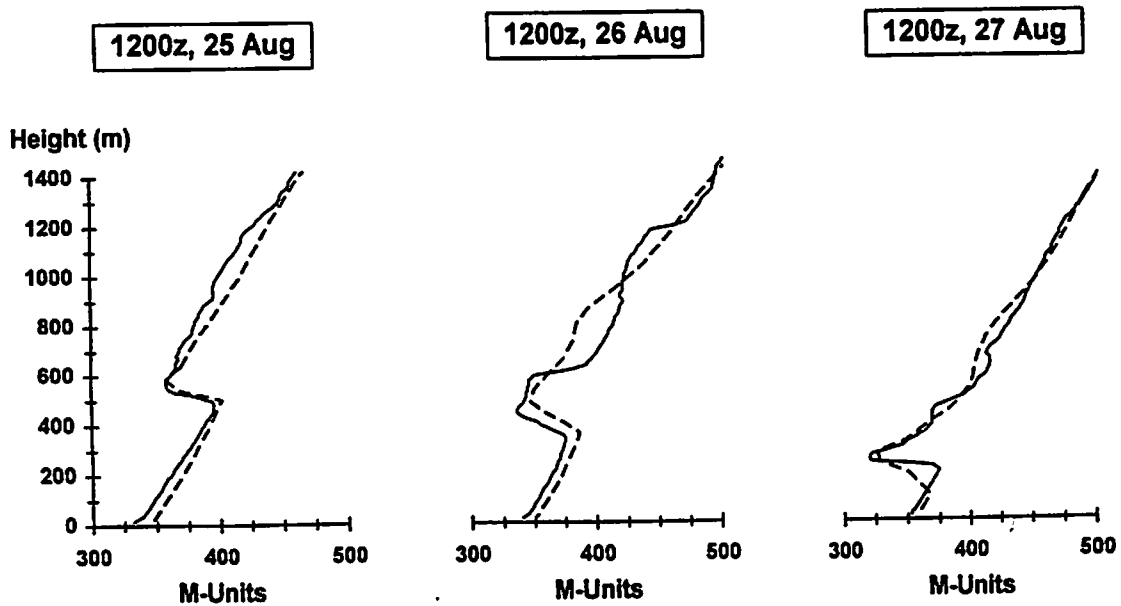


Figure 2. Observed (solid) and MM5-simulated (dashed) modified refractivity (M) at San Nicolas Is. versus height (m) on three consecutive days (25-27 August 1993) at 0500 PDT (1200 GMT). M-profiles show a trapping layer ($dM/dz < 0$) and a ducting layer. MM5 results from 12-km domain.

Long Range Propagation-Relevant Sound Speed Profiles: Synoptic Scales and Seasonal Variability

William J. Syrett* and Dennis W. Thomson**

Department of Meteorology

503 Walker Building

The Pennsylvania State University

University Park, PA 16802

**syrett@essc.psu.edu, telephone: 814-865-6172, fax: 814-865-3663*

***thomson@essc.psu.edu, telephone: 814-863-1585, fax: 814-865-3663*

I. Introduction

Audible sound signals that have propagated a few tens to hundreds of meters through the atmosphere depend critically upon conditions in the atmospheric surface layer. For sounds propagated over hundreds of meters to tens of kilometers, the conditions in the atmospheric boundary layer are of major importance. The state of, and variations in the atmospheric boundary layer and its lowermost part, the atmospheric surface layer, depend not only upon the properties of the earth's surface (including type and state of the vegetative cover) but also upon the time of day and the general weather conditions. Important factors include time of year, cloudiness, and whether or not the site is under the influence of high or low pressure. In the atmospheric boundary layer the critical meteorological variables are the vertical gradients of velocity and temperature. Path-integrated relative humidities are important only if the frequencies of concern are greater than 1-2 kHz. By contrast, the properties of ambient turbulence are very important, particularly for scattering easily detectable sound into regions that traditionally have been regarded as "shadow zones."

In order to understand "really" long-range sound propagation, signals that have traveled hundreds to thousands of kilometers, occasionally even completely around the earth, it is necessary to switch meteorological hats. Turbulence, always present in the atmospheric boundary layer, is of lesser importance because its largest scales, a km or so, correspond to the shortest of the infrasound wavelengths (roughly 300 m at 1 Hz, 30 km at 0.01 Hz). Instead what becomes critically important are the velocity and temperature gradients throughout the entire troposphere, stratosphere, and well into the mesosphere, essentially "inner" space. Thus, the relevant atmospheric dynamics are those from weather to planetary scales, and the features of interest are weather systems and seasonally changing, latitude- and longitude-dependent so-called long wave patterns.

Since WWII several schools of engineers and scientists, who have been concerned with problems of environmental signal propagation, have depended heavily upon climatological profiles of, for example, radio refractivity in the atmosphere and sound speed in the ocean. This approach has worked to some extent only because the radio refractivity doesn't depend upon atmospheric winds, and in the slowly varying oceans sound speeds are much higher than those of ambient currents. In the atmosphere the natural spatial and temporal variabilities of temperature, pressure, and winds are such a large fraction of the mean sound speed at any given location that it is unwise to define or depend upon profiles of a climatological mean type.

The application of some climatological data is necessary because there are few routine observations available for altitudes in excess of 30 km. However, for the troposphere and lower stratosphere the analyzed observations used today for daily global weather forecasts are of such high quality and so readily accessible that it only makes sense to use what is routinely available. Furthermore, the "observations" that are potentially available for uses in propagation models are even "better" than the actual atmospheric measurements.

All of the operational weather analysis and forecast models use some form of dynamic initialization. Therefore, the state of the atmosphere is "filled in" in a dynamically consistent fashion between the relatively sparse, in space and time, actual measurement locations. In addition, the time steps in the forecast models are typically a few minutes. Thus, by using data in the models for shorter times than the 3- to 12-hour forecast intervals, it is possible to intelligently infer the evolution of the atmospheric sound propagation medium at the resolution of the model over global scales.

The remainder of this paper provides some examples of meteorological and computed sound speed profiles over the continental United States during January and July 1996.

II. Examples of Long Range Propagation-Relevant Profiles

To illustrate the sensitivity of the sound speed profiles to weather- (synoptic-) scale-imposed changes in the ambient velocity and temperature profiles, we chose to examine the profiles relevant to propagation of a large burst of infrasound from an arbitrary location in southern Nevada. Thus, the source location was defined to be 36.75 N, 116.5 W. During the early years of above-ground nuclear weapons testing this general area was occasionally a source of large infrasound signals. Figure 1, thus, shows radials extending from southern Nevada along which one might be interested in knowing the sound velocity profiles for purposes of predicting the magnitude of signals received at hypothetical sensors deployed to the east in an array across the U.S. and Canada.

Having above disparaged the use of climatological profiles as input to various signal propagation models, it may now seem strange for us to have computed monthly mean, January and July 1996, profiles for use in this paper. Remember, however, that the sound velocity profiles, or sound speed along any particular specified bearing, at any particular time depend upon the ambient atmospheric velocity and temperature profiles that are constantly changing as the weather systems advect and evolve. Defining the advection and evolution of these systems is essentially the meteorologist's weather analysis and forecasting challenge. If the models used to solve that problem are working well, then the profiles from them necessary to predict infrasound propagation will provide the best available environmental data.

Our choice to evaluate monthly means also was somewhat arbitrary. The two months were chosen to represent cold-season versus warm-season statistics, while the year was chosen for its high data availability and lack of extreme weather. By calculating monthly means, it meant that two analyses per day, 00 and 12 UTC, or 62 profiles were used in estimating the profiles of, for example, standard deviations of sound speed during the month.

Figure 2 shows the mean temperatures as a function of latitude and pressure altitude along 80 W during January 1996. The nearly vertical orientation of the isotherms reflects the normal, substantial, wintertime north-south gradient of temperature at the surface. Recall that in the absence of daylight, and with large areas of snow cover, the earth's surface is essentially constantly cooling north of the Arctic Circle.

Figure 3 illustrates the mean zonal (west to east) winds in July. The dominant feature is the core of roughly 24 m/s winds at 42 N and about 200 mb pressure altitude (about 11.5 km MSL). In the winter this jet stream core was about 7 or 8 degrees further south and the wind speeds were roughly twice as fast.

Figures 4 and 5 show the source-referenced sound speed profile along 80 W as a function of north latitude and pressure altitude for January and July, respectively. Note the substantial difference in the pattern of the profiles. During the winter there is a sound speed maximum at about 30 N and 600 mb height (at about 4 km MSL) that would produce through downward refraction a zone of enhanced sound pressure levels somewhere "downstream." On the other hand, there are almost no significant wintertime vertical gradients at the mid-latitudes, and at the northernmost latitudes the atmosphere is upward refracting at altitudes above 3 km.

Figure 6 shows the standard deviation of the sound speeds as a function of latitude and pressure altitude for January. Note that standard deviation of sound speed in the vicinity of the jet core is about 18 m/s or roughly 5 percent of the mean sound speed. This variation is essentially due to changes throughout the month in both the location and speed of the jet stream.

In order to illustrate the longitudinal variabilities in the mean sound speed profiles, we show in Figures 7 and 8, respectively, the mean sound speed profiles (again referenced to a hypothetical Nevada source) at eight different latitudes for 70 W and 110 W. In these examples the obvious differences are essentially the result of the influence of the wintertime, over-continent cooling of the air masses passing over North America. For the same longitudes in the summer (Figures 9 and 10) the differences are not nearly so large.

III. Concluding Remarks

For any serious analysis or forecast of long range infrasound propagation, data of the sort that we used to produce the illustrations shown in this paper must be combined (appropriately splined) with climatological data for the upper stratosphere, mesosphere, and lower thermosphere to produce the best possible set of latitudinally and longitudinally varying sound speed profiles referenced to a potential source of interest. This is not a trivial exercise for it is necessary to apply the data as precisely as possible to the location and magnitude of a possible source, and the profile set needs to be reevaluated on time scales corresponding to significant changes in the tropospheric weather conditions, almost certainly at hourly or shorter intervals.

Fortunately, there are a number of atmospheric analysis and forecast models that are available and capable of producing the state-of-the-art meteorological fields necessary as input to various sound propagation prediction codes. For global scales these include the CCM3 (NCAR),

SKYHIGH (GFDL-Princeton), and ECMWF and UGAMP (European Center) models. For finer, mesoscale, high spatial resolution analyses and forecasts some of the better known models in the meteorological community are the following: MM5 (Penn State/NCAR), ETA (National Meteorological Center), NOGAPS (Fleet Numerical Operations Center) and ARPS (Univ. of Oklahoma).

At infrasonic frequencies there are a number of meteorological phenomena, including gravity waves, clear air turbulence, and convective storms, which produce pressure fluctuations at precisely the sound frequencies of interest. What is noise to the acoustician is signal to the meteorologist, and vice-versa! In the computer codes used for large eddy simulation, part of the output includes information regarding pressure fluctuations as a function of time at every grid point. Unfortunately, to the authors' knowledge, this is not done in any of the above- referenced global or mesoscale models. Perhaps a study of the potentially available pressure fluctuation data should be conducted. It could be useful in defining preferred or worst case conditions for locating globally dispersed infrasonic sensors. Hopefully, we will be able to report on the results of such a study at the next symposium.

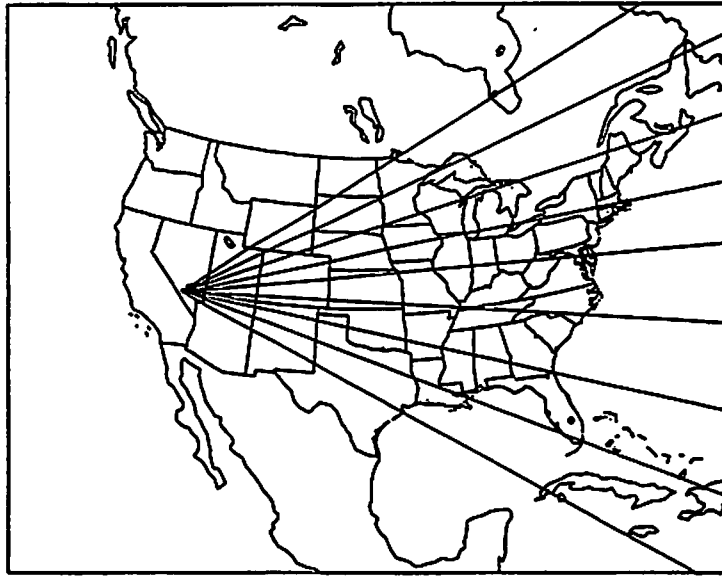


Figure 1. Radials extending from a hypothetical sound source in southern Nevada.

Mean Temperature (C) January 1996
Longitude: 80 W

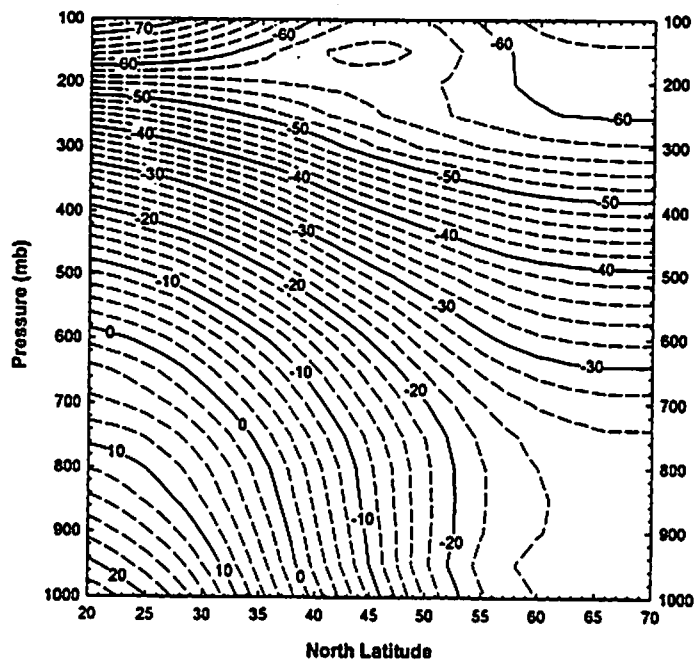


Figure 2. The mean temperatures as a function of latitude and pressure altitude along 80W longitude during January 1996.

Mean Zonal Wind (m/s) July 1996
Longitude: 80 W, Source: 36.75 N, 116.50 W

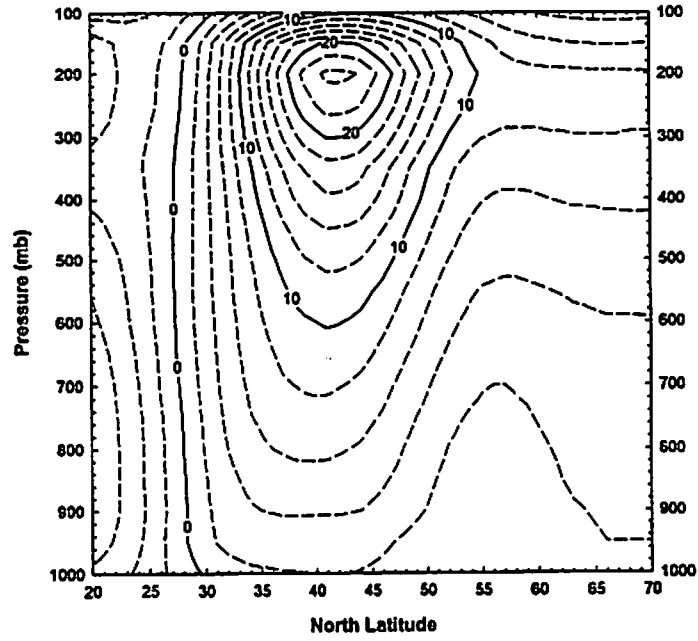


Figure 3. The mean zonal (west to east) winds in July 1996.

Mean Sound Velocity (m/s) January 1996
Longitude: 80 W, Source: 36.75 N, 116.50 W

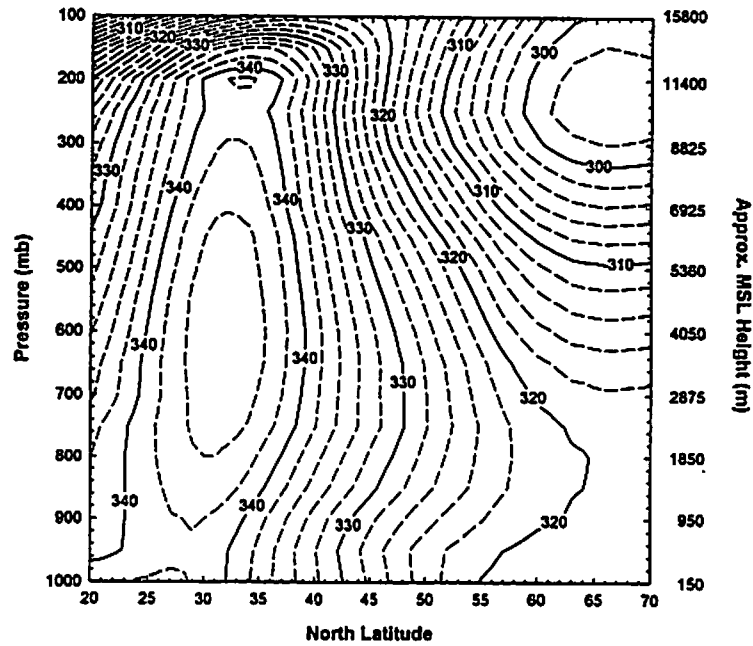


Figure 4. Source-referenced sound speed profile along 80W longitude as a function of north latitude and pressure altitude for January 1996.

Mean Sound Velocity (m/s) July 1996
Longitude: 80 W, Source: 36.75 N, 116.50 W

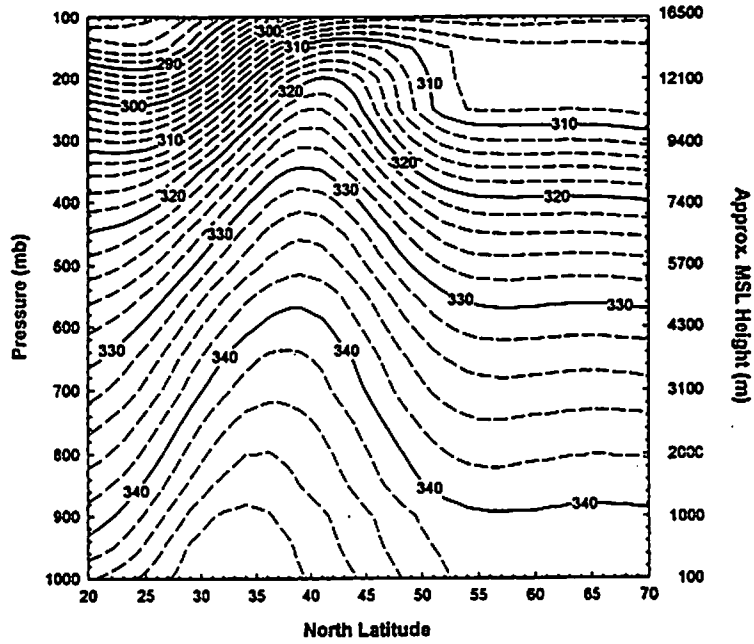


Figure 5. Source-referenced sound speed profile along 80W longitude as a function of north latitude and pressure altitude for July 1996.

Std Dev Sound Velocity (m/s) January 1996
Longitude: 80 W, Source: 36.75 N, 116.50 W

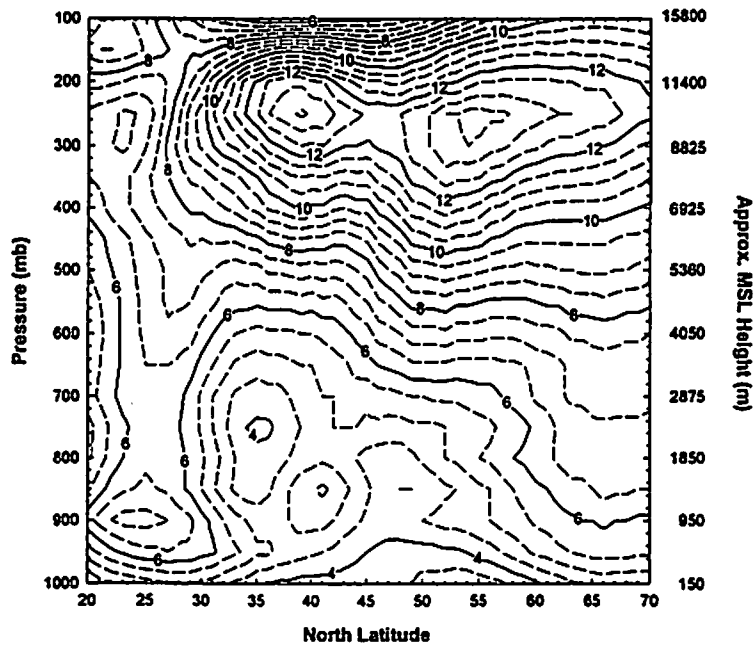


Figure 6. The standard deviation of the sound speeds as a function of latitude and pressure altitude for January 1996.

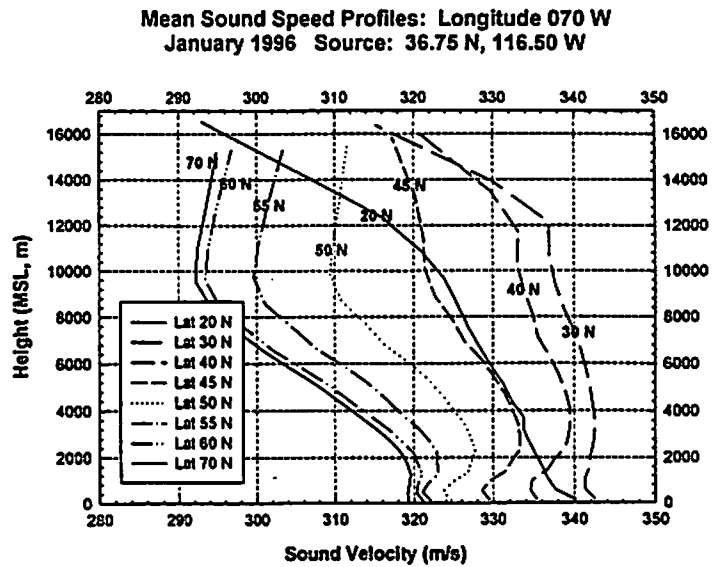


Figure 7. Variabilities in the mean sound speed profiles in January 1996 at eight different latitudes for 70W longitude.

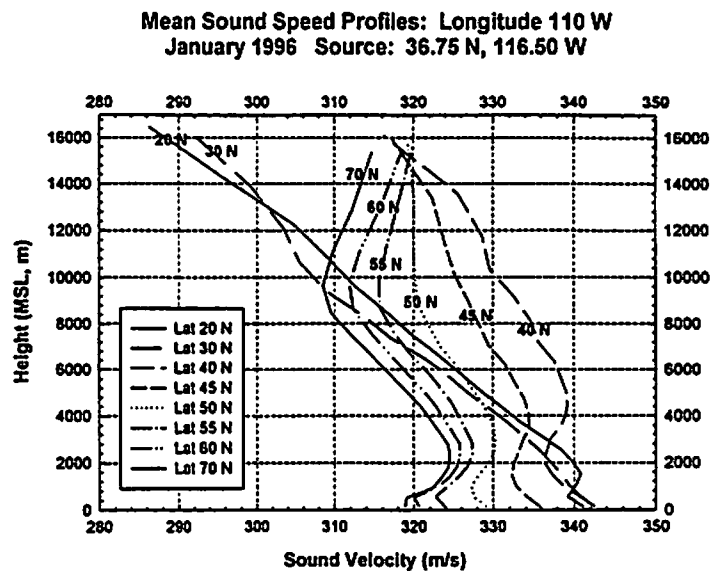


Figure 8. Variabilities in the mean sound speed profiles in January 1996 at eight different latitudes for 110W longitude.

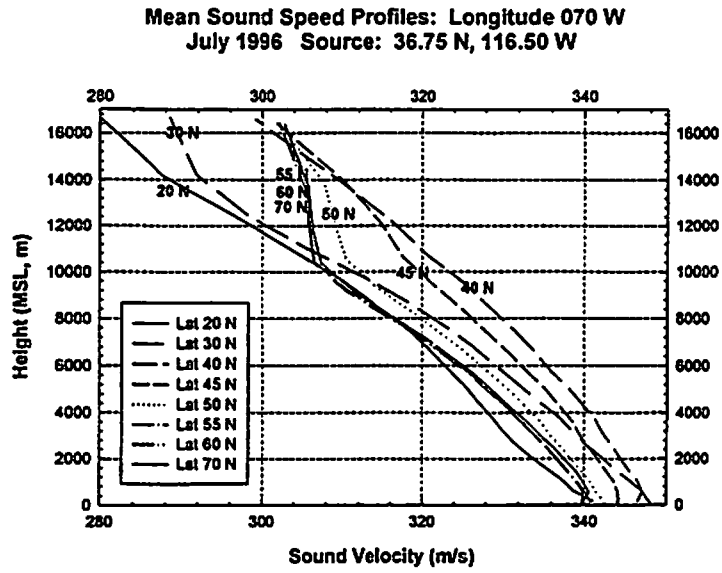


Figure 9. Variabilities in the mean sound speed profiles in July 1996 at eight different latitudes for 70W longitude.

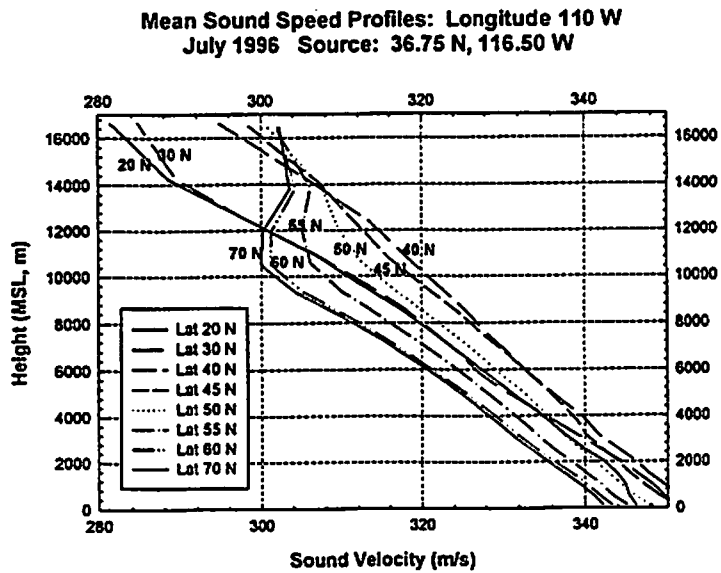


Figure 10. Variabilities in the mean sound speed profiles in July 1996 at eight different latitudes for 110W longitude.

... ..

Field Observations

... ..

... ..

... ..

Environmental Sensors for Long Range Sound Propagation Measurements

Karl Reichard¹, Jason Estep and David Swanson
The Applied Research Laboratory
The Pennsylvania State University
P.O. Box 30, State College, PA 16804

¹Voice: (814) 863-7681, FAX: (814) 863-9918, email: kmr5@psu.edu

Abstract

A remote, wireless, intelligent environmental and acoustic sensor node is described. Remote sensor nodes that incorporate environmental and acoustic sensors to provide both acoustic measurement capability and characterization of local meteorological conditions have been developed and tested. Remote environmental sensors permit measurement of temperature, temperature gradient, humidity, barometric pressure, wind speed and direction, and insolation (the ratio of incident to reflected solar radiation). The sensor nodes include automatic data logging and wireless communication capability. Wireless communications permit remote data collection and sensor networking. The design and performance characteristics of the sensors are discussed, and typical measurement results are presented. Local environmental data from the remote sensors is combined with upper level wind and temperature data from weather databases to predict the sound velocity profile for the observed environmental conditions and predict received sound pressure levels from a remote source.

Introduction

Complete characterization of long range sound propagation includes not only the measurement of acoustic source and receiver sound pressure levels, but also the environmental parameters affecting sound propagation. The availability of inexpensive, accurate, and reliable sensors, powerful microprocessors, and wireless communications technology greatly simplify the real-time measurement of remote acoustic and environmental data. The use of integrated environmental and acoustic sensor packages with wireless communications eliminates the need for long cables, improves the reliability of measurements, and can reduce staffing requirements for long range sound propagation measurement. A series of remote environmental and acoustic sensor nodes used in conjunction with a central sensor node at an acoustic source can simultaneously characterize sound propagation in multiple directions over a wide area.

The dependence of acoustic propagation on the weather is well known. This dependence is driven by two main components: the wind and temperature gradients. The wind and temperature profiles (variation with height above the surface) both affect the sound velocity profile (the speed of sound as a function of height above the surface). By combining measurements from surface environmental sensors with upper atmosphere

data, the temperature and wind profiles (and consequently the sound velocity profile) can be calculated. Fortunately the necessary upper level atmospheric wind and temperature data are available from weather forecast models over the Internet [1,2]. Such models are updated every few hours and are used to predict surface winds and temperatures as well as barometric pressure, humidity (dew/frost point), wind and temperature over elevations of interest for air traffic. The surface meteorological data gathered at each remote node includes temperature at two heights (e.g. 0.2m and 1.0m), wind speed and direction, humidity, barometric pressure, and solar flux.

Remote Sensor Node

The remote sensor node has three functional components: a collection of environmental and acoustic sensors, a data logger, and communications electronics. The environmental and acoustic sensors are mounted in or attached to the outside of a cylindrical tube as shown in Figure 1. The suite of environmental sensors includes 2 temperature sensors for measuring air temperature and the temperature gradient, 2 differential pressure sensors for measuring wind speed and direction, a humidity sensor, an absolute pressure sensor for measuring barometric pressure, and a pair of optical thermopile sensors for measuring insolation (the ratio of incident to reflected solar radiation).

The temperature sensors are attached to the outside of the main sensor tube. The lower temperature sensor measures the air temperature at a height of approximately 0.15-m above the ground, while the upper temperature sensor measures the air temperature at approximately 1 m above the ground. Figure 1 shows the two temperature sensors attached to the side and top of the main sensor tube.

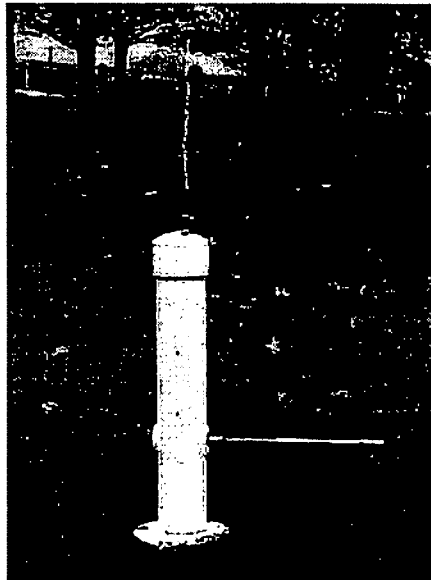


Figure 1. Remote sensor node sensor tube.

The humidity, barometric pressure and wind sensors are all housed inside the main sensor tube. The operation of the wind sensor is described in the next section of this paper. The optical thermopiles used to measure the incident and reflected solar radiation must be

mounted on the outside of the tube. A microphone can also be mounted on the outside of the tube for acoustic measurements.

The differential pressure sensors used to measure the wind speed and direction and the absolute pressure sensor used to measure the barometric pressure are all micro-machined silicon devices. The temperature sensors are also silicon devices. The humidity sensor is a capacitive device, which requires an external timer circuit to measure the humidity dependent capacitance. The optical thermopiles operate as photodiodes.

The remote sensor node uses a Tattletale model TT8 data logger to acquire, process, and log data from the node's environmental and acoustic sensors. The Tattletale model TT8 is manufactured by Onset Computers and includes a Motorola 68332 microprocessor, 1 MB of dynamic RAM, 8 channels of 12-bit analog to digital conversion, and 2 RS-232 serial data ports. An add-on module provides 15 MB of non-volatile compact flash memory. The Tattletale data logger and sensor interface electronics are mounted in a portable metal case. Figure 2 shows a photograph of the Tattletale. Additional sensors are mounted in the case with the data logger and sensor interface electronics to monitor temperature, humidity, and battery voltage.

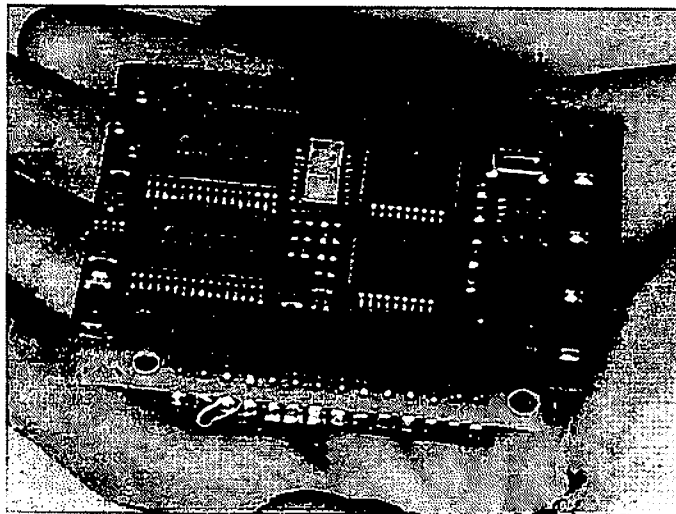


Figure 2. Tattletale data logger.

Data from the remote sensor nodes can be stored on the compact flash cards or transferred to a central monitoring location via wireless modems. The remote sensor node uses a FreeWave® wireless modems connected to data logger's serial port. At the central monitoring node, another wireless modem is connected to a laptop or desktop PC. The FreeWave wireless modems operate in the 902-928 MHz frequency band and use frequency-hopping spread spectrum technology to avoid interference. The modem's range can be extended to 20 mi. with the addition of a directional YAG antenna. Configuring an intermediate modem as a repeater can also extend the modem's range. Data transfer rates of up to 115.2 k baud have been achieved. Figure 3 shows a photograph of the FreeWave modem.



Figure 3. FreeWave wireless modem.

Wind Speed and Direction Measurement

The remote sensor node used 2 micro-machined differential pressure sensors mounted in the main sensor tube to measure wind speed and direction. Flow due to wind causes small pressure differences on opposite sides of cylinder [3,4]. The differential pressure sensors are mounted inside the tube and connected to ports on opposite sides of the tube as shown in the drawing in Figure 4.

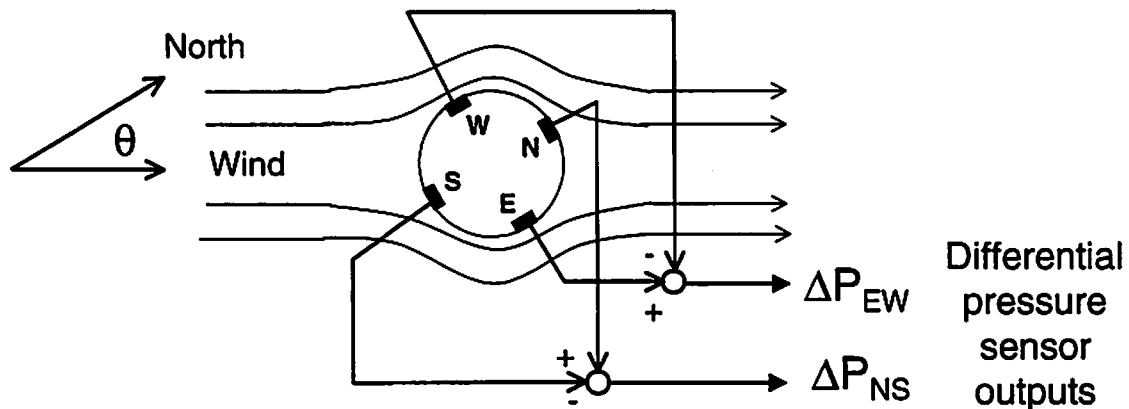


Figure 4. Differential pressure sensors mounted on opposite sides of cylindrical sensor tube.

The wind speed and direction are computed from the differential pressure measured across the North –South (NS) and East-West (EW) pressure ports in the cylinder walls. Given the measured differential pressures, the corresponding orthogonal components of the wind vector are

$$U_{NS} = \text{sgn}(\Delta P_{NS}) * \sqrt{2|\Delta P_{NS}| / \rho}$$

$$U_{EW} = \text{sgn}(\Delta P_{EW}) * \sqrt{2|\Delta P_{EW}| / \rho}$$

The overall wind speed and direction are given by

$$|\bar{U}| = \sqrt{U_{NS}^2 + U_{EW}^2}$$

$$\angle \bar{U} = \tan^{-1}(U_{EW} / U_{NS})$$

Figure 5 shows the results of wind tunnel tests of the remote sensor's wind speed and direction measurement capability. The plot shows that the wind speed calculation is more accurate at higher speeds and most sensitive to measurement errors at low flow speeds.

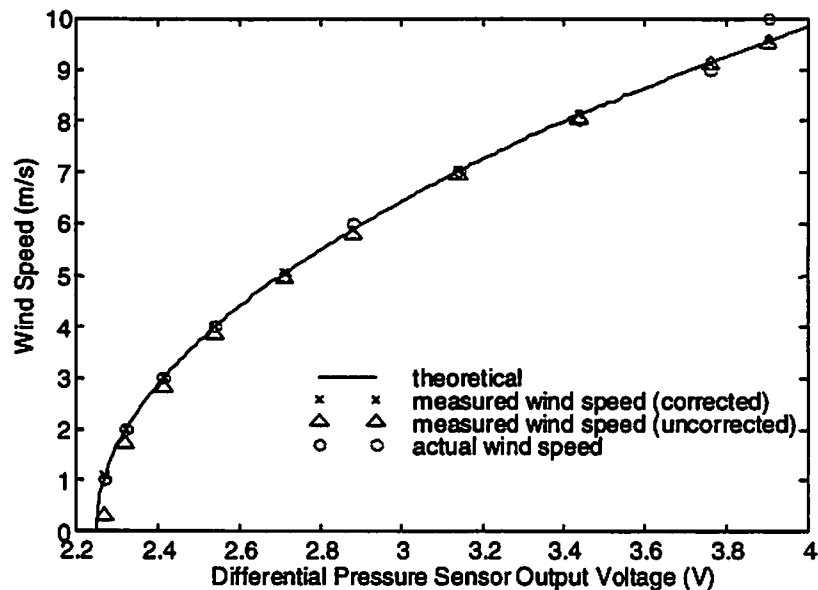


Figure 5. Wind tunnel test of remote sensor wind speed and direction measurement.

Reducing the diameter of the sensor tube significantly improves the accuracy of the sensor. The data in Figure 5 were taken with the differential sensors mounted in the walls of a 3-in diameter pipe. Figure 6 shows the results of wind tunnel tests of the wind sensor with the differential pressure sensors mounted in a 1-in diameter pipe. The upper plot shows wind direction measured using the differential pressure sensors on the y-axis versus the true wind bearing angle on the x-axis. The bearing data is for a 3 m/s flow in the wind tunnel. Only one data point shows any significant error. The lower plot in Figure 6 shows the computed and measured wind speed, and again shows good agreement.

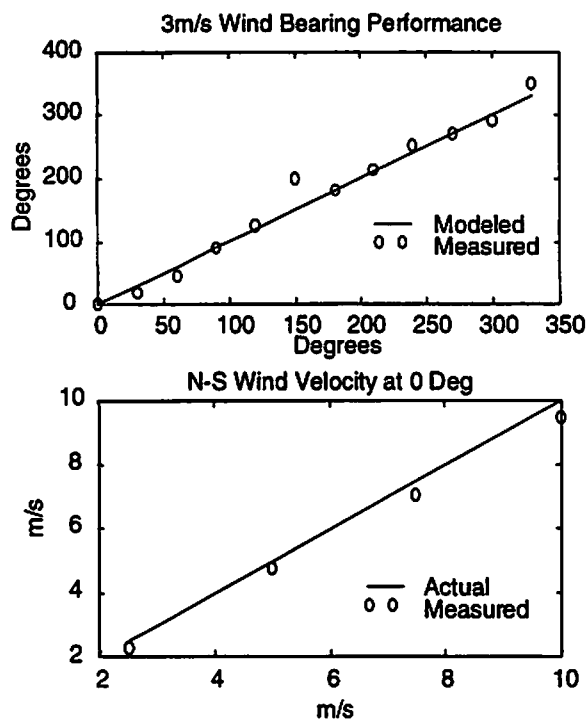


Figure 6. Wind sensor results for 1-in diameter tube.

Sound Propagation Prediction

The ultimate goal in building the remote sensor nodes is to improve the accuracy and reliability of long range sound propagation measurements and to acquire correlated measurements of environmental and acoustic data. Figure 7 shows an example of the type of data collected by the remote environmental and acoustic sensors. The upper plot in Figure 7 shows the temperature measured by the upper and lower temperature sensors over approximately 60 hours. The lower plot in Figure 7 shows the corresponding received sound pressure level for a 54 Hz tone, with the source approximately 450 m from the receiver. The data presented in Figure 7 verify the general relationship between the measured temperature gradient and sound propagation – sound travels farther (less attenuation) when the temperature gradient is positive and is attenuated less when the temperature gradient is negative (warmer air near the ground). When the temperature gradient is positive the air near the ground is cooler than the air aloft and the sound refracts downward, increasing the received sound pressure level. Downward refracting conditions typically occur in the early evening. A negative temperature gradient corresponds to the case where the air is warmer near the ground and cooler aloft, and the sound refracts upward. This condition typically occurs during a hot afternoon due to solar heating of the ground.

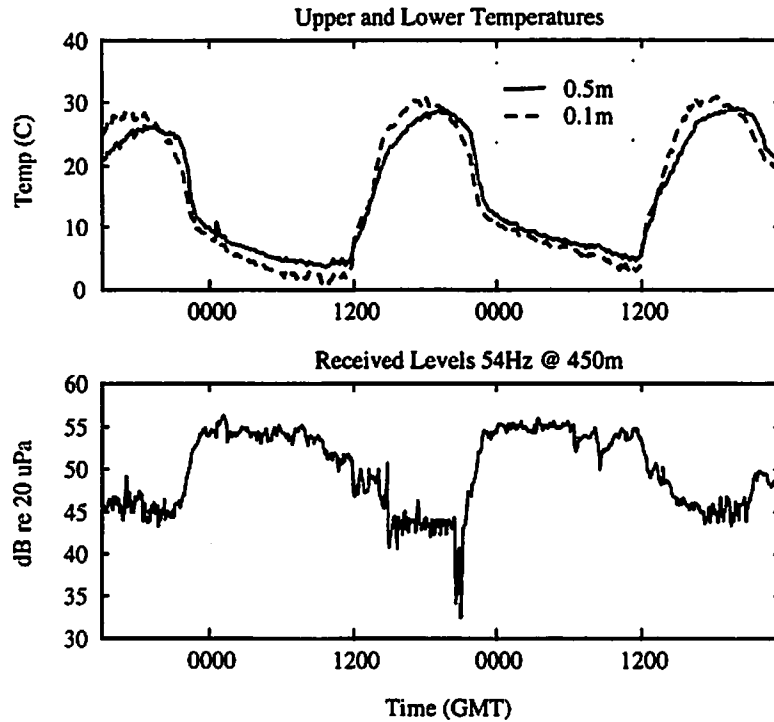


Figure 7. Measured temperature and acoustic data.

In addition to obtaining correlated long-term measurements of the environmental and acoustic data we also want to develop and verify models for predicting the sound velocity profile from measurements of the local meteorological conditions and upper atmosphere data available over the Internet. Figure 8 and Figure 9 show comparisons of modeled and measured temperature and wind velocity profiles. The modeled temperature and wind speed profiles are computed based on temperature and wind data measured at the remote sensor node and upper atmosphere temperature and wind data. Figure 8 shows that the modeled temperature profile agrees very well with temperature data measured using a RASS. Figure 9 shows that the modeled and measured (using a SODAR) wind speed profiles have the same overall shape but differ by a constant of approximately 3 m/s over the first 200 m height.

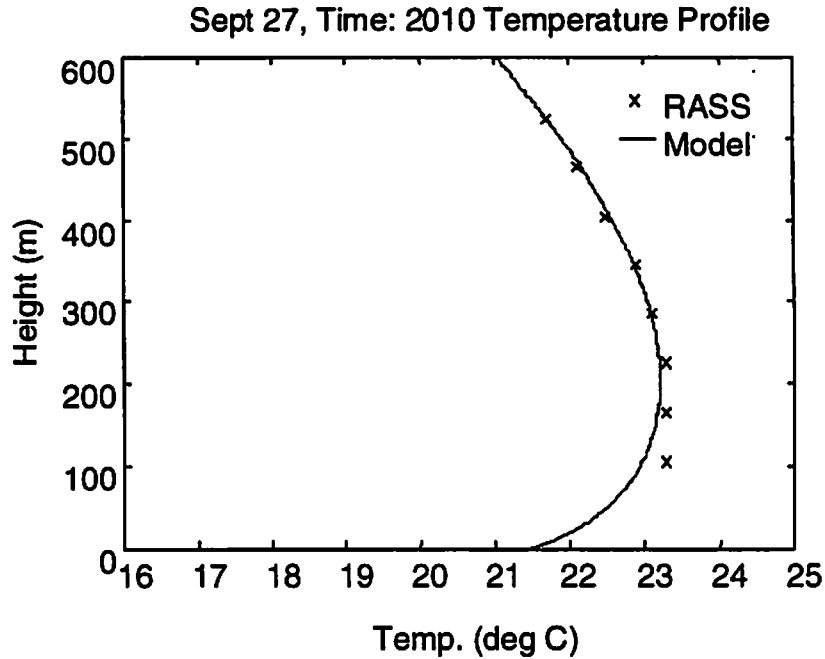


Figure 8. Modeled and measured temperature profiles.

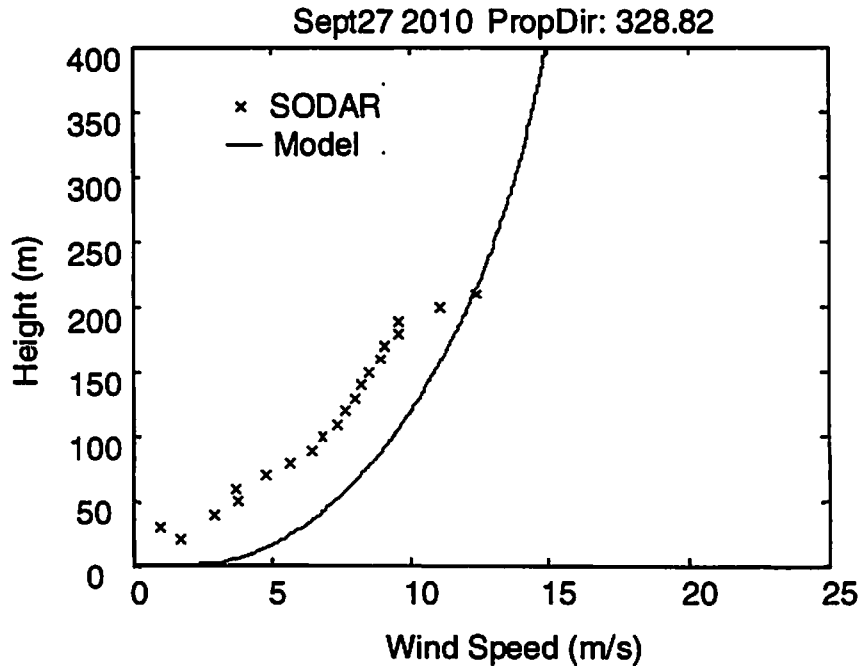


Figure 9. Modeled and measured wind speed profiles.

The modeled temperature and wind speed profiles are used to compute the corresponding sound velocity profile [2]. The sound velocity profile is then used in the Green's function PE to generate propagation loss tables for the measured meteorological conditions [5]. Finally, the propagation loss tables are used to predict received sound pressure levels for

continuous sources at specified frequencies and ranges. Figure 10 shows measured and predicted receiver sound pressure levels. The predicted sound pressure levels are based on data measured at a remote sensor node in downward refracting (nighttime) conditions. The measured levels were acquired using a microphone attached to the remote node. Figure 10 shows very good agreement between the predicted and measured sound pressure levels at 4 out of 5 source tone frequencies, with less than a 10 dB difference at the 5th frequency.

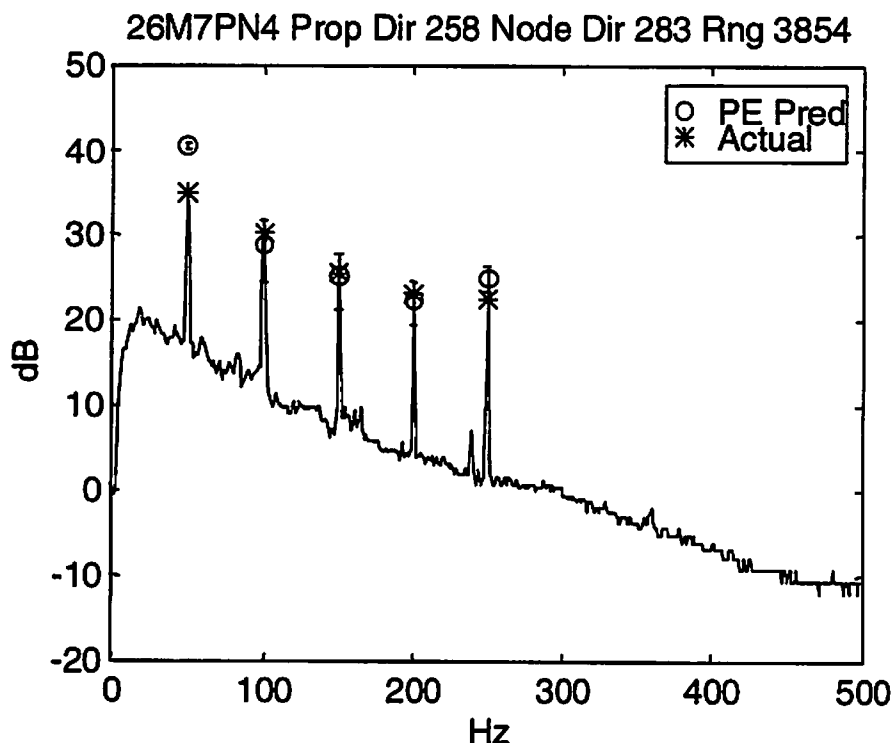


Figure 10. Measured and predicted receiver sound pressure levels.

Conclusions

A system of remote, wireless, intelligent environmental and acoustic sensor nodes designed for long range sound propagation measurements was described. Each remote sensing node includes environmental and acoustic sensors to facilitate characterization of the received acoustic signals and the local meteorological conditions affecting sound propagation. The suite of environmental sensors includes two temperature sensors for measuring the temperature gradient near the ground, two micro-machined differential pressure gauges to sense wind speed and direction, optical thermopile sensors to measure solar flux, a capacitive humidity sensor, and a micro-machined pressure sensor for measuring barometric pressure. The measured surface temperature gradient and wind speed and direction are combined with upper elevation wind and temperature data from aviation weather allow a sound velocity profile (SVP) to be modeled. The SVP is used in

a parabolic equation sound propagation model to predict sound attenuation vs frequency and range for the environment.

Experimental data were presented to demonstrate the measurement of wind speed and direction from pairs of differential pressure sensors located on opposite sides of a cylinder placed in the flow. Additional experimental data demonstrated the correlation between diurnal variations in the temperature gradient measured by the sensor node and variations in received sound levels. The computation of sound velocity profiles from sensor node and upper elevation meteorological data was described and an example was presented that demonstrated the agreement between predicted and measured sound pressure levels.

References

1. D. Swanson, and K. Reichard, "Environmental Sensors and Algorithms for Ground-Based Passive Acoustic Sensors," presented at the 12th SPIE Annual International Symposium on Aerospace/ Defense Sensing, Simulation and Controls, Orlando, FL, 13-17 April, 1998.
2. D. Swanson, K. Reichard, K. McClintic, and D. Norris, "Atmospheric boundary layer sound velocity profile model for wind and temperature." Presented at the 133rd meeting of the Acoustical Society of America, 15-20 June, 1997
3. F. W. Hagen and R. V. DeLeo, "Solid State Orthogonal Anemometer," Rosemont Inc., Eden Prairie, MN.
4. "Measuring Wind, Ice, and Fog in the Home of the World's Worst Weather", Sensors Magazine, January 1995.
5. Kenneth E. Gilbert and Xiao Di, "A fast Green's function method for one-way sound propagation in the atmosphere", Journal of the Acoustical Society of America, 94(4), pp. 2343-2352, 1992.

The Influence of Wind Noise on the Performance of Helicopter Detection and Classification Algorithms.

A.C. van Koersel

TNO Physics and Electronics Laboratory,
PO box 96864, 2509 JG The Hague, The Netherlands,
Tel. +31703740357, Fax +31703740651, email vanKoersel@fel.tno.nl.

Abstract

This paper describes the method and the results of the investigation into the performance of two acoustic helicopter detection and classification algorithms, for a range of meteorological conditions. A measurement station was developed to automatically record wind and environmental noise for different meteorological conditions. Meteorological parameters were measured simultaneously. Sound speed profiles were estimated from the measured meteorological data. Simulated data of a helicopter was used as a source signal. The Fast Field Program (FFP) was used to calculate the acoustic attenuation for a chosen range of frequencies and source receiver distances. The received signal was calculated at 4 ranges, using the acoustic attenuation and the recorded noise files, and was subsequently submitted to both classification algorithms. Both algorithms performed well, up to and including a downwind force 5, and up to and including upwind force 3.

1. Introduction

In the project "Acoustic Helicopter Classification" a number of algorithms to detect and classify helicopters were developed at TNO-FEL. The possibility of detecting and classifying helicopters using their acoustic signature, raised interest in the performance of the algorithms in realistic outdoor conditions. To estimate the effect of different meteorological conditions (wind speed, turbulence) information about the acoustic propagation and the properties of the noise caused by wind and turbulence was needed.

This paper describes the theoretical approach, the data collection procedure, the measurement station, the calculation of the propagation effects, and the effect on the classification performance. The algorithms used for detection and classification were presented at the 6th symposium on LRSP [1]. Only two algorithms were chosen for further analysis (template matching and harmonic series), since they can easily be adapted to classify additional types of helicopters.

2. Theory

The problem stated in the introduction is to estimate the influence of meteorological conditions, environmental noise, and acoustic propagation on the performance of helicopter detection and

classification algorithms. We assume that such an algorithm operates on the output from a single acoustic sensor. We regard the received signal at the sensor position as the convolution of the source (helicopter) signal and the impulse response of the atmosphere, with noise added:

$$r(t) = s(t) * h(t) + n(t) \quad (2.1)$$

r = received signal at microphone
 s = source signal
 h = impulse response of the atmosphere
 n = received noise at microphone

Or, if the calculation is performed in the frequency domain:

$$R(f) = S(f)H(f) + N(f) \quad (2.2)$$

This procedure has the benefit that it speeds up the calculations significantly, since the convolution of $s(t)$ and $h(t)$ is replaced by a Fourier transform and subsequent multiplication of $S(f)$ and $H(f)$. As source signal we decided to use simulated helicopter data, since there are no measurements available to us recorded under free space conditions. The helicopter noise simulation procedure uses the lift and drag forces on the rotor blade calculated with a helicopter preliminary design program by de Vreeze [2]. The simulation procedure is described in van Koersel [3].

2.1 Wind Noise and Turbulence

Wind noise on a microphone is essentially fluctuation of the air pressure caused by the movement of the medium. Morgan and Raspert [4] have shown that for outdoor measurements sound pressure variations are mainly caused by the turbulence of the airflow passing over the microphone. For low frequencies a microphone acts as a point receiver, and responds to the dominating turbulent flow rather than the interaction between the flow and the microphone itself. The rms pressure fluctuation can be approximated by:

$$p = \rho UV \quad (2.3)$$

ρ = medium density [kg/m^3]

U = turbulence [m/s]

V = average velocity [m/s]

Formula 2.3 shows that the average wind velocity V and the turbulence U are the main parameters that determine the magnitude of the wind noise p . V is the average of the wind speed v . U is the rms value of u , which is the deviation of v from its average value v . (U is equivalent to the standard deviation of the wind speed). We have set up classes for V and U , and record noise samples $N(t)$ measured with a set of microphones for these classes. The class limits for the average wind speed are the well-known Beaufort scale limits, the turbulence class limits were chosen after trial measurements. Both are shown in table 2.1. In our case v is measured at 3.4 s intervals and V is the average over 10 minutes. U is calculated every 10 minutes from the stored values of v and V . How and where the measurements were performed and the number of noise samples collected is described in chapter 3.

Table 2.1: Wind speed and turbulence classes set up to record noise data.

Class Number	Wind speed [m/s]	Turbulence [m/s]
0	<.3	< 0.42
1	0.3- 1.6	0.42-0.83
2	1.6- 3.4	0.83-1.25
3	3.4- 5.5	1.25-1.67
4	5.5- 8.0	1.67-2.08
5	8.0-10.8	2.08-2.50
6	10.8-13.9	2.50-2.92
7	13.9-17.2	2.92-3.33
8	17.2-20.8	3.33-3.75
9	20.8-24.5	> 3.75
10	24.5-28.5	
11	> 28.5	

2.2 Propagation Influence

The noise generated by a source outdoors is attenuated by propagation through the atmosphere. To calculate the attenuation of the source signal a sound propagation model is used, which is described in detail by Raspert et al [5]. The acoustic propagation problem is formulated in terms of a Green's function integral, and is solved using the Fast Field Program Technique. The program uses a layered model of the atmosphere, bounded by a ground surface. The properties of the medium are assumed constant along the distance of propagation. The FFP program was made available to us by the U.S. Department of Army, Construction Engineering Research Laboratory (CERL), Corps of Engineers, Champaign, IL, USA. Usually the model is applied to calculate the sound pressure or the attenuation as a function of the distance for a specific frequency. For our purpose however we are interested in the attenuation as a function of the frequency at a specific distance. Therefore a "shell" was written around the FFP, to perform a number of calculations (for a chosen range of frequencies) and produce a table of the attenuation as a function of frequency $H(f)$ for 4 chosen ranges.

Parameters that determine the accuracy of the FFP calculation are the extra loss ($<7.5/\text{range}$), the atmospheric absorption, the number of FFT panels, and the FFT length in relation to the maximum range and the frequency. The adapted program was tested for a specific case. This case was used in an earlier report [6] to compare the results of a ray tracing program (Rayflux) to results from another ray tracing program by Vermaas [7], and a wave field extrapolation model by Nijs and Wapenaar [8]. The FFP results show excellent agreement with the results of all models for the used test case.

2.3 Atmospheric Profiles

For the calculation of the propagation attenuation with FFP, accurate information of the speed of sound as a function of height $c(z)$ is essential. The speed of sound is determined by the air density and the component of the wind speed in the direction of propagation. In our case direct measurement of the speed of sound was not practical, since acoustic data was collected for different meteorological conditions during an entire year. Measurement of the temperature and wind speed at different heights was not possible for the same reason. This problem was solved using a model developed by Monin-

Obukhov (Huisman et al [9], Salomons et al [10] and Huisman [11]) that describes the wind speed and temperature as a function of height with different functions for either a stable, unstable or neutral atmosphere. The parameters that are used in the Monin-Obukhov model are estimated using the values of wind speed, temperature and surface roughness that are measured during data collection:

- wind speed at 2 m height
- wind speed at 10 m height
- temperature at 2 m height
- relative humidity
- atmospheric pressure
- surface roughness of the measurement site

The wind speed at 10 m height is obtained from the KNMI, who operate a meteorological station close to our site (distance approximately 5 m). The Monin-Obukhov model and the estimated parameters are used to calculate the profile of wind speed $v(z)$ and temperature $T(z)$ as a function of height. From these profiles a sound speed profile $c(z)$ is calculated using formula 2.4. This sound speed profile $c(z)$ is used as input for FFP.

$$c(z) = v(z) + 335.1 \sqrt{1 + \frac{T(z)}{273.15}} \quad (2.4)$$

c = sound speed [m / s]
 v = wind speed [m / s]
 T = temperature [° C]

For all collected data files belonging to a class of wind speed and turbulence the meteorological data is averaged, and sound speed profiles are estimated using a procedure that takes z_0 , $u(2)$, $u(10)$ and $t(2)$ as input, and produces the parameters that are needed to calculate the profiles. The profiles (45 downwind cases and 45 upwind cases) are calculated and written into a file formatted to be read by the FFP input processing program. A sample profile calculated for wind speed class 6 and turbulence class 6 (neutral atmosphere) is shown in figure 2.2.

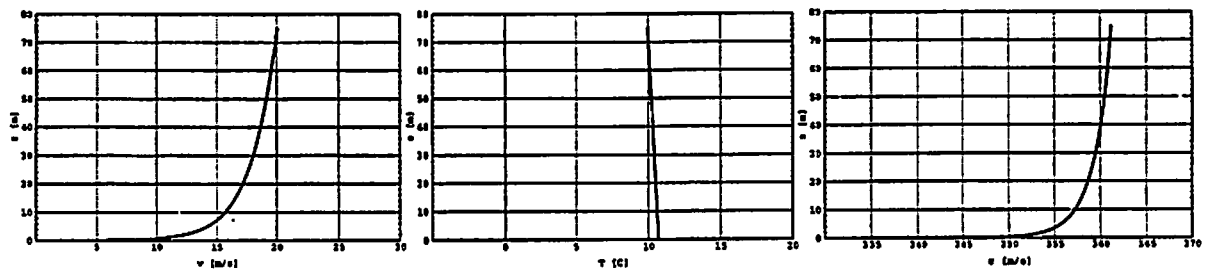


Figure 2.2 Wind speed and temperature profile as a function of height, and resulting sound speed profile for wind class 6 and turbulence class 6.

3. Data Collection

The measurement station was manufactured in-house for this project. The objective of the station was to record acoustic windnoise automatically for different classes of wind speed and turbulence. The data collection hardware consisted of:

- 486/66N PC with 200 Mb hard disk
- TransEra model 410 data acquisition board with 16 single or 8 differential input channels, a 13 bit A/D converter and programmable gain
- a Sensor SM6B vertical geophone, a Bruel & Kjaer 1/2 inch pre-polarised condenser microphone (type 4129) and a TNO-weatherproof condenser microphone
- geophone and microphone amplifier (2) with manual gain adjustment
- 8 order Butterworth anti-aliasing filters
- a “watchdog” that switched off power to the PC after 8 restarts
- a Rheinhardt CWS7 meteo station that measured relative humidity, temperature, solar radiation, wind direction, atmospheric pressure, wind speed, and precipitation

The hardware was built into a steel housing, and a mast (2 m height) was constructed for the meteo station. For prolonged use outdoors the B&K microphone was built into a PVC container with an “umbrella” on top. An in-house developed condenser microphone for outdoor use was placed next to the B&K for comparison. A picture of the steel housing with the PC and signal conditioning hardware is shown in figure 3.1.

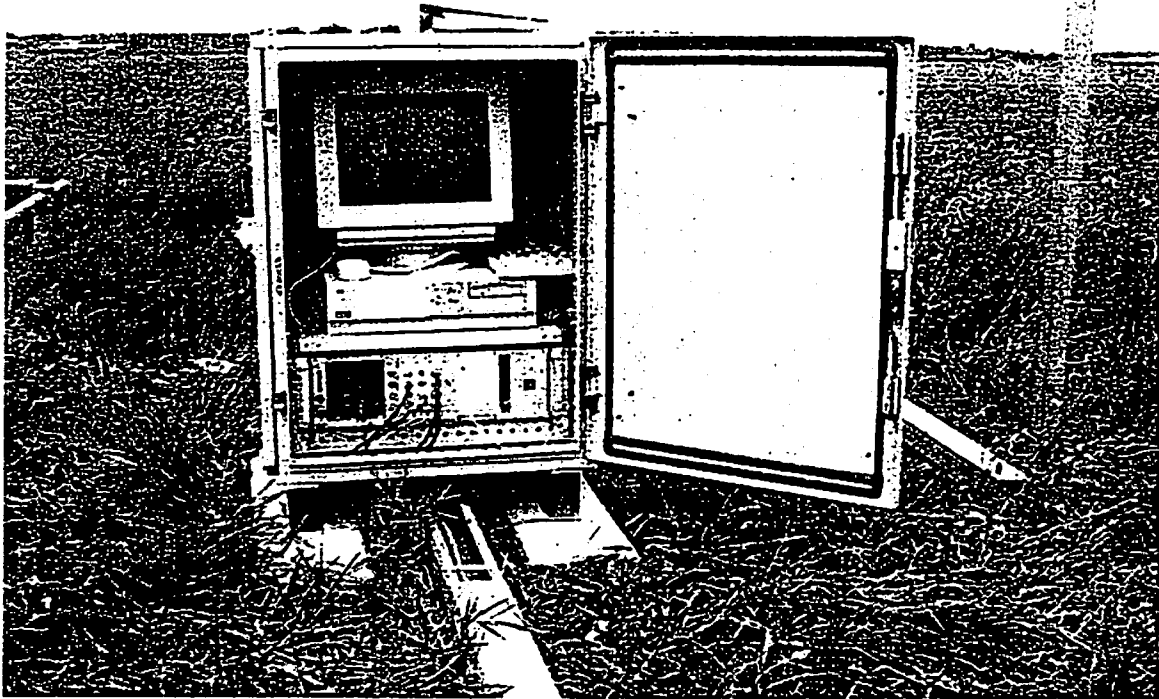


Figure 3.1: The measurement hardware (PC, filters and amplifier) in the steel housing.

The entire set-up (sensors, PC, and meteo station) was placed at the Naval airfield at Valkenburg (MVKV) in the Netherlands, from May 29 1996 up to June 1 1997.

Meteo data for the same period (wind speed and wind direction at 10 m, temperature at 1.5 m and precipitation) was acquired from the nearby KNMI measurement station.

To control the data-acquisition a HT basic program was been written. The program read data from the meteo station, and processed the data into 10 minute averages of wind speed, wind direction, turbulence, temperature and precipitation. From the averages the program determined the meteo class (wind 0-11, turbulence 0-9, rain 0-9) and the hour of the day (0-23). Every 32 seconds two arrays with

acoustic- and one with seismic data were read from the data acquisition board. The data was stored on disk and in a 3D matrix a flag was set for the combination of wind class 01, turbulence class 1, and hour class 23. If the same combination (in this example 01123) occurs again, the data is discarded. The storage matrix is manually reset every month, during inspection of the station. The number of files stored during the year for each wind speed and turbulence class is shown as a distribution of wind speed and turbulence classes, in table 3.1.

Table 3.1: The distribution of the recorded files over the chosen wind speed (W0-W8) and turbulence (T0-T8) categories, during the measurement period from June 1996 to July 1997.

	W0	W1	W2	W3	W4	W5	W6	W7	W8
T0	276	329	291	13	1	0	0	0	0
T1	13	239	364	375	195	4	0	0	0
T2	1	46	152	361	406	126	0	0	0
T3	0	11	40	92	271	230	43	0	0
T4	0	0	7	17	43	113	69	8	0
T5	0	0	1	5	4	21	39	7	0
T6	0	0	0	1	2	4	8	7	1
T7	0	0	0	0	0	0	1	2	1
T8	0	0	0	0	0	0	0	0	1

Note that the number of files stored for each class is a rough indication of the probability of occurrence of the classes during the year. For the frequency of occurrence of the wind speed and turbulence classes, the collected meteo data has been analysed. The result of this analysis is presented in chapter 5.

4. Propagation calculation

The FFP is used to calculate propagation attenuation from source to receiver, for a chosen geometry and a sound speed profile corresponding to the measured classes (see paragraph 2.4). For all classes an upwind case (wind vector pointing from receiver to source) and a downwind case (wind vector pointing from source to receiver) was chosen. As mentioned earlier we used averaged meteorological parameters as input for the calculation of the sound speed profile. The reason for using average parameters is that for each class a different, and sometimes a large number of noise files was recorded (see table 3.1). It was not feasible to calculate a sound speed profile and the corresponding propagation attenuation for all recorded noise files separately. Calculating propagation attenuation for the up- or downwind case for 45 recorded classes already takes approximately 36 hours of batch processing on a DEC 3000 Model 800 AXP¹. Doing the same for all (4240) stored noise files would take approximately half a year of processing time on our machine.

Typical FFP output for a sound speed profile $c(z)$ calculated for meteorological conditions corresponding to wind speed class 4 and turbulence class 3, for receiver distances of 90, 1000, 2000, and 4000 m is shown in figure 4.1.

¹ Specifications of the processor are approximately: Clock speed 200 MHz, specfp92 187.2, specfp95 4.64.

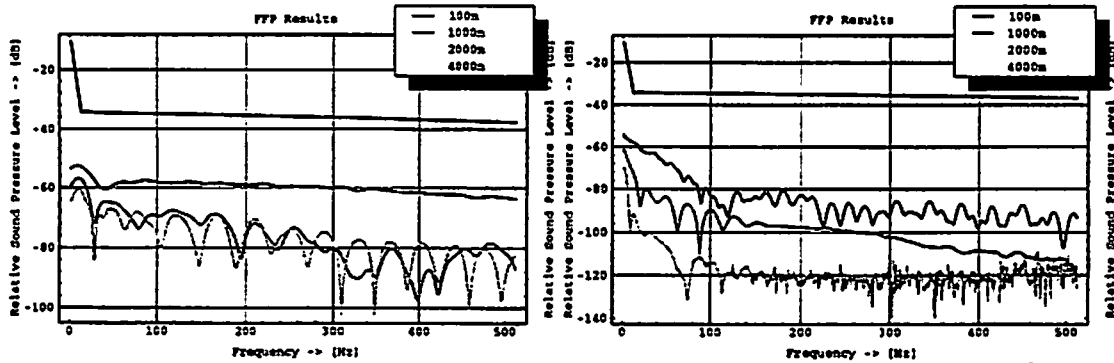


Figure 4.1 FFP output for a sound speed profile $c(z)$ belonging to wind class 4 and turbulence class 3 (left downwind case, right upwind case).

Source height is 5 m, receiver height is 0.1 m, ground impedance is modelled using the Delany and Bazley model, with effective flow resistivity $\sigma = 2.5 \cdot 10^5$ mks Rayls (which is typical for grass-covered soil).

Note that the FFP propagation model used for this project does not include the effect of turbulence and variation of the meteorological parameters in the atmosphere on the acoustic attenuation. The attenuation is calculated using $c(z)$, the geometry, and the surface as the most important parameters. Models that include turbulence are being developed however, see for example [12] and [13].

5. Results

As mentioned in paragraph 2.1 we use simulated helicopter data as input for the performance calculations. Figure 5.1 shows the sound pressure level as a function of frequency of the simulated helicopter signal. The sound pressure level is calculated at 90 m from the source (head on), and normalised to a source level at 1 m distance from the source with a reference value of $20 \mu\text{Pa}$.

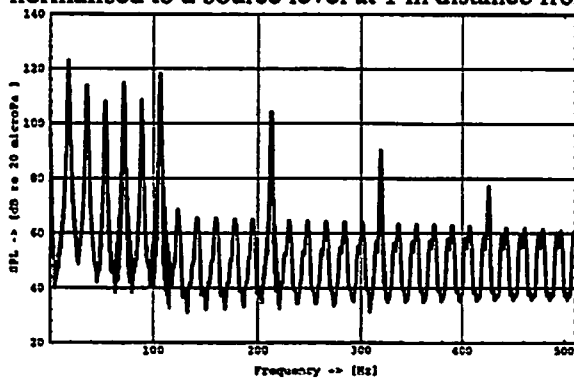


Figure 5.1 The simulated helicopter spectrum used as input for the performance estimation, normalised to source level at 1 m from the source with a reference value of $20 \mu\text{Pa}$.

In this procedure the assumption is made that the helicopter acts as a point source. In real situations this is far from true. For our application where we are interested in the helicopter noise level at 1 km or more from the source, the assumption is regarded as valid.

To show the signal degradation caused by propagation and the addition of wind noise, we show the same helicopter spectrum as in figure 5.1, but now as if received downwind from the source at 1000

m, with wind noise recorded for wind speed class 7 and turbulence class 7 added (figure 5.2 left). The propagation attenuation has been calculated with FFP, using a sound speed profile estimated for the corresponding meteorological class, as described in paragraph 2.4. Figure 5.2 (left) shows one of the more extreme cases of signal degradation. To present another example, we show the same helicopter spectrum as in 5.1, also propagated 1000 m downwind, but with wind noise recorded for wind speed class 1 and turbulence class 3 added.

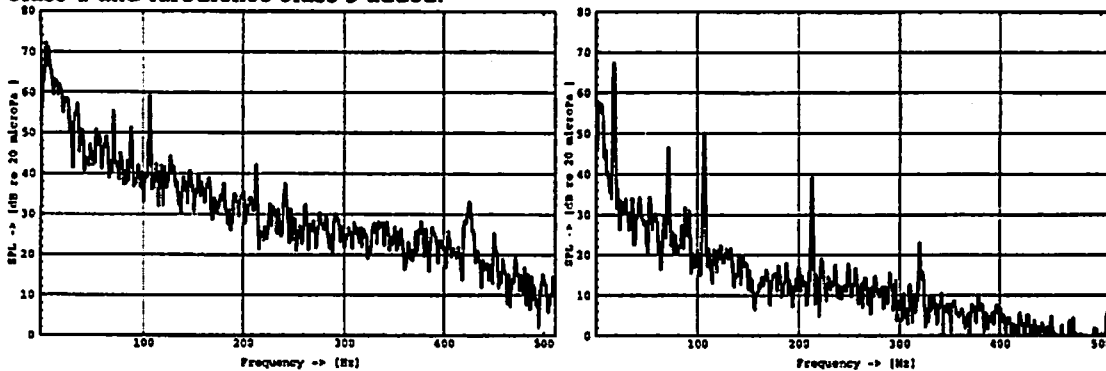


Figure 5.2 The simulated helicopter spectrum, as seen at the receiver position at 1000 m from the source (downwind), with wind noise of class 7 and turbulence class 7 added (left), and with wind noise of class 1 and turbulence class 3 added (right).

5.1 Classification Results

The analysis of the performance of the classifiers was performed for all classes measured, as mentioned in paragraph 4. The propagation filter (up and downwind for 1, 2 and 4 km range) was applied to the helicopter spectrum using formula 2.2. All noise files were added for the measured classes using the same formula, resulting in tables with classifier performance for different range, and wind speed and turbulence combinations. To obtain clearer insight into the classifier performance as a function of the wind speed, the classification results were averaged over the turbulence classes for each wind speed class. The results of the template matching algorithm and the harmonic series algorithm at source receiver distance of 1000 m are shown in figure 5.3 and 5.4 respectively. The results at other ranges are not shown in this paper.

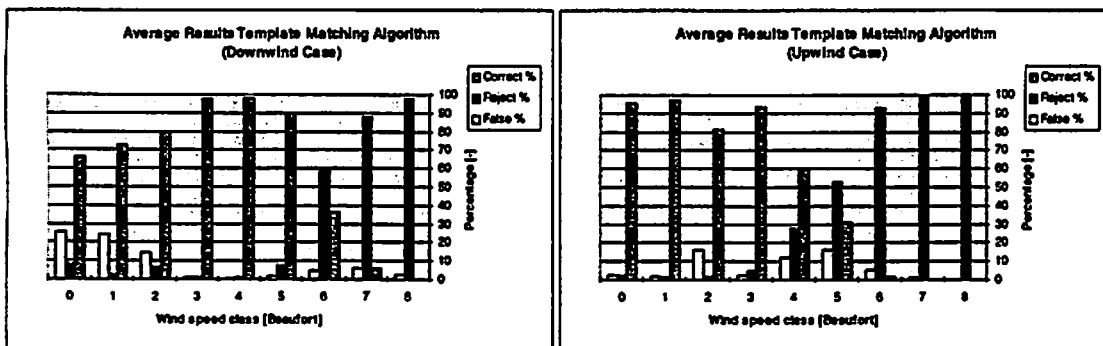


Figure 5.3 Average results of the Template Matching Algorithm (left downwind case, right upwind case), at source receiver distance 1000m.

Figure 5.3 (left) shows an unexpected decrease in performance at low wind speed. Detailed analysis of the classification results shows that this is caused by a large sharp dip in the calculated acoustic attenuation, near the frequency of the main rotor of the helicopter. This dip which occurs in some cases only, and causes a biased main rotor frequency estimation, which leads to false classifications. The magnitude and frequency of this attenuation dip depends on the chosen geometry, the chosen ground absorption model, and its parameter values. Such sharp dips in the acoustic propagation however are not likely to be observed during measurements, at least not as large and steady in level and frequency for a longer period of time. One of the reasons is that atmospheric turbulence causes variation in the propagation conditions. This effect however is not included in the FFP model, as mentioned in chapter 4. Therefore the low performance as seen in figure 5.3 at low wind speed classes should be interpreted as resulting from the calculation method, rather than as a realistic drop of the performance under these conditions. We can also observe that the classifier performance drops above wind speed 5, with a low false classification percentage at higher wind speeds. In figure 5.3 (right) we observe a slightly lower performance at wind speed class 2 (explained earlier). The performance decreases above wind speed 3, with a low false classification percentage at higher wind speeds. Only in the intermediate range (wind speed class 4-6) the number of false classifications increases.

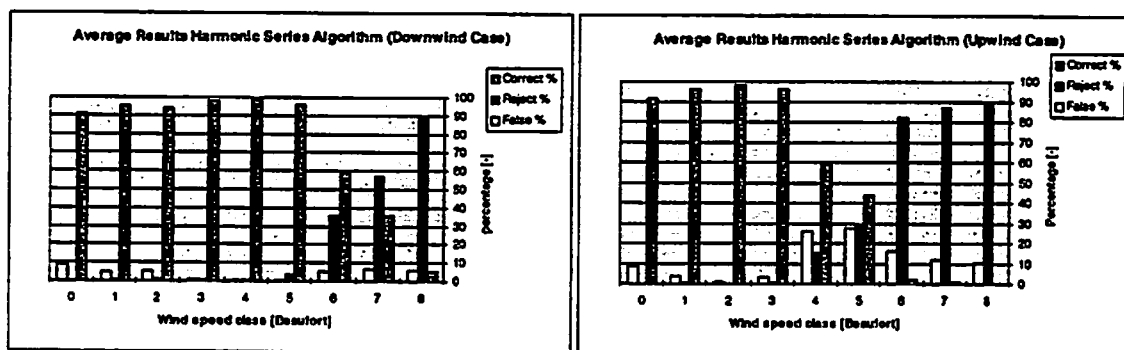


Figure 5.4 Average results of the Harmonic Series Algorithm (left: downwind case, right: upwind case), source receiver distance 1000m.

From figure 5.4 we observe that for the harmonic series algorithm the performance starts to decrease above wind speed 5, in the downwind case, with a low number of false classifications. The overall performance is slightly higher than the performance of the template matching algorithm. From figure 5.4 we also observe that for the upwind case the performance decreases above wind speed class 3, with a slightly higher number of false classifications than the template matching algorithm. Important for the interpretation of the results is the probability of occurrence of the wind and turbulence classes during the year of measurement. For instance the probability of occurrence of wind speed class 7 is lower than the probability of occurrence of wind class 4. To obtain an indication of the probability of occurrence of the wind speed classes, the relative occurrence of the wind speed classes during the year of measurement is determined from the measured meteorological data at MVKV. The result is shown in figure 5.5. Note that this relative wind speed occurrence is site specific. Data on the distribution of wind speeds over a longer period of time on different sites in the Netherlands can be found in [14] and [15]. For example, during the period 1971-1990 the occurrence of wind speeds larger and equal to 5 Beaufort at de Kooy was 30,3 %, and at Soesterberg it was only 4,15 %.

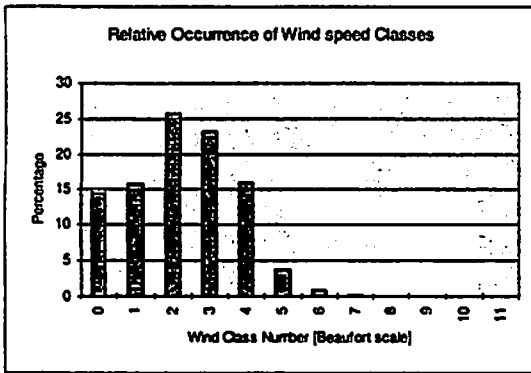


Figure 5.4 Relative occurrence of wind speed classes during the year of measurement, at MVKV as a function of the class number which corresponds with the Beaufort scale.

5.2 Wind noise spectra

To obtain an indication of the shape of the wind noise spectrum, some recorded data files were analysed in more detail. From the recorded signal, 32 spectra (0-512 Hz) were calculated and averaged. The result of this analysis is shown for three wind speed classes (wind speed class 0, 4 and 8). For each of these 3 wind speed classes 3 files with increasing turbulence were analysed. The result is shown in figure 5.5.

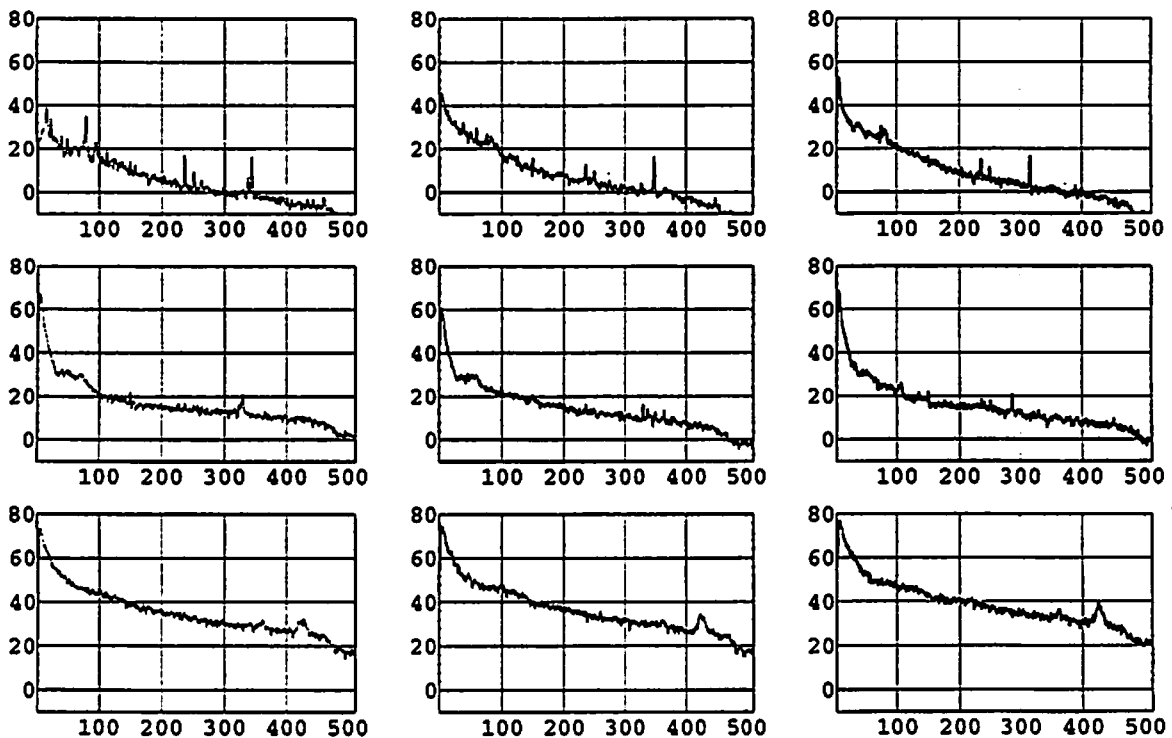


Figure 5.5 The individual spectra, top graphs: wind speed class 0, turbulence class 0-1-2, middle graphs: wind speed class 4, turbulence class 0-1-2, bottom graphs: wind speed class 8, turbulence class 6-7-8. The y axis shows the sound pressure level with a reference of $20 \mu\text{Pa}$, the x axis is the frequency in Hz.

To gain insight into the increase of the level as a function of wind speed and frequency, the data was analysed further. The spectra for wind speed 0 and 8 were averaged, and subtracted. The result is shown in figure 5.6.

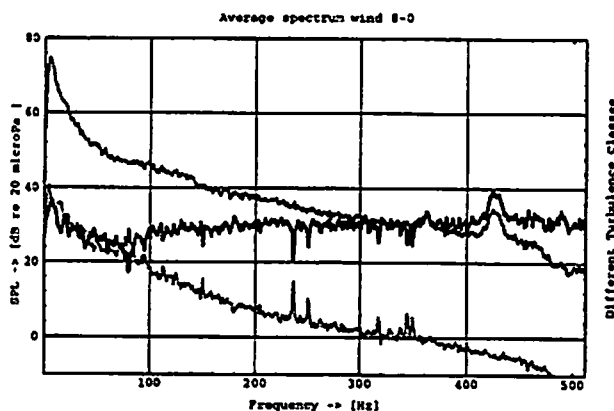


Figure 5.6 Average wind noise spectra for wind speed 8 (Dark gray line) and 0 (Light gray line), and the difference between these noise spectra (Black line) in one graph. The y axis shows the sound pressure level with a reference of 20 μ Pa, the x axis is the frequency in Hz.

From figure 5.6 we see that the wind noise level increases approximately 30 dB if the wind speed increases from wind speed class 0 to class 8. The increase in level is approximately constant in the frequency range from 0 to 500 Hz.

6. Conclusions

The method developed to estimate the performance of two classification algorithms was applied to measured data. The results give a useful estimation of the performance of the algorithms for a range of meteorological conditions.

Overall both algorithms perform very well (more than 90 % of the signals classified correctly) at source receiver distance of 1000 m, up to and including wind force 5 in the downwind situation (wind from source to receiver), and up to and including wind force 3 for the upwind situation. In the intermediate range of wind speeds (downwind speed class 6-7, upwind speed 4-6) the number of false classifications increases. For higher wind speed almost all processed segments are rejected. At high wind speed the noise level caused by wind and turbulence increases. The increase is approximately constant in level from 0 to 500 Hz. The result is that the algorithms reject the processed signal. The number of false classifications increases only slightly. The template matching algorithm performs slightly better in this respect than the harmonic series algorithm.

Acknowledgements

The research was performed under contract of the Dutch Army. For the successful completion of this project we have depended on the help of a number of people at TNO and other institutions. Specifically the Royal Netherlands Navy for the use of the Naval Airfield at Valkenburg and the

friendly co-operation during the year of measurements, the Royal Netherlands Meteorological Institute for the wind speed data, the US Department of Army, Construction Engineering Research Laboratory (CERL) for the use of the Fast Field Program, and Dave Havelock of the Canadian National Research Council for his comments on the original project proposal.

References

- [1] Ton van Koersel, Martijn Miedema and Chris Nieuwenhuize, Acoustic Helicopter Classification, proceedings of the Sixth International Symposium on Long-Range Sound Propagation, NRC Canada, 1994.
- [2] M. de Vreeze, CVH Helicopter design study, TU Delft, Dept of Aerospace Engineering, A2 Design & Performance, Delft, The Netherlands, 1987.
- [3] A.C. van Koersel, Simulation of Helicopter Rotor Noise, FEL-95-A099.
- [4] S. Morgan and R Raspet, Investigation of the mechanisms of low frequency wind noise generation outdoors, J. Acoust. Soc. Am. 92 (2), p 1180-1183.
- [5] R. Raspet, S.W. Lee, E. Kuester, D.C. Chang, W.F. Richards, R. Gilbert and N. Bong, A fast-field program for sound propagation in a layered atmosphere above an impedance ground, , J. Acoust. Soc. Am. 77 (2), p 345-352.
- [6] A.C. van Koersel, Beschrijving van het Rayflux ray tracing programma en vergelijking met andere modellen en metingen, FEL-91-B335, november 1991.
- [7] E.A. Vermaas, A new approach in calculating the outdoor sound propagation with a ray-tracing model in the presence of atmospheric gradients, TU Delft, feb 1989.
- [8] L. Nijs, C.P.A. Wapenaar, The influence of wind and temperature gradients on sound propagation, calculated with the two-way wave equation, J. Acoust. Soc. Am. 87(5), may 1990.
- [9] W. H. T Huisman, K. Attenborough, Reverberation and Attenuation in a pine forest, JASA 90(5), November 1991, pp. 2664-2677.
- [10] E.M. Salomons, F.H.A. van den Berg and H.E.A. Brackenhoff, Long-term average sound transfer through the atmosphere: predictions based on meteorological statistics and numerical computations of sound propagation, Proceedings of the sixth International Symposium on Long-range Sound propagation, NRC Canada, June 1994.
- [11] Huisman, W., Sound Propagation over vegetation-covered ground, dissertation, KU Nijmegen, nov. 1990.
- [12] M. R. Stinson, D.I. Havelock and G.A. Daigle, Simulation of scattering by turbulence into a shadow region using the GF-PE method, Proceedings of the sixth International Symposium on Long-range Sound propagation, NRC Canada, june 1994.
- [13] Xiao Di and K.E. Gilbert, The effect of turbulence and irregular terrain on outdoor sound propagation, Proceedings of the sixth International Symposium on Long-range Sound propagation, NRC Canada, june 1994.
- [14] KNMI, Climatological data of stations in the Netherlands, publication number 150-27, Normals and extreme values of the fifteen principal stations for the period 1961-1990, Ministry of Transport, Public works and Water management, 1992.
- [15] J. Wieringa en P.J. Rijkoort, Windklimaat van Nederland, Staatsuitgeverij, Den Haag, 1983.

Acoustic Propagation, Prediction, Validation, and Training Models for Civilian Applications

D.C. Swanson, K.T. McClintic, M.P. Mahon, and K.M. Reichard
The Applied Research Laboratory
The Pennsylvania State University
P.O. Box 30, State College, PA 16804-0030
(814) 865-2448, fax 863-9918, dcs5@psu.edu

Abstract

Sound propagation models have been developed to a high degree of performance in that if an accurate estimate of the ground impedance and sound velocity profile is used, one can expect a good prediction of the propagated sound levels. However, the general public and governments have needs for simple answers regarding noise pollution and atmospheric conditions which are possible if a few additional assumptions can be applied. Assuming the source is in a relatively open area, the ground is fairly flat and homogeneous, and the weather conditions lead to a sound velocity profile which depends mainly on height and propagation direction, a table-based sound level prediction model is developed. Using literally hundreds of pre-computed sound transmission loss tables for upwind, downwind, and crosswind weather conditions, and for various ground impedances, the user can select a source signature and appropriate background noise to determine the range contour where the source is detectable. Baseline detection is modeled using a 1 Hz resolution spectrum and a "figure-of-merit", or FOM curve, is used to model better or worse detection performance by ground sensors or even humans. The FOM curve represents the noise suppression by sensor algorithms such as beamforming or the SNR variability with frequency of the human ear. Using this approach, a rough estimate of acoustic detectability of sound sources can be made accessible to non-scientists so long as the underlying environmental assumptions are accurate. Some examples of the approach are presented along with a simplified model relating the human ear to 1 Hz resolution FFT-based detection. Some details are also given on the sound velocity profile modeling employed.

Assumptions for a Simplified Model

While computing efficiency has made impressive gains in recent years, it is still not practical to calculate parabolic equation (PE) propagation models for every conceivable source location and propagation direction of interest for a given environment. Furthermore, to make such information accessible to non-scientists for a rough assessment of acoustic detectability some choices have to be made on bounding the problem into a useful and representative set of environments and weather conditions. The corresponding sound propagation attenuation calculated for a range of frequencies and distances of interest is then pre-computed into tabular form for the upwind, downwind, and crosswind propagation directions. Pre-computing of the propagation data for a discrete number of environments allows the detectability prediction model to run on rather modest laptop computers. However, the associated underlying assumption is that the ground impedance is homogeneous, the ground surface is flat compared to wavelength, and the sound velocity profile varies with altitude and propagation direction, but not from site to site within the propagation region of interest.

These assumptions are broad and practical, but still workable for long range propagation detection prediction. We claim this because at ranges beyond a few hundred meters, outdoor grasses, vegetation, and small surface roughness variations likely scatter significantly the sound ray(s) which travel along the surface directly from a ground-based source to a ground-based receiver. At long ranges, we expect the majority of received sound energy to either refracted or scattered from the atmosphere to the ground-based receiver. Therefore, the variations in the ground height are really more on an issue to source and receiver height (relative to the mean ground height). Obviously, the rougher the ground, the weaker this assumption becomes. Our reason for making a "flat ground" assumption is driven by practical reasons of using tables of propagation loss for an entire region, rather than a single source and receiver location. This is very useful for predicting detectability of moving sources. Another important bit of physics our assumptions disregard is the affect of the varied ground on surface winds (including katabatic and anabatic winds) and local surface-driven turbulence. Putting all these assumptions into place (and we recognize the broad scope) we can provide a rough estimate in a simple model for non-scientists to use to make a reasonable estimate of the detectability of various sounds in particular environments. This is not to say that the discarded physics are unimportant - they are extremely important for inhomogeneous environments, but rather, by making these assumptions we can only do a good job predicting acoustic detectability in environments where our assumptions hold. Figure 1 shows the basic process for predicting the detection range in a particular environment.

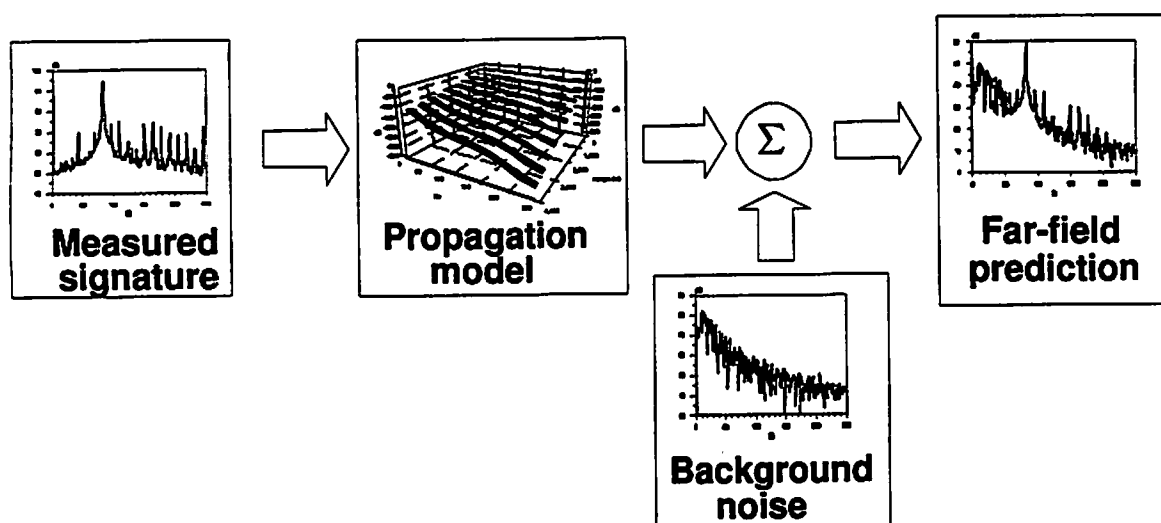


Figure 1 Basic application of the sonar equation using a tabularized propagation model result to predict the detectability as a function of range

The detection of the far-field signature seen in Figure 1 is done using a straightforward narrowband detection algorithm. Typically, a detection threshold is set about 6 dB above the background noise, which for 1 Hz resolution FFT's, works out to be 0.1% false alarm rate, or about 1 detection false alarm every 15 minutes on 1-second sensor updates. When a narrowband peak is at or above the detection threshold, the probability of detection is 50% or greater. Detection modeling for the human ear will be explained later in the paper. Figure 2 shows the general scheme for selecting the representative environments for the simplified model.

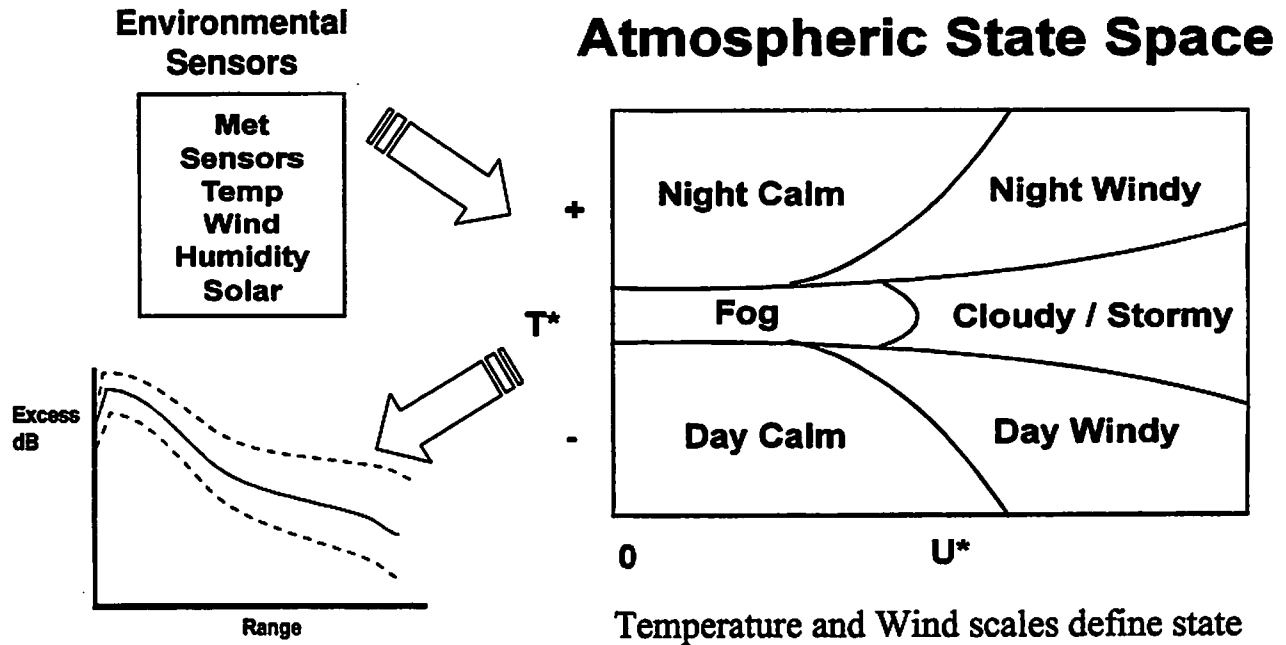


Figure 2 Using surface-layer similarity theory [1], the temperature and wind scaling parameters, T^* and U^* , respectively, help define an atmospheric state with a correspond wind and temperature profile which are used to derive a sound velocity profile for a direction on interest

Figure 3 shows the systematic relationship between atmospheric state and sound propagation over a 3-day lite wind period in October, 1995 at Penn State’s Rock Springs test site which is very flat and homogeneous.

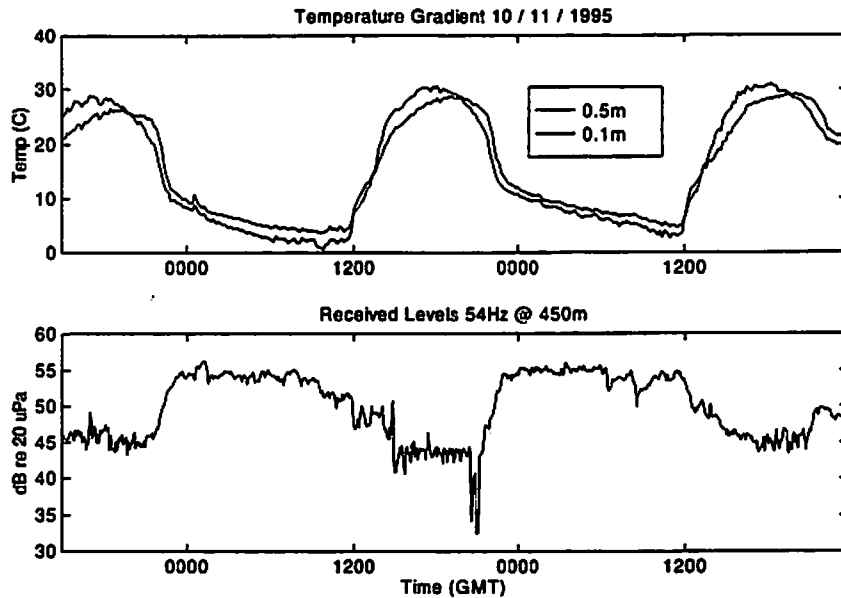


Figure 3 A systematic relationship between surface temperature gradient and sound propagation received level of a 54 Hz sinusoid over a 3-day period.

Sound Velocity Profile (SVP) Modeling

The first step in modeling the SVP is to fit a model to the available temperature data. Since the receiver and the target are on the ground, and the temperature varies significantly near the ground, the temperature (and wind) profile over the bottom 100m is extremely important for sound propagation modeling. Since it's impractical for the receiver sensors to measure the temperature directly over the bottom 100m (typically done using meteorological sensor towers), we use an aspect of meteorology called surface-layer similarity theory [2-5] to estimate the wind and temperature profiles. Similarity theory is only valid for the surface layer, where the thickness is taken as approximately twice the magnitude of the Monin-Obukov length scale L_{mo} , where g in equation (1) is the gravitational constant and T_0 is the absolute temperature at the surface (measured from the bottom temperature sensor).

$$L_{mo} = \frac{u_*^2 T_0}{k_v g T_0} \quad (1)$$

Clearly, equation (1) shows that for little temperature gradient (T_0 is near zero), the thickness of the surface layer is quite large. As the gradient approaches zero we place an upper limit on the magnitude of L_{mo} of 100m. In cases of light winds, L_{mo} approaches zero which will lead to other scaling problems in our profile generator, so a low limit on the order of 1-2 m is assumed. Note that direct-measured meteorological profile data from weather balloons (radiosonde), SODAR, or RASS usually start reading data at around 100m on upward. Modeled data is available over the internet from the Forecast Systems Laboratory (<http://www.fsl.noaa.gov/>), where we use rapid update cycle (RUC) data which is in the form of a 2-dimensional grid with a layer for every 25 mbars of barometric pressure from the ground up. The height of the layer varies at each grid point (60 km spacing between grid points on the map) depending on the weather condition. By sorting the data in the RUC file, one can obtain the barometric pressure, height, temperature humidity (dew/frost point), and wind speed and direction for the nearest 3 or 4 grid points to the receiver location of interest and interpolate to get the upper atmosphere wind and temperature profiles needed for the SVP. However, none of this modeled or measured data is very reliable at the surface where the receiver is located. The surface layer meteorological sensors are required to complete the profile model data.

The temperature profile model used is given in equation (2)

$$T(z) = \frac{T_*}{k_v} \left\{ \ln \frac{z}{z_0} - \Psi_r \left(\frac{z}{L_{mo}} \right) + \beta \frac{z}{H_{sl}} \ln \frac{z}{H_{sl}} \right\} + T_0 \quad (2)$$

where H_{sl} is the thickness of the surface layer (twice the magnitude of L_{mo}) and the temperature is in degrees Kelvin. The first two terms in equation (2) are straight out of similarity theory while the third term we have added as part of a least-squares fit to match the upper level data to the surface layer. In similarity theory, the temperature profile is for potential temperature (removing the adiabatic lapse rate of about -1 degree Kelvin per 100m increase in altitude). Since we are

doing a least squared error model fit, the adiabatic decrease in temperature with height is assumed part of our temperature profile model. The mixing function $\Psi_T(z/L_{mo})$ depends on the L_{mo} length scale [4,5] and is fairly complicated as seen in equation (3). The profile of the temperature is governed by the mixing function only in the surface layer, which is why we chose a “z lnz” structure to our least-squares fit function for the upper atmosphere data. Note that “z lnz” tends to be zero near the ground.

Figure 4 shows a typical daytime profile model result. The sharp negative temperature gradient near the ground is physically the result of solar heating and the result of similarity theory in the first two terms of the profile model in equation (2). The smooth transition from the surface layer to the least-squares fit on the upper atmosphere is both physical and desirable because any artificial fluctuation of the profile will result in erroneous sound scattering in the sound propagation model. The surface layer transition is important to accurate sound propagation modeling when both target source and receiver are on the ground.

$$\begin{aligned}
 L_{mo} < 0 \quad \Psi_T\left(\frac{z}{L_{mo}}\right) &= 2 \ln\left(\frac{1 + \sqrt{1 - 16\frac{z}{L_{mo}}}}{2}\right) \\
 |L_{mo}| \approx 100 \quad \Psi_T\left(\frac{z}{L_{mo}}\right) &= 0 \\
 L_{mo} > 0 \quad \Psi_T\left(\frac{z}{L_{mo}}\right) &= -5 \frac{z}{L_{mo}}
 \end{aligned} \tag{3}$$

The wind profile is split into “u” and “v” components for the “east-west” and “north-south” components of the wind, respectively (w is typically used for the vertical wind component). We note that compass bearings θ_c differ from trigonometric bearings θ_t by $\theta_t = 90 - \theta_c$. We also note that convention has winds coming out of the North as having a bearing of 0 degrees, while the velocity direction is actually along the negative y-axis, or -90 degrees using a trigonometry polar system. Therefore, the trigonometric velocity angle θ_t for a wind direction θ_c is $\theta_t = -90 - \theta_c$. The wind profile along the “east-west” direction is given in equation (4) and along the “north-south” direction in equation (5). This separation of the u and v wind components allows for twisting wind profiles, which are quite common. In particular, during the night “drainage winds” of cold air flowing down to the bottom of valleys (katabatic winds) can have the opposite direction of winds several hundred meters aloft.

$$u_u(z) = \frac{u_s}{k_v} \cos\left(\frac{\pi}{180}[-90 - \theta_c]\right) \left\{ \ln\frac{z}{z_0} - \Psi_u\left(\frac{z}{L_{mo}}\right) + \gamma_u \frac{z}{H_{st}} \ln\frac{z}{H_{st}} \right\} \tag{4}$$

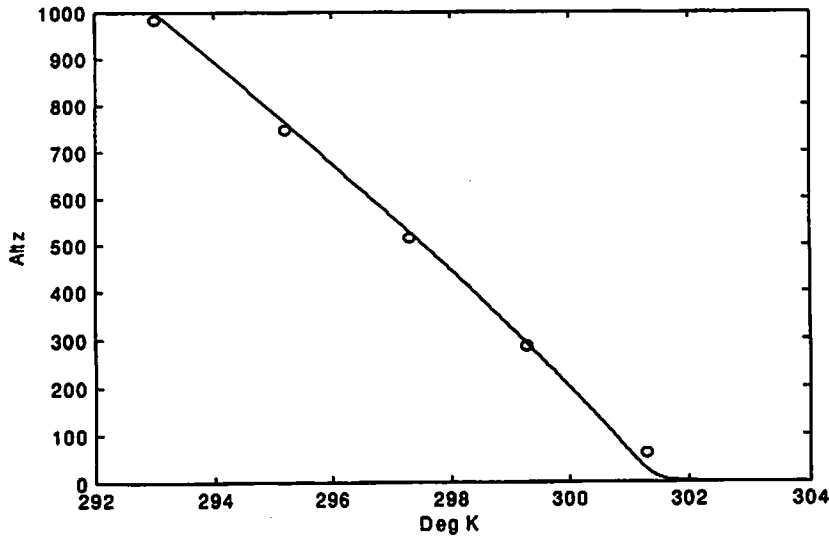


Figure 4 Daytime temperature profile using least-squares fit for upper atmosphere data and similarity theory for surface layer temperatures.

$$u_v(z) = \frac{u_*}{k_v} \sin\left(\frac{\pi}{180}[-90 - \theta_c]\right) \left\{ \ln \frac{z}{z_0} - \Psi_u\left(\frac{z}{L_{mo}}\right) + \gamma_u \frac{z}{H_{sl}} \ln \frac{z}{H_{sl}} \right\} \quad (5)$$

The mixing functions for the wind are given in equation (6).

$$\begin{aligned}
 L_{mo} < 0 \quad \Psi_u\left(\frac{z}{L_{mo}}\right) &= 2 \ln\left(\frac{1+x}{2}\right) + \ln\left(\frac{1+x^2}{2}\right) - 2 \tan^{-1}(x) + \frac{\pi}{2} \\
 x &= \left(1 + 16 \frac{z}{L_{mo}}\right)^{\frac{1}{4}} \\
 |L_{mo}| = 100 \quad \Psi_u\left(\frac{z}{L_{mo}}\right) &= 0 \\
 L_{mo} > 0 \quad \Psi_u\left(\frac{z}{L_{mo}}\right) &= -5 \frac{z}{L_{mo}}
 \end{aligned} \quad (6)$$

The mixing functions in equations (3) and (6) are found by empirical fitting measured data to the dimension-less model equations provided by similarity theory. This approach is based on a technique known as Buckingham-pi theory, where a complex set of differential equations is reduced by deriving a number of independent dimension less equations (pi variables) equal to the number of independent dimensions (physical units) governed by the differential equations. Much of boundary-layer meteorology is rooted in Buckingham-pi theory and is well accepted in the scientific community. Figure 5 shows a twisting wind profile typical of the environment spanning the surface to elevations of several hundred meters.

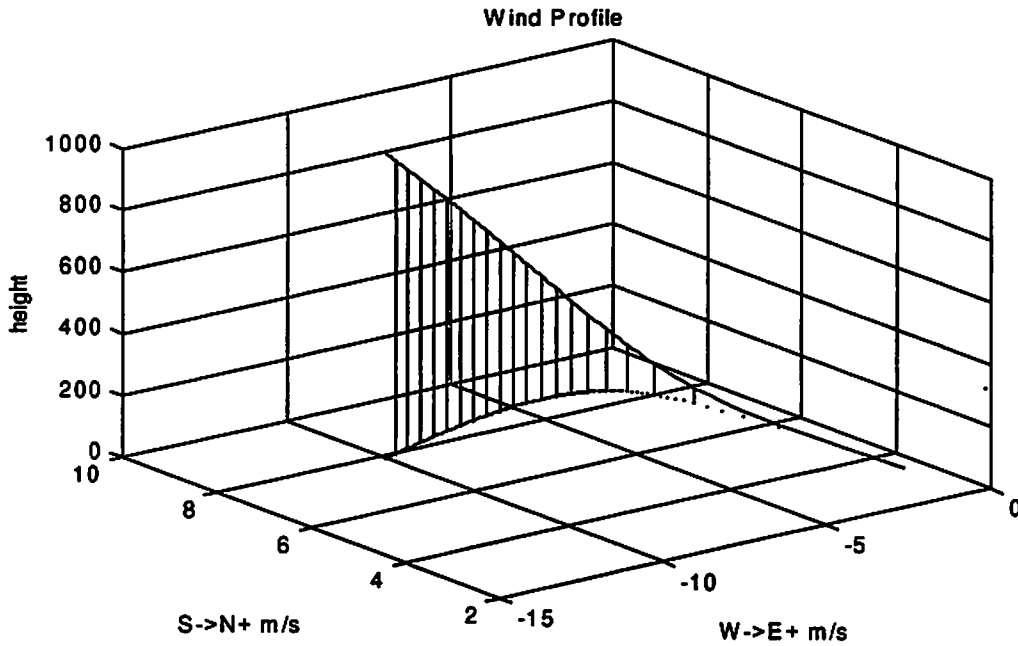


Figure 5 Twisting wind profile can be seen when the terrain is not flat allowing katabatic winds "draining" from hillsides to shift the surface wind direction

The SVP is found by combining the wind and temperature profiles. The speed of sound in the atmosphere is well known to be dependent upon temperature as

$$c = c_0 \sqrt{\frac{T}{273}} \quad (7)$$

where c_0 is 331.6 m/s (the speed of sound in air at 0 degrees C) and T is absolute temperature in degrees Kelvin. The wind velocity components simply add to the sound speed velocity, making the SVP a function of propagation direction θ_p and height. Equation (8) gives the SVP for a compass propagation direction θ_p (sound propagating to the southeast will have a compass heading of 135 degrees and a trigonometric angle of $90 - \theta_p = -45$ degrees).

$$c(z, \theta_p) = c_0 \sqrt{\frac{T(z)}{273}} + u_u(z) \cos\left(\frac{\pi}{180}[90 - \theta_p]\right) + u_v(z) \sin\left(\frac{\pi}{180}[90 - \theta_p]\right) \quad (8)$$

Propagation and Detection Models

Once we have a reasonable estimate for the SVP, a Green's function PE model [6] is used to calculate the total (spreading plus excess attenuation) propagation loss from source to receiver in the upwind, downwind, and crosswind directions. We have streamlined this processing intensive task into a C++ Windows application to efficiently generate propagation tables. For example, on a Pentium II 266 MHz processor, 8192 point FFT's (0.5m vertical sampling) are used in 20 range steps out to 6 km for 50, 100, 150, 200, and 150 Hz in the upwind, downwind, and crosswind directions to compute a complete set of tables in under 5 minutes time.

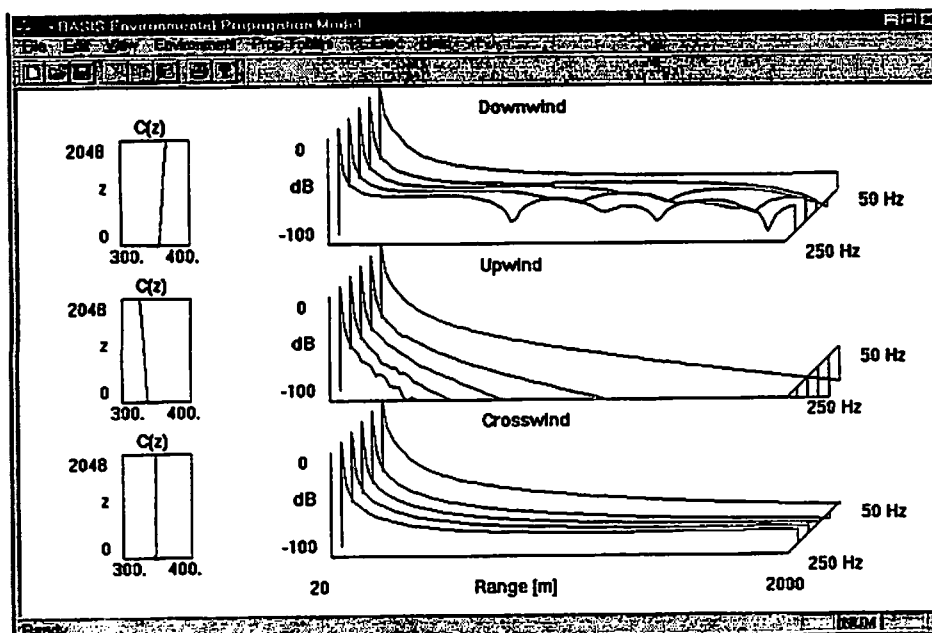


Figure 6 The GFPE propagation model showing the sound speed profiles and transmission loss curves for 5 frequencies in the upwind, downwind, and cross wind directions

Figure 7 shows what the user sees in the simplified acoustic detection model for a typical commercial truck and 3 different receiving positions. The contours represent a 50% probability of detection for the largest propagated peak of the truck signature. If the truck is located anywhere inside the contour, a 1 Hz resolution FFT of a single microphone should be able to easily detect it. A beamforming sensor array would obviously be able to detect the truck at a much farther distance. We use a FOM curve to objectively represent the SNR improvement from an array's directivity index as well as other signal processing enhancements to improve performance. Figure 8 shows the FOM curve for an 8 element 2m circular array. The FOM curve is negative (on a dB scale) when the noise is suppressed relative to a single microphone with a 1 Hz resolution FFT.

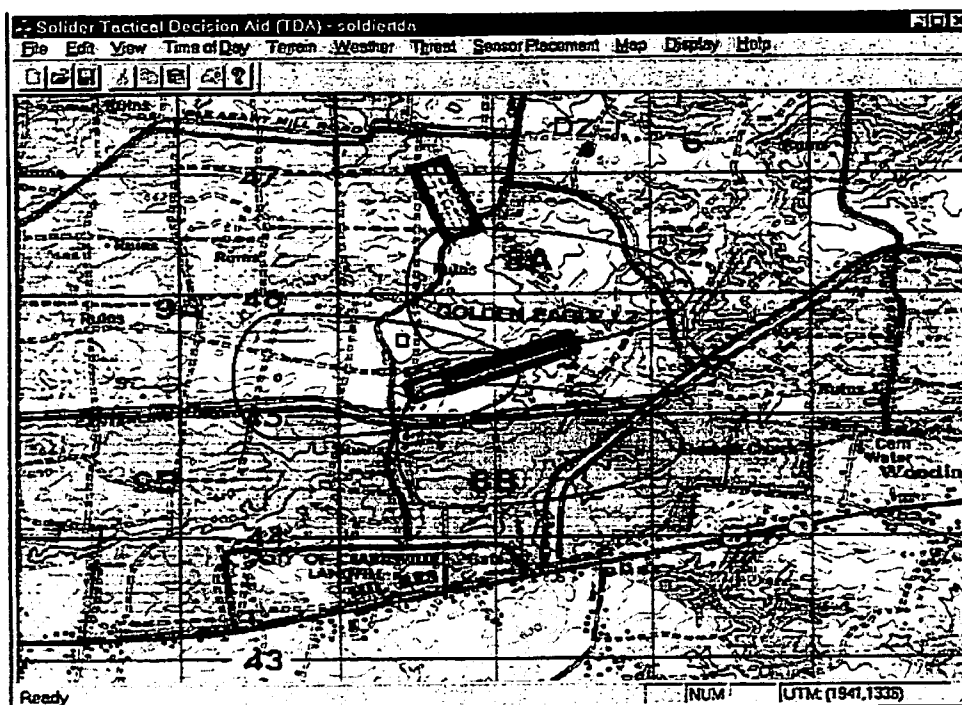


Figure 7 The detection footprints at 3 receiver locations for the noise from a cargo truck with moderate winds out of the East.

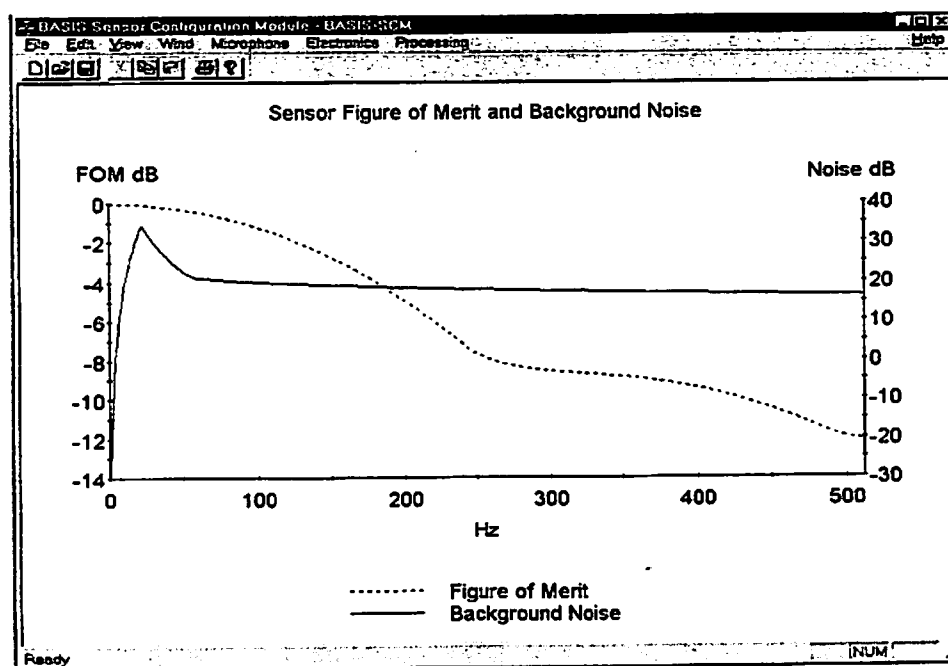


Figure 8 Modeled sensor background noise and SNR figure-of-merit curves from BASIS-SCM

Some Validation Results

During a sound propagation experiment in the desert near Yuma, AZ in late July 1997, the environmental sensors and detection performance modeling were employed. To fully observe the effect of the environment on sound propagation and acoustic detection, testing was done at all hours over a five day period. Acoustic calibration of the test range is done using a calibrated loudspeaker source playing 50, 100, 150, 200, and 250 Hz at a level of 115 dB at 1m. About once per hour these acoustic calibrations are broadcast from a single location and recorded by multiple remote unattended ground sensor (UGS) nodes, also equipped with surface meteorological sensors. The UGS meteorological data was augmented by several 10m towers, and SODAR system for measuring boundary layer winds, and radiosonde weather balloons. A RASS (Radio-Acoustic Sounding System) was also on site, but did not provide useful data due to the extremely dry conditions.

The meteorological data gathered in the field during the acoustic calibrations is used to estimate the SVP in the upwind, downwind, and cross wind directions, and PE models are run for the 50, 100, 150, 200, and 250 Hz calibration tones. The PE sound level predictions for the calibration tones are then compared to the available acoustic spectral measurements from the UGS nodes around the range. A good match indicates that the propagation model is valid and can be used to accurately predict detection ranges for the various UGS sensors. Figures 9 and 10 show the PE predicted and measured calibration tone results for an UGS node 3.85 km from the loudspeaker during the hot windy afternoon and at around midnight. The "*" symbols merely highlight the spectrum at the frequency bins where the tones should be. The "o" symbols and error bars are the PE predictions. The wind background noise and upward refraction typical of a hot desert afternoon clearly show poor detection performance in Figure 9. The same calibration tone levels, at the same UGS node on the same day are seen for midnight in Figure 10. Clearly, the reduced wind noise and downward refraction greatly enhance UGS acoustic detection performance at night. *In fact, acoustic UGS work so much better at night, and especially during the pre-dawn hours, that they should be referred to as nocturnal sensors.*

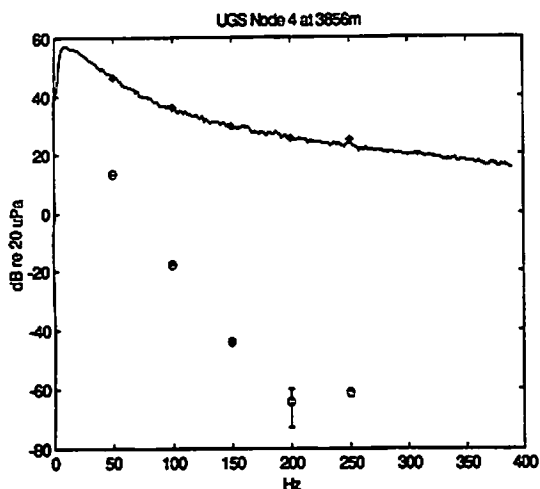


Figure 9 Loudspeaker calibration during a hot afternoon

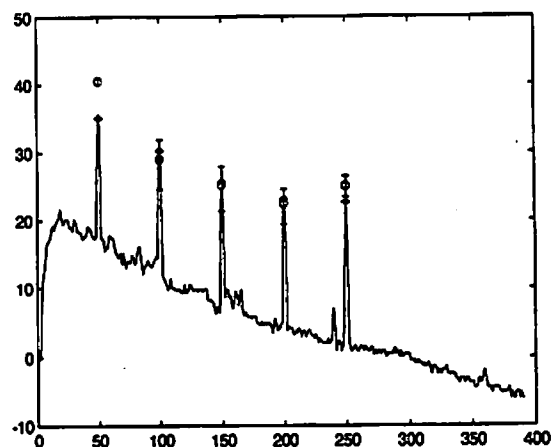


Figure 10 Loudspeaker calibration at midnight

Human Detection of Narrowband Tones

Of primary interest to civilian and government needs for acoustic predictions outdoors is the detection performance of humans. This of course leads to community noise complaints, legal actions between people and businesses, and so on. We have just established an objective approach to systematically make predictions for narrowband frequencies measured by microphones and processed by computer. For human detection, we have to cross over into the subjective discipline of audiology [7]. There are at least three relevant facts about all human hearing which, as physicists, we can embrace to develop a FOM model to relate human hearing to our signal processing model. The first is that the frequency response of human hearing is loudness-dependent. For sounds louder than about 85 dB, the human ear has a relatively flat frequency response, or C-weighting response. For sounds quieter than about 55 dB, the ear's sensitivity is concentrated in the speech range from 500 Hz to around 3 kHz, or an A-weighting. In between sound levels of 55 and 85 dB there is actually a B-weighting curve which is used by audiologists. Figure 11 shows the A, B, and C weighting curves in dB relative to 1 kHz.

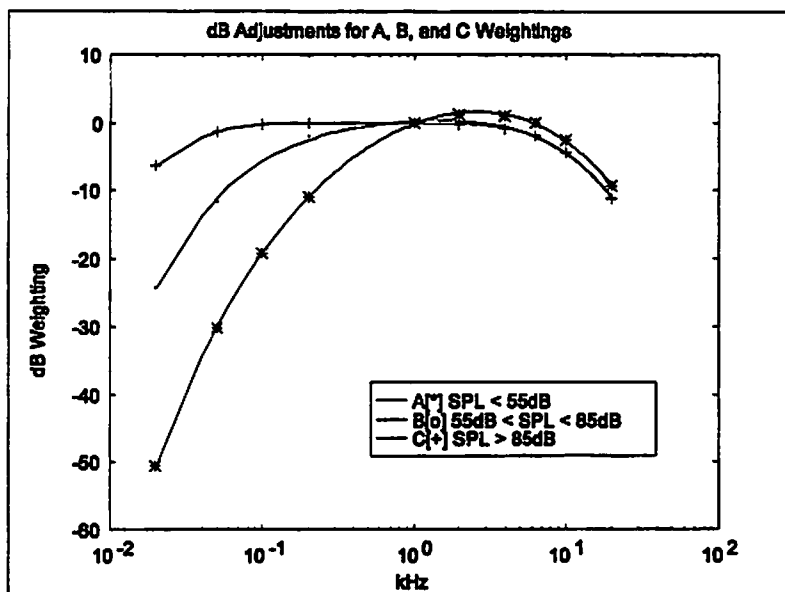


Figure 11 A, B, and C, weighting curves for modeling the human ear's relative frequency response to sound at various levels of loudness

Second, we know the ear responds neurologically in the range of 25 msec to as long as 150 msec, indicating the integration time is in the 200 msec range. This corresponds to an equivalent frequency resolution of about 5 Hz. We also know that the lowest frequency to be perceived by most humans as a sound (rather than vibration) is in the 20 Hz range, and that beat frequencies faster than about 10-20 beats per second will be perceived as an inter-modulation tone rather than amplitude modulation of a sinusoid. While highly subjective, it is plausible to say that the ear's detection capability (SNR enhancement) is roughly equivalent to a 5 Hz

resolution FFT at low frequencies, and perhaps has less resolution at higher frequencies (faster integration times). There is one more observable from audiology which supports the 5 Hz low frequency resolution hypothesis. It has been reported that at low frequencies, the ear's critical bandwidth is approximately a 1/3 octave band. The critical bandwidth is the narrowest bandwidth of noise which will mask a narrowband sinusoid with the same total power. The bandwidth of a 1/3 octave filter is about 23% of the center frequency, or 5 Hz at 20 Hz center frequency, 23 Hz at 100 Hz center frequency, and so on. The FOM for the human ear at low frequencies is seen to be around +7 dB (7 dB worse SNR enhancement than a 1 Hz resolution FFT) at best, and the SNR enhancement worsens as one goes to higher frequencies. However, for low intensity sounds, the ear's sensitivity increases remarkably as one approaches the 1-3 kHz range.

Third, a quantity called the minimum audible field, or MAF, represents the minimum sound pressure levels the best human ears can detect. Its about 43 dB at 100 Hz, 15 dB at 200 Hz, 4-5 dB in the 1-2 kHz range, -5 dB at 4 kHz, and 13.5 dB at 8 kHz [7]. The astonishing sensitivity at 4 kHz is due to the part of the cochlea closest to the oval window in the inner ear. The MAF represents an "internal background noise" of the human ear. In extremely quiet environments, the biological noise internal to our bodies, along with neurological noise such as tinnitus (ringing of the ears) will prevent detection of sound.

Putting the human detection model together still requires further research, but it can be included in our acoustic detection model as follows. 1) the source signature predicted at some range of interest is evaluated for an overall sound pressure level, SPL; 2) the signature is weighted by either A, B, or C-weighting curves depending on the overall SPL. 3) the weighted background noise is added to the "internal noise" of the MAF to produce the modeled noise presented to the ear; 4) the FOM for ear is used to adjust the signature (A, B, or C weighted) SNR prior to a detection calculation in the model. For low level, low frequency sounds, the effect of A-weighting will diminish the signal and noise substantially, perhaps so much that the MAF masks the signal from being detected. But at higher frequencies this is much less of a problem. A-weighting at say 1 Hz leaves the sound relatively unscathed while at the same time the MAF is extremely small. This explains why human hearing is so acute in the speech range. But, this is also the current state of our work on outdoor sound detection modeling.

Conclusions

We have shown a simplified acoustic detection model for use in outdoor sound propagation source level predictions of narrowband sinusoids in environmental noise. The simplifications are done to allow a large number of pre-computed sound propagation attenuation tables to be employed for modeling the sound attenuation efficiently. This is done for a representative set of environments assuming a "flat ground" terrain and temperature and wind profiles which vary vertically only. This allows a detection contour derived from upwind, downwind, and crosswind detection ranges to be applied anywhere in the region. However, the underlying assumptions restrict this application to relatively flat open areas. We have also presented some preliminary work towards a human detection capability to be added to the model

in the future. The human detectability problem requires that physical aspects of the ear be cast into signal processing parameters which allow the ear model to be integrated into the acoustic detection model. We have found very good model performance results in relatively low wind homogeneous environments. However, much more validation work is anticipated.

References

1. R. Stull, *An Introduction to Boundary Layer Meteorology*, Kluwer Academic Publishers, 1991.
2. D. Swanson, "Digitization of the battlefield using unattended ground sensors," SPIE 96, paper no. 2764-21
3. D. Swanson and K Reichard, "Environmental Sensors and Algorithms for Ground-Based Passive Acoustic Sensors," SPIE 98, paper no. 3393-28
4. J.A. Brusinger, J.C. Wyngaard, Y. Izumi, and E.F. Bradley, "Flux profile relationships in the atmospheric surface layer," *J. Atmospheric Science*, 28, pp181-189, 1971.
5. F.T.M. Nieuwstadt, *Boundary Layer Meteorology*, 14 (1978), p235-246.
6. Kenneth E. Gilbert and Xiao Di, "A fast Green's function method for one-way sound propagation in the atmosphere", *Journal of the Acoustical Society of America*, 94(4), pp. 2343-2352, 1992.
7. H.A. Newby, *Audiology*, 4th ed., (Englewood Cliffs: Prentice-Hall), 1979.

Comparison of Seismic and Acoustic Signals from Moving Vehicles.

Roy J. Greenfield,
 Dept. of Geosciences, Penn. State Univ.
 441 Deike Building
 University Park, PA 16802
 Tel: 814-865-5723 roy@geosc.psu.edu

Mark L. Moran, and Donald G. Albert
 U.S. Army Cold Regions Research and Engineering Laboratory,
 72 Lyme Rd., Hanover, NH 03755
 Tel: 603-646-4274
 mmoran@crrel.usace.army.mil
 dalbert@crrel.usace.army.mil

ABSTRACT

Moving vehicles generate both acoustic and seismic signals. The seismic signal received on a geophone can contain some energy that has propagated as seismic waves and some energy that couples from acoustic waves to seismic waves at the geophone. In the frequency domain, the coherence between the microphone and geophone signal can be used to determine if the seismic signal is predominantly due to acoustic wave coupling. If the latter predominates the ratio of the seismic ground particle velocity to sound pressure can be determined, giving the frame strength of the ground. The method is applied to data from both summer and snow covered winter ground. For the winter data a 15 meter array of 10 microphones is used to look at the spatial coherence of the sound. Results can be applied to removing the sound generated portion of the seismic signal.

Introduction

It is well established that sound waves move the earth and create signals on a geophone. The coupling of sound to geophones has been studied using speakers as sources (e.g. Sabatier et al, 1986) and using pistol shots (Albert and Orcutt, 1989). The measurement normally made is the ratio of the seismic ground velocity (the quantity measured by a geophone) divided by sound pressure. We denote this quantity by SAR. This SAR has been used with other measurements to get properties of the ground (e.g. Sprague et al, 1993). It is also important to measure and understand this coupling if full use is to be made of seismic signals in monitoring activities.

In the present work we investigate the possibility of determining SAR using the signals that are generated by moving vehicles. From a source such as a moving vehicle signal reaches a geophone in several ways. Energy is put into seismic waves directly by the vehicle tread. Next energy can couple from sound waves into seismic waves near the vehicle, then travel to geophone as seismic waves. Finally energy propagates as sound waves and couples to ground motion near the geophone. Thus the use of a moving vehicle rather than a speaker or pistol source may require care in data reduction.

This work attempts to determine which part of the total seismic signal has propagated as sound waves. To do this we look at the coincidence of spectral peaks in the microphone and geophone signals, and at the coherence (coherence function) between the microphone and geophone signals.

Method

Data Sources

Data will be discussed from two field experiments. The first, called the Alaska data, uses data taken at the Texas Range test site in Ft. Greely, AK. The data was taken 1/27/98 during a day with low wind, and air temperatures below -17°C . The site is characterized by deep glacial tills. The ground was frozen and snow cover was between 15 and 60 cm deep. The area is largely open with only short (<1 m) scrubby vegetation. Geophones were mounted on spikes and forced into the ground. The microphones were mounded on stands 1 m above the snow surface. Data was take with a 10 element microphone array and, a 12 element, three component geophone array. The data analyzed is from a microphone separated by 3 m from a vertical geophone. The seismic sensors were Mark Products 4.5-Hz geophones and the microphones were Bruel & Kjaer 4165 all-weather capacitance microphones with windscreens. Custom amplifiers were used to remove the DC offset from the microphone signals. Figure 1 shows Alaska data.

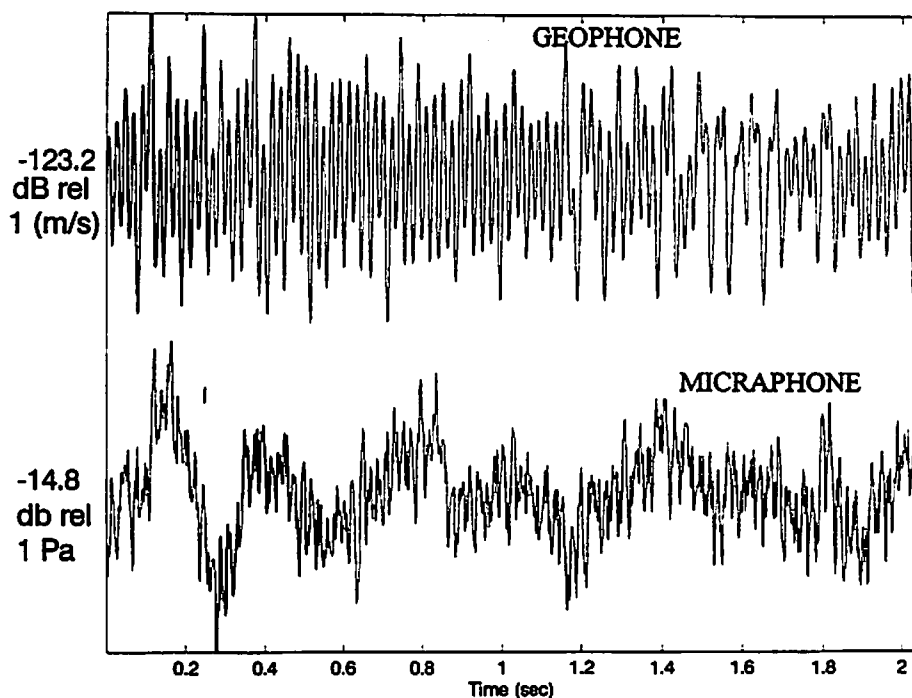


Figure 1. Sample Data from Alaska. Source distance is 330 m.

The second data set to be discussed was taken at Aberdeen, MD. Data was taken in a large open field, with grass cover, throughout the evening of 10/28/98. . Topographic relief between source

and sensor locations is less than 1 m. Air temperatures were approximately 60° and average wind speeds over the course of the recording period were less than 1 m/s. A shallow hole, roughly the height of the geophone, was stamped in the ground and the spiked geophones pushed into the hole. The microphone and vertical geophone used for the coherence measurement were separated by approximately 9 m.

Calculation methods

The coherence is a measure of the similarity of the seismic and acoustic signal. The geophone signal may be thought of as composed of energy that propagates through the earth and is uncorrelated with the sound signal, G_U and a part that is generated by the sound to ground motion coupling, G_C , as shown in Figure 2. The sound picked up by the microphone is composed of that couples into the ground, M_C , and other sound, for example wind noise, that does not couple to the ground, M_U . The total microphone signal is then the correlated and the uncorrelated parts, $M_C + M_U$, while the total geophone signal is $G_C + G_U$. The coherence is defined as

$$C \equiv \frac{(P_{MG})^2}{(P_{MM})(P_{GG})} = \frac{(P_{M_C} P_{G_C})}{(P_{G_U} + P_{G_C})(P_{M_U} + P_{M_C})} \quad (1)$$

where

P_{MM} \equiv microphone power spectra

P_{MG} \equiv microphone - geophone cross power spectra

P_{M_C} \equiv coherent part of the microphone power spectra

and analogous definitions hold for the other variables.

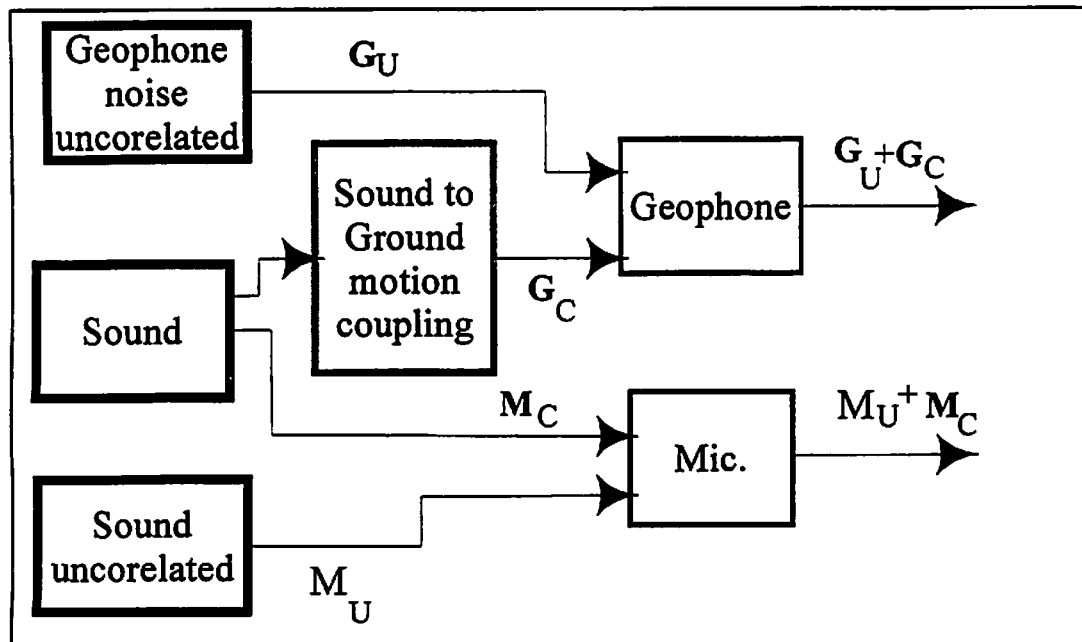


Figure 2. Diagram of signal formation.

If the block averaging method is used to measure the coherence, the coherence may be thought of as a measure of how constant the phase difference between microphone and geophone signals is from block to block. Thus the coherence is a measure of how much of the energy is common to both traces, as given by equation (1).

The power spectral density calculations were made using the Matlab routine PSD. The coherence measurement were made using the Matlab routine COHERE. For the Aberdeen data 5 seconds of data were used, a 1.024 s data blocks gives about 1 Hz. resolution. A 1 s window was used, with 50% overlap between blocks. This give approximately 5 degrees of freedom in the measurement. For Alaska data a 2 second data section was used, with a .48 s data block, with 50% block overlap, giving approximately 4 degrees of freedom.

Results

Figure 3A shows PSD (the Power Spectral Density) for Aberdeen data. The source was a common main battle tank, with a velocity of 35 km/h at a distance of approximately 300 m. The top two traces have been normalized to bring out the coincidence of the spectral peaks of the microphone and geophone traces in the frequency range of 60 to 150 Hz. The spectral peaks in the signals are believed to be the engine noise spectral peaks normally seen in tank acoustic noise (e.g. Wellman, 1996). The coherence between the two traces, shown in Figure 3B, indicates that the two signals are highly coherent between 80 and 150 Hz, and have low coherence outside of that band. Figure 4 shows the true PSD for the two sensor signals. The difference in signal level of the microphone minus the geophone (dB rel to 1 [(m/s)/Pa]). Is shown in the lower panel.

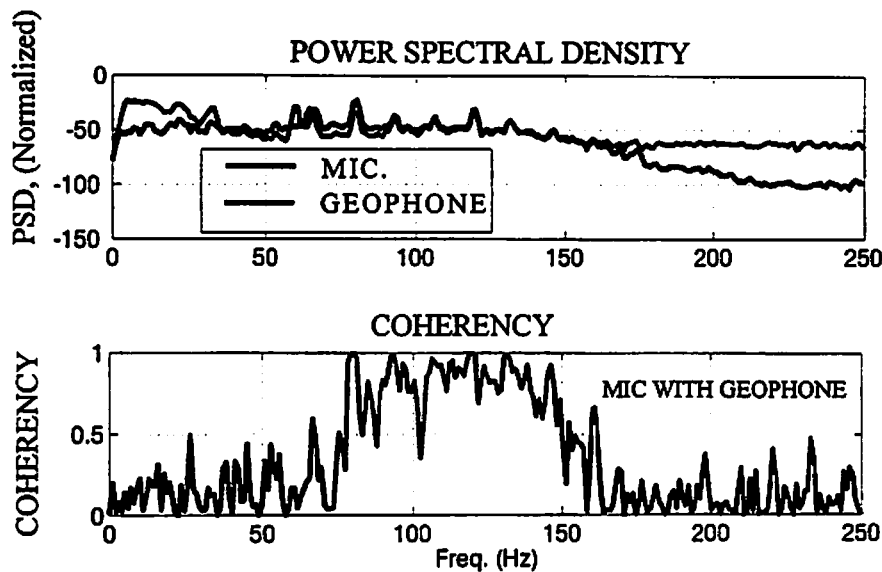


Figure 3. A. PSD For mic and geophone. B. Coherence. File 84, Aberdeen.

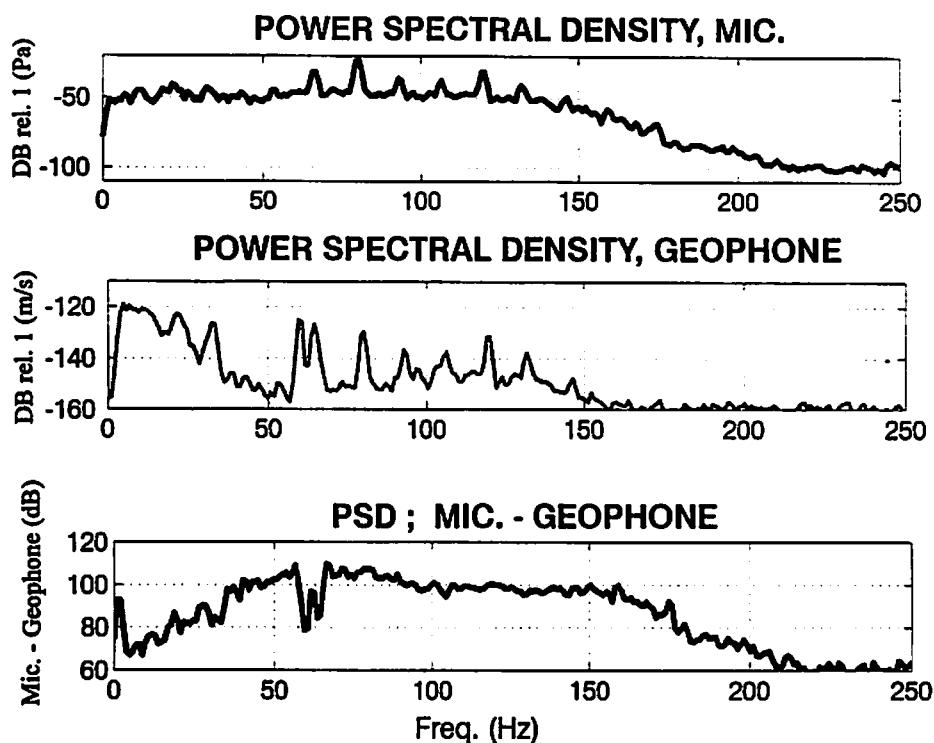


Figure 4. PSD for mic, PSD for geophone, and PSD (mic – geophone) vs frequency. File 84 Aberdeen.

The results for this data section are similar for the whole record. When the source was approximately 700 m from the sensors, the coherence was still high over the 80 to 150 Hz band. The SAR for several different portions of data are shown in Figure 5. Figures 5 A, C, and D are for the same run at different portions of the record. Figure 5B is for the same vehicle run but uses a different geophone, also at a distance of 9 m from the microphone. In all cases the SAR's are similar. There is a peak centered at about 55 Hz which is common to all. This corresponds to a peak in the seismic spectra, indicating that this peak is due to energy that propagated from the source as seismic energy, and not a place where the seismic to acoustic coupling became large. The SAR is about 3×10^{-6} (m/s)/Pa at 70 Hz. Rising to about 10×10^{-6} (m/s)/Pa at 150 Hz.

SEISMIC/ACOUSTIC RATIO VERSUS FREQUENCY

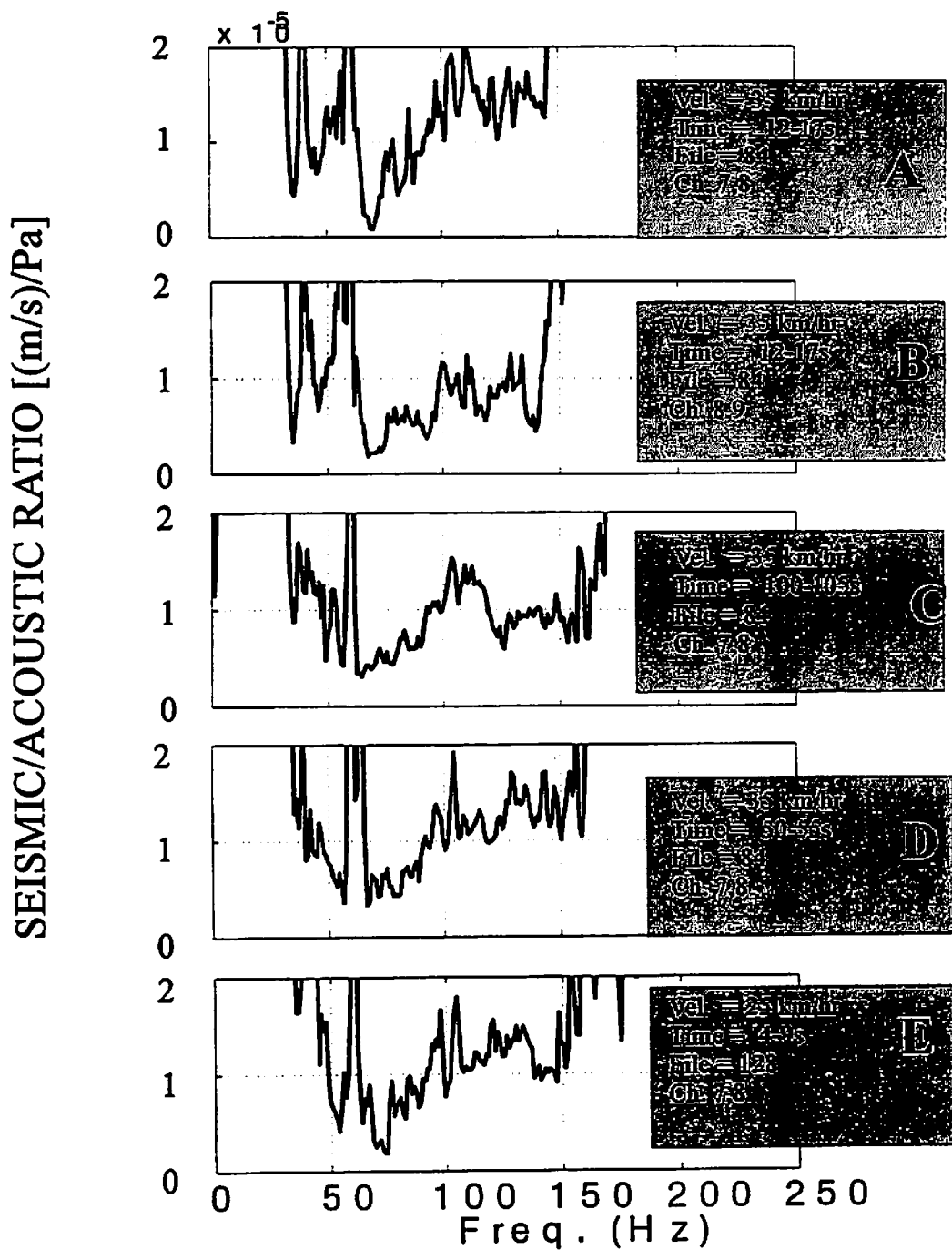


Figure 5. Seismic/Acoustic ratio for 5 samples. A, B, C, and D are for tank with reciprocating engine. E is for a tank with a turbine engine. B uses a different seismic channel than other ratios.

The Alaska data use the same type of main battle tank as the majority of the Aberdeen data. In this data the vehicle is at distance of 330 m. The microphone PSD, coherence, and SAR are shown in Figure 6. The coherence are generally high from 100 to 200 Hz, however there are dips in coherence where the microphone PSD is low. This illustrated by the right-most vertical line on the figure, where the microphone PSD is high the coherence is high. Note that at the frequencies where the coherence is relatively low the SAR is high. This indicates that there is significant seismic energy on the geophone that is not coherent with the microphone signal. However at frequencies where the microphone signal is high the major portion of the geophone power is from acoustic coupling. Thus by following the lower portion of the SAR curve a reliable estimate of the SAR is obtained. The SAR are around 1.3×10^{-6} [(m/s)/Pa] at 120 Hz. Rising to about 2×10^{-6} [(m/s)/Pa] at 180 Hz.

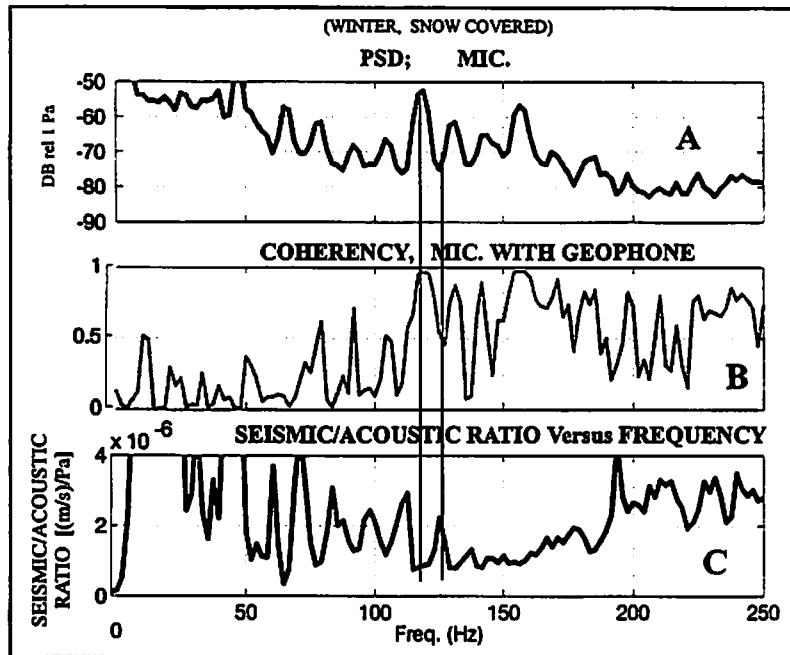


Figure 6. A. PSD for mic. B. Coherence between mic and geophone. C. SAR. For Alaska, File 42. Vertical lines show frequency alignment for a peak and for a trough of the three time series.

Finally the average inter element coherence of the 10 element microphone array is shown in Figure 7. This was formed by averaging at each frequency, the 45 combinations of microphones taken two at a time. The diameter of the array was approximately 15 m. The microphones are generally coherent from 150 to 350 Hz. In addition there are high coherence peaks from 50 to 80 Hz.

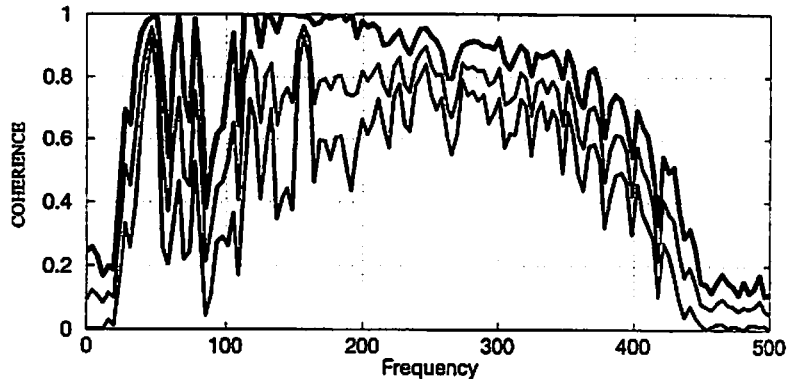


Figure 7. Average coherence versus frequency. Average of 45 combinations. Error limit curves are above and below the coherence curve.

Discussion

The SAR values found for Aberdeen were consistent with the 6×10^{-6} to 10×10^{-6} [(m/s)/Pa] given in the literature (e.g. Albert and Orcutt, 1989; Sabatier et al, 1986). The SAR values are roughly a factor of 2 to 4 lower for Alaska than for Aberdeen. Rayleigh wave velocity at Aberdeen was on the order of 250 m/s. Array processing of seismic data showed P wave velocities of 1500 m/s for Rayleigh surface waves, and up to 4,000 m/s for signals thought to be P-waves. These are consistent with permafrost. Figure 8 shows a plot of the theoretical SAR versus V_s (shear wave velocity) for a plane wave in air incident on a Poisson solid. Calculations were done with the solution in Ewing, Jardetsky, and Press (1957, p79). Calculations were for an air velocity of 340 m/s. Note the general decrease of SAR with V_s . This trend is consistent with the low SAR for the Alaska data. The peak in calculated SAR around 370 m/s is due to the air coupled Rayleigh wave phenomenon (Press et al, 1955). Even though the measurements of SAR only go up to 200 Hz using more complex models for the earth incorporating layering and poroelastic material (e.g. Albert, 1993; Attenborough, 1985) would give a better fit to the observed SAR curve.

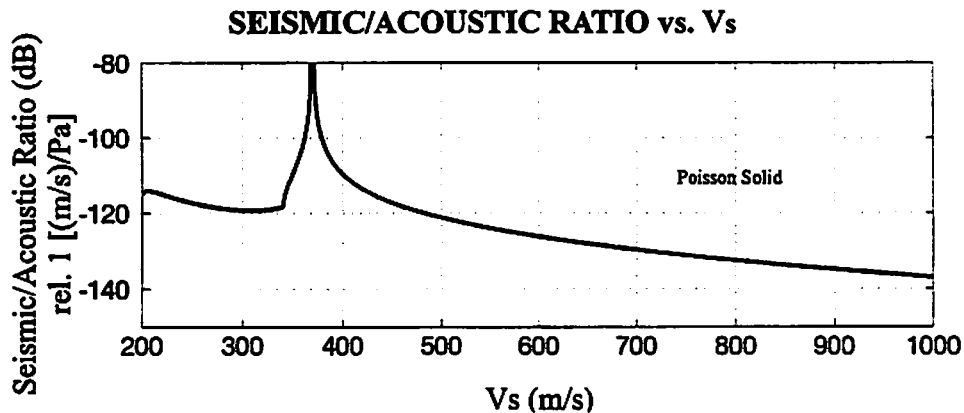


Figure 8. SAR for a wave in air incident on an elastic halfspace vs frequency. Poisson solid. Density of solid 2000 kg/m^3 .

Conclusions

Microphone and geophone signals were observed to be coherent at frequencies of approximately 60 to 150 Hz at a grass covered site, at 100 to 200 Hz at a frozen snow covered site. Evidence was presented that use of passive signals from vehicles can be used to estimate the SAR. The use of coherence is useful in determining what part of the seismic signal is energy that has propagated as seismic wave, and what part is due to sound to ground motion coupling. It is possible that prediction error filtering may be useful in removing the sound to seismic coupled noise on the geophone (Albert, 1984). A through investigation of the SAR values from a variety of settings may lead to methods for estimating the acoustic ground impedance and the near surface stiffness of the earth's surface. These are important parameters in autonomous remote monitoring systems.

REFERENCES

- Albert, D.B., 1984, The effect of snow on vehicle-generated seismic signatures: CRREL Rpt. 84-23, U. S. Army Corps of Eng., Cold Regions Research and Engineering Laboratory, Hanover, N.H.
- Albert, D.G., and J.A. Orcutt, 1989: *J. Acoust. Soc. Am.*, 86, 351-359.
- Albert, D.G., 1993, A comparison between wave propagation in water-saturated and air-saturated porous materials: *J. Appl. Phys.*, 73, 28-36.
- Attenborough, K. 1985, Acoustical impedance models for outdoor ground surfaces: *J. of Sound and Vib.*, 99, 521-544.
- Ewing, W.M., W.S. Jardetzky, and F. Press, 1957, "Elastic Waves in Layered Media", McGraw-Hill.
- Press, F., J. Oliver, and M. Ewing, 1955, Model study of air-coupled surface waves: *J. Acoust. Soc. Am.*, 27, 43-46.
- Sabatier, J.M., H.E. Bass, L.N. Bolen, and K. Attenborough, 1986: Acoustically induced seismic waves: *J. Acoust. Soc. Am.*, 80, 646-649.
- Sprague, M.W., R. Raspet, and H.E. Bass, 1993: Low frequency acoustic ground impedance measurement techniques, *Applied acoustics*, 39, 307-325.
- Wellman, M. 1996, Acoustic feature extraction for target ID: 4th Annual Battlefield Acoustics Symposium, Ft. Meade, MD, 24-26 Sept. 1996.

Review of Models for Ground Effects over Level Terrain

Keith Attenborough

Faculty of Technology, The Open University, Milton Keynes, MK7 6AA, England; Tel.44 1908 652766;
Fax 44 1908 652192; e-mail k.attenborough@open.ac.uk

0. Introduction

The last few years have seen the development and use of several means of characterizing the ground when predicting outdoor sound propagation. In this paper we review some of these developments and discuss them in the light of recent data. In the first section several surface impedance models are introduced. Impedance models are compared with data in section 2. A method of deducing surface impedance from short-range complex excess attenuation measurements is described in section 3. Progress in modelling roughness effects is reported in section 4. Evidence of ground roughness effects are reported in section 5. Finally some concluding remarks are offered.

1. Ground Impedance models

A widely-used, semi-empirical single-parameter model, due to Delany and Bazley, for propagation constant and relative normal surface impedance [1,2] suggests that

$$k = (\omega/c_f) [1 + 0.0978X^{-0.700} + i0.189X^{-0.595}] \quad (1)$$

$$Z_c = 1 + 0.0571X^{-0.754} + i0.087X^{-0.732}, \quad (2)$$

where $X = \rho_f f / R_s = f / R_{eff}$, R_{eff} being an effective flow resistivity.

Rasmussen [3] found it possible to improve agreement with short range propagation data over grass-covered surfaces by assuming a hard-backed layer structure and by using equations (1) and (2) with the formula for the impedance of a hard-backed layer of thickness d ,

$$Z(d) = Z_c \coth(-ikd). \quad (3)$$

Hamet and Berengier [4] have used a modified form of the phenomenological model published by Morse and Ingard [5] to predict the acoustical properties of porous asphalt. Their model may be written

$$Z_c = \left(\frac{1}{\Omega} \right) \left(\frac{K}{\gamma} \right)^{\frac{1}{2}} \left\{ 1 + \frac{\gamma-1}{\gamma} \left(\frac{1}{F_0} \right)^{\frac{1}{2}} \right\} F_\mu^{\frac{1}{2}}, \quad k = \gamma \Omega k_0 Z_c$$

$$F_\mu = 1 - \omega_\mu / \omega, \quad F_0 = 1 - \omega_0 / \omega, \quad \omega_\mu = (R_s / \rho_0) (\Omega / K), \quad \omega_0 = \omega_\mu (K / N_{PR}). \quad (4)$$

where N_{PR} is the Prandtl number for air and $k_0 = \omega / c_f$.

The acoustical properties of the ground may be modelled as those of a rigid-porous material and characterized by a complex density, containing the influence of viscous effects, and a complex compressibility, containing the influence of thermal effects. Thermal effects are much greater in air-filled materials than in water-filled materials. The precise forms of these quantities may be obtained by considering a microstructure of narrow pores or tubes. This offers a more rigorous basis for ground impedance prediction than phenomenological [5] or semi-empirical [2] approaches.

According to Stinson [6], if the complex density in a uniform pore of arbitrary shape, is written as

$$\rho(\omega) = \rho_0 / H(\lambda) \quad (5)$$

where λ is a dimensionless parameter, then the complex compressibility is given by

$$C(\omega) = (\gamma P_0)^{-1} [\gamma - (\gamma - 1)H(\lambda\sqrt{(NPR)})] \quad (6)$$

Where $(\gamma P_0)^{-1} = (\rho_0 c_0^2)^{-1}$ is the adiabatic compressibility of air.

$H(\lambda)$ has been calculated for many ideal pore shapes [6-9] including circular capillary, infinite parallel sided slit, equilateral triangle and rectangle.

The dimensionless parameter λ may be related to the (steady) flow resistivity (R_s) of the bulk material through use of the Kozeny-Carman formula [10], $R_s = \frac{2\mu q^2 s_0}{\Omega r_h^3}$, where the

hydraulic radius, $r_h = \frac{\text{'wetted' area}}{\text{perimeter}}$, s_0 is a steady flow shape factor and q^2 is tortuosity,

defined as the square of the increase in path length per unit thickness of material due to deviations of the steady-flow path from a straight line.

The bulk propagation constant ($k(\omega)$) and relative characteristic impedance ($Z_c(\omega)$) of the bulk porous material may be calculated from¹

$$k(\omega) = \omega[(q^2)\rho(\omega)C(\omega)]^{0.5} \quad (7)$$

$$Z_c(\omega) = (\rho c)^{-1} [(q^2/\Omega^2)\rho(\omega)/C(\omega)]^{0.5} \quad (8)$$

There are various published methods that allow for arbitrarily-shaped pores. Attenborough [11] scales the complex density function directly between pore shapes and introduces an adjustable dynamic pore shape parameter (s_A). For example, the bulk complex density function for arbitrarily-shaped pores is given by [9]

$$\rho_b(\lambda) = (q^2/\Omega)\rho_0[1 - \tanh(\lambda\sqrt{-i})/(\lambda\sqrt{-i})]^{-1} \quad (9)$$

where

$$\lambda = s_A \left(\frac{3\rho_0 \omega q^2}{\Omega R_s} \right)^{1/2}$$

$s_A = 1$ for slit-like pores and $0.745 < s_A < 1$ for pore shapes varying between equilateral triangles and slits. If circular cylindrical pore shapes are used as the basis, then the dimensionless parameter may be written

$$\lambda = s_A \left(\frac{8\rho_f \omega q^2}{\Omega R_s} \right)^{1/2}$$

This formulation retains explicit dependence on s_A even in the low frequency limit.

Champoux and Stinson [7] have pointed out that to satisfy the correct limiting behaviour for the complex density, in particular that $-i\omega\rho_b \rightarrow R_s$ as ω tends to zero, this method requires s_A to be frequency-dependent.

Their method of allowing for arbitrary pore shape is closer to that originally suggested by Biot [12] and the resulting pore shape parameter (s_B) has the advantage of being frequency-independent. Using this approach, with reference to the functions for slit-like pores, we write the complex density for the bulk material as

¹Equation (3.8) implies that the bulk compressibility $C_b(\omega) = \Omega C(\omega)$

$$\rho_b(\lambda) = (q^2/\Omega)\rho_0 + \frac{iR_s}{\omega}F_s(\lambda) \quad (10)$$

where

$$F_s(\lambda) = \frac{1}{3} \frac{(\lambda\sqrt{-i}) \tanh(\lambda\sqrt{-i})}{[1 - \tanh(\lambda\sqrt{-i})/(\lambda\sqrt{-i})]} \quad (11)$$

$$\lambda = s_B \left(\frac{3\rho_0\omega q^2}{\Omega R_s} \right)^{1/2}$$

and $1 < s_B < 1.342$ for pore shapes varying from slits to equilateral triangles. This approach scales the viscosity correction or dynamic viscosity function $F(\lambda)$ instead of the complex density function. Since $F(\lambda)$ tends to unity in the low frequency limit this method of defining $\rho_b(\lambda)$ does not have any explicit dependence on a dynamic pore shape factor. In the low frequency limit, the dependence on pore shape is only that implicit in the flow resistivity.

For a given bulk flow resistivity, porosity and tortuosity, the complex density and complex compressibility, calculated from (5) and (6) are found to depend on pore shape. However the complex bulk propagation constant, complex characteristic impedance and corresponding surface impedance of a hard-backed layer, are predicted to be relatively insensitive to pore shape [9]. This is true particularly for low flow resistivities and frequencies less than a few thousand Hz.

Other microstructural factors of significance in pore-based modeling are the variation of pore cross-sections along their lengths and the associated distributions of pore sizes and shapes. To allow simultaneously for arbitrary pore shapes and for pore cross-sections that change along their lengths, Johnson *et al* [13] interpret $1/H(\lambda)$ as a dynamic tortuosity and introduce two characteristic lengths. In effect, the characteristic lengths introduce two 'dynamic' pore shape factors s_p (equivalent to s_B) and s_C into complex density and complex compressibility respectively. The need for two shape factors may be argued from the fact that the wider parts of each pore tend to be more important for the complex compressibility while the narrower pore cross-sections dominate the complex density. This formulation has been adopted by Allard *et al.* [8].

A method of allowing for a log-normal pore size distribution, while assuming pores of identical (slit-like) shape has been developed by Attenborough [9] based on the work of Yamamoto and Turgut [14].

Several authors have considered the surface impedance of a high flow resistivity rigid porous medium in which the porosity decreases exponentially with depth [15-18]. The most rigorous approximation for a high flow resistivity surface [16] is

$$Z = \frac{1+i}{\sqrt{\pi}\rho_0} \sqrt{\frac{R_s}{f}} + \frac{ic_0\alpha_r}{8\pi f} \quad (12),$$

where $\alpha_e = (n' + 2)\alpha/\Omega$, where n' is a grain shape factor such that the tortuosity is given by $\Omega^{-n'}$.

This implies that $X > R$ (as long as α_e is positive), and may be written generically in the form

$$Z = a(1+i)\sqrt{\frac{R_e}{f} + \frac{ib\alpha_e}{f}} \quad (13),$$

where $a = 1/\sqrt{\pi\rho_0\gamma}$ and $b = c_0/8\pi\gamma$. For a non-hard backed thin layer, $\alpha_e = 4/d_e$.

An approximation for the surface impedance of a high flow resistivity porous medium with the porosity *increasing* exponentially with depth is given by (3.32) with negative α_e .

If α_e is negative then (3.32) predicts a resistance that exceeds the reactance at all frequencies.

An improved approximation at high frequencies may be written either [19]

$$\begin{aligned} Z &= Z_e + \frac{ic_0\alpha_e}{8\pi\gamma f} \\ &= \frac{1}{\sqrt{\pi\gamma\rho}}(1+i)\sqrt{\frac{R_e}{f}} + \frac{1}{3}\sqrt{\frac{\pi\rho}{\gamma}}(1-i)T_e\sqrt{\frac{f}{R_e} + \frac{ic_0}{8\pi\gamma}\frac{\alpha_e}{f}} \end{aligned} \quad (14)$$

$$\text{or} \quad Z = \frac{1}{\sqrt{\pi\gamma\rho}}(1+i)\sqrt{\frac{R'_e}{f}} + \sqrt{\frac{\pi\rho}{\gamma}}(1-i)T_e\sqrt{\frac{f}{R'_e} + \frac{ic_0}{8\pi\gamma}\frac{\alpha_e}{f}} \quad (15)$$

where $R'_e = \frac{R_e}{4\Omega}$. Note that R_e and R'_e are identical if $s_p = 0.5$.

These introduce a third parameter $T_e = T/\Omega^2$ which depends on the tortuosity and porosity and influences the high frequency values of the impedance.

By viewing the viscous and thermal diffusion in porous materials as a relaxation process, Wilson [20 – 22] has obtained models for the acoustical properties of porous materials in simple forms that, nevertheless, enable accurate predictions over wide frequency ranges. His results may be expressed as

$$Z = \frac{\sqrt{T}}{\Omega} \left[\left(1 + \frac{\gamma-1}{\sqrt{1-i\omega\tau_e}} \right) \left(1 - \frac{1}{\sqrt{1-i\omega\tau_e}} \right) \right]^{-1/2} \quad (16)$$

$$k = \frac{\omega\sqrt{T}}{c_0} \left[\left(1 + \frac{\gamma-1}{\sqrt{1-i\omega\tau_e}} \right) \left(1 - \frac{1}{\sqrt{1-i\omega\tau_e}} \right) \right]^{1/2} \quad (17)$$

where, for identical uniform pores, τ_e and τ_v , the thermodynamic and aerodynamic characteristic times respectively, are given by

$$\tau_e = 2\rho_0 T / \Omega R, \quad (18)$$

$$\text{and} \quad \tau_v = N_{PK} s_b^2 \tau_e, \quad (19).$$

Essentially this represents a single parameter model for a given pore shape, flow resistivity and porosity.

For materials in which the pore cross sections vary, Wilson has suggested a slightly more complicated form, in which $\sqrt{1-i\omega\tau_e}$ and $\sqrt{1-i\omega\tau_v}$ are replaced by $\sqrt{1 + \frac{\tau_e}{\tau_v} \left(\sqrt{1-i\omega\tau_e} / \tau_e - 1 \right)}$

where τ_l and τ_h are appropriate low- and high-frequency versions of τ_e and τ_v . He has shown that results equivalent to the Johnson/Allard model may be obtained with $\tau_{kr} = \tau_{kr} = N_{pk} s_k^{-2} \tau_v$, and $\tau_{kr} = s_p^{-2} \tau_{kr} = 2\rho_0 T / \Omega R_i$. In its most general form this represents a four- or five- parameter model.

3. Comparisons with impedance and short range propagation data

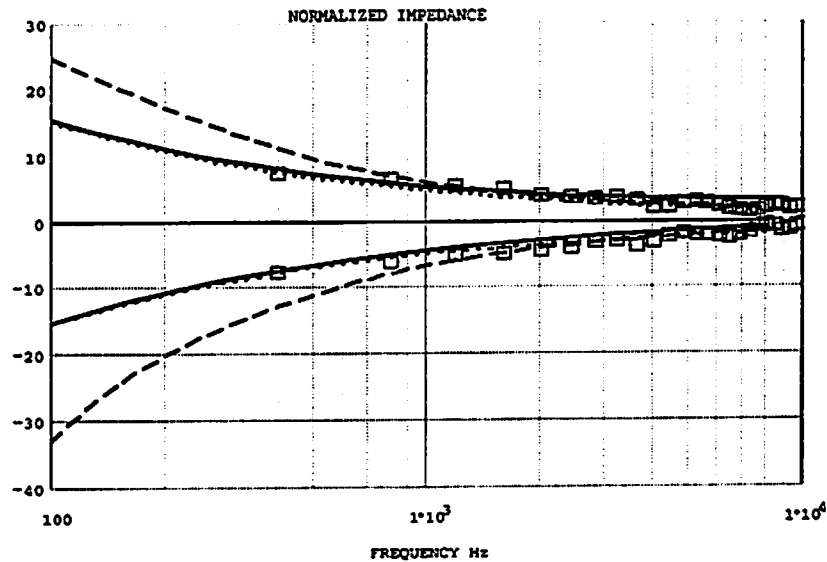


Figure 1 Impedance of compacted soil measured by Cramond and Don [3.65] and predictions using equation (2) with effective flow resistivity 450 kPa s m^{-2} (broken lines), equations (8) and (9), and equation (16) (solid lines) with flow resistivity 200 kPa s m^{-2} , porosity 0.4 and tortuosity 1.5.

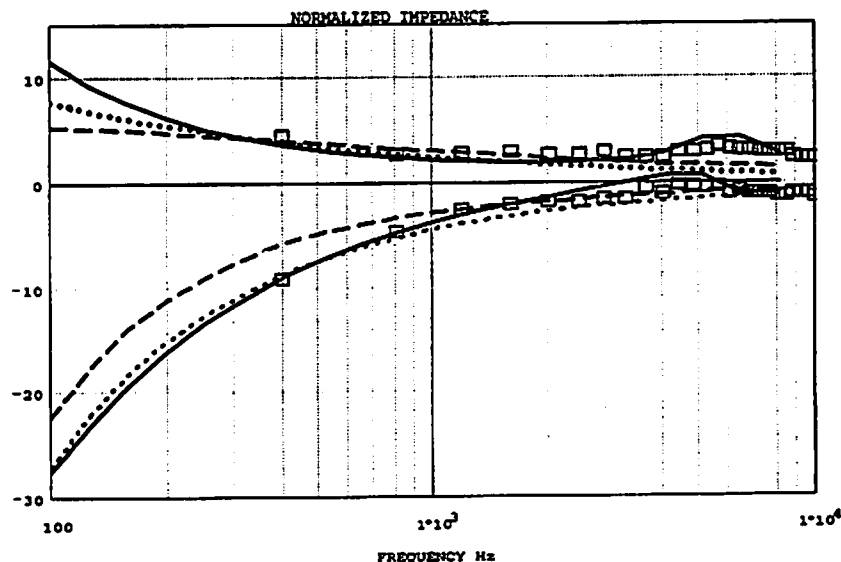


Figure 2 Impedance of loosened soil (0.02 m thick) above compacted soil measured by Cramond and Don [37] and predictions using equation (2) with effective flow resistivity 450 kPa s m^{-2} (broken lines), equations (3), (8) and (11) (solid lines), with upper layer flow resistivity 50 kPa s m^{-2} , porosity 0.4, tortuosity 1.5 and thickness 0.02 m; substrate flow resistivity 800 kPa s m^{-2} , porosity 0.2 and tortuosity 3 and equation (12) (dotted lines) in which $R_e = 31.2 \text{ kPa s m}^{-2}$ and $\alpha_e = 200 \text{ m}^{-1}$.

Example results of the pulse method used by Cramond and Don are shown in Figures 1 and 2 together with predictions obtained from the semi-empirical model due to Delany and Bazley (equations (2)), and pore-based models (equations (3), (5), (6), (8) and (16)-(19)). The data are for compacted earth and the same soil with the top 0.02 m loosened. There are significant differences between the measured impedances of compacted and loose soil. Although it is possible to obtain reasonable fits with the semi-empirical model in both cases, improved agreement is possible with models based on an assumed slit-pore microstructure.

The dotted lines represent predictions of the relaxation model with $s_b = 1$. The dashed lines represent predictions of the Hamet-Berengier phenomenological model and the dash-dot lines represent predictions of the Delany-Bazley model with effective flow resistivity given by the product of measured flow resistivity and porosity.

Figure 3 Shows impedance data for a hard-backed sample of snow obtained in an impedance tube by Buser [36]. The measured flow resistivity and bulk density of this sample were 9.6 kPa s m^{-2} and 208 kg m^{-3} respectively. Assuming an ice density of 913 kg m^{-3} , the latter value corresponds to a porosity of 0.774. The continuous lines in Figure 3 correspond to predictions of an identical slit-pore model with tortuosity equal to inverse porosity.

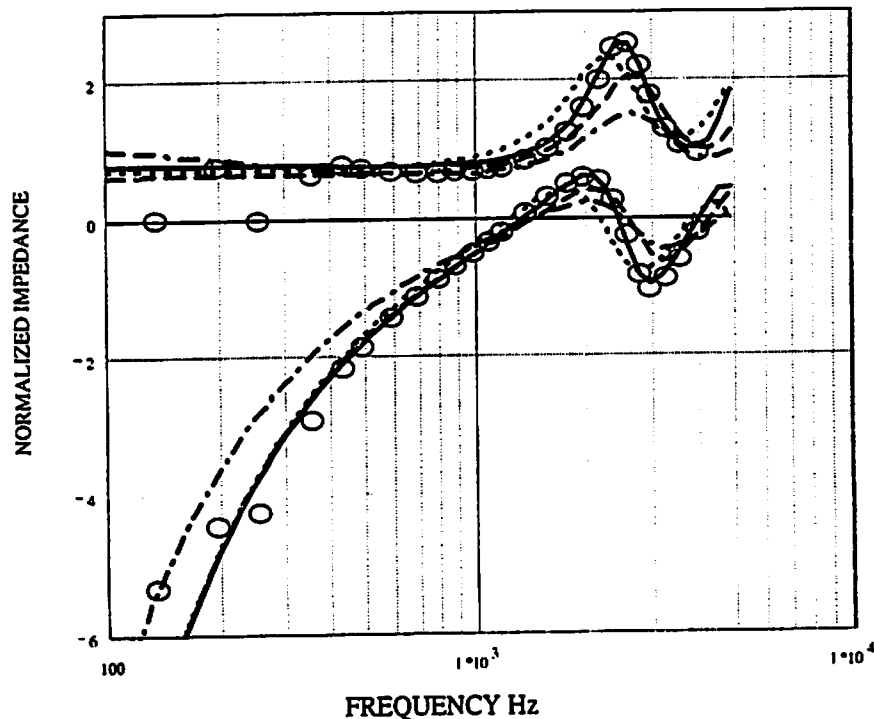


Figure 3 Measured and predicted impedance of a 0.05 m thick layer of snow with measured flow resistivity 9.6 kPa s m^{-2} and porosity 0.774 [36]. Predictions use identical slit pore model with measured flow resistivity and porosity and tortuosity = $1/\text{porosity}$ (solid lines), Hamet-Berengier (dashed), Wilson-relaxation (dotted) and Delany-Bazley (dash-dot) with $\text{Re} = \Omega R_s$.

The predictions of the relaxation model can be improved by adjusting the value of s_b (1.4 gives better agreement with data). However it should be noted that this removes one of its advantages as a simple model. Moreover the slit-pore predictions are obtained without

any adjustment apart from the assumption that tortuosity is given by the inverse of porosity. It is noticeable that the Delany-Bazley model gives relatively poor predictions for these data.

Figure 4 shows measurements [23] and predictions of the spectrum of the level difference between vertically-separated microphones 1 m from a point source over a dry flat silt soil (at Pendleton, Oregon).

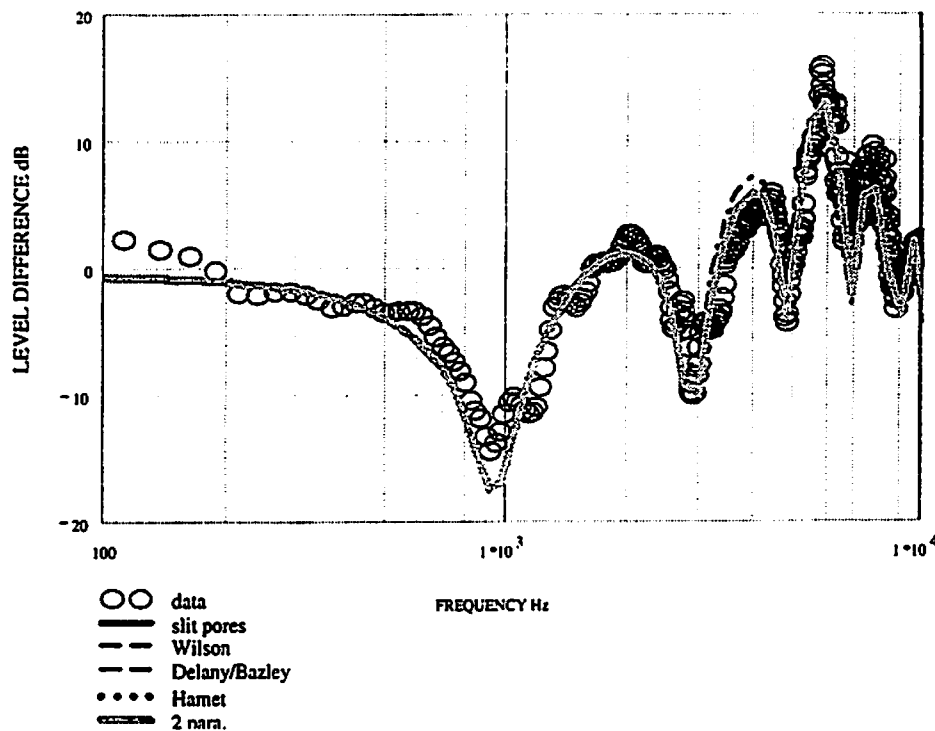


Figure 4 The spectrum of the difference in levels between two microphones at 0.288m and 0.0385m due to a point source at 0.3285m height and separated by a horizontal distance of 1 m over a dry flat silt soil and predictions of the various impedance models cited in the legend.

4. Impedance measurement by excess attenuation fitting

A method of deducing impedance from excess attenuation or level difference spectra has been proposed based on two-dimensional minimization of the difference between data and theory at each frequency [24]. The first step is to calculate the spherical reflection coefficient (Q) from measured excess attenuation spectra at short ranges. The next step is to search for a theoretical value of the impedance that best fits the measured Q at each frequency point. This requires considerable computation and is rather inefficient. An alternative numerical method uses root-finding [25] and takes advantage of the fact that the classical approximation to the spherical wave reflection coefficient is an analytic function of the impedance. The resulting saving in computation time can be up to a hundred-fold without any loss in accuracy. Figures 5 and 6 show examples of impedances obtained in this way from (complex) excess attenuation data over two different grass covered surfaces and over a mixed woodland floor with and without leaf litter.

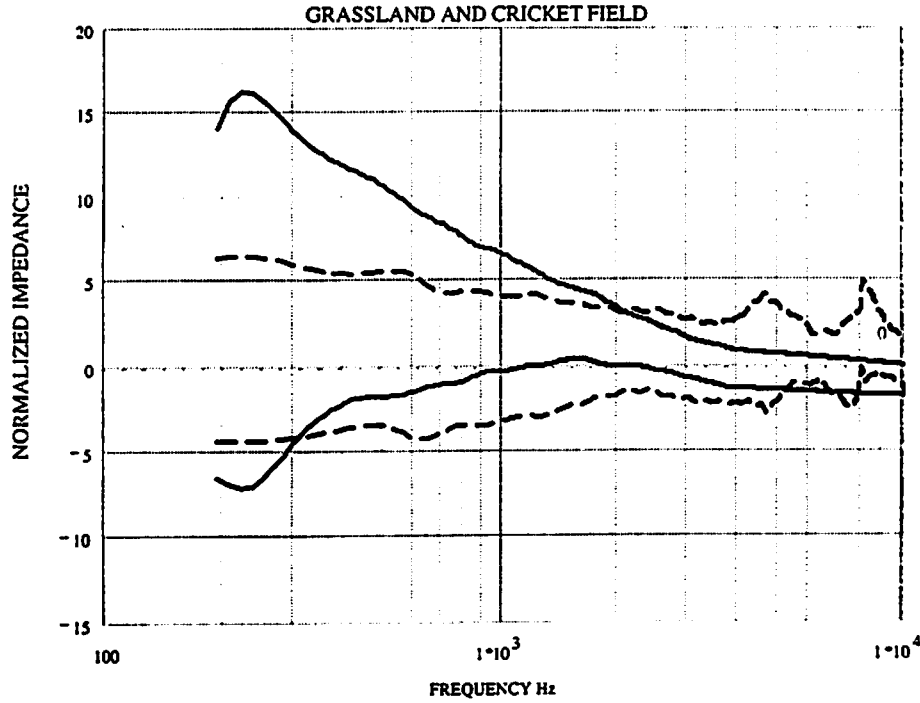


Figure 5 Impedances deduced by root-finding from (complex) excess attenuation measurements using short-range geometries over farm grassland (solid lines) and a carefully-maintained cricket field (broken lines).

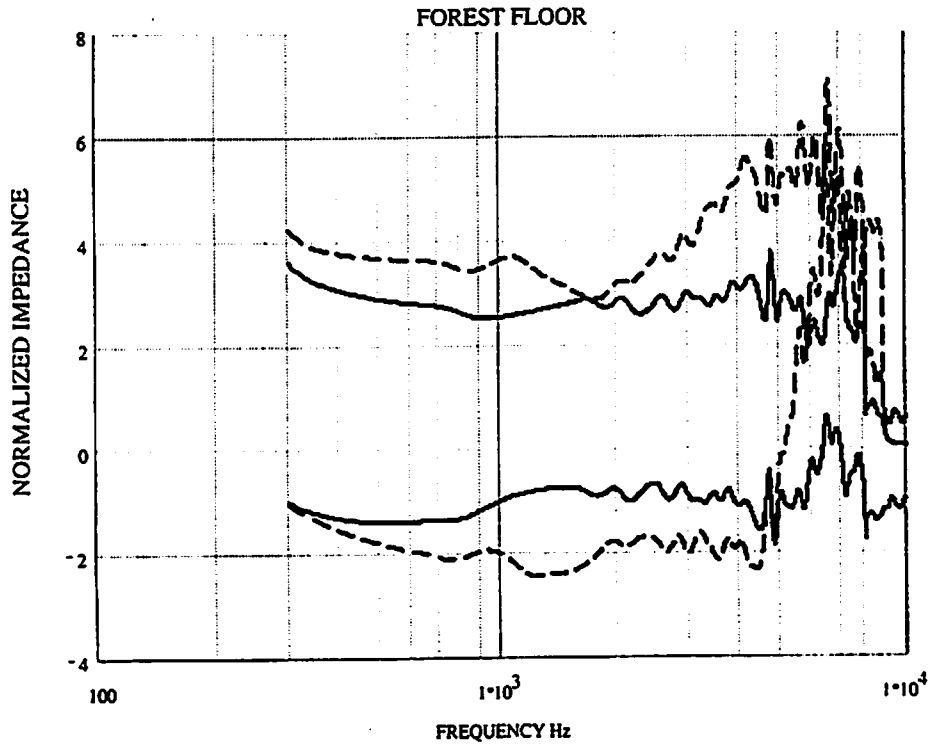


Figure 6 Impedances of a mixed woodland floor deduced from (complex) excess attenuation measured at short range (1 m) with source and microphone heights 0.1 m with (solid lines) and without (broken lines) the litter layer.

5. Models for effects of surface roughness

As well as being porous many outdoor surfaces are rough. Surface roughness scatters the sound coherently and incoherently. The relative strengths of the coherent and incoherent parts of the scattered energy depend on the mean size of the roughness. On disked soil, the roughness is small compared to the wavelengths of sound for the frequency range of interest (100 Hz – 2000 Hz). Such roughness may be described as small-scale and gives rise to mainly coherent scattering. The impedance or admittance of the boundary is modified by the presence of small-scale roughness. This can be considered to have an influence on the (spherical-wave) reflection coefficient and hence the ground effect [26]. However once the roughness size approaches the wavelengths of interest, incoherent scattering dominates and ground effect is reduced.

Twersky has developed a boss model [27-31] to describe coherent reflection from a hard surface containing semi-cylindrical roughnesses in which the contributions of the scatterers are summed to obtain the total scattered field. Sparse and closely-packed distributions of bosses have been considered and interaction between neighbor scatterers has been included. His results lead to a real part of the effective admittance of the rough hard surface which may be attributed to incoherent scattering. Consider a plane wave incident on an array of semi-cylinders of radius a and mean center-to-center spacing b on an otherwise plane hard boundary. Denote the angle of incidence with respect to the normal by α and the azimuthal angle between the wave vector and the roughness axes by φ . Twersky's results for the effective relative admittance β of a rough *hard* surface containing non-periodically-spaced 2-D circular semi-cylinders are [32]

$$\beta = \eta - i\xi. \quad (20)$$

with

$$\xi(\alpha, \varphi) = kV \left[-1 + (\delta \cos^2(\varphi) + \sin^2(\varphi)) \sin^2(\alpha) \right] + O(k^3) \quad (21)$$

$$\eta(\alpha, \varphi) = \frac{nk^3\pi^2a^4}{8}(1-W^2) \left\{ \left[1 - \sin^2\alpha \sin^2\varphi \right] \left[1 + \left(\frac{\delta^2}{2} \cos^2\varphi - \sin^2\varphi \right) \sin^2\alpha \right] \right\} + O(k^5). \quad (22)$$

$V = n\pi a^2/2$ is the raised cross sectional area per unit length, n is the number of semi-cylinders per unit length ($= 1/b$), $\delta = \frac{2}{1+I}$ is a measure of the dipole coupling between the

semi-cylinders, $I = \frac{a^2}{b^2} I_1$, where

$$I_1 \cong 2W(1 + 0.307W + 0.137W^2) \quad \text{for } W < 0.8,$$

$$I_1 \cong \frac{\pi^2}{3} \left[1 - \frac{2(1-W)}{W} \right] + 6 \frac{(1-W)^2}{W^2} \left[\frac{\pi^2}{6} + 1.202 \right] \quad \text{for } W \geq 0.8$$

$$I \cong \frac{(\pi a)^2}{3b^2} \quad \text{for } W = 1 \text{ (periodic),}$$

$(1-W)^2$ is a packing factor introduced for random distributions, $W = nb^* = \frac{b^*}{b}$, b^* is the minimum (center to center) separation between two cylinders and k is the wave number.

The real part η of the admittance (which represents the incoherent scattering) is zero only for periodic distributions of bosses. For grazing incidence normal to the

cylinder axes, $\alpha = \pi/2$ and azimuthal angle $\varphi = 0$ we obtain the effective admittance of a rough hard boundary containing 2-D roughness as

$$\beta = \frac{na^2k}{2} \left((1-W^2) \frac{(1+\delta^2/2)k^2\pi^2a^2}{4} - i\pi(\delta-1) \right) \quad (23).$$

According to Lucas and Twersky [31], for semi-elliptical cylinders with eccentricity K , so that $V = n\pi a^2 K/2$,

$$\delta = \frac{1+K}{1+I \frac{K(1+K)}{2}}. \quad (24)$$

Twersky's cylindrical boss theory may be generalized to scatterers of arbitrary shape by comparison with equivalent results from Tolstoy's work. Equations (20) to (24) may be contrasted with the equivalent results from Tolstoy's boss theory [33] for the effective admittance of a surface containing 2-D roughnesses of arbitrary shape, after correcting his expression for a missing coefficient σ : According to Tolstoy,

$$\beta = -ik\varepsilon(\cos^2\varphi - \sigma \cos^2\alpha), \quad (25)$$

where

$$\varepsilon = V \left(\frac{2s_2}{v_2} - 1 \right), \quad \sigma = \left(\frac{2s_2}{v_2} - 1 \right)^{-1}, \quad (26)$$

$s_2 = \frac{1}{2}(1+K)$ is a shape factor, K is a hydrodynamic factor depending on steady flow around a scatterer, $v_2 = 1 + \frac{2\pi V s_2}{3b}$ is a scatterer interaction factor, and V is the cross-sectional scatterer area above the plane per unit length. Values of K are known for various shapes [26]. Twersky's and Tolstoy's expressions for the imaginary part of the effective admittance are equivalent for circular semi-cylinders if δ is replaced by $\frac{\varepsilon}{V} + 1 = \frac{2s_2}{v_2}$. By comparing their results [32] it is possible to generalize (22) to give

$$\eta(\alpha, \varphi) = \frac{k^2 b V^2}{2} (1-W^2) \left\{ (1 - \sin^2\alpha \sin^2\varphi) \left[1 + \left(\frac{\delta^2}{2} \cos^2\varphi - \sin^2\varphi \right) \sin^2\alpha \right] \right\} + O(k^2) \quad (27),$$

where V represents the scatterer volume per unit area (raised area per unit length in 2-D). These results allow predictions of propagation over bosses of the various shapes for which K is known. In addition to the known values for semi-cylinders, semi-ellipsoids and triangular wedges, K for thin slats may be deduced by assuming that each slat affects the fluid flow as if it were a lamina [34]. The expression for the virtual mass of a lamina of width $2a$ is identical to the one for a cylinder of radius a i.e. $K = 1$. Equations (20), (21) and (27) have been shown to give tolerable agreement with laboratory data over rough hard boundaries, although predictions of a boundary element code have been more successful [32].

Tolstoy has considered sound propagation at the rough interface between two fluids [33] and hence allows predictions of propagation over a rough impedance boundary [26]. Consider the general case involving a planar distribution of small fluid scatterers, N per unit area, embedded in a fluid half-space with density and sound speed ρ_3 and c_3 beneath a fluid half-space characterized by ρ_1 and c_1 . The scatterers have

density ρ_2 and c_2 , height h , centre-to-centre spacing l and occupy a total volume σ_v above the plane.

where

If $\rho_1 \ll \rho_2$ and $c_1 < c_2$, or $\rho_2 = \rho_1$ and $c_2 = c_1$, and for 2-D scatterers, the effective admittance is given by

$$\beta_2^* = -ik \cos^2(\vartheta) \epsilon_{12}^* + \beta_s \quad (28),$$

where β_s represents the impedance of the imbedding plane,

$$\begin{aligned} \epsilon_{12}^* &= a_{12}^* - b_{12}^*, \quad a_{12}^* = 2\sigma_v \left[\frac{\rho_2 - \rho_1}{\rho_2 + \rho_1} \right] \frac{s_{2D}}{v_{12}^*}, \\ b_{12}^* &= \sigma_v (1 - m_2 / m_1) \\ v_{12}^* &= 1 + \frac{\pi^2 h^2}{3 l^2} \frac{\rho_2 - \rho_1}{\rho_2 + \rho_1} s_2 \\ s_{2D} &= \frac{\rho_1 + \rho_2}{\rho_2 + K\rho_1} s_2, \quad v_{2D} = 1 + \frac{2\pi\sigma_v}{3Nl^2} \left[\frac{\rho_2 - \rho_1}{\rho_2 + \rho_1} \right] s_{2D} \end{aligned} \quad (29)$$

and $\theta (= \pi/2 - \varphi)$ is the angle between the source-receiver axis and the normal to the scatterer axis.

If the embedding material and scatterers are rigid and porous then they can be treated acoustically as if they are fluids but with complex densities and sound speeds. These complex quantities may be calculated from any of the models described in the previous section.

If $|\rho_2| \gg \rho_1$, $s_2 = s_3 = v_2 = v_3 = 1$, equations (28) and (29) may be approximated by

$$\beta_2^* = -ik \cos^2(\theta) \sigma_v + \beta_s (1 - ik_s \sigma_v) \quad (30),$$

where k_s is the complex wave number within the lower half-space (i.e. the imbedding material).

As remarked earlier, Tolstoy's results for hard rough surfaces ignore incoherent scatter. It is a straightforward heuristic extension to write the effective surface admittance of a porous surface containing sparse 2-D roughnesses as

$$\beta_2^* = \eta - ik \cos^2(\theta) \sigma_v + \beta_s (1 - ik_s \sigma_v) \quad (31)$$

where η is given by (27), $\delta = (2s_2/v_2)$, s_2 and v_2 are calculated from (29).

Figure 7 shows predictions of the change in the effective surface impedance of a porous material consisting of identical triangular pores with increasing semi-cylindrical roughness (including incoherent scatter). Figure 8 shows that the predicted normalised surface impedance of a rough porous surface may be approximated by that predicted by formula (2) with an effective flow resistivity given by $0.8 \times$ the actual flow resistivity. Also shown in Figure 8 are predictions of the formula

$$Z_r = Z_s - \left(\frac{2\sigma_v R_s}{\gamma \rho_0 c_0} \right) \left(\frac{2}{v} - 1 \right) \quad (32).$$

Results such as those shown in Fig. 8 may indicate why equation (2) has been successful in modelling the impedance of outdoor ground surfaces. The predictions using Equation (32) suggest that the effective normalised impedance of a rough surface is that of the smooth surface but with a reduced real part.

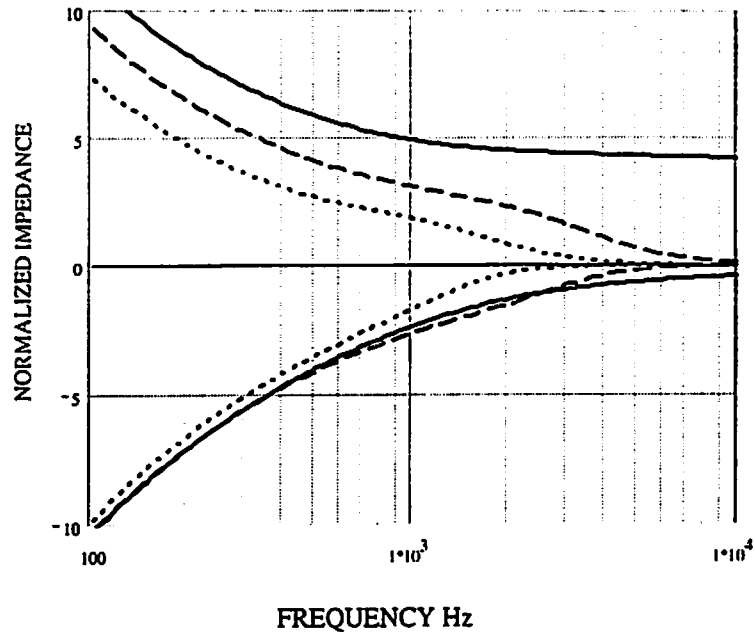


Figure 7 Predicted influence on the effective normalised surface impedance of increasing the surface roughness of a porous material containing identical triangular pores with flow resistivity 200 kPa s m^{-2} , porosity 0.4, tortuosity 2.5. The predicted normalised surface impedance of the smooth surface is represented by the solid lines. The dashed lines represent the predicted result of adding 5/m 0.02 m radius semi-cylinders of the same material. The dotted lines show the predicted result of adding 20/m 0.02 m radius roughnesses.

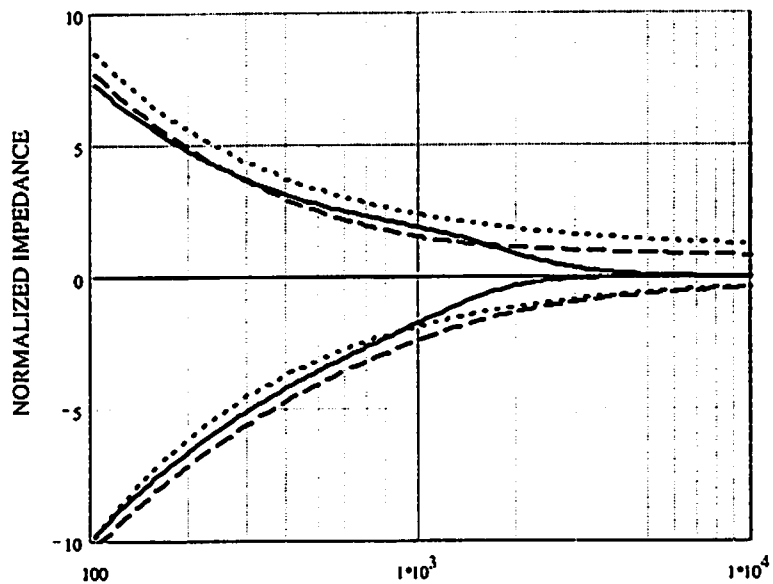


Figure 8 Solid lines represent the predicted normalised surface impedance of porous surface as in Fig. 3.5 with 20/m semi-cylindrical roughness. The dotted lines represent the result predicted by equation (3.2) with $R_{sr} = 0.8 \times$ the actual flow resistivity. The dashed lines are predictions of equation (3.57).

For high flow resistivities and low frequencies, $\beta_s k_s \approx \gamma \Omega$. If the same approximations that produce (30) apply, and if it is assumed that $\alpha = 0$ (grazing-incidence) and $\theta = 0$, then $\eta = \frac{3\sigma_v^2 k^3 b}{4}(1 - W^2)$ and (31) may be written

$$\beta_2^* = -i\sigma_v(k + \gamma\Omega) + \frac{3\sigma_v^2 k^3 b}{4}(1 - W^2) + \beta_s. \quad (33)$$

This might be a basis for the acoustic determination of roughness in some circumstances.

5. Measurements of roughness effects outdoors

Data reported by Aylor [35] in 1971 demonstrates a considerable change in excess attenuation over approximately 50 m range after disking a soil and without any significant change in meteorological conditions. More recent short range level difference measurements by Rickman [23] show significant differences between dry, wet and ploughed conditions in a silt soil. These data are shown in Figure 9

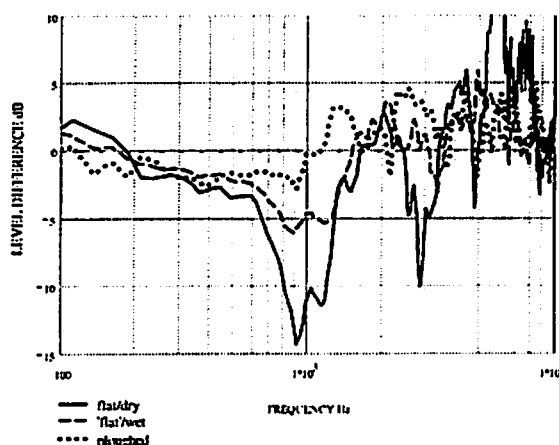


Figure 9 The spectrum of the difference between vertically-separated microphones at a range of 1 m from a source situated approximately 0.3 m above a silt soil surface when dry (solid line), after rain and with visible roughness (broken line) and subsequent to ploughing (dotted line). The source heights are 0.3285, 0.29 and 0.356 m respectively and the microphone heights are (0.288m, 0.0385m); (0.27m, 0.04m) and (0.38m, 0.039m) respectively.

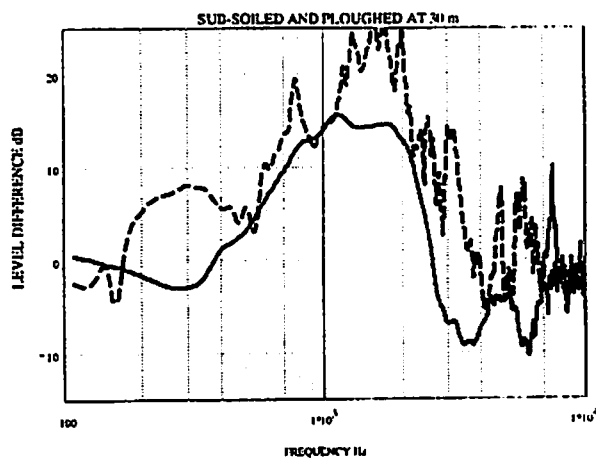


Figure 10 Level difference spectra obtained at a horizontal range of 30 m from a 1.65 m high source with microphones at 1 m and 0.1 m height over sub-soiled (solid line) and ploughed (broken line) clay soil.

Other level difference data obtained recently over sub-soiled and ploughed clay soils [38] show considerable changes in acoustic propagation (see Figure 10). The short range level difference data in Figure 9 are fitted to some extent by assuming reduced flow resistivity (see Figure 11).

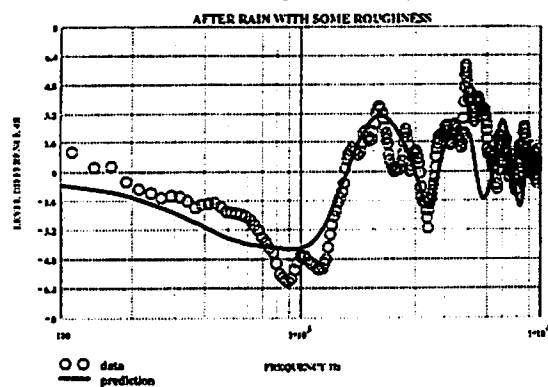


Figure 11(a) Measured and predicted level difference spectra over wet silt soil. Predictions use the identical slit pore hard-backed layer model with flow resistivity 55 kPa s m^{-2} , tortuosity = $1/\text{porosity}$, porosity 0.44 and thickness 0.063 m.

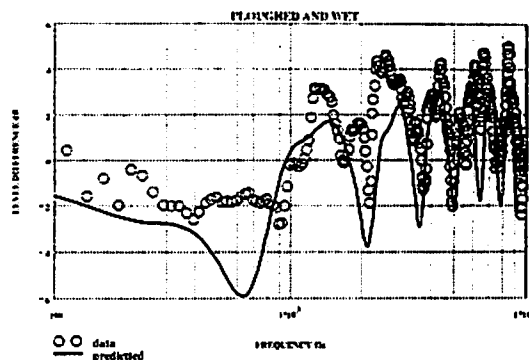


Figure 11(b) Measured and predicted level difference spectra over wet silt soil. Predictions use the identical slit pore hard-backed layer model with flow resistivity 20 kPa s m^{-2} , tortuosity = $1/\text{porosity}$, porosity 0.44 and thickness 0.15 m.

On the other hand (see Figure 12)) a combination of reduced resistivity and roughness (through equation (33)) has proved to be tolerably successful in predicting the longer range data shown in Figure 10.

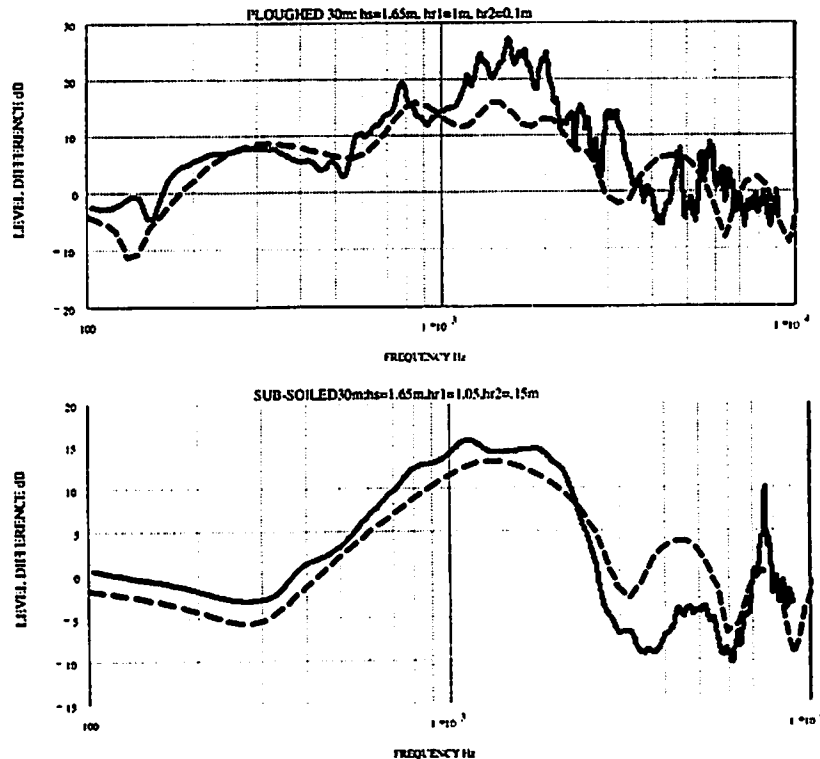


Figure 12 Data from Figure 10 for ploughed and sub-soiled clay soils and predictions using slit pores; flow resistivities 8 and 80 kPa s m^{-2} , porosities 0.5 and 0.4; thicknesses 0.175 and 0.08 m; roughness volumes 0.06 and 0.07 m^3 , respectively

6. Concluding remarks

Recent developments in modeling the acoustical properties of rigid porous materials and of rough surfaces together with impedance data and short-range propagation data have been reviewed. A root-finding algorithm offers a convenient method for deducing surface impedance from short-range propagation data. Both data and predictions indicate that surface treatments have a significant influence on propagation. Comparisons of predictions and data indicate that there can be some confidence in the models. However further work is needed to enable prediction of roughness effects.

Acknowledgements

This work was supported by BBSRC and EPSRC (UK) through grants CTE 02649 and GR/L15326.

References

- 1 M.E. Delany and E.N. Bazley *Applied Acoustics* 3 105-116 (1970)
- 2 Delany and Bazley *NPL Report* (1970)
- 3 K.B. Rasmussen, *J. Sound Vib.* 78 (2) 247-255 (1981)
- 4 M.C. Berengier, M.R. Stinson, G.A. Daigle and J.F. Hamet, *J. Acoust. Soc. Am.*, 101 155-162 (1997)
- 5 P.M. Morse and K.U. Ingard, *Theoretical Acoustics*, New York,
- 6 M.R. Stinson, *J. Acoust. Soc. Am.* 89 (1) 550-558, 1991
- 7 Y. Champoux and M.R. Stinson, *J. Acoust. Soc. Am.* 92 (2) 1120-1131 (1992)
- 8 J.F. Allard, *Propagation of sound in porous media*, Elsevier Applied Science, London 1993
- 9 K. Attenborough, *Acta Acustica* 1, 213-226 (1993)
- 10 P.C. Carman, *Flow of gases through porous media* Butterworths, London, 1953
- 11 K. Attenborough, *J. Acoust. Soc. Am.*, (1992)
- 12 M.A. Biot, *J. Acoust. Soc. Am.* 28 168-191 (1956)
- 13 D.L. Johnson, J. Koplik, and R. Dashen, *J. Fluid Mechanics*, 176 379-402 (1987)
- 14 T. Yamamoto and A. Turgut, *J. Acoust. Soc. Am.*, 83 (5) 1744-1751, (1988)
- 15 K. Attenborough, *J. Acoust. Soc. Am.* 92 418-427 (1992); see also R. Raspet and K. Attenborough, *J. Acoust. Soc. Am.* 92 3007 (1992)
- 16 R. Raspet and J.M. Sabatier, *J. Acoust. Soc. Am.*, 99(1) 147 - 152 (1996)
- 17 Donato 'Impedance models for grass-covered surfaces' *J. Acoust. Soc. Am.*, (1976)
- 18 K. Attenborough, *J. Sound Vib.*, 99 521-544 (1985)
- 19 S. Taherzadeh, Private Communication (1997)
- 20 Wilson, D.K. *J. Acoust. Soc. Am.* 94 1136-1145 (1993)
- 21 Wilson, D.K., *Applied Acoustics* XX (1997)
- 22 Wilson, D.K., *Proc. NOISE-CON 97*, Pennsylvania State University, 85-90 (1997)
- 23 R. Rickman (private communication, August 1998)
- 24 C. Nocke, V. Mellert, T. Waters-Fuller, K. Attenborough, and K.M. Li, *Acustica*, 83 1085-1090 (1997).
- 25 S. Taherzadeh, K. Attenborough and K.M. Li "Deduction of ground impedance from excess attenuation data", accepted for publication in *J. Acoust. Soc. Am.*
- 26 K. Attenborough and S. Taherzadeh, *J. Acoust. Soc. Am.*, 98(3) 1717-22 (1995)
- 27 V.F. Twersky, *J. Acoust. Soc. Amer.* 29 209-225 (1957)
- 28 V. Twersky, *J. Acoust. Soc. Am.* 40, 883-895 (1966).
- 29 V. Twersky, *J. Acoust. Soc. Am.* 73, 68-84 (1983)
- 30 V. Twersky, *J. Acoust. Soc. Am.* 73, 85-94 (1983).
- 31 R. J. Lucas and V. Twersky, *J. Acoust. Soc. Am.* 76, 1847-1863 (1984).
- 32 P.M. Boulanger, K. Attenborough, T. Waters-Fuller and K.M. Li, "Rough hard boundary ground effects", *J. Acoust. Soc. Am.* (in press).
- 33 I. Tolstoy, *J. Acoust. Soc. Am.* 72 (3) 960 - 972 (1982)
- 34 H. Lamb *Hydrodynamics* Dover, New York (1945). p85
- 35 D. Aylor, *J. Acoust. Soc. Am.* 51 (1) 197-205 (1971).
- 36 O. Buser, *J. Sound Vib.* 111, 71-92 (1986).
- 37 A.J. Cramond and C.G. Don, *J. Acoust. Soc. Am.* 77 382-389 (1984).
- 38 T. F. Waters-Fuller (private communication 1998).

Interpretation of Ground and Terrain Effects

The following text is extremely faint and largely illegible. It appears to be a series of paragraphs or a list of points, but the specific content cannot be discerned. The text is scattered across the page, with some lines appearing in the left margin and others in the main body. The overall appearance is that of a very low-quality scan of a document page.

Measurement of ground impedance with the level difference method

Mikael Ögren

SP Swedish National Testing and Research Institute, Box 857, S-501 15 Borås, Sweden

+46 33 16 54 25, Fax +46 33 13 83 81, mikael.ogren@sp.se

Introduction

The acoustical properties of the ground, or the ground impedance, can be found by making two or more simple propagation measurements. It is also possible to use some form of correlated measurements or short impulses, but such methods are generally more complex and expensive than propagation measurements. Nordtest (Nordic cooperation for standardization of measurement methods) has initiated a project which aims at developing a simple and useful method to measure the ground impedance, and this paper describes some of the experiences and conclusions reached during this project.

In the following text the harmonic time dependence is assumed to be $e^{-i\omega t}$.

The level difference method

To compare a propagation measurement with theoretical calculations, one has to know the sound power that our source emits and the distances involved. However, by using two microphones one can study the level difference between the two microphones, and thus avoid the need to know the sound power of the source. This is the fundamental idea behind the level difference method. To extract information of the ground surface from the measurements, one must compare them with some form of theoretical calculation. When an acceptable match has been achieved, the ground impedance can be extracted from the theoretical model.

The theoretical model must describe the sound propagation, but more importantly, it must describe how the ground impedance changes with frequency. The impedance model

$$Z = 1 + 9,08 \left(\frac{1000f}{\sigma} \right)^{-0.75} + i11,9 \left(\frac{1000f}{\sigma} \right)^{-0.73} \quad (1)$$

,first published in [1], is used for most of the calculations in this text for this purpose. The method in [2] is used to calculate the level differences from the geometrical situation and the impedance, including the effect of third octave band smoothing.

A typical level difference curve has a distinctive dip and a peak, see figure 1. These come from the interference between the direct and reflected rays, see the dotted and solid lines in figure 2, and they are changed in frequency location and shape by the ground impedance. Most of the information about the ground impedance can be found around the dip and the peak, so it is useful to have them spread out in frequency. When we use our impedance model to fit the theoretical curves to the measured ones, what we do is in principle to extrapolate the information obtained around the dip and the peak to lower and higher frequencies.

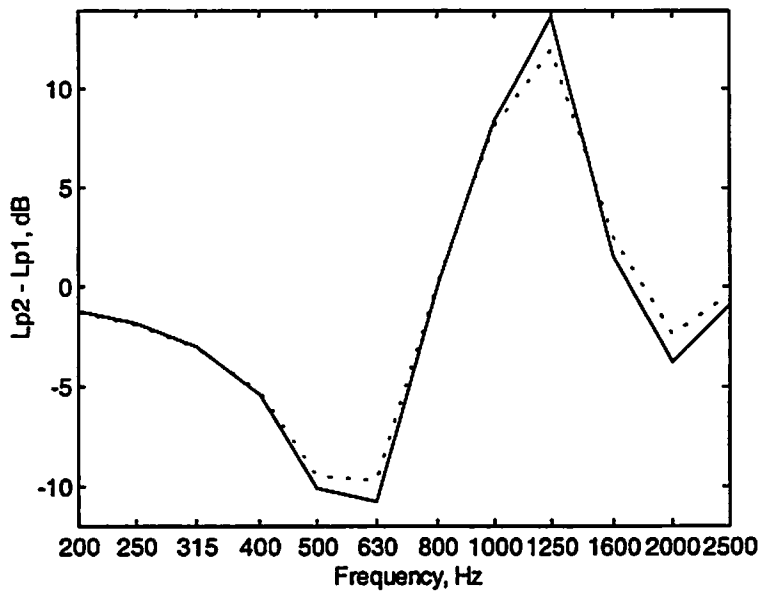


Figure 1
Level difference in
third octaves,
 $h_s=0.5$ m, $h_{r1}=0.2$ m,
 $h_{r2}=0.5$ m,
 $d=1.75$ m
 Solid - measured
 values
 Dotted - calculated
 values with
 $\sigma=400\,000$ (Ns/m⁴)

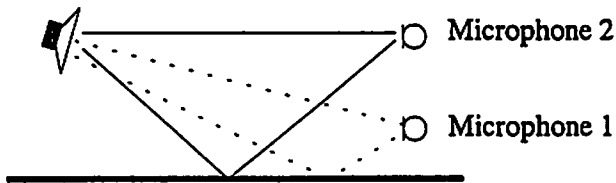


Figure 2
Measurement geometry
for the level difference
method

Method limitations

The level difference method has limitations and source of errors that can throw the unwary user off the track. One obvious limitation is, of course, that the theory must be valid. Some surfaces might not even be locally reacting and for other surfaces, the impedance model might not be valid. Typical surfaces that cause problems are snow and other layered surfaces. For the surfaces measured in this project the impedance model gave very good results, so for most ground types, and within a certain frequency range, the model seems to be accurate enough.

Another limitation is that the method is not well suited for hard surfaces. If the surface is very hard, the only change in the level difference in comparison to an infinitely hard surface is a small frequency shift of the dip and peak. If we use a third octave band analyzer this effect is hard to detect, but even if we use a narrow band analyzer, we have to know the geometry to an unrealistic precision in order to get a correct result.

Little or no information about the ground impedance can be extracted for very low frequencies with the level difference method. Well below the first dip both the microphones measure the same pressure, and thus no information can be found there. The impedance model (1) predicts high real

and imaginary parts of the impedance for low frequencies, so the ground is hard there, which further complicates the situation. To get the first dip low in frequency, a large ray path difference between the direct and the reflected wave is needed, so the source and the top microphone must be high up from the ground. Then the reflection angle decreases (angle to the surface normal), making the ground harder (the spherical reflection coefficient Q is dependent on the reflection angle). This can be compensated with a larger distance between the source and the microphones, but that leads to a greater sensitivity to refraction and turbulence. The atmospheric turbulence affects the higher frequencies more, so in principle we have a frequency band where the measurements are possible. The lower frequency limit depends on how soft the ground is and on the geometry, and the high frequency limit depends on weather conditions. A more thorough investigation of the weather dependence of the method can be found in [3].

Nordtest method background

During 1997 a Nordtest (Nordic cooperation for standardization of measurement methods) project for determination of ground impedance was initiated. New outdoor sound propagation models for rail and road traffic noise have been under development for some years in the Nordic countries. The old models used only two ground types, hard and soft. The new models will use a more complex description of the ground, but very little data was found on the impedance of typical Nordic ground types. Therefore Nordtest wanted to develop a method that any reasonably equipped laboratory or consultant could use to measure ground impedance. This would simplify the survey of Nordic impedances.

After initial studies the frequency range of interest was set to the octaves 250 - 2000 Hz (Third octaves 200 - 2500 Hz), and the geometry was set to: source height 0.5 m, receiver 1 height 0.5 m, receiver 2 height 0.2 m and the horizontal distance 1.75 m.

Ground classes

The level difference method does not require any complex equipment other than a third octave band analyzer, and a source of some kind. It does require that you can evaluate the spherical reflection coefficient, which involves the complementary error function for complex arguments. A way around that is to use pre-calculated curves that the user can use to fit his measurements to as proposed in [4]. Another way is to use pre-calculated tables of level differences for different impedances and define some kind of error which the user can calculate and then use to pick the best fit impedance. Both these methods require that the impedance, or flow resistivity if we use the impedance model (1), is divided into classes. The class that fits the measurements the best is the result. They also require that the same geometry is used always, or that tables or curves can be obtained for all desired measurement geometries.

The table method was chosen for the Nordtest method. The classes were chosen so that the error between a class and its closest neighbor would be approximately constant, which lead to a logarithmic spacing in flow resistivity, except for very hard surfaces where the steps had to be larger (table 1). Note that these classes were not chosen to represent a useful set of classes for sound propagation purposes. They were simply chosen to provide a uniform coverage of what was possible to measure within the given geometry and frequency range. The level difference curves for the classes in table 1 can be found in figure 3.

Table 1 Ground classes for the impedance model (1)

Class number, k	1	2	3	4	5	6	7	8	9	10	11	12
Flow res. kNs/m ⁴	10	16	25	40	63	100	160	250	400	630	2000	20000

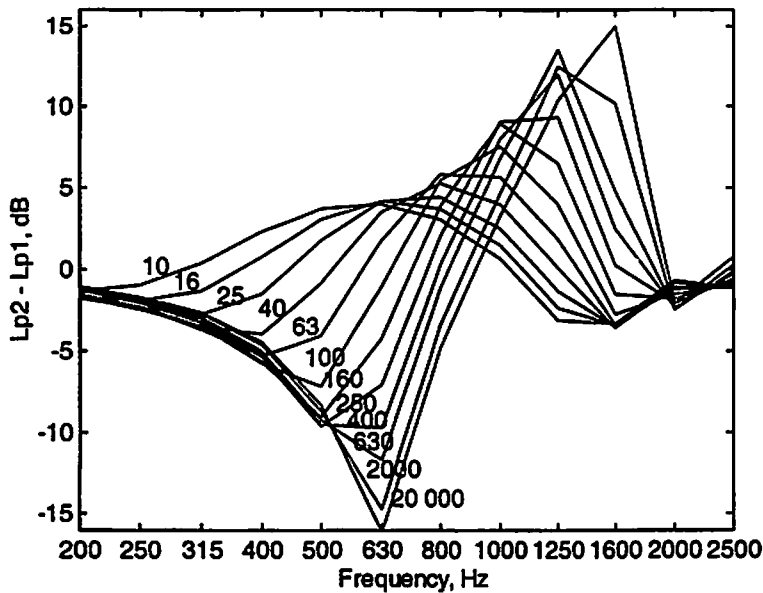


Figure 3
Level difference in third octaves. The number adjacent to each line is the flow resistivity class from table 1.
[imp model (1)]
hs=0.5 m, hr1=0.2 m,
hr2=0.5 m,
d=1.75 m

The error E is defined as the sum over the frequency range of the absolute values of the difference between the measurement and the reference, see (2). k is the class number (table 1), and the best fit class is the class where the error E has its minimum value e , see (3).

$$E(k) = \sum_{f=200\text{ Hz}}^{2500\text{ Hz}} |\Delta L_M(f) - \Delta L_R(f, k)| \quad (2)$$

$$e = \min_k (E(k)) \quad (3)$$

It is more common to use the squared differences, but this leads to a stronger dependence of deviations in isolated frequencies than if we use just the absolute value. This effect can be seen in figure 4. The minimum error e obtained is a quality measure of the measurement. If it is low the impedance model describes the true ground behavior well and the measurement is free from disturbing noise. It can be high due to noisy measurements, turbulence and refraction effects, ground unevenness and deviations in the true ground behavior from the impedance model. It can also be higher if the actual flow resistivity is just between two classes, but this effect is small if the classes are tightly spaced. But too many classes lead to difficulties in determining what class a ground surface really belong to since it can vary between different measurements in that case.

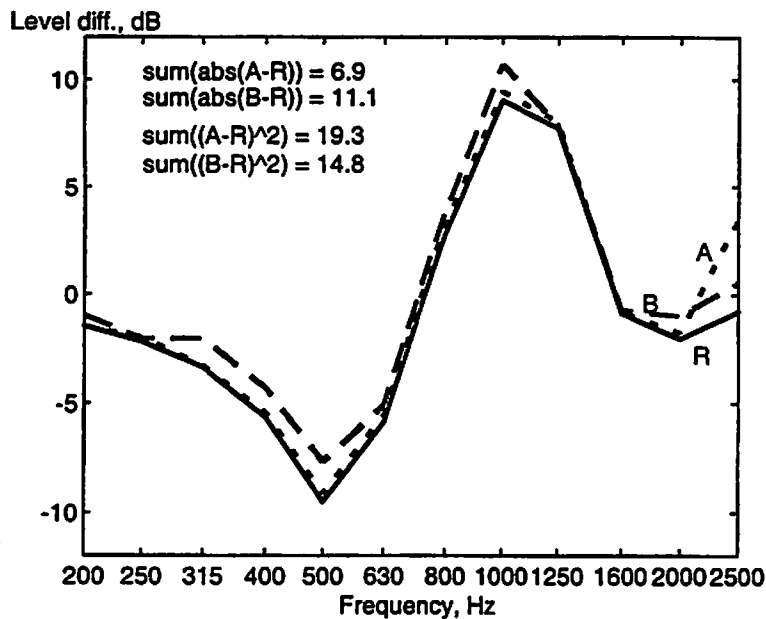


Figure 4
 Level difference in
 third octaves. The
 solid line (R)
 represents the
 reference, and A and
 B are simulated
 measurements.

Mean spectrum

During initial measurements it was discovered that one single measurement could give quite unstable results. It was therefore decided to make at least four independent measurements. If the four measurements are evaluated each in turn, one will have four classes, possibly different, as the result. If we use the measurements to make a mean spectrum (mean value of the SPL's in each third octave band), we will get only one result. In table 2 a number of measurements are presented with the four different measurements evaluated, and then the evaluation of the mean spectrum. Although the four measurements can vary quite a lot it seems as though the mean spectrum gives quite stable results. The measurements are described in the next chapter.

Table 2 *Evaluation of measurements with the mean spectrum.*
1-4 are the separate measurements, MV is the mean spectrum.
Measurement conditions and surfaces are described in the next chapter.

A		SP		DELTA		VTT		SINTEF	
M.NR	CLASS	e	CLASS	e	CLASS	e	CLASS	e	
1	63	22.7	160	13.5	63	22.8	63	21.0	
2	100	14.6	100	22.0	63	27.6	100	13.9	
3	100	11.8	100	8.8	63	12.0	100	20.5	
4	160	15.0	160	9.0	100	24.4	100	9.7	
MV	100	10.6	160	12.7	63	19.5	100	11.9	
B		SP		DELTA		VTT		SINTEF	
M.NR	CLASS	e	CLASS	e	CLASS	e	CLASS	e	
1	250	7.4	400	6.5	400	9.9	400	9.9	
2	250	10.1	160	9.9	400	8.4	160	11.2	
3	250	4.5	400	10.5	250	12.4	250	6.9	
4	250	6.9	250	11.6	400	10.2	250	4.1	
MV	250	5.0	250	7.4	250	8.5	250	5.9	
C		SP		DELTA		VTT		SINTEF	
M.NR	CLASS	e	CLASS	e	CLASS	e	CLASS	e	
1	630	8.8	630	5.1	400	7.8	250	18.0	
2	2000	11.9	630	5.5	400	7.1	400	6.9	
3	2000	11.6	630	7.8	400	10.8	630	7.8	
4	2000	14.1	630	6.6	630	6.8	2000	9.3	
MV	630	10.1	630	5.2	400	7.2	630	8.1	
D		SP		DELTA		VTT		SINTEF	
M.NR	CLASS	e	CLASS	e	CLASS	e	CLASS	e	
1	2000	10.5	2000	10.3	630	13.1	2000	8.1	
2	2000	7.2	2000	9.6	630	9.0	2000	8.6	
3	2000	12.4	2000	12.3	2000	15.6	2000	11.6	
4	2000	11.3	2000	10.6	2000	18.5	2000	10.6	
MV	2000	10.2	2000	10.0	2000	13.9	2000	9.2	

Nordtest verification measurements

During the 13-14 of May 1998 a series of measurements were made at Sjömarken outside Borås in Sweden, in an effort to establish the reliability and versatility of the Nordtest method. The participants were from four Nordic countries: SP from Sweden, VTT from Finland, DELTA from Denmark and SINTEF from Norway. Four ground surfaces, A-D, were measured by all participants, all with their own equipment and personnel. In addition, SP made a few extra measurements with help from SINTEF. All groups used the B&K sound power source type 4205 except SP, which used a special built source with a 1½" compression driver connected to a flexible tube.

The temperature was around 19°C both days, and the sky was mostly clear, with scattered clouds. Wind speeds one meter above ground were 1-2 m/s.

Table 3 contains a description of the ground type at the different positions, and table 4 contains the measured ground class according to the preliminary Nordtest method.

Table 3 *Ground description for the reference measurements*

Ground	Description
A	Rough grassland
B	Exercise track, earth mixed with sawdust
C	Soccer field grass
D	Gravel parking lot
E	Sandy forest floor
F	Soft forest floor covered with pine needles
G	Soft forest floor with small blueberry bushes and moss

Table 4

Reference measurements at Sjömarken. The result is the flow resistivity in kNs/m^4 , see (?). Results within parenthesis indicate an error difference E-e of less than 4 dB for those classes.

Site	Lab	Min error	Max std dev	Result
A	SP	10.7	3.32	100
A	DELTA	12.2	3.26	160 (100)
A	VTT	19.5	3.50	63 (100)
A	SINTEF	11.9	3.55	100
B	SP	5.0	1.52	250
B	DELTA	7.4	2.27	250
B	VTT	8.5	2.38	250 (400)
B	SINTEF	6.0	2.91	250
C	SP	10.1	2.20	630 (2000)
C	DELTA	5.2	0.94	630
C	VTT	7.2	1.73	400 (630)
C	SINTEF	8.2	3.50	630 (400)
D	SP	10.2	1.37	2000 (630)
D	DELTA	10.1	0.89	2000
D	VTT	13.9	5.24	2000 (630)
D	SINTEF	9.2	1.80	2000
E	SP	7.2	2.83	2000 (630)
F	SP	5.0	2.86	160
G	SP	4.5	1.76	40

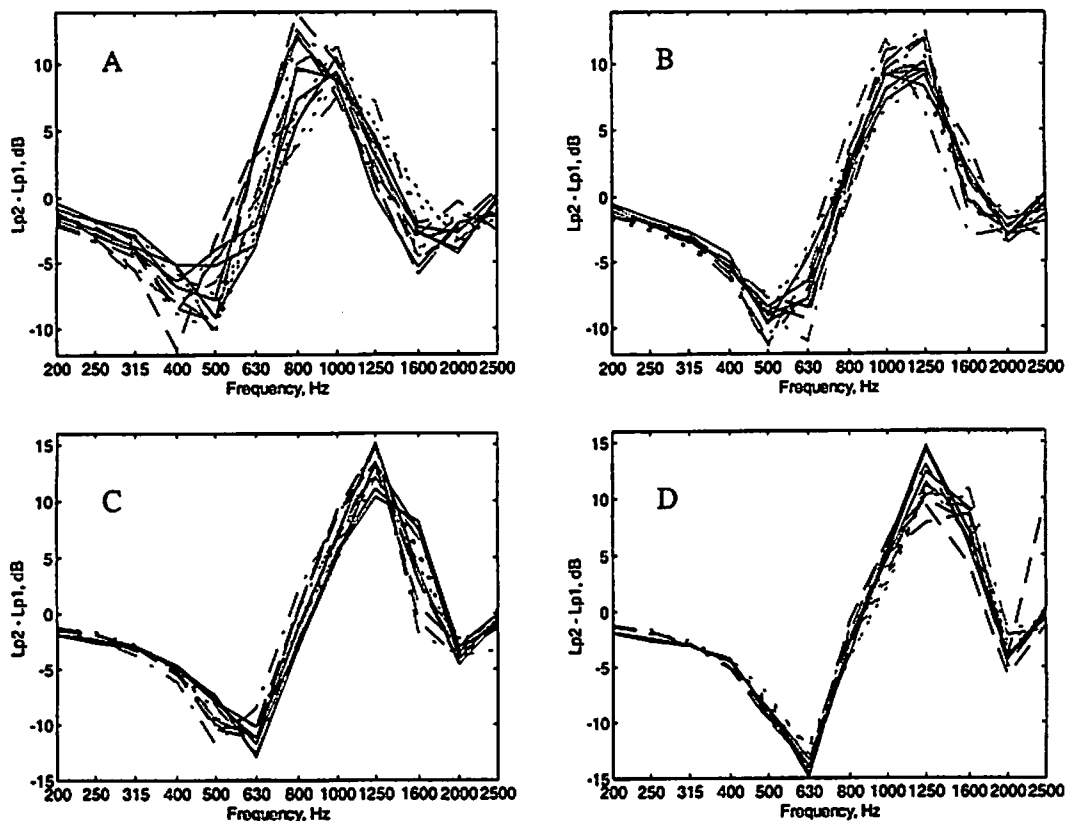


Figure 5
All of the measurements for each site A-D

The multiple height method

The level difference method uses an impedance model. If the model does not describe the ground behavior correctly, then the method will give erroneous results. The purpose of the model is to extrapolate the information obtained around the dip and peak in the spectrum in frequency. But if one could obtain a peak or dip for all frequencies, would it be possible to directly obtain the real and imaginary part of the impedance?

Using more than two microphones will make it possible to get a dip in height instead of frequency, see figure 6. For each frequency the dip will change height as the wavelength and impedance change. If one assumes a locally reacting surface, and that the impedance is constant within a third octave band, one can theoretically calculate the level behavior as a function of the height, and compare with the measurements. This method was used, in principle, in [5]. The question is if a SPL measurement with a number of microphones will give a unique solution for the real and imaginary part of the impedance. Due to the complexity of the expressions involved, this is very hard to evaluate.

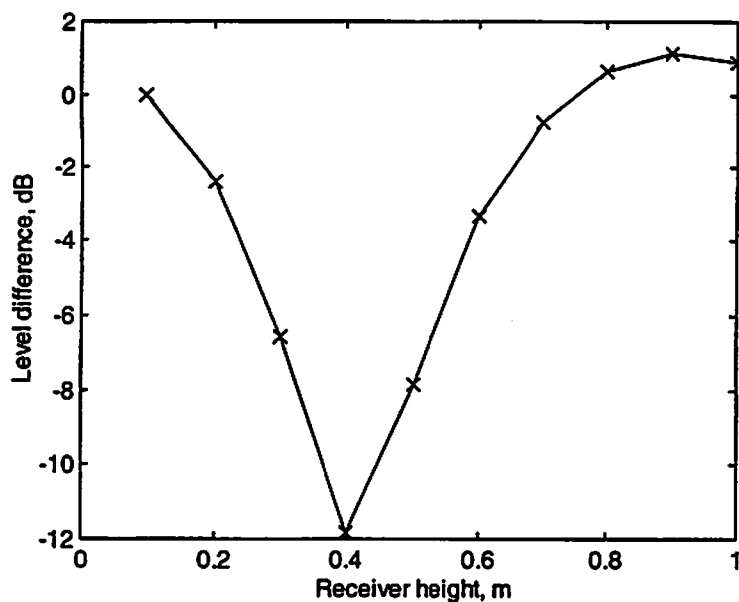
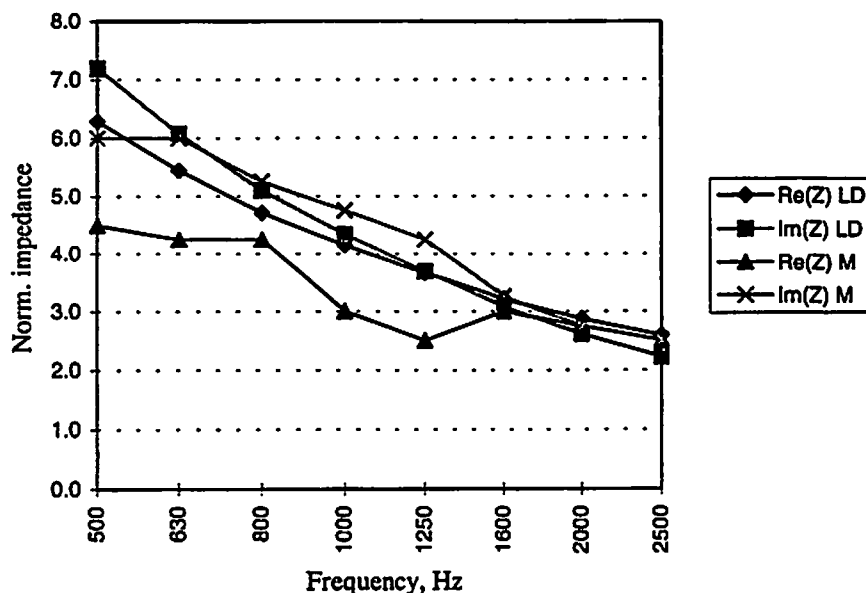


Figure 6
Level difference,
 $h_s=1.5$ m, $h_r=0.1-1$ m, $d=4$ m. Third octave band 500 Hz. Calculated with $\sigma=200\,000$, impedance model (1)

Figure 7 displays a measurement of the ground impedance on a grass surface with both the level difference method, and the multiple height method. The 12 different heights from table 5 were used. The source height was 0.5 m, and the distance was 1.75 m. The error was defined as the sum of the absolute value of the difference in level difference, with the lowest microphone as the reference. The calculations were made with constant step of 0.25 (no unit, normalized impedance) in both the real and the imaginary part.

Table 5 Receiver heights for the multiple height method (cm)

15	20	25	30	35	40	45	50	55	60	65	70
----	----	----	----	----	----	----	----	----	----	----	----



*Figure 7
Normalized
impedance
measured on a
grass surface with
the level difference
method (LD), and
with the multiple
height method (M).*

Conclusions

- The ground impedance can be measured, within a limited frequency band and for non-layered surfaces, with a number of simple level difference measurements.
- None of the measured surfaces showed any strong deviations from the basic impedance model within the measured frequency range.
- Hard surfaces are difficult to evaluate with the level difference method.

Acknowledgments

I would like to acknowledge the help and inspiration obtained during numerous discussions on the subject of sound propagation with Jens Forsén, and other PhD students, from Chalmers University of Technology. I would also like to thank Tomas Ström for his advice and insight into acoustic measurements, Hans Jonasson for making the project financially and academically possible, and the inter-Nordic group that helped during the measurements at Sjömarken: Birger Plovsing, Jørgen Kragh, Svein Storheier and Raimo Eurasto.

References

- [1] Acoustic Properties of Fibrous Absorbent Materials
M. E. Delaney, E. N. Bazley
Applied Acoustics 3(2), 1970
- [2] Noise propagation along an impedance boundary
C. I. Chessel
J. Acoust. Soc. Am. 62(4), 1977

- [3] A note on short-range ground characterization
K. Attenborough
J. Acoust. Soc. Am. 95(6), 1994
- [4] Template Method for Ground Impedance
ANSI S1.x - 199x, Third draft 03/1997
(Draft - Not approved)
- [5] Sound propagation over ground with and without barriers
Hans G. Jonasson
Lund Institute of Technology, 1971

Measurement of Multipath Outdoor Sound Propagation with Spread-Spectrum Signals

T. Douglas Mast, David C. Swanson, Mark P. Mahon, and David E. Norris

Applied Research Laboratory, The Pennsylvania State University
University Park, Pennsylvania 16802

Abstract

A method for measurement of multipath acoustic propagation is presented and applied to outdoor sound propagation. The method employs spread-spectrum signals, in which a low-frequency sinusoidal carrier is bi-phase modulated by a pseudorandom maximal-length sequence. The spreading of the signal spectrum is determined by the chip rate, or the rate at which the carrier is modulated; faster chip rates result in broader spectra. Deconvolution of the received acoustic signals with respect to the transmitted signals provides a filtered version of the channel impulse response, which in turn can be analyzed to obtain time delay and amplitude estimates for each path in the propagation channel. This method has been tested in an outdoor sound propagation experiment in the presence of atmospheric turbulence. Multiple spread-spectrum signals were transmitted from a loudspeaker and received by a three-axis microphone array. Deconvolution processing of the received signals clearly resolved a direct wavefront and a ground-reflected wavefront. The measured path lengths and arrival directions for these wavefronts were confirmed by a three-dimensional ray-tracing model that incorporated sound-speed and wind-velocity profiles determined from meteorological measurements.

I. Theory

Spread-spectrum and other coded-pulse signals have proven useful for high-SNR measurements in several areas of acoustics, including sonar [1]–[3] and ultrasonics [4]–[7] applications. Work performed in architectural acoustics [8]–[10] has also shown that the impulse response of rooms, which includes complicated high-order multipath propagation, can be measured accurately using direct-sequence coded-pulse methods. The work reported here shows that high-resolution acoustic detection and ranging can be performed using spread-spectrum methods in the presence of atmospheric turbulence. In the method outlined below, deconvolution of spread-spectrum source signals from received signals results in a filtered form of the channel impulse response. This method is presented in greater detail in Ref. [11].

For linear acoustic propagation through complicated media, the general effects of propagation can often be approximated as a convolution:

$$y(t) = x(t) \otimes h(t), \quad (1)$$

where $x(t)$ is the transmitted signal, $y(t)$ is the received signal, and $h(t)$ is the impulse response of the acoustic channel. The impulse response can, in theory, be determined by straightforward Fourier deconvolution.

When the input signal x has finite bandwidth, however, wideband deconvolution may not be possible to perform stably. This problem can be overcome, at a loss of temporal resolution, by applying a bandpass filter ϕ_{BP} to the output signal g before deconvolution:

$$\tilde{h}(t) \approx \mathcal{F}^{-1} \left[\frac{\hat{y}(\omega) \phi_{BP}(\omega)}{\hat{x}(\omega)} \right], \quad (2)$$

where \tilde{h} is the estimated channel impulse response. For numerical stability, the filter ϕ_{BP} can be specified such that its frequency-domain support is similar to that of the input signal $x(t)$.

Even for idealized propagation through a homogeneous acoustic path, the impulse response estimated from Eq. (2) has finite temporal resolution if the system bandwidth is finite. In general, the methods presented here for impulse response measurement result in temporal resolution limits that are inversely proportional to the window bandwidths employed.

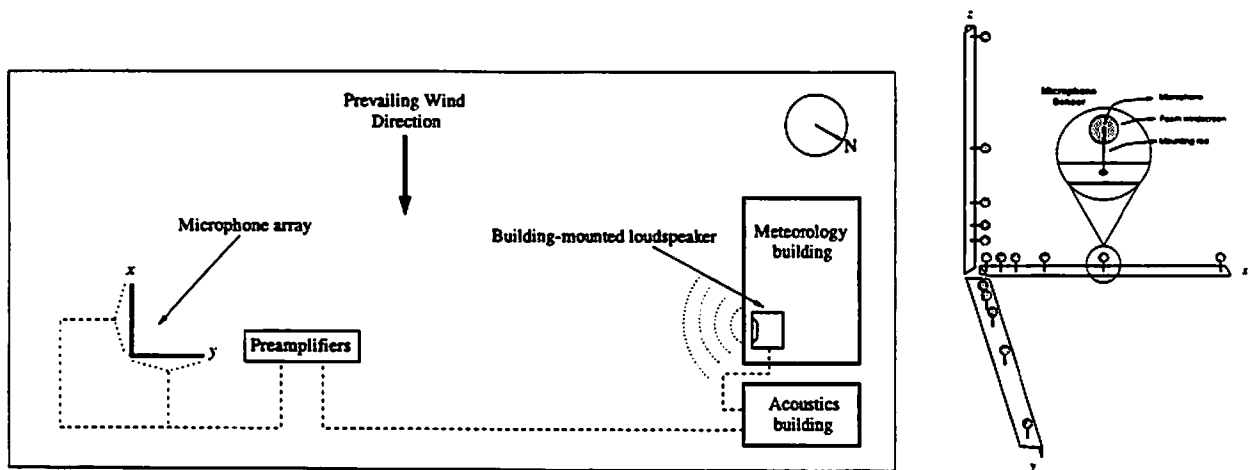


Figure 1: Sketch of measurement configuration (top view). A spread-spectrum acoustic signal is continuously emitted from a loudspeaker mounted on a building. After propagation, acoustic signals are received by a three-axis microphone array and digitally recorded. The right panel shows a sketch of the microphone array.

II. Methods

The signals employed in this study are spread-spectrum signals obtained by bi-phase modulation of a sinusoidal carrier by a maximal length sequence at a specified chip rate. Maximal length sequences were generated synthetically using shift-register algorithms summarized in Table 3.7 of Ref. [12], then used to modulate sinusoidal carrier waves at a sampling frequency of 4000 Hz.

The measurement configuration employed is sketched in Fig. 1 and discussed in greater detail in Ref. [11]. During the measurements, the temperature averaged 9.1°C and the wind speed at 10 m above ground averaged 7.9 m/s with a bearing of 264° . Signals were played back from a single channel of a two-channel digital audio tape recorder and broadcast from a loudspeaker mounted on a building 4.8 m above ground. A microphone was mounted directly in front of the loudspeaker driver to record the acoustic near field of the source. Signals were received by a three-axis microphone array mounted on a scaffold tower at a height of 6 m. Fourteen microphone sensors were spaced logarithmically on the array. Sixteen signal channels, including the original digitally recorded source signal, the signal from the near-field microphone, and the fourteen array microphone signals, were recorded synchronously to a sixteen-channel digital audio tape recorder.

The digitally recorded signals were processed using custom software to obtain the filtered impulse response of each channel. Spectra were computed using discrete Fourier transforms (obtained by FFT), taken over non-overlapping rectangular windows for all available temporal data. The transform length for each discrete Fourier transform was the number of samples corresponding to the temporal duration of a single MLS sequence for the signal employed. The transfer function $H(\omega) = \hat{y}(\omega)/\hat{x}(\omega)$ was computed separately for each rectangular window and all transfer functions were averaged to obtain an estimate of the channel transfer function. The estimated channel transfer function was then used in the deconvolution operation described by Eq. (2) to obtain the filtered impulse response of the medium. The corresponding impulse response envelope was obtained by discrete Hilbert transformation. Impulse responses were converted to range units using an assumed sound speed of 340 m/s. For the deconvolution, a Hanning-shaped filter, with value unity at zero frequency and zero for $|f| \geq 1200$ Hz, was applied to the received signals. To determine the direction of incidence for each arrival relative to each array axis, the peak positions corresponding to the first and second arrival were located in the impulse response for each channel and a least-squares linear fit of path lengths vs. array position was applied.

For comparison, propagation paths and corresponding arrival times were predicted using a three-dimensional ray-tracing program. The program was based upon the ray-trajectory equations for a moving, inhomogeneous medium [13, 14]. The trajectory of each ray was determined by integrating the ray-trajectory equations using a fourth-order Runge-Kutta method with a fixed time step of 0.5×10^{-4} s. The mean sound speed and wind velocity profiles employed were estimated from meteorological data and Monin-Obukhov similarity theory [11, 15].

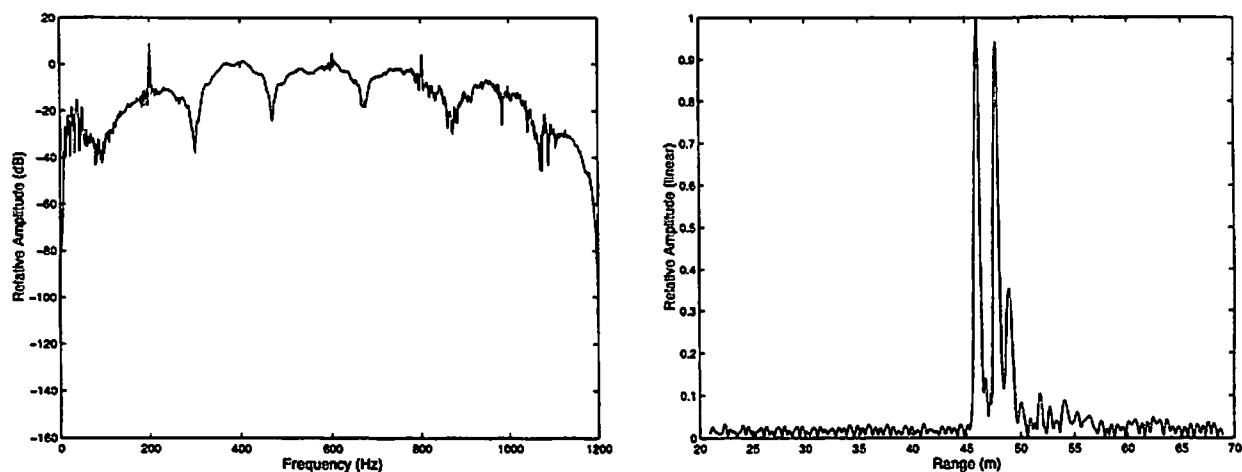


Figure 2: Illustration of impulse response computation for a center frequency of 400 Hz, chip rate of 200 Hz, and sequence length of 127 chips. Left panel: transfer function. Right Panel: corresponding impulse response envelope.

III. Results

The measurement of impulse response is illustrated by Fig. 2. The results shown there were obtained using data from a measurement employing a 400 Hz carrier wave, 200 Hz chip rate, and 127 chip sequence length. The computed transfer function is depicted in the left panel of Fig. 2, while the impulse response obtained by inverting this filtered transfer function is shown in the right panel. This impulse response clearly shows two peaks, which correspond to a direct wave and a ground-reflected wave. A third peak, which is also discernible in most of the measured impulse responses, is of unknown origin; this peak may be caused by scattering from a structure or from atmospheric turbulence.

Comparison of simulated and measured propagation paths is given in Table 1. The results show that the direct and reflected paths measured experimentally correspond closely to those simulated by a three-dimensional ray-tracing model based on measured temperature and wind profiles. It may also be noted that the average sound speed computed from the ray simulations was 339.7 m/s, which is close to the speed of 340 m/s assumed for computation of propagation path lengths in the measurements.

Results shown in Ref. [11] show that, for a variety of spread-spectrum signals with center frequencies between 200–400 Hz, chip rates of 50–300 Hz, and sequence lengths between 127 and 1023, the filtered impulse response shows direct and reflected arrivals with peak positions and widths close to those shown in Fig. 2. The mean 3 dB peak width is 0.408 m for the direct arrivals and 0.438 m for the reflected arrivals. These widths are as small as a quarter-wavelength at the 200 Hz carrier frequency; they correspond closely to theoretical resolution limits based on the system bandwidth employed [11, 16].

IV. Conclusions

A method for precise measurement of multipath acoustic propagation has been presented and tested for outdoor sound propagation in the presence of atmospheric turbulence. Filtered impulse-response functions, obtained by deconvolution processing of spread-spectrum signals, show multiple arrivals that have been shown to correspond to direct and reflected propagation paths. Measured path lengths and arrival angles for these paths agree well with simulated results.

It has also been shown that impulse-response measurements with resolution of features much smaller than the carrier period can be achieved. The range resolution achieved using the present method is nearly independent of the carrier frequency, modulation frequency, and sequence length employed, but is instead determined primarily by the effective system bandwidth used in computation of the filtered impulse response.

The methods presented here have potential for further studies of atmospheric sound propagation. The inherently high SNR and high resolution of spread-spectrum methods should allow measurement of long-distance multi-modal propagation like that that occurs in the presence of atmospheric temperature inversions. Since high resolution can be achieved for fairly narrow-band signals, the current methods may also be useful for accurate measurement of

	Direct Path		Reflected Path	
	Experiment	Simulation	Experiment	Simulation
Elevation angle	1.6°	2.4°	13.7°	13.9°
<i>x</i> -axis bearing	-19.4°	-21.9°	-19.4°	-22.0°
<i>y</i> -axis bearing	-72.8°	-68.1°	-72.2°	-68.0°
Range (m)	46.1	46.8	47.9	48.2

Table 1: Measured arrival angles and path lengths for direct and reflected paths in a turbulent atmosphere, obtained using spread-spectrum processing with a carrier-wave frequency of 400 Hz, chip rate of 200 Hz, and sequence length of 127 chips.

frequency-dependent effects such as propagation through atmospheric turbulence and reflection from an absorbing ground. However, assessment of the potential for measurement of frequency-dependent effects using spread-spectrum signals requires further investigation.

References

- [1] J. L. Stewart and E. C. Westerfield, "A theory of active sonar detectors," Proc. IRE, 872-881 (1959).
- [2] D. R. Dowling, "Acoustic pulse compression using passive phase-conjugate processing," J. Acoust. Soc. Am. **95**, 1450-1458 (1994).
- [3] R. Pinkel, M. Merrifield, J. Smith, and H. Ramm, "Advances in Doppler sonar technology," Proc. IEEE Working Conference on Current Measurement, 37-41 (1995).
- [4] E. S. Furgason, V. L. Newhouse, N. M. Bilgutay, and G. R. Cooper, "Application of random signal correlation techniques to ultrasonic flaw detection," Ultrasonics, 11-17 (January 1975).
- [5] Y. Takeuchi, "An investigation of a spread energy method for medical ultrasound systems, Part one: theory and investigation," Ultrasonics, 175-182 (July 1979).
- [6] O'Donnell, M., "Coded excitation system for improving the penetration of real-time phased-array imaging systems," IEEE Trans. Ultrason. Ferroelect. Freq. Control **39**, 341-351 (1992).
- [7] G. A. Gordon, "Spread spectrum ultrasound for inspection of Spectrum UT integrated circuits and material interfaces," Internal Report, Applied Research Laboratory, The Pennsylvania State University, SP No. 268-95 (1995).
- [8] J. Borish, *Electronic Simulation of Auditorium Acoustics*, Ph.D. thesis, Stanford University, 1984.
- [9] D. D. Rife and J. Vanderkooy, "Transfer-function measurement with maximum-length sequences," J. Audio Eng. Soc. **37**, 419-444 (1989).
- [10] P. S. Kovitz, *Extensions to the Image Method Model of Sound Propagation in a Room*, Ph.D. thesis, The Pennsylvania State University, 1994.
- [11] T. D. Mast, D. C. Swanson, M. P. Mahon, and D. E. Norris, "Resolution of multipath outdoor sound propagation using spread spectrum signals," submitted to J. Acoust. Soc. Am. (1998).
- [12] R. C. Dixon, *Spread Spectrum Systems*, Second Edition (New York: Wiley), 1984.
- [13] R. Engelke, "Ray trace acoustics in unsteady inhomogeneous flow," J. Acoust. Soc. Am. **56**, 1291-1292 (1974).
- [14] A. D. Pierce, "Wave equation for sound in fluids with unsteady inhomogeneous flow," J. Acoust. Soc. Am. **87**, 2292-2299 (1990).
- [15] D. E. Norris, *Atmospheric Acoustic Propagation: Characterization of Magnitude and Phase Variability*, Ph.D. Thesis, The Pennsylvania State University, 1998.
- [16] T. D. Mast and R. C. Waag, "Wave space resolution in ultrasonic scattering measurements," J. Acoust. Soc. Am. **98**, 3050-3058 (1995).

Sound Propagation in a Refracting Medium Above an Uneven Terrain

Shahram Taherzadeh, Kai Ming Li and Keith Attenborough

Faculty of Technology, The Open University, MK7 6AA, UK

Abstract

A hybrid Boundary Integral Equation – Fast Field Program (BIE-FFP) procedure is described and used to simulate the propagation of sound in a medium with an arbitrary sound speed profile above an irregular, impedance ground. The method uses the boundary integral equation to allow for the non-uniformity of the ground boundary (impedance mismatch, a barrier or hilly terrain) while utilising the FFP formulation to model a refracting atmosphere by discretising it as horizontal layers. Steps and approximations taken to increase the efficiency of the procedure are discussed, as well as methods for allowing for the effect of turbulence in the calculations. The hybrid BIE-FFP is validated by comparing its predictions with scale model measurements available in the literature.

Introduction

The Boundary Integral Equation (BIE) is a powerful numerical procedure in predicting sound pressure field in the presence of noise barriers and other scattering objects. It is able to account for both forward and back scattering. But the method requires that the sound field be known in the absence of the scattering object (the so-

called Green's function). There have been many applications of the Boundary Integral Equation to prediction of the sound field beyond a barrier in a neutral atmosphere but few studies exist that attempted to include the refracting atmosphere⁽¹⁻⁴⁾. Recently, a hybrid method to account for the non-homogeneous atmosphere was outlined⁽⁵⁾ and used to predict the performance of noise barriers in down wind conditions. Here, this procedure is described and applied to the prediction of the sound field in a refracting medium above a non-uniform boundary. Other

Theory

Let a line source produce a time harmonic sound field in a medium, D , bounded by a locally reacting impedance surface, S . This impedance plane can have features such as barriers, hills, impedance discontinuities etc. The Boundary Integral form of the wave equation can be written as

$$\varepsilon\phi(r, z) = G(r, r_0) - \int_S \left\{ G(r, r_s) \frac{\partial\phi(r_s, z_s)}{\partial n(r_s)} - \phi(r_s, z_s) \frac{\partial G(r, r_s)}{\partial n(r_s)} \right\} ds \quad (1)$$

where r_s is the position vector of the boundary element ds , and n is the unit normal vector out of ds . The parameter, ε , is dependent on the position of the receiver. It is equal to 1 for r in the medium, $1/2$ for r on the flat boundary and equal to the $\Omega/2\pi$ at edges where Ω is the solid angle. The Green's function, $G(r, r_0)$, is the solution of the wave equation in the domain in the absence of scatterers. The integral is then the contribution of the scatterer elements to the total sound field at a receiver position. This integral formulation is the so-called Helmholtz-Kirchhoff wave equation. By allowing the observer points (r) to fall on the boundary, an integral equation for the

field potential at the boundary is obtained. The equation, the BIE, is a Fredholm integral equation of the second kind. Once solved, the contribution of the scatterers can be determined by evaluating the integral in eqn. (1) and hence the total field for any point in the entire domain, D . This is the main BIE equation for the acoustic field potential in the presence of non-uniform boundary. The BEM is concerned with reducing the acoustic propagation in a medium to the boundary integral equation and solving this integral equation numerically.

The derivative of the unknown field can be reduced if we assume a locally reacting impedance boundary condition on all surfaces:

$$\frac{d\phi}{dn} - ik_0\beta\phi = 0 \quad (2)$$

where β , the admittance, is a function of the position on the boundary. One would then have:

$$\varepsilon\phi(r, z) = G(r, r_0) - \int_S \phi(r_s, z_s) \left\{ ik_0\beta G(r, r_s) - \frac{\partial G(r, r_s)}{\partial n(r_s)} \right\} ds \quad r, r_s \in S \quad (3)$$

The boundary surface is discretized in some fashion assuming the unknown potential to be constant in each element, thereby reducing the integral equation to a set of linear equations.

$$\int_S \phi(r_s, z_s) \left\{ ik_0\beta G(r, r_s) - \frac{\partial G(r, r_s)}{\partial n(r_s)} \right\} ds = \sum_{m=1}^M \phi(r_m, z_m) \int_{r_m-h/2}^{r_m+h/2} \left\{ ik_0\beta G(r, r_s) - \frac{\partial G(r, r_s)}{\partial n(r_s)} \right\} ds \quad (4)$$

In principle, the integral on the right-hand side can be evaluated numerically. Then the BIE becomes

$$\varepsilon\phi(\mathbf{r}) = G(\mathbf{r}, \mathbf{r}_0) - \sum_{m=1}^M \phi(\mathbf{r}_m) \Lambda(\mathbf{r}, \mathbf{r}_m) \quad (5)$$

where Λ denotes the integral on the right-hand side of eqn. (4). Substitution of $\mathbf{r} = \mathbf{r}_n$, $n=1 \dots M$, produces a set of M linear equations.

$$\varepsilon\phi(\mathbf{r}_n) + \sum_{m=1}^M \phi(\mathbf{r}_m) \Lambda(\mathbf{r}_n, \mathbf{r}_m) = G(\mathbf{r}_n, \mathbf{r}_0) \quad n=1 \dots M \quad (6)$$

It is easily seen that the Greens function $G(\mathbf{r}, \mathbf{r}_s)$ will be singular at $\mathbf{r} = \mathbf{r}_s$ i.e. at diagonal elements when $n=m$. One can use the principal value of the integral for the integrals involving the singularities. For further discussions on the stability and uniqueness of the solution see reference 6 and references therein. It is sufficient here to state that the solution of the eqn. (3) is unique except near characteristic frequencies of the space enclosed by the barrier.

The Green's Function $G(\mathbf{r})$

The Green's function represents the sound field derivative in the medium in the absence of the 'boundary'. In order to minimize the number of elements, the Green's function includes the reflection from the flat impedance ground surface.

The Greens function for a line source radiating cylindrical waves above a locally reacting impedance plane can be written as

$$G(\mathbf{r}_1, \mathbf{r}_2) = \frac{1}{\sqrt{2\pi}} \int_0^{\infty} \bar{\varphi}(z_1, z_2, k_r) \exp(ik_r R) dk_r \quad (7)$$

Where $\mathbf{r}_2 [= (x_2, z_2)]$ and $\mathbf{r}_1 [= (x_1, z_1)]$ are the source and receiver position vectors respectively and R is the horizontal separation between them. For a neutral medium it can be evaluated analytically in terms of Hankel functions^[6,7]. In a refracting medium, the integral in eqn. (7) is evaluated by the FFP method.

The infinite integral is truncated at a suitable value, say k_{max} , and the integral is replaced by a finite Fast Fourier Transform (FFT) sum. The variable of integration, k_r , can be thought of as the horizontal component of the wavenumber. To avoid the possible poles on or near the real k axis, the path of integration is deformed below the real axis. To avoid artificial oscillations in the solution caused by the truncation of the integral at a finite value a Hanning window is multiplied to the kernel of the integral as suggested by K. Wilson^[8].

The kernel function φ is now independent of range and is in one dimension only. This function is the solution of the one dimensional Helmholtz equation in presence of a plane impedance boundary. For a homogeneous fluid this solution is known and is given in terms of up and down going plane waves. In an inhomogeneous medium such as a refracting atmosphere or in upwind or downwind conditions with an arbitrary sound speed profile, the potential function cannot be determined analytically. Instead, a scheme similar to the finite element method can be utilised whereby the fluid is divided into uniform horizontal layers. The boundary conditions at the layer boundaries determine the wave potential amplitudes in each layer. These conditions are continuity of normal particle displacement and pressure across the boundary. The resulting equations are set in a global matrix, which is solved to produce the wave amplitudes in all layers. The value of the kernel function at one or more desired positions can then be derived easily. The main advantage of the Global Matrix formulation of the FFP is that the wave field in the entire x - z plane is evaluated at once thus reducing the computation time considerably. The derivative of

the Green's function can also be evaluated easily and at the same time. The derivative term is recognized as the dipole field oriented in the direction of $\mathbf{R}^{[9,10]}$.

A high level of accuracy is required in evaluating the Green's functions in the Boundary Integral Equation. The FFP values for the pressure are accurate only at the spatial grid points and an interpolation scheme for range values in between the grid points, while providing accurate values for the magnitude of the pressure, fails to give adequate accuracy for the phase values. This means that the midpoint of barrier elements must be made to fall on the grid points of the FFP scheme. This requirement puts constraints on the integration parameters such as truncation value (k_{max}) and the number of integration points (N_k). There are three stages where calculations involving the Green's function and its derivatives are performed (figure 1):

- A. Evaluating the Green's function in the absence of the barrier.
- B. Calculation the radiation from the source to each element on the barrier (the right hand sides of the equation); and
- C. Evaluating the radiation from each element to every other one (i.e. evaluating the matrix elements in equation (4));
- D. The contribution of each barrier element to the sound received at the observation point (i.e. evaluating the boundary integral after the matrix equation has been solved).

In theory a single FFP step is sufficient to evaluate sound pressure at all points in the x - z plane. In practice though, memory and storage considerations make this impractical. Nevertheless, considerable time saving steps can still be taken in each of the three stages.

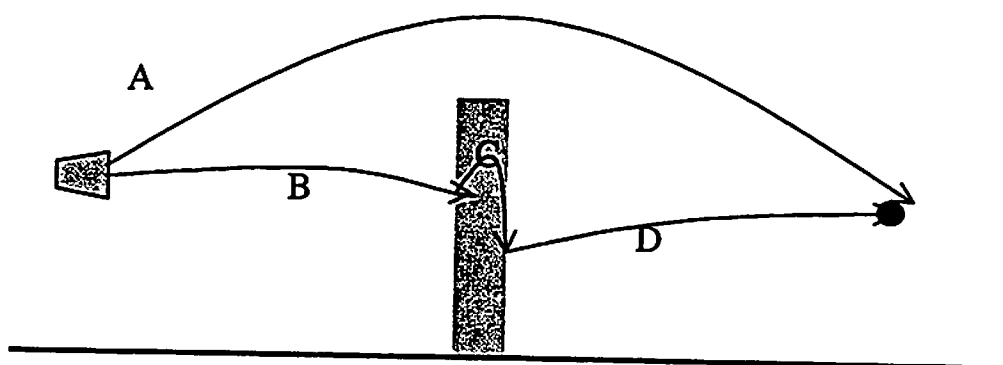


Figure 1 The stages required in solving the BIE

Apart from the case where a large area of the boundary has to be discretized (as in an uneven ground surface) the physical size of the scatterer is small compared with the radius of curvature. If then the horizontal separation between the elements is small, the sound speed profile plays very little role. In this case the Hankel functions approximate the Green's function sufficiently. Even when a large area is discretized and the separation between elements can be large the main contribution to the field in each element comes from its neighbours. It is therefore still a good approximation to ignore the effect of refraction and use Hankel functions instead. Thus, the effect of refraction has been ignored in evaluating stage C.

Use of the FFP approach in evaluating the Green's function allows one to make efficient computations in certain typical cases. In particular, if the scatterer has vertical sides, the right hand sides for each vertical section (stage B above) is be evaluated with a single FFP step.

The same is true for the last stage (i.e. contributions from each element to a single observer point) if one uses the reciprocity property of the Green's function and its horizontal (or x) derivative.

The effect of atmospheric turbulence in sound propagation at long ranges is significant. The only method available in the literature to include effects of turbulence in the FFP formulation is that suggested by Raszpet and Wu^[11]. In their formulation of the FFP, the average pressure squared is given by

$$\overline{\langle p^2(r,t) \rangle} = \frac{1}{2} \operatorname{Re} \left(\frac{1}{\pi r} \int_0^{\infty} \int_0^{\infty} \hat{p}(K) \hat{p}^*(K') e^{-i(K-K')r} T(K, K') \sqrt{KK'} dK dK' \right) \quad (8)$$

where $T(K, K')$ is the average effect of the decorrelation in phase and amplitude on the interference of horizontal wavenumbers K and K' . Evaluation of the pressure clearly requires a double summation instead of the FFP with huge increase in computational effort and memory requirements. For these reasons, the effect of turbulence has been omitted in this report.

RESULTS AND CONCLUSIONS

The numerical scheme outlined above has been compared to scale model measurements carried out by Rasmussen^[12] in a wind tunnel. Their measurement set up consisted of a thin barrier 2.5m high at a distance of 20.m from a point source 2. m above an impedance surface. The Excess Attenuation of sound re free field was measured at a microphone positioned 40.m behind the barrier and 1.m above the surface. A wind speed gradient of approximately $1.0 \text{ m s}^{-1}/\text{m}$ was generated by a fan.

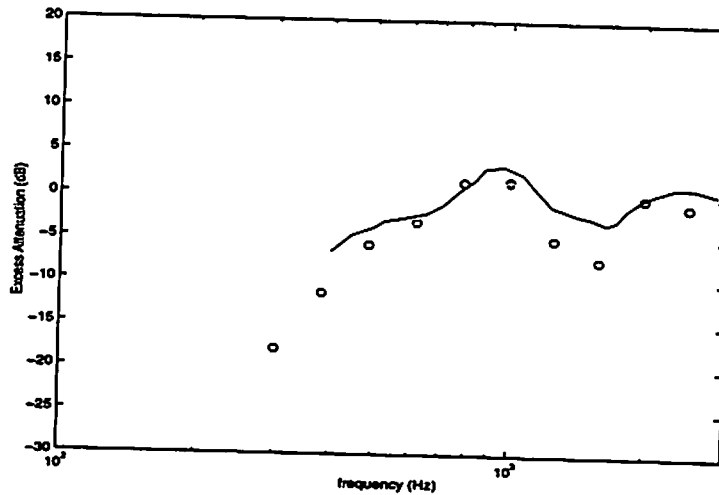


Figure 2 Measured (solid line) and predicted (circles) excess attenuation of sound at a receiver behind a barrier 2.5 m high in down wind conditions.

Figure 2 shows the measured (solid line) and predicted (circles) Excess Attenuation spectra for this geometry. The data has been taken from figure 11 of reference (5). It is seen that there is a reasonable agreement between predictions and the data. The greatest divergence is at the minimum at 1500 Hz which is probably due to the influence of turbulence which has not been taken into account here.

Figure 3 shows an example of Sound Pressure level above a ground where the first 400m of the range is a hard ground while beyond the distance of 400m the ground is acoustically soft (low flow resistance). Also plotted is the predicted SPL over the hard ground (solid line). It is seen that the interference patterns of the two theoretical plots match up to about 450m. In this example, a frequency of 50Hz has been assumed with the source and receiver heights at 5.0 and 1.2m respectively. A positive sound speed gradient of 1.0s^{-1} has been assumed. The hard ground is assumed to have an impedance of $(19.5+25.3i)$ and the soft ground an impedance of $(6.2+12.0i)$.

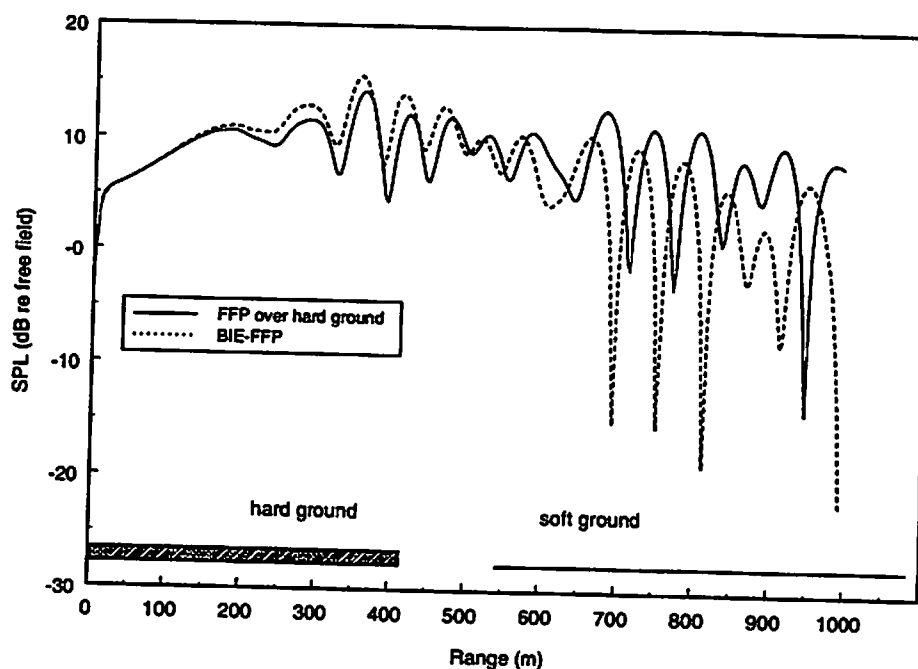


Figure 3 Predicted SPL (re free field) above an acoustically hard ground (solid line) and one where the ground becomes acoustically soft after 400.m. The source and receiver heights are 5.0m and 1.2m respectively and the frequency is 50.0 Hz. The sound speed gradient is 1.0 s^{-1} .

In conclusion, the method proposed in this paper integrates the Boundary Integral equation and the Fast Field Method to simulate the sound field in a medium with an arbitrary sound speed profile above an uneven terrain. It has been compared to scale model data available in the literature favourably

Acknowledgement

This research was supported by EPSRC of UK under grant no. GR/L15326

References

- [1] R. DeJong, and E. Stusnick, *J. Noise Control Eng.* 6(3), 101-109 (1976)
- [2] W.E. Scholes, A.C. Salvidge and J.W. Sargent, *J. Sound Vib.* 16, 627-642 (1971)
- [3] E.M. Salomons, *J. Acoust. Soc. Am* 95, 3109-3117 (1994)
- [4] K.M. Li and Q. Wang, *J. sound Vib.*, Vol.211, .663-681, 1998

- [5] S. Taherzadeh, K.M. Li and K. Attenborough, Proceedings of the 16th ICA and 135th ASA Meeting, Seattle, USA, 475-477, June 1998.
- [6] S.N. Chandler-Wilde, *Ph.D. Thesis*, University of Bradford, (1988)
- [7] D.C. Hothersall, S.N. Chandler-Wilde and M.N. Hajmirzae, *J. Sound Vib.*, **146**(2), 303-322, (1991)
- [8] D. K. Wilson, *J. Acoust. Soc. Am.* **89**, 448-450 (1991)
- [9] S. Taherzadeh and K. Attenborough, Proc. Symposium on Computational Acoustics, Editor C.A. Brebbia, Southampton, UK, p45-54, 1995
- [10] S. Taherzadeh, *Ph.D. Thesis*, The Open University, 1996
- [11] R. Raspet and W. Wu, *J. Acoust. Soc. Am.* **97**, 147-153 (1995)
- [12] K.B. Rasmussen, *J. Acoust. Soc. Am.* **100**, 3581-3586 (1996)

Donald G. Albert

U.S. Army Cold Regions Research and Engineering Laboratory (USACRREL), 72 Lyme Road, Hanover, NH 03755, USA, (603)646-4459, fax (603)646-4397, dalbert@crrel.usace.army.mil

Lars R. Hole*

University Courses on Svalbard (UNIS), Box 156, 9170 Longyearbyen, Norway, larshole@unis.no

ABSTRACT

A rigid-porous model of a snow cover, rather than a viscoelastic treatment, has been used to simulate measured, horizontal acoustic waveform propagation above a dry snow cover 11 to 20 cm thick. The waveforms were produced by explosions of 1-kg charges and propagated from 100- to 1400-m distances. These waveforms, with a peak frequency around 50 Hz, show pulse broadening effects similar to those seen for higher frequency waves over shorter propagation distances. The predicted average snow cover depth of 15 cm and effective flow resistivities of 30 - 41 kPa s m⁻² agree with snow pit observations and with previous acoustic measurements over snow. For propagation in the upwind direction, the pulse broadening caused by the snow cover interaction is lessened, but the overall amplitude decay is greater because of refraction of the blast waves.

1 INTRODUCTION

Military training activities and firing ranges can produce loud sounds that cause significant annoyance to civilian populations. To minimize this annoyance, noise prediction models are often used to schedule military activities during periods when atmospheric and other environmental conditions are favorable. However, a better understanding of environmental effects on sound propagation and predictive models capable of including these effects are still needed.

A series of blast noise measurements has been conducted in Norway to investigate the effects of forest vegetation, micro-meteorological conditions, and winter ground conditions, and their temporal variations, on the propagation of low-frequency impulse noise. The goal of these measurements was to elucidate these environmental effects and to provide data suitable for validating more realistic propagation models.¹ In an earlier analysis of some of the Norwegian experimental data, Hole² used a viscoelastic Fast Field Program³ to predict pulses for propagation distances up to 1400 m. Predictions of overpressure amplitudes correlated well with experimental data in strongly upward and downward refracting atmospheres when a wet, slushy snow surface was present. However, the predicted amplitudes and waveforms did not agree with the measured results when a dry snow cover was present. In this paper, we analyze a subset of these measurements to examine the effect of a snow cover on the blast waves. Our purpose here is to determine whether a rigid-porous model of the snow can predict the measured waveforms better than does the viscoelastic model.

Many authors have predicted overpressure as function of distance from the source,^{4, 5} but there have been fewer predictions of the entire waveform.⁶⁻⁹ Albert and Orcutt¹⁰ compared

*Permanent address: Norwegian Defence Construction Service (NDCS), Oslo, Norway

predictions and measured waveforms for short range propagation above a snow cover, and showed that the rigid frame porous model of Attenborough¹¹ (and its low-frequency approximation) gave good agreement with the large waveform changes that were observed. Subsequently, the Attenborough model has been applied¹² to similar measurement data in an inversion process to find the snow parameters that control the acoustic effects of the snow cover. This paper applied this rigid-porous model to predict waveforms at much longer distances and lower frequencies than were previously examined.

In the next section, we describe the measurements and the experimental data. This is followed by a brief outline of the theory of acoustic pulse propagation above a rigid-porous medium and the waveform inversion method used to determine the snow parameters. The results of these theoretical calculations are compared with the measurements, and conclusions are presented in the following sections.

2 FIELD EXPERIMENT

2.1 Description of site

Acoustic measurements were obtained on 22 February 1995 in an open field of pastureland at a site about 200 km north of Oslo, Norway. The field was virtually flat, with a dry snow cover about 0.1 to 0.2 m deep. Below the snow, there was a frozen crust of soil, 0.5 m thick, which had very high compressional wave speeds (around 3000 m s^{-1})¹³, and a density of 2100 kg m^{-3} . Apart from this thin frozen layer, conditions were *superseismic*; i.e., air pressure waves traveled faster than seismic compressional body waves, which had a typical speed of 300 m s^{-1} . Below the frozen soil crust, the soil density was around 1600 kg m^{-3} .

2.2 Meteorological and snow conditions

Meteorological measurements were carried out using tower-mounted instruments and a tethered balloon¹⁴. During the acoustic measurements, the average wind at 10 m above ground was around 5 m s^{-1} , blowing approximately from the south towards the north, and the air temperature was around 0°C . The atmospheric sound velocity profile was almost constant with time and with height during the acoustic measurements. However, because of the influence of the wind, the value of the sound velocity was 326 m s^{-1} towards the south (upwind) and 336 m s^{-1} towards the north (downwind) in Figure 1. Figure 2 shows the meteorological conditions during the acoustic measurements. Even though the wind profiles are almost constant with height, the wind shear close to the ground (which is not visible in Figure 2) caused a difference in propagation conditions for the two directions studied. This will be described in section 4.

Observations were made in two snow pits, concurrent with the blast noise measurements^{15, 16}. The total snow cover thicknesses in the two pits were 18 and 16 cm. A hard snow layer just above the ground surface was overlain by an ice crust, and topped by a layer of newly fallen, partially broken precipitation grains. The bottom layer was 9-10 cm thick with a density of $300\text{-}350 \text{ kg m}^{-3}$. The grain size in this layer ranged from 1 to 4 mm, with rounded clusters and mixed faceted grain types, indicating that some metamorphosis was occurring. The ice layer at the bottom was 1 - 2 cm thick. The top layer was 5-6 cm thick, with smaller grain sizes (0.5-1 mm) and a low density of 125 kg m^{-3} . Snow cover depths measured at other locations in the field on the day of the blast tests ranged from 11 to 20.5 cm, with most values between 14 and 16 cm.

2.3 Acoustical measurements

The Department of Applied Acoustics, University of Salford, England, carried out the acoustical measurements. We analyze only the acoustical data recorded using microphones placed at the snow surface. Table 1 contains a description of acoustical instrumentation used at both locations; 2048 samples were recorded for each shot at a sampling rate of 6.4 kHz. The reader is referred to a special section in the *Inter-noise'96* proceedings for further details on all these measurements^{1, 17-21}.

The experimental geometry is presented in Figure 1. 1-kg charges of C4 explosive^{2, 22, 23} were detonated 2 m above the surface along a line between the two acoustic measurement stations, which were 1500 m apart. The blast waveforms for both the north and south locations are shown in Figure 3. For both recording locations, the duration of the waveforms increases as the propagation distance increases, and the peak amplitude decreases with distance. The amplitude decay is caused in part by spherical spreading of the blast wavefront, and in part by environmental effects, as will be discussed below. The measured pulses have a broad frequency content from about 10 to 100 Hz. For the source, the central frequency for the 1 kg C4 detonations used here is around 50 Hz, compared to a frequency of around 200 Hz for the blank pistol shots used in previous measurements¹⁰. For the snow surface present during these measurements, we observed that the highest frequencies were quickly attenuated as the blast waves propagated.

The waveforms recorded at the north location last longer than those recorded at the south location, and they also exhibit small irregularities in their early portions that do not appear in the south location waveforms. Except for the shortest propagation distance (100 m), the north location waveforms also have higher peak pressure amplitudes than those at the south location. These differences with respect to propagation direction will be discussed below.

3 THEORY

3.1 Pulse waveform for a rigid-porous medium and homogeneous atmosphere

Although a method of calculating pulse shapes based on an empirical model of ground impedance²⁴ has been developed^{6-8, 25} and works well for grass-covered ground, we have included a more complicated, but physically based, model of ground impedance in our calculations to give better agreement with observed measurements for snow¹⁰. This model gives increased accuracy at low frequencies compared to the empirical model. We briefly outline the procedure for calculating theoretical acoustic pulse waveforms from a known (or assumed) surface. For a monofrequency source (with frequency ω) in the air and a receiver on the surface, the acoustic pressure P at a slant distance r away from the source is given by

$$\frac{P}{P_0} = \frac{e^{ikr}}{kr} (1 + Q) e^{-i\omega t} \quad (1)$$

where P_0 is a reference source level, k is the wave number in air, and Q is the image source strength representing the effect of the ground. At high frequencies ($kr \gg 1$), Q can be written as²⁶⁻²⁸

$$Q = R_p + (1 - R_p)F(\omega), \quad (2)$$

where R_p is the plane wave reflection coefficient, F is the ground wave term, and w is a numerical distance, all of which depend on the specific impedance $Z(\omega)$ of the ground. By determining Q_n at a given frequency f_n , the response P_n can be written as,

$$P_n = \frac{P_0}{4\pi r} S_n W_n Q_n e^{i2\pi f_n r/c}, \quad n = 0, 1, 2, \dots, N-1 \quad (3)$$

where S_n and W_n represent the source and instrument effects at frequency index n and c is the speed of sound in air. An inverse FFT,

$$P_m = \frac{1}{N} \sum_{n=0}^{N-1} P_n e^{-i2\pi mn/N}, \quad m = 0, 1, 2, \dots, N-1 \quad (4)$$

is used to construct theoretical pulse waveforms in the time domain. An explicitly layered model of the ground must be used to represent thin snow covers²⁹ using (omitting the frequency subscripts),

$$Z = Z_2 \frac{Z_3 - iZ_2 \tan k_2 d}{Z_2 - iZ_3 \tan k_2 d} \quad (5)$$

where d is the snow layer thickness, k_2 is the wave number in the snow layer, and Z_2 and Z_3 are the impedances of the snow layer and substratum, respectively.³⁰

The acoustic behavior of the soil or snow is specified by the impedance Z_2 and wave number k_2 , which are used in equations (5) and (2) to find the theoretical waveform. We use Attenborough's four-parameter model of ground impedance¹¹ to calculate these parameters. The four input parameters are the effective flow resistivity σ , the porosity Ω , the pore shape factor ratio s_f , and the grain shape factor n' . The snow depth d and the substrate properties are also required in a layered model.

After some experimentation, a simple analytic source pulse $S(t)$ was adopted for the calculations. This source pulse has been previously used in other wave propagation codes^{3, 31}. The form of $S(t)$ is

$$S(t) = \sin(2\pi f_c t) - 0.5 \sin(4\pi f_c t) \quad (6)$$

where t is time and f_c is the central frequency. A value of $f_c = 50$ Hz was used for the 1-kg charges. The waveform and spectrum of the source are shown in Figure 4.

3.2 Inversion technique

The acoustic pulse calculation method can be used in a waveform inversion procedure to determine the acoustic model parameters needed to correctly model the observed waveforms¹². The calculated pulses are directly compared to the observed pulses, and the input parameters

are varied in a systematic way using an iterative search procedure³² until good agreement is obtained.

For our rigid-porous medium calculations, the grain shape factor n' was set to 0.5, corresponding to spherical grains, and the porosity $\Omega = 0.698$ was determined from the measured average density, 275 kg m^{-3} , of the entire snow cover. We fixed the pore shape factor ratio s_f at 0.8 for dry snow¹². Parameters for the frozen soil beneath the snow were fixed at $\sigma = 3000 \text{ kPa s m}^{-2}$, $\Omega = 0.27$, $s_f = 0.73$, and $n' = 0.5$.¹² Only the effective flow resistivity σ of the snow and the snow depth d were varied in the inversion procedure.

Waveform inversion to determine the snow parameters was performed independently for each source-receiver distance. We compared calculated and observed pulses using time-aligned, normalized waveforms.

4 RESULTS

The measured and automatically calculated waveforms are compared in Figure 5. The snow parameters determined from the inversion procedure are listed in Table 2. In general there is good agreement, except at the shortest range of 100 m. This distance would be most affected by inaccuracies in the estimated source pulse used in the calculations. The waveforms measured at this short distance also seem to be affected by some nonlinear effects, due to the large pressure arrival, that are ignored in the theoretical calculations.

Figure 6 compares the experimentally measured waveform for the north measurement location with the rigid-porous snow cover calculations of this paper and with a viscoelastic Fast Field Program (FFP) calculation that did not take the dry snow cover into account². The propagation distance was 1300 m. The improvement in the modeling accuracy using the porous treatment of the snow is clear from this figure.

The snow cover depths determined by the theoretical waveform inversions were consistently near 15 cm, in agreement with the measured snow depths. The effective flow resistivities are nearly constant for the north location, with values between 30 and 41 kPa s m^{-2} . For the south location, the values are higher, 46 - 78 kPa s m^{-2} , and they seem to fluctuate randomly with distance.

These results can be explained by the effects of the snow cover and the wind. At the north location, the propagation of the blast wave is "downwind," so that the waves tended to be refracted downwards causing them to interact strongly with the porous snow. While the refraction by the wind tends to increase the wave amplitude, compared with the case of a homogeneous atmosphere, the interaction with the snow decreased the amplitude and elongated the waveform. This pulse broadening leads to a low effective flow resistivity in the inversion process. The inversion results are consistent, as the propagation distance increases because the snow cover was fairly uniform.

The pulse broadening observed at the south location was less than at the north, so the effective flow resistivities are higher. Here, the propagation was into the wind, so that the waves tended to be refracted upwards, away from the snow surface. Although these waves interacted less with the snow cover, they have lower peak pressure amplitudes because some of the energy that was refracted upwards never reaches the microphone on the ground. The amplitudes, and the inversion parameters, fluctuate more than for the north waveforms because they are strongly affected by slight fluctuations in the wind. The waveform and amplitude

changes in this case are caused more by the wind-generated refraction than by snow cover interaction.

A single frequency (50-Hz) poroelastic calculation³³ demonstrates the effect of the wind shear close to the ground (Figure 7). A snow depth of 0.2 m, an effective flow resistivity of 30 kPa s m⁻², and a porosity of 0.689 were used. At the ground, the model sound velocity was 331 m s⁻¹, while at 10 m height above the ground, the sound velocity was 336 m s⁻¹ towards the north and 326 m s⁻¹ towards the south. Figure 7 clearly demonstrates the wind effect at this low frequency. The calculation predicts a 4 dB difference between up- and downwind propagation at 100 m, and a 24-dB difference at 1 km, which agrees reasonably well the measured amplitudes, but shows that the downwind enhancement was overpredicted. The measured difference of 11 dB at 1.1 km is large, probably because of the simple atmospheric model that was used and because the snow cover effect was underestimated in the calculation.

The effective flow resistivities, 30 - 41 kPa s m⁻², determined for the snow cover from the north location waveforms are slightly higher than has been determined from most previous pulse measurements on snow^{12, 15, 21}. The relatively high flow resistivities are not attributable to the use of an incorrect source pulse in the calculations, as waveform inversion tests with higher frequency source pulses ($f_c = 75$ and 100 Hz) gave nearly the same results (depth and effective flow resistivity) for the longer propagation ranges.

While the higher effective flow resistivity values for snow are believed to be accurate, the possibility that the waveform inversion method and the parameters resulting from this technique have some dependency on frequency cannot be eliminated. As additional evidence for these values, impedance tube measurements³⁴ done the day after the blast measurements also gave relatively high values for the effective flow resistivity of 59-69 kPa s m⁻². However, rain had fallen on the snow by that time, and the warm air temperature overnight may have caused substantial changes in the snow structure by that time.

5 SUMMARY AND CONCLUDING REMARKS

Blast waves propagating in the up- and downwind directions above a dry snow exhibit pulse broadening caused by wave interaction with the snow cover. By modeling the effect of the snow cover using a porous medium model, our predicted pulses are in much better agreement with experimental results than are previously published calculations using the viscoelastic Fast Field Program that did not take the dry snow cover into account. Our results indicate that a porous boundary condition will need to be included for non-homogeneous atmospheric conditions when a snow cover is present.

ACKNOWLEDGEMENTS

We thank the following persons: Robert L. Guice at ARA, USA, for organizing acoustic and seismic data; Geoffrey Kerry at University of Salford, UK, for providing the measured acoustic data; Amir M. Kaynia and Christian Madshus at NGI, Norway, for determining the seismic properties of the test site; and Steve Arcone and Mark Moran, CRREL, for technical reviews. The field experiment was initiated and managed by Arnfinn Jenssen at NDCS, Norway. This work was funded by NDCS and the Directorate of Research and Development, US Army Corps of Engineers.

REFERENCES

1. G. Kerry, "An overview of the long range impulse sound propagation measurements made in Norway," *Inter-noise 96*, Liverpool, UK, 583-588 (1996).
2. L.R. Hole, "An experimental and theoretical study on propagation of acoustic pulses in a strongly refracting atmosphere," *Appl. Acoust.* **53**, 583-588 (1997).
3. H. Schmidt, *SAFARI: Seismo-acoustic fast field algorithm for range-independent environments. User's guide*, Report SR-113 (SACLANTCEN, 1987).
4. J.W. Reed, *BLASTO, a PC program for predicting positive phase overpressure at distance from an explosion*, (JWR Inc, Albuquerque, NM, n.d.).
5. G. Kerry, D.J. Saunders, and A. Sills, "The use of meteorological profiles to predict the peak sound pressure level at distance from small explosions," *J. Acoust. Soc. Am.* **81**, 888-896 (1987).
6. R. Raspet, J. Ezell, and H.E. Bass, "Additional comments on and erratum for 'Effect of finite ground impedance on the propagation of acoustic pulses' [*J. Acoust. Soc. Amer.* **74**, 267-274 (1983)]," *J. Acoust. Soc. Am.* **77**, 1955-1958 (1985).
7. R. Raspet, H.E. Bass, and J. Ezell, "Effect of finite ground impedance on the propagation of acoustic pulses," *J. Acoust. Soc. Am.* **74**, 267-274 (1983).
8. C.G. Don and A.J. Cramond, "Impulse propagation in a neutral atmosphere," *J. Acoust. Soc. Am.* **81**, 1341-1349 (1987).
9. I.P. Chunchuzov, G.A. Bush, and S.N. Kulichov, "On acoustical impulse propagation in a moving inhomogeneous atmospheric layer," *J. Acoust. Soc. Am.* **88**, 455-461 (1990).
10. D.G. Albert and J.A. Orcutt, "Acoustic pulse propagation above grassland and snow: Comparison of theoretical and experimental waveforms," *J. Acoust. Soc. Am.* **87**, 93-100 (1990).
11. K. Attenborough, "Acoustical impedance models for outdoor ground surfaces," *J. Sound Vib.* **99**, 521-544 (1985).
12. D.G. Albert, "Acoustic waveform inversion with application to seasonal snow covers," *J. Acoust. Soc. Am.* (1997, submitted).
13. A.M. Kaynia and C. Madshus, *Blast propagation through forest- NOR 95/1 tests*, NGI report 515137-4 (Norwegian Geotechnical Institute, Oslo, Norway, 1995).
14. L.R. Hole, Y. Gjessing, T. de Lange, and J.W. Reed, "Meteorological measurements and conditions during Norwegian Trials," *Noise Cont. Eng. J.* (1997, submitted).
15. D.G. Albert, "Snow cover properties from impulsive noise propagation measurements," *Noise Cont. Eng. J.* (1997, submitted).
16. S. Bakkehøi, *Snow classification during tests at Haslemoen, February 1995*, NGI Report 51537-4 (Norwegian Geotechnical Institute, Oslo, Norway, 1995).
17. R. Guice and A. Jenssen, "Impulse noise measurements in a forest during summer and winter - an overview of measurements," *Inter-Noise 96*, Liverpool, UK, 2589-2594 (1996).
18. M. Trimpop and H.K. W., "On the advantage of relational data structures and client/server applications for shooting noise data using ODBC, SQL and OLE standards," *Inter-noise 96*, Liverpool, UK, 549-554 (1996).
19. L.R. Hole, Y. Gjessing, and T. de Lange, "Meteorological measurements during Norwegian Trials," *Inter-noise 96*, Liverpool, UK, 605-610 (1996).
20. C. Madshus and A.M. Kanyia, "Ground response to propagating airblast," *Inter-Noise 96*, Liverpool, UK, 1433-1438 (1996).
21. D.G. Albert, "Snow cover effects on impulsive noise propagation in a forest," *Inter-Noise 96*, Liverpool, UK, 663-668 (1996).
22. L. Kennedy, S. Hikida, and R. Ekler, *Overpressure and dynamic pressure waveforms for small C4 charge detonations*, Report no SSS-DFR-94-14507 (Maxwell S-Cubed Division, Albuquerque, NM, 1994).
23. R. Ford, D.J. Saunders, and G. Kerry, "The acoustic pressure waveform from small unconfined charges of plastic explosive," *J. Acoust. Soc. Am.* **94**, 408-417 (1993).
24. M.E. Delaney and E.N. Bazley, "Acoustical properties of fibrous absorbent materials," *Appl. Acoust.* **3**, 105-116 (1970).
25. A.J. Cramond and C.G. Don, "Reflection of impulses as a method of determining acoustic impedance," *J. Acoust. Soc. Am.* **75**, 382-389. (1984).

26. K. Attenborough, S.I. Hayek, and J.M. Lawther, "Propagation of sound above a porous half-space," *J. Acoust. Soc. Am.* **68**, 1493-1501 (1980).
27. K.U. Ingard, "On the reflection of a spherical wave from an infinite plane," *J. Acoust. Soc. Am.* **23**, 329-335 (1951).
28. I. Rudnick, "Propagation of an acoustic wave along a boundary," *J. Acoust. Soc. Am.* **19**, 348-356 (1947).
29. J. Nicolas, J.-L. Berry, and G.A. Daigle, "Propagation of sound above a finite layer of snow," *J. Acoust. Soc. Am.* **77**, 67-73 (1985).
30. L.M. Brekhovskikh, *Waves in Layered Media*, (Academic Press, New York, 1980), 2nd ed.
31. K. Fuchs and G. Mueller, "Computation of synthetic seismograms with the reflectivity method and comparison with observations," *Geophys. J. Royal Astron. Soc.* **23**, 417-433 (1971).
32. W.H. Press, B.P. Flannery, S.A. Teukolsky, and W.T. Vetterling, *Numerical recipes: The art of scientific computing*, (Cambridge University Press, New York, 1986).
33. L.R. Hole, A.M. Kaynia, and C. Madshus, "Measurement and simulation of low frequency impulse noise and ground vibration from airblasts," *J. Sound Vib.* (1998, in press).
34. S. Storeheier, *A preliminary investigation on the acoustic characterization of snow at the Haslemoen site*, Report 40-NO950182 (Sintef Delab, Trondheim, Norway, 1995).

TABLE 1
Acoustical instrumentation for each station.

Microphones	4 B&K, 4147
Preamplifiers	4 B&K, 2639
Recorders	1 of 4 ch., SONY PC 204 DAT
Analyzers	2 Oni Sokki
Sampling heights	0, 2, 4, and 8 m

TABLE 2
Waveform inversion results.

<i>Range (m)</i>	<i>North Location</i>		<i>South Location</i>	
	<i>Effective flow resistivity (σ) kPa s m²</i>	<i>Snow depth (cm)</i>	<i>Effective flow resistivity (σ) kPa s m²</i>	<i>Snow depth (cm)</i>
100	17	30	(38)	(23)
200	24	20	(31)	(24)
400	30	16	46	17
750	38	15	65	14
1100	41	15	48	13
1300	34	14	67	14
1400	40	15	78	12

Values in parentheses are loosely determined by the waveform inversion process.

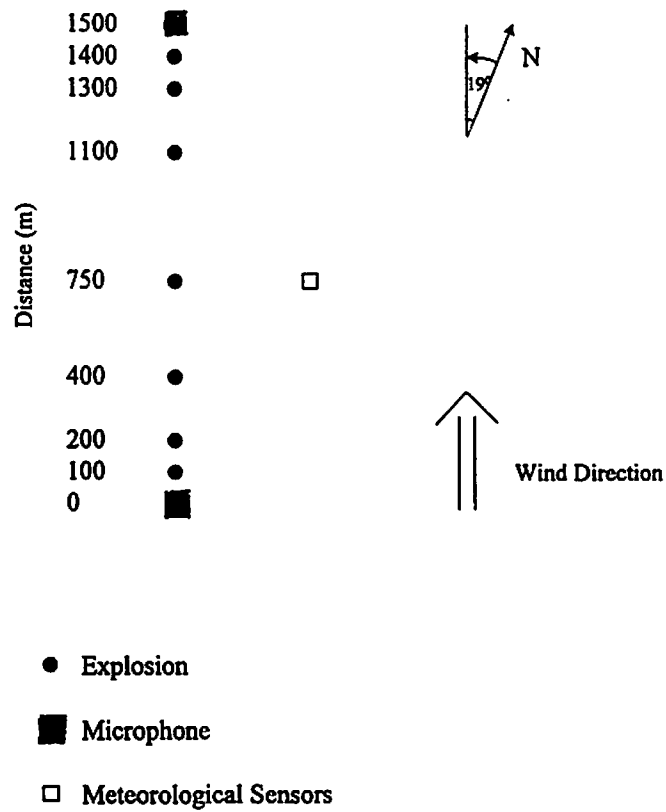


Figure 1. Plan view of the experimental layout. The orientation of the sensor line is 341° true. Detonation height was 2 m, and the acoustic waveforms were recorded using surface microphones at the 0 (upwind) and 1500 m (downwind) locations.

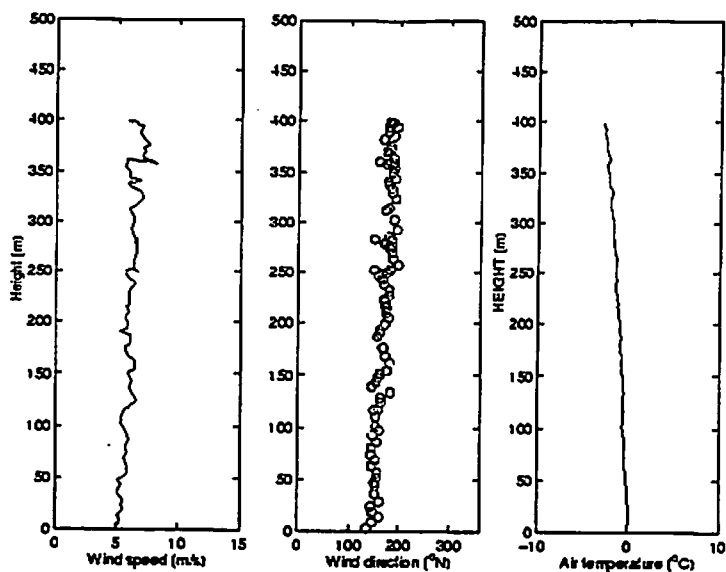


Figure 2. Meteorological conditions during the blast noise measurements, 22 February 1252-1308 UTC, measured by Tethersonde¹⁹. The wind speed was approximately $4\text{-}5\text{ m s}^{-1}$ during the tests, and always blowing approximately from the south along the detonation line.

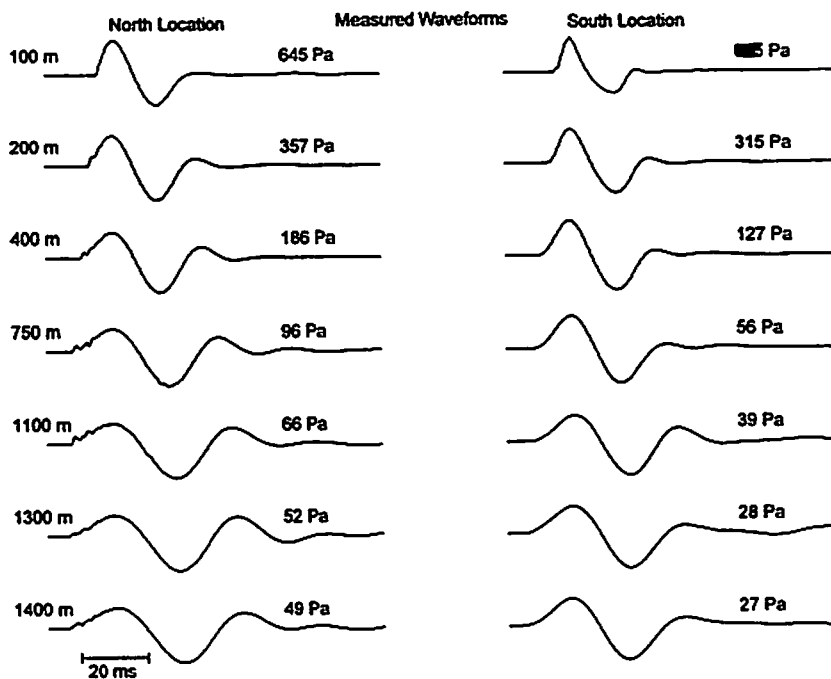


Figure 3. Normalized blast waveforms experimentally observed by surface microphones for 1-kg explosive charges detonated 2 m above the surface. Although the propagation distances are the same for both observation locations, the waveforms recorded at the downwind location are longer than those measured at the upwind location.

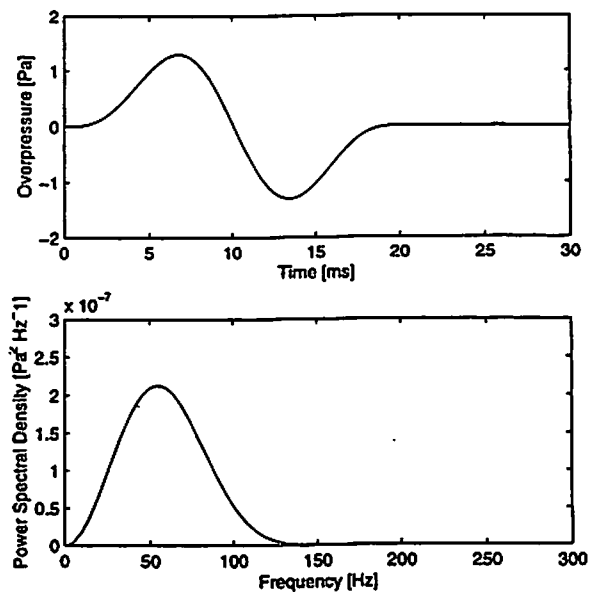


Figure 4. Assumed source waveform (a) and its power spectrum (b) used in the theoretical calculations.

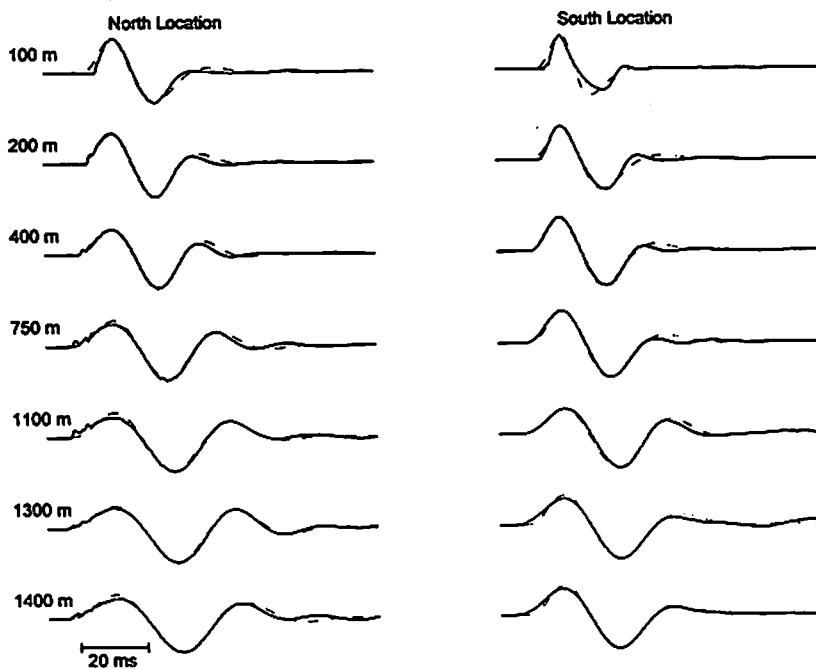


Figure 5. Observed and predicted waveforms at the snow surface, made using the rigid-porous medium model, for both the north and south measurement locations.

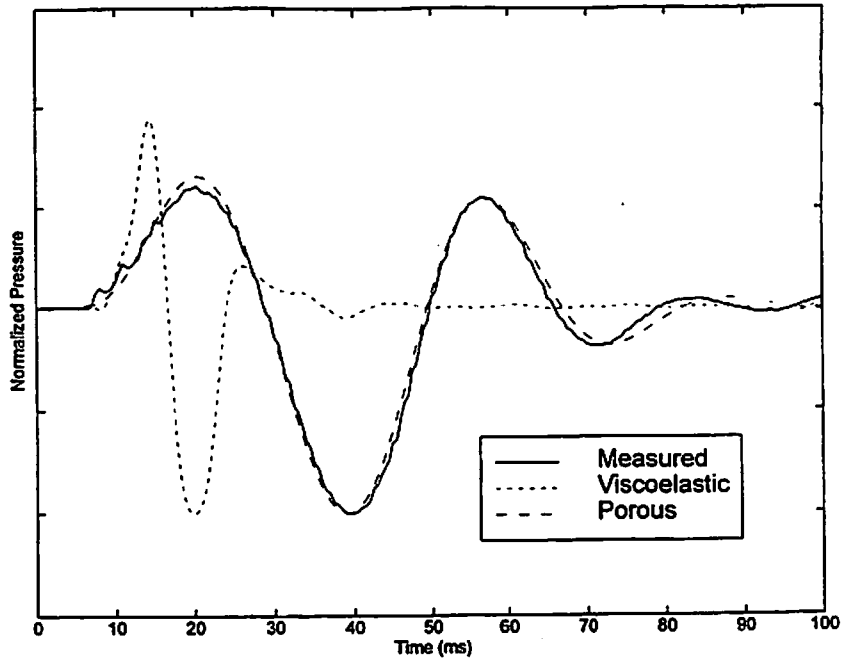


Figure 6. Comparison of the experimental waveform (solid line) at north measurement location, 1300 m from the source with a viscoelastic Fast Field Program (FFP) calculation (dashed line, same result as in Figure 9 in Hole²), and with the rigid-porous medium calculations of this paper (dotted line). All waveforms have been normalized.

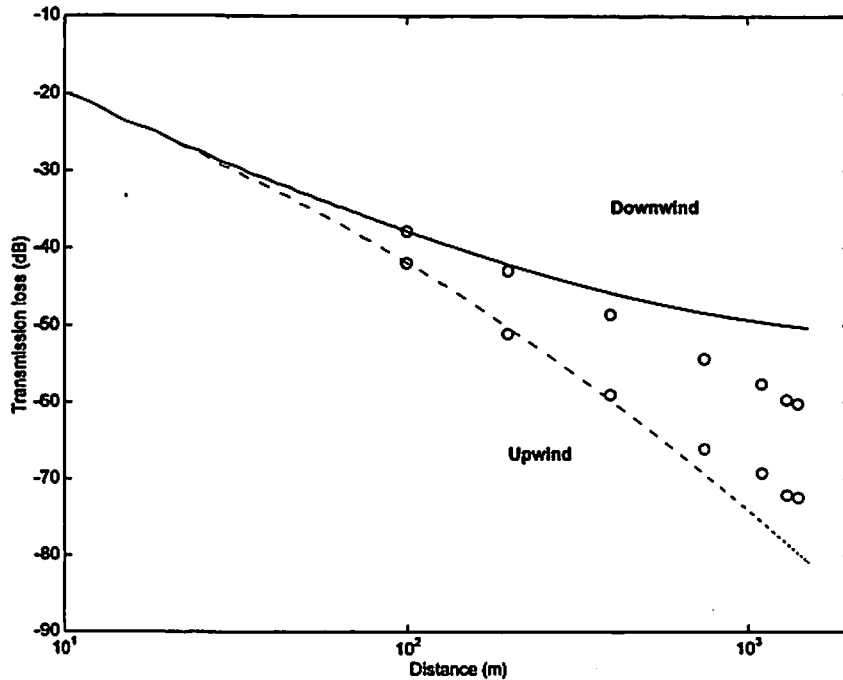


Figure 7. Poroelastic FFP calculations at 50 Hz, for upwind (north, solid line) and downwind (south, dashed line), measurement locations. Points are the peak amplitudes of the measured waveforms, scaled to match the calculated levels at 100 m.

THEORETICAL ANALYSIS OF PULSE PROPAGATION ABOVE A CURVED SURFACE WHICH SUPPORTS A SURFACE WAVE.

Richard Raspet, National Center for Physical Acoustics, University of Mississippi, University, MS 38677

Keith Attenborough, Kai Ming Li and Qiang Wang, Engineering Mechanics Discipline, The Open University, Milton Keynes MK7 6AA, UK

At the recent Acoustical Society of America meeting in Seattle, K. M. Li and Q. Wang [J. Acoust. Soc. Am. 103 (No.5, Pt 2), 2802 (1998)] reported measurements of pulse propagation over a convex impedance surface whose imaginary part of impedance was much larger than the real part. The theory of Raspet et. al. [J. Acoust. Soc. Am. 89(1), 107-114 (1991)] predicts that one of the residue series contributions corresponds to the complex impedance surface wave. As such it displays a much reduced phase velocity. Li and Wang observed the splitting of a pulse into two parts, even though a single mode dominated the prediction for the carrier frequency. They speculated that each mode may contain components of an ordinary creeping wave and a surface wave. In this talk we demonstrate that the shape of the pulse envelope is critical in measurements of single frequency phase velocity measurements over the complex impedance curved surface and present calculations of diffracted pulse shapes with and without surface waves.

Introductions

At the spring meeting of the Acoustical Society of America, K. M. Li and Qiang Wang presented measurements of acoustic pulses propagation over a convex cylindrical surface.¹ The surface was designed to produce complex surface impedance whose imaginary part is much larger than the real part. The theoretical research of Raspet, Baird and Wu² predicts that such a surface should support a surface wave of much reduced phase velocity in addition to the ordinary residue series contributions. Li and Wang observed the separated residue series and surface wave pulses as expected but also found pulse splitting for frequencies which were predicted to only support surface waves. In this paper we investigate the pulse shapes predicted for Li and Wang's surface using the theory of Raspet et al² in the pulse propagation prediction of Daigle and Raspet.³

Calculations

Li and Wang fit level difference measurements for their surface to Attenborough's exponentially varying impedance model.⁴ They found an effective flow resistivity of 4.0 kPa s m^{-2} and an exponential rate of porosity change of 570 m^{-1} . Figure 1 displays the transfer function predicted for the geometry of Li and Wang's Figure 2: $z_1 = 4.0 \text{ cm}$, $z_2 = 2.0 \text{ cm}$, $r = 1.5 \text{ m}$. The surface wave component clearly dominates below 4200 Hz.

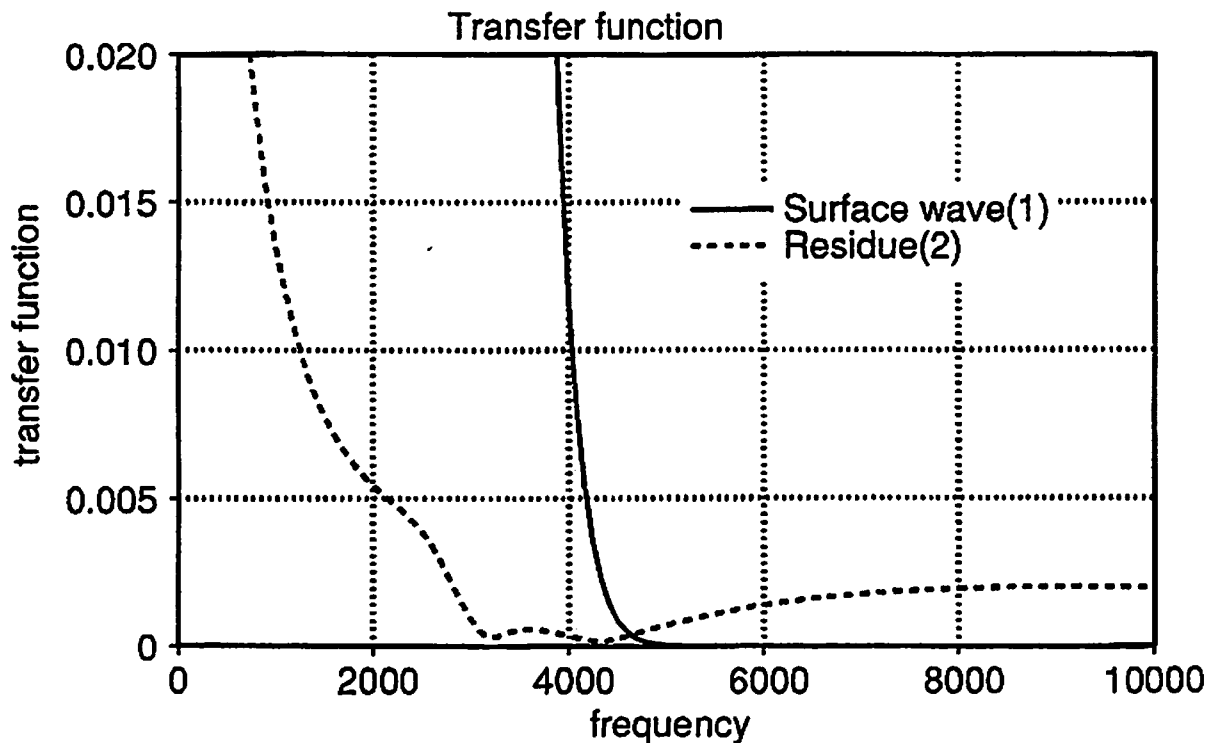


Fig 1. Magnitude of the transfer function for the surface wave and first residue series for sound propagation above a 25m radius cylinder
 $z_s = 02n$, $Z_r = B_r = 04m$, $r = 1.5m$

If a 12 cycle 400 Hz pulse with a Gaussian three cycle transition at the front and back is input into the pulse propagation prediction (Figure 2), the result is the waveform shown in Figure 3. It appears as if two wave components are present although the surface wave should be the only measurable contribution at 4000 Hz. Careful examination of Figure 3 reveals that the frequency context of the pulses is quite different from 4000 Hz. The spectral broadening of the pulse creates lower and higher frequency components which travel at different velocities.

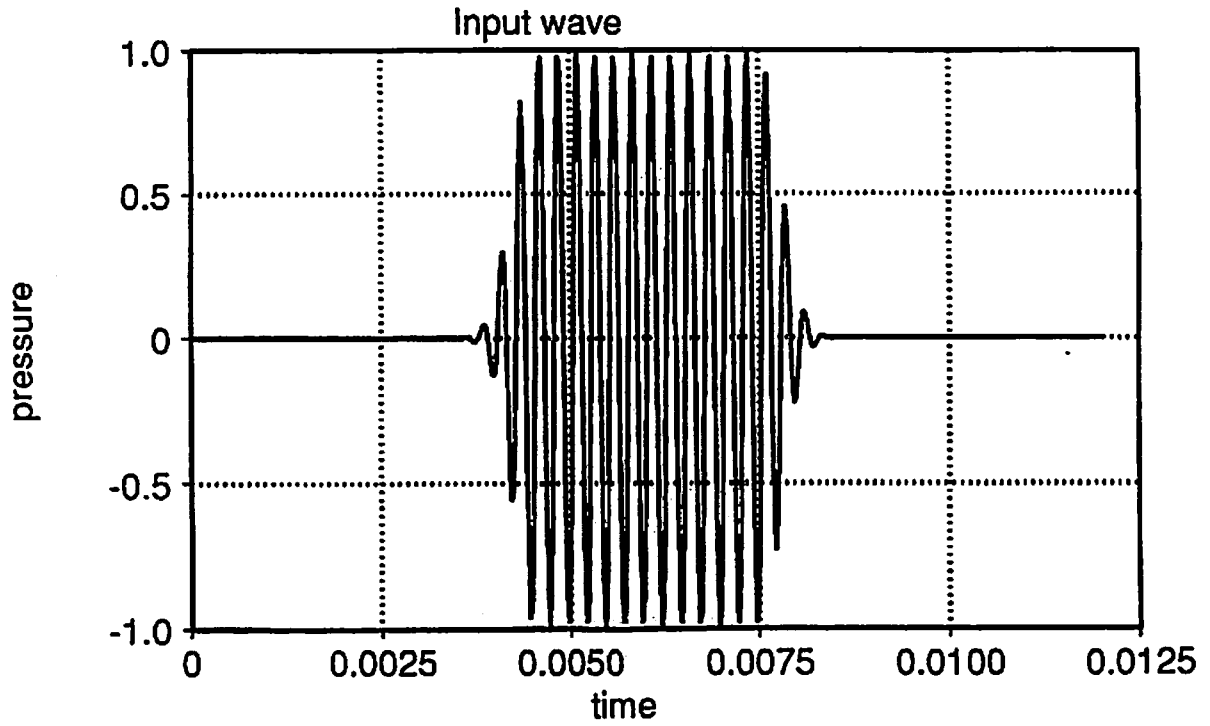


Fig 2. Input wave for calculation 4000 Hz.

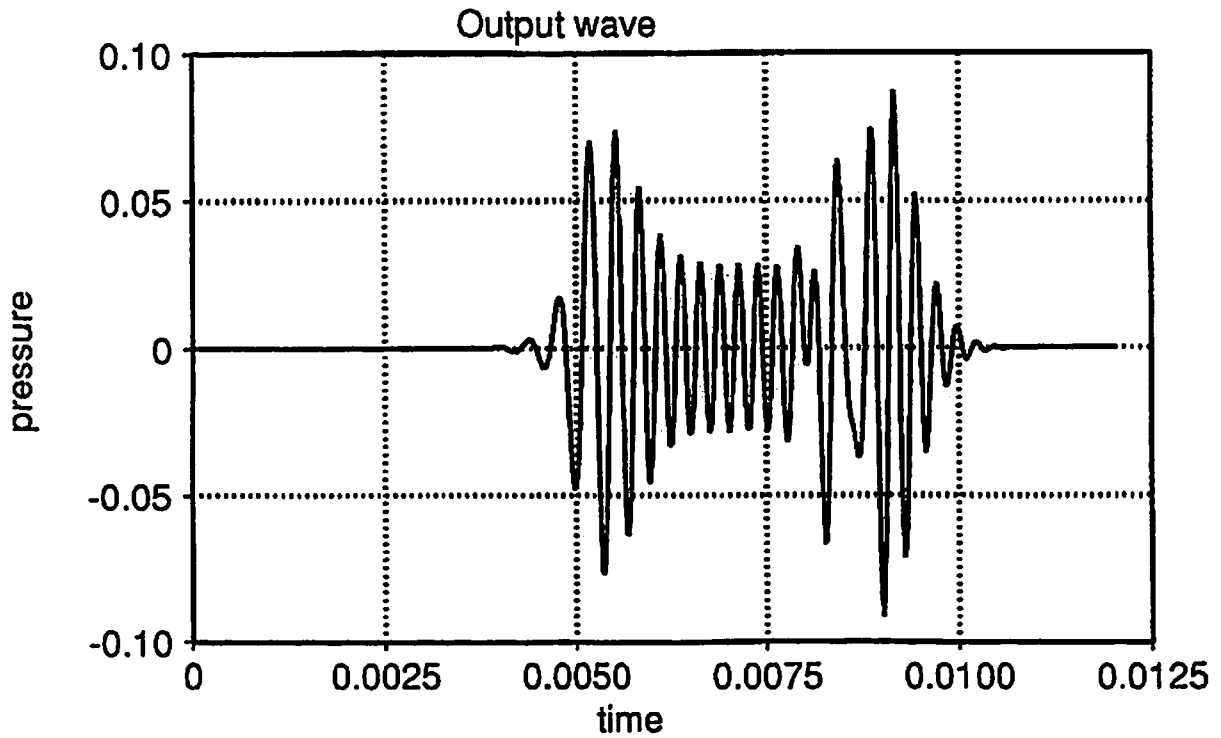


Fig 3. Output wave for the 4000 Hz pulse

A 24 cycle 4000 Hz pulse with a Gaussian envelope was then run. This pulse shapes minimizes spectral broadening of the 4000 Hz line. The output from this signal is shown in Figure 4. The output pulse is a single attenuated replica of the input pulse.

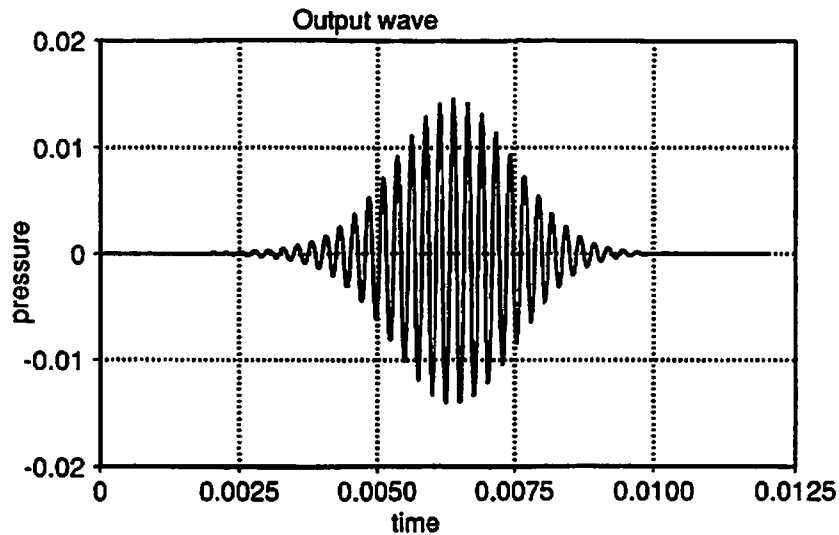


Fig 4. Output wave for a 4000 Hz pulse with a Gaussian envelope.

Next, the same input pulse scaled to 4650 Hz was input into the prediction. According to Figure 1, the output pulse should contain significant surface wave and residue series components. This is in fact the case, as is illustrated in Figure 5.

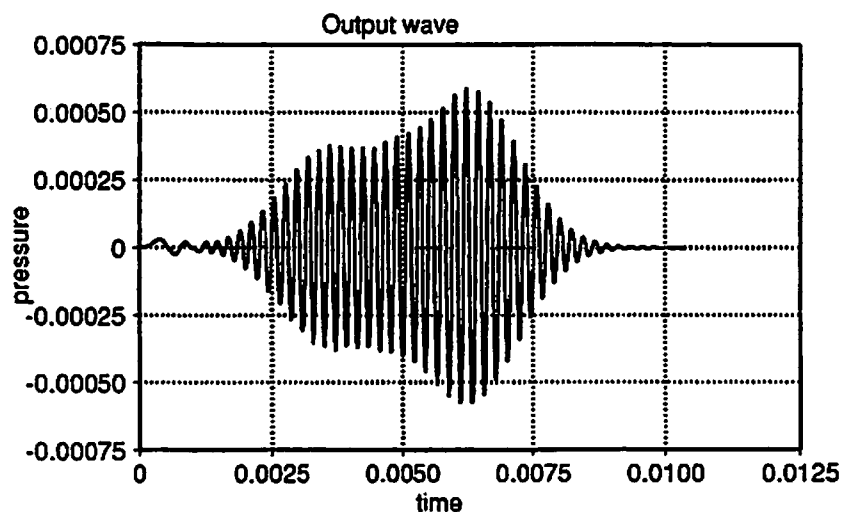


Fig 5. Output wave for a 4650 Hz pulse with a Gaussian envelope.

The phase and group velocities of the two components were calculated in order to investigate the separation velocity of the two wave contributions. These velocities, as a function of frequency, are displayed in Figure 6. The separation velocity in Figure 5 corresponds to the group velocities in Figure 6.

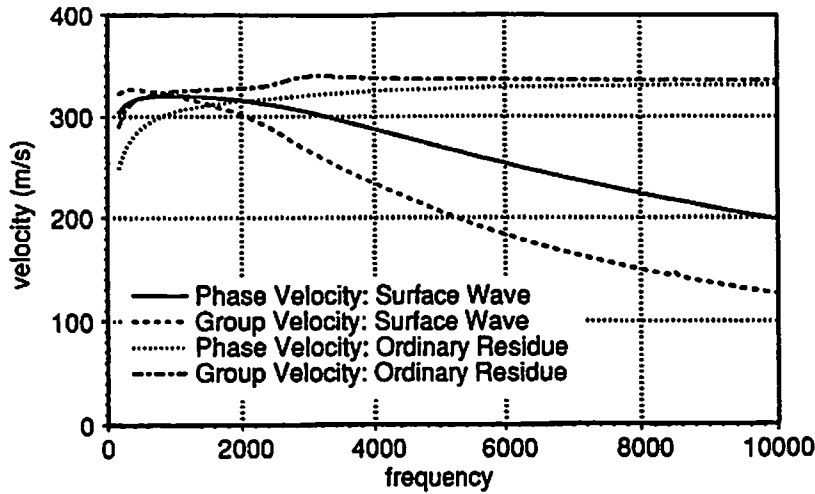


Fig 6. Phase and group velocity for the surface wave and residue series.

As a final calculation, the pulse shape due to a single cycle at 4650 Hz was input to the theory. The output pulse from this is shown in Figure 7. If the first two maxima are considered as separate pulses, the separation velocity approximates to the phase velocity. Group velocity is only a valid concept if the pulse retains its original shape.

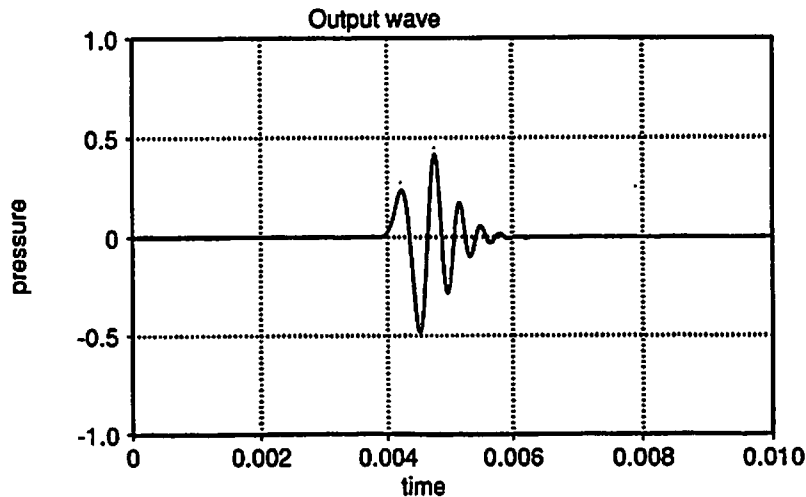


Fig 7. Output wave for a single cycle 4650 Hz pulse.

Conclusion

Care must be taken in using acoustic pulses to investigate the surface wave over a complex impedance curved surface. The dispersion and attenuation of the surface wave contribution vary so rapidly with frequency and distance that conventional ideas of phase and group velocity may not be valid. Further analytic investigations will be pursued in the future. The experimental results of Li and Wang will also be analyzed in the near future.

REFERENCES

1. Kai Ming Li and Qiang Wang, "Surface wave over a convex impedance", Proceedings of the 16th International Congress on acoustics and the 135th Meeting of the Acoustical Society of America, June 20-26, 1998, page 477-478
2. Richard Rasset, Gordon E. Baird and Wenliang Wu, "The relationship between upward refraction above a complex impedance plane and the spherical wave evaluation for a homogeneous atmosphere", J. Acoust. Soc. Am. **89**, 107-114 (1991).
3. Gilles A. Daigle, Richard Rasset, "Dispersion of impulse sound above a curved surface", J. Acoust. Soc. Am. **89**, 101-106 (1991).
4. Keith Attenborough, "Ground parameter information for propagation modeling", J. Acoust. Soc. Am. **92**, 418-427 (1992).

Survey of Research of Sound Propagation in Forests
Michelle Swearingen, David Swanson, and Karl Reichard
Applied Research Laboratory, Penn State University, P.O. Box 30, State College, PA 16802
(814)865-0422 (P), (814)863-9918 (Fax), swear@sabine.acs.psu.edu
(814)865-2448 (P), (814)863-9918 (Fax), dcs5@psu.edu
(814)863-7681 (P), (814)863-9918 (Fax), kmr5@psu.edu

Abstract:

An overview of research in sound propagation in forested areas is presented and directions for future research are identified. Although much research has been done in the area of sound propagation within and through forested and densely vegetated areas, the available literature is scattered and varied. Furthermore, the different findings are sometimes contradictory: one researcher may find a large attenuation, while the next finds only minimal effects. Some of the differences are due to variations in the methods employed, such as source and receiver locations and heights, noise sources, and how the data are presented. Comparisons are not immediately obvious because some of the data are presented in dB/100m, dB/100ft, and other length scales, and different test sites are used. Also, meteorological conditions are rarely noted, as many researchers felt that the conditions were constant and/or small enough to neglect. Advances in measurement techniques and sound propagation models have opened the doors to new possibilities in research. Improved measurement equipment now allows researchers to gain a more accurate view of what really happens to sound in a forest and better meteorological sensors assist in determining what effect the microclimate under a forest canopy really has on the propagation of sound. Developments in outdoor sound propagation models, such as the parabolic equations method, allow scientists to more efficiently and accurately model the sound propagation around and through forested areas.

Introduction:

A limited amount of research has been done in the area of sound propagation within and through forested and densely vegetated areas. Unfortunately, this literature is scattered throughout many publications, and has not yet been summarized in a major refereed journal. The literature available is scattered and varied. Articles pertaining to this topic can be found primarily in acoustical journals, conference proceedings, theses, and biological journals. The different interpretations of findings are sometimes contradictory. Most research has found some attenuation in the forest, but not all researchers consider the amounts to be significant. Some of the differences are due to variations in the methods employed, such as source and receiver locations and heights, pure tones vs. random noise, point sources vs. line sources, and how the data are interpreted and presented. Comparisons are not immediately obvious because some of the data are presented in dB/100m, dB/100ft, and other length scales, and different test sites are used. Also, meteorological conditions are rarely noted, as many researchers felt that the conditions were constant and/or small enough to neglect.

Figure 1 shows the frequency ranges studied in each paper cited here. Note that the low-range frequencies have been largely neglected.

This compilation of the major research to date will benefit many different groups, including community noise boards, private companies, and biologists. Community noise boards will be interested because it will help them to better evaluate noise problems and determine potential solutions. Private companies will be able to use the information to better secure their facilities through acoustic detection. Biologists can use the information to develop new, non-intrusive ways to study wildlife populations.

Advances in measurement techniques and propagation models have opened the doors to new possibilities in research. Better equipment will allow researchers to gain a more accurate view of what really happens to sound in a forest. Better meteorological sensors will assist in determining what effect the microclimate under a forest canopy really has on the propagation of sound. More powerful computers will help process data more efficiently. Developments in outdoor sound propagation models, such as the parabolic equations method, will allow scientists to more efficiently and accurately model the sound propagation around and through forested areas.

Previous Research in the Forests of the World:

Work in the area of sound propagation in forested areas has been done all over the world, from the jungles of Panama to the dense forests of Maine and the Netherlands. Surprisingly, much of the information extracted from these various tests agrees reasonably well, although factors such as tree type, forest density, forest age, terrain features, and density of undergrowth all cause the numbers to vary.

The earliest article published in the area of sound propagation through forested areas was in 1946 by Carl Eyring¹. He investigated octave band noise for frequencies between 150 Hz and 10 kHz in the jungles of Panama. He defined the term "excess attenuation" (EA) to mean any attenuation above and beyond that due to spherical spreading. He assumed that any excess attenuation was due to the jungle, since he determined that wind velocity and temperature gradients were negligible in the jungle. He located both the source and receiver inside the Panamanian jungles studied, and he raised the receiver ~1.5 m (5 ft) above the ground in order to mimic the placement of a human ear. Eyring determined that optical visibility is related to the excess attenuation, i.e. less optical visibility related to more excess attenuation. In 1959, Wiener and Keast² performed a similar study in the dense woodlands of Eastern Maine. Their data agreed with Eyring's data of comparable optical visibility. Wiener and Keast state that absorption effects dominate over scattering effects. However, it should be noted that the receiver was located ~1 m (3 ft) above the ground.

In 1963, T. F. W. Embleton³ found larger average excess attenuations by around 2-3dB/100m. However, he placed the source outside of the forest and the receiver inside, instead of both source and receiver inside, as Eyring and Wiener and Keast did. The extra 2-3 dB of attenuation present in his data could be because of the source and receiver locations. Previous studies didn't include the edge effect of the forest. Embleton found the attenuation to follow an S-shaped curve. He postulated that the curve shape could be indicative of absorption due to branch oscillations. Further analysis showed that while the frequency dependence could follow from branch oscillations, the magnitude of excess attenuation did not. In his 1971 Master of Science thesis, Alan Bjornsen⁴ showed that attenuation is indeed greater when the source is located outside the forest, thus forcing the sound to travel through the forest edge. He studied three different forest types, and found similar results for each, although the frequency of maximum attenuation differed for the three forest types. In that same year, Richard Frank⁵ published his Master's thesis on the effectiveness of plants as highway noise barriers. He studied heterogeneous deciduous forests, and homogeneous deciduous forests. He found that the heterogeneous forest attenuated sound better, possibly due to the thick understory. He determined that forest plantings, although not very effective noise barriers, still have merit as highway barriers for aesthetic and safety reasons. Cook and van Haverbeke⁶ published a study for the U. S. Department of Agriculture in 1971 with their recommendations for the use of trees and shrubs for noise abatement. They found that a belt 20 feet thick would be adequate for residential noise abatement, while 100 feet was needed for freeway noise reduction. They also found that the belts of trees must be wide, dense, and preferably made up of coniferous trees. These recommendations would lead to a 5 to 12 dB reduction in noise levels. Their measurements were through the belts of trees, i.e. source on one side and receiver on the other side.

In 1972, researchers started to look into the causes of attenuation in more detail. Donald Aylor^{7 8} found in his two studies that foliage was the main attenuation device for mid to high frequencies, while the ground was mainly responsible for low frequency attenuation. He also found broad leaves attenuate sound better than narrow ones. In 1976, Leslie Frank⁹ studied tree bark and the forest floor as absorbing elements in the forest. He found that tree bark has a low absorption coefficient (approximately 0.05), while the ground has a much higher absorption coefficient, ranging from 0.15 to 0.60 for low frequencies and from 0.45 to 0.90 for high frequencies. He also determined that the ground absorption is greater when the soil is moist, and when covered by leaf litter. In that same year, Linskens et al¹⁰ published a study of the dependence of season on attenuation. They found that low frequencies were more attenuated in the forest during the winter, while high frequencies were more attenuated in the summertime. Herrington and Brock¹¹ studied attenuation as a function of height. They found that above 15 feet, there is no significant difference in attenuation with height. However, below 15 feet, the ground absorption plays an increasingly larger role.

In 1977, Carlson, McDaniel, and Reethof¹² studied the absorbing characteristics of tree bark and the ground. They found the absorption of tree bark and the ground using impedance tube measurements. They found that thicker bark provides more absorption than thin bark, with absorption coefficients ranging from 0.02 to 0.10. This is a larger range than L. Frank obtained, although his results do fall within that range. They measured the ground absorption to be as large as 0.9 at 2000 Hz, and less for lower frequencies. This agrees well with the findings of L. Frank. The

sound propagation measurements used the source and receiver in the forest, with heights between 1.5 and 2.4 meters (5 and 8 feet), as well as temperature gradient measurements up to 15 m (50 ft). These studies showed that the absorption acts like spherical spreading over short distances, and then diverges to become greater at longer propagation distances. Marten and Marler¹³ (1977) and Marten, Quine, and Marler¹⁴ (1977) studied the effects of receiver height in a forest and in the jungle. They found similar results for both cases. In each case, they found that trees improved transmission for frequencies below 3 kHz for heights above 1m. However, frequencies below 2 kHz were quite attenuated near the ground. They found that height affected attenuation more than the habitat type. That same year, M. J. M. Martens¹⁵ published a study that looked exclusively at the influence of the soil on sound propagation. He constructed a computer model of the ground interference that takes care of the phase shift that occurs when the sound wave reflects off the ground, assuming the soil is reflecting. He took some propagation and weather data, and found that the low SPL in the 200 to 600 Hz range was caused by interference of the direct and reflected sound waves. By comparing the calculated and experimental SPL's, he was able to calculate the reflection coefficient of the ground, and therefore its acoustic impedance.

As advances in technology allowed for smaller sensors and Laser-Doppler vibrometers, both of which had less mechanical impact on the physical systems than earlier devices, researchers started to investigate smaller and more specific components of the forest. This allowed for more detailed information about which components effect which frequencies the most. Thermoviscous absorption was found to be the major contributing factor in attenuation due to pine boughs (Burns, 1979)¹⁶. That same study also looked at effects due to the flexing of trunks and branches, flexing of needles, and scattering. Martens and Michelsen¹⁷ (1981) found the absorption due to a single plant leaf by using a Laser-Doppler vibrometer to study the leaf vibrations. They found the absorption to be quite small on a per leaf basis, but speculate that since the typical tree has 2×10^5 leaves, the absorption could be significant. In 1986, Geveling, Martens, and Roebroek¹⁸ did another study with a Laser-Doppler Vibrometer, and found the leaves to be linear systems for frequencies between 75 Hz and 2000 Hz. They also state that the vibrational response of a leaf depends on its structure, physiology, and amount of energy loss. Tang, Ong, and Woon¹⁹ (1986) simulated sound propagation through six different types of leafy foliage using a Monte Carlo technique. They measured leaf vibrations for six different types of leaves to determine the amount of sound energy transferred into heat. They report that leaves may alter or scatter sound via diffraction, reflection, and interference. The leaves were modeled as circular disks over some "leaf area density", randomly arranged in position and angular orientation. The results compared well with Martens "Foliage as a low-pass filter" (1980).

Through these same times, research continued on a larger scale as well. Many studies included computer models as computational power grew. Yamada, Watanabe, Nakamura, Yokoyama, and Takeoka²⁰ measured similar locations with and without hedges to determine the absorption due to the hedges. They calculated the absorption coefficient of an individual tree, and found it to be proportional to \sqrt{f} . Although the hedges didn't attenuate much on their own, they are still desirable as a barrier for visual purposes. They also looked at the masking effect of wind noise in the trees, and found that it ranged from 30-70 dB, depending on wind speed. In 1980, Martens²¹ modeled a forest in an anechoic chamber. He found that foliage acts as an amplifier in the mid-range frequencies, and a noise filter in the high frequencies. Martens's model is effective for frequencies between 200 Hz and 12.5 kHz. In his 1980 Masters thesis, Talaske²² speculated that the absorption in a forest is caused more by the thick organic layers that the trees produce, which lowers the impedance of the forest floor, than by the trees themselves. In 1981, Martens²³ found that more excess attenuation occurred at 1.2 m above then ground than at 3.9 m. He also found that at least 12 m of trees are necessary for any noise control, and that the trees need to be planted in rows perpendicular to the direction of the sound field for maximum attenuation.

In 1982, Bullen and Fricke²⁴ modeled propagation through a large number of trees as a classical diffusion problem. They derived a general differential equation and compared the predictions to a small scale model study and to field measurements. They found trees to be transparent below 1 kHz at 60 m. In 1984, Fricke²⁵ contradicted Martens (1981), finding that directionality didn't matter for attenuation. Fricke found that the attenuation was caused by three main phenomena: interference between direct and ground reflected sound, scattering by tree boles, and the ground. He found that the attenuation was due to the size and spacing of trees for high frequencies, due to scattering for mid-range frequencies, and due to the ground for low frequencies. Then in 1986, Fricke²⁶ postulated that he had been in error about the low frequency attenuation. His new evidence pointed to the effects of the temperature gradients near the ground. He also found that attenuation generally increased with increasing relative humidity over a wide range of frequencies and forest types.

1986 saw the Workshop on Sound Propagation in Forested Areas and Shelterbelts in Nijmegen, the Netherlands. This workshop brought many fine researchers together from the fields of acoustics and biology. At this workshop, Martens and Huisman²⁷ presented their findings that close-planted forests attenuate sound better than belts of trees, conifers attenuate better than deciduous trees, and deciduous trees attenuate better than grass with no trees. Price, Attenborough, and Heap²⁸ presented a study on propagation in three different types of woodlands: a 30 year old Norway spruce plantation, a 38 year old mixed stand of oaks and Norway spruce, and a 15 year old mixed coniferous stand. They found that the mixed coniferous stand had the highest attenuation. Huisman and Martens²⁹ developed a ray-tracing model for sound propagation that included effects of vegetation. It attempted to include wind and thermal effects, but the model only worked reliably for isothermal, windless conditions and did not allow for changes in topography. In actuality, the program (called RAYFLUX) was composed of four separate models: a micrometeorology model, a ground impedance model, a vegetation absorption model, and a ray-tracing model. Brown³⁰ reported on acoustical measurements of background noise, broadcast signal attenuation, and reverberation for three East African habitats: rain forest, riverine swamp, and savanna. He found four factors that determine the maximum audible distance of representative primate vocalizations. These are 1) signal amplitude and spectrum at its source, 2) transmission characteristics of signals of various frequencies in the natural habitat, 3) amplitude and spectra of background noise, and 4) masked auditory threshold of the signal embedded in environmental background noise. He found that over short distances, there is no difference in propagation for the three habitat types, but for distances over 50 m, loud calls traveled better in the rain forest than over the savanna. It is important to note that the data for this finding was taken during the day, and that the savanna receiver height was lower than that in the forest. Reijnen and Thissen³¹ studied the effects of road traffic on breeding bird populations. They found that bird populations near major roadways had fewer birds than those populations away from major roadways. The lesser numbers can be attributed to noise emission, visual stimuli, air pollution, vibrations in the ground, and individual deaths due to collisions.

Several more papers came out from 1988 on that incorporated more intricate models. For example, as a follow-up to their 1986 paper, Price, Attenborough, and Heap³² (1988) compared their previous measurements to a model. The model summed up the separate contributions of the ground, trunks and branches, and foliage. The trunks and branches, and foliage were modeled by a modified multiple scattering approach. The characteristic shape of the attenuation curve obtained was low-frequency peak(s), a mid-frequency dip, and a net increase with frequency above the dip. The model predicted the characteristic shape quite well, but not the actual numbers. Tang and Ong³³ (1988) used a Monte Carlo technique again, this time to model traffic noise with and without trees alongside the roadway. The situation modeled was high rise buildings on both sides of the street, with a single row of trees on either side. They found that the trees attenuate high frequencies, especially higher up in the buildings, but that there is no attenuation below 1 kHz. In 1991, Huisman and Attenborough³⁴ published a report that studied the reverberation and attenuation in a pine forest at 10 m and 100m from the source. They looked at meteorological conditions and the effect of the receiver location with respect to height. Several different models were employed in trying to understand the data. For low frequencies, a point source calculation using a two-parameter ground impedance model worked. They tried a multiple scattering model for high frequencies. It worked reasonably well, but failed to explain the height dependence. For the middle range of frequencies, they attempted to simply add the two models. Unfortunately, the forest is too complicated, and this approach did not yield satisfactory results. In the course of their search for an appropriate model, they determined, contrary to Bullen and Fricke, that a diffusion model is inappropriate for sound propagation in forested areas. The meteorological data that they took allowed them to determine that meteorological conditions have little effect on the data at a distance of 100 m. In 1996, Watanabe and Yamada³⁵ used rectangular plates to model trees. They did experiments in an anechoic chamber, and found directionality in the attenuation. This directionality was attributed to non-spherical spreading. They assumed that attenuation is mainly due to scattering and absorption in the stems, branches, and leaves. They found the absorption coefficient for trees to be proportional to \sqrt{f} , which agrees with Yamada, Watanabe, Nakamura, Yokoyama, and Takeoka.

Future Research Needs:

While the research to date covers many aspects of sound propagation through forests, many more measurements need to be done in a more standardized fashion. Sound level measurements with respect to range and frequency

need to be done in forests with known statistics. These statistics include tree size, type, and spacing, and terrain type. Wind and temperature profiles must be taken below the canopy. Scattering measurements are needed to determine the arrival direction of a signal. Finally, ambient noise measurements are needed for a variety of forest types and microclimates. These ambient noise measurements will include wind and rain noise, as well as wildlife and insect noise. To date, most researchers have neglected the meteorological conditions below the canopy. They justify it by taking measurements during neutral meteorological conditions. Very few studies have taken ambient noise measurements, and fewer have incorporated the masking effects of the ambient noise in their reports.

Advances in atmospheric sound propagation models³⁶ should allow researchers to incorporate forests into these models. It is now possible to do wind and temperature profile modeling accurately. These improved models allow faster computation times, thus making them more reasonable to use.

The research needed will have many practical applications for many varying fields of interest. One of these applications will be to community noise planning. If the planners know how much a given stand of trees should attenuate noise, they can predict the noise impact of an installation, such as a factory or an outdoor amphitheater on a community. The research will also be of interest to companies and citizens who want to employ some trespasser alert system. The companies would use a network of sensors to determine whether or not there is a trespasser on the site. Finally, this research will be of great interest to those interested in wildlife management. Knowing ambient noise levels and signal propagation, they will be able to do things such as count endangered species and determine the impact of man on animals, all in a non-intrusive manner. The non-intrusive manner will allow for more accurate representations of the situations, since there would be minimal human involvement. People would only be needed to place, repair, and retrieve the sensors. Theoretically, the sensors could be in place for long periods of time.

Although much work has been done in the area of sound propagation through forested areas, there is much more that needs to be done. The work to date has resulted in varied data, with little or no attempts to correlate to forest type more specific than simply tree type. Therefore, no statistical data is available for people to draw upon to make decisions regarding the use of forested areas for sound attenuation or wildlife study. This paper has compiled much of the research to date to assist others in making judgements regarding the use of forests, but a substantial amount of research is still needed to better quantify the effects of forests on sound propagation.

- ¹ C. F. Eyring, "Jungle acoustics," *J. Acoust. Soc. Am.* **18**, 257-270 (1946).
- ² F. M. Wiener and D. N. Keast, "Experimental study of the propagation of sound over ground," *J. Acoust. Soc. Am.* **31**, 724-732 (1959).
- ³ T. F. W. Embleton, "Sound propagation in homogeneous deciduous and evergreen woods," *J. Acoust. Soc. Am.* **35**, 1119-1125 (1963).
- ⁴ A. B. Bjornsen, "The effect of some meteorological conditions on sound propagation in three North American forest types," Master Thesis, State University of New York, Syracuse (1971).
- ⁵ R. A. Frank, "The effectiveness of plants for highway noise abatement," Master Thesis, Pennsylvania State University (1971).
- ⁶ D. I. Cook and D. F. Van Haverbeke, *Trees and shrubs for noise abatement* (U.S. Department of Agriculture Forest Service, Washington D.C., 1971), Final Report.
- ⁷ D. Aylor, "Noise reduction by vegetation and ground," *J. Acoust. Soc. Am.* **51**, 197-205 (1972).
- ⁸ D. Aylor, "Sound transmission through vegetation in relation to leaf area density, leaf width, and breadth of canopy," *J. Acoust. Soc. Am.* **51**, 411-414 (1972).
- ⁹ L. D. Frank, "Tree bark and the forest floor as sound absorbing elements within a forest," Master Thesis, Pennsylvania State University (1976).
- ¹⁰ H. F. Linskens, M. J. M. Martens, H. J. G. M. Hendricksen, A. M. Rostenberg-Sinnige, W. A. J. M. Brouwers, A. L. H. C. van der Staak, and A. M. J. Strick-Jansen, "The acoustic climate of plant communities," *Oecologia* (Berlin) **23**, 165-177 (1976).
- ¹¹ L. P. Herrington and C. G. Brock. *Vertical acoustic energy profiles as affected by vegetation and atmospheric conditions*. (U.S. Department of Agriculture, Forest Service, Northeastern Forest Experiment Station, Syracuse, NY, 1976) 10-5002A.
- ¹² D. E. Carlson, O. H. McDaniel, and G. Reethof, "Noise control by forests," *Proc. Inter-Noise '77: Zurich*, B576-B586 (1977).
- ¹³ K. Marten and P. Marler, "Sound transmission and its significance for animal vocalization, I. Temperate habitats," *Behavioral Ecology and Sociobiology* **2**, 271-290 (1977).
- ¹⁴ K. Marten, D. Quine, and P. Marler, "Sound transmission and its significance for animal vocalization, II. Tropical forest habitats," *Behavioral Ecology and Sociobiology* **2**, 291-302 (1977).
- ¹⁵ M. J. M. Martens, "The influence of the soil on the acoustic climate of plant communities," *Proc. Inter-Noise '77: Zurich*, B593-B598 (1977).
- ¹⁶ S. H. Burns, "The absorption of sound by pine trees," *J. Acoust. Soc. Am.* **65**, 658-661 (1979).
- ¹⁷ M. J. M. Martens and A. Michelsen, "Absorption of acoustic energy by plant leaves," *J. Acoust. Soc. Am.* **69**, 303-306 (1981).
- ¹⁸ S. M. Geveling, M. J. M. Martens, and J. G. H. Roebroek, "Sound-induced vibration patterns of plant leaves," in *Proceedings of the Workshop on Sound Propagation in Forested Areas and Shelterbelts*, edited by M.J.M. Martens (Fac. Sciences, Nijmegen, 1986), pp. 153-160.

- ¹⁹ S. H. Tang, P. P. Ong, and H. S. Woon, "Monte Carlo simulation of sound propagation through leafy foliage using experimentally obtained leaf resonance parameters," *J. Acoust. Soc. Am.* **80**, 1740-1744 (1986).
- ²⁰ S. Yamada, T. Watanabe, S. Nakamura, H. Yokoyama, and S. Takeoka, "Noise reduction by vegetation," *Proc. Inter-Noise '77: Zurich*, B599-B606 (1977).
- ²¹ M. J. M. Martens, "Foliage as a low-pass filter: Experiments with model forests in an anechoic chamber," *J. Acoust. Soc. Am.* **67**, 66-72 (1980).
- ²² R. H. Talaske, "The acoustic impedance of a layered forest floor," Master Thesis, Pennsylvania State University (1980).
- ²³ M. J. M. Martens, "Noise abatement in plant monocultures and plant communities," *Applied Acoustics* **14**, 167-189 (1981).
- ²⁴ R. Bullen and F. Fricke, "Sound propagation through vegetation," *J. Sound and Vibration* **80**, 11-23 (1982).
- ²⁵ F. Fricke, "Sound attenuation in forests," *J. Sound and Vibration* **92**, 149-158 (1984).
- ²⁶ F. Fricke, "Sound propagation and relative humidity," in *Proceedings of the Workshop on Sound Propagation in Forested Areas and Shelterbelts*, edited by M. J. M. Martens (Fac. Sciences, Nijmegen, 1986), pp. 93-106.
- ²⁷ M. J. M. Martens and W. H. T. Huisman, "Ecosystem acoustics research," in *Proceedings of the Workshop on Sound Propagation in Forested Areas and Shelterbelts*, edited by M. J. M. Martens (Fac. Sciences, Nijmegen, 1986), pp. 13-24.
- ²⁸ M. A. Price, K. Attenborough, and N. W. Heap, "Sound propagation results from three British woodlands," in *Proceedings of the Workshop on Sound Propagation in Forested Areas and Shelterbelts*, edited by M. J. M. Martens (Fac. Sciences, Nijmegen, 1986), pp. 107-118.
- ²⁹ W. H. T. Huisman and M. J. M. Martens, "A ray tracing model of forest acoustics," in *Proceedings of the Workshop on Sound Propagation in Forested Areas and Shelterbelts*, edited by M.J.M. Martens (Fac. Sciences, Nijmegen, 1986), pp. 161-180.
- ³⁰ C. H. Brown, "Forest noise and sound transmission in east African primate habitats," in *Proceedings of the Workshop on Sound Propagation in Forested Areas and Shelterbelts*, edited by M.J.M. Martens (Fac. Sciences, Nijmegen, 1986), pp. 185-196.
- ³¹ M. J. S. M. Reijnen and J. B. M. Thissen, "Effects of road traffic on woodland breeding bird populations," in *Proceedings of the Workshop on Sound Propagation in Forested Areas and Shelterbelts*, edited by M.J.M. Martens (Fac. Sciences, Nijmegen, 1986), pp. 97-205.
- ³² M. A. Price, K. Attenborough, and N. W. Heap, "Sound attenuation through trees: Measurements and models," *J. Acoust. Soc. Am.* **84**, 1836-1844 (1988).
- ³³ S. H. Tang and P. P. Ong, "A Monte Carlo technique to determine the effectiveness of roadside trees for containing traffic noise," *Applied Acoustics* **23**, 263-271 (1988).
- ³⁴ W. H. T. Huisman and K. Attenborough, "Reverberation and attenuation in a pine forest," *J. Acoust. Soc. Am.* **90**, 2664-2677 (1991).
- ³⁵ T. Watanabe and S. Yamada, "Sound attenuation through absorption by vegetation," *J. Acoust. Soc. Jpn. (E)* **17**(4), 175-182 (1996).

³⁶ K. Attenborough, S. Taherzadeh, H. E. Bass, C. Di, R. Raspet, G. R. Becker, A. Gudesen, A. Chrestman, G. A. Daigle, A. L'Esperance, Y. Gabillet, K. E. Gilbert, Y. L. Li, M. J. White, P. Naz, J. M. Noble, and H. A. J. M. van Hoof, "Benchmark cases for outdoor sound propagation models," *J. Acoust. Soc. Am.* **97**, 197-205 (1995).

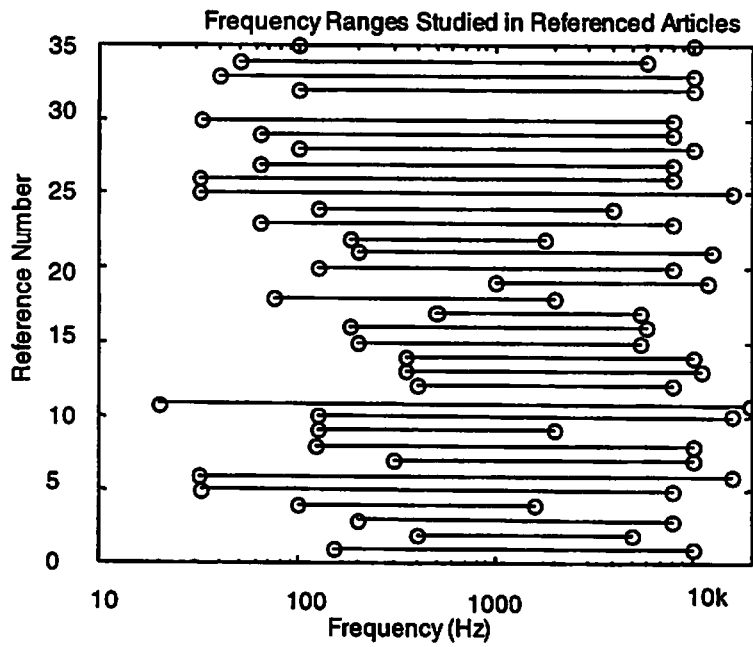


Figure 1: Note that Reference 31 does not have an entry. That article used real traffic noise as its source.

Using a Boundary Element Method for Predicting Noise Barriers Efficiency with Meteorological Effects

E. Premat *, Y. Gabillet **

* Ecole Nationale des Travaux Publics de l'Etat, DGCB CNRS URA 1652

2 rue Maurice Audin, 69518 Vaulx-en-Velin Cedex, France

Tél : +33.4.72.04.70.31 - Fax : +33.4.04.72.04.70 41

eric.premat@entpe.fr

** Centre Scientifique et Technique du Bâtiment

24 rue Joseph Fourier, 38400 Saint-Martin d'Hères, France

Tél : +33.4.76.76.25.25 - Fax : +33.4.76.44.20.46

gabillet@cstb.fr

Abstract

In real conditions meteorological effects (wind and temperature profiles, turbulence) have to be taken into account in order to calculate the efficiency of noise barriers.

Boundary Element Methods are nowadays widely used for describing the acoustic field around complex noise screens (various absorbing properties and shapes) in homogeneous atmosphere.

Besides, in order to assess for the acoustic propagation in inhomogeneous media a few models have been recently designed (Normal Modes, Residue Series, Parabolic Equation, Fast Field Program ...).

The aim of this work is to take advantage of the power of the Boundary Element Methods and to include in these formulations meteorological effects using as the appropriate Green's function these recent propagation models in inhomogeneous media.

In this paper this new hybrid formulation, called Meteo-BEM, and the methodology used is presented. The academic case of a rigid thin noise barrier on a flat ground under a known sound speed gradient condition is studied. Numerical simulations compared to experimental results show that this method is a powerful tool for outdoor sound propagation prediction and offers interesting possibilities for further developments.

1. INTRODUCTION

Most country regulations concerning traffic noise are today more and more demanding, leading to lower and lower maximum acceptable sound levels. There is consequently now a need of sound prediction at long ranges. Besides, noise barriers are nowadays widely used as traffic noise control devices and it is commonly found that the insertion loss of barriers measured outdoors at long range is often much lower than predicted. This appears to be due to the influence of meteorological conditions: wind and temperature gradients, turbulence. So there is a need to investigate the meteorological influence on the performance of noise barriers.

For predicting noise barriers efficiency a few now well-known tools (empirical [1], semi-empirical models [2], ray theory [3, 4, 5, 6, 7], Boundary Element Methods -BEM- [8,9,10]) exist but very few of them do take into account meteorological effects. Among these tools valid in homogeneous media, the Boundary Element Methods have the advantage, although being rather computer time consuming, to allow to assess for any kind of shape and absorption of the propagation domain boundaries (in particular uneven terrains, various shapes of sound barriers, impedance discontinuities).

On the other hand recent models [11] have been developed in order to describe the acoustic propagation in inhomogeneous media (Normal Modes, Residue Series, Parabolic Equation, Fast Field Program, Gaussian Beams).

So the aim of the work presented in this paper is to show that it is possible to keep the advantages of the BEM and to extend these methods to inhomogeneous media using an appropriate Green's function taking meteorological effects into account, coming from these recent inhomogeneous models.

We present here this new approach, called Meteo-BEM, combining a Boundary Element Method with an appropriate meteorological Green's function. The methodology used is first given and then comparisons are made with experimental results.

At first we recast briefly in section 2 the Boundary Element Method in homogeneous media and point out the power of the Green's function; then we present the inhomogeneous model taking meteorological effects in section 3; section 4 presents the hybrid method; comparisons between theory and experiments are given in section 5, and finally we conclude and give perspectives of our work in section 6.

2. THE BOUNDARY ELEMENT METHOD IN HOMOGENEOUS ATMOSPHERE

Let us consider a harmonic point source S in a semi-infinite domain Ω whose boundary σ is the ground and a barrier (figure 1).

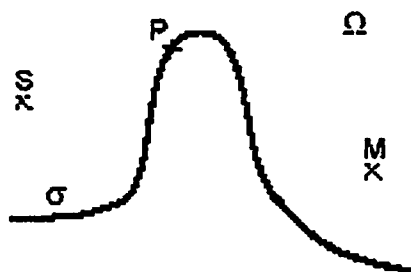


Figure 1: Notations.

Considering linear acoustics assumptions and temporal dependency $\exp(-i\omega t)$, the problem in homogeneous atmosphere can be described by the following system:

$$\left\{ \begin{array}{l} (\Delta + k^2) p = \delta_s, M \in \Omega \end{array} \right. \quad (1)$$

$$\left\{ \begin{array}{l} \lim_{M \in \Omega \rightarrow P \in \sigma} \left[\partial_{n(M)} p(M) - ik \frac{\rho c}{Z_n} p(M) \right] = 0 \end{array} \right. \quad (2)$$

$$\left\{ \begin{array}{l} \text{Sommerfeld conditions for } p \end{array} \right. \quad (3)$$

p is the total acoustic pressure, k the wave number, δ_s represents the point source radiation, ρ is the air density, c the sound speed and Z_n is the normal acoustic impedance of σ .

The acoustic pressure can be expressed as a sum of the incident pressure (the pressure radiated by the source) plus a linear combination of simple and double layer potentials (the pressure scattered by the boundary) [12,13].

$$p(M) = p_0(M) + \alpha p_s(M) + \beta p_d(M) \quad (4)$$

where the incident acoustic field in free space is:

$$p_0(M) = -\frac{\exp(ikr(S,M))}{4\pi r(M,S)} \quad \text{in 3D} \quad p_0(M) = -\frac{i}{4} H_0(kr(S,M)) \quad \text{in 2D} \quad (5)$$

and the simple and double layer potentials p_s and p_d are:

$$p_s(M) = \int_{\sigma} v(P) G(M,P) d\Gamma(P) \quad p_d(M) = \int_{\sigma} \mu(P) \partial_{n(P)} G(M,P) d\Gamma(P) \quad (6)$$

In this direct integral formulation G is the key Green's function that is indeed an elementary solution of the problem satisfying to certain boundary conditions. The more boundary conditions are included in the Green's function the smaller is the integration domain being considered as a secondary source so that the total acoustic field is the superposition of the incident field and the contributions of these secondary sources.

v and μ denote respectively the simple layer and the double layer potential densities. These functions are unknown and have to be determined using the boundary conditions. The

introduction of the acoustic pressure in the boundary conditions leads to a boundary integral equation that has to be solved in order to get the unknown layer potential densities.

Using for example a collocation method a linear system gives then these unknown functions and then the acoustic field is known in the whole space via the direct integral formulation.

This BEM is called indirect because v and μ have to be first determined to lead to the acoustic pressure anywhere in the space Ω via the equation (4). The mathematical method presented here is exact and the pressure solution of the boundary value problem is unique provided that both the propagation medium and its complementary are infinite.

The keypoint in this formulation is the use of the adequate Green's function: we said that the more information you put in the Green's function the smaller the integration domain is. That is why different authors have first concentrated on the ground effects in order to reduce the domain σ to the noise barrier Γ (see figure 2) but all these works have been restricted to a homogeneous atmosphere. In this work meteorological effects are introduced via the Green's function.

For the sake of clarity consider without any restriction the case of a rigid thin noise barrier on a rigid flat ground (figure 2). The boundary condition (2) is then a Neumann condition:

$$\lim_{M \in \Omega \rightarrow P \in \Gamma} \partial_{n(M)} p(M) = 0 \quad (7)$$

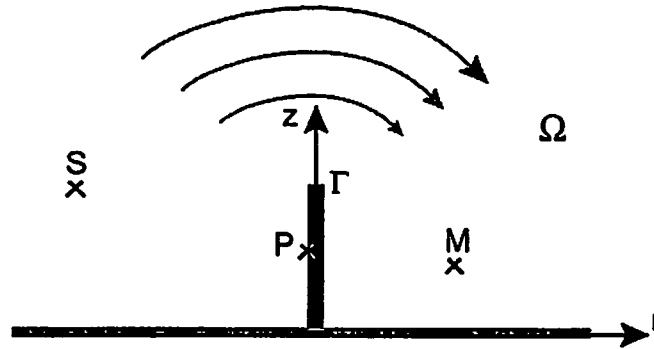


Figure 2: Thin noise barrier on a flat ground.

Daumas [8] showed that the solution could be represented by a double layer potential:

$$p(M) = p_0(M) + \int_{\Gamma} \mu(P) \partial_{n(P)} G(M, P) d\Gamma(P) \quad \forall M \in \Omega \quad (8)$$

Including ground effects in the Green's function G allows one to reduce the integration domain to the sound barrier Γ . This Green's function is given by:

$$G(P, M) = -\frac{i}{4} H_0(kr(P, M)) - \frac{i}{4} H_0(kr(P', M)) \quad (9)$$

where P' is the image source corresponding to P with respect to the ground plane. H_0 is the Hankel function of the first kind and of order zero. The incident pressure due to the source S is then given by:

$$p_0(M) = G(S, M) \quad (10)$$

Expressing the Neumann condition on the screen the following Fredholm integral equation of the first kind is obtained:

$$-\partial_{n(M)} p_0(M) = PF \int_{\Gamma} \mu(P) \partial_{n(M)} \partial_{n(P)} G(M, P) d\Gamma(P) \quad \forall M \in \Gamma \quad (11)$$

Because of the singularity of the Green's kernel the integral is taken in the sense of the Hadamard finite part. The definition used is according to Filippi [14] the limit of the normal component of the gradient of the double layer potential when the point M approaches the screen.

This integral equation is solved using N collocation points M_j on the screen. Looking for a piecewise constant approximation for the unknown double layer potential density the sound barrier Γ is discretized into subelements Γ_i and yields the linear system:

$$-\partial_{n(M)} p_0(M_j) = \sum_{i \neq j} \mu_i \int_{\Gamma_i} \partial_{n(M)} \partial_{n(P)} G(M_j, P) d\Gamma(P) + \mu_j PF \int_{\Gamma_i} \partial_{n(M)} \partial_{n(P)} G(M_j, P) d\Gamma(P) \quad j = 1..N \quad (12)$$

This equation represents indeed the contribution of the interaction between the source in presence of the ground and the screen.

Equation (12) can be rewritten as:

$$[A][\mu] = [B] \quad (13)$$

$$\text{with} \quad \begin{cases} [B] = [B_j] = [-\partial_{n} p_0(M_j)] \\ [\mu] = [\mu_i] \\ [A] = [A_{ji}] = \left[PF \int_{\Gamma_i} \partial_{n(M)} \partial_{n(P)} G(M_j, P) d\Gamma(P) \right] \end{cases} \quad (14)$$

The integrals are computed using an adaptative Gauss-Legendre scheme and the linear system is solved using a full pivoting Gauss strategy.

Once the layer density μ is known the acoustic pressure can be calculated at any receiver point with the direct formulation (8). The integral formulation of the double layer potential represents then the contribution of the radiation of the sound barrier to the total acoustic field.

The results obtained with this Boundary Element Method were compared to Time Delay Spectrometry -TDS- measurements made at CSTB [15]. Figure 3 shows a comparison for the case of a rigid barrier on a rigid flat ground. The source, receiver and screen heights were respectively 1.5 cm, 10 cm and 15.25 cm. The sound barrier was 50 cm far from the source and the distance between the source and the receiver was 150 cm.

The comparisons give good agreement between the BEM results and the measured data.

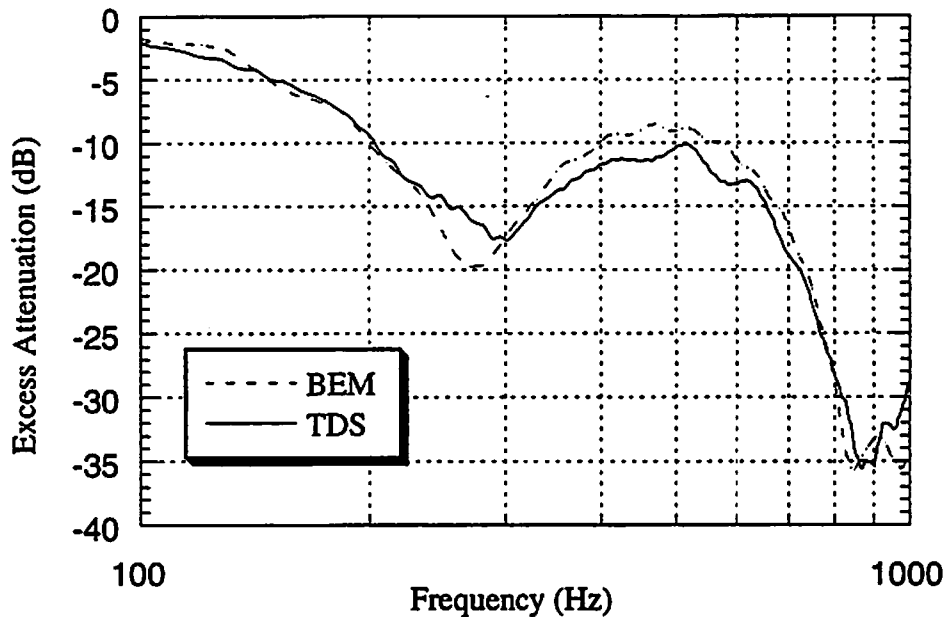


Figure 3: Comparison between TDS measurements and the homogeneous BEM.

3. THE GREEN'S FUNCTION ACCOUNTING FOR METEOROLOGICAL EFFECTS

Meteorological effects (wind and sound speed gradients, turbulence) are important in outdoor sound propagation particularly at long ranges.

In the classical Boundary Element Methods the Green's functions can include the ground effects [16,17]. The idea of this work is to take advantage of recent propagation models in inhomogeneous media taking meteorological effects as well as ground effects into account. One will concentrate here on refraction phenomena. These recent models describing sound speed gradients are mainly Normal Modes for downward refraction, the Residue Series for upward refraction, the Fast Field Program and the Parabolic Equation for both situations [11].

In order to illustrate the methodology used for including this inhomogeneous Green's function in the BEM, consider without restricting the generality the case of a positive sound speed gradient condition.

Furthermore, the above acoustic pressure formula is valid in 3-D so it needs to be adapted to 2-D configurations because the BEM approach used in this work is written in 2-D.

This is done using the idea outlined in [20] p.276, considering the form of the normal modes in 2-D and 3-D. A trivial change has to be performed to get the 2-D solution and (19) becomes:

$$P_s(r,z) = \frac{i}{2l} \sum_n \frac{\exp(ik_n r) \text{Ai}(\tau_n + z_s/l) \text{Ai}(\tau_n + z_r/l)}{k_n \tau_n [\text{Ai}(\tau_n)]^2 - [\text{Ai}'(\tau_n)]^2} \quad (22)$$

The results obtained with the Normal Modes program were compared satisfactorily to results from the benchmark [11] for downward refraction. Figure 4 shows the results for the case 2 fig.12 p.187 at 100 Hz, the source and receiver heights are 5m and 1m, the range varies from 0.1 to 10000m, the specific surface impedance of the ground is $Z_c=(12.81,11.62)$ and the sound speed gradient is 0.1 s^{-1} .

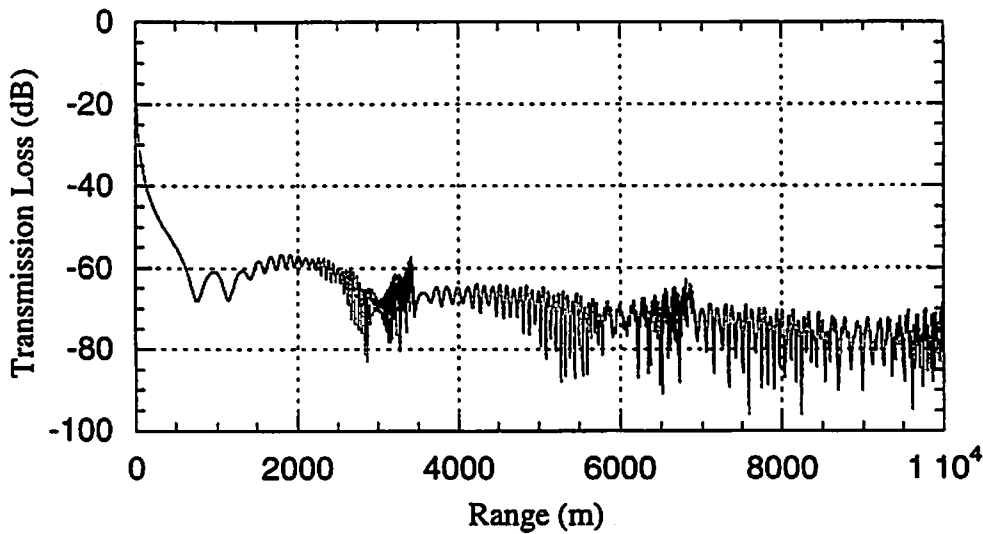


Figure 4: Normal Modes Transmission Loss versus range for the case 2, 100 Hz, fig. 12, p.187, JASA 97(1), 1995.

Figure 5 shows the comparison between measured data (fig.8c JASA 93(6), 1993,p.3111) and 2-D/3-D results from the Normal Modes theory. The source and receiver heights are 0.1 and 0.15m, the frequency is 1000 Hz, the radius of curvature of the rays R is 20m.

In the case of a linear sound speed profile, the Normal Modes solution [18] is particularly well adapted to this situation since the variables involved in the analytical formulation are uncoupled and straightforward to derive.

The pressure wave equation solution satisfying on the one hand the same conditions as for the homogeneous problem and on the other hand the height dependent sound speed condition for inhomogeneous media can be written as follows:

$$p(r, z) = - \int_{-\infty}^{+\infty} H_0^1(kr) P(z, k) k dk \quad (15)$$

In the case of a linear profile, $c(z) = c(0)(1 + z/R)$ (16)

the height dependent Green function $P(z, k)$ can be expressed in terms of Airy functions and their derivatives:

$$P(z, k) = -2\pi e^{i\pi/6} \text{Ai}(\tau + y_>) \left[\text{Ai}(\tau + y_<) e^{2i\pi/3} - \left(\frac{\text{Ai}'(\tau e^{2i\pi/3}) + q \text{Ai}(\tau e^{2i\pi/3})}{\text{Ai}'(\tau) + q \text{Ai}(\tau)} \right) \text{Ai}(\tau + y_<) \right] \quad (17)$$

where $k_0 = 2\pi f / c(0)$, $q = (ik_0 \rho c) / Z$, $l = (R / 2k_0^2)^{1/3}$, $R = c / (dc/dz)$
 $\tau = (k^2 - k_0^2) l^2$, $y = z/l$, $z_> = \max(z_s, z_r)$, $z_< = \min(z_s, z_r)$ (18)

R is the ray paths curvature radius, z_s is the source height and z_r the receiver height.

Then, using the residue theorem, the poles of the integrand are calculated and the contributions of the integrand residue at each pole are summed up to obtain the expression for the acoustic pressure in downward refraction for a point source radiating spherical waves above a locally reacting impedance plane:

$$p_s(r, z) = \frac{i\pi}{1} \sum_n \frac{H_0^1(k_n r) \text{Ai}(\tau_n + z_s/l) \text{Ai}(\tau_n + z_r/l)}{\tau_n [\text{Ai}(\tau_n)]^2 - [\text{Ai}'(\tau_n)]^2} \quad (19)$$

where $\tau_n = (k_n^2 - k_0^2) l^2$ (20)

are the zeros of $\text{Ai}'(\tau_n) + q \text{Ai}(\tau_n) = 0$ (21)

k_n represents the horizontal wave number of the n th mode. The zeros of (21) are trapped in the complex plane with an adapted Powell hybrid method for nonlinear systems solutions.

One must point out that this derivation is an exact analytical formulation but in the last result the continuous spectrum contribution has been neglected, which leads to negligible error at long range.

Besides, concerning the numerical implementation, a significant numerical instability gives rise to some oscillations in the predicted sound field due to the oscillatory behaviour of Airy functions for large arguments. This drawback is overcome assuming that near to the vertical, sound speed gradients do not affect the propagation, so for small k_n the propagation happens as if the medium were homogeneous (see [19]).

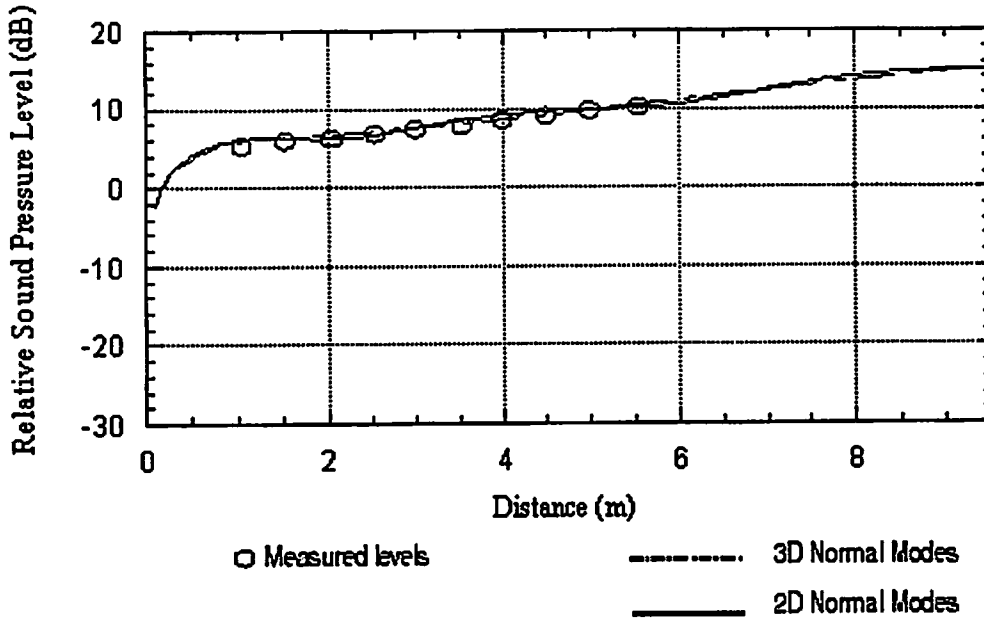


Figure 5: Excess Attenuation versus Range for fig.8c p.3111, JASA 93(6), 1993. Comparison between measured data, 2D and 3D Normal Modes results.

We can notice that the results for 2-D and 3-D excess attenuation match perfectly and are very close to the measurement results.

4. THE NEW HYBRID MODEL: METEO-BEM

Using the results of both theories described above (BEM for noise barriers efficiency in homogeneous atmosphere and Normal Modes for sound propagation in inhomogeneous media), the hybrid formulation Meteo-BEM combining the advantages of both methods is now presented.

For the sake of clarity, without loss of generality, consider the case of a rigid thin noise barrier on a flat ground in the presence of downward refraction. In the homogeneous case eq. (8) section 2 is rewritten as:

$$p(M) = p_0(M) + \int_{\Gamma} \mu_{\text{inhom}}(P) \partial_{n(P)} G(M, P) d\Gamma(P) \quad \forall M \in \Omega \quad (23)$$

But now, the Green's function describes the acoustic propagation in an inhomogeneous medium, so the results of section 3 equation (22) are used:

$$G(S, M) = p_S(r(M), z(M)) = \frac{i}{2l} \sum_n \frac{\exp(ik_n |r_M - r_S|) \text{Ai}(\tau_n + z_S/l) \text{Ai}(\tau_n + z_M/l)}{k_n \tau_n [\text{Ai}(\tau_n)]^2 - [\text{Ai}'(\tau_n)]^2} \quad (24)$$

Since the ground is rigid, the parameter q in (18) is equal to zero. So the equation (21) shows that the τ_n are the zeros of the derivative of the Airy function called a'_n and finally:

$$G(S,M) = \frac{i}{2l} \sum_n \frac{\exp(ik_n|r_M - r_S|) \text{Ai}(a'_n + z_s/l) \text{Ai}(a'_n + z_M/l)}{k_n a'_n [\text{Ai}(a'_n)]^2} \quad (25)$$

The new inhomogeneous integral equation corresponding to (11) must be solved with the Normal Modes Green's function:

$$-\partial_{n(M)} p_0(M) = \text{P.F.} \int_{\Gamma} \mu_{\text{in hom}}(P) \partial_{n(M)} \partial_{n(P)} G(M,P) d\Gamma(P) \quad \forall M \in \Gamma \quad (26)$$

The normal derivative of the pressure for the left hand side of this integral equation is:

$$\partial_{n(M)} p_0(M) \Big|_{\Gamma} = \frac{\partial G(S,M)}{\partial r_M} = -\frac{1}{2l} \sum_n \frac{\exp(ik_n|r_S|) \text{Ai}(a'_n + z_s/l) \text{Ai}(a'_n + z_M/l)}{a'_n [\text{Ai}(a'_n)]^2} \quad (27)$$

For the right hand side, an approximation following the idea of Rasmussen [19] exposed above in section 3 can be made considering that vertical propagation is weakly affected by the refraction, so this term is at first approximated by the homogeneous term presented in section 2.

So a new linear system involving the Normal Modes Green's function derivative for the right member and the same matrix as for the homogeneous system equations (13) and (14) is obtained:

$$[A_{\text{in hom}}] [\mu_{\text{in hom}}] = [B_{\text{in hom}}] \quad (28)$$

$$\text{with } \begin{cases} [B_{\text{in hom}}] = [B_{j,\text{in hom}}] = [-\partial_n p_{0\text{in hom}}(M_j)] \\ [\mu_{\text{in hom}}] = [\mu_{i,\text{in hom}}] \\ [A_{\text{in hom}}] = [A_{j,\text{in hom}}] = \left[\text{P.F.} \int_{\Gamma_i} \partial_{n(M)} \partial_{n(P)} G(M_j,P) d\Gamma(P) \right] \approx [A_{\text{hom}}] \end{cases} \quad (29)$$

The subscripts "inhom" and "hom" denote respectively propagation in inhomogeneous medium and in homogeneous medium.

Once solved this new inhomogeneous linear system provide the layer density for inhomogeneous media calculated using the same numerical schemes as in section 2.

The last step is then to use the direct formulation with the Normal Modes Green's function for the incident field as well as for its derivative involved in the integral in the same way as for the left hand side of the inhomogeneous integral equation above.

The acoustic pressure is then computed at any receiver point using the following equation:

$$\begin{aligned} p(M) &= p_0(M) + \int_{\Gamma} \mu_{\text{in hom}}(P) \partial_{n(P)} G(M,P) d\Gamma(P) \\ &\approx p_0(M) + \sum_i \mu_{i,\text{in hom}} \partial_{n(P)} G(M,P_i) \Delta\Gamma_i \end{aligned} \quad (30)$$

5. RESULTS

Calculations obtained from this new Boundary Element Method (Meteo-BEM) are compared (figs.6 to 9) to results from experimental measurements made above a concave surface indoors that simulates propagation under downward refraction in the case of a hard impedance surface and in the presence of a barrier ([21] fig.2 and 3, and [4] figs.15 a, b, c). Results about the acoustic field without sound barrier in the presence of downward refraction (Normal Modes) and with barrier in homogeneous medium (BEM) are also given. The source height is for all cases 10 cm, and at a distance of 4 m from the sound barrier which is 15 cm high. Ground and barrier are rigid. The receiver is respectively 1 m (fig.6), 2 m (fig.7 and 8) and 3 m far from the noise screen. The receiver heights are 5 cm (fig.6), 10 cm (fig.7 and 9) and 15 cm (fig.8). The radius of curvature R is 20 m.

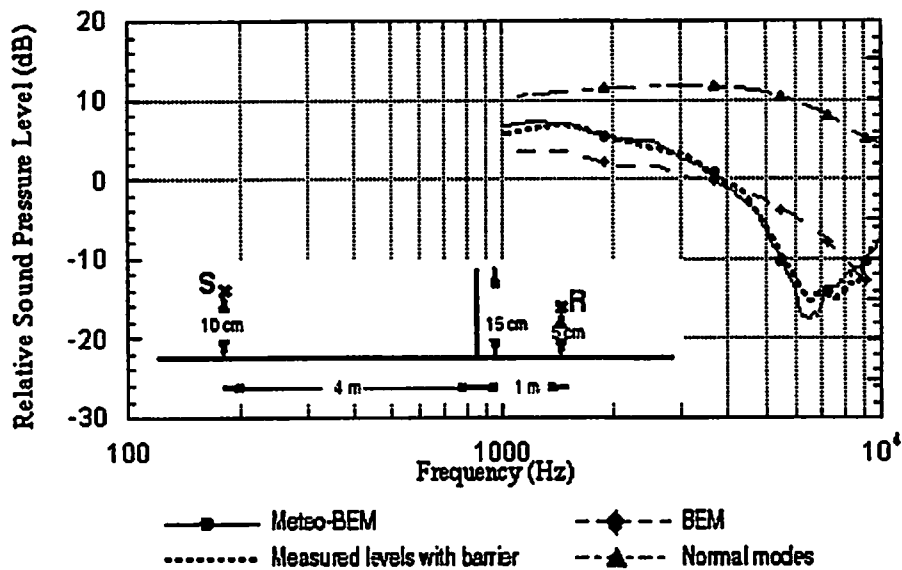


Figure 6: Excess Attenuation versus Frequency, $z_s=5\text{cm}$, $r=1\text{m}$.

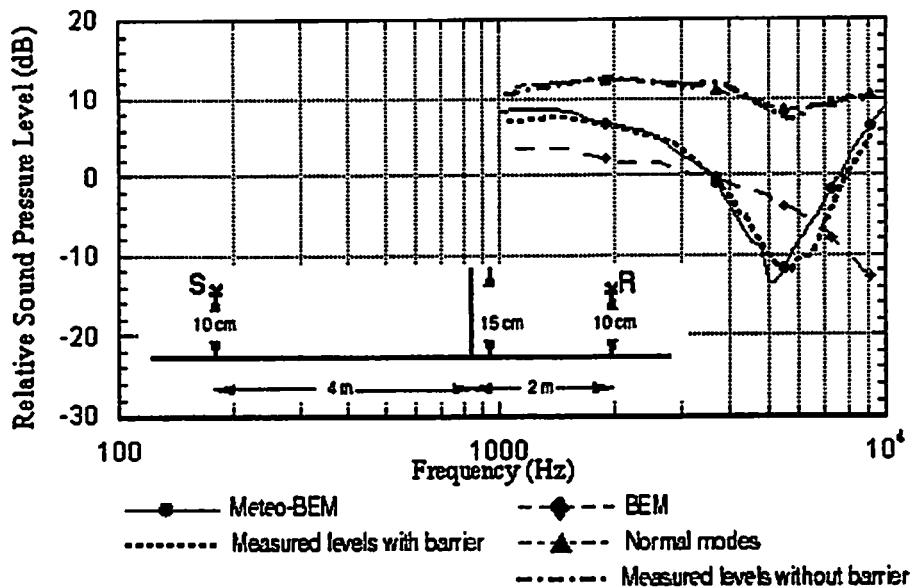


Figure 7: Excess Attenuation versus Frequency, $z_r=10\text{ cm}$, $r=2\text{ m}$.

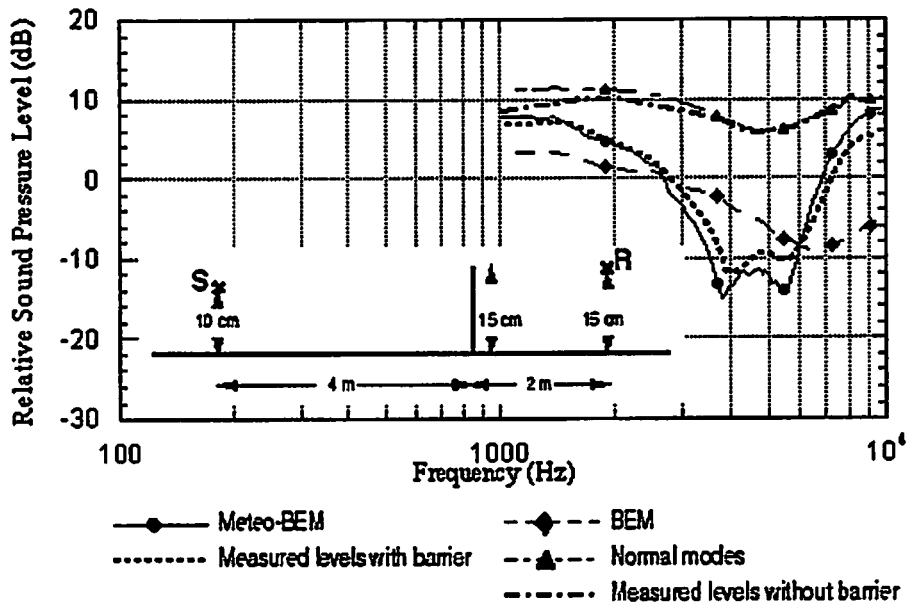


Figure 8: Excess Attenuation versus Frequency, $z_r=15\text{ cm}$, $r=2\text{ m}$.

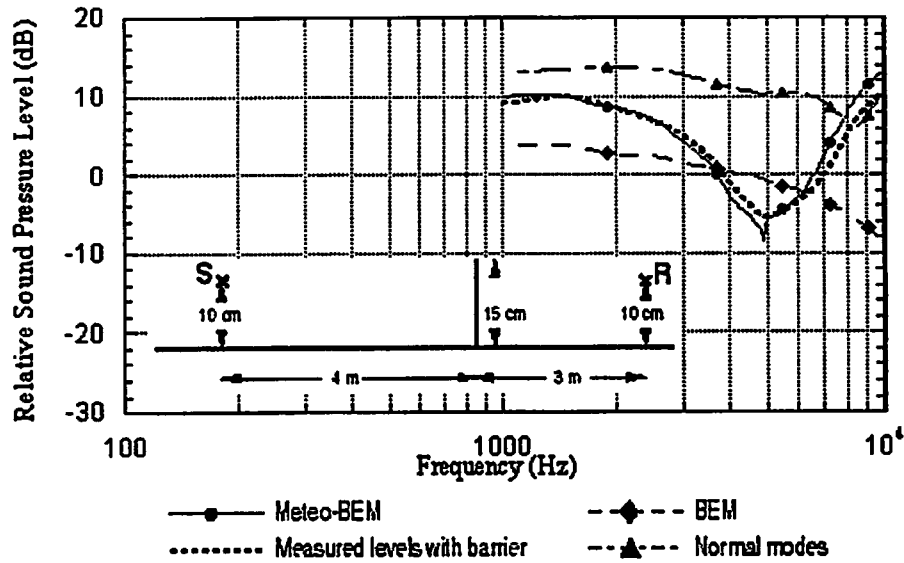


Figure 9: Excess Attenuation versus Frequency, $z_r=10\text{cm}$, $r=3\text{m}$.

The results show that the Meteo-BEM model agrees very well with the experimental data.

6. CONCLUSION

In this paper a hybrid method for calculating the acoustic field in a medium with a sound speed profile above complex boundaries has been presented. First of all, the theory of BEM together with that of sound propagation in inhomogeneous media has been briefly recalled. Each step of the work has been justified and validated. Then the new model Meteo-BEM has been derived, using results of both theories. Finally in order to validate this innovative approach, comparisons have been made with experimental results. The results prove that a BEM can be adapted to complex atmospheric sound propagation problems using the adequate Green's function and give good agreement with experimental data.

This hybrid method allows to calculate the sound field in a medium with a sound speed profile above an uneven impedance ground provided that the non flat part of the terrain is included in the integration domain σ of formulas (2)-(6). The influence of various diffracting shapes of the sound barriers combined to meteorological effects on the acoustic field is going to be studied. Other validations with more realistic configurations (finite impedance of the ground for instance) are engaged. Investigations need also to be done in order to give insight on physical phenomena in complex outdoor sound propagation. Besides, further work is in progress in order to use the power of the Parabolic Equation for predicting range dependent propagation in both conditions of downward and upward refraction. Other investigations are pursued with other inhomogeneous models like the Residue Series for upward refraction, or F.F.P. for both situations. Turbulence could also be included in such a formulation using the adequate Green's function.

7. REFERENCES

- [1] Z. Maekawa, *Applied Acoustics*, 'Noise reduction by screens', 1, 1968, 157-173.
- [2] U.L. Kurze, G. Anderson, *Applied Acoustics*, 'Sound attenuations by barriers', 4, 1971.
- [3] J.B. Keller, *J. Opt. S. A.*, 'Geometrical theory of diffraction', 52, p233, 1962.
- [4] Y. Gabillet et al., *J.A.S.A.*, 'Application of the Gaussian beam approach to sound propagation in the atmosphere: theory and experiments', 93(6), 1993, 3105-3116.
- [5] K.B. Rasmussen, *J.A.S.A.*, 'On the effect of terrain profile on sound propagation outdoors', 98(1), 35-44, 1985.
- [6] A. L'Espérance et al., *J.A.S.A.*, 'Insertion loss of absorbant barriers on ground', 86(3), 1060-1064, 1989.
- [7] J. Defrance, Y. Gabillet, 7th LRSP, 'New Analytical Expressions for Predicting Diffraction and Ground Effects', 1996, 63-78.
- [8] A. Dumas, *Acustica*, 'Etude de la diffraction par un écran mince disposé sur le sol', 40(4), 213-222, 1978.
- [9] D.C. Hothersall et al., *J.S.V.*, 'Efficiency of single noise barriers', 146(2), 1991, 303-322.
- [10] A. Tekatlian, E. Premat, 7th LRSP, 'Computer cost of a 3-D numerical model for noise barrier insertion loss', 1996, 307-322.
- [11] K. Attenborough et al., *J. Acoust. Soc. Am.*, 'Benchmark cases for outdoor sound propagation models', 97(1), 173-191, 1995.
- [12] P. Filippi, *J. Sound Vib.*, 'Layer potential and acoustic diffraction', 54(4), 473-500, 1977.
- [13] A. Tekatlian and E. Premat, *Inter-Noise 96*, 'Computer cost of a 3-D numerical model for noise barriers insertion loss', 3075-3079, 1996.
- [14] P. Filippi, G. Dumery, *Acustica*, 'Etude Théorique et Numérique de la Diffraction par un Ecran Mince', 21, 343-350, 1969.
- [15] J. Defrance, Ph. D. Dissertation, 'Analytical method for the calculation of outdoors sound propagation', Université du Maine, 180 p., 1996.
- [16] D. Habault, *J. Sound Vib.*, 'Sound propagation above an inhomogeneous plane: boundary integral equation methods', 100(1), 55-67, 1985.
- [17] S. Chandler-Wilde, *J. Sound Vib.*, 'Sound propagation above an inhomogeneous impedance plane', 98(4), 475-491, 1985.
- [18] R. Raspet and G. Baird, *J. Acoust. Soc. Am.*, 'Normal mode solution for low-frequency sound propagation in a downward refracting atmosphere above a complex impedance plane', 91(3), 1341-1352, 1992.
- [19] K.B. Rasmussen, *J. Sound Vib.*, 'Sound propagation over ground under the influence of a sound speed profile in the atmosphere', 139(1), 71-81, 1990.
- [20] F.B. Jensen et al., 'Computational Ocean Acoustics', AIP Series in Modern Acoustics and Signal Processing, New-York, 1994, 612p.
- [21] Y. Gabillet et al., *Journal de Physique IV, sup. au Journal de Physique III*, vol. 2, avril 1992, 'Application de la méthode de sommation de faisceaux gaussiens au calcul du champ sonore diffracté par un écran en atmosphère inhomogène', 553-556.

Scale Model Experiments On The Insertion Loss Of Wide And Double Barriers And Barriers Under Turbulent Conditions.

James P. Chambers, Glenn J. Wadsworth, Mark Kelly, and Richard Raspet
National Center for Physical Acoustics, University of Mississippi, University, MS 38677

ABSTRACT

The insertion loss of wide and double barriers is investigated through scale model experiments. Such configurations and conditions are common in outdoor sound propagation problems such as highway barriers and raised or depressed roadways. The Biot-Tolstoy-Medwin (BTM) time domain wedge formulation for multiple diffraction [J. Acoust. Soc. Am. 72, 1005-1013] is used to predict the acoustic field directly in the time domain for non turbulent conditions. Evaluating the insertion loss at discrete frequencies is accomplished via the Fast Fourier Transform (FFT). For the non turbulent conditions, comparisons between the BTM model and other frequency based models will also be presented.

INTRODUCTION

The Federal Highway Department (FHWA) is in the process of introducing and refining a new, state of the art, computational model to describe sound propagation near highways. The motivation for the present work was to investigate the portion of the Traffic Noise Model (TNM) that handles multiple diffraction to investigate its usefulness and to possibly suggest alternate computational methods to address the problem of scattering by multiple barriers or terrain features. An additional charge was to begin to investigate the effects of atmospheric variations on sound propagation in an attempt to include these features in future upgrades of the model.

The diffraction model utilized by the TNM is that of De Jong et al. [1] The model was found to be lacking for multiple diffraction problems and alternate computational models were investigated for their suitability. A wide barrier model developed by Pierce [2] was investigated along with an extension of a model developed by Medwin et al [3] Both models are capable of handling a wide or three sided barrier while the latter is capable of handling arbitrary barrier configurations. Therefore, the Medwin model was investigated further and the results are presented here.

Biot-Tolstoy-Medwin (BTM) Diffraction Model

The Biot-Tolstoy-Medwin[3-6] theory involves the introduction of a source strength, S , such that the pressure at a distance R is given by

$$p = \frac{\rho S}{4\pi R} \delta\left(t - \frac{R}{c}\right) \quad (1)$$

where ρ is the density of the propagating medium, and c is the speed of sound. The delta function in Eq. 1 has a value of zero for all times except $t = R/c$, where it has the value of 1. Hence the propagating pressure pulse spherically diverges as $1/R$ and is proportional to the source strength. This type of source lends itself easily to convolution, allowing transient sources to be considered.

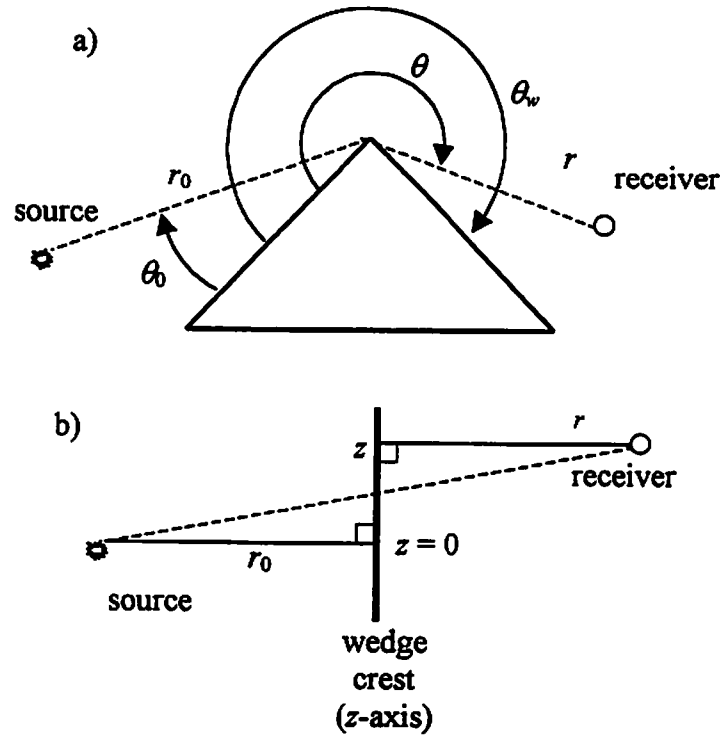


Figure 1 BTM model wedge geometry: a) side view; b) top (unfolded) view. Dashed lines indicate least time paths from source to receiver.

The geometry is based in a cylindrical coordinate system where the z -axis extends along the crest of the wedge, as shown in Figure 1. Source coordinates are given by r_0 , θ_0 , and $z = 0$; receiver coordinates are given by r , θ , and z . The wedge angle, θ_w , is measured from one face of the wedge through the propagating medium to the other face. For the thin plate, this angle is 2π , and such a barrier is referred to as a *knife-edge* barrier.

Receivers in the region where $\theta - \theta_0 < \pi$ are said to be in the *bright zone* and receive both the unobstructed, direct signal as well as the edge diffracted signal. Otherwise, they are in the *shadow zone* and receive only the diffracted signal. In this region, the diffracted pressure is given by Medwin [3,6] as

$$p(t) = -\frac{S\rho c}{4\pi\theta_w} \frac{\beta}{rr_0 \sinh Y} e^{-\pi r/\theta_w}, \quad (2)$$

where

$$\beta = \frac{\sin[(\pi/\theta_w)(\pi \pm \theta \pm \theta_0)]}{1 - 2e^{-\pi r/\theta_w} \cos[(\pi/\theta_w)(\pi \pm \theta \pm \theta_0)] + e^{-2\pi r/\theta_w}}, \quad (3)$$

and

$$Y = \operatorname{arccosh} \frac{c^2 t^2 - (r^2 + r_0^2 + z^2)}{2rr_0}. \quad (4)$$

This expression is valid for times $t \geq \tau_0$, where

$$\tau_0 = \frac{\sqrt{(r+r_0)^2 + z^2}}{c} \quad (5)$$

is the least time over the wedge. Note that for $t = \tau_0$, Y is identically zero, and by Eq. 2, the pressure is undefined. The numerical method for calculating $p(t = \tau_0)$ is described in Appendix 1.A of reference [7].

The \pm signs in Eq. 3 indicate that all possible combinations of source, receiver, image source, and image receiver angles are considered. The β factor in Eq. 2 is the sum of four values which include paths from image sources and receivers located within the wedge. A more complete discussion of these image contributions is found in Section 5 of reference [4]. The use of the term *image* in this context should not be confused with similar terminology used later in this work, where the term *image* is used in treating reflections by a rigid surface.

The impulse formulation can provide valuable insight into the relative contributions of each arriving pulse. In addition, ray-tracing techniques allow comparison of distinct reflected and diffracted components. It is often more desirable, however, to quantify the diffracted sound field in the frequency domain. Although at this time no analytical transform of Eqs. 2 to 5 have been found, the frequency response is easily obtained by digital means. In order to represent the diffracted field digitally, instantaneous values of Eq. 2 are calculated for discrete values of time. The frequency content of the diffracted field is obtained via the Fast Fourier Transform (FFT). The desired frequency range governs the choice of the discrete time step, ΔT , of the impulse response.

This discrete, digital representation of the pressure diffracted by a barrier follows from a classical Huygen's wavelet description of the spherical wave. Secondary sources are defined at interception points between the wavefront and the edge. The first secondary source, $S_{s,0}$, is the intercept of the diffracting edge and the least time path. As the wavefront propagates, secondary sources on both sides of the least time path contribute to the sound field in pairs. The paths defined by the positions of the secondary sources are referred to as *partial least time paths*, and pulses propagating along these paths arrive at intervals of $n\Delta T$. The complete time-domain waveform is composed of N points whose values are written as $p(n\Delta T)$.

Insertion Loss

The quantity of interest in this work is the insertion loss defined here as

$$IL = 20\log\left(\frac{P_{\text{barrier}}}{P_{\text{no barrier}}}\right) = 20\log\left(\frac{p_2}{p_1}\right) \quad (6)$$

where p_1 and p_2 are the pressures as a function of frequency before and after inserting the object, respectively. Many authors insert a "-" sign to make the insertion loss a positive quantity. In this work we chose to keep the format consistent with that used by Medwin et al.[3,6] since we compare to his work. The reference pressure, p_1 is the total field which includes ground bounces and acts to give a more realistic depiction of barrier losses for a given geometry.

When a single knife-edge barrier is placed on a rigid surface, four ray paths from the source to a receiver in the shadow zone are possible. Throughout this work the symbols r_0 and r refer to the source-edge distance and the receiver-edge distance for one ray path, including paths with image

sources and/or image receivers. The diffracted signal for each ray path is calculated independently using the method described above and then superimposed.

For the single knife-edge barrier, the agreement between the DeJong, Pierce and BTM models is excellent although this data is not presented for the purposes of brevity. The comparison can be found in reference [7].

Multiple Diffraction

Multiple diffraction effects are easily handled by the BTM model in the context of the classical Huygen's Principle. These effects must be considered when predicting the insertion losses of thick and/or multiple barriers. Although the wide barrier has been addressed by Medwin et al.[3], it is reexamined in the presence of a rigid ground surface. In addition, diffraction over double knife-edge barriers of various widths is investigated.

The double diffraction method treats each diffracting edge independently. Each secondary source along the first edge in turn radiates a new, weaker pulse which then diffracts over the second edge in the same manner as the first. Although similar, the calculations used for the wide and double knife-edge barriers have a few subtle differences; therefore the two barriers are addressed separately. The BTM model does not require that the diffracting edges of the barriers be parallel, nor does it place any stipulations on the relative heights of the two edges. In this discussion, however, the barriers' edges are parallel with constant width W and of the same height h in order to minimize the logistical difficulty of the corresponding experiment. Furthermore, the source-receiver axis is normal to the z -axis in all cases.

Cartesian coordinates are used to conveniently give the locations of the source and receiver throughout this discussion. For both the wide and double barrier, the origin of the cylindrical coordinate system depends on which edge is being treated in the double diffraction method. In the Cartesian system, used only for measurement convenience, the origin is placed at the point of contact between the first diffracting edge and the ground surface. The case of the double knife-edge barrier is illustrated in Figure 2. The conversion is the same for the wide barrier.

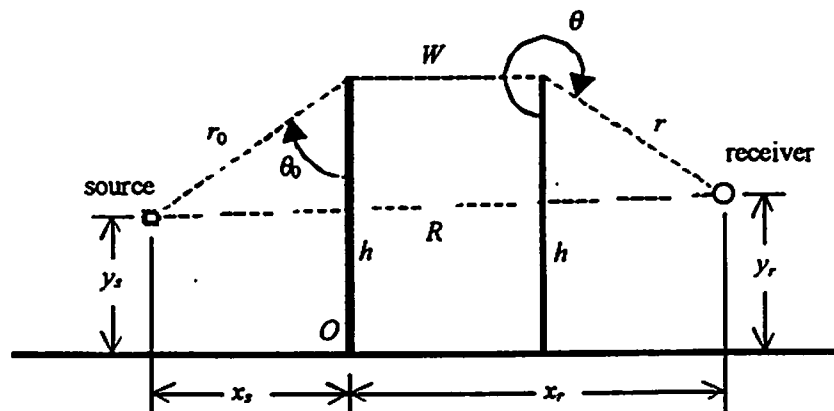


Figure 2 Conversion from cylindrical to Cartesian coordinate system for the wide or double knife-edge barrier. The origin of the Cartesian system is at point O .

Wide Barrier Diffraction

A typical wide barrier geometry is shown in Figure 3. Like the single knife-edge, there are four possible paths from source to receiver. Each of these paths includes two diffracting edges at points A and B . Diffraction effects beyond double diffraction (e.g. path $SABABR$) were neglected.

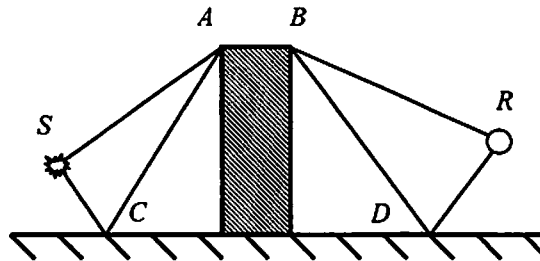


Figure 3 Typical wide barrier geometry showing four ray paths $SABR$ (the least time path), $SCABR$, $SABDR$, and $SCABDR$.

Figure 4 illustrates the double diffraction technique. The wide barrier is extended to form a single right-angle wedge, and a virtual receiver is placed at coordinates $(r', \theta, 0)$ where $r' = W + r$ and $\theta = \theta_w = 3\pi/2$. Using Eqs. 2, to 5, N values of $p(n\Delta T)$ are calculated at the virtual receiver. The fractional strength of the 0^{th} secondary source, $S_{ss,0}$, is then determined.

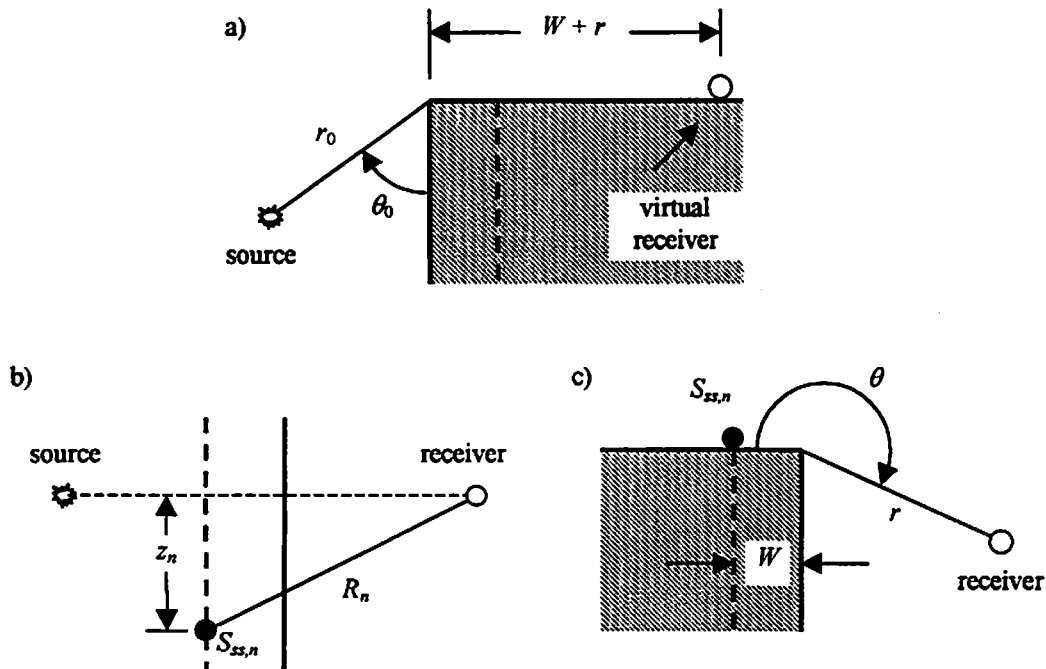


Figure 4 Wide barrier double diffraction method. a) Placement of virtual receiver, side view. b) The n^{th} partial least time path, top view. The least time path is shown as the thin dashed line. c) Diffraction over the second edge from the n^{th} secondary source, side view.

This source strength is simply $S_{ss,0} = F_0 S$, where

$$F_0 = \frac{p(0\Delta T)}{p_{\delta,0}} \quad (7)$$

The value of $p_{\delta,0}$ gives what the pressure "would have been" at the virtual receiver had the pulse originated from the 0th secondary source location, and is given by

$$p_{\delta,0} = \frac{S\rho}{2\pi R_0 \Delta T} \quad (8)$$

where $R_0 = W + r$. The factor of 2 in the denominator of Eq. 8 replaces the usual factor of 4 for a point source due to pressure doubling at the face of the wedge. Subsequent secondary source strengths are calculated in pairs as $S_{ss,n} = F_n S$, where

$$F_n = \frac{1}{2} \frac{p(n\Delta T)}{p_{\delta,n}} \quad (9)$$

and

$$p_{\delta,n} = \frac{S\rho}{2\pi R_n \Delta T} \quad (10)$$

for $R_n = [(W + r)^2 + z_n^2]^{1/2}$. The expression for z_n , the location of the n th secondary source along the z -axis, shown in Figure 4, can be found in Appendix 1.B of reference [7]. Contributions from secondary sources cumulate until the cut-off criteria is met.

$$F_n = \frac{S_{ss,n}}{S} < 0.5\% \quad (11)$$

This cut-off criteria (also used by Medwin et al. in reference [3]) defines N_{ss} , the value of n when Eq. 3-10 is satisfied. Once these secondary source strengths have been found, diffraction over the second edge can be treated.

A second right-angle wedge is formed as shown in Figure 4c, such that each secondary source has coordinates (r_0', θ_0', z_n) where $r_0' = W$ and $\theta_0' = 0$. Again using Eqs. 2, to 5, N_{ss} individual waveforms are obtained and added arithmetically at the appropriate arrival times to give the final pressure signal due to that ray path. These steps will be repeated to yield four individual signals, each corresponding to one of the ray paths shown in Figure 3. The superposition of these four signals gives the total impulse response for diffraction over the wide barrier. A typical time domain impulse response for a wide barrier is shown in Figure 10

Double Barrier Diffraction

In order to facilitate comparison of the wide and double knife-edge barriers, both plates of the double barrier are of the same height and are separated by width W . The same basic technique as described in the previous section is applied to the double knife-edge barrier to calculate the effects of double diffraction. However, since the double knife-edge barrier consists of two plates rather than a solid object, several distinct differences arise.

For both diffracting edges, the wedge angle used in Eqs. 2, to 5 is 2π rather than $3\pi/2$. An additional ground bounce in between the two plates is introduced to each of the four ray paths of the wide barrier, effectively doubling the number of possible ray paths to eight. These ray paths are shown in Figure 5. Internal reflections between the two plates are neglected, as are multiple diffraction effects beyond double diffraction (e.g. path *SABABR*).

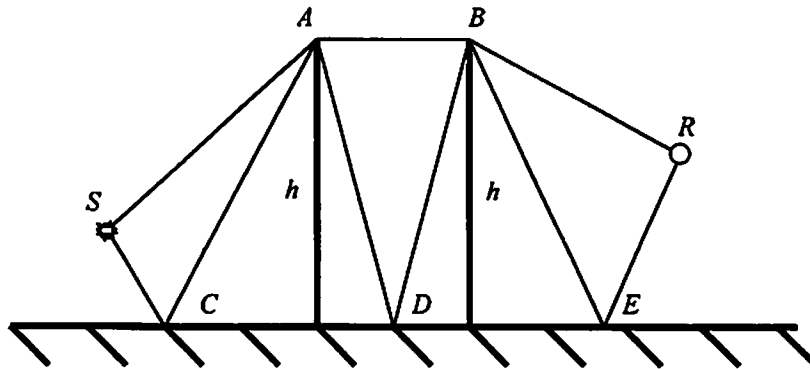


Figure 5 Typical double knife-edge barrier geometry showing eight possible ray paths *SABR* (the least time ray path), *SCABR*, *SADBR*, *SABER*, *SCADBR*, *SCABER*, *SADBER*, and *SCADBER*.

The coordinates of the virtual receiver and secondary sources depend on the path taken. Paths that include the ground bounce use a virtual receiver at coordinates $(r', \theta, 0)$ where $r' = [W^2 + (2h)^2]^{1/2} + r$ and $\theta = 2\pi - \arctan(W/2h)$ and secondary sources at (r_0', θ_0', z_n) where $r_0' = [W^2 + (2h)^2]^{1/2}$ and $\theta_0' = \arctan(W/2h)$. Paths that do not include the ground bounce have secondary source and virtual receiver coordinates that are the same as those of the wide barrier with the exception of θ_0' , which is $\pi/2$.

In using Eq. 8 and Eq. 10 to calculate the secondary source strengths, the effect of pressure doubling at the virtual receiver is no longer applicable. Spherical spreading takes its usual form with

$$p_{\delta,0} = \frac{S\rho}{4\pi R_0 \Delta T} \quad (12)$$

and

$$p_{\delta,n} = \frac{S\rho}{4\pi R_n \Delta T} \quad (13)$$

Table 1 shows a summary of the differences between the double diffraction techniques for the wide and double knife-edge barriers.

Table 1 Summary of differences between double diffraction techniques for the wide and double knife-edge barriers.

		Wide Barrier	Double Knife-Edge Barrier	
			no internal ground bounces	with internal ground bounce
θ_w		$3\pi/2$	2π	2π
# of ray paths		4	8	8
virtual receiver coordinates	r'	$W+r$	$W+r$	$[W^2+(2h)^2]^{1/2}+r$
	θ	$3\pi/2$	$3\pi/2$	$2\pi - \arctan(W/2h)$
$P\delta_n$		$\frac{S\rho}{2\pi R_n \Delta T}$	$\frac{S\rho}{4\pi R_n \Delta T}$	$\frac{S\rho}{4\pi R_n \Delta T}$
secondary source coordinates	r_0'	W	W	$[W^2+(2h)^2]^{1/2}$
	θ_0'	0	$\pi/2$	$\arctan(W/2h)$

A typical time domain impulse response for the double knife-edge barrier, in which eight distinct arrivals can be observed, is shown in Figure 12

Comparison of Models

As with the single knife-edge barrier, the BTM double diffraction method for the wide barrier was compared to the models of Pierce and De Jong. Like the case of the single knife-edge barrier, the BTM and Pierce wide barrier models agree quite well. Figure 6 shows this agreement for the case of a 20cm thick barrier normalized to the total field.

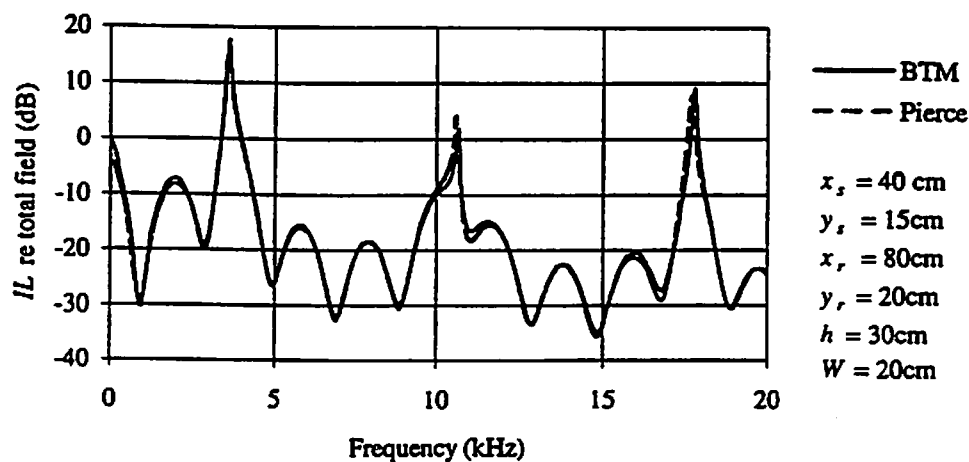


Figure 6 Insertion loss, normalized to the total field, of a wide barrier as predicted by the BTM and Pierce models.

The De Jong model for double diffraction, however, had significant discrepancies which were attributed to phase mismatches between the direct and image sources. [7]

While the Pierce model is well suited to predict multiple diffraction effects, it requires adjacent diffracting edges to have a common side plane. This configuration is often referred to as a three-sided barrier in the literature. In Section 2.2.2 of reference [8], Salomons offers a heuristic modification to Pierce's model in which diffraction effects from an arbitrary number of edges can be calculated without the common side plane requirement. Salomons further states, however, that by using this modification, discontinuities occur in the resulting spectrum and can be avoided only by limiting the calculation to a fixed frequency. This shortfall is overcome by the BTM impulse formulation which gives a continuous broadband response through a transformation of the time domain.

Experiment

Experiments were conducted in a well-controlled indoor environment. The source was an electric spark and the receiver was a 1/4" B&K microphone. Time domain data was captured for surface with and without barriers and windowed to avoid unwanted reflections and diffractions from walls and surface edges, etc. The time domain data was Fast Fourier Transformed to investigate the insertion loss in the frequency domain. A sketch of the experimental geometry is presented in Figure 7 for the double barrier experiment. Similar geometries were used for the single and wide barrier geometries

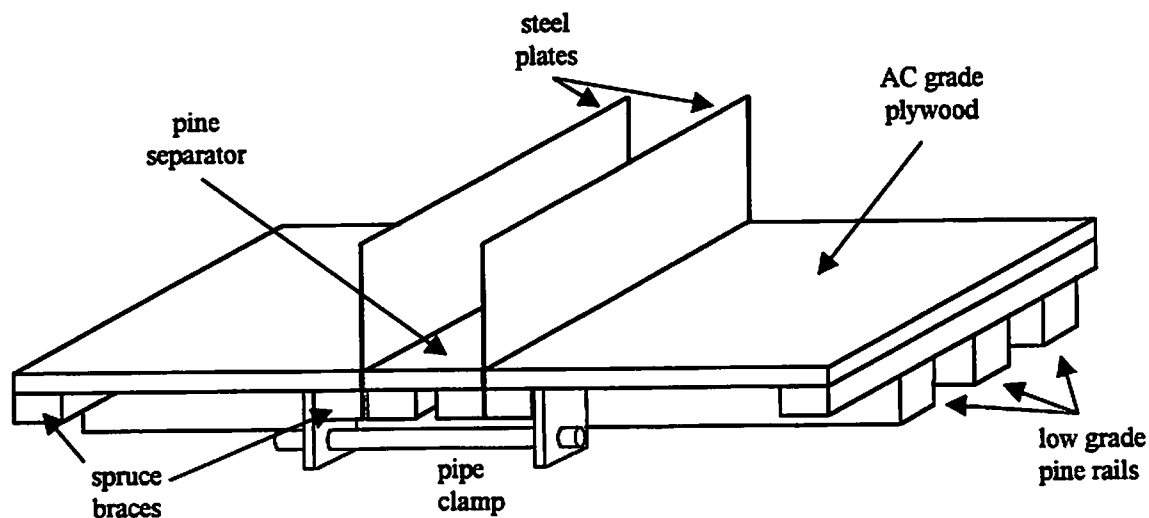


Figure 7 Configuration of surface and barrier materials.

Barrier Measurements

Five similar configurations were tested and for each configuration the three types of barriers were compared by keeping the pre-insertion range from source to receiver constant (120cm) and placing the barriers such that the centerline of each was in the same location. The primary variation among the five configurations was the width, W , of the wide and double knife-edge barriers. Configurations for the single knife-edge were determined by adding half the value of W

to both x_s and x_r . The graphs to be presented correspond to one of the geometries in which, for the wide and double barrier configuration, $x_s = 50$ cm, $y_s = 15$ cm, $x_r = 70$ cm, $y_r = 20$ cm, $h = 3.7$ cm and $W = 24.2$ cm. For the single barrier, $W = 0$ and x_s and x_r are adjusted accordingly to keep the centerline in the same location.

Single Knife-Edge Barrier

This section presents data for two experimental configurations and the corresponding BTM predictions, both in the time domain and in the frequency domain. The time domain impulse response in Figure 8 shows excellent agreement between theory and experiment with minor exceptions. The first is the slight discrepancy between the predicted arrival times of the pulses following ray paths including ground bounces. This could be due to (1) an error in the speed of sound used for calculations, (2) an improper placement of the source and receiver and/or (3) a slight warping of the plywood surface. The latter effect could cause the effective barrier height to change along the z -axis.

The second exception is a very weak arrival at ~ 5.3 ms for the two configurations shown. Geometrical analysis confirms that this pulse, shown by a "?" in the figures, is not backscatter from the edges of the plywood surface or diffraction from the side edges of the steel plate. Most likely, it is the result of reflection(s) from the acrylic structure of the spark source or from the ring stands and clamps used to support the source and receiver. These extraneous "sources," present in all five data sets, are believed to be the primary source of error in the insertion loss analysis.

In the insertion loss data presented in Figure 9, excellent agreement is found from 2kHz to ~ 10 kHz. Beyond 10kHz, the curves appear slightly shifted although the general trends of the two curves are very similar. This condition can also be seen for both the wide barrier and the double knife-edge barrier.

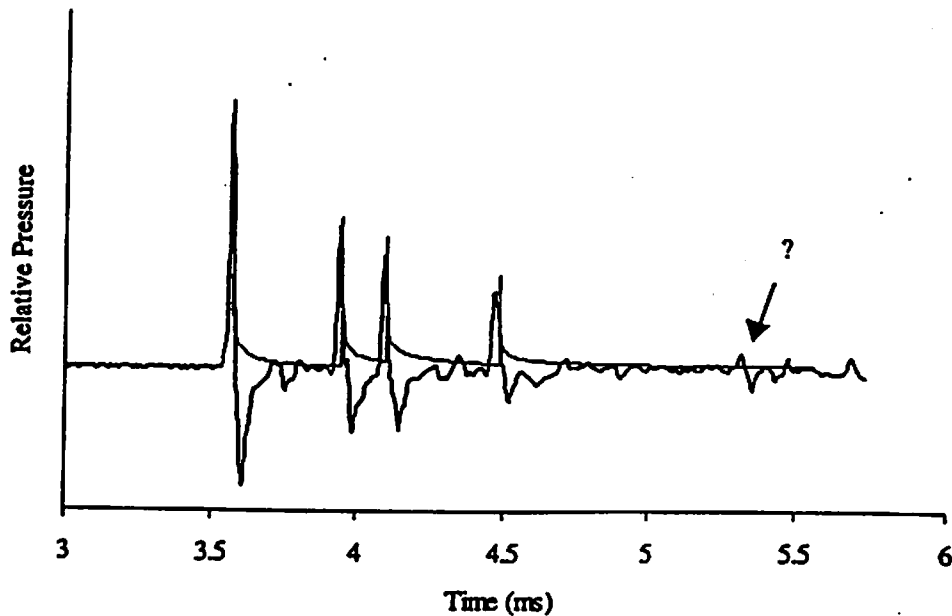


Figure 8 Single knife-edge barrier impulse response. BTM prediction (thin line) and experimental data (thick line).

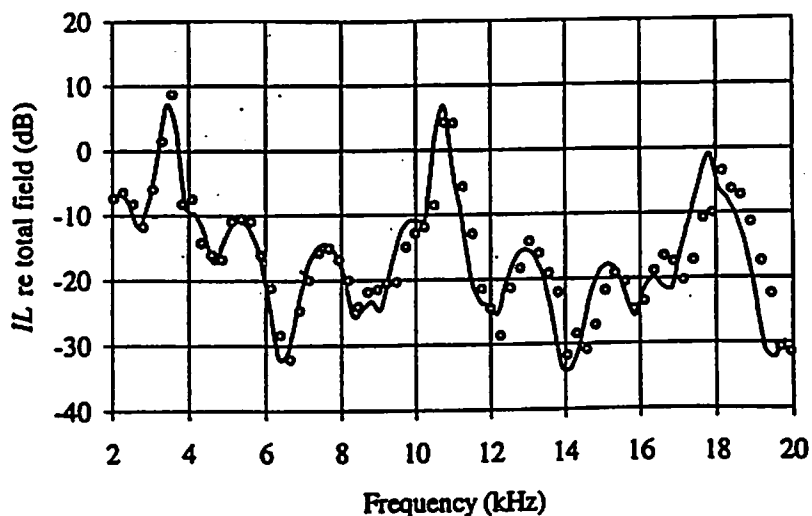


Figure 9 Single knife-edge barrier insertion loss. BTM prediction (solid line) and experimental data (hollow dots).

2. Wide Barrier

As with the single knife-edge barrier, both the time domain and insertion loss results for the wide barrier are presented. Not surprisingly, it is found that the wide barrier generally gives an improved insertion loss (i.e. lower sound level) as compared to the single knife-edge barrier. This improvement is especially seen at frequencies whose wavelengths are comparable to the thickness of the barrier. By blocking certain destructively interfering ray paths, however, the wide barrier can actually be less effective than the single-knife edge barrier at some frequencies when normalizing by the total field.

The time domain traces comparing the BTM prediction to the experimental data, is shown in Figure 10. The corresponding insertion loss curves are shown in Figure 11. Again, there is good agreement between the BTM model and the experimental data. The shift of the data from the BTM prediction, observed at frequencies above ~ 10 kHz for the single knife-edge barrier, is less pronounced for the wide barrier.

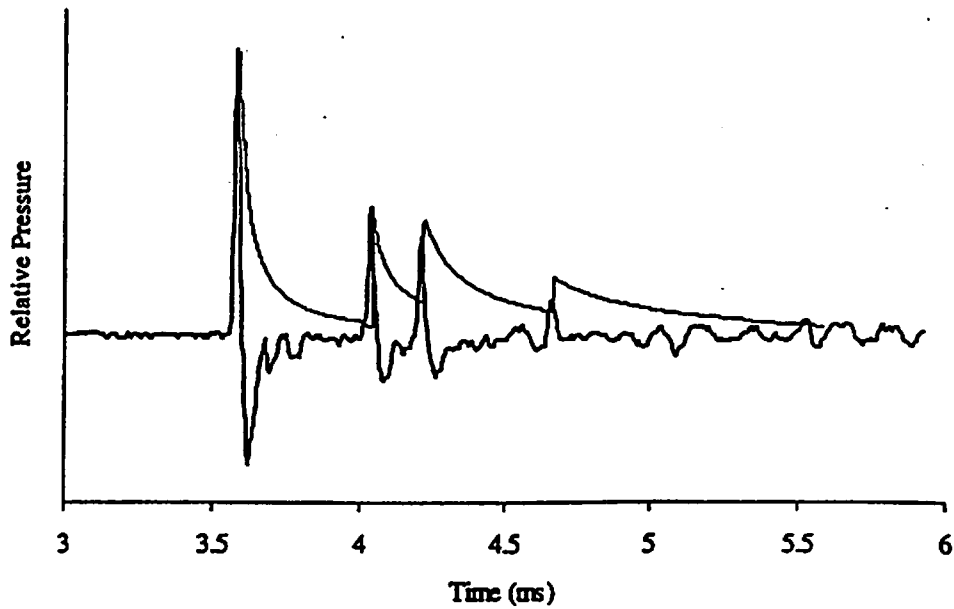


Figure 10 Wide barrier impulse response. BTM prediction (thin line) and experimental data (thick line).

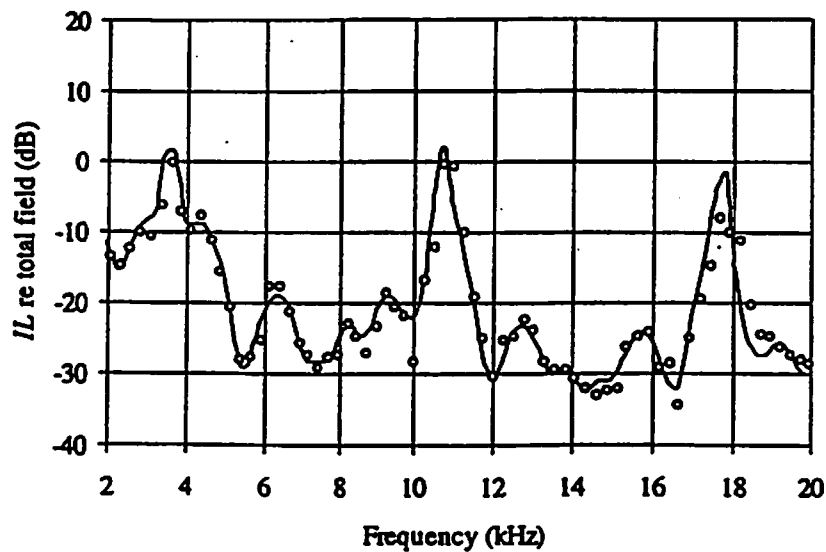


Figure 11 Wide barrier insertion loss. BTM prediction (solid line) and experimental data (hollow dots).

Double Knife-Edge

A further improvement in sound level mitigation is observed for the double knife-edge barrier, as compared to the wide barrier. Figure 12 presents the impulse response for this configuration. It is more difficult, however, to distinguish individual pulses arriving later in time due to the abundance of source clutter. In addition, the discrepancies in the relative amplitudes of the individual diffracted pulses are much larger than observed in either the single knife-edge

barrier or the wide barrier. The double knife-edge barrier insertion loss data is shown in Figure 13.

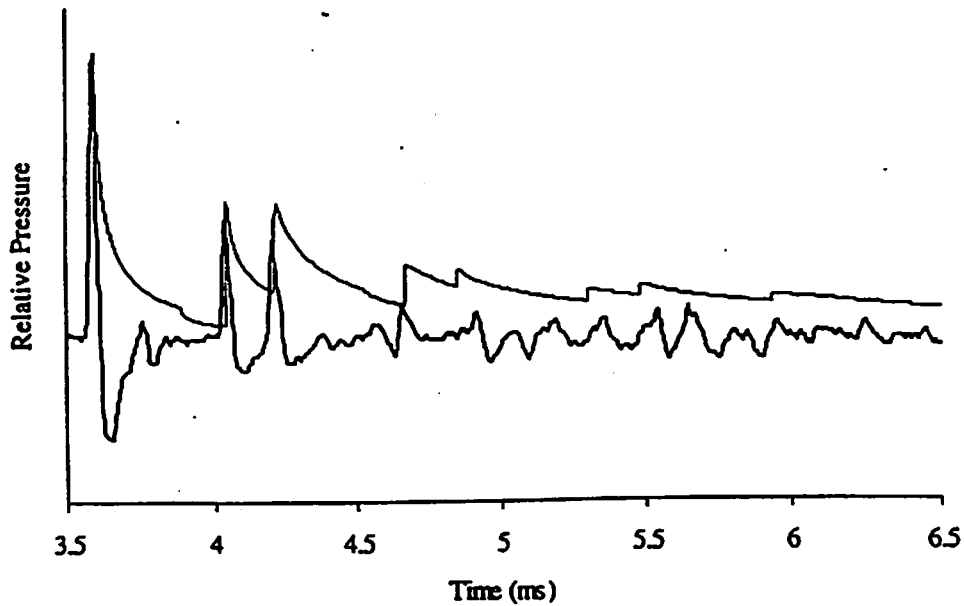


Figure 12 Double knife-edge barrier impulse response. BTM prediction (thin line) and experimental data (thick line).

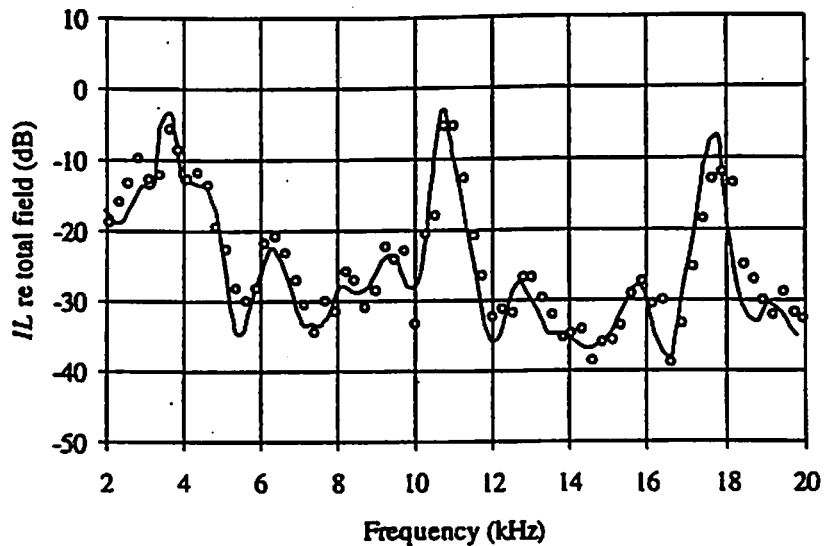


Figure 13 Double knife-edge barrier insertion loss. BTM prediction (solid line) and experimental data (hollow dots).

It is intriguing to note that the insertion loss of the double knife edge barrier is systematically 2 to 3 dB lower than the wide barrier and the difference is independent of

frequency. This relation can be more easily seen in Figure 14 where the insertion loss for a typical model geometry, given in Table 2, is presented for the knife edge, wide and double barriers. This finding suggests that 1) The added 4 ray paths in the double barrier geometry are a negligible contribution to the problem, 2) it may be possible to reduce the number of calculated ray paths to certain key ones 3) the principle cause of the difference is the change in wall angle from 270° to 360° . These last two findings may open avenues for quick empirical optimization algorithms.

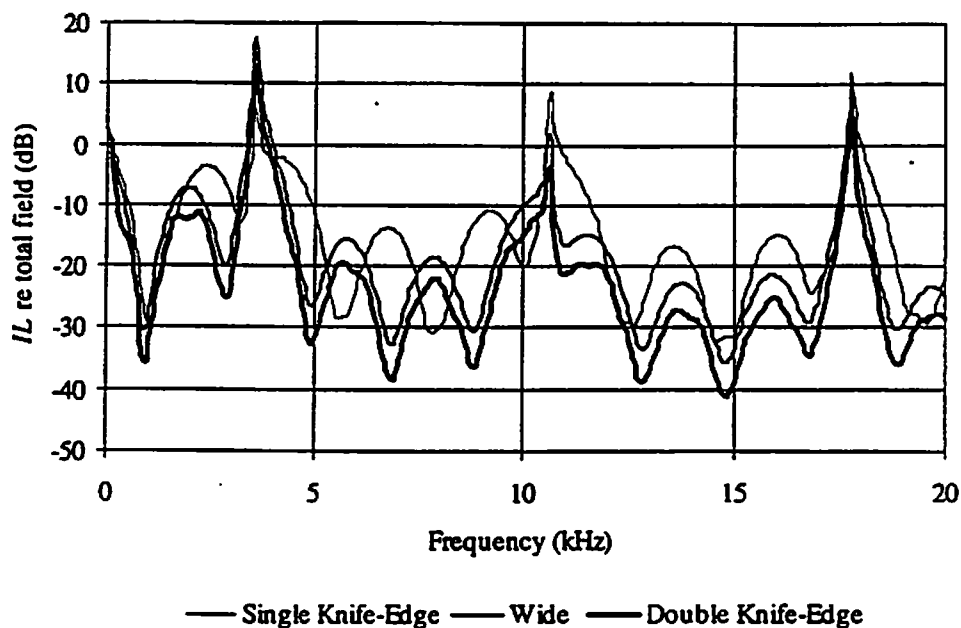


Figure 14 Insertion loss curves for the single knife-edge, wide, and double knife-edge barriers.

Table 2 Geometry used for Figure 14

	source coordinates		receiver coordinates		h (cm)	w (cm)
	x_s (cm)	y_s (cm)	x_r (cm)	y_r (cm)		
Single Knife-Edge Barrier	50	15	70	20	30	—
Wide and Double Knife-Edge Barriers	40	15	80	20	30	20

CONCLUSIONS

Diffraction effects on various configurations of acoustical barriers have been investigated. Barriers that have two diffracting edges were the primary focus of the research. A rigid ground surface was also included in the investigation in order to study interference patterns that can result from various possible ray paths. The De Jong, model, Pierce model and the Biot-

Tolstoy-Medwin (BTM) model were investigated for their ability to predict the diffracted sound field associated various barrier configurations. These predictions were initially compared to data found in the literature and it was determined that the Pierce and BTM models could properly account for multiple diffraction effects over wide barriers. The Pierce model is not properly posed to handle arbitrarily separated barriers, such as the double knife edge, so the BTM model was extended and examined in greater detail in the hopes that it might provide an alternate solution for arbitrary configurations of multiple barriers.

In conjunction with the modeling efforts, a series of scale model experiments were conducted to verify the usefulness of the developed model and to provide a data set for future models if needed. While agreement between the BTM model and the experimental data was quite good the model may have limited value as an alternate solution for diffraction effects in noise prediction software. At present it is too computationally prohibitive and its time domain formulation may not mix well with other models that handle other propagation features such as impedance effects and vegetation.

REFERENCES

- ¹B. A. De Jong, A. Moerkerken and J. D. Van Der Toorn, "Propagation of sound over grassland and over an earth barrier," *J. Sound Vib.*, **86**(1), pp. 23-46 (1983).
- ²A. D. Pierce, "Diffraction of sound around corners and over wide barriers," *J. Acoust. Soc. Am.*, **55**(5), pp. 941-955 (1974).
- ³H. Medwin, E. Childs and G. M. Jebsen, "Impulse studies of double diffraction: a discrete Huygens interpretation," *J. Acoust. Soc. Am.*, **72**(3), pp. 1005-1013 (1982).
- ⁴M. A. Biot and I. Tolstoy, "Formulation of wave propagation in infinite media by normal coordinates with an application to diffraction," *J. Acoust. Soc. Am.*, **29**(1), pp. 381-391 (1957).
- ⁵I. Tolstoy, "Exact, explicit solutions for diffraction by hard sound barriers and seamounts," *J. Acoust. Soc. Am.*, **85**(2), pp. 661-669 (1989).
- ⁶H. Medwin, "Shadowing by finite noise barriers," *J. Acoust. Soc. Am.*, **69**(4), pp. 1060-1064 (1981).
- ⁷G. J. Wadsworth, *Scale Model Experiments on the Insertion Loss of Wide and Double Barriers*, pp. (1998).
- ⁸E. M. Salomons, "Sound propagation in complex outdoor situations with a non-refracting atmosphere: model based on analytical solutions for diffraction and reflection," *Acustica*, **83**, pp. 436-454 (1997).

Wave Propagation in a 3-D Turbulent Atmosphere: Horizontal Coherence

Xiao Di and Kenneth E. Gilbert

*Applied Research Laboratory and the Graduate Program in Acoustics
The Pennsylvania State University, University Park, PA 16802, USA*

Telephone: 814-863-5399 (X. D.), 814-863-8291 (K. E. G.)

Email: di@seaair.acs.psu.edu, keg5@psu.edu,

ABSTRACT

A 3-D version of the "Green's function parabolic equation" (GF-PE) is used to investigate horizontal coherence of the acoustic field versus cross range and height at a distance of 1 km from a point source. The purpose of the investigation is to assess the feasibility of using long (10 m to 100 m) elevated horizontal arrays to beamform on the acoustic field of a distant source. The cross-range correlation function for daytime propagation (upward-refracting) is computed at a range of 1 km for array heights of 0 m, 25 m, and 100 m, and for frequencies of 50 Hz, 100 Hz, and 200 Hz. It is found that, at 50 Hz, beamforming is possible at all three heights. At 100 Hz, beamforming can possibly be done at 25 m and 100 m, but not on the ground. At the highest frequency investigated, 200 Hz, beamforming appears to be feasible only at the greatest height, 100 m. Hence, it is apparent that, for daytime beamforming to be feasible, technological advances are badly needed that will permit acoustic sensing at greater heights than is now possible with ground-based microphones.

I. INTRODUCTION

For many years, long horizontal arrays have been used in the ocean to usefully beamform on distant sources. In the ocean, the use of long horizontal arrays at substantial depths is relatively easy due to Archimedes' Principle: ships float on the surface and hydrophones sink. In atmospheric acoustics, because of the difficulty of making measurements at any significant height, almost all measurements have been made near the ground. In the daytime, because of upward refraction and scattering from turbulence, the acoustic field near the ground has little coherence [Havelock et al., 1995; Di and Gilbert, 1997; Gilbert and Di, 1998]. Consequently, long, near-ground horizontal arrays have limited use as a means for locating the bearing of a distant source. It is well known in atmospheric acoustics, however, that the coherence of the sound field increases with height above the ground. [Havelock et al., 1995; Di and Gilbert, 1997; Gilbert and Di, 1998]. Hence, in this paper we investigate the possibility of useful beamforming with long, elevated horizontal arrays. Methods for deploying such arrays are beyond the scope of the present paper and, consequently, are not discussed here.

II. THEORY AND COMPUTATIONAL METHODS

The model used for the 3-D propagation calculations presented here is an extension of a 2-D model known as the "Green's Function Parabolic Equation" (GF-PE) model [Gilbert and Di, 1993]. The 3-D GF-PE method, which has been reported recently [Di and Gilbert; 1997, Gilbert and Di, 1998], computes the acoustic field of a point source in a "pie-slice" region with periodic boundary conditions imposed on the straight sides of the slice. The geometry of the computational domain is indicated by the 3-D pie-slice shown in Fig. 1. On the bottom of the pie slice, a finite impedance boundary condition is used, where the normalized value of the impedance is Z_g . At the top of the pie slice, an artificial absorptive "sponge" is used to elimination spurious reflections from the top of the computational domain. Because periodic boundary conditions are imposed on the two straight sidewalls of the pie slice, acoustic energy going out one side of the pie slice reenters on the opposite side. The motivation for using periodic boundary conditions is the need for a numerically tractable method that conserves energy and preserves the statistical properties of the scattered acoustic field. The azimuthal angle of the pie slice shown in Fig. 1 is given by δ , where δ can be any value from 0° (2-D calculation) to 360° (a full 3-D calculation). For the sake of computational speed, in calculations done thus far, δ has been limited to a relatively small angle, 11.5° . Within the pie slice itself, the usual out-going wave propagation condition is assumed.

a. Mathematical formulation

The following is a brief description of the 3-D GF-PE formulation. We start from the 3-D wave equation for acoustic pressure P ,

$$\frac{\partial^2 P}{\partial x^2} + \frac{\partial^2 P}{\partial y^2} + \frac{\partial^2 P}{\partial z^2} + k^2(x, y, z)P = 0 \quad (1)$$

where $k(x, y, z)$ is the wavenumber. In a cylindrical coordinated system, (r, ϕ, z) , a scaled variable $\Psi = \sqrt{r}P$ is introduced to replace the acoustic pressure, P . Substituting $P = \Psi / \sqrt{r}$ into Eq. (1), and applying the usual far-field approximation, we obtain a far-field 3-D wave equation,

$$\frac{\partial^2 \Psi}{\partial r^2} + \frac{\partial^2 \Psi}{r^2 \partial \phi^2} + \frac{\partial^2 \Psi}{\partial z^2} + k^2(r, \phi, z)\Psi = 0 \quad (2)$$

The one-way, outgoing-wave equation corresponding to Eq. (2) is given by,

$$\frac{\partial \Psi}{\partial r} = i\sqrt{Q}\Psi \quad (3)$$

where

$$\begin{aligned}
 Q' &\equiv \sqrt{\frac{\partial^2}{\partial z^2} + \frac{\partial^2}{r^2 \partial \phi^2} + k^2(r, \phi, z)} = \sqrt{\frac{\partial^2}{\partial z^2} + \frac{\partial^2}{r^2 \partial \phi^2} + k_0^2 + (k^2 - k_0^2)} \\
 &\approx \sqrt{\frac{\partial^2}{\partial z^2} + \frac{\partial^2}{r^2 \partial \phi^2} + k_0^2} + (k - k_0) \equiv Q + (k - k_0)
 \end{aligned} \tag{4}$$

and k_0 is a reference wavenumber.

The formal solution of Eq. (3) is,

$$\Psi(r + \Delta r) = \exp[i\Delta r(k - k_0)] \exp[i\Delta r \sqrt{Q}] \Psi(r) \tag{5}$$

which, written in explicit form, is given by,

$$\Psi(r + \Delta r, \phi, z) = \exp[i\Delta r(k - k_0)] \frac{1}{i\pi} \int_C e^{i\kappa \Delta r} \kappa d\kappa \int_0^\delta r d\phi' \int_0^\infty dz' G(\kappa, z, z', \phi, \phi', r) \Psi(r, \phi', z') \tag{6}$$

where C is a contour integral enclosing the spectrum of the Green's function, G . The Green's function itself is the solution of the following boundary value problem:

$$\frac{\partial^2 G}{\partial z^2} + \frac{\partial^2 G}{\partial (r\phi)^2} + k_T^2 G = -\delta(z - z') \delta(r\phi - r\phi') \quad z \geq 0 \tag{7}$$

where k_T is the transverse wavenumber. The boundary condition at $z=0$ is $\partial G / \partial z = -i\beta G$, where $\beta = k_f Z_g$, and Z_g is the normalized ground impedance. With the periodic boundary condition $G(\phi + \delta) = G(\phi)$, the explicit solution for the Green's function is,

$$\begin{aligned}
 G &= \frac{1}{2\pi r \delta} \sum_{m=-\infty}^{\infty} \int_{-\infty}^{\infty} \frac{e^{ik_z(z-z') + \frac{2\pi}{\delta} m(\phi-\phi')}}{k_z^2 + \left(\frac{2\pi m}{\delta r}\right)^2 - k_T^2} dk_z + \frac{1}{2\pi r \delta} \sum_{m=-\infty}^{\infty} \int_{-\infty}^{\infty} R(k_z) \frac{e^{ik_z(z+z') + \frac{2\pi}{\delta} m(\phi-\phi')}}{k_z^2 + \left(\frac{2\pi m}{\delta r}\right)^2 - k_T^2} dk_z \\
 &\quad + \frac{2i\beta}{r\delta} \sum_{m=-\infty}^{\infty} \frac{e^{-i\beta(z+z') + \frac{2\pi}{\delta} m(\phi-\phi')}}{\beta^2 + \left(\frac{2\pi m}{\delta r}\right)^2 - k_T^2}
 \end{aligned} \tag{8}$$

where k_z is the vertical wavenumber and m is the azimuthal modal rank. By substituting the explicit form of the Green's function into Eq. (6), we arrive at the final formulation for the 3-D GF-PE:

$$\begin{aligned} \Psi(r + \Delta r, \varphi, z) = & \frac{e^{i\Delta r(k-k_0)}}{2\pi\delta} \sum_{m=-\infty}^{\infty} e^{i\frac{2\pi}{\delta}m\varphi} \left\{ \int_{-\infty}^{\infty} e^{ik_z z} dk_z \int_0^{\delta} e^{-i\frac{2\pi}{\delta}m\varphi'} e^{i\Delta r \sqrt{k_0^2 - k_z^2 - (\frac{2\pi m}{\delta r})^2}} \int_0^{\infty} e^{-ik_z z'} dz' \Psi(r, \varphi', z') \right. \\ & + \int_{-\infty}^{\infty} R(k_z) e^{ik_z z} dk_z \int_0^{\delta} e^{-i\frac{2\pi}{\delta}m\varphi'} e^{i\Delta r \sqrt{k_0^2 - k_z^2 - (\frac{2\pi m}{\delta r})^2}} \int_0^{\infty} e^{ik_z z'} dz' \Psi(r, \varphi', z') \\ & \left. + e^{i\Delta r \sqrt{k_0^2 - \beta^2 - (\frac{2\pi m}{\delta r})^2}} \int_0^{\delta} e^{-i\frac{2\pi}{\delta}m\varphi'} d\varphi' 4\pi i \beta e^{-i\beta z} \int_0^{\infty} e^{-i\beta z'} dz' \Psi(r, \varphi', z') \right\} \end{aligned} \quad (9)$$

where the reflection coefficient R is given by,

$$R(k_z) = \frac{k_z - \beta}{k_z + \beta} \quad (10)$$

As in the 2-D version of the GF-PE, the final solution for the 3-D GF-PE in Eq. (9) consists of three terms, each having a clear physical interpretation: the first term is the direct wave, the second term is the specular reflection, and the third term is the surface wave. Equation (9) is used below to investigate horizontal coherence of the acoustic field versus cross range and height at a distance of 1 km from a point source

III. RESULTS OF A NUMERICAL INVESTIGATION OF COHERENCE

To provide some physical insight on the 3-D structure of the acoustic field from a point source, we present here gray-scale plots of the down-range and cross-range acoustic levels at 50 Hz, 100 Hz, and 200 Hz. In addition, we show the cross-range, two-point correlation function at selected heights: 0 m, 25 m and 100 m. The source height is 1 m, and the ground is taken to be rigid ($Z_g = \infty$). The mean sound-speed profile is upward-refracting and is shown in Fig. 2. Realizations for the turbulent part of the sound speed are generated using a homogeneous, isotropic, 3-D Kolmogorov spectrum with random phases for each of the Fourier components. The azimuthal angle of the pie slice, δ , is 11.5° in all the calculations.

Since the results given here are for a particular mean sound-speed profile and a particular turbulence model, one should use care in extrapolating the conclusions to other atmospheric scenarios. Nevertheless, from the results shown, it is clear that significant performance improvements can be expected with elevated horizontal arrays.

a. Visualization of the 3-D acoustic field

Figures 3 and 4 show, respectively, a single realization of the down-range and cross-range variation in the relative sound-pressure level for a point source obtained using the inputs described above. In Fig. 3, the geometric (ray) shadow boundary is approximated by the gray-scale plot at 200 Hz. At lower frequencies, the geometric shadow is partially filled by diffraction, with significant levels near the ground at the lowest frequency, 50 Hz. Although "snapshots" of the down-range variation of the acoustic field provide useful information on the effect of upward refraction in the presence of turbulence, they provide little useful information on the important issue of the cross-range correlation. To address the issue, we present, in Fig. 4, gray-scale plots of the cross-range levels at 50 Hz, 100 Hz, and 200 Hz. At 50 Hz, the field is relatively uniform horizontally, showing that, at 50 Hz and a range of 1 km, turbulence effects are small. There appears to be only a little focusing or de-focusing of the nearly spherically spreading acoustic wave. Near the ground, there is some noticeable horizontal variation of the field and a few "dead spots" due to de-focusing of the field. Above about 75 m, the field is uniform except for a few small white "hot spots" due to focusing of the field. At 100 Hz, focusing and de-focusing of the acoustic field has generated significant patchiness in the field over the whole height shown (0 - 200 m). Notice, in particular, the large hot spots (white) where the level is about 10 dB above spherical spreading. Even though the field is patchy at 100 Hz, the patches are large enough above 20 - 30 m to maintain significant horizontal correlation in the field. Near the ground, in contrast, the patches are quite small and there is no noticeable correlation except over distances of a few meters. At the highest frequency, 200 Hz, the field has broken up into a myriad of patches of all sizes. At a heights greater than 75 m, the patches are large enough that one can still distinguish high intensity regions with dimensions of many 10's of meters. Below 75 m, the field quickly breaks up into patches of only a few meters.

b. Two-point horizontal correlation function

In this section, to augment the above "patch-ology" discussion with a quantitative measure of cross-range correlation, we present in Fig. 5 the horizontal correlation function versus separation distance at heights of 0 m, 25 m, and 100 m, computed with the average over 50 realizations. Essentially everything shown in Fig. 5 is consistent with the qualitative discussion of Fig. 4 in the previous section.

At 50 Hz the horizontal cross-range correlation function is above .9 at all frequencies, with the higher values associated with the greater heights. Thus, for beamforming at 50 Hz, there appears to be little advantage to using elevated sensors. Except for special sources such as helicopters, however, one cannot expect significant energy at such a low frequency. At more common frequencies, such as 100 Hz and 200 Hz, Fig. 5 shows that near-ground beam-forming at 1 km may not be feasible. At 100 Hz, one could possibly construct a useful beam using two 25 m towers to support a horizontal array. At 200 Hz, in contrast, the field is reasonably coherent only at 100 m. Since 100 m towers would not be mobile, remote sensing at 100 m would require technology that is not readily available at present.

c. Physical explanation of daytime horizontal correlation

The essential features of Figs. 4 and 5 can be understood in a simple way. Consider the acoustic field to be the sum of two components: (1) a fairly strong, coherent field that is composed of small-angle components generated by upward refraction together with diffraction into the shadow zone; (2) a fairly weak, incoherent field that is generated by larger-angle scattering from turbulence. Although both fields are present at all heights and all frequencies, the degree of coherence is governed by the relative contribution of each component. At 50 Hz, for example, the total field is dominated by field number one, so that the acoustic field has substantial coherence at all heights. As the frequency increases, the shadow boundary approaches the geometric boundary, so that near the ground, the field is dominated more and more by field number 2, which because of its source, stochastic scattering, is inherently incoherent. Thus, as one progresses from 50 Hz to 200 Hz, higher and higher altitudes are required to sample field number one, which is the more coherent component. Clearly, as the frequency or range are increased, the simple model proposed here will break down, since field number one will become more and more incoherent and finally reach "saturation." At saturation, the field has reached its maximum complexity and generally has a small but stable coherence length [Flatte' et al., 1979]. Under such conditions, beamforming with long horizontal arrays is probably not feasible at any height.

IV. CONCLUSIONS

The numerical investigation of horizontal coherence presented here indicates that beamforming with long, elevated horizontal arrays is feasible provided that, at a given range, the frequency is low enough and the horizontal array is high enough. At 50 Hz and a range of 1 km, for example, useful beamforming was possible at any height. At 100 Hz, the study indicated that useful beamforming should be possible at heights above about 25 m. At the highest frequency investigated, 200 Hz, useful beamforming required a height of 100 m. Measurement of the acoustic field at such heights is not easily done with presently available technology.

Finally, we point out the need for field measurements to test the model predictions given here. Although measurements with elevated sensors remain problematic, plans are underway for cross-range, two-point coherence measurements at considerable heights, hopefully up to 300 m.

ACKNOWLEDGMENTS

The authors gratefully acknowledge support from the Defense Advanced Research Projects Agency (DARPA).

REFERENCES

S. M. Flatte', R. Dashen, W. H. Munk, K. M. Watson, and F. Zachariasen, 1979: *Sound Transmission Through A Fluctuating Ocean..* Cambridge University Press, New York, pp. 299

K. E. Gilbert and X. Di, "A fast Green's function method for one-way sound propagation in the atmosphere", *J. Acoust. Soc. Am.*, Vol. 94, No.4, pp. 2343-2352, Oct. 1993

D. I. Havelock, X. Di, G. A. Daigle, and M. R. Stinson, "Spatial coherence of a sound field in a refractive shadow: Comparison of simulation and experiment", *J. Acoust. Soc. Am.*, 98, October 1995, pp. 2289-2302

X. Di and K. E. Gilbert, "Strategies for computing sound propagation through realistic three-dimensional turbulence," presented at the 134th meeting of the Acoustical Society of America, San Diego, California, December, 1997

K. E. Gilbert and X. Di, "Modeling the effects of refraction and diffraction on wave propagation in a 3-D turbulent atmosphere," *Proceedings of 16th International Congress on Acoustics and the 135th meeting of the Acoustical Society of America*, Vol. 1, pp. 479-480, June, 1998

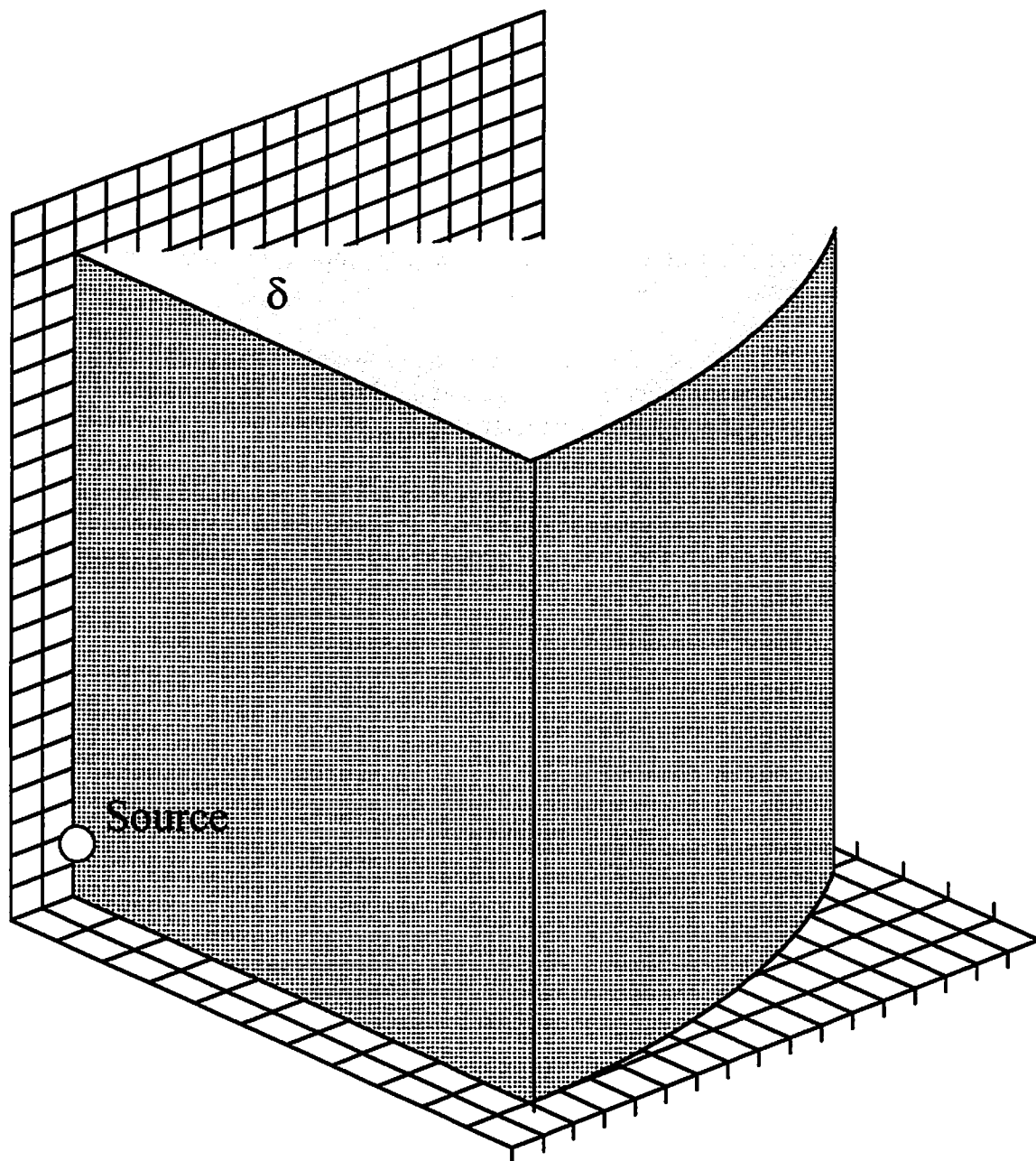


Figure 1. Geometry of the three-dimensional computational domain of GF-PE calculations (pie slice). The lower boundary is a finite impedance surface. The upper portion of the pie slice is an absorptive sponge. Periodic boundary conditions are enforced on the two straight side walls of the pie slice.

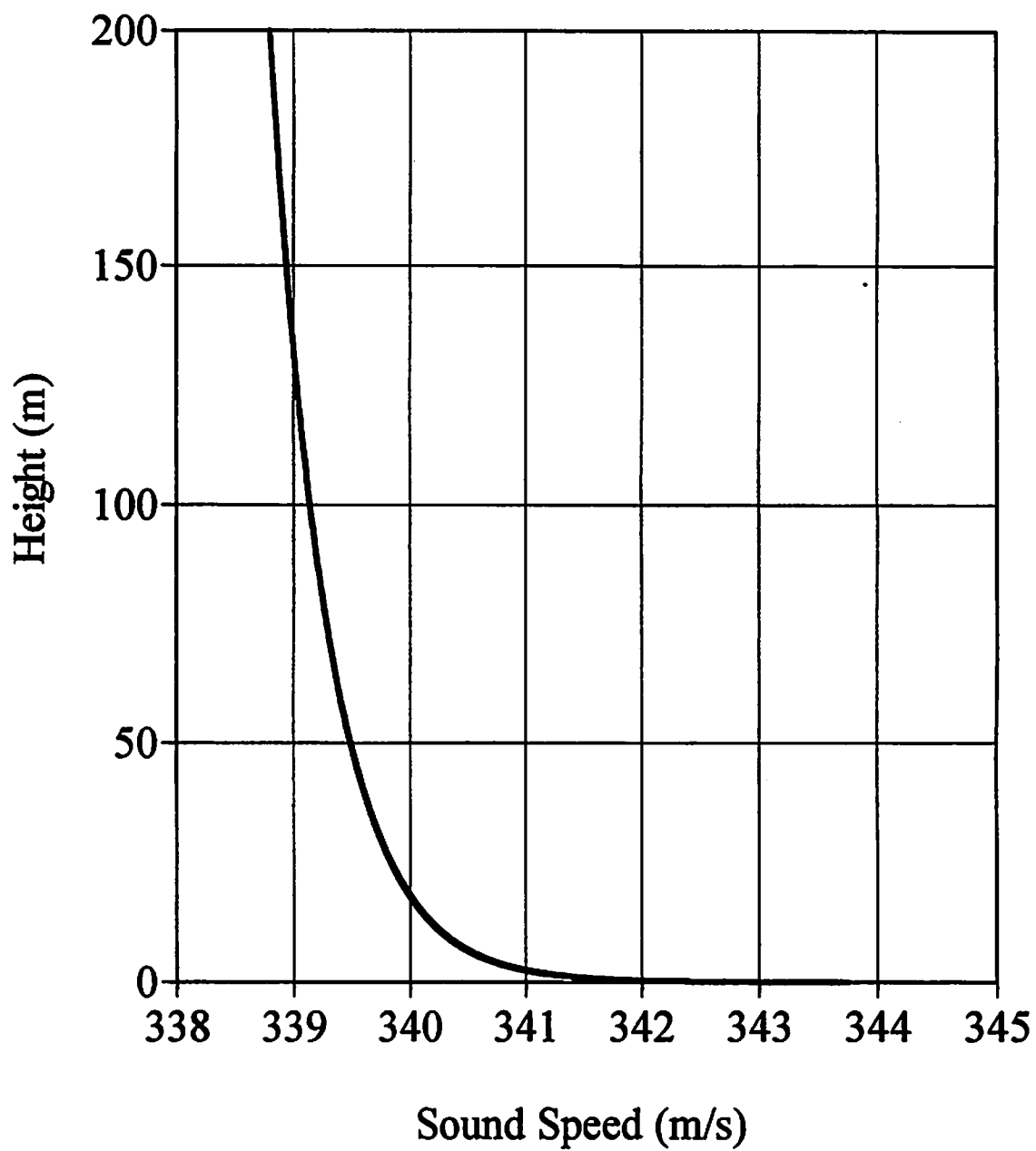
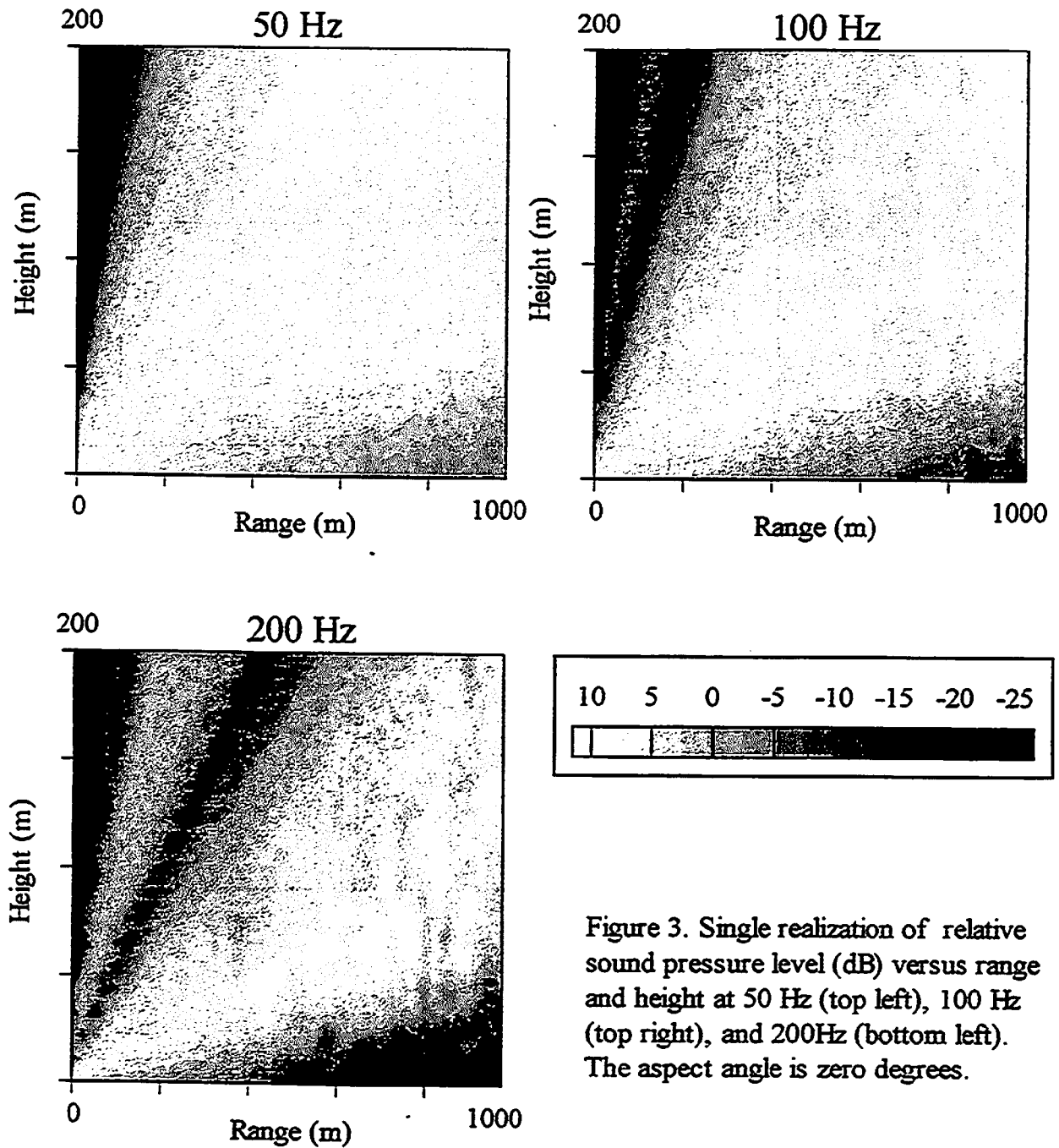


Figure 2. Upward-refracting sound-speed profile used for the GF-PE calculations in Figs. 3-5.



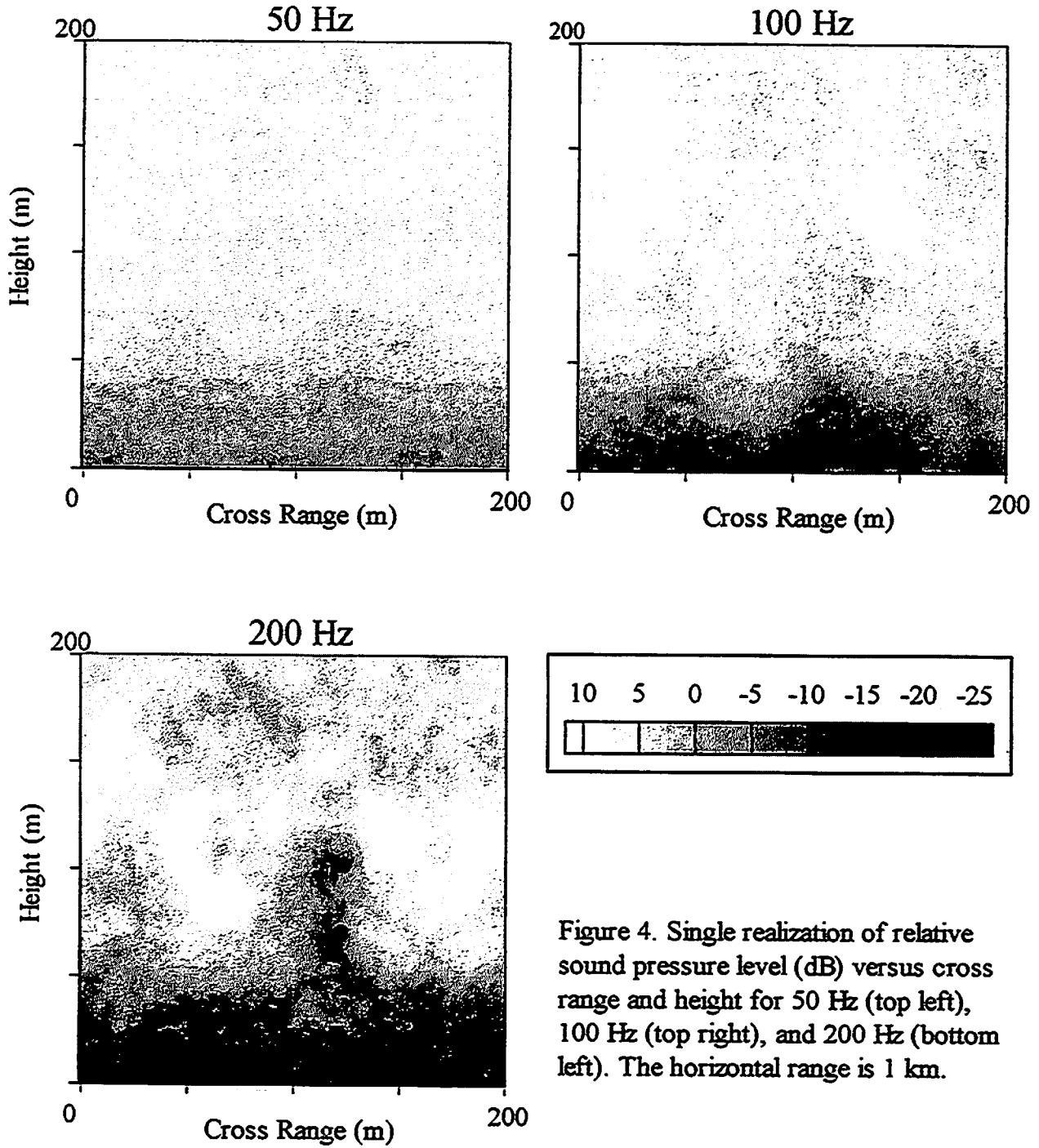


Figure 4. Single realization of relative sound pressure level (dB) versus cross range and height for 50 Hz (top left), 100 Hz (top right), and 200 Hz (bottom left). The horizontal range is 1 km.

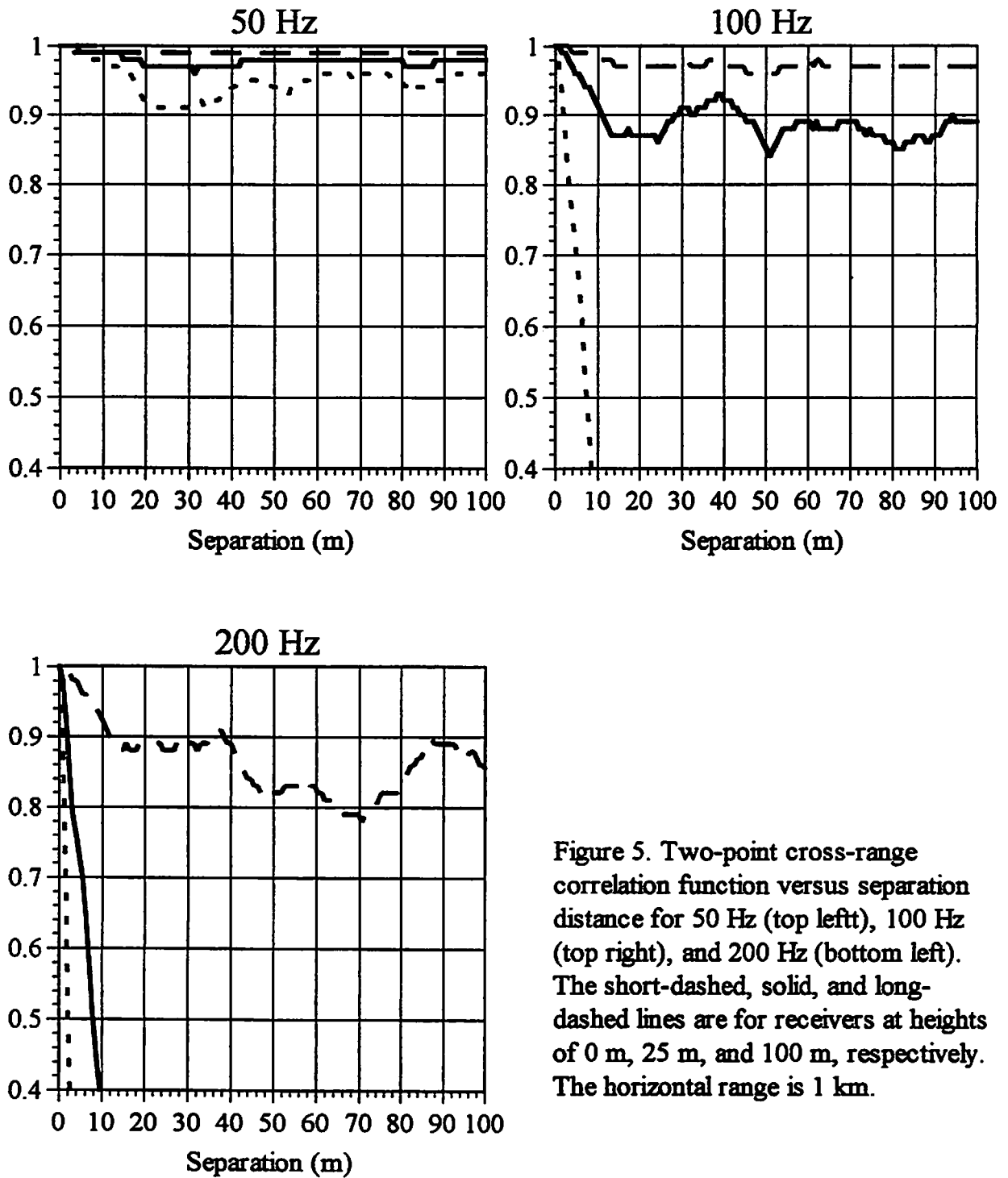


Figure 5. Two-point cross-range correlation function versus separation distance for 50 Hz (top left), 100 Hz (top right), and 200 Hz (bottom left). The short-dashed, solid, and long-dashed lines are for receivers at heights of 0 m, 25 m, and 100 m, respectively. The horizontal range is 1 km.

**A Large Vertical Step Parabolic Equation (LVS-PE)
for Long Range Propagation in the Atmosphere**

M. West and R A Sack

Department of Acoustics and Audio Engineering

University of Salford

Salford, M5 4WT, England

Tel: +44 (0)161 295 5490, Fax 5427

e-mail: m.west@acoustics.salford.ac.uk

1. Introduction

Examination of a typical full field prediction for a vertical atmospheric section often shows that most of the SPL variation occurs in the bottom 100 - 300m for a low frequency source. This variation in level is due to the complex interaction of the refracted field with the ground reflected field. Higher up in the atmosphere the variation in level is much smaller with height, z , and it would seem possible therefore to consider using large z intervals at these locations in a numerical solution scheme.

The use of a variable vertical mesh interval is not new. Gilbert¹ used a finite element formulation for the z dependent operator in his PE which allowed a variable vertical mesh. Close to the ground, where the field is most complicated and where the spatial scale of the pressure variation is very small, Gilbert used tiny intervals in z . He increased these intervals gradually with z , but only up to a maximum of $\frac{1}{3}$ rd of a wavelength, $\lambda/3$. This limit was set by the need to maintain an error free solution with no accumulated error at each range step.

A great deal of progress in using large *range*, x , steps has been made in the last few years. Most noteworthy is Gilbert and Di's GF-PE² and Sack and West's LP-PE³, both procedures allowing the use of massive x steps typically up to 100λ . In the GF-PE very accurate solutions are obtained at the selected coarse range steps by computing the z dependent Green's function. In the LP-PE the accuracy of the calculation at each range step is enhanced by using the LP expanded operator with its set of Padé terms. The LP-PE also makes use of a sub-range structure to ensure stability and minimise errors where the propagation is not mainly in the x direction.

The success of the above large range step models depended on the use of new formulations of the z dependent operator to give much more accurate solutions at each chosen range step. They both however implicitly assume that changes in the modulator, φ , solution over a coarse range step are small.

If we are to construct a coarse z step algorithm we must therefore find a means of improving numerical accuracy. In this paper novel procedures for doing this, based on addition of a new z dependent carrier function, Ψ_1 , are presented. The total potential is then

$$\Psi(x, z) = \Psi_0(x) \Psi_1(z) \varphi(x, z) \quad (1 - 1)$$

and we retain the original x dependent carrier, $\Psi_0(x) = e^{ik_x x}$.

In the first versions of the new LVS-PE we used a co-ordinate transformation which allowed the PE algorithm to operate with equal intervals in the transformed domain. This was thought to be necessary for formulation of a stable PE algorithm. By using improved discretisations of φ and its z derivatives however, we found that the co-ordinate transformation could be avoided.

2. Derivation of the Modulator Wave Equation (MWE) for a Potential Containing a Matched Vertical Wave Carrier (MVWC)

We substitute the potential in (1 - 1) into the two dimensional Helmholtz equation in the usual way⁴ and noting that Ψ_0 itself satisfies the Helmholtz equation we get the MWE

$$\frac{\partial^2 \varphi}{\partial x^2} + 2ik_0 \frac{\partial \varphi}{\partial x} + L\varphi = 0 \quad (2 - 1)$$

where L is the z dependent operator given by

$$L = \frac{\partial^2}{\partial z^2} + 2i \Phi_z(z) \frac{\partial}{\partial z} + \left(k^2 - k_0^2 - \Phi_z^2 + i\chi\Phi_{zz} \right) \quad (2 - 2)$$

and

$$\Phi_z = \frac{\partial \Psi_1}{\partial z} / i \Psi_1 ; \quad \Phi_z = \frac{\partial^2 \Psi_1}{\partial z^2} / i \Psi_1 \quad (2 - 3)$$

Our first choice of a MVWC was an exponential, $\Psi_1 = \exp(i k_1 z)$, so that $\Phi_2 = k_1$, $\chi = 0$ with k_1 selected to match the vertical wavenumber for a source at a "representative" location. In order to produce a soluble PE the coefficients of L must be constants.

3. Co-ordinate Transformations

Whatever transformation we choose, $(x, z) \rightarrow (\xi, \eta)$, we must ensure the resulting PE remains soluble. Here we only need to transform the z to η . For the PE to retain its original form the coefficients of L in the transformed MWE (see below) must still be constants.

3.1 Exponentially Increasing z Step

The transformation is chosen here to allow z steps which rapidly increase as we move upwards starting from very small steps close to the ground. The 2D co-ordinate transformation is

$$\xi = x; \quad \eta = \frac{1}{\varepsilon} \ln \left[\frac{z + z_0}{z_0} \right] \quad (3 - 1)$$

The z steps will increase exponentially with η , $\Delta z = z_0 e^{\varepsilon \eta} (e^{\Delta \eta} - 1)$.

The parameters ε and z_0 are set to give Δz values which start small near the ground and increase rapidly with height such that over each Δz interval the change in ϕ is always small even for the largest intervals (for example choose $\Delta \eta = 1$, $\varepsilon = 0.1$ and $z_0 = 0.01$ so that for $\eta = 1$, $\Delta z \approx 0.02\text{m}$ and for $\eta = 100$ $\Delta z \approx 380\text{m}$).

We can obtain all the derivatives of ϕ in x and z appearing in (2 - 1) and (2 - 2) now in terms respectively of derivatives in ξ and η :

$$\frac{\partial \phi}{\partial z} = \frac{1}{Z_1} \frac{\partial \phi}{\partial \eta} ; \quad \frac{\partial^2 \phi}{\partial z^2} = \frac{1}{Z_1^2} \frac{\partial^2 \phi}{\partial \eta^2} - \frac{Z_2}{Z_1^2} \frac{\partial \phi}{\partial \eta} \quad (3 - 2)$$

where here

$$Z_1 = \frac{dz}{d\eta} = \frac{1}{\varepsilon(z + z_0)} , \quad Z_2 = \frac{d^2z}{d\eta^2} = \varepsilon \quad (3 - 3)$$

This transformation turned out to be very unsatisfactory not allowing sufficient control over the Δz values - Δz had to be far too small close to the ground to set up a reasonable value higher up.

3.2 Arctan Function for Δz

We choose a z transformation here with a more gradual increase in Δz with η (and z)

$$\frac{\partial z}{\partial \eta} = V_m + V_b \tan^{-1} \left[\frac{\eta - \eta_T}{W} \right] \quad (3 - 4)$$

Taking $\Delta \eta = 1$, $\frac{\partial z}{\partial \eta} \approx \Delta z$.

The parameters V_m , V_b , η_T and W are set up from

- (1) η_{TOP} the largest η ; $\eta_T = \eta_{TOP}/2$
- (2) z_{TOP} the largest z ; $V_m = z_{TOP}/\eta_{TOP}$
- (3) Δz_0 the smallest Δz close to the ground
- (4) $\Delta z_{1/4}$ the Δz at $\eta = \eta_{TOP}/4$.

From items (3) and (4) we can obtain an equation in $q = \eta_T/2W$, $f(q) = 0$, whose root can be found using a Newton - Raphson procedure. This allows us to obtain W and from

item (3), V_b . Equations (3 - 2) are applicable in this case but here Z_1 is given in (3 - 4) and Z_2 is obtained by differentiation of (3 - 4) with respect to η .

This transformation was much easier to use than the exponential one and allowed a sensible variation of Δz .

4. Transformed Modulator Wave Equation

We replace the derivatives in (2 - 1), which can be expressed in terms of the transform variables ξ and η , using (3 - 2).

$$\frac{\partial^2 \varphi}{\partial \xi^2} + 2ik_0 \frac{\partial \varphi}{\partial \xi} + L\varphi = 0 \quad (4 - 1)$$

The operator L is now η dependent and can be written

$$L = \alpha(\eta) \frac{\partial^2}{\partial \eta^2} + \beta(\eta) \frac{\partial}{\partial \eta} + \gamma(\eta) \quad (4 - 2)$$

with

$$\alpha = \frac{1}{Z_1^2}; \quad \beta = \frac{2i\Phi_z}{Z_1} - \frac{Z_2}{Z_1^2}; \quad (4 - 3)$$

$$\gamma = k^2 - k_0^2 - \Phi_z^2 + i\chi\Phi_{zz}$$

We obtain the second order accurate wide angle PE from (4 - 1) using the procedure described in detail in references 5 and 6. We integrate over a range step $\xi = a$ to $\xi + \Delta\xi = b$ replacing $\partial\varphi/\partial\xi$ by $iL(\varphi)/2k_0$ which gives an equation containing a sum of three integrals

$$I_\alpha = \alpha \int_a^b \varphi^{(2)} d\xi; \quad I_\beta = \beta \int_a^b \varphi^{(1)} d\xi; \quad I_\gamma = \gamma \int_a^b \varphi d\xi \quad (4 - 4)$$

where

$$\varphi^{(n)} = \frac{\partial^n \varphi}{\partial \eta^n}$$

These integrals are evaluated as a linear combination of $\varphi^{(n)}$ at the ends of the interval. From references 5 and 6 we can show

$$\begin{aligned} I_\alpha &= \frac{\alpha \Delta \xi}{2} \{ \varphi^{(2)}(a) + \varphi^{(2)}(b) \} \\ I_\beta &= \frac{\beta \Delta \xi}{2} \{ \varphi^{(1)}(a) + \varphi^{(1)}(b) \} \\ I_\gamma &= \frac{\gamma \Delta \xi}{2} \{ \varphi(a) + \varphi(b) \} \end{aligned} \quad (4-5)$$

The vertical operator L can then be discretised in η in the usual way⁵ allowing the core PE matrix-vector equation to be written

$$L(b) \varphi(b) = L(a) \varphi(a) \quad (4-6)$$

where

$$L = u_\pm \left[\frac{\alpha}{\Delta \eta^2} \delta^2 + \frac{\beta}{\Delta \eta} \delta + \gamma \right] + 2ik_0 \quad (4-7)$$

and

$$u_\pm = \frac{i}{2k_0} \pm \frac{\Delta \xi}{2}, \quad + \text{for } b, - \text{for } a \quad (4-8)$$

$$\delta^2 = \varphi_{m+1} - 2\varphi_m + \varphi_{m-1}, \quad \delta = \varphi_{m+1} - \varphi_m \quad (4-9)$$

If $\alpha \rightarrow 1$, $\beta \rightarrow 0$ and $k_1 = 0$ (4-6) is a standard wide angle CN-PE with $\Delta \eta \rightarrow \Delta z$ and $\eta \rightarrow z$.

5. Ground Boundary Condition

At $z = 0$ we can apply the normal impedance condition

$$\left. \frac{\partial \Psi}{\partial z} \right|_{z=0} = ik_0 \beta_A \Psi \quad (5 - 1)$$

where β_A is the normal admittance of the ground. Replacing Ψ with (1 - 1) gives

$$\left. \frac{\partial \varphi}{\partial z} \right|_{z=0} = ik_0 \beta_A - i\Phi_z \quad (5 - 2)$$

when the vertical transformation is applied (5 - 2) becomes

$$\left. \frac{\partial \varphi}{\partial \eta} \right|_{\eta=0} = Z_1 (ik_0 \beta_A - i\Phi_z) \quad (5 - 3)$$

This has a similar form to the original flat ground boundary condition and is easily incorporated into the matrix vector equation (4 - 6) when discretised (see reference 7).

6. Upper Boundary Condition

In order to obtain approximate Sommerfeld radiation conditions we have shown (see ref. 7) that for the untransformed CN-PE, if the top of the computational mesh is located at $z = z_M$, then

$$\varphi_{M+1} = 2f\varphi_M - f^2\varphi_{M-1} \quad (6 - 1)$$

with

$$f = e^{ik\sin\theta \Delta z}$$

We can show similarly that when we have our z dependent function; Ψ_1 , present then (6 - 1) still applies but now

$$f = e^{i(k\sin\theta - \Phi_z)\Delta z} \quad (6 - 2)$$

The boundary condition in (6 - 1) refers only to the z dependence and maintains a Sommerfeld radiation condition at the upper boundary for the z dependent part of the solution. For still air conditions or when the sound speed gradients near the upper boundary are small this condition works well. Under more severe meteorological

conditions the above condition can give spurious upper boundary reflections. These tend to increase in magnitude with range. Since we are dealing with only a z dependence in the above equations the transformed version is obtained simply by replacing Δz by $\Delta \eta$.

7. Appraisal of the Prototype Algorithm

The program was run initially with no sound speed gradient and gave erroneous predictions within a few hundred metres at 50 Hz because of the large amount of upper boundary reflection. Once these errors had grown, the PE could not maintain sufficient stability to allow the range marching solution to proceed. The errors could only be minimised by increasing the number of vertical mesh points which removed the speed advantages of the LVS algorithm.

7.1 Subrange Configuration for Variable k_1

In the case where $\Psi_1 = \exp(i k_1 z)$ the choice of k_1 appears to be very important in terms of PE stability. We set k_1 to match the vertical component of the wavenumber $k_v(z_{\text{rep}})$ taken at a "representative" height, z_{rep} . This height can be estimated on the basis of the known still air solution. Ignoring ground reflection we guess a z_{rep} value, find the corresponding k_1 and E with the expression below. The required z_{rep} value is found by iterating until E is a minimum

$$E = \sum_m | e^{ik_1 z_m} - e^{ik_v(z_{\text{rep}}) z_m} |^2$$

The representative height, z_{rep} , decreases with range. We therefore used a set of subranges, typically 15, within each of which k_1 must be roughly constant. The subranges increase in width typically approximately logarithmically starting at 250m.

At the interface of two subrange zones we must carry out an interpolation on the last set of solutions in subzone N , $\varphi^{(N)}$, to generate the starting solutions in subzone $N + 1$, $\varphi^{(N+1)}$, to allow for the change in Ψ_1 from zone N to zone $N+1$

$$\varphi^{(N+1)}(\xi, \eta) = \frac{\Psi_1^{(N)}}{\Psi_1^{(N+1)}} \varphi^N(\xi, \eta) \quad (7 - 1)$$

The subrange configuration produced a considerable improvement in prediction accuracy for still air conditions. However when more realistic met profiles were used the erroneous results and instabilities in section 7 recurred.

8. A Matched Vertical Wave Function Based on Ray Paths

The weakness of the LVS algorithm lies in the poor match achieved between $\Psi_1 = \exp(i k_1 z)$ and the actual vertical field variation. If the large vertical steps are not to introduce errors which accumulate as the solution proceeds it is vital that Ψ_1 is sufficiently close to the actual vertical component of the field that the residual φ only changes very slowly with z . We introduce here a new matching function which is based on the phase change produced along a ray path between the source and the chosen point (x, z)

$$\Psi_1 = e^{i\Phi(x, z)} \quad (8 - 1)$$

The function must be exclusively z dependent if we are to produce a soluble PE form. We remove the x dependence by setting x at a representative value, \hat{x} . This type of function clearly demands a subrange configuration so that \hat{x} can be reset for each subrange (typically at the centre of the subrange). A ray may be traced from the source through to a point, P, (\hat{x}, z_m) using the well known ray tracing equations (see reference 8) provided we know its launch angle, θ , and the sound speed profile, $c(z)$. Φ is found by integrating along the ray path, ℓ

$$\Phi(\hat{x}, z_m) = \omega \int_{Origin}^P \frac{d\ell}{c(z)} \quad (8 - 2)$$

In the simple case of constant sound speed gradient the ray will be a circular arc, θ is known and the integral can be performed analytically. In the general case we will need to launch rays which arrive close to (\hat{x}, z_m) from which we can deduce $\Phi(\hat{x}, z_m)$ using

an interpolation method.

In our derivation of the MWE in equation (2 - 1) we were careful to use a general Ψ_1 so that all the equations in this paper will hold for either the exponential or ray based matching functions. For the ray based function we can see from (2 - 3) that we will need the first and second z derivatives of Ψ_1 . We note that now

$$\Phi_z = \frac{\partial \Phi}{\partial z} ; \quad \Phi_{zz} = \frac{\partial^2 \Phi}{\partial z^2} + i\Phi_z^2 \quad (8 - 3)$$

The argument Φ must be constant along any wavefront passing through (x, z) hence

$$\Phi_z = k(z) \sin \theta \quad (8 - 4)$$

where θ is the ray direction at (x, z) which is known.

8.1 Tests for Constant Sound Speed Gradient Case

The predictions for still air and small gradient values (less than 0.05) were excellent showing little upper boundary error. Predictions obtained with the new algorithm were compared with those from our standard CN-PE using the same boundary conditions. The new LVS algorithm did however generate a little more upper boundary error than the CN-PE. The overall speed increase was not as large as we had hoped because the minimum number of vertical points needed lay between $\frac{1}{3}$ and $\frac{1}{6}$ of the number required in the CN-PE. In an attempt to improve run times we introduced logarithmically increasing range, x , steps using the existing subrange configuration. This did give the required increase in speed but at the expense of solution accuracy where the x step size was large.

9. An Untransformed Version of the LVS-PE

The z transformation in section 3 could be dispensed with provided the discretisations used in the z dependent operator can be set up for the unequal z steps. The existing transformed version uses an η discretisation based on equal η steps. We use a parabolic

fit to give an improved z discretisation

$$\left. \begin{aligned} \frac{\partial \varphi}{\partial z} &= \hat{\alpha}_1 \varphi_{m-1} + \hat{\beta}_1 \varphi_m + \hat{\gamma}_1 \varphi_{m+1} \\ \frac{\partial^2 \varphi}{\partial z^2} &= \hat{\alpha}_2 \varphi_{m-1} + \hat{\beta}_2 \varphi_m + \hat{\gamma}_2 \varphi_{m+1} \end{aligned} \right\} \quad (9 - 1)$$

The coefficients can easily be obtained as linear functions of $d_1 = z_{m+1} - z_m$ and $d_2 = z_m - z_{m-1}$. In this case we must use the untransformed MWE in equation (2 - 2) to give our PE algorithm. In principle the derivation given in section 4 for the transformed case is applicable for the untransformed case with z now replacing η (and x replacing ξ). The only change required will be the discretisations for the first and second η derivatives of φ , δ and δ^2 , which are now z derivatives obtained from (9 - 1).

The untransformed LVS was tested as described above in section 8.1. There was a small improvement in numerical accuracy and speed compared with the transformed version. At 50 Hz for a 10 km range we have obtained a 5 times speed improvement over the equivalent CN-PE performance.

10. Concluding Remarks/Future Developments

The LVS concept has been shown to be viable. We expect to improve run times to around 10 - 50 times CN-PE values by improving the formulation of the upper boundary condition, which will cut down upper boundary reflection even when we have large Δz values near the top of the atmosphere.

The algorithm tested in sections 8 and 9 was limited to the constant sound speed gradient case. The algorithm for more general conditions is nearing completion and testing will commence soon.

The formulation of the LVS-PE presented here has been carefully structured to permit adaptation to the undulating terrain case. A new large step terrain algorithm is under development, the formulation and testing will be presented at a later date.

11. References

1. K E Gilbert and M J White. Application of the Parabolic Equation to Sound Propagation in a Refracting Atmosphere. *J. Acoust. Soc. Amer.* 85, 630-637, (1989).
2. K E Gilbert and X Di. A Fast Green's Function Method for One-Way Sound Propagation in the Atmosphere. *J. Acoust. Soc. Amer.* 94, 2343-2352, (1993).
3. R A Sack and M West. The Lagrange Padé Parabolic Equation (LP-PE) for the Prediction of Long Range Sound Propagation in the Atmosphere. *Applied Acoustics*, 49, 2, 105-125, 1996.
4. R A Sack and M West. Representation of Elliptic by Parabolic Partial Differential Equations with an Application to Axially Symmetric Sound Propagation. *Applied Acoustics*, 37, 141-149, (1992).
5. R A Sack and M West. A Parabolic Equation for Sound Propagation in Two Dimensions over Any Smooth Terrain Profile: The Generalised Terrain Parabolic Equation (GT-PE). *Applied Acoustics* 45, 113-129, (1995).
6. M West and R A Sack. A New Generalised Terrain Parabolic Equation (GT-PE). *Proceedings of the 6th International Symposium on Long Range Sound Propagation, Ottawa*, 385-393, (1994).
7. M. West and R A Sack Development of an Algorithm for Prediction of the Sound Field from a Spherical Acoustic Source Using the Parabolic Approximation. *Proceedings of the 5th International Symposium on Long Range Sound Propagation, Milton Keynes* 115-127, (1992).

8. F Walkden and M West. Prediction of Enhancement Factor for Small Explosive Sources in a Stratified Moving Atmosphere. J. Acoust. Soc. Amer 84(1), 321-326 (1988).

Acknowledgement

The authors wish to acknowledge the financial support for this work provided by the Telford Institute at the University of Salford.

A wide angle parabolic equation for sound waves in moving media

L. Dallois, Ph. Blanc-Benon, D. Juvé

Laboratoire de Mécanique des Fluides et d'Acoustique,

U.M.R. C.N.R.S. 5509, Ecole Centrale de Lyon,

B.P. 163, 69131 Ecully Cedex, France

V.E. Ostashev

Department of Physics,

New Mexico State University,

Las Cruces, Box 30001, NM 88003-8001, USA

Abstract

This paper studies the sound propagation in a moving atmosphere using the parabolic equation (PE) method. In the literature available PE models are usually based on a narrow angle approximation. Furthermore, the moving medium is replaced by a motionless one with the effective sound speed which is a sum of the sound speed and wind velocity component in the direction of sound propagation. Here, to describe more accurately the effects of the mean wind velocity and its fluctuations on sound propagation and scattering, a new wide-angle parabolic equation and its Padé (1,1) approximation are derived. Numerical predictions of sound pressure levels are presented in two situations; in the first one a mean wind profile is considered, and, in the second one a turbulent velocity field is superimposed on a mean sound speed profile. The influence of each terms occurring in the new PE model are discussed.

Introduction

Parabolic equations have been used widely to predict sound fields in inhomogeneous media with variations in the sound speed c , density ρ and fluid velocity \vec{v} . For numerical simulations of outdoor sound propagation, parabolic equations have been derived using the approximation of the effective sound speed. In this conventional approach the real moving atmosphere is replaced by a hypothetical motionless medium with the effective sound speed $c_{eff} = c + v_x$. Here v_x is the wind velocity component along the direction of propagation between source and receiver. When the source and receiver are close to the ground, the preferred direction of sound propagation is nearly horizontal, and standard

parabolic equations can be used to predict sound pressure levels. However, in many problems of atmospheric acoustics, refracted sound waves and those scattered by turbulence propagate in directions which may significantly differ from the horizontal axis. A great effort has been done to derive wide angle parabolic equations (see for example Lee et al. [1], Gilbert et al. [2], Chevret et al.[3]). However, the equations derived do not take into account accurately the effects of moving media. Using linearized equations of fluid-dynamics, Ostashev et al. [4] recently derived a new wide-angle parabolic equation in which the effects of the fluid motion are included correctly. Note that a similar approach has been used by Godin [5].

In this paper we calculate the sound field due to a source located in a moving medium above a rigid ground when both medium velocity and medium velocity gradients exist. In a first section we describe the derivation of new wide-angle parabolic equations and their Padé(1,1) approximations. The standard PE based on the approximation of the effective sound speed c_{eff} will also be reminded. In second section, we present 2D numerical simulations of propagation of sound waves in a stratified and turbulent moving atmosphere. Two geometries are considered : (1) sound propagation in the presence of a mean wind which is not necessarily colinear to the direction of propagation, and (2) sound scattering into a shadow zone due to the random fluctuations of the wind velocity vector. Furthermore, the predicted sound pressure levels based on the new wide-angle PE and the standard PE are compared, and the influence of each terms in new PE are discussed. And in conclusion we summarize the results obtained.

1 New wide angle parabolic equations

1.1 Starting equations

To derive a wide-angle parabolic equation for sound propagation in a moving medium, the following heuristic equation based on the approximation of the effective sound speed has often been used in the past:

$$\left[\Delta + k^2(1 + \epsilon_{eff}) \right] P(\mathbf{r}) = 0. \quad (1)$$

where $P(\mathbf{r})$ is the sound pressure field, Δ is the Laplacian operator, ω is the angular frequency of the sound field, $k = \omega/c_0$ is the wave number, $\epsilon_{eff} = (c_0/c_{eff})^2 - 1$, and c_0 is the mean value of the sound speed. (Hereinafter, the subscript 0 denotes a mean value of a variable). The Cartesian coordinates are denoted by $(x, y, z) = (x_1, x_2, x_3)$ where $x = x_1$ is the direction of propagation and $z = x_3$ is the vertical axis. It should be noted that the heuristic Eq.(1) may lead to significant phase and amplitude errors when the direction of sound propagation differs from the horizontal axis, or when there are regular and random inhomogeneities in c , ρ and \mathbf{v} (see [4] for a detailed analysis).

An exact equation for sound propagation in a homogeneous medium with a uniform wind velocity is given by [6]:

$$\left(\frac{\partial}{\partial t} + \mathbf{v} \cdot \nabla \right)^2 P(\mathbf{r}, t) = c^2 \Delta P(\mathbf{r}, t) \quad (2)$$

To evaluate the sound pressure field $P(\mathbf{r}, t)$ in an inhomogeneous medium, equation (2) is still a reasonable approximation if the characteristic scale of wind velocity variations, L , is large in comparison with the acoustic wavelength, λ . In this high-frequency approximation, the operator $(\mathbf{v} \cdot \nabla)^2$ can be represented as:

$$(\mathbf{v} \cdot \nabla)^2 = v_i \frac{\partial}{\partial x_i} \left(v_j \frac{\partial}{\partial x_j} \right) = v_i v_j \frac{\partial^2}{\partial x_i \partial x_j} + \mathcal{O}\left(\frac{\lambda}{L}\right)$$

Then, for a monochromatic sound field, Eq.(2) becomes:

$$\left[\Delta + k^2(1 + \epsilon) + 2ik \sqrt{1 + \epsilon} \frac{v_i}{c} \frac{\partial}{\partial x_i} - \frac{v_i v_j}{c^2} \frac{\partial^2}{\partial x_i \partial x_j} \right] P(\mathbf{r}) = 0 \quad (3)$$

By comparison with the Helmholtz equation (1), terms of second order in the Mach number $M = v/c$ are incorporated in equation (3), so better sound level amplitude predictions are expected especially in the case of strong wind velocity.

In inhomogeneous moving media, where both velocity and velocity gradients exist, the sound pressure field is solution of the following equation ([6],[7]):

$$\left[\underbrace{\Delta + k^2(1 + \epsilon)}_{(1)} - \underbrace{\left(\nabla \ln \frac{\rho}{\rho_0} \right) \cdot \nabla}_{(2)} + \underbrace{\frac{2ik}{c_0} \mathbf{v} \cdot \nabla}_{(3)} - \underbrace{\frac{2i}{\omega} \frac{\partial v_i}{\partial x_j} \frac{\partial^2}{\partial x_i \partial x_j}}_{(4)} \right] P(\mathbf{r}) = 0. \quad (4)$$

When comparing with the Helmholtz equation (1), the new terms represent the wave scattering by dipoles through the wind terms (3) and by quadrupoles through the gradient terms (4). Therefore, for sound propagation through turbulence, this equation will describe more accurately scattering effects. The relative magnitude order of gradient terms (4) in equation (4) with respect to the wind term (3) is λ/L . In the following part of the paper we assume that the density ρ is uniform, so the term (2) disappears in equation (4). Note that equation (3) does not contain terms of the order $M \lambda/L$.

1.2 Derivation of wide angle parabolic equations

Parabolic equations derived from equations (1) and (4) have already been presented in [3] and [4], respectively. Here, a wide-angle parabolic equation will be derived starting from (3). On a first step, equation (3) is rewritten as :

$$\left\{ \frac{\partial^2}{\partial x^2} + k^2 Q_1^2 \right\} P(\mathbf{r}) = 0, \quad (5)$$

where :

$$Q_1^2 = 1 + \mathcal{F}_1 + \mathcal{M}_1 \frac{\partial}{\partial x}, \quad (6)$$

with :

$$\mathcal{F}_1 = \frac{1}{c^2 - v_x^2} \left[c_0^2 + 2i c_0 \frac{\mathbf{v}_\perp \cdot \nabla_\perp}{k} + \sum_{i,j=2}^3 \frac{c^2 \delta_{i,j} - v_i v_j}{k^2} \frac{\partial^2}{\partial x_i \partial x_j} \right] - 1, \quad (7)$$

$$\mathcal{M}_1 = \frac{2v_x}{k(c^2 - v_x^2)} \left(i c_0 - \frac{v_\perp \cdot \nabla_\perp}{k} \right). \quad (8)$$

If the medium is slowly varying with the distance of propagation x , the commutator $\left\{ \frac{\partial}{\partial x}, \mathcal{Q}_1 \right\}$ can be neglected and the operator $\left\{ \frac{\partial^2}{\partial x^2} + k^2 \mathcal{Q}_1^2 \right\}$ can be split into two independent operators. Then for forward propagating waves, the equation to solve is :

$$\left(\frac{\partial}{\partial x} - ik \mathcal{Q}_1 \right) P(\mathbf{r}) = 0.$$

To approximate the square root of the operator \mathcal{Q}_1^2 , we use a Padé (1,1) approximation. After simple algebra we get the following equation :

$$\left[1 + q \mathcal{F}_1 \right] \frac{\partial}{\partial x} P(\mathbf{r}) + q \mathcal{M}_1 \frac{\partial^2}{\partial x^2} P(\mathbf{r}) = ik \left[1 + p \mathcal{F}_1 \right] P(\mathbf{r}) + ikp \mathcal{M}_1 \frac{\partial}{\partial x} P(\mathbf{r}) \quad (9)$$

where $p = \frac{3}{4}$ and $q = \frac{1}{4}$. Now according to equation (5), the operator $q \mathcal{M}_1 \frac{\partial^2}{\partial x^2}$ on the left-hand side of Eq.(9) is replaced by $-qk^2 \mathcal{M}_1 \mathcal{Q}_1$. Finally we introduce the complex amplitude of the sound field $\psi(\mathbf{r})$, so that $P(\mathbf{r}) = e^{ikx} \psi(\mathbf{r})$, and obtain a wide-angle parabolic equation:

$$\begin{aligned} & \left[1 + q \mathcal{F}_1 - ipk \mathcal{M}_1 - qk^2 \mathcal{M}_1^2 \right] \frac{\partial \psi}{\partial x}(\mathbf{r}) \\ & = ik \left[(p - q) \mathcal{F}_1 + ik(p - q) \mathcal{M}_1 - iqk \mathcal{M}_1 \mathcal{F}_1 + qk^2 \mathcal{M}_1^2 \right] \psi(\mathbf{r}). \end{aligned} \quad (10)$$

1.3 2D wide-angle parabolic equations

The numerical simulations presented in this paper deal with two dimensional (2D) geometries. Here we summarize 2D wide-angle parabolic derived from equations (1), (3) and (4):

- starting from equation (1) (see [4])

$$\left[1 + q \mathcal{L}_c \right] \frac{\partial \psi}{\partial x}(\mathbf{r}) = ik \left[(p - q) \mathcal{L}_c \right] \psi(\mathbf{r}), \quad (11)$$

where:

$$\mathcal{L}_c = \epsilon_{eff} + \frac{1}{k^2} \frac{\partial^2}{\partial z^2}.$$

- starting from equation (3) (see Eqs.(7), (8) and (10))

$$\begin{aligned} & \left[1 + q \mathcal{F}_1 - ipk \mathcal{M}_1 - qk^2 \mathcal{M}_1^2 \right] \frac{\partial \psi}{\partial x}(\mathbf{r}) \\ & = ik \left[(p - q) \mathcal{F}_1 + ik(p - q) \mathcal{M}_1 - iqk \mathcal{M}_1 \mathcal{F}_1 + qk^2 \mathcal{M}_1^2 \right] \psi(\mathbf{r}), \end{aligned} \quad (12)$$

where:

$$\mathcal{F}_1 = \frac{1}{c^2 - v_x^2} \left[c_0^2 + 2i c_0 \frac{v_x}{k} \frac{\partial}{\partial z} + \frac{c^2 - v_x^2}{k^2} \frac{\partial^2}{\partial z^2} \right] - 1,$$

$$\mathcal{M}_1 = \frac{2v_x}{k(c^2 - v_x^2)} \left(i c_0 - \frac{v_x}{k} \frac{\partial}{\partial z} \right).$$

- starting from equation (4) (see [4])

$$\left[1 + q\mathcal{F}_2 - ipk\mathcal{M}_2 \right] \frac{\partial \psi}{\partial x}(\mathbf{r}) = ik \left[(p - q)\mathcal{F}_2 + ik(p - q)\mathcal{M}_2 - \frac{iq}{k}\mathcal{M}_2 \frac{\partial^2}{\partial z^2} \right] \psi(\mathbf{r}), \quad (13)$$

where:

$$\mathcal{F}_2 = \epsilon + \frac{2i}{k} \frac{1}{c} \left(\frac{\partial v_x}{\partial x} + v_x \frac{\partial}{\partial z} \right) + \frac{1}{k^2} \left[1 + \frac{2i}{k} \frac{1}{c} \left(\frac{\partial v_x}{\partial x} - \frac{\partial v_z}{\partial z} \right) \right] \frac{\partial^2}{\partial z^2},$$

$$\mathcal{M}_2 = \frac{2i}{k} \frac{v_x}{c} - \frac{2i}{k^3} \frac{1}{c} \left(\frac{\partial v_x}{\partial z} + \frac{\partial v_z}{\partial x} \right) \frac{\partial}{\partial z}.$$

Note that these three parabolic equations (11), (12) and (13) are reduced to the same equation if $v = 0$. In the presence of a uniform wind velocity the differences between equation (12) and equation (13) are due to second order terms in Mach number M .

2 Two-dimensional numerical simulations

In this section we present numerical simulations that validate the numerical schemes of solving new parabolic equations (Eq.(12) and Eq.(13)) We also compare differences in predictions of sound transmission losses derived from the use of Eq.(11) based on the approximation of the effective sound speed c_{eff} and correct wide-angle parabolic equations (12) and (13). We consider the two-dimensional propagation of sound from a point source located at $x = 0$ and $z = h_s$ (see figure 1). Numerically, each of previous parabolic equations (Eqs.(11), (12) and (13)) is discretized on a uniform mesh ($i \Delta x, j \Delta z$) using a standard finite difference method. z -derivatives are evaluated with centered difference approximations, and Crank-Nicholson scheme is implemented as a marching algorithm. The horizontal step Δx and the vertical step Δz are equal to the smallest characteristic scale of the problem divided by factor 5 and 10, respectively. The ground is modelled as a perfectly reflecting plane by introducing a source at $z = h_s$ and its image at $z = -h_s$. The source is initialized by a Gaussian starter ([8]). A non reflecting boundary condition is imposed at the top of the computational domain by adding an absorbing layer of several wavelength thickness. In addition, to reduce the vertical size of the computational domain, we choose to vary the altitude of the receiver and to keep the source close to the ground. Note that the transmission loss TL is defined below as $20 \log(P/P_0)$ where P_0 is the sound pressure level in free space at a distance of 1 m from the source.

2.1 Validation and comparison with an analytical solution

In order to validate the sound pressure levels predicted by the use of new PEs (Eqs.(12) and (13)), we consider a simple model of a moving atmosphere in which the wind velocity

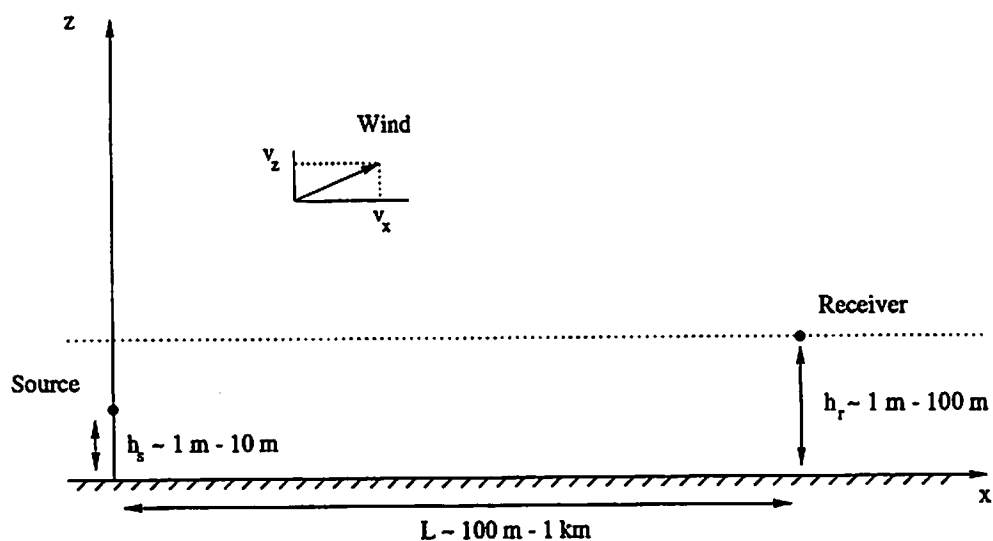


Figure 1: Geometry of the problem, which is numerically solved by using three PE.

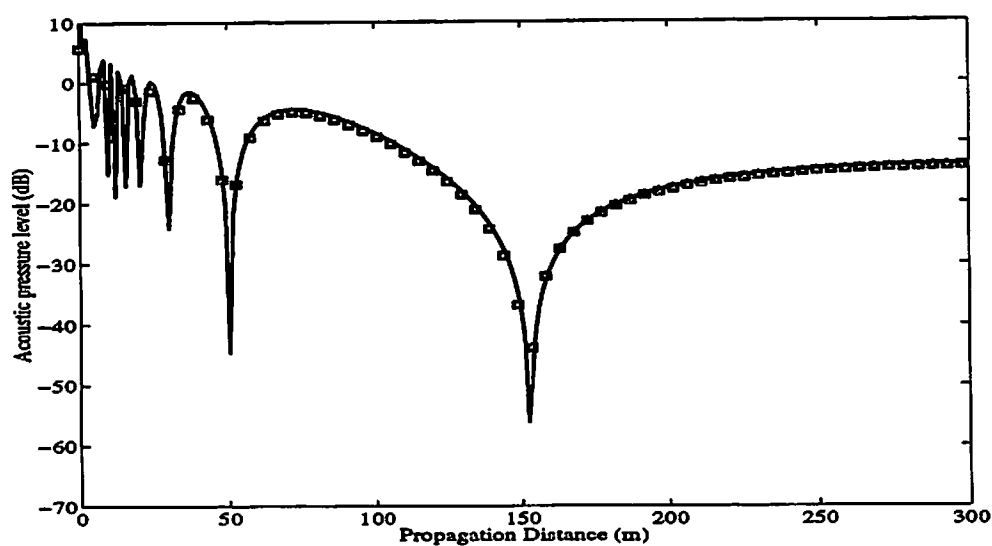


Figure 2: Comparison between analytical solution [—] and the results obtained with new parabolic equations : $[\Delta]$ Eq. (12), $[\square]$ Eq. (13). The horizontal velocity is constant and equal to 5 m s^{-1} . $\nu = 400 \text{ Hz}$, $h_s = 5 \text{ m}$ and $h_r = 5 \text{ m}$.

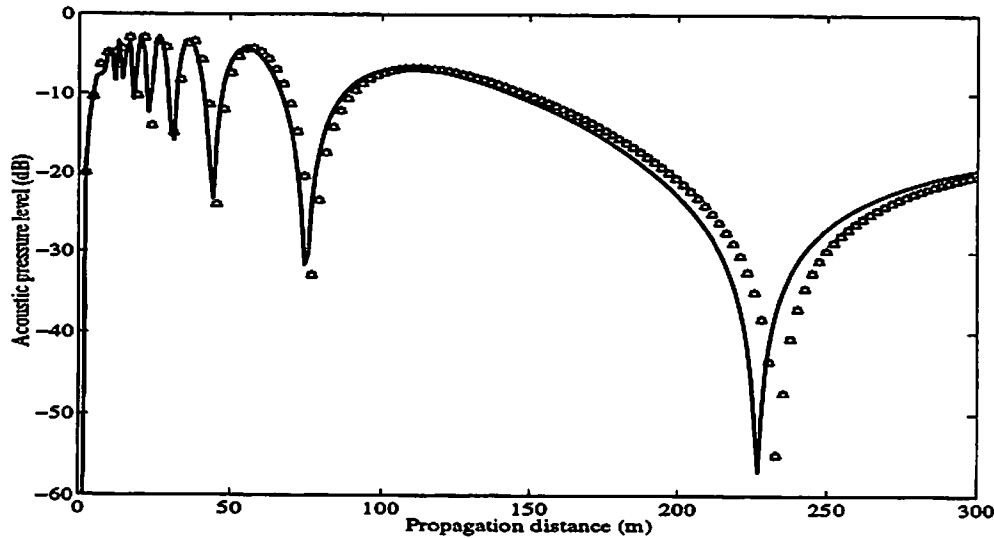


Figure 3: Comparison between the three PE : [—] the standard PE (11), [Δ] the PE (13) and [\square] the convective PE (12). The horizontal velocity is constant and equal to $v_x = 10 \text{ ms}^{-1}$. $\nu = 400 \text{ Hz}$, $h_s = 5 \text{ m}$ and $h_r = 10 \text{ m}$.

vector is constant and parallel to the horizontal axis (i.e. $v_x = v$, $v_z = 0$). In the presence of a perfectly reflecting plane boundary, it is possible to evaluate the sound pressure field using the method of image source. Using the analytical solution of Ostashev ([6]), we obtained:

$$P(r) = \sum_{j=1}^2 \frac{1}{\sqrt{r_j}} \exp \left[ik_0 r_j \frac{M \cos \alpha_j - \sqrt{1 - M^2 \sin^2 \alpha_j}}{M^2 - 1} \right] \quad (14)$$

where $j = 1$ and $j = 2$ correspond to the source and its image, respectively, α is the angle between the horizontal axis and the line-segment connecting source and receiver, and r_j is the distance between the receiver and the source or its image. Note that in this solution, the phase is calculated to any order of the Mach number M to preserve possible changes in the interference pattern due to the effects of the wind velocity. On Figure 2 we compare the transmission loss evaluated with the PEs (12) and (13) to the transmission loss given by the analytical solution (14). The horizontal velocity is constant and equal to 5 ms^{-1} . $\nu = 400 \text{ Hz}$, $h_s = 5 \text{ m}$ and $h_r = 5 \text{ m}$. The agreement between the analytical and new parabolic solutions is excellent.

2.2 Effects of a mean wind velocity

Figure 3 presents the results obtained with the new PE's (12) and (13) and the standard PE (11). The sound frequency ν is still 400 Hz , the wind velocity vector is parallel to the x axis, $v_x = 10 \text{ ms}^{-1}$ and $v_z = 0 \text{ ms}^{-1}$. The height of the source is 5 m and the receiver is located at 10 m from the ground. As expected, the prediction obtained with the standard parabolic equation (11) is different from two other predictions based on new parabolic equations. This difference increases with the distance of propagation. In terms

of geometric acoustics, the receiver is reached by two different paths: a direct ray and a reflected ray. The sound speed, $c + v \cos \theta$, varies on each ray with θ and the use of the effective sound speed, $c + v_x$, introduces a cumulative phase error in standard parabolic equation. This error increases with the receiver height, the distance of propagation and the wind velocity.

Now we consider the sound propagation in an inhomogeneous medium with a constant vertical wind gradient dv_x/dz . The wind profile is the linear wind profile used in [9]: $v_x = 0.1 \cdot z$ for $z < 200$ m, $v_x = 20 \text{ m}\cdot\text{s}^{-1}$ for $z > 200$ m, and $v_z = 0$. This downward propagation geometry is very sensitive to the wind velocity. First, for long distances, because of the occurrence of caustics, more than two rays reach the receiver. Secondly, the paths are curved downward so directions of sound propagation differ from the horizontal axis. On Figure 4 we compare the transmission losses obtained with standard PE (Eq.(11)) and new wide-angle PE (Eq.(13)) for three different heights of the receiver ($h_r = 1$ m, 10 m, 50 m). We notice significant differences between two predictions. Again, as expected the difference depends on the receiver height and the distance of propagation. For example with a receiver located at the altitude of 50 m when the distance of propagation is greater than 1000 m, the positions of interference maxima and minima are totally shifted and the difference in the transmission loss level is of the order of 5 dB.

For the next geometry, the direction of wind velocity is perpendicular to the direction of sound propagation from source to receiver. In a 2D medium we will have: $v_x = 0$ and $v_z = v$. On Figure 5 we compare predictions of the transmission losses using three PEs. The frequency of the source is $\nu = 400$ Hz. The heights of the source and receiver are $h_s = 5$ m and $h_r = 10$ m, respectively. As expected, standard PE (Eq.(11)) does not take into account the vertical wind velocity and the phase errors in the sound field dramatically increase with range. For example at a distance of 240 m the use of standard PE (11) results in destructive interference while new PEs (12) and (13) do not reveal it. We also plotted on Figure 5 the transmission losses calculated using a ray tracing algorithm. There is a concern whether the geometric acoustics method is able to include the velocity vector in exact way ([10]). One of the difficulties of this method is related to the finding out of all eigenrays, which are necessary for computation of the transmission losses. Of course, this approach will fail in a shadow zone. Nevertheless up to a distance of propagation of 200 m, the comparison is in favor of new PEs which incorporate rigorously the wind velocity.

Finally, for all geometries considered so far in this section, two new PEs (Eq.(12) and Eq.(13)) give the same numerical predictions.

2.3 Sound scattering into a shadow zone

We now consider sound scattering into a shadow zone due to random fluctuations of the wind velocity vector. The vertical profile of the sound speed is given by:

$$c(z) = c_0 + A \log \left(\frac{z+d}{d} \right) \quad (15)$$

where $A = 2 \text{ m}\cdot\text{s}^{-1}$ and $d = 6.10^{-3} \text{ m}$ as in [11]. Then, a homogeneous and isotropic turbulent wind velocity is superimposed on the mean sound profile. This random vectorial

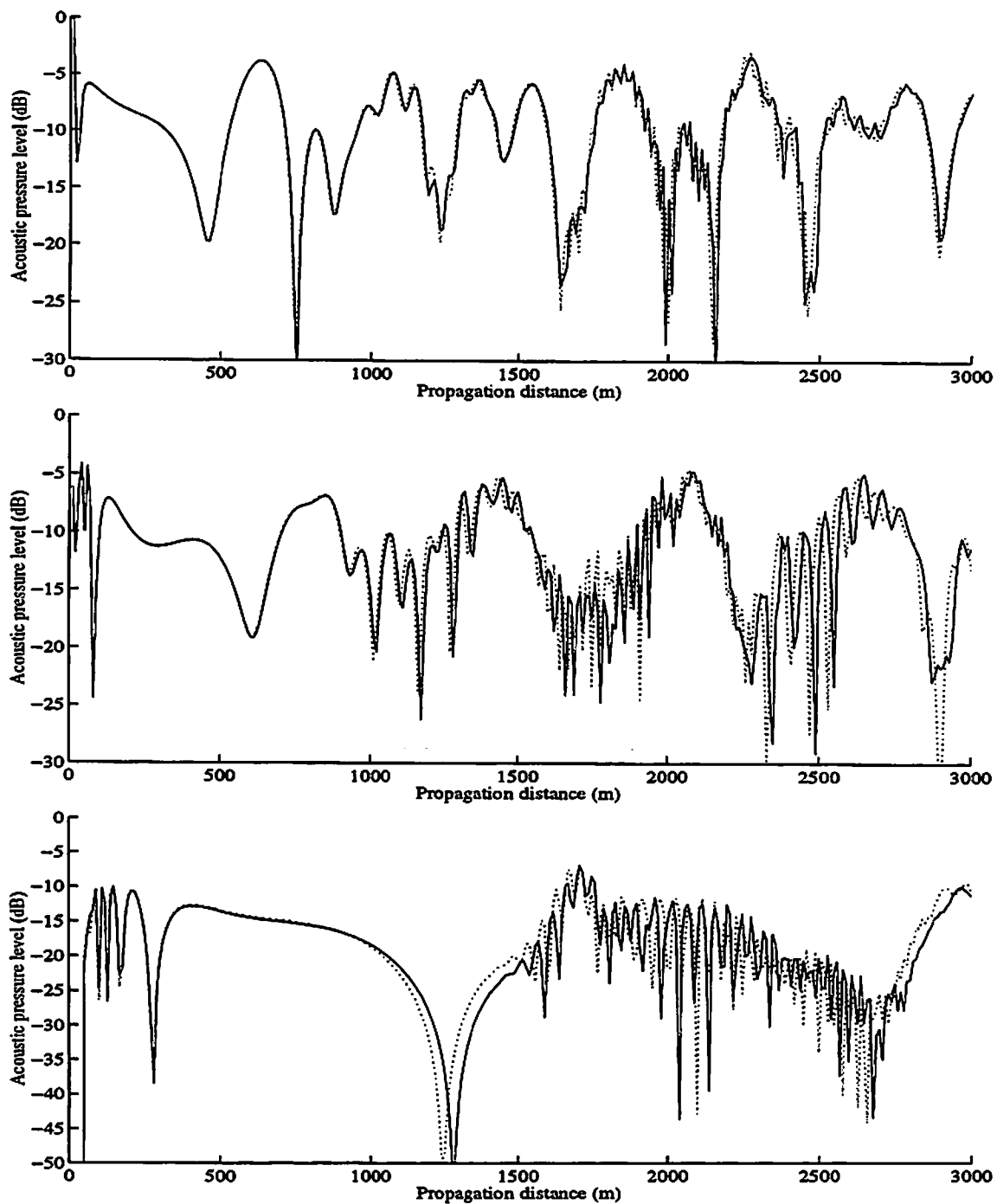


Figure 4: Comparison between two PE : [· · · · ·] standard PE (11) and [—] new PE (13). dv_x/dz is constant and equal to 0.1 s^{-1} . $\nu = 400 \text{ Hz}$ and $h_s = 5 \text{ m}$. From the top to the bottom h_r is equal to 1 m , to 10 m and to 50 m , respectively.

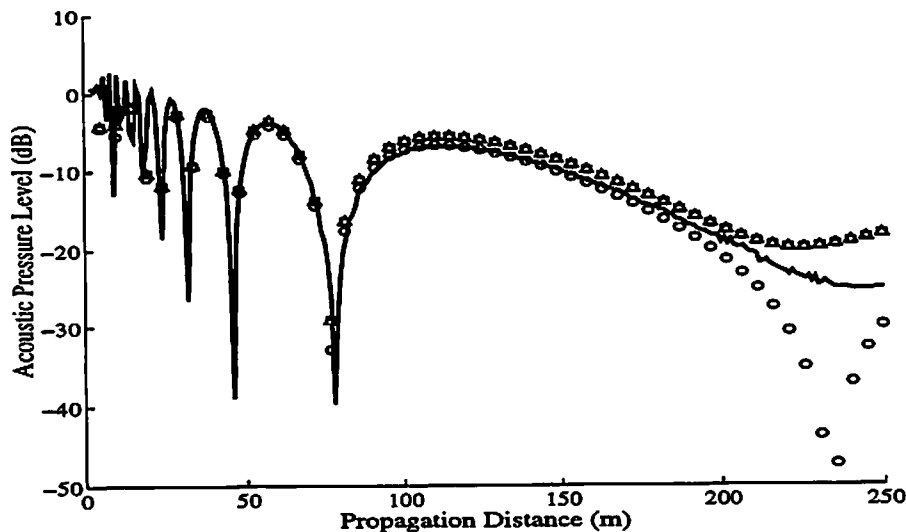


Figure 5: Comparison between results obtained by the ray tracing program [—], the PE (13) [Δ] and PE (12) [\square]. Standard PE (11) solution is plotted with [\circ]. The vertical velocity is constant and equal to $v_z = 5 \text{ m s}^{-1}$. $\nu = 400 \text{ Hz}$, $h_s = 5 \text{ m}$ and $h_r = 10 \text{ m}$.

field is generated using a Random Fourier Modes (R.F.M.) method with a von Karman spectrum model for the turbulent kinetic energy repartition [10] and [12]:

$$E(k) = \frac{8 \sigma_u^2}{9 k_e} \frac{(k/k_e)^3}{[1 + (k/k_e)^2]^{14/6}} \exp \left[-2 \left(\frac{k}{k_\eta} \right)^2 \right] \quad (16)$$

Here $k_e = 0.586/L$, k_η is the Kolmogorov wavenumber, σ_u^2 is the velocity variance and L is the outer scale of turbulence. In our numerical simulations, $L = 2 \text{ m}$ and $\sigma_u = 1 \text{ m.s}^{-1}$.

On two Figures 6 and 7 we compare the results obtained with standard PE (11) and new PE (13) which includes velocity and its gradient. Each curve corresponds to a single realization, and the same realization of the turbulent medium is used for both PEs. Figure 6, corresponding to the sound frequency 400 Hz , shows some important differences between two PE. At large distances of propagation this difference increases up to 10 dB . However, for a higher frequency of the source, 1000 Hz (see Fig.7), the difference is less. In fact, the order of magnitude of the additional gradient terms in equation (13) is $M\lambda/L$ ($1/\lambda^2$ is taken as reference value). Therefore, for heigher frequencies, a contribution from these terms is smaller. Nevertheless, after averaging over 30 realizations a difference between two numerical predictions is less than 3 dB (see Figures 8 and 9). On Figure 10 we detail the difference between these two solutions for each frequency of the source $\nu = 400 \text{ Hz}$ (top graph) and $\nu = 1000 \text{ Hz}$ (bottom graph). We notice that the variation in the mean sound level is greater for smaller acoustic frequencies. Thus, we can assume that the effects of large structures of the turbulence are well describe with the use of standard parabolic equation. Note that the use of a PE with accurate description of the wind velocity does not influence the average sound scattered level even if the instantaneous behaviour of the sound propagation is strongly affected.

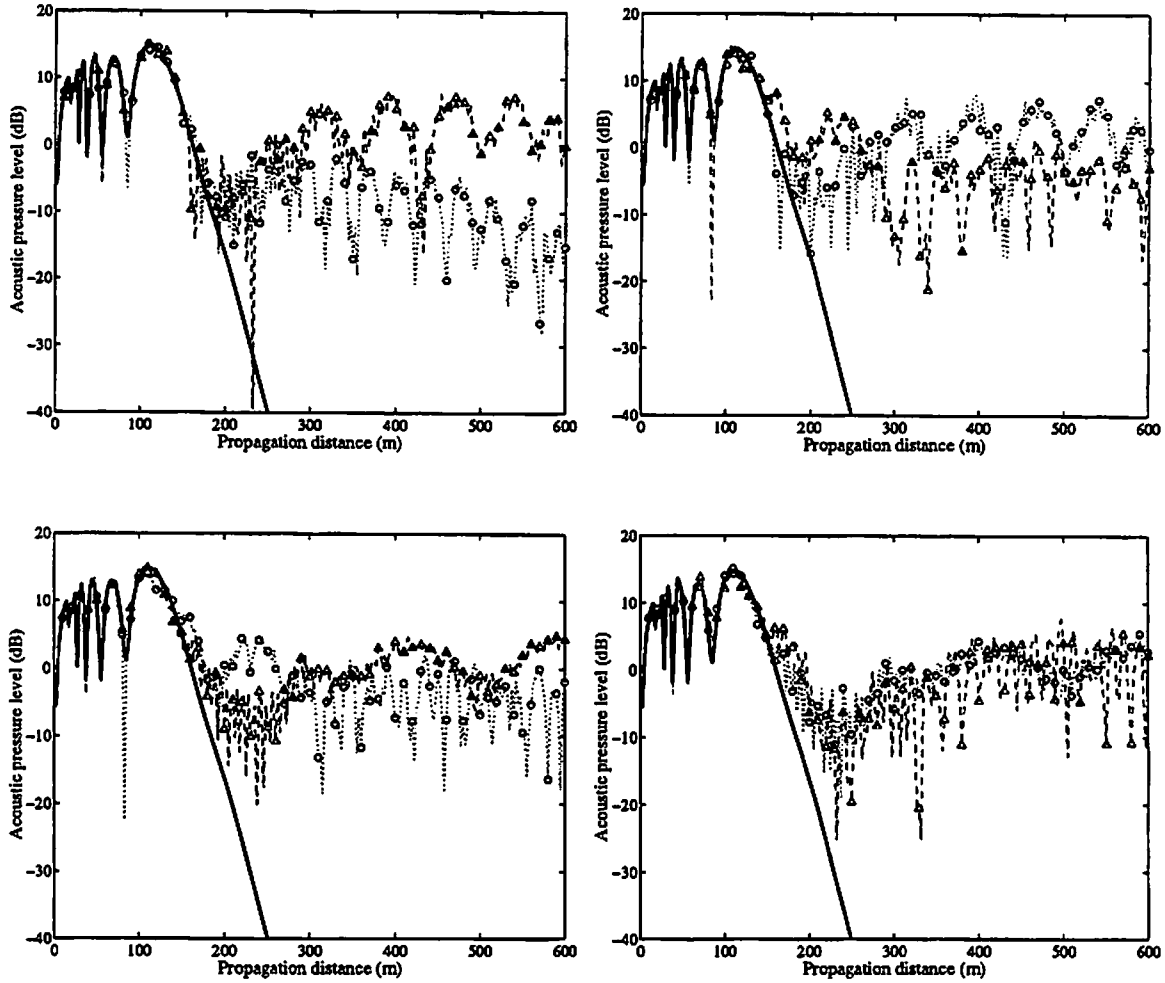


Figure 6: Comparison between standard and new PE for four single realisations. [—] without turbulence, [$\cdot \cdot \cdot$] standard PE (11) and [$-\Delta-$] new PE (13). The wind turbulence is generated by a RFM method using a von Karman spectrum with $\sigma_u = 1 \text{ m s}^{-1}$ and $L = 2 \text{ m}$, $\nu = 400 \text{ Hz}$, $h_s = 5 \text{ m}$ and $h_r = 10 \text{ m}$.

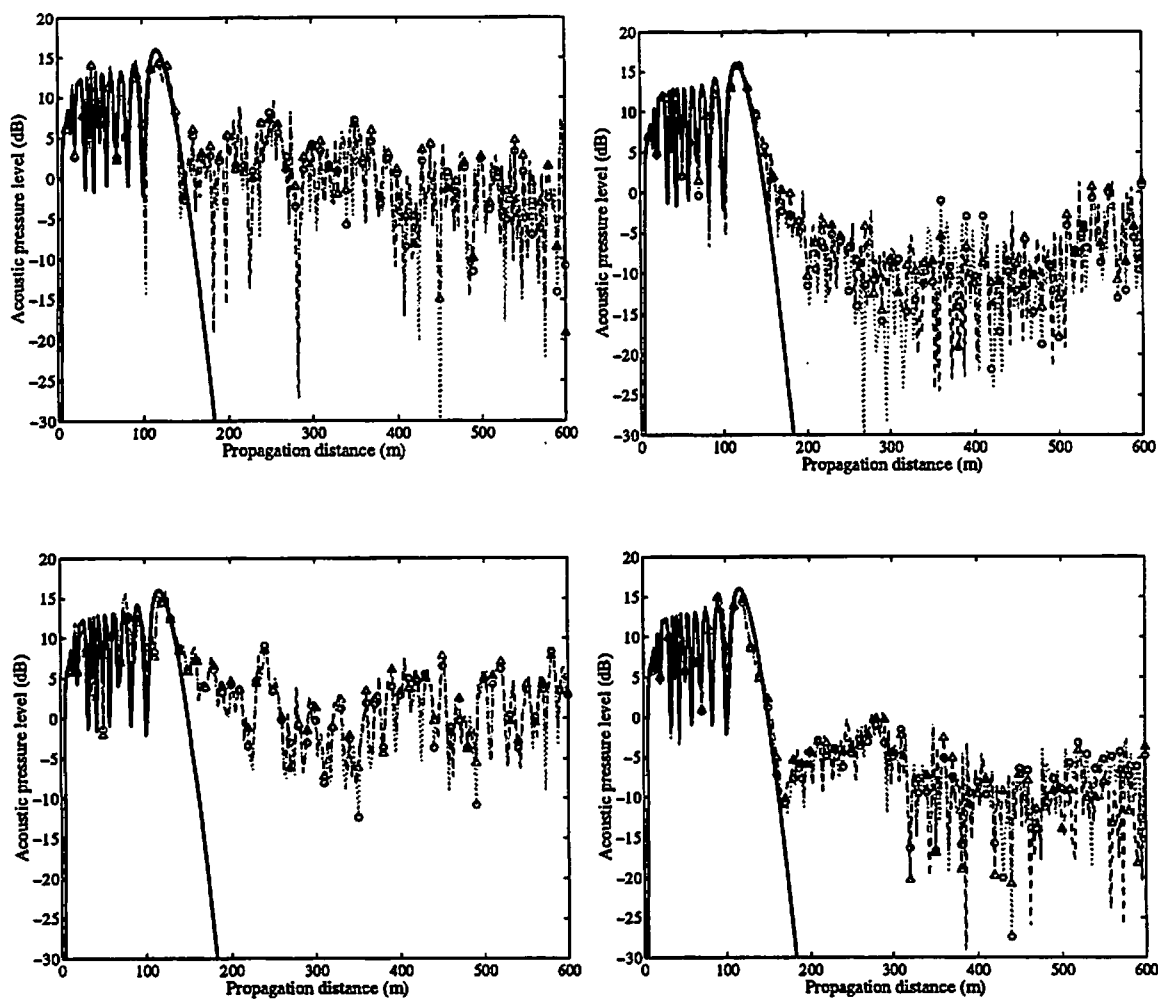


Figure 7: Comparison between standard and new PE for four single realisations. [—] without turbulence, [$\cdot \cdot \circ \cdot \cdot$] standard PE (11) and [$-\Delta-$] new PE (13). The wind turbulence is generated by a RFM method using a von Karman spectrum with $\sigma_u = 1 \text{ m s}^{-1}$ and $L = 2 \text{ m}$. $\nu = 1000 \text{ Hz}$, $h_s = 5 \text{ m}$ and $h_r = 10 \text{ m}$.

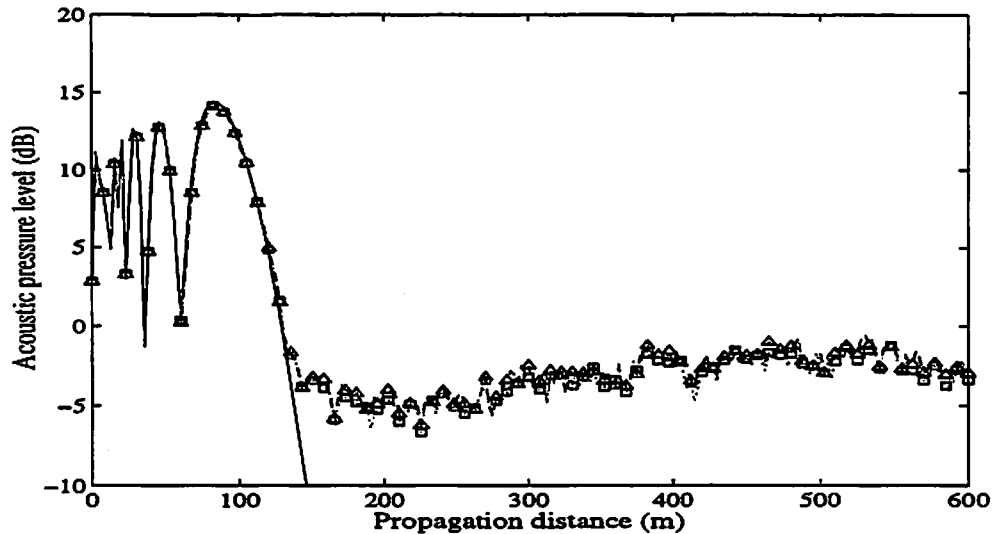


Figure 8: Comparison between the results of standard PE (11) [Δ] and new PE (13) [\square]. The plain curve [—] is the solution without turbulent wind field. The wind turbulence is generated by a RFM method using a von Karman spectrum with $\sigma_u = 1 \text{ ms}^{-1}$ and $L = 2 \text{ m}$. $\nu = 400 \text{ Hz}$, $h_s = 5 \text{ m}$ and $h_r = 10 \text{ m}$.

However at this point it is important to note that a real turbulent atmosphere is not isotropic and homogeneous and the recent work of Wert et al. ([12]) demonstrate the importance of the variation of the outer scale of turbulence with altitude. Another important parameter is the time evolution of the turbulent atmospheric boundary layer and the effect of intermittency of the ABL on the scattered sound ([13],[14],[15]). In this case, the use of accurate PEs which incorporate the wind and gradient terms are of great interest for a rigorous modelisation of sound propagation (as an example note on FIG. 6 and FIG. 7 the transmission loss variations from one realization to another).

The results obtained here are in a qualitative agreement with the ratio $\sigma(\theta)/\sigma_{\text{eff}}(\theta) = \cos^2 \theta$, obtained in Reference [4]. Here, θ is the scattering angle, and σ and σ_{eff} are the sound scattering cross-sections derived from Eqs.(4) and (1), respectively. The sound pressure in a shadow zone is believed to be depended on σ . For small θ , which are probably delt with in sound scattering into a refractive shadow zone, the difference between σ and σ_{eff} is small. For large θ , which might be a case of sound scattering into a shadow zone in a presence of a barrier, the difference between σ and σ_{eff} is large.

Conclusions

In this paper we have presented 2D numerical simulations of sound propagation and scattering in random moving media. We derived a new wide-angle parabolic equation and its Padé(1,1) approximation. We have shown that the use of the effective sound speed assumption is not sufficient to describe accurately the effects of mean and random wind velocity on sound propagation through moving media. In particular our numerical simulations reveal that all the components of the wind velocity vector and the associated gradient terms have to be considered in order to obtain an accurate modeling of sound

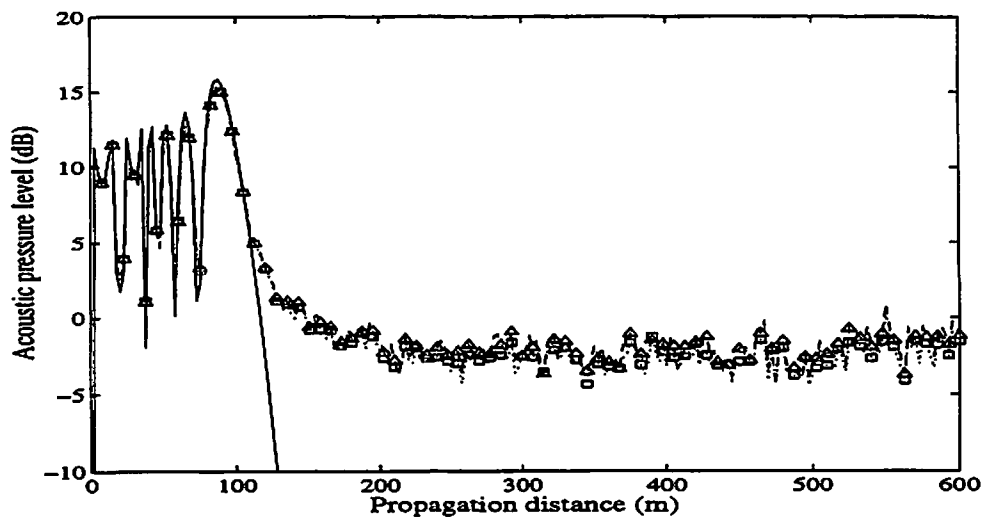


Figure 9: Comparison between the results of the standard PE (11) [Δ] and new PE (13) [\square]. The plain curve [—] is the solution without turbulent wind field. The wind turbulence is generated by a RFM method using a von Karman spectrum with $\sigma_u = 1 \text{ m s}^{-1}$ and $L = 2 \text{ m}$. $\nu = 1000 \text{ Hz}$, $h_s = 5 \text{ m}$ and $h_r = 10 \text{ m}$.

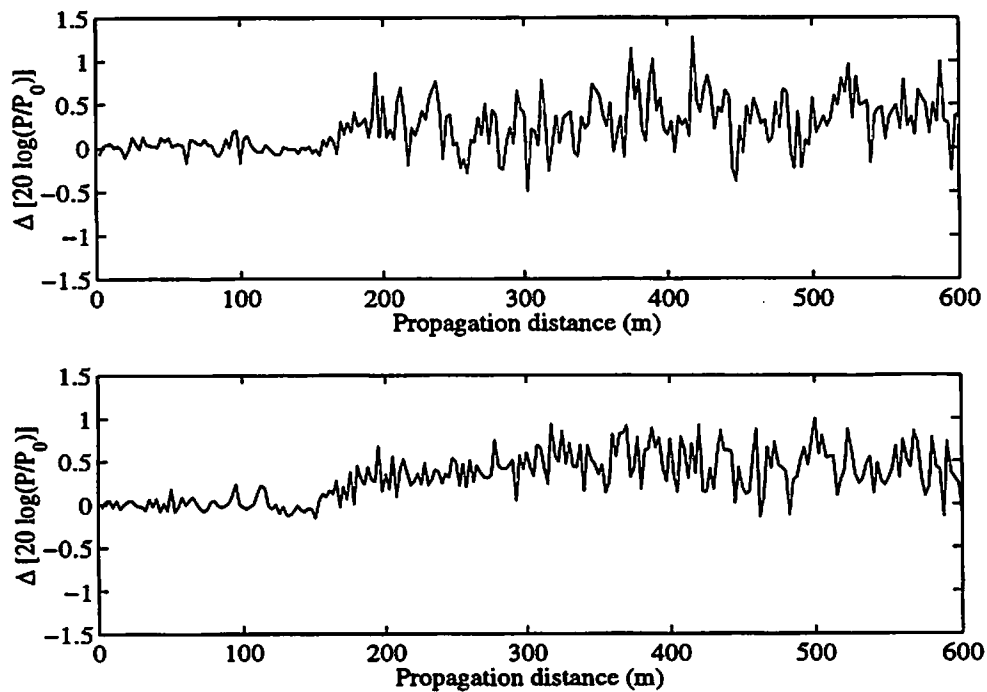


Figure 10: Difference between the transmission losses of FIG. 8 and of FIG. 9. Upper graph : $\nu = 400 \text{ Hz}$, Lower graph : $\nu = 1000 \text{ Hz}$.

propagation in the turbulent atmosphere.

Acknowledgments

This material is based upon work supported in part by the U.S. Army Research Office under contract DAAH04-95-1-0593. It has been started while V.E. Ostashev was a Visiting Professor at Ecole Centrale de Lyon awarded by the French Ministry of Education.

References

- [1] Lee D. and Pierce A.D. Parabolic equation development in recent decade. *J. Comp. Acoust.*, 3(2):95-173, 1995.
- [2] Gilbert K.E. and White M. Application of the parabolic equation to sound propagation in a refracting atmosphere. *J. Acoust. Soc. Am.*, 85:630-637, 1989.
- [3] Chevret P., Blanc-Benon Ph., and Juvé D. A numerical model for sound propagation through a turbulent atmosphere near the ground. *J. Acoust. Soc. Am.*, 100:3587-3599, 1996.
- [4] Ostashev V.E., Juvé D., and Blanc-Benon Ph. Derivation of a wide-angle parabolic equation for sound waves in inhomogeneous moving media. *Acustica united with Acta Acustica*, 83(3):455-460, 1997.
- [5] Godin O. A. A wide-angle, energy-conserving parabolic equation for sound in moving medium. In *Proceedings of Third International Conference on Theoretical and Computational Acoustics*, Columbia University, New York, 1997. to appear.
- [6] Ostashev V.E. *Acoustic in moving inhomogeneous media*. E & FN SPON, 1997.
- [7] Abdullaev S.S. and Ostashev V.E. Propagation of sound waves in three-dimensionally inhomogeneous and randomly inhomogeneous moving media. *Izv. Acad. Sci. USSR Atmos. Ocean. Phys.*, 24:417-426, 1988. Engl. transl.
- [8] Tappert F.D. *Wave propagation in underwater acoustic*, chapter 5, pp. 224-285. Springer-Verlag, 1977.
- [9] Kai Ming Li and Qiang Wang. Analytical solution for outdoor sound propagation in the presence of wind. *J. Acoust. Soc. Am.*, 102(4):2040-2049, 1997.
- [10] Karweit M., Blanc-Benon Ph., Juvé D., and Comte-Bellot G. Simulation of the propagation of an acoustic wave through a turbulent velocity field : A study of phase variance. *J. Acoust. Soc. Am.*, 89(1):52-62, 1991.
- [11] Chevret P. *Simulation numérique des effets de la turbulence sur la propagation du son dans l'atmosphère*. PhD thesis, Ecole Centrale de Lyon 94-18, 1994.
- [12] Wert K., Blanc-Benon Ph. and Juvé D. Effect of turbulence scale resolution on numerical simulation of atmospheric sound propagation. *19th Aeroacoustics Conference, CEAS/AIAA Paper*, 98-2245, 1998.
- [13] Thomson D.W. Wilson D.K. and Havelock D.I. The effect of turbulent intermittency on scattering into a shadow zone. *J. Acoust. Soc. Am.*, 99:3393-3400, 1996.
- [14] Khanna S. and Brasseur J.G. Analysis of Monin-Obukhov similarity from large-eddy simulation. *J. Fluid Mech.*, 345:251-286, 1997.
- [15] Blanc-Benon Ph. and Juvé D. Propagation of acoustic pulses in a turbulent refractive atmosphere. In *Proceedings of 7th International Symposium on Long Range Sound Propagation*, pp. 359-372, Ecole Centrale de Lyon, Ecully France, 1996.

Numerical Modeling of Long Range Propagation from Explosion Sources

Rod Whitaker, James H. Hunter, and Kalpak Dighe

**Earth and Environmental Sciences Division
Los Alamos National Laboratory**

Using a modified version of the Pierce-Posey-Kinney normal mode code, we present results of long range propagation calculations for explosions sources. Our modifications include a WKB approximation for mode location and porting the code to Fortran 90 on a Unix workstation. We will summarize results for ideal ducts, with and without winds, which serve as excellent test cases. Then results for surface bursts will be given for realistic atmospheres with and without winds at long range, several hundred to a thousand kilometers. Finally, numerical results and observations will be compared for a large surface explosion. The observations were made with infrasound arrays operated by Los Alamos National Laboratory.

Using Modified Mode-Ray Theory To Understand
Counter-wind Propagation Effects
from Atmospheric Explosions

D. O. ReVelle

Earth and Environmental Sciences - 8,
Los Alamos National Laboratory
Los Alamos, New Mexico 87545 USA
(505) 667-1256
(505) 665-3681 FAX
email: dor@vega.lanl.gov

ABSTRACT:

Modifications have been made to the standard ray-mode theory of Tindle and Guthrie (1974) to incorporate steady state horizontal winds in the inviscid, linearized flow approximation for a range-independent environment. It has been found that the formal inclusion of winds is limited to a certain range of launch angles and a specific criterion has been developed to evaluate this fundamental limitation of the method. This method does not predict the wave amplitude, but only the relative distance, i.e., the ray-mode skip distance, where wave energy will be present at any direction surrounding a sound source. The goal of this work has been to be able to develop a tool to understand the nature of the counter-wind return from explosions compared to its down-wind counterpart. Thus, we have applied this new method to seasonal model atmospheres with winds that simultaneously satisfy the combined constraints of a geostrophic and thermal wind balance for a hydrostatic atmosphere. It was found that ray-mode skip distances increase for the counter-wind flow case and decrease for the down-wind case in comparison to the cross-wind (or no wind case). (This is exactly the opposite of what is predicted for an ideal iso-velocity duct.) Also, the frequency of the counter-wind flow is lower than that corresponding to the down-wind situation. This result means that diffraction effects are more likely to contribute to the nature of the counter-wind signal from near-surface explosions. The height regime of the free wave modal zeros is very different for the two extreme wind cases and gives rise to two ducts in the down-wind direction, i.e., the Stratospheric and Thermospheric ducts and to a single duct in the up-wind direction, i.e., the Thermospheric duct. This approach allows us to evaluate the propagation differences for monochromatic inviscid propagation through realistic model atmospheres. In addition to the deterministic sound and wind speed profiles, we have also added a chaotic perturbation function to the sound speed profiles to illustrate the effects of waves and turbulence on acoustic wave propagation. Significant propagation changes are predicted to occur for the up-wind propagation case at the lowest free wave mode numbers where the horizontal wave number is largest. From the results of this model these latter effects seem to be the only way to allow acoustic energy to reach up-wind locations at a similar delay time to the downwind returns. This study was undertaken because of the current CTBT IMS (Comprehensive Test Ban Treaty, International Monitoring System) monitoring needs for a better understanding of long range propagation of sound waves in the atmosphere.

I. Introduction and Overview

A. Mode-ray theory

Systematic studies of the combined predictions of ray and mode theory have led to a deeper understanding of both mathematical types of analyses for computing acoustical propagation effects in stratified media in the linear, WKB limit. The ray-mode theory is based on the concept of an interference length between two adjacent modes of unequal amplitude and the production of an associated ray-mode skip distance for each mode at each frequency as a function of the thermodynamic structure of the environment in which the acoustic wave is propagating.

Some of the earliest attempts to connect these two fundamental alternative approaches were made by Tolstoy and Clay (1966) and by Weston (1968) and later by Weston and Rowlands (1979). Tindle and Guthrie (1974) brought the subject to a culmination for the case of perfectly stratified media, whereas similar work by Rutherford (1979) accomplished the same level of understanding for simple range-dependent environments. The basic result is that the constructive interference effects for a certain group of modes is physically linked to an equivalent ray angle obeying Snell's law. Similar work has apparently not proceeded for understanding propagation effects in the atmosphere.

B. Snell's Law Propagation Predictions

The geometrical optics version of Snell's law of wave refraction dates back to at least 1621 (Pierce, 1989). Its acoustic counterpart seems to have been recognized much more recently however, for example as presented in Milne (1921). This subject is also discussed in the geometrical acoustics kinematic approaches of Groves (1955). Other references to the history of this subject include the work of Thompson (1972).

It has long been recognized that for atmospheric propagation in the summertime when the prevailing Stratospheric winds reverse from their middle latitude westerly origins to easterly, that an asymmetry in wave normal propagation existed for the upwind and downwind directions. Specifically for wave normals emanating in the downwind direction (with the wind), returns from about 50 km are readily predicted using Snell's law due to the combined presence of warm temperatures and strong winds in the middle of the Stratosphere. For propagation against the prevailing Stratospheric wind in summer however, no returns are predicted from the 50 km region, but instead only from the lower thermosphere region near 100-110 km (Donn and Rind, 1972). Despite this prediction of no arrivals from the lower sound channel, full wave propagation codes, such as those developed by Pierce and co-workers (1976) and many earlier researchers have consistently predicted the presence of signals at the appropriate range against the wind in summer, albeit much weaker in amplitude than for the corresponding downwind summertime case. The corresponding problem has not been addressed in the case of underwater sound propagation simply because the prevailing currents such as the Gulf Stream are sufficiently slow compared to the phase speed of acoustic waves in the ocean (about 1.5 km/sec) that the corresponding effects do not materialize to any substantial degree. This is also true because the corresponding maximum oceanic sound channel depth is much shallower (Jensen et. al., 1994) than for the dominant sound channels considered for long distance atmospheric sound propagation.

The key unanswered question has been by what mechanism(s) does the sound reach ground level for such cases when Snell's law does not predict possible refractive returns on the basis of the observed atmospheric temperature and wind

structure. For example, diffraction effects not explicitly accounted for in the ray theory could be responsible as could wave scattering effects. Using our current approach we will show that the combined-ray mode theory predicts arrivals for the counterwind summertime returns from both the 50 km and the 100 km regions under appropriate conditions. Based on results discussed in section III. it seems likely that these differences are due to diffraction effects.

II. Mathematical Development

A. Standard Ray-Mode Theory: No inclusion of winds/currents

Traditional ray-mode theory, as applied to the underwater acoustics environment, does not include mass average motions of the ambient medium, i.e., winds or currents since they are so slow in comparison to the thermodynamic sound speed. Thus the maximum oceanic Mach number is about $\arcsin(2/1500) \cong .001$, whereas in the atmosphere it can be as much as 1/3 or even higher on occasion. Thus, for the oceanic case, the neglect of winds is not even a second order effect except at very close range unless travel times between source and receiver are extremely short.

Thus, starting from the simplest ray-mode equations of Tindle and Guthrie (1974), we have the following perfectly stratified atmosphere relations, derived for a static medium with no mass average motions, i.e., winds:

- a) Perfectly Reflecting,
Homogeneous Sound Channel (Iso-velocity):

$$D = 2 \cdot H \cdot K_x / K_z \quad (1)$$

where

- n = Free wave mode number (0,1,2,3,)
- K_x = horizontal wavenumber of the nth mode
- K_z = vertical wave number of the nth mode
- D = Mode cycle skip-distance
- H = vertical sound channel thickness

- b) WJKB Approximation: For normal modes with 2 turning points at z_1, z_2 :

$$D = 2 \cdot K_x \cdot \int \{ dz / K_z \} \quad (2)$$

More generally (Jenkins, et. al., 1995), we can write an expression for D as:

$$D = \left| 2 \cdot \pi / \partial K_x / \partial n \right| \quad (3)$$

Also, following Weston and Rowlands (1979), we can also set an upper limit on the effective number of modes that need to be considered in an ideal waveguide in the limit where K_x approaches zero.

$$N_{\max} = 2 \cdot H / \lambda_x \quad (4)$$

where

λ_x = Wavelength of the acoustic wave

In this analysis we have maintained the full acoustic-gravity wave regime definitions of K_z , as given in Beer (1974). We have also utilized both the local isothermal and the non-isothermal definitions of the Brunt-Vaisalla and the

acoustic waveguide cut-off frequencies to evaluate their effect on the results. The Piere-Posey-Kinney normal mode code utilizes the local isothermal definition during the numerical calculations and we wanted an independent check of how the non-isothermal definition of these frequencies could influence the results.

B. Propagation effects from near-surface explosions

It is also well known that there is a strong asymmetry in the propagation of acoustic waves from near-surface explosions. Downwind the waves travel in two ducts, one between the ground and the top of the Stratosphere and the other between the ground and the base of the Thermosphere. In the up- or counter-wind direction, high frequency ray theory (using Snell's law including both temperature and winds) predicts that propagation should occur solely in a Thermospheric waveguide between the ground and about 110 km. Observations indicate that both directions receive sound at the canonical 200 km range, but that downwind maximum amplitudes exceed those up-wind by 20-30 times. Full wave theory modal analyses using the Pierce-Posey-Kinney (1976) normal mode code also indicate these amplitude levels as well using completely realistic sound and wind speed profiles (personal communication with R.W. Whitaker, 1997). Bush et al. (1997) and Kulichkov (1998) has also analyzed this situation and found that scattering from quasi-permanent turbulence in the vicinity of the Stratopause can produce the observed up-wind signal.

It is also very clear that the sole mechanism in the full wave theory that is not accounted for in ray theory is diffraction and not scattering, but the precise way in which the sound arrives at 200 km up-wind with an associated timing for Stratospheric waveguide propagation is not clear. Because of these apparent conflicts we undertook an analysis of the ray-mode theory while incorporating steady state horizontal winds in a range independent environment for the first time as will be discussed below.

C. Scattering and Diffraction Processes and Associated Scales

We can identify numerous vertical length scales in the atmosphere that have direct relevance to the propagation of acoustic waves. These include the pressure and density scale heights (H_p , H_r) the vertical depths of the main upper and lower acoustic sound channels in the atmosphere (H_u , H_l), scales of characteristic eddies in the planetary boundary layer and within the surface layer where the waves are observed (H_{pbl} , H_s), etc.. We must also compare these scales considered as acoustic frequencies to the relevant resonant frequencies of the atmosphere and of the acoustic waveguide in the frequency band of interest. Here we use the conventional isothermal, windless atmosphere definitions for simplicity of the relevant angular oscillation frequencies associated with atmospheric propagation processes and associated dynamics, etc., namely (Beer, 1974):

Following Draganov and Spiesberger (1995), and letting $C_s = 331$ m/s and using standard isothermal acoustic resonant frequency definitions (Beer, 1974):

$$\begin{aligned}\Omega_a &= \text{acoustic cut-off frequency} = 2.08 \cdot 10^{(-2)} \text{ /s} \\ F_a &= \text{linear cut-off frequency} = 3.31 \cdot 10^{(-3)} \text{ Hz} \\ \Omega_{bv} &= \text{Brunt frequency} = 1.88 \cdot 10^{(-2)} \text{ /s} \\ F_{bv} &= \text{linear Brunt frequency} = 2.99 \cdot 10^{(-3)} \text{ Hz}\end{aligned}$$

Assigning the numerical values:

$$H_p = 8 \text{ km}, \quad H_r = 10 \text{ km}$$

Hu = 100 km, Hl = 50 km
 Hpbl = 1 km, Hs = 10 m

we can calculate the following linear frequencies in association with these vertical scale sizes:

Fp = $4.1 \cdot 10^{-2}$ Hz, Fr = $3.3 \cdot 10^{-2}$ Hz
 Fu = $3.3 \cdot 10^{-3}$ Hz, Fl = $6.6 \cdot 10^{-3}$ Hz
 Fpbl = $3.3 \cdot 10^{-1}$ Hz, Fs = $3.3 \cdot 10^{+1}$ Hz

By associating these frequencies with the Brunt and acoustic waveguide cut-off frequencies as in Draganov and Spiesberger, (1995), we can infer the associated vertical length scales for which diffraction effects are important compared to scattering effects during acoustic wave propagation through the atmosphere. To do this we make use of the size parameter:

$$L = 2\pi a / \lambda_x \quad (5)$$

where a is the radius of the "scatterer" and λ_x is the acoustic wavelength of the wave. For $L \gg 1$, the geometrical acoustics regime, i.e. ray theory is evident, whereas for $L \ll 1$ scattering is evident. For $L = O(1)$, diffraction is important. Thus, scattering is important when the size of the eddies in the fluid are small compared to an acoustic wavelength, whereas diffraction effects are important if the eddy size is comparable to the acoustic wavelengths of interest. In the geometric acoustics limit the radius of the features that are redirecting the sound waves are very large compared to the acoustic wavelengths (Thompson, 1972).

Thus, we can see that vertical scales associated with e-folding of pressure and density are about 1 order of magnitude higher in frequency than the atmospheric resonant frequencies. In contrast, the scales associated with the acoustic ducted propagation are of the same order of magnitude as the resonant frequencies, whereas the boundary layer frequency scales are two to four orders of magnitude greater than the atmospheric resonant frequencies. As discussed in Draganov and Spiesberger (1995), for the higher frequencies, the scales controlling the diffraction process are the dimensions of the wave focussing regions. When the effects of wave scattering are negligible, the focussing regions are comparable to the acoustic wavelength and diffraction effects are important. Conversely if the scattering processes act to diffuse the spatial scales of the wave focussing regions, diffraction effects are negligible on the associated ray travel times. In addition, the scale of the source of the waves itself can produce associated focussing regions which can effect the propagation.

On the basis of the numerical values presented above, we can conclude that diffraction effects are negligible for wave frequencies significantly less than the duct height associated frequencies (which are also comparable to the resonant frequencies). Thus, we expect for atmospheric acoustic waves, that diffraction should be of importance at all frequencies below the geometrical acoustics limit, $\lambda_z \ll gH_p$ or $\ll \sim 11.2$ km (Thompson, 1972b), until $L \sim 1$. Using $L = 0.1$ for example, this condition occurs for $\lambda_z = 1$ km for $a = 0.1 \cdot (1/(2\pi)) = 1.59 \cdot 10^{-2}$ km = 15.9 m. Using $\lambda_z = 1$ km, we have an effective lower frequency limit of about 0.33 Hz for the utility of the geometrical acoustics ray concepts.

Since we are only concerned in this analysis with distance and time scales and not amplitude (except in a qualitative sense), we can adopt these operational definitions for our current purposes.

III. Fundamentals of Ray-Mode Modeling Ray-Mode Theory with Winds (in the linearized, inviscid, WKB Limit)

A. Mode Theory

If winds are added to the problem at hand, they must be added in a self-consistent way to both the ray and to the modal theories. Thus, for the mode theory, we have the kinematic Doppler-shift relationship, which assumes that the wavelength of the sound source is a conserved quantity:

$$\Omega(z) = \Omega_0 + K(z) \cdot V(z) = \Omega_0 * (1 + \{V(z)/C_s(z)\} * \cos\delta) \quad (6)$$

where

- Ω = angular wave frequency in the non-moving Earth frame
- Ω_0 = intrinsic angular frequency in the moving medium (= constant)
- $K(z)$ = Total wavenumber vector in two dimensions
(With K_y assumed to be =0).
- $V(z)$ = Vector wind speed
- δ = Angle between the wave heading and the wind vector

B. Ray Theory

In the ray theory we must add the zonal, meridional and vertical winds (u, v, w) as indicated in Jones (1969) and in Thompson (1972) to the ray equations which for a perfectly stratified atmosphere and plane waves ($\beta = 0$), reduce to:

$$dx/dt = \alpha \cdot C_s(z) + u(z); \quad \alpha = \cos\theta \quad (7a)$$

$$dy/dt = v(z) \quad (7b)$$

$$dz/dt = \pm \gamma \cdot C_s(z) + w(z); \quad \gamma = \sin\theta \quad (7c)$$

Briefly, we proceed exactly as with standard ray-mode theory, but now explicitly include the effects of the wind terms in the expression for the total ray path travel distance and in the angular wave frequency in (6). After this process is repeated as outlined in Tindle and Guthrie (1974), we find that the identical expression for the ray-mode skip distance is predicted if the launch angles are sufficiently shallow combined with other limits on $C_s(z)$ as well.

IV. Representation of Atmospheric Acoustical Structural Parameters

Subsequently, we consider applications of the above, simple cases of ray-mode equations to the Stratospheric and Thermospheric atmospheric sound channels for the mean summer and winter propagation conditions respectively. We assume from the onset that the effects of a finite ground impedance are not significant for the low-frequency sound propagation being considered, with associated frequencies $\ll 10$ Hz (see for example the recent work of Robertson et. al., 1995). Thus, we will not explicitly consider the effects of the surface and of the boundary layer on the surface reflection effects, etc..

We have used the combined geostrophic and thermal wind balance for the large scale horizontal atmospheric motions, in order to predict the wind structure as a function of altitude. Here we have made use of Egnell's law (Humphreys, 1964)

which connects the density scale height and the air density of the atmosphere to the zonally averaged horizontal winds using the relationships:

$$(1/u(z)) * du(z) / dz = 1/H_r \quad (8a)$$

$$(1/\rho(z)) d\rho(z) / dz = - (1/H_r) \quad (8b)$$

Briefly, using (8a) and (8b) in combination with the zonally averaged North-south temperature gradient at 1 km (above the boundary layer since this is an inviscid relationship) and the altitudes where the temperature gradient switches sign, we can fully predict the horizontal, steady state winds as a function of height. This process also conserves the horizontal momentum flux as well.

The mean winter temperature and sound speed profile that has been determined using this approach and which has subsequently been fitted smoothly using a high order polynomial function is plotted in Figure 1. The mean isothermal and non-isothermal acoustic waveguide cut-off and Brunt-Vaisalla resonant frequencies have been computed from these basic curve data and are plotted in Figure 2. Similarly the mean winter horizontal zonal wind as a function of height are indicated in Figure 3 (assuming a N-S temperature gradient of 40 deg K/10,00 km)

We have also introduced a special chaotic function from Lorentz (1976) to calculate chaotic deviations of atmospheric structural parameters. Here we have used $a=0.9$, which corresponds to a chaotic perturbation which can change its sign with respect with height. This is a very convenient way to add chaotic perturbations to the propagation problem since the function can be completely controlled by appropriately modifying the initial value and/or the nonlinear control parameter, a . The effects of the inclusion of this nondeterministic propagation term will also be discussed again briefly in Section V.C.

V. Predictions of Modified Ray-Mode Theory: Interference Length Variations

A. Ideal versus seasonal atmospheric model solutions

An analytic solution is readily available for the case of a homogeneous iso-velocity duct for propagation in a windless environment as indicated earlier. We have used this ideal standard to compare all of our numerical calculations against, i.e., to act as a calibration check of all of our results.

B. General Cases:

1) Cross-wind case:

As should be expected this is fully equivalent to the case of no winds. We have found by direct numerical integration that ducting between the ground and the lower Thermosphere is the only possibility for this case.

2) Down-wind case:

We have determined that ducting can occur either between the ground and the Stratopause or between the ground and the base of the Thermosphere. Also, the higher order free wave mode numbers correspond to steeper angle propagation paths.

3) Counter-wind case: In this case, we have determined that propagation can only occur in a duct between the ground and the base of the Thermosphere at quite high free wave mode numbers.

In Figure 4. We have plotted the predicted skip distance as a function of the free wave mode number for the mean winter profile indicated earlier. Notice that the down-wind solutions are all quite small compared to the up-wind case. This is also the case for the mean summer profiles considered as well. Thus weaker winds do not change the conclusions that have been reached. The very largest counter-wind skip-distance values correspond to propagation between ~60 and 120 km and are not relevant to ground based observations.

All of the above results are fully consistent with the predictions of Snell's law and of ray theory in the high frequency limit (Donn and Rind, 1972).

C. Inclusion of a chaotic propagation term into the thermodynamic sound speed:

In order to examine non-deterministic effects, we have also included the presence of a chaotic perturbation propagation term in the thermodynamic sound speed profile. We have found that the inclusion of this term in the sound speed relationship is very significant for the counter-wind case. It can allow acoustic energy to reach the ground which otherwise would not occur using solely deterministic sound and wind speed values. In Figure 5. we have plotted the sound speed, wind speed and effective sound speed as a function of the geopotential height for the case of counter-wind propagation in the winter, including these perturbation values. In Figure 6., we have also plotted the corresponding counter-wind propagation skip-distance with and without the inclusion of any chaotic terms in the sound speed profiles. Here we can clearly see that the presence of small amounts of variations in the sound speed as a function of height can make a dramatic difference in the presence of sound at the corresponding first bounce range from the Stratosphere (~200 km).

VI. Summary and Conclusions

A. Mode-ray theory

We have successfully incorporated winds into the standard ray-mode theory of Tindle and Guthrie (1974). We have found that the exact inclusion is limited to a range of shallow launch angles and other variations of the slowly varying, thermodynamic sound speed profile. We have successfully applied this new theory to a specific propagation problem in the atmosphere that has long defied a solution, namely the case of up-wind propagation.

B. Atmospheric Propagation Effects

An analysis has been made of the anomalous, propagation of sound wave energy against the prevailing winds in the Stratosphere. Even though Snell's law predicts no arrivals from the lower sound channel in this direction, waveguide mode theory predicts an arriving signal and such signals are also observed. These observed signals are far weaker however than the corresponding downwind case at a range of about 200 km. Since the waveguide theory contains diffraction

effects and since we predict that lower frequencies enter this anomalous zone upwind of the source, we can conclude that the wave energy enters the region through diffractive effects which are implicit in the full wave modal waveguide theory. The full details of this work will be submitted to J.A.S.A. for publication.

VII. ACKNOWLEDGMENTS

This work was supported by the Department of Energy, Office of Nonproliferation and International Security, DOE HQ, NN-20. I would also like to thank Dr. Rod Whitaker for many useful comments on this subject.

VIII. REFERENCES

- Beer, T., *Atmospheric Waves*, John Wiley and Sons, New York, 300 pp., 1974.
- Bush, G.A., S.N. Kulichkov and A.I. Svertilov, Some Results of the Experiments on Acoustic Wave Scattering from Anisotropic Inhomogeneities of the Middle Atmosphere, *Izv. Atmos. And Oceanic Physics*, 33, 445-4452, 1997.
- W.L. and D. Rind, Microbaroms and the Temperature and Wind of the Upper Atmosphere, *J. Atmos. Sci.*, 29, 156-172, 1972.
- Draganov, A. and J. Spiesberger, Diffraction and Pulse Delay in A Structured Ocean, *J. Acous. Soc. Amer.*, 98, 1065-1074, 1995.
- Groves, G.V., *Geometrical Theory of Sound Propagation in the Atmosphere*, *J. Atmos. Terr. Phys.*, 7, 113-127, 1955.
- Humphreys, W.J., *Physics of the Air*, Dover Publications, Inc., New York, 676 pp., 1964.
- Jensen, F.B., W.A. Kuperman, M B. Porter and H. Schmidt, *Computational; Ocean Acoustics*, AIP Press, New York, 612 pp., 1994.
- Jones, W.L. Ray Tracing for Internal Gravity Waves, *J. Geophys. Res.*, 74, 2028-2033, 1969.
- Kulichkov, S.N., Acoustic Sounding of Inhomogeneous Structures in the Middle Atmosphere, *Izv. Atmos. And Oceanic Physics*, 34, 1-6, 1998.
- Lorentz, E. N., Nondeterministic Theories of climatic change, *Quart. Res.*, 6, 495-506, 1976.
- Pierce, A.D. *Acoustics: An Introduction to its Physical Principles and Applications*, ISBN 0-88318-612-8, Second Edition, Acoustical Society of America, American Institute of Physics, 678 pp., 1989.
- Milne, E.A., Sound Waves in the Atmosphere, *Philos. Mag.*, 42, 96-114, 1921.
- ReVelle, D.O., Chaos and "Bursting" in the Planetary Boundary Layer, *J. Appl. Meteor.*, 32, 1169-1180, 1993.
- Robertson, J.S., W.L. Siegmann and M.J. Jacobson, Low-Frequency Sound Propagation Modeling Over A Locally R Reacting Boundary with the Parabolic Approximation, *J. Acous. Soc. Amer.*, 98, 1130-1137, 1995.
- Rutherford, S.R., An examination of multi-path processes in a range dependent ocean environment within the context of adiabatic mode theory, *J.A.S.A.*, 66, 1482-1486, 1979.
- Thompson, P.A., *Compressible-Fluid Dynamics*, McGraw-Hill Book Co., 665 pp., New York, 1972.
- Tindle, C.T. and K.M. Guthrie, Rays as Interfering Modes in Underwater Acoustics, *J. Sound Vib.*, 34, 291-295, 1974.
- Tolstoy, I. and C.S. Clay, *Ocean Acoustics*, Mc-Graw-Hill, New York, 1966.
- Weston, D.E., Sound Focussing and Beaming in the Interference Field Due to Several Shallow Water Modes, *J. Acous. Soc. Amer.*, 44, 1706-1712, 1968.
- Weston, D.E. and P.B. Rowlands, Guided Acoustic Waves in the Ocean, *Rep. Prog. Phys.*, 42, 347-387, 1979.

Temperature and Thermodynamic Sound Speed In Winter

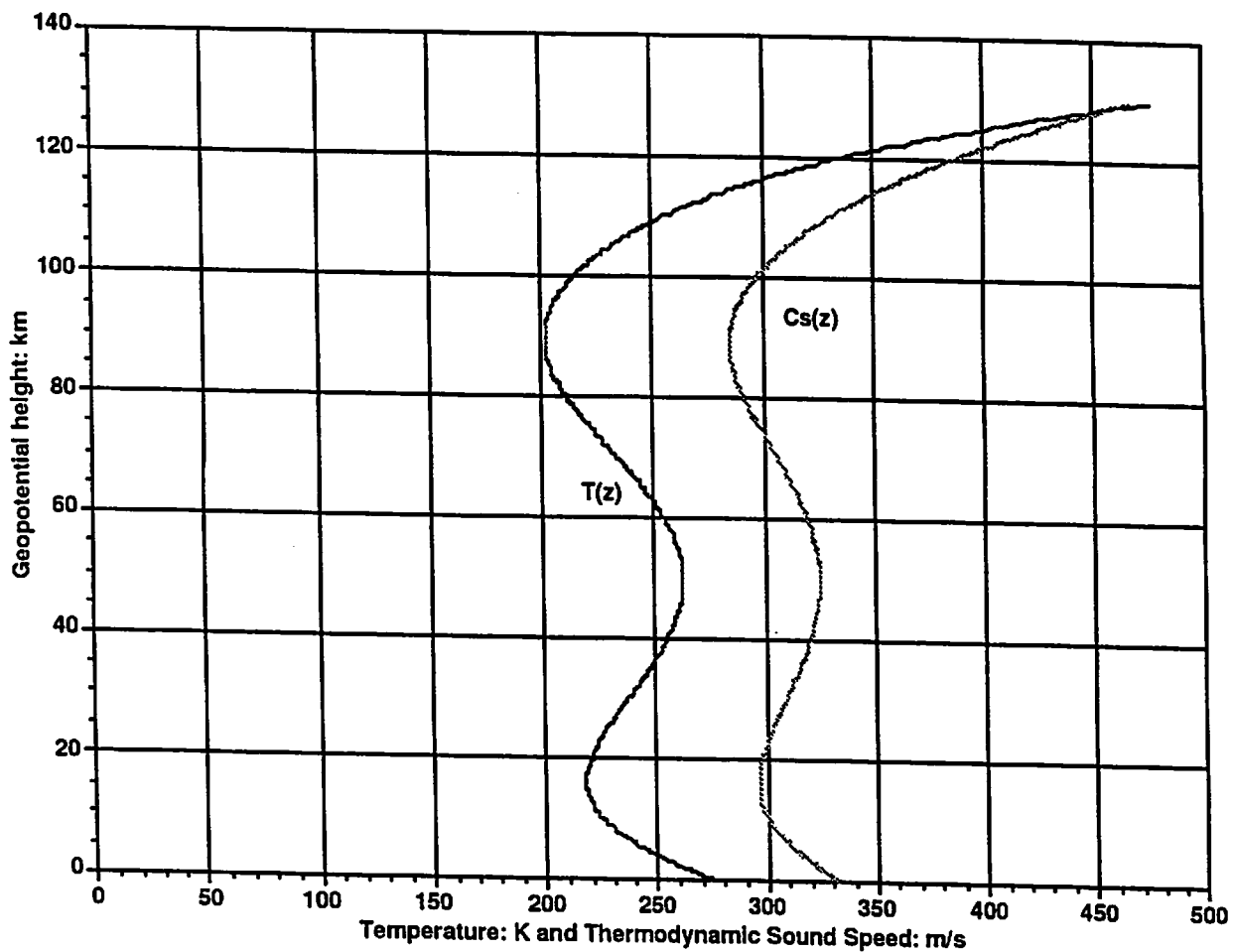


Figure 1. Mean winter curve fit of the temperature and computed thermodynamic sound speed as function of geopotential height

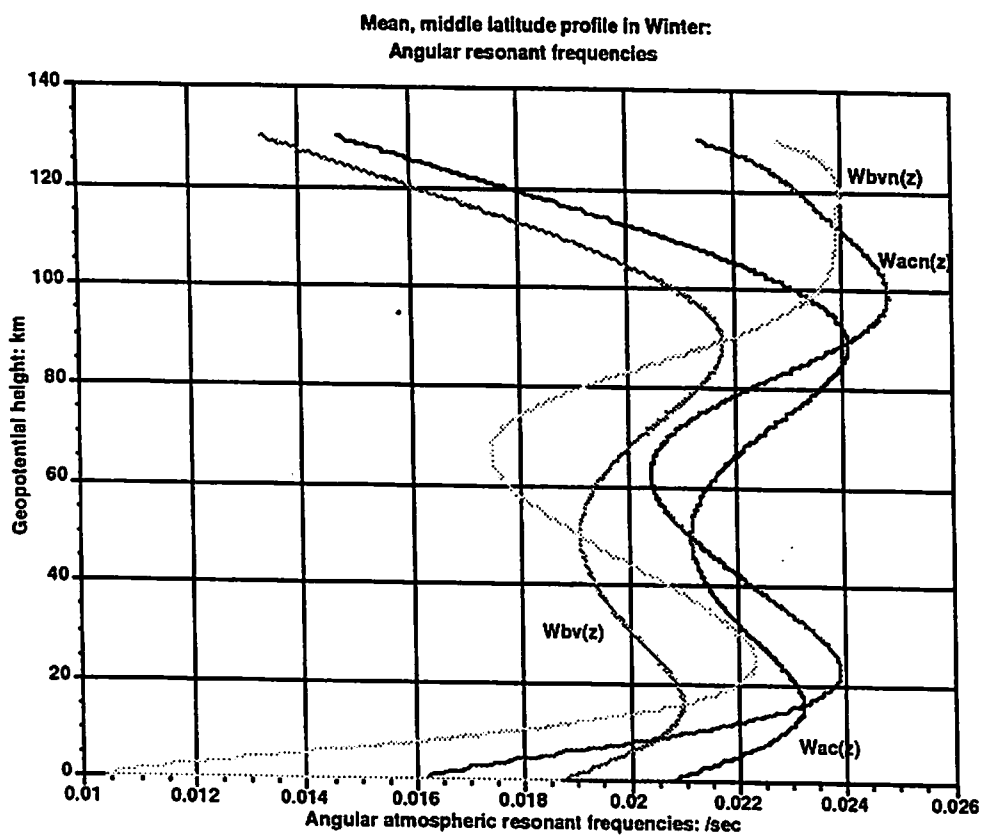


Figure 2. Mean winter isothermal and non-isothermal atmospheric resonant frequencies as a function of geopotential height.

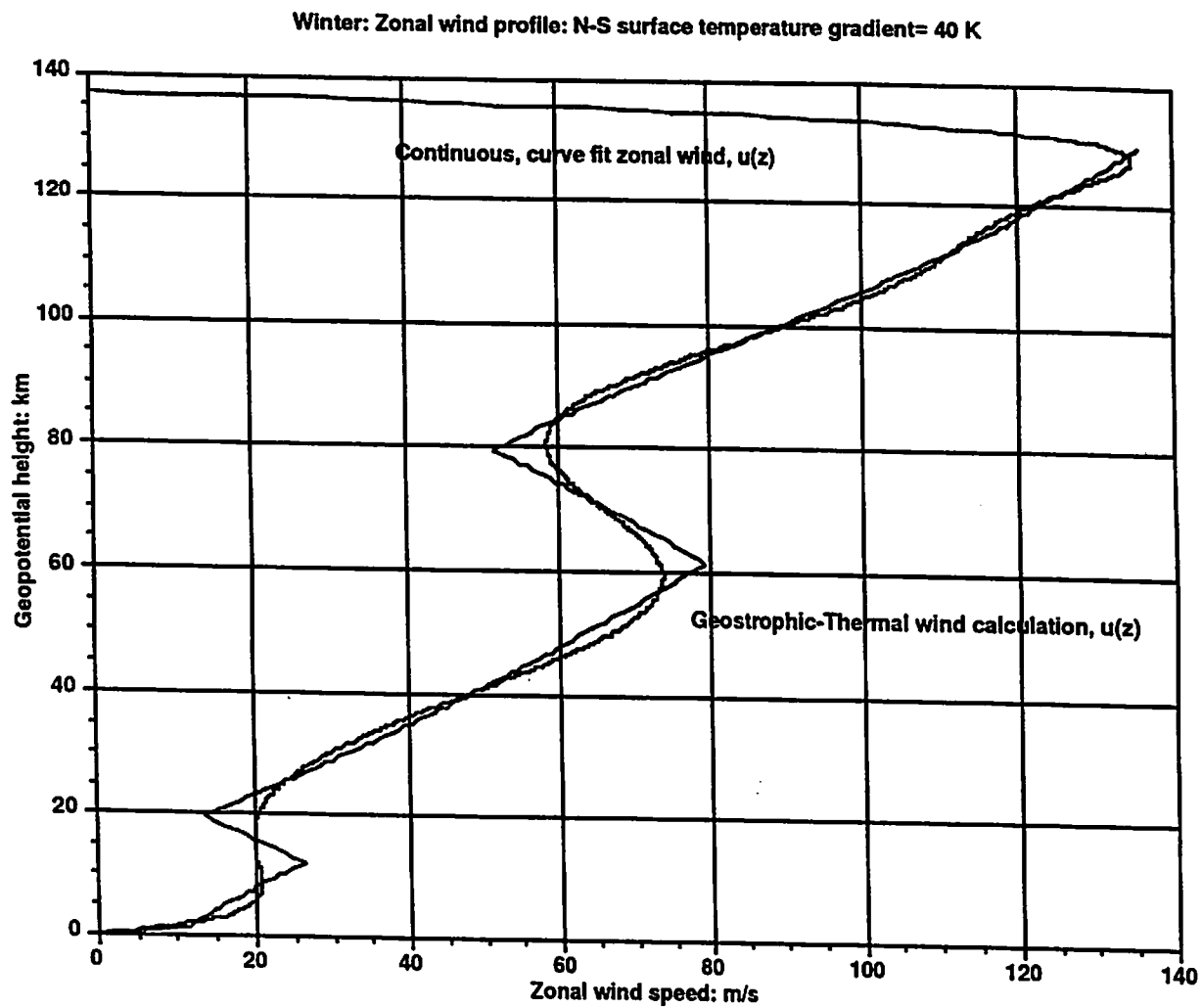


Figure 3. Mean winter zonal wind speed as a function of geopotential height: km. Directly calculated Geostrophic-Thermal winds and high order polynomial curve-fitted result. (N-S. temperature gradient= 40 K/10,000 km).

Winter: Ray-mode skip distance versus free wave mode number:
 $f=0.1$ Hz, Vertical step =0.25 km, Curve-fit winds for all heights

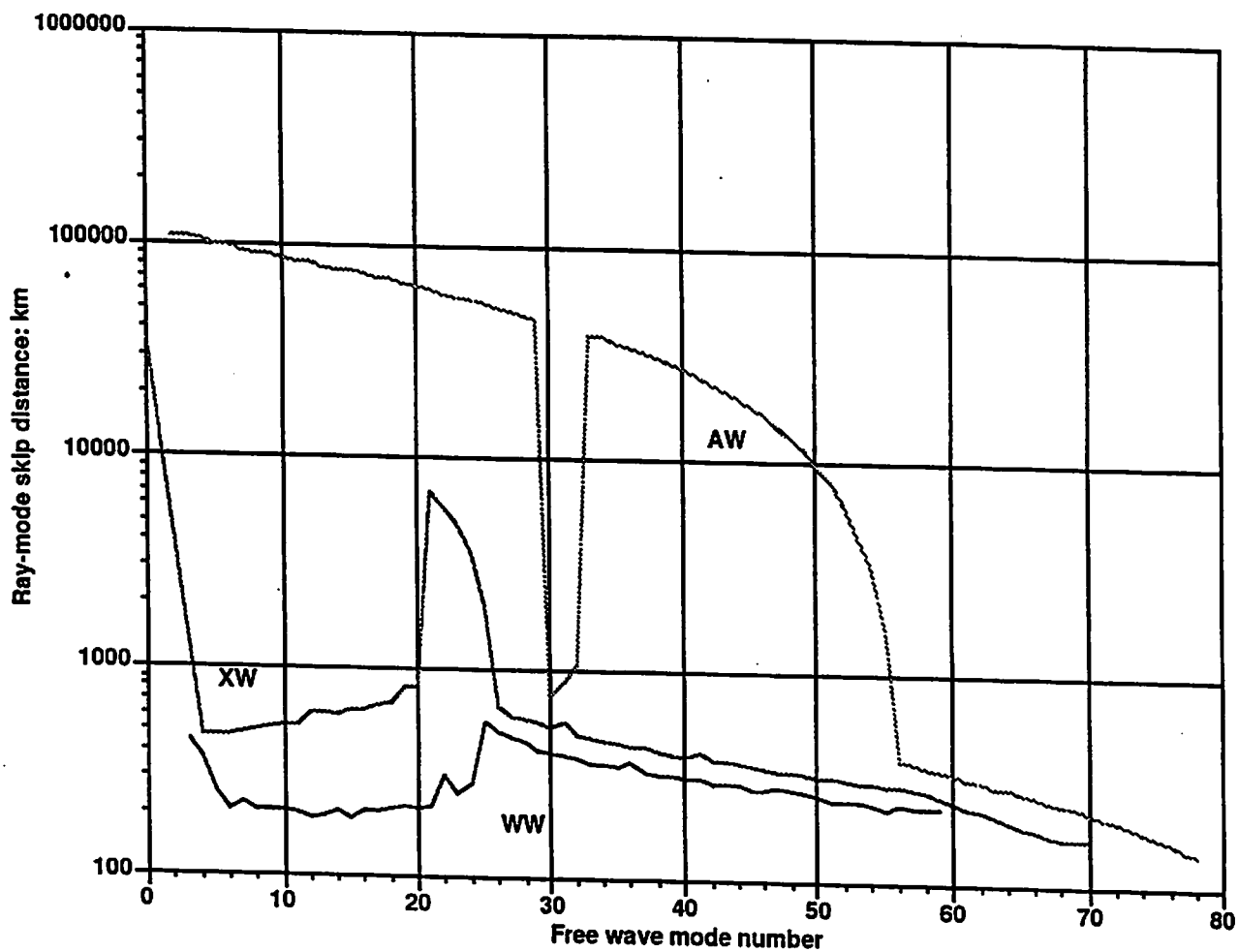


Figure 4. Skip-Distance versus the free wave mode number for with-wind and for counter-wind propagation in Winter without the inclusion of chaotic perturbations in the vertical sound speed profile.

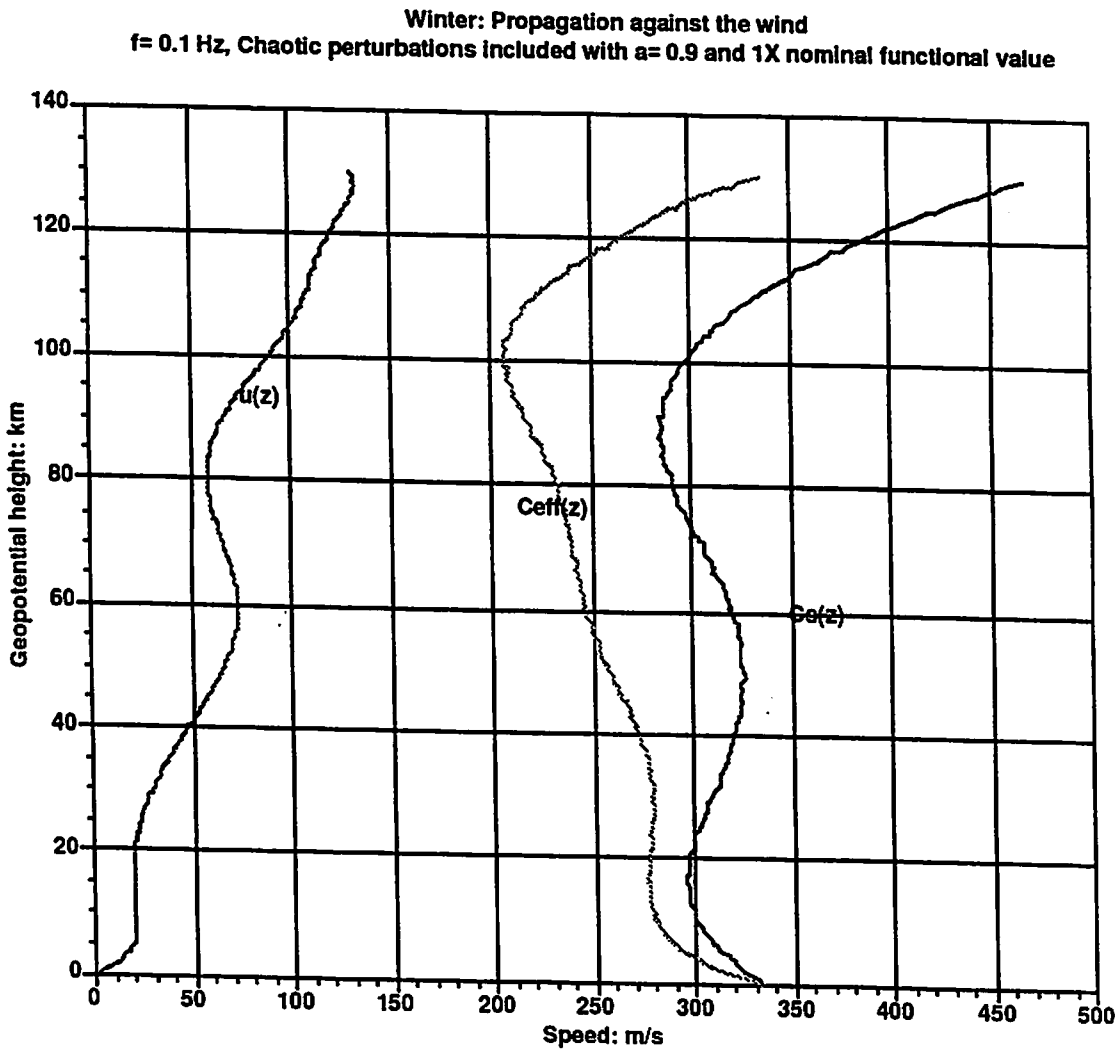


Figure 5. Sound speed, wind speed and effective sound speed as a function of geopotential height for the case of counter-wind propagation in Winter (with respect to the Stratospheric winds). The sound speed profile has been perturbed using the special function discussed in the text for $a=0.9$.

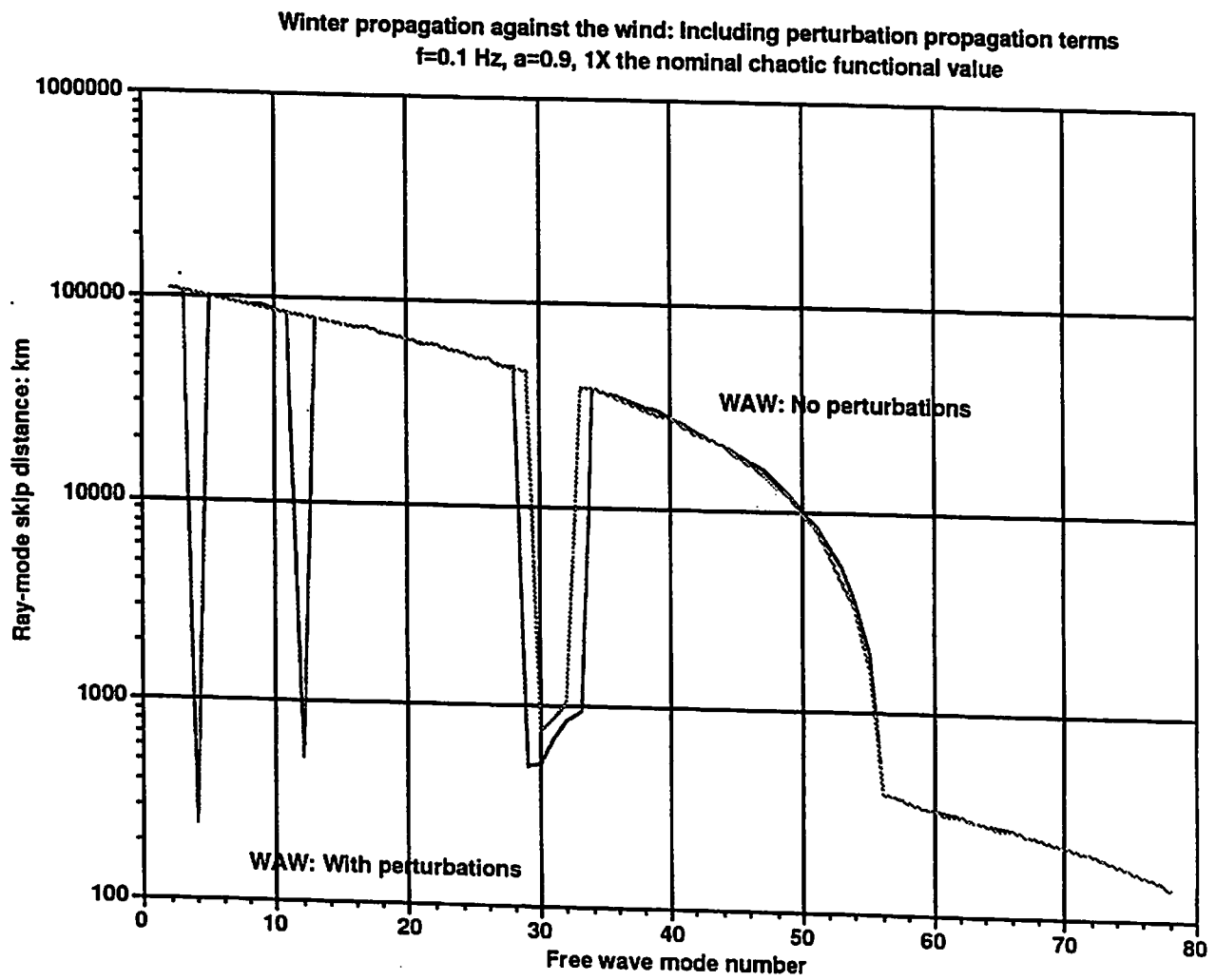


Figure 6. Skip-distance versus the free wave mode number for counter-wind propagation in Winter with and without the inclusion of chaotic perturbations in the vertical sound speed profile.

IMPEDANCE DISCONTINUITY AND RANGE DEPENDENT REFRACTION PROFILE : A NUMERICAL STUDY.

**Benoit GAUVREAU ⁽¹⁾, Michel BERENGIER ⁽¹⁾, Philippe BLANC-BENON ⁽²⁾, and
Claude DEPOLLIER ⁽³⁾**

⁽¹⁾ Laboratoire Central des Ponts et Chaussées, DGER, Cellule Acoustique, BP19, 44340 BOUGUENAIS, France - Phone : +33 (0)2 40 84 59 03 - Fax : +33 (0)2 40 84 59 98
e-mail : benoit.gauvreau@lcpc.fr, michel.berengier@lcpc.fr

⁽²⁾ Laboratoire de Mécanique des Fluides et d'Acoustique de l'Ecole Centrale de Lyon, UMR CNRS 5509, BP 163, 69131 ECULLY, France - Phone : +33 (0)4 72 18 60 19
Fax : +33 (0)4 72 18 91 43 - e-mail : phbb@selene.mecaflu.ec-lyon.fr

⁽³⁾ Laboratoire d'Acoustique de l'Université du Maine, UMR CNRS 6613, BP 535, 72017 LE MANS, France - Phone : +33 (0)2 43 83 32 86 - Fax : +33 (0)2 43 83 35 20
e-mail : depol@laum.univ-lemans.fr

The split-step Padé method for the resolution of the 2D parabolic equation (PE) is used to study traffic noise propagation in a stratified atmosphere.

Our study focuses on the propagation of mechanical noise from a highway, typically represented by a very low monopole source height and by the presence of an impedance discontinuity (infinite/finite representative of asphalt/grass) and of an acoustic barrier (screen, berm, ...) along the sound wave path.

Thus, after the validation of the code for simple cases, an impedance jump is firstly introduced. The split-step Padé results are presented for an atmosphere either homogeneous or stratified, qualitatively in one hand by maps showing diffraction by the discontinuity, and quantitatively in the other hand by comparison with other numerical, analytical or experimental data.

Finally, a range dependent gradient of celerity is introduced to model the air flow perturbation induced by a noise barrier for instance. Several gradient profiles are presented, for different geometrical configurations.

INTRODUCTION

During this last decade, the propagation of sound above a plane and heterogeneous ground (with an impedance discontinuity) with or without refraction phenomena has been extensively studied ¹⁻¹², analytically, numerically and/or experimentally. When a noise barrier (or berm, slope, etc) is located between the source and the receiver, a perturbation due to wind conditions occurs. This perturbation has an important effect on the refraction and modifies the celerity profile in the screen proximity ¹³. Moreover, a change in the impedance value can appreciably alters the vertical temperature gradient, and thus the celerity gradient.

The traffic noise is a practical application of such a situation. Beyond 60 km/h, the tire-road noise predominates over the mechanical noise. Recent experimental works carried out in the Laboratoire Central des Ponts et Chaussées (LCPC) showed that the sound source equivalent height is very low (of the order of a few centimetres, typically 3 cm) and that this source can be correctly modelled by a monopole sound source ¹⁴. Moreover, traffic sound is most

commonly generated above an acoustically hard surface (asphalt or concrete), and crosses an impedance discontinuity along its propagation from the source to the receiver above a softer surface such as grass or snow.

The purpose of this study is to quantify the influence of a modification of the refraction profile on the acoustic field due to the presence of a virtual obstacle on the sound path. The frequency range is [100 Hz ; 5 kHz] and the distances involved are of the order of hundreds metres, in order to take into account the celerity gradient effects.

Numerical results are obtained using the parabolic equation and the split-step Padé method for its resolution¹⁵. Even if the acoustic scattering by the turbulent flow is not (yet) beyond the scope of our study, it must be noticed that this marching algorithm has been recently improved by the acoustic group of the Ecole Centrale de Lyon (ECL), particularly in the way of generating and introducing turbulence in the code^{16,17}. In the present work, we introduce an impedance discontinuity in the marching algorithm, and we set the celerity gradient to be range-dependent with a linear evolution between two profiles.

The results are firstly compared to numerical and experimental data existing in the litterature, in order to validate the code for gradually more realistic cases. The split-step Padé method still shows its accuracy and its efficiency in terms of CPU time. Finally, we study several cases for which there is no experimental data available.

I. THEORY

I. A. The Parabolic Equation

In the linear acoustic approximation, the acoustic pressure p is solution of the elliptic (two-way) Helmholtz equation $\Delta p + k^2 p = 0$, where $k = \frac{2\pi f}{c(r, z)} = k_0 n(r, z)$ is the wave number, k_0

is a reference wave number, f is the frequency, c is the vertical sound celerity gradient and n is the refraction index (c and n both depend on the range and height coordinates, respectively r and z). If the azymuthal symmetry is assumed for the acoustic field, this equation is then written in the 2D cylindrical coordinates system :

$$\left(\frac{\partial^2}{\partial r^2} + \frac{1}{r} \frac{\partial}{\partial r} + \frac{\partial^2}{\partial z^2} + k^2 \right) p = 0 \quad (1)$$

The sound pressure is next split up into two components : an outgoing cylindrical wave represented by the Hankel function and its far field approximation ($k_0 r \gg 1$), and an envelope function $u(r, z)$ which is assumed to vary *slowly* with range :

$$p(r, z) = u(r, z) H_0^{(1)}(k_0 r) \approx \frac{1}{\sqrt{r}} u(r, z) \exp(ik_0 r) \quad (2)$$

where the carrier wave number k_0 is now chosen close to the dominant horizontal wave number in the spectral decomposition of $u(r, z)$. An approximate value for the carrier wave number is $k_0 = \frac{\omega}{\bar{c}}$, where \bar{c} is the average sound speed¹⁸.

Assuming that $n(r,z)$ is weakly range dependent and that the back propagated acoustic energy is negligible, the evolution of $u(r,z)$ is governed by the one-way parabolic equation :

$$\frac{\partial u(r,z)}{\partial r} = i(\sqrt{Q} - 1)u(r,z) \quad (3)$$

where the pseudo-differential operator Q is defined as $Q = \frac{\partial^2}{\partial z^2} + k_0^2 n^2$.

According to the series expansion order of the square root of the pseudo-differential operator Q , the different approximations lead to different angle limitations for the acoustic propagation and to different numerical (finite-difference) schemes.

I. B. The split-step Padé method

Defining a new pseudo-differential operator Q' as $Q'^2 = 1 + \xi + \eta$ where $\xi = \frac{1}{k_0^2} \frac{\partial^2}{\partial z^2}$ and $\eta = n^2 - 1$, the parabolic equation (3) is rewritten :

$$\frac{\partial u}{\partial r} = ik_0(Q' - 1)u \quad (4)$$

Like the split-step Fourier method¹⁹, the first idea is to solve the Eq. (4) *before* applying a Padé approximation¹⁵. Given the field at an arbitrary range r_0 , and assuming that Q' varies very slowly on the interval $[r_0, r_0 + \Delta r]$, the solution of Eq. (4) at the range $r_0 + \Delta r$ is :

$$u(r_0 + \Delta r, z) = \exp[ik_0(Q' - 1)\Delta r]u(r_0, z) = \exp[\sigma(Q' - 1)]u(r_0, z) \quad (5)$$

Defining $\mathfrak{I} = Q'^2 - 1$, the next and major idea of the method is to approximate the *whole* operator $\exp[\sigma(Q' - 1)]$, where $\sigma = ik_0\Delta r$. This is realized by a second order Padé expansion of $Q' = \sqrt{1 + \mathfrak{I}}$ which yields^{16,17} :

$$\exp[\sigma(Q' - 1)] = \exp[\sigma(\sqrt{1 + \mathfrak{I}} - 1)] \approx \frac{1 + p_1\mathfrak{I} + p_2\mathfrak{I}^2}{1 + q_1\mathfrak{I} + q_2\mathfrak{I}^2} \quad (6)$$

The coefficients p_1 , p_2 , q_1 and q_2 are easily deduced from a fourth order Taylor development of the exponential operator $\exp[\sigma(Q' - 1)]$:

$$p_1 = \frac{3 + \sigma}{4}; p_2 = \frac{\sigma^2 + 6\sigma + 3}{48}; q_1 = \frac{3 - \sigma}{4}; q_2 = \frac{\sigma^2 - 6\sigma + 3}{48} \quad (7)$$

Finally, the marching algorithm is expressed in terms of the coefficients p_1 , p_2 , q_1 , q_2 ,

$\eta = n^2 - 1$ and of the operator $\xi = \frac{1}{k_0^2} \frac{\partial^2}{\partial z^2}$ as :

$$\boxed{[1 + q_1(\eta + \xi) + q_2(\eta + \xi)^2]u(r_0 + \Delta r, z) = [1 + p_1(\eta + \xi) + p_2(\eta + \xi)^2]u(r_0, z)} \quad (8)$$

The numerical scheme deduced from Eq. (8) leads to a linear system with pentadiagonal matrices, solved at each step with a standard LU decomposition method ²⁰. Its stability is guaranteed by imposing that the denominator and the numerator elements of the rational approximation in Eq. (6) are complex conjugates of each other, so that the resulting rational function is always of modulus one. This second order Padé scheme can accommodate propagation angles as high as 54°, which is a wider angle than existing finite-difference techniques having similar cost step per step ^{16,17}.

The ground is modelled as a locally reacting plane with a complex impedance, which is allowed to change along the sound wave path. The impedance values are calculated from the single parameter (air flow resistivity) Delany & Bazley's model ²¹.

A nonreflecting boundary condition is imposed at the top of the computational domain by adding an absorption layer of several wavelengths thickness, so that no significant acoustic energy is artificially introduced by reflection on the upper boundary of the wave guide.

The initial pressure field required for the initialization of the marching algorithm has a Gaussian shape, an adjustable width and takes into account the image source weighted by a complex reflection coefficient.

At last, the mean sound speed profiles are those previously used by Gilbert & White ¹⁸, but are now set range dependent :

$$c(r, z) = \begin{cases} c_0 + a(r) \ln(z / z_0) & \text{for } z \geq z_0 \\ c_0 & \text{for } z < z_0 \end{cases}$$

where $c_0 = 340$ m/s, $z_0 = 6 \cdot 10^{-3}$ m (rugosity parameter) and where the coefficient $a(r)$ varies from -2 m/s for strong upward refraction to 2 m/s for strong downward refraction, with a *linear* evolution versus range between two values.

II. VALIDATION OF THE CODE

The stability and the accuracy of the split-step Padé method have been largely tested for trivial cases involving both homogeneous ground and homogeneous atmosphere. For the frequency range [100 Hz ; 5 kHz], for propagation distances up to several kilometres and for different geometrical configurations, we obtained a very good agreement with analytical methods based on the ray theory.

The numerical results presented here are those obtained for more realistic configurations, representative of traffic noise always involving an impedance discontinuity (infinite/finite) and a very low sound source height (a few centimetres), except when indicated.

We used a vertical step Δz of $\lambda/4$ for the cases of propagation in an homogeneous atmosphere, and $\lambda/6$ in an heterogeneous atmosphere. The horizontal marching step Δr is of the order of λ in the case of a constant refraction profile, and $\lambda/2$ for a range-dependent refraction profile in order to satisfy the condition on $n(r, z)$ from step to step in Eq. (5). With those last space gridding values and for a 1 km long wave guide for example, the CPU time on a Sun Ultra1 work station (143 MHz) do not exceed 1 minute for 100 Hz and 2 hours for 5 kHz.

The physical and geometrical parameters involved are defined in Fig. 1 :

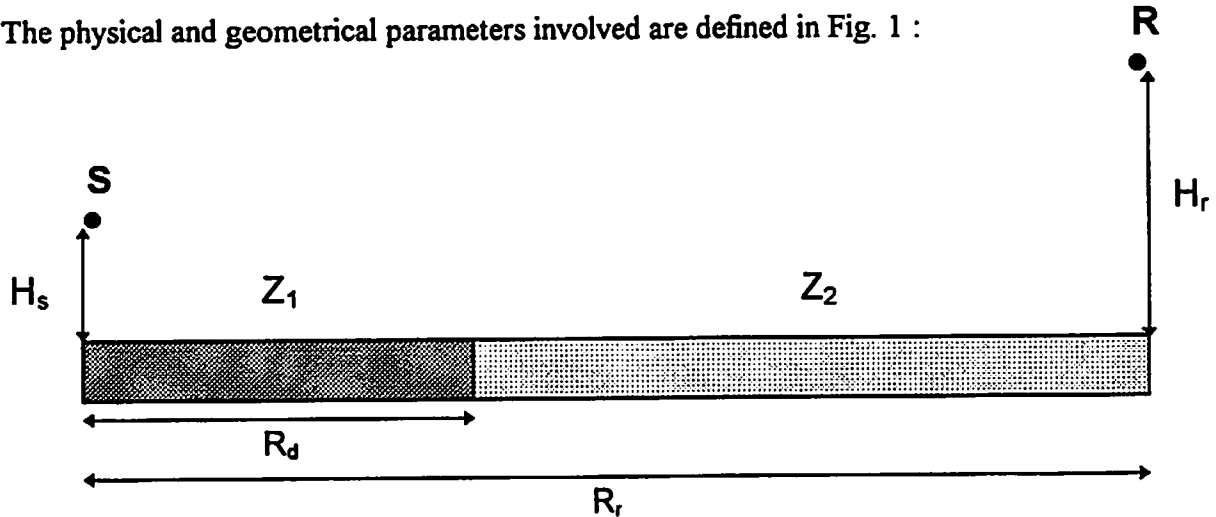


Fig. 1 : Physical and geometrical parameters notations

II. A. Qualitative validation

For concision, we present here only the results for the 4 kHz frequency, for heights up to 20 m and for distances up to 200 m. Other maps with higher sound source have clearly shown interference figures, whose number increases with the frequency and with the source height.

II. A. 1. Homogeneous atmosphere

In Fig. 2 and 3, we have plotted the sound pressure levels (SPL) relative to a reference microphone placed close to the source. For both figures, the sound source is 10^{-2} m high, the frequency is 4 kHz and the SPL range [-40 dB ; 0 dB], with a color step each 4 dB. In Fig. 2, the impedance (or flow resistivity) is homogeneous and « infinite » along the whole sound wave path, while in Fig. 3, the air flow resistivity turns rapidly from $3 \cdot 10^5$ kNsm $^{-4}$ (asphalt for instance) to $3 \cdot 10^2$ kNsm $^{-4}$ (grass) 5 m after the source position in range.

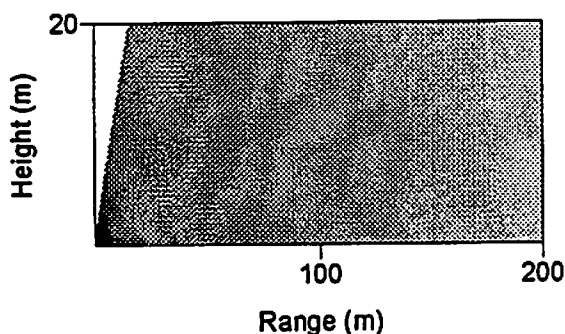


Fig. 2 : $f = 4$ kHz ; $H_s = 10^{-2}$ m ;
 $\sigma_1 = \sigma_2 = 3 \cdot 10^5$ kNsm $^{-4}$

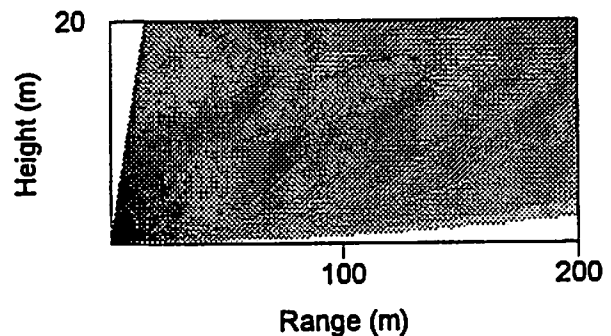


Fig. 3 : $f = 4$ kHz ; $H_s = 10^{-2}$ m ; $R_d = 5$ m
 $\sigma_1 = 3 \cdot 10^5$ kNsm $^{-4}$; $\sigma_2 = 3 \cdot 10^2$ kNsm $^{-4}$

For a source very close to the ground ($H_s/\lambda \ll 1$) and for homogeneous and acoustically perfectly hard ground, not any interference figure occurs and the propagation lobes turn rapidly to plane wave foreheads (Fig. 2).

The introduction of a breakdown in the impedance (Fig. 3) leads to diffraction of the acoustic energy on this discontinuity, which then acts as a secondary source role and which generates new propagation lobes. In comparing Fig.3 to Fig.2, we also observe the intuitive phenomena that the ground absorption is reinforced and that the sound energy is considerably less important than in the previous case for the lowest receiver heights. In both cases, the angular limitation of the method is easily visible.

II. A. 2. Stratified atmosphere

In this case, we observe the influence on the SPL of an homogeneous celerity gradient, either negative ($a = -1$ m/s - Fig. 4) or positive ($a = 1$ m/s - Fig. 5). Except for the celerity profile, all the previous values of the parameters are conserved (cf Fig. 3).

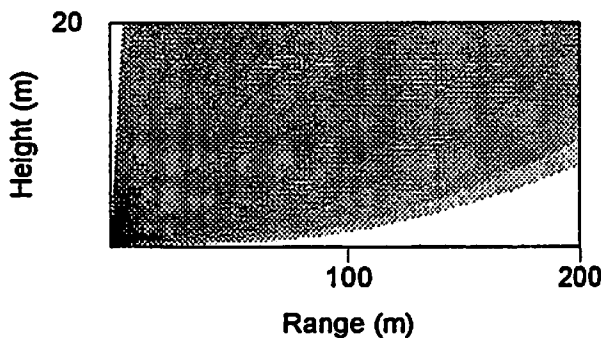


Fig. 4 : upward refraction
Same parameters values as in Fig. 3

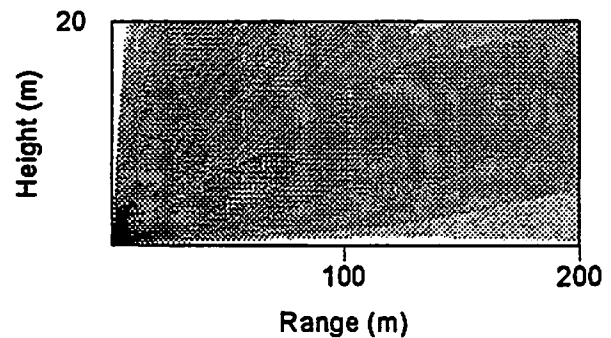


Fig. 5 : downward refraction
Same parameters values as in Fig. 3

In that case too, the map illustrations are consistent with the intuitive predictions : the main propagation lobes due to the impedance discontinuity are turned either upward or downward whether the celerity gradient is respectively negative or positive, and sonorise respectively less or more the lowest region of the wave guide. The color step is still 4 dB, but the SPL range is [-60 dB ; 0 dB] for Fig. 4 and [-40 dB ; 0 dB] for Fig. 5. A shadow zone appears on Fig. 4, in which the sound pressure levels decrease down to -80 dB. Moreover, we verified that the gradient effects increase with frequency.

II. B. Quantitative validation

We have shown that the split-step Padé results are consistent with the physical predictions. We now compare them with other numerical results or experimental data. We want to emphasize again the fact that the validation of the code for simple cases (either homogeneous ground or atmosphere) and for the whole traffic noise frequency range [100 Hz ; 5 kHz] has been widely done by comparing its results with those of an other model developed in the LCPC (program « DISC »). This model is essentially based on the ray theory. It takes into account the impedance discontinuity through the Rasmussen technique^{22,23}. This model has already been validated by many experimental data available in the LCPC.

The results presented are those compared to the data found in the litterature, involving more and more complex cases.

II. B. 1. Homogeneous atmosphere - Heterogeneous ground

Craddock & White ⁵ have first introduced an impedance discontinuity in a numerical code based on the PE (finite differences with the Crank-Nicolson scheme). They validated their results for two particular geometrical configurations, for which Daigle & al. had made an excellent review ¹. Craddock & White compared their results with the predictions according to Rasmussen ²³, DeJong & al. ²⁴ and Koers ²⁵. They next chose a SPL representation versus distance (and thus for a fixed frequency) to better illustrate the jump in the impedance value, but for which there were neither experimental nor numerical data available for comparison. Their results for either an homogeneous and perfectly reflective ground (« C&W hard ») or heterogeneous hard/soft ground (« C&W disc ») are plotted in Fig. 6. and compared to the split-step Padé results for the same cases (« SSP hard » and « SSP disc »). We also mentioned in Fig. 6 the results given by the analytical model « DISC » developed in the LCPC.

The agreement between the three methods is excellent, except in the destructive interference region where the sound pressure levels fall dramatically and where the accuracy in the geometrical configuration is of primary importance (since the position of both source and receiver are numerically determined by the space gridding, their precisions decrease with the frequency). The parameters values are those indicated in Fig. 6.

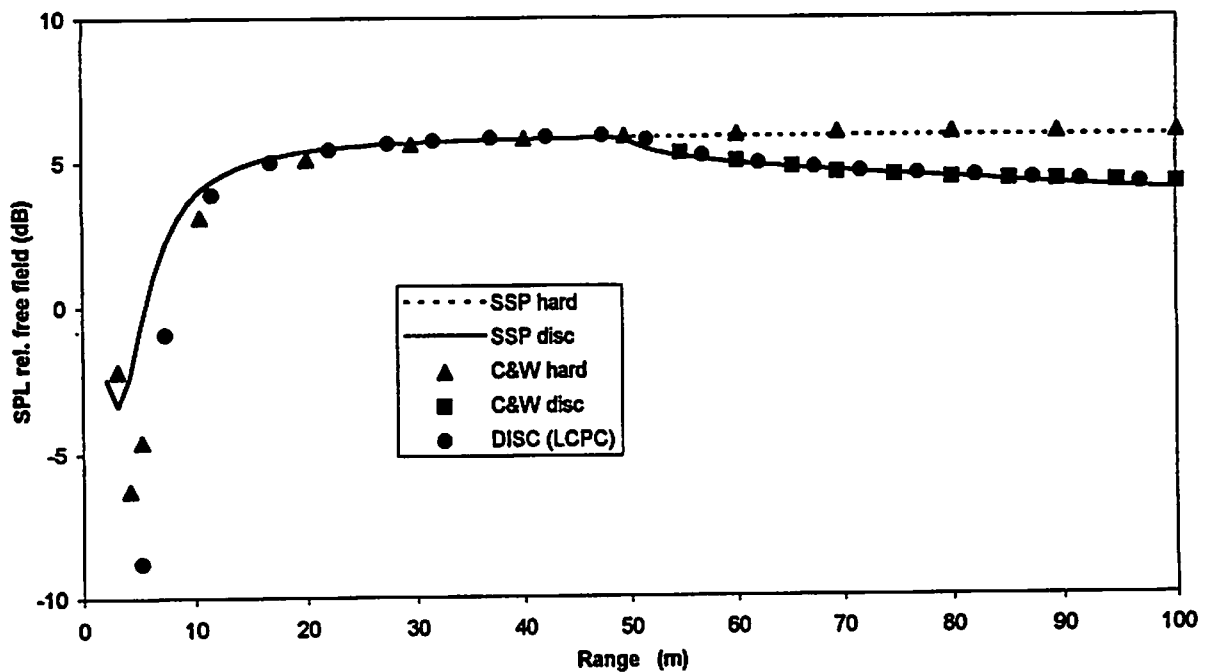


Fig. 6 : Predictions according to Eq. (8) compared with Craddock & White ⁵
 $f = 160 \text{ Hz}$; $H_s = 1.5 \text{ m}$; $H_r = 1.8 \text{ m}$; $R_d = 50 \text{ m}$; $\sigma_1 = 2 \cdot 10^5 \text{ kNsm}^{-4}$; $\sigma_2 = 2 \cdot 10^2 \text{ kNsm}^{-4}$

More recently, M. Galindo ^{7,10} compared her PE calculations for long range propagation over an impedance jump with those given by Rasmussen's method ^{22,23} for two geometrical configurations. For easier comparison in those particular configurations, we plotted the results relative to free field versus frequency, issued from numerical split-step Padé (« SSP ») and finite differences (« CN-PE ») methods, and analytical LCPC (« DISC ») and Rasmussen (« Rasmussen ») models. The agreement is very good for both configurations. The set of those numerical data for the first configuration is recapitulated in Fig. 7. The parameters values are the same as in ref. 7 and ref. 10.

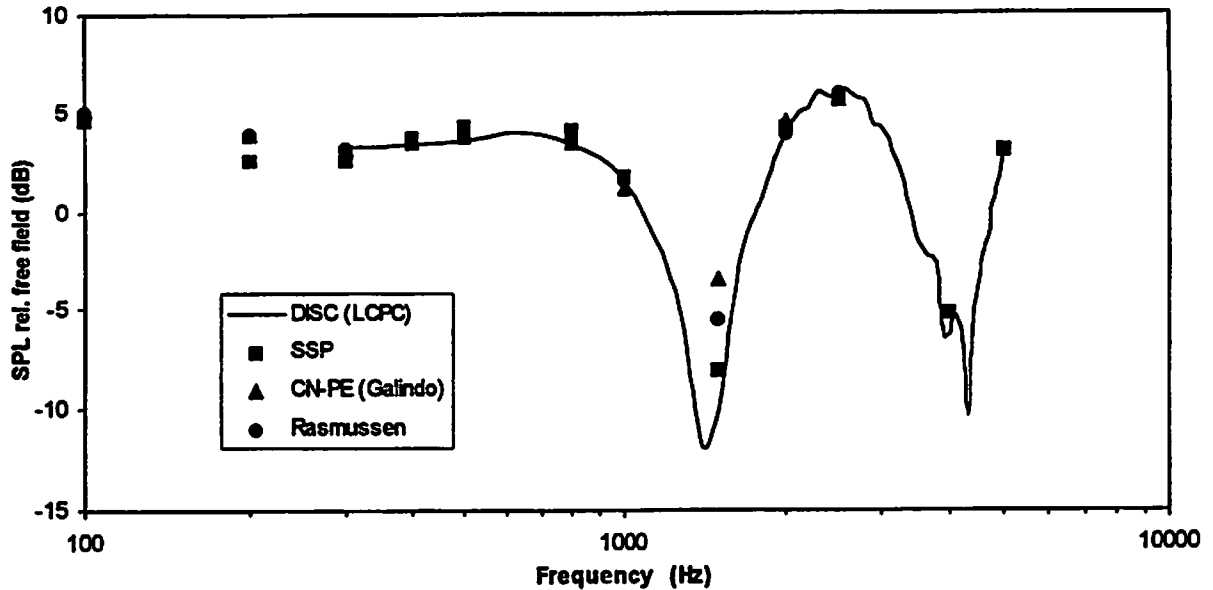


Fig. 7 : Predictions according to Eq. (8) compared with Galindo ^{7,10} (configuration 1)
 $H_s = 3 \text{ m}$; $H_r = 2 \text{ m}$; $R_d = 25 \text{ m}$; $R_r = 100 \text{ m}$; $\sigma_1 = 2 \cdot 10^2 \text{ kNsm}^{-4}$; $\sigma_2 = 5 \cdot 10^4 \text{ kNsm}^{-4}$

II. B. 2. Homogeneous ground - Stratified atmosphere

The SPL representation versus distance from the source position for a monochromatic acoustic sound wave is also treated by M. Galindo ¹⁰. She compares her PE calculations (CN-PE) with Green's Function Parabolic Equation (GF-PE) data ²⁶ and with Fast Field Program (FFP) predictions ²⁷. For distances from the sound source up to 1 km, the agreement is very satisfactory. Her results for homogeneous negative and positive celerity gradient are respectively plotted in Fig. 8 and Fig. 9. The frequency is always 500 Hz and the other parameters values are as indicated.

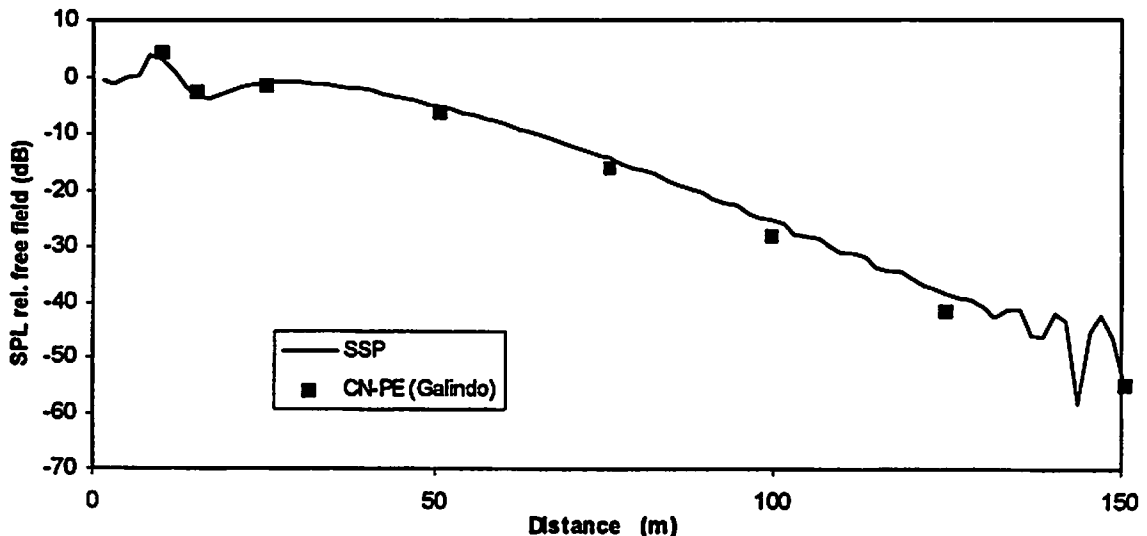


Fig. 8 : Predictions according to Eq. (8) compared with Galindo ¹⁰
 for an upward refracting atmosphere
 $f = 500 \text{ Hz}$; $H_s = 1.5 \text{ m}$; $H_r = 2 \text{ m}$; $\sigma_1 = \sigma_2 = 2 \cdot 10^2 \text{ kNsm}^{-4}$; $a(r) = a = -2 \text{ m/s}$

Fig. 8 shows a rapid decay in the sound level, as pronounced with the SSP predictions as with the CN-PE ones. After 150 m, the levels are less than -60 dB and strong oscillations occur, with a mean value nearly constant : this is identified with the acoustic shadow zone, where analytical theories do not predict any acoustic energy. In reality, we now know that the atmospheric turbulence scatter acoustic energy in this region. When the range and the frequency increase, the introduction of these effects is necessary to obtain reliable numerical predictions. It will be achieved in a further communication.

The calculations plotted in Fig. 9 have been obtained with exactly the same parameter values as in Fig. 8, except the homogeneous velocity gradient which turned to +2 m/s. For distances up to 1 km (in that case, no numerical data exist outside this range) the tendencies obtained with the two numerical methods are identical, and the respective SPL values are very closed to each other except, of course, for the destructive interference regions. A slight difference appears in those values and increases with the distance. The nature of these errors has been presented by M. Galindo ¹⁰ in terms of a *level* error introduced by the selection of the starting field, and a *phase* error generated by the rational linear approximation [Eq. (6)] and worsened in strong downward refraction conditions.

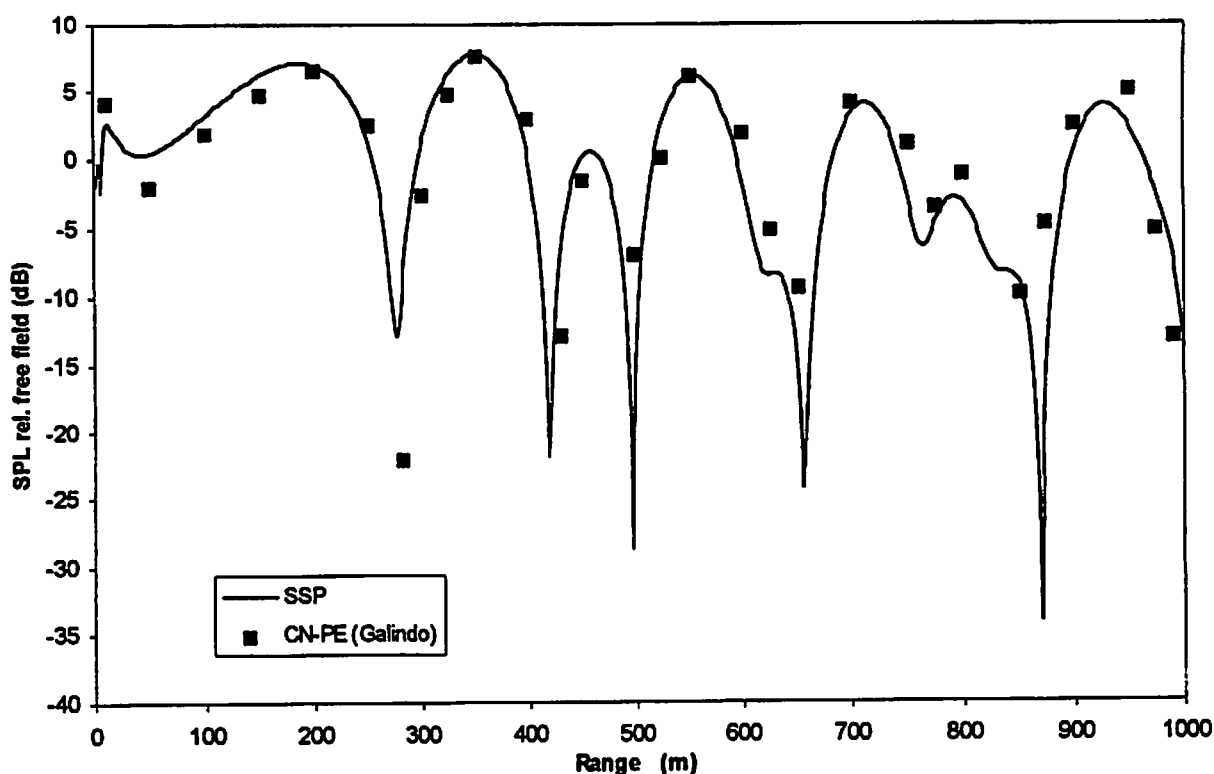


Fig. 9 : Predictions according to Eq. (8) compared with Galindo ¹⁰
for a *downward* refracting atmosphere
 $f = 500 \text{ Hz}$; $H_s = 1.5 \text{ m}$; $H_r = 2 \text{ m}$; $\sigma_1 = \sigma_2 = 2 \cdot 10^2 \text{ kNsm}^{-4}$; $a(r) = a = +2 \text{ m/s}$

II. B. 3. Heterogeneous ground - Stratified atmosphere

For this more complex situation involving a sound wave propagating above an heterogeneous ground (without screen) and through a stratified atmosphere, only upward refraction cases exist in the literature. In ref. 3, Bérengier & Daigle compared indoor experimental data obtained for propagation of sound above a curved surface having an impedance discontinuity, with analytical predictions given by a residue series solution. The parabolic equation assuming a far field approximation, we proceed to a scale change in order to compare correctly our results to theirs. We thus multiply by 10 the geometrical parameters, and divide by 10 the frequency and the air flow resistivity.

The shorter range numerical (« SSP ») results in Fig. 10 best fit the experimental data (« B&D exp. ») than their analytical predictions (« B&D th. »). According to the authors, this deviation beyond the discontinuity could be attributed to setting the edge diffraction coefficient $D = 1$ in their model.

The discrepancy between the split-step Padé calculations and the experimental acquisitions in Fig. 10 could be attributed to both the unaccuracy in the experimental air flow resistivity measurement and in the impedance discontinuity localisation amplified by the scale factor, and to the very strong linear gradient value (due to the analogy between the sound propagation in an homogeneous atmosphere above a curved surface and the sound propagation in a stratified atmosphere above a plane surface).

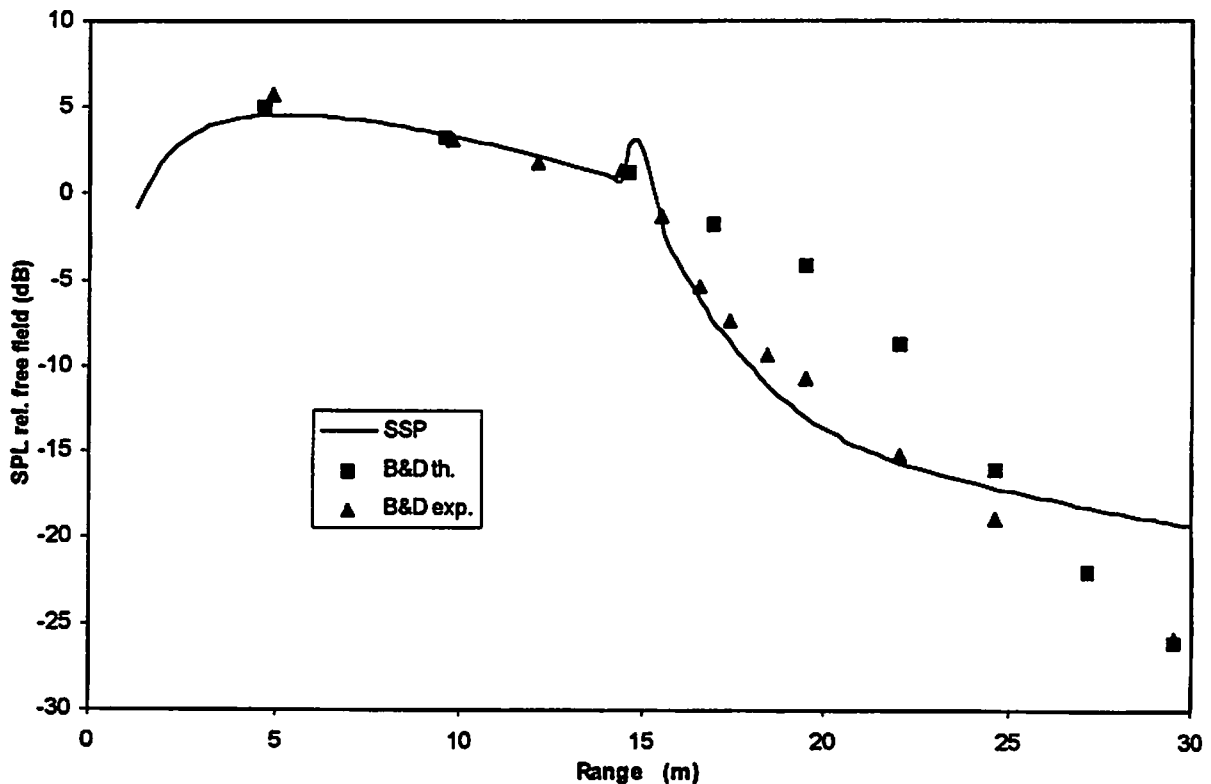


Fig. 10 : Predictions according to Eq. (8) compared with Bérengier & Daigle ³ for an upward refracting atmosphere *and* an heterogeneous ground
 $f = 400 \text{ Hz}$; $H_s = H_r = 0.5 \text{ m}$; $R_d = 15 \text{ m}$; $\sigma_1 = 5 \cdot 10^4 \text{ kNsm}^{-4}$; $\sigma_2 = 5 \text{ kNsm}^{-4}$;
 $a(r) = a = -68.8 \text{ m/s}$ (linear gradient until the altitude $z = 1.2 \text{ m}$)

III. COMPLEX CONFIGURATIONS

If a screen (or other physical obstacle) is introduced along the sound wave path, its presence considerably modifies the air flow in its close vicinity, and thus alters the celerity gradient. Rasmussen & Galindo¹³ have shown that the profile could even turn to its opposite (negative to positive celerity gradient for instance) above the screen edge. Here, the purpose is to study such a situation, focusing on the evolution of a refraction profile and the consequences on the sound pressure levels rather than on the diffraction by the barrier edge. For the moment, the obstacle is *virtual*, leaving the global case with a physical screen to a further work.

So, the sound wave now propagates above an heterogeneous ground (impedance discontinuity at R_d metres from the source) and in a *horizontally* heterogeneous medium : the refraction parameter has a *constant* value until R_{inf} metres from the source, then varies *linearly* between R_{inf} and R_s from a_{inf} to a_s , next from a_s to a_{sup} between R_s and R_{sup} , and is finally set constant again, with the value a_{sup} below R_{sup} . The major parameters involved are displayed in Fig. 11 :

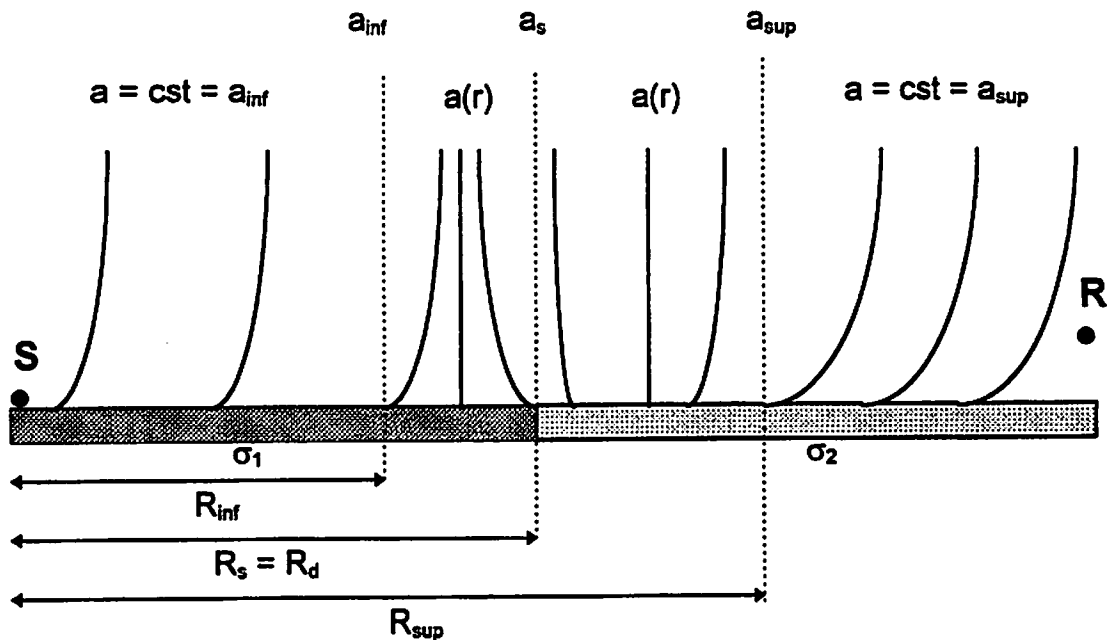


Fig. 11 : Parameters notations for a typical configuration

Even if the impedance discontinuity and the pseudo-screen positions (R_d and R_s respectively) are set identical in the presented configurations, they are allowed to differ in our SSP code. The same holds true for the refraction parameters a_{inf} and a_{sup} .

For the lowest frequencies, the refraction effect is weak and the results are not of prime interest. In Fig. 12, 13, 14 and 15, we plotted the SSP calculations (SPL relative to free field as a function of distance) for a refraction parameter either constant or variable along the sound wave path. The results are firstly presented for a mainly *negative* celerity gradient (Figures 12 and 13 for the frequencies 1 and 5 kHz respectively), and next for a mainly *positive* one (Figures 14 and 15 for the same frequencies). Each time, the homogeneous celerity profile case calculations are mentioned as a reference. Other parameter values are indicated.

III. A. Mainly *upward* refracting atmosphere

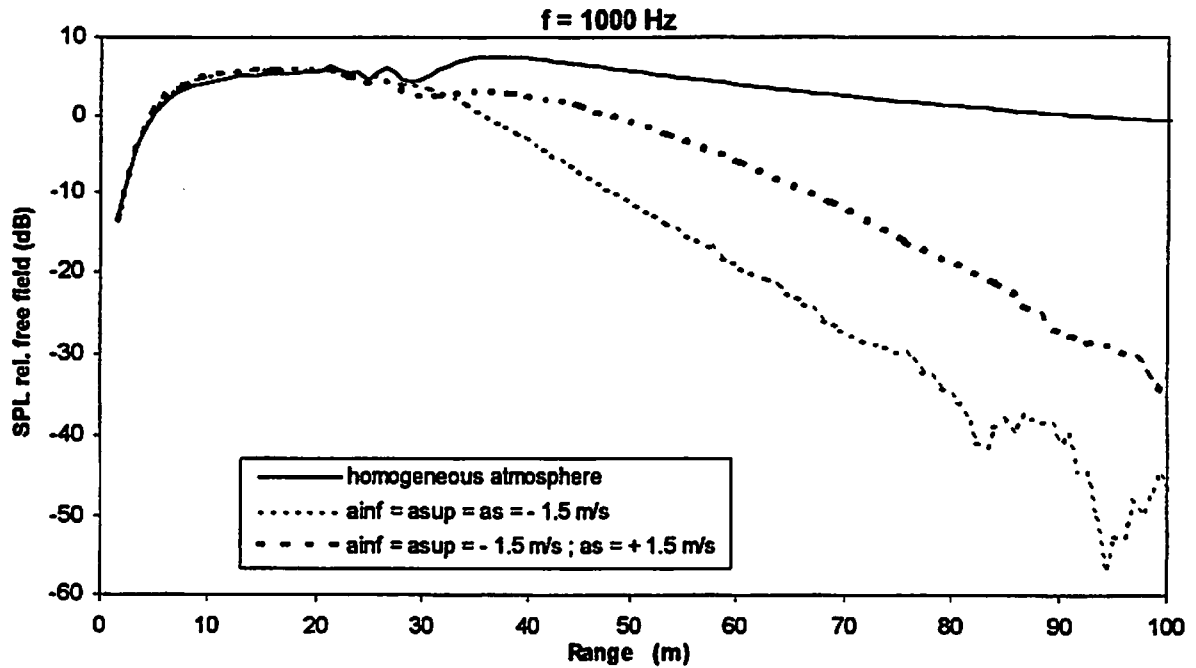


Fig. 12 : Influence of an *upward* range dependent refraction profile in the presence of an impedance discontinuity. $f = 1000 \text{ Hz}$; $H_s = 3 \cdot 10^{-2} \text{ m}$; $H_r = 3 \text{ m}$; $R_s = R_d = 20 \text{ m}$; $R_{inf} = 10 \text{ m}$; $R_{sup} = 30 \text{ m}$; $\sigma_1 = 3 \cdot 10^5 \text{ kNsm}^{-4}$; $\sigma_2 = 3 \cdot 10^2 \text{ kNsm}^{-4}$

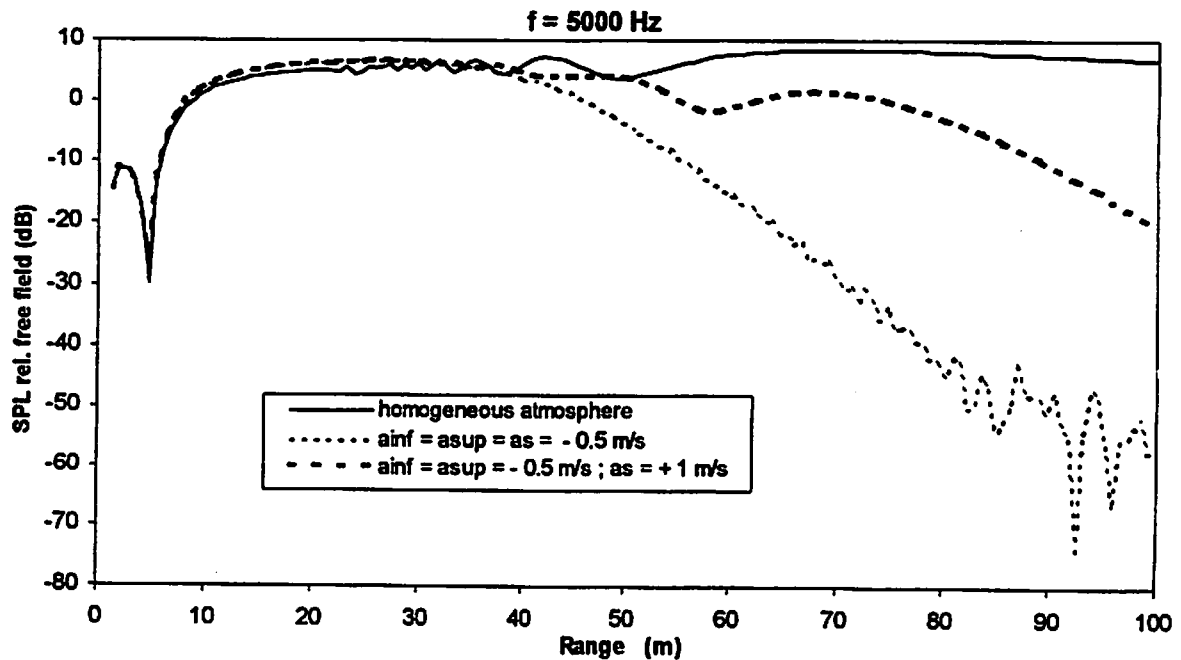


Fig. 13 : Influence of an *upward* range dependent refraction profile in the presence of an impedance discontinuity. $f = 5000 \text{ Hz}$; $H_s = 3 \cdot 10^{-2} \text{ m}$; $H_r = 3 \text{ m}$; $R_s = R_d = 20 \text{ m}$; $R_{inf} = 10 \text{ m}$; $R_{sup} = 30 \text{ m}$; $\sigma_1 = 3 \cdot 10^5 \text{ kNsm}^{-4}$; $\sigma_2 = 3 \cdot 10^2 \text{ kNsm}^{-4}$

III. B. Mainly *downward* refracting atmosphere

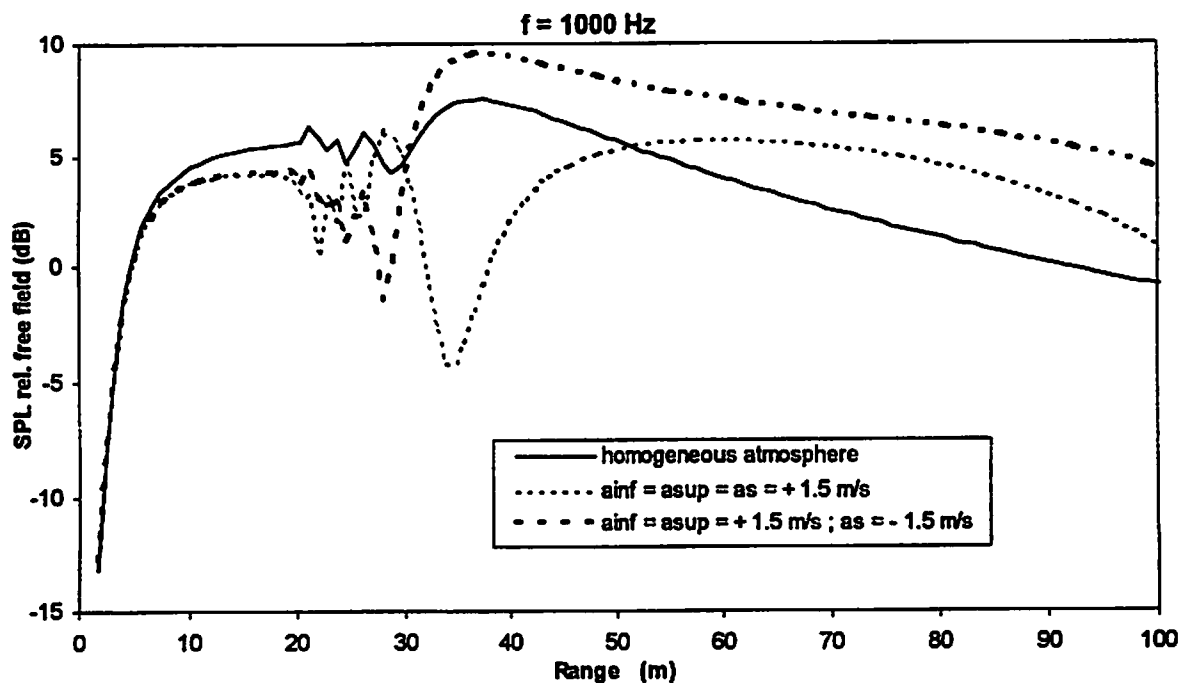


Fig. 14 : Influence of a *downward* range dependent refraction profile in the presence of an impedance discontinuity. $f = 1000 \text{ Hz}$; $H_s = 3 \cdot 10^{-2} \text{ m}$; $H_r = 3 \text{ m}$; $R_s = R_d = 20 \text{ m}$; $R_{inf} = 10 \text{ m}$; $R_{sup} = 30 \text{ m}$; $\sigma_1 = 3 \cdot 10^5 \text{ kNsm}^{-4}$; $\sigma_2 = 3 \cdot 10^2 \text{ kNsm}^{-4}$

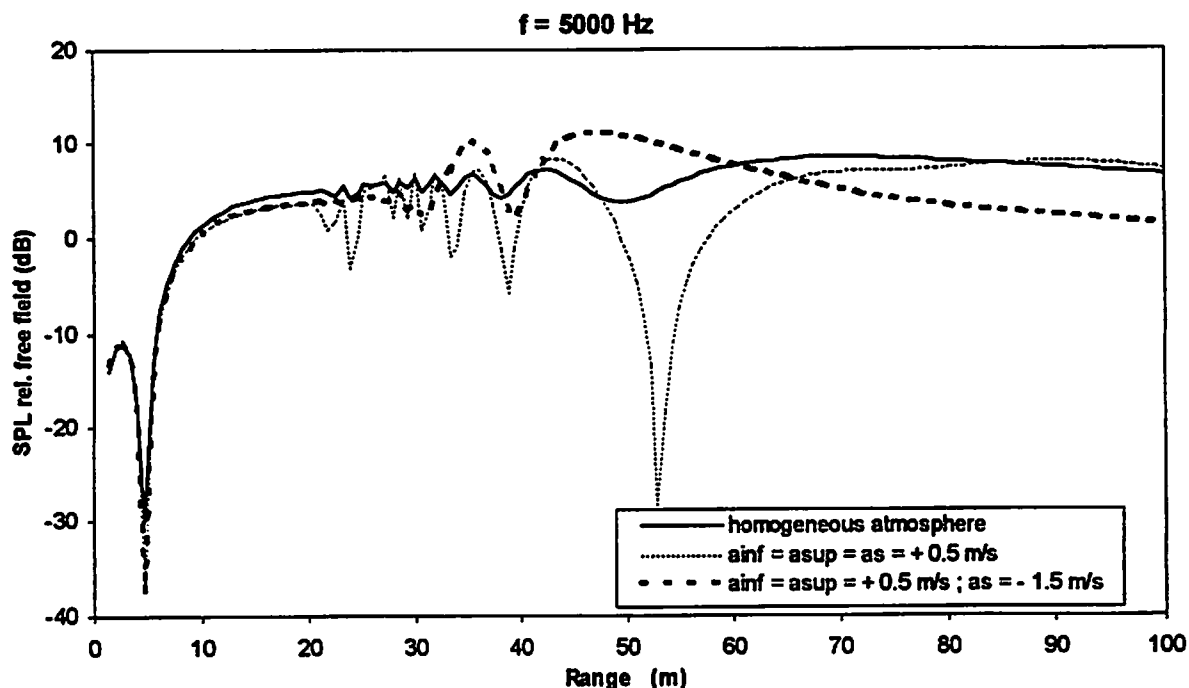


Fig. 15 : Influence of a *downward* range dependent refraction profile in the presence of an impedance discontinuity. $f = 5000 \text{ Hz}$; $H_s = 3 \cdot 10^{-2} \text{ m}$; $H_r = 3 \text{ m}$; $R_s = R_d = 20 \text{ m}$; $R_{inf} = 10 \text{ m}$; $R_{sup} = 30 \text{ m}$; $\sigma_1 = 3 \cdot 10^5 \text{ kNsm}^{-4}$; $\sigma_2 = 3 \cdot 10^2 \text{ kNsm}^{-4}$

III. C. Comments

All the curves drawn in Figures 12, 13, 14 and 15 show numerical instabilities just beyond the impedance discontinuity, followed by softer « humps » which explain the crossing through propagation lobes due to the diffraction by the discontinuity (see Fig. 3, 4 and 5). Those phenomena are all the more pronounced as the celerity gradient value is important. An other observation is that either a negative or positive celerity gradient value has a *delayed* effect on the sound pressure levels. This physical event, due to the source and receiver relative heights, is already visible comparing constant gradient and variable gradient curves : they are of course the same until R_{inf} (10 m for instance) and stay very close to each other even after the celerity gradient begin its linear evolution. Moreover, considering the relative positions of source and receiver, the « near field » SPL (generally before the impedance discontinuity) are qualitatively reversed according to the sign of the celerity gradient : in this region, the levels in upward and downward refraction conditions are respectively higher and lower than for an homogeneous atmosphere. This is easily understandable by imaging the upward refracting atmosphere case for example : in the source vicinity, the negative celerity gradient bends the acoustic rays toward the receiver and firstly increases the sound pressure levels at this point, before taking place in the shadow zone (Fig. 12 and 13). In the opposite case, the inverse phenomena occurs (Fig. 14 and 15).

For mainly *upward* refraction conditions (Fig. 12 and 13), the inversion of the celerity gradient sign between R_{inf} and R_{sup} brings back acoustic energy with regard to the constant negative celerity gradient case, and delays the appearance of the numerical instabilities in the shadow zone. This yields the intuitive result that the SPL stands in this case between the values obtained in the homogeneous atmosphere case and those obtained in the constant negative celerity gradient case.

Finally, Fig. 14 and 15 (mainly *downward* refracting atmosphere cases) show strong interference figures due to the multiple reflections of the acoustic rays on the ground. By modifying the celerity gradient value along the sound wave path, the position and the amplitude of these interferences are also altered. This yields complex situations, where the SPL for a variable celerity gradient is alternatively higher and lower than those calculated with a constant positive celerity gradient.

IV. CONCLUSION

We have developed an efficient means of allowing the ground impedance *and* the celerity gradient to vary with range in the split-step Padé code for the resolution of the parabolic equation. For a constant (and eventually set to zero in an homogeneous atmosphere) celerity gradient along the sound wave path, the model has been validated both qualitatively and quantitatively, for homogeneous or heterogeneous (impedance discontinuity) ground by comparison with other numerical, analytical or experimental data found in the litterature. The agreement is generally very good. For the configurations involving strong upward conditions and long range propagation, the atmospheric turbulence must be taken into account. This will

be done in a future work, which will also introduce a physical screen along the sound wave path.

The situations involving a range dependent celerity gradient of sound propagating above a ground with an impedance discontinuity have not been previously studied. Thus, neither experimental nor theoretical data exist yet, and that is the reason why results can only be examined qualitatively rather than quantitatively. Anyway, the variation of the celerity gradient value seems to have a strong effect on the sound pressure and this numerical study shows that it has to be taken into account. Controlled experiments are in progress in the Laboratoire Central des Ponts et Chaussées in order to validate the code for such complex cases.

ACKNOWLEDGEMENTS

The authors would like to gratefully acknowledge the French Acoustical Society (SFA) for its financial support.

REFERENCES

- ¹ G. A. Daigle, J. Nicolas & J. L. Berry, "Propagation of noise above ground having an impedance discontinuity", *J. Acoust. Soc. Am.* 77(1), 127-138 (1985)
- ² A. Berry & G. A. Daigle, "Controlled experiments of the diffraction of sound by a curved surface", *J. Acoust. Soc. Am.* 83(6), 2047-2058 (1988)
- ³ M. Bérengier & G. A. Daigle, "Diffraction of sound above a curved surface having an impedance discontinuity", *J. Acoust. Soc. Am.* 84(3), 1055-1060 (1988)
- ⁴ M. Bérengier, G. A. Daigle et A. Berry, "Etude du champ acoustique en présence d'une discontinuité d'impédance et d'un effet de gradient de vitesse du son", *Rapport de recherche LPC 155* (1989)
- ⁵ J. M. Craddock & M. J. White, "Sound propagation over a surface with varying impedance: A Parabolic Equation approach", *J. Acoust. Soc. Am.* 91(6), 3184-3191 (1992)
- ⁶ K. B. Rasmussen, "Scale model simulation of sound propagation over an impedance discontinuity", *Proceedings of Inter-Noise 93*, 1711-1714 (1993)
- ⁷ M. Galindo, "Application of the parabolic approximation method to sound propagation above ground with impedance variations", *Proc. 6th Intern. Symp. on Long Range Sound Propagation*, Ottawa, 394-407 (1994)
- ⁸ D. C. Hothersall & J. N. B. Harriott, "Approximate models for sound propagation above multi-impedance plane boundaries", *J. Acoust. Soc. Am.* 97(2), 918-926 (1995)
- ⁹ J. S. Robertson, P. J. Schlatter & W. L. Siegmann, "Sound propagation over impedance discontinuities with the parabolic approximation", *J. Acoust. Soc. Am.* 99(2), 761-767 (1996)
- ¹⁰ M. Galindo, "The parabolic equation method for outdoor sound propagation", Ph.D. Thesis, Technical University of Denmark (1996)
- ¹¹ M. R. Stinson & G. A. Daigle, "Surface wave formation at an impedance discontinuity", *J. Acoust. Soc. Am.* 102(6), 3269-3275 (1997)

- ¹² P. Boulanger, T. Waters-Fuller, K. Attenborough & K. M. Li, "Models and measurements of sound propagation from a point source over mixed impedance ground", Proc. 7th Intern. Symp. on Long Range Sound Propagation, 291-305 (1996)
- ¹³ K. B. Rasmussen & M. Galindo Arranz, "The insertion loss of screens under the influence of wind", Proceedings of Inter-Noise 97, 313-318 (1997)
- ¹⁴ J. F. Hamet, M. A. Pallas, D. Gaulin & M. Bérengier, "Acoustical modeling of road vehicles for traffic noise predictions : determination of the source height", 16th ICA-ASA Congress, Seattle, J. Acoust. Soc. Am. 103(5), 2919 (1998)
- ¹⁵ M. D. Collins, "A split-step Padé solution for the parabolic equation method", J. Acoust. Soc. Am. 93(4), 1736-1742 (1993)
- ¹⁶ P. Chevret, "Simulation numérique des effets de la turbulence atmosphérique sur la propagation du son dans l'atmosphère", Ph.D. Thesis, Ecole Centrale de Lyon n°94-18, 1994
- ¹⁷ P. Chevret, Ph. Blanc-Benon & D. Juvé, "A numerical model for sound propagation through a turbulent atmosphere near the ground", J. Acoust. Soc. Am. 100(6), 3587-3599 (1996)
- ¹⁸ K. E. Gilbert & M. J. White, "Application of the Parabolic Equation to sound propagation in a refracting atmosphere", J. Acoust. Soc. Am. 85(2), 630-637 (1989)
- ¹⁹ F. D. Tappert & R. H. Hardin, "Computer simulation of long-range ocean acoustic propagation using the parabolic equation method", Proc. 8th Intern. Cong. on Acoustics, 452 (1974)
- ²⁰ W. H. Press, B. P. Flannery, S. A. Teukolsky & W. T. Vetterling, "Numerical Recipes", Cambridge University Press, 1992
- ²¹ M. E. Delany & E. N. Bazley, "Acoustical properties of fibrous absorbent materials", Appl. Acoust. 3, 105-116 (1970)
- ²² K. B. Rasmussen, "Propagation of road traffic noise over level terrain", J. Sound Vib. 82(1), 51-61 (1982)
- ²³ K. B. Rasmussen, "A note on the calculation of sound propagation over impedance jumps and screens", J. Sound Vib. 84(4), 598-602 (1982)
- ²⁴ B. A. de Jong, A. Moerkerken & J. D. van der Toorn, "Propagation of sound over grassland and over an earth barrier", J. Sound Vib. 86(1), 23-46 (1983)
- ²⁵ P. Koers, "Diffraction by an absorbing barrier or by an impedance transition", Proc. Inter-Noise 83, 311-314 (1983)
- ²⁶ X. Di & K. E. Gilbert, "Application of a Fast Green's Function method to long range sound propagation in the atmosphere", Proc. 5th Intern. Symp. on Long Range Sound Propagation, 128-141 (1992)
- ²⁷ R. Raspet, S. W. Lee, E. Kuester, D. C. Chang, W. F. Richards, R. Gilbert & N. Bong, "A fast-field program for a layered medium bounded by complex impedance surface", J. Acoust. Soc. Am. 77, 345-352 (1985)

Lamb Waves from Small Explosions: Boundary Layer Effects

D. O. ReVelle (*), R.W. Whitaker (**)

Earth and Environmental Sciences - 8,
Los Alamos National Laboratory
Los Alamos, New Mexico 87545 USA
(505)-667-1256
(505)-665-3681 FAX

(*) email: dor@vega.lanl.gov
(**) email: rww@lanl.gov

S.N. Kulichkov

Obukhov Institute of Atmospheric Physics
Russian Academy of Sciences
3 Pyzevsky
Moscow, 109017 Russia
7 (095) 233-4876
7 (095) 233-1652 FAX
email: snk@omega.ifaran.ru

ABSTRACT:

We have used the Pierce-Posey-Kinney (P-P-K) normal mode waveguide code which has been modified at Los Alamos to efficiently search for the WKB acoustic modes from smaller energy releases of current interest to the CTBT IMS (Comprehensive Test Ban Treaty, International Monitoring System) program. We have chosen a specific explosion to simulate, namely the ~60 t energy release on April 14, 1991 near Moscow that was subsequently detected some 310 km to the north in Saratov by an array of 3 pressure sensors that was operated by the Obukhov Institute of Atmospheric Physics of the Russian Academy of Sciences. The array detected three types of signals from this near-surface explosion. These included Lamb wave arrivals (L type), possibly Stratospheric arrivals (S type) and Thermospheric arrivals (Th type). The simulation also produced three arrivals, but the Stratospheric type arrived later than expected if it has been properly interpreted (0.27 km/s signal speed rather than the more typical value of 0.29 to 0.30 km/s). Computed wave periods and duration of the Lamb waves were quite similar to those observed, but the computed amplitudes were much too small (~30X). This close range amplitude deficiency of the P-P-K code has been known for some time, but we felt that an attempt to model data at the smaller explosive source energies, which are of current interest to CTBT, would allow us to find ways of eventually improving our modal simulations.

I. Introduction and Overview

Historically, Lamb waves from large explosions have been very extensively studied because they are the first distinct arrival with rather large amplitude and long period at very large detection ranges (ReVelle, 1996; ReVelle and Whitaker, 1996). For the smaller sources of current interest to the CTBT IMS program, i.e., ~ 1 kt (TNT equivalent), it is not at all clear that this will be the case. ReVelle and Whitaker (1996) have shown by systematically analyzing

the properties of Lamb waves from smaller yield near-surface sources that it is doubtful that significant Lamb wave amplitudes will be detected at ranges of interest to the 60 array IMS infrasound system. On the other hand, Busch et. al. (1997) and ReVelle and Kulcihkov (1997, 1998) have shown that significant Lamb wave amplitudes can be observed from smaller yield explosions under the right conditions, i.e., when the planetary boundary layer (PBL) has a significant inversion or low-level wind maximum near the surface or further aloft. To evaluate these possibilities further we undertook a discrete waveguide modal analysis for one of the small Russian explosive tests conducted at the Obukhov Institute of Atmospheric Physics near Moscow between 1985-1992.

II. The Pierce-Posey-Kinney: Waveguide Modal Analysis Code

A. The Physics of Normal Mode Analyses

Los Alamos has developed a full working version of the Pierce-Posey-Kinney Waveguide Normal mode code (Pierce and Kinney, 1976) which has been modified to search more efficiently for the WKB modes of smaller yield atmospheric explosions (Hunter and Whitaker, 1998). The gravity waves modes and their properties have been explicitly neglected during this code development process. The source function for a 1 kt nuclear explosion is an input to the model in order to compute, by hydrodynamic scaling arguments for sources that are not at ground level, the expected positive phase duration and amplitude of the wave which is subsequently allowed to propagate further to very large ranges. Thus, in the near field the code is initially calibrated using the theoretical point source explosion waveform which has also been directly checked by careful atmospheric measurements.

Briefly, the physics revolves around the solution of the depth separated wave equation in cylindrical coordinates for a point source explosion in a perfectly stratified, steady state medium having slowly varying vertical gradients of temperature (or of thermodynamic sound speed) and of the horizontal winds. The isothermal definitions of the atmospheric resonant frequencies, i.e., the acoustic wave-guide cut-off and the Brunt-Vaisalla frequency were used during the analysis of the resulting linearized set of equations. The analysis is completely inviscid so that dissipative mechanisms are assumed to be small. For smaller source yields at concomitantly greater ranges at higher wave frequencies this may no longer be a good assumption however. In a companion paper, ReVelle (1998) has examined the effects of the non-isothermal resonant frequency on the predicted skip distance of the Ray-mode theory, etc.

The explosive pulse is then allowed to disperse in the specified atmospheric model and allowed to propagate as a wave using the complete set of modal characteristics available from the linearized acoustic-gravity wave theory (Pierce and Kinney, 1976). All of the ramifications of accurately specifying the upper and lower boundary conditions, constructive and destructive interference phenomena, Doppler shifting of the wave frequency by the horizontal winds, etc. are handled by the P-P-K code. In addition, the code assumes a large scale atmospheric hydrostatic, non-rotating system with zero basic state vertical velocities at all levels, etc. Range dependence properties are no handled with the current version, although there is interest in extending the code to include this important atmospheric property.

B. P-P-K Code Characteristics

The code has been thoroughly tested at Los Alamos. One of its characteristics that has been identified is that at ranges of one bounce or less (<~200-300 km), its predicted amplitude can be greatly underestimated compared to observations, even from larger yield sources, i.e., it is truly a long distance, linear code. The mode code produces the steady state phase velocity versus angular wave frequency for all the acoustic modes specified as a function of horizontal range and of the azimuth direction towards which the signal is beamed from the source.

Depending on the whether the signal is heading upwind (counter-wind) or downwind (with-wind), the atmospheric modal characteristics are very different. A separate synthesis of the amplitude of the waveform is made for downwind compared to up-wind propagation, depending on the details of the resulting duct structure of the atmosphere in the direction(s) of interest. In the downwind case, two atmospheric ducts are evident, one from the ground to the top of the Stratosphere (S type returns) and the other is from the ground to the base of the Thermosphere (Th type) as discussed in ReVelle and Whitaker (1996).

For the computer simulations to be discussed below, the following relevant characteristics have been used for the WKB waveform analysis:

Time resolution of waveform synthesis	0.2 s
Number of modes	100
Phase speed search limits:	
a) Downwind	0.345 to 0.378 km/s
b) Upwind	0.379 to 0.70 km/s
c) crosswind	0.345 to 0.70 km/s
Number of intervals for the phase speed search	60

III. Comparisons of P-P-K Predictions against Infrasonic Observations on April 14, 1991.

We have set up the Pierce-Possey-Kinney (P-P-K) code to analyze the properties of the signal from the 60 T test (TNT equivalent) near Moscow for four directions, i.e., 5 degrees E of N, 5 degrees S of East, 5 degrees W of S and finally for 5 degrees N of West. All pressure waveforms were evaluated at a fixed horizontal range of 310 km corresponding directly to the array measurements made at Saratov by personnel of the Obukhov Institute of Atmospheric Physics of the Russian Academy of Science. These observations included Lamb (L type), Stratospheric (S type) and Thermospheric (Th type) waves recorded at a 3 element array of pressure sensors with a baseline separation between elements of about 20 m. The basic sensors were B&K NO. 4147 condenser microphones with a frequency response from 0.02 Hz to 10 kHz. No noise reduction devices were used during the infrasonic detection of any of these tests. Shots were repeated quite frequently with four shots total having been detonated on this particular day.

A. Discussion of Vertical Temperature and Wind Profiles

The following vertical profiles were used during the analysis:

- a) Boundary Layer Profile: Vologograd
0000 GMT, 4/14/1991 (3 am Moscow time)
- b) Middle Atmosphere Temperature and wind profile:
Vologograd
0128 GMT, 4/17/1991

In Figure 1. And 2. below we have plotted the vertical profiles of the measured temperature and of the horizontal winds in terms of the zonal and meridional components that were measured during this time period. The winds above the Tropopause were actually measured about 3 days after the shot origin time. These winds were characterized by a strong meridional jet near the Tropopause of almost 20 m/s to the North and an almost equally strong zonal wind to the West at about the same height level. In the Stratosphere, there was also a 40 m/s zonal jet heading Eastward at about 55-65 km altitude and a weaker meridional jet peaking at about 50 km at about 20 m/s with vector winds to the South. The combination of these features with the sound speed profile discussed below produced a Stratospheric wave-guide to the East and to the South during the time of this test. Thus, directions to the North and West of Moscow, such as Saratov were in a zone of acoustic shadow for Stratospheric ducting during this time period. For a return at 0.29-0.30 km/s as expected from the Stratosphere (ReVelle and Whitaker, 1996), we expect an arrival time of ~1033-1069 seconds at 310 km range. For Thermospheric returns, we expect an arrival time at this range of ~1292-1409 seconds, corresponding to possible signal speeds of 0.22-0.24 km/s. For Lamb waves we correspondingly expect arrival times of ~886-912 seconds, based on a signal speed of about 0.34-0.35 km/s for these waves.

There may also have been small changes in these wind systems in the Stratosphere since they were recorded some 3 days after the shot. Generally these large scale features tend to remain relatively stable on a time scale of many days, except during rapid changes in the Spring and Fall such as Sudden warmings etc.

The measured air temperature (or thermodynamic sound speed) shown in Figure 1. are characterized by a strong temperature inversion (~ +7 to +15 degrees K/km) in the PBL at quite low levels, i.e., at about 200-250 m above the ground. This was the consequence of a strong nocturnal temperature inversion that developed during the nighttime hours. Even with the strong positive gradient the effective sound speed that was calculated near the ground did not exceed the ground level effective sound speed so that an effective low-level acoustic duct was apparently not evident during these tests. As dawn approached however changes in the boundary layer may have also changed the ducting possibilities of the lowest kilometer of the atmosphere which may have contributed to the variable amplitudes of L and S type returns that were observed throughout the testing period.

Above 80 km, model winds and temperatures were provided by Kulichkov and colleagues since there was no data available above this level.

B. Comparisons With Observations

In order to illustrate the propagation variability as a function of the azimuth launch angle, we have decided to pick four directions each 90 degrees apart, starting at the known location at 310 km range at a direction of 5 degrees East of North in order to compare results.

In Figures 3.-6., we have plotted the P-P-K normal mode calculations in the respective directions indicated in the table below. Examining our simulated arrival times from P-P-K, we have the following distinct arrival types for each of these propagation directions, with approximate peak to peak amplitudes INDICATED in microbars.

		Lamb	Stratosphere	Thermosphere
a)	5 degrees	0.5	?	3.6
b)	95 degrees	< 0.1	9.6	3.9
c)	185 degrees	0.35	0.50	4.0
d)	275 degrees	< 0.1	---	9.0

Thus, our P-K_P results indicate what was mentioned briefly earlier on the basis of the available temperature/sound speed and horizontal wind speed profiles, i.e., a Stratospheric duct existed to the East and to the South of Moscow during these tests. The arrival time of Stratospheric signals is about 1000 - 1050 seconds as indicated in Figures 4. and 5. This is fully consistent with the nominal arrival time range indicated earlier. To the West, only a Thermospheric duct is possible with the ground and this duct is very strong because all the available acoustic energy in this direction is confined to this duct. Only the Stratospheric return at a direction of 95 degrees is slightly larger than the Thermospheric amplitude at a direction of 275 degrees. The predicted Lamb wave return at a direction of 5 degrees, although much smaller than the observed signal at Saratov has the largest computed amplitude for all four directions that were considered.

There is also a distinctive feature that appears in Figures 2 and 4 at an arrival time of about 1150 sec, which is clearly too late to be Stratospheric in origin. This return has a signal speed of about 0.27 km/s, which is too large to be a typical Thermospheric type return. Based on this value of signal speed all we can say is that it is consistent with being a return from the region between 50 and 100 km, i.e., from the Mesosphere.

The detonation site was located at 48.78 N and 45.74 E (near Moscow) and all infrasonic recordings were made at Saratov at 51.54 N and 46.03 E, some 310 km away and at a bearing of about 5 degrees E of N.

The Saratov recordings all showed evidence of returns from Lamb waves, and also returns from the Stratosphere and from the Thermosphere ducts as well. As discussed in ReVelle and Kulichkov (1997), the measured Lamb wave to Stratospheric type amplitude varied quite irregularly during the four tests on the early morning of 4/14/1991. The registered Lamb wave amplitudes, periods and duration during these measurements can be summarized as follows (ReVelle and Kulichkov, 1997):

4/14/1991	Lamb wave signal speed: km/s	Lamb wave amplitude: Pa	Lamb wave period: seconds	Lamb wave duration: seconds
To=09:35 GMT	0.34	1.8+	1.8	8.0
To=10:05 GMT	0.34	1.5	0.9	5.6+
To=13:15 GMT	0.35	2.4	13.3+
To=15:20 GMT	0.33	2.4	7.8

The Lamb wave amplitudes that were measured varied by a factor of up to 4.5 times compared to the amplitude of the measured Stratospheric returns during the experiment. For the earliest test shot on this date, the Lamb amplitude was 2.25 times greater than the S type signal whereas for the shot at 15:20 GMT, its amplitude was only one-half as large as the S type return.

Our predicted Lamb wave amplitudes are clearly much too small (by about 30X), although their period and duration are not too unreasonable given that this is the first test of this code at these very small yields and at such a close range. A. Pierce, the original developer of the numerical code, also commented that the predicted amplitudes should improve at much longer ranges. Further tests are clearly needed to verify all of these predictions. Another factor that needs to be examined is the original waveform needed at the weak shock matching range that is already provided in the P-P-K code. This code was originally setup to examine nuclear explosions for yields of many hundreds of kt and greater and at very long ranges from the explosion. If the equivalent source function for these tests was significantly different in either scaled amplitude or period, these source function parameters could produce at least part of the current discrepancy between theory and experiment as well.

IV. Summary and Conclusions

A. The Pierce-Posey-Kinney Normal Mode Code

We have made four computer simulations using the P-P-K normal mode waveguide code to evaluate the amplitude, period and duration of infrasonic signals from small yield, near-surface chemical explosions at very close range, i.e., ~310 km. This test allowed us to use our WKB mode evaluation system for four directions surrounding the source so that the differences in propagation in each of these directions could be systematically examined. All three types of wave arrivals, i.e., L, S and Th were predicted in differing directions and with different amplitudes, periods and duration.

B. Comparisons against Infrasonic Observations on April 14, 1991

We have compared our predictions against the Russian measurements made at Saratov on April 14, 1991. In general we find a much weaker Lamb wave signal than was measured. We have known for a long time however that the P-P-K code results at such a close range would be expected to be quite low compared to reality. Further detailed tests of the code with additional data is clearly

warranted so that the degree of agreement between theory and observations can be steadily improved for such small yield sources at quite short observation ranges.

V. ACKNOWLEDGMENTS

This work was supported by the Department of Energy, Office of Nonproliferation and International Security, DOE HQ, NN-20.

VI. REFERENCES

- Busch, G.A., S.N. Kulichkov and A.I. Svertilov, Some Results of the Experiments on Acoustic Wave Scattering from Anisotropic Inhomogeneities of the Middle Atmosphere, *Izv. Atmos. And Oceanic Physics*, 33, 445-452, 1997.
- Hunter, J.R. and R.W. Whitaker, Numerical Modeling of Long Range Infrasonic Propagation, Proceedings: Infrasonic Workshop for CTBT Monitoring, Santa Fe, New Mexico, August 25-28, pp. 451-475, 1998 (Available as LA-UR-98-56).
- Pierce, A.D and W.A. Kinney, Computational Techniques for the Study of Infrasonic Propagation in the Atmosphere, Final Report, AFGL-TR-76-0056, 186 pp., March 13, 1976 (Available as AD-A024951 from the National Technical Information Service, Washington, D.C.).
- ReVelle, D.O., The Development and Propagation of Lamb Waves from Airborne Explosion Sources, Available as LA-UR-96-881, 12 pp., 1996.
- ReVelle, D.O. and R.W. Whitaker, Lamb Waves from Airborne Explosive Sources: Viscous Effects and Comparisons to Ducted Acoustic Arrivals, 7th International Symposium on Long Range Sound Propagation, Eds. D. Juve, H.E. Bass and K. Attenborough, Ecole Centrale De Lyon, Ecully, France, July 24-26, pp. 323-337, 1996 (Available as LA-UR-96-3594).
- ReVelle, D.O. and S.N. Kulichkov, Examining Lamb Wave Generation from Small Surface Explosions, Paper A52C-11, EOS, Trans. American Geophysical Union, 78, p. F138, November 18, 1997.
- ReVelle, D.O. and S.N. Kulichkov, On Lamb Wave Propagation from Small Surface Explosions in the Atmospheric Boundary Layer, ISARS'98 (Intern. Soc. Acoustic Remote Sensing of the Atmosphere and the Oceans, Vienna, Austria, July, 3 pp., 1998.
- ReVelle, D.O., Using Modified Mode-Ray Theory to Understand Counter-wind Propagation Effects from Atmospheric Explosions, 8th Symposium on Long Range Sound Propagation, Pennsylvania State University, State College, PA, 15 pp., September 9-11, 1998 (This volume).

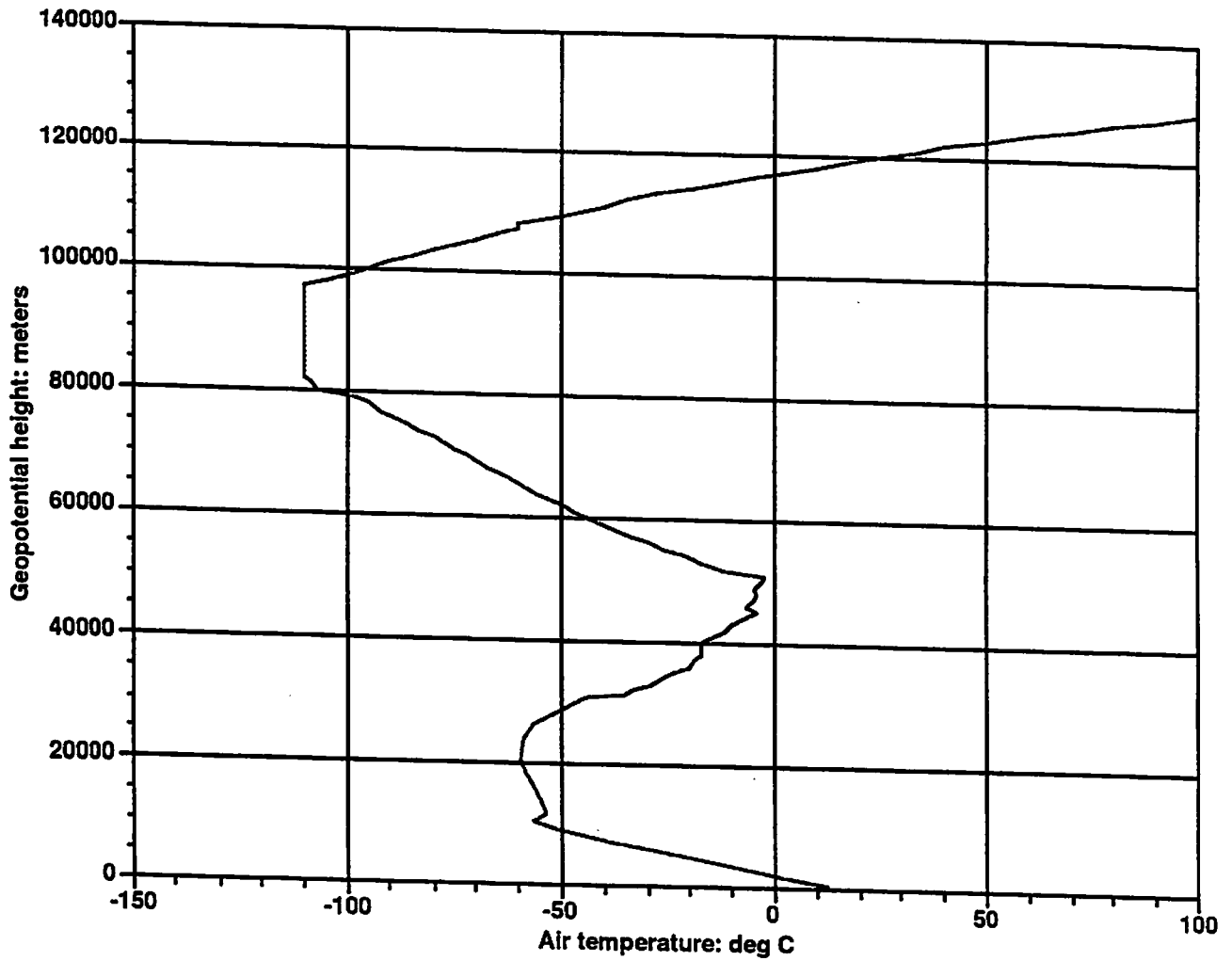


Figure 1. Measured vertical profile of the air temperature (deg C) on April 14, 1991 at Volgograd (< 30 km) and on April 17, 1991 (> 30 km).

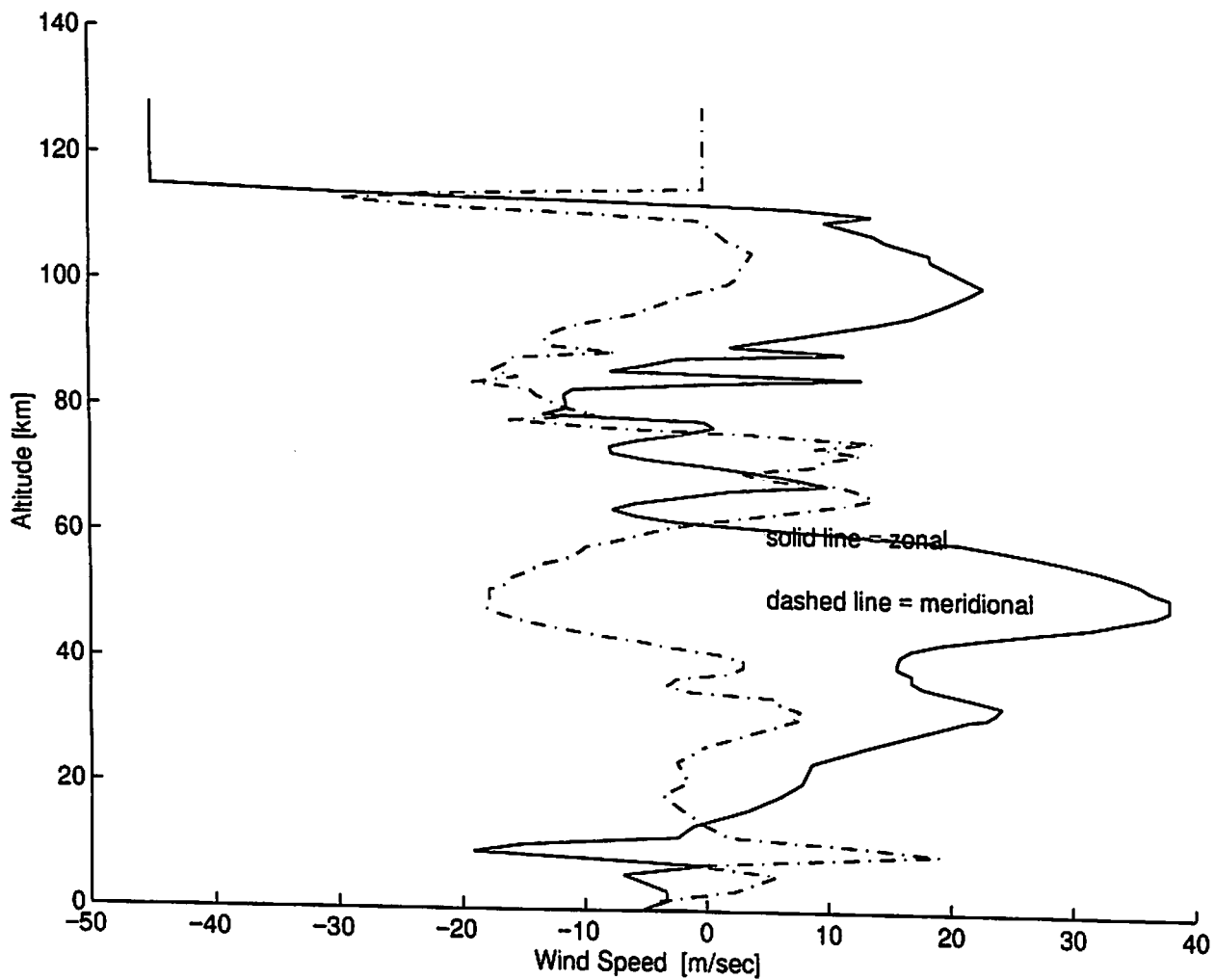


Figure 2. Vertical profiles at Volgograd of zonal and meridional winds for the planetary boundary layer (000 GMT, 4/14/1991) and of the tropospheric and middle atmospheric winds (0128 GMT, 4/17/1991).

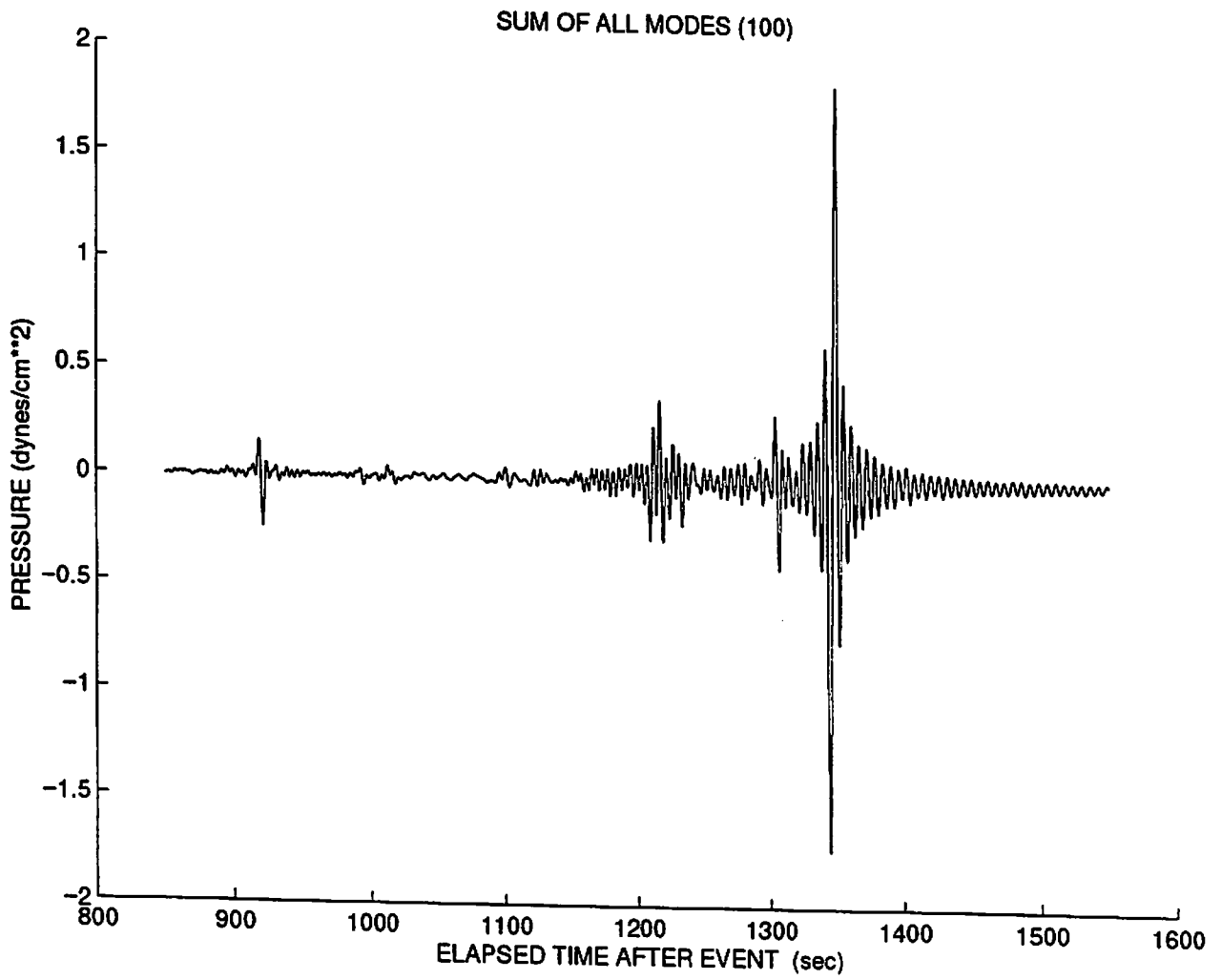


Figure 3. Mode theory prediction for propagation to 310 km range towards 5 degrees East of North (5 deg).

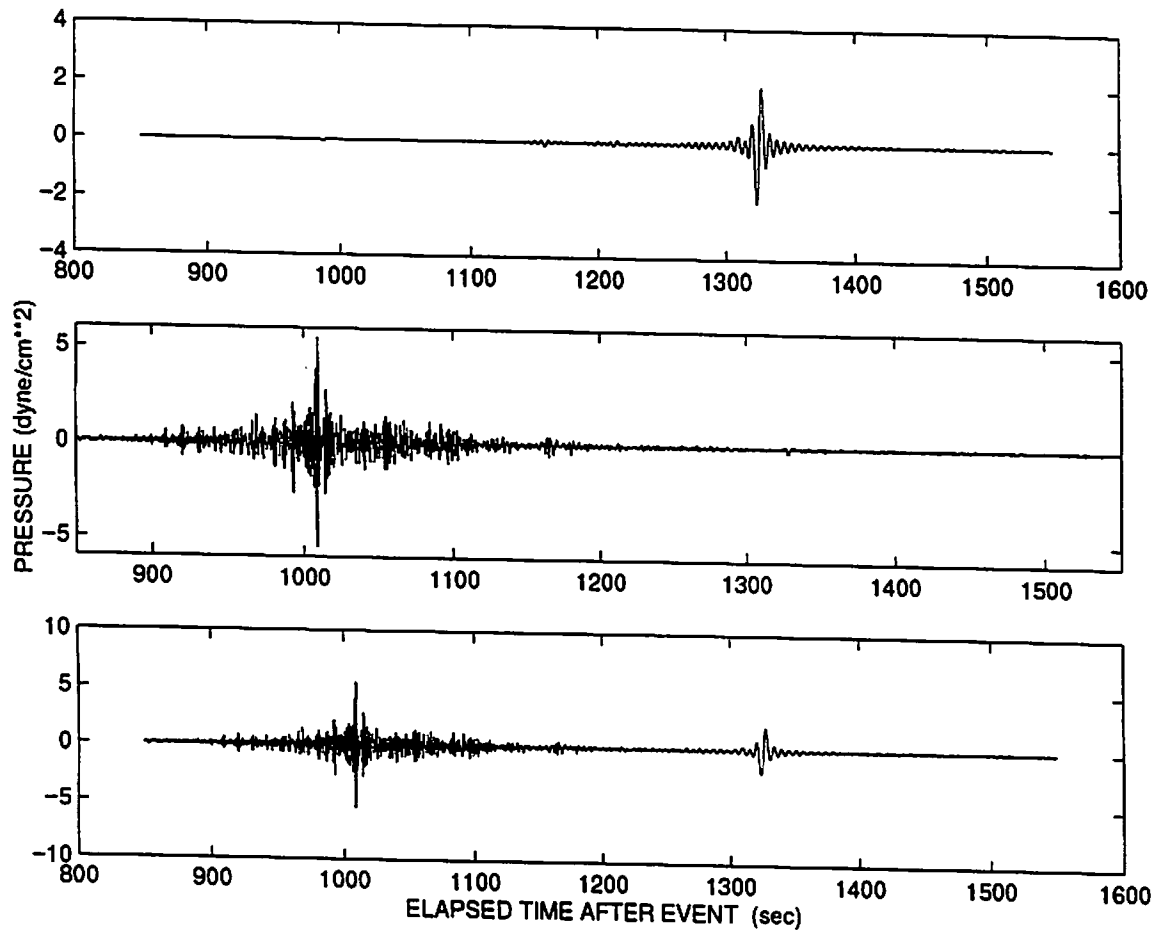


Figure 4. Mode theory prediction for propagation to 310 km range towards 5 degrees South of East (95 deg).

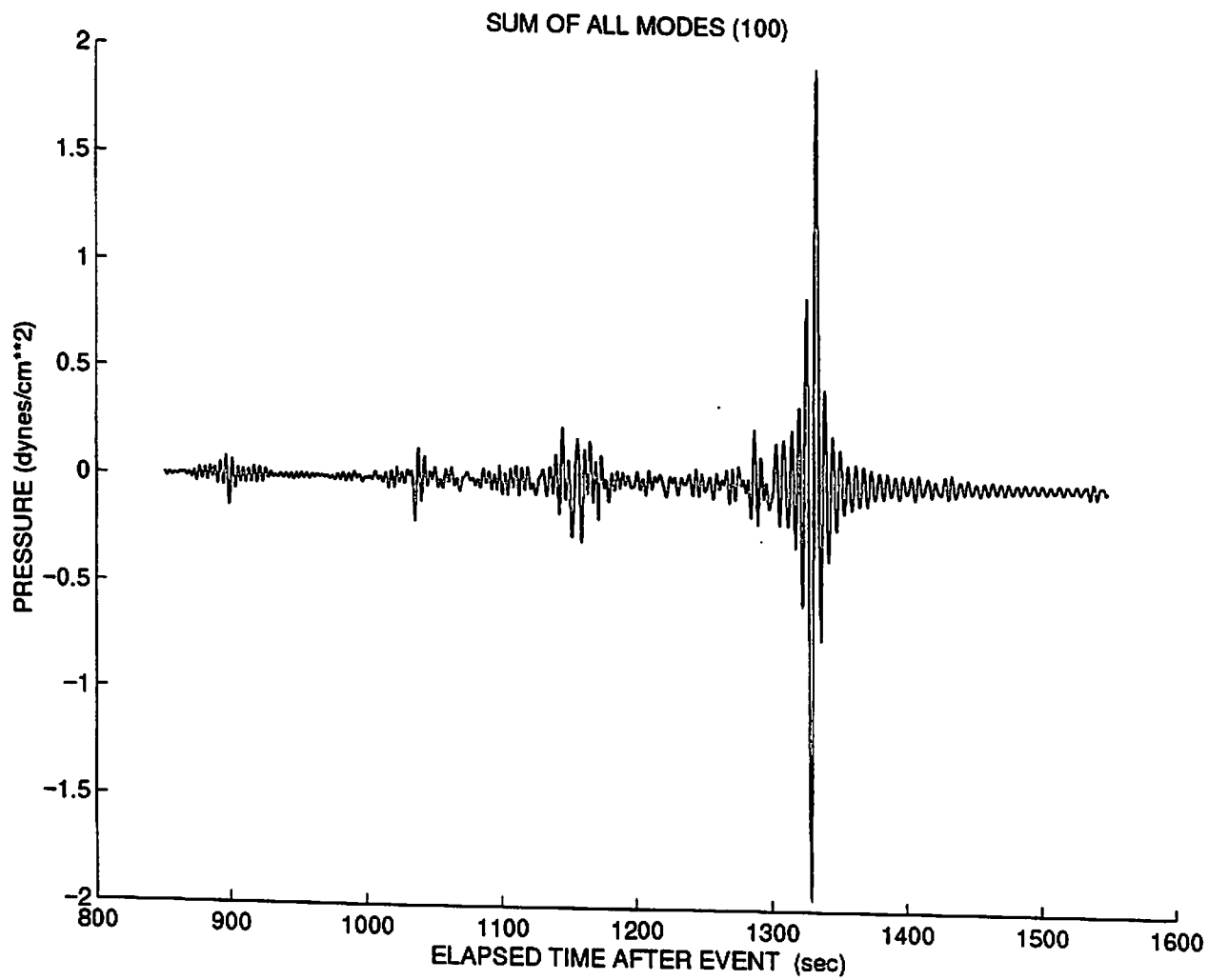


Figure 5. Mode theory prediction for propagation to 310 km range towards 5 degrees West of South (185 deg).

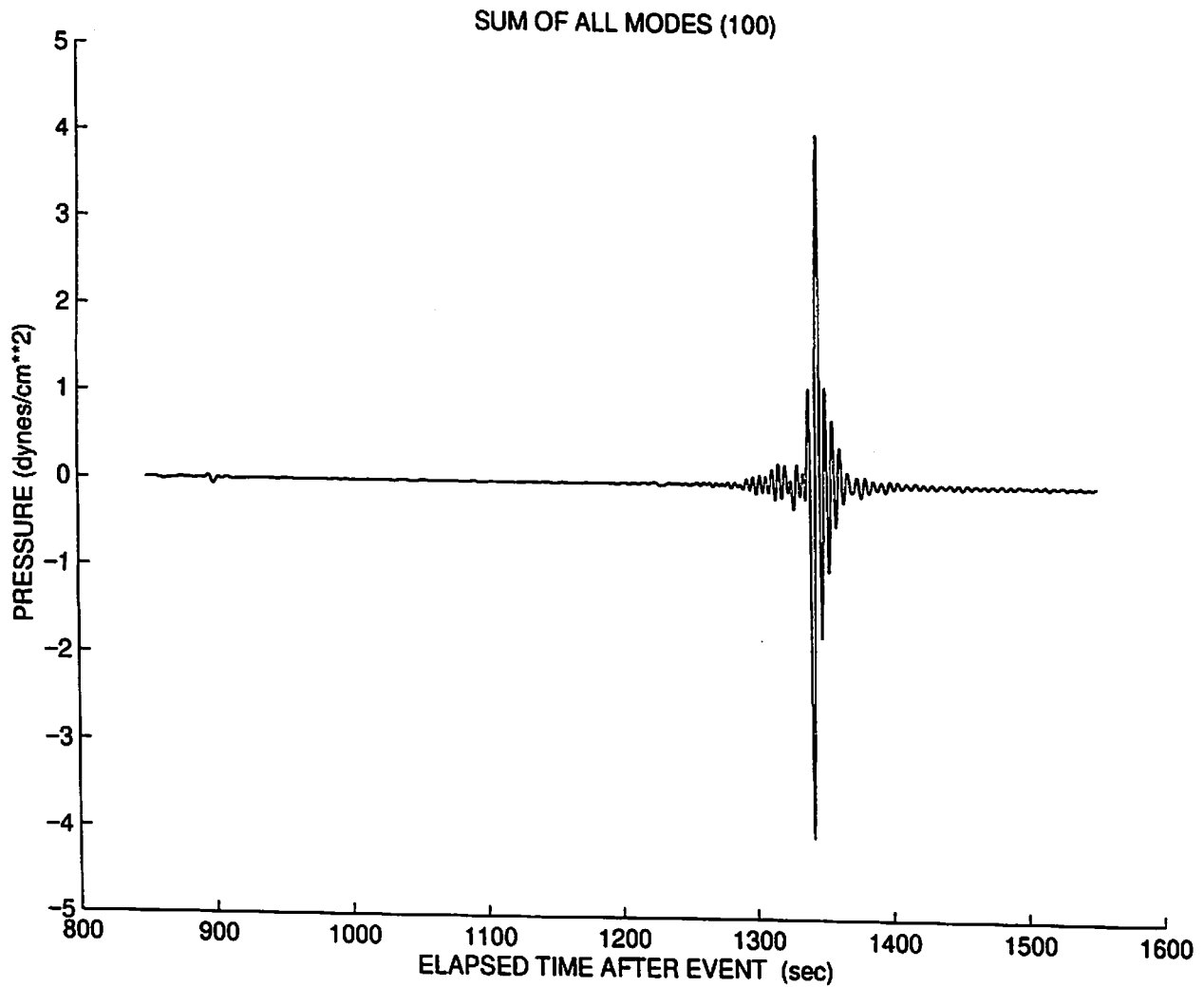


Figure 6. Mode theory prediction for propagation to 310 km range toward 5 degrees North of West (275 deg). The three panels indicate respectively, the individually predicted Thermospheric return, the Stratospheric return and finally the composite prediction of modes from both of the atmospheric ducts.

A PROPAGATION MODEL BASED ON GAUSSIAN BEAMS THAT ACCOUNTS FOR WIND AND TEMPERATURE INVERSIONS

R. L. Bronsdon [1] and H. Forschner [2]

[1] Walt Disney Imagineering, 1401 Flower Street, Glendale, CA 91221, USA

[2] Navcon Engineering Network, 701 W. Las Palmas Drive, Fullerton, CA 92835, USA

1. INTRODUCTION

The model discussed has sought to more accurately predict sound propagation in inversion conditions so as to provide an engineering tool for the placement of sound sources in sensitive urban environments. It is based on Gaussian Beams to preserve the fundamental concept of a propagation path which allows the use of standardized calculation routines for barrier insertion loss. Validation studies have shown that continuous variations in wind, temperature, and ground absorption all along the propagation path have profound effects on the received level. Any model which fails to deal with these parameters is not likely to have much success in accurately predicting the impact of a sound source on the community. This paper will present results from the validation testing and compare them with results both from the Gaussian Beam and PE models.

2. THE GAUSSIAN BEAM MODEL AND SOUNDPLAN

The Walt Disney Company and Braunstein and Berndt GmbH, the company producing the SoundPlan program, have undertaken to develop a more accurate model for long range sound propagation. The problem faced by many noise producing activities in urban environments is that certain atmospheric conditions, temperature inversions and wind, tend to either reduce or totally eliminate the effectiveness of noise barriers leading to complaints in the surrounding community. Traditional models such as the General Prediction Method (GPM) and the German VDI 2720 account for this bent path propagation by employing an empirical curved path based on an arc. This curved transmission path is used to calculate barrier insertion losses in place of a straight path and degrades the barriers effectiveness.

Experiences at current installations indicated that the standard approaches tended to underestimate the amount of sound which reached the community by a considerable amount. The problems occurred during times of strong radiational cooling; clear skies and very low wind. The apparent effect was obviously related to a more strongly downward bending sound field but the GPM and VDI are only calculated for one meteorological condition. The CONCAWE method does attempt to account for various types of conditions but the corrections are based on experimental data and, being anecdotal in nature, are applied as a constant degradation behind the barrier.

An approach was developed with Drs. Ken Gilbert, Xiao Di, and Alan Stuart which is based on the concept of Gaussian Beams. The basic program, Gausbeam, calculates the beam paths for a given set of temperature and wind conditions for a full 180 degrees around an arbitrary sound source of known height above an absorptive plane. This model has the benefit of preserving the concept of propagation path while enabling a path computation based on actual conditions. The path and Transmission Loss data are then handed over to the SoundPlan program which calculates barrier insertion losses based on the newly calculated curved paths. Gausbeam employs the concept of Similarity in determining from either two or three temperature data points and two wind data points what the average sound speed profile will be for each angle relative to the direction of the wind. SoundPlan then employs these path calculations in the generation of noise estimates and grid maps.

Figure 1 shows that the Gausbeam path estimate for a range of 2200 meters is considerably higher than the GPM. This means that the actual barrier insertion loss should be considerably lower than the GPM would predict. As inversion conditions strengthen, the arch becomes more pronounced and more

and more receivers are exposed to propagation paths which are unaffected by the barriers which normally provide some relief.

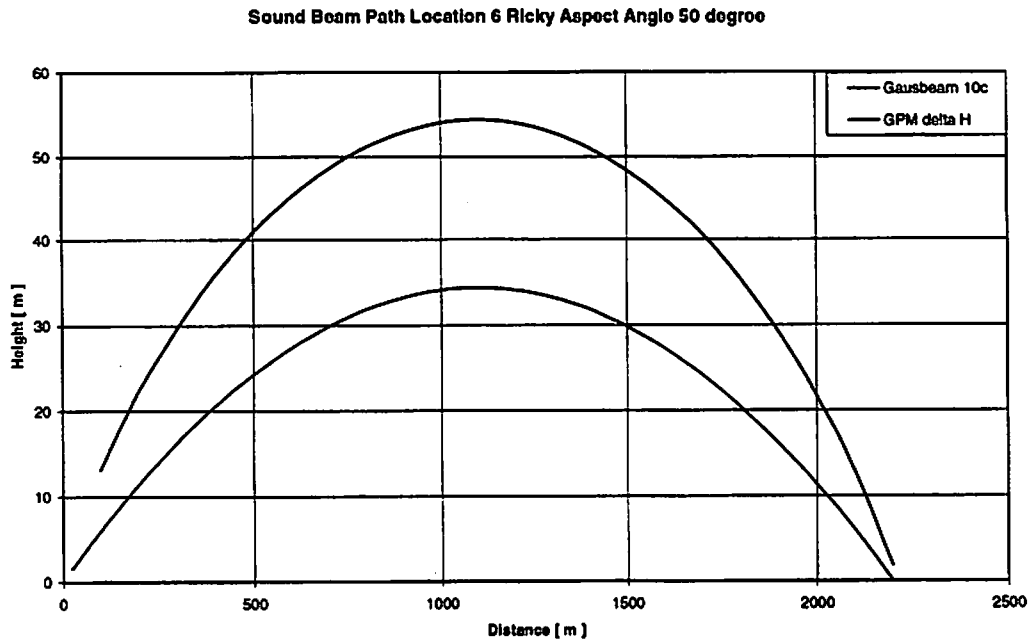


Figure 1: Comparison of Gausbeam and GPM Propagation Paths

The output files generated by Gausbeam are shown in Figure 2. Figure 2.a shows the temperature and wind profiles for a typical inversion condition. If wind is a factor, the program must then calculate a sound speed profile for each ten degree increment for 180 degrees around the source as the effect of the wind on the sound speed profile will be dependent on the aspect angle. This is shown in Figure 2.b. The predicted propagation paths and the TL are shown in Figures 2.c and 2.d respectively.

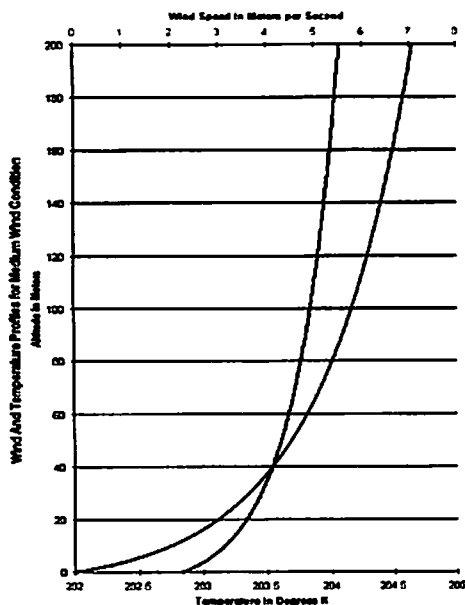


Figure 2.a: Wind and Temperature Profiles

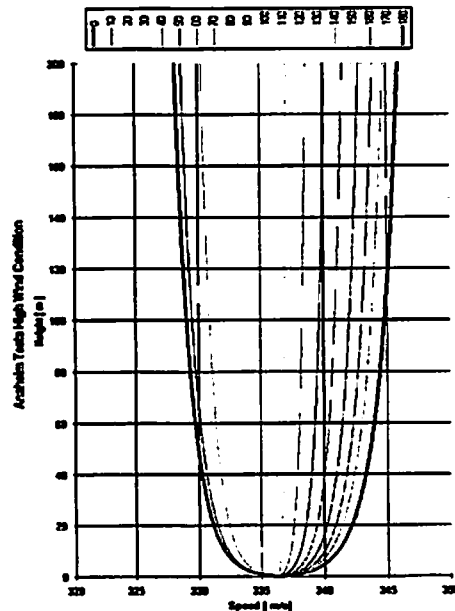


Figure 2.b: Sound Speed Profiles for 180°

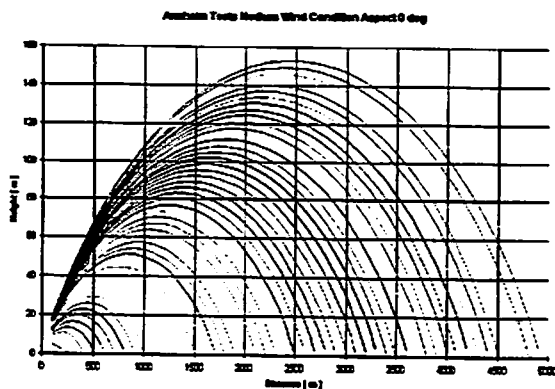


Figure 2.c: Predicted Beam Paths for Upwind Condition

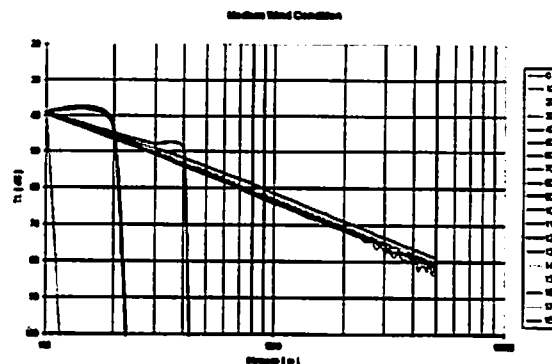


Figure 2.d: Predicted Transmission Loss

The SoundPlan model takes the aspect angle into account when looking up the propagation path information for every source/receiver combination and can either do a point to point calculation for a specific receiver, or generate a grid map for an entire project area. Figure 3 shows a grid map for the testing done in Anaheim. The sound shadow of the buildings and the effect of the inversion can be clearly seen.

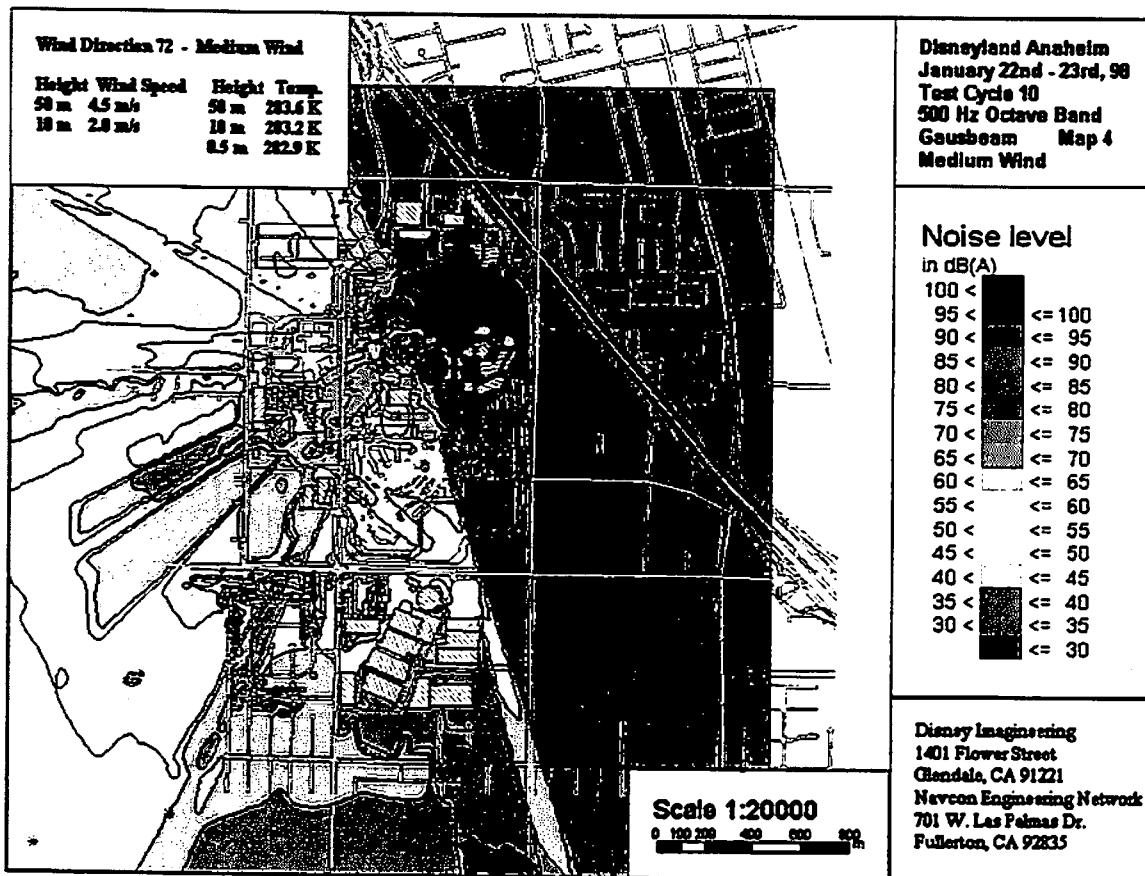


Figure 3: SoundPlan Grid Map for Anaheim Testing

3. VALIDATION TESTING

Validation testing was undertaken at the end of 1997 to provide both validation of the modeling technique and also hard data for final programming modifications. Tests were performed at both Edward's AFB and in Anaheim at the Disneyland facility. The tests at Edward's made use of a simplified environment with a flat ground plane and a single building as a barrier. The source was a single speaker playing band limited pink noise. Logging sound level meters were placed at intervals along a straight line behind the building. Meteorological data was collected continuously at four heights and logged on a ground station for the duration of the testing. Similar systems were employed in Anaheim, as shown in Figure 4, but the locations of the sound level meters was dictated by the roads and buildings and were, therefore, more dispersed. Sound data were collected out to a range of 2600 meters and the source was a speaker array already installed in the park.

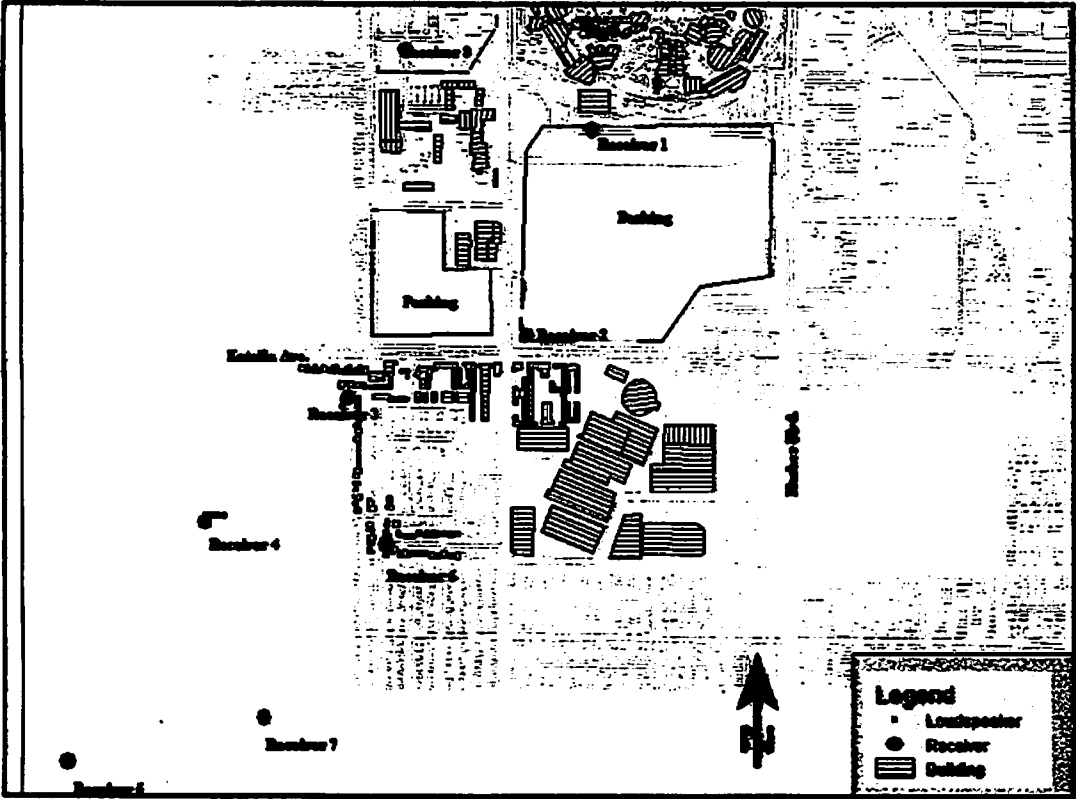


Figure 4. Testing setup in Anaheim

Figure 5 compares the testing results from Anaheim with the various prediction models available in SoundPlan. The data points are averaged received levels for the two minute tests at 500 Hz. There were ten tests in all over one nights testing. The black data points represent the highest level received during that test period, independent of the time period over which that maximum was experienced. Overall, there is excellent agreement between the predicted average performance from Gausbeam and the measured average performance. The General Prediction Method tracks almost as well with better predictions at short ranges and more error at long ranges. The CONCAWE and VDI standard both seem to do a poorer job of predicting the results. None of the models is consistently predicting the maximum. The VDI does appear to come close at several locations, but the prediction is not consistently high.

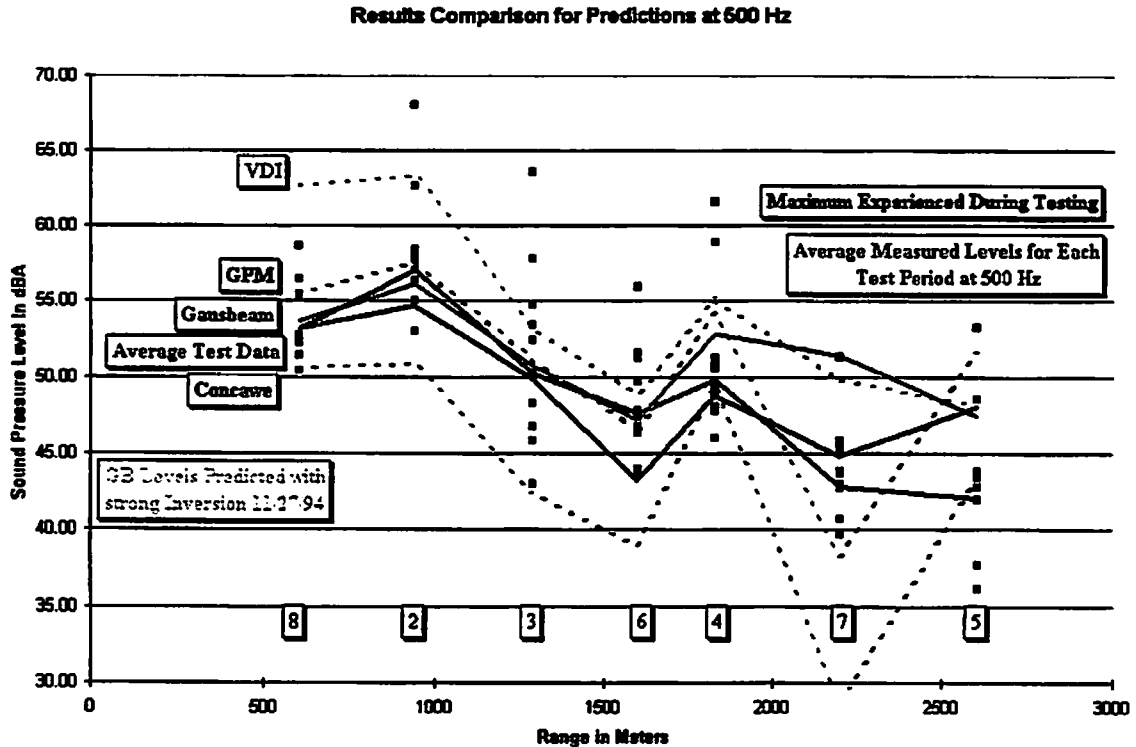


Figure 5: Comparison of Test Results and Predictions for Anaheim Testing

All of the models used were designed in some way to account for inversion propagation so they each show some modification to the barrier insertion loss at increasing range. The variations reflect the appropriateness of each models assumptions as to what constitutes an "average" condition, and how that average condition relates to the actual conditions experienced on the night of testing. The advantage that Gausbeam has over the other models is that actual meteorological conditions can be used. The grid map shown in Figure 3 demonstrates another important consideration. When wind is a strong influencing factor, as it is almost always bound to be, Gausbeam can provide accurate predictions and even show upwind ducting as a function of angle relative to the wind. None of the other models takes wind into account at all. The accuracy of the other models is due in large part to the fact that the wind, which was a strong factor in the actual inversion that was experienced on the night of testing, was predominately blowing from the source to the receivers. If the wind had been blowing from the receivers to the source, the other models would have failed to predict the upward bending sound field and would therefore have strongly over predicted the results.

The detailed analysis possible with SoundPlan allows one to determine what constituents are most important in determining the received sound level at each location. The model is quite sensitive to local barriers at both the source and receiver, ground attenuation, and local reflecting surfaces. We found that placing the houses around the sources was important as at least one measurement location was in the shadow of a two story house and another was impacted by multifamily units. The inclusion of these barriers reduced the level considerable, but extraneous houses also added as much as 5 dB in reflected sound to the prediction.

Figure 6 shows how received levels varied over the time of one test in Anaheim. The conditions during these tests were dominated by a subsidence wind from the mountains out to sea. This wind is characterized by a pronounced increase in wind velocity just above tree level to a height of about 50 to 60 meters where it then returns to a velocity which remains fairly steady with increasing height. The large fluctuations in level are most likely due to short term fluctuations in the wind. Figure 7

shows how variable the wind was during the testing. This plot displays wind speed and temperature as a function of height. It was obtained by raising and lowering a single sonde on a tethered balloon. The ascent and descent required about 13 minutes each so the data represents the variability over less than one half hour.

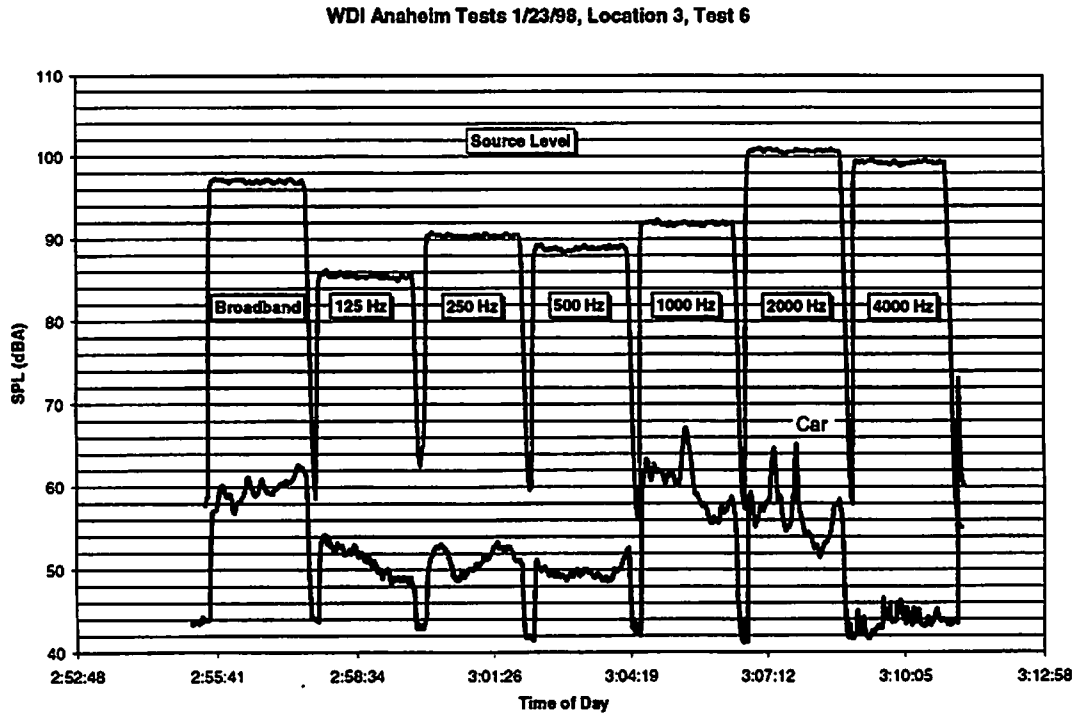


Figure 6: Variation in Received Level with time in Anaheim

The data points represent the average wind and temperature data for the time period of each test. The curves show how the instantaneous wind and temperature deviate from the average. A PE model was run with the inputs shown in Figure 7. The results are shown in Figure 8. It is clear from this that variations in wind speed profile could have accounted for the short term fluctuations in the received level.

These fluctuations are caused by sound channels, or elevated ducts, which form and dissolve as the wind conditions change with time. It is clear from Figure 5 above that average conditions do not always predict the impact of noise on a surrounding community. The response to a level near 50 in a urban environment is probably going to be a lot less severe than the response to levels in the high 60's. These sound channels may only exist for less than a minute but the impact is profound. The problem is that in an urban setting, there is almost always somebody sitting in the HOT ZONE when a sound channel forms.

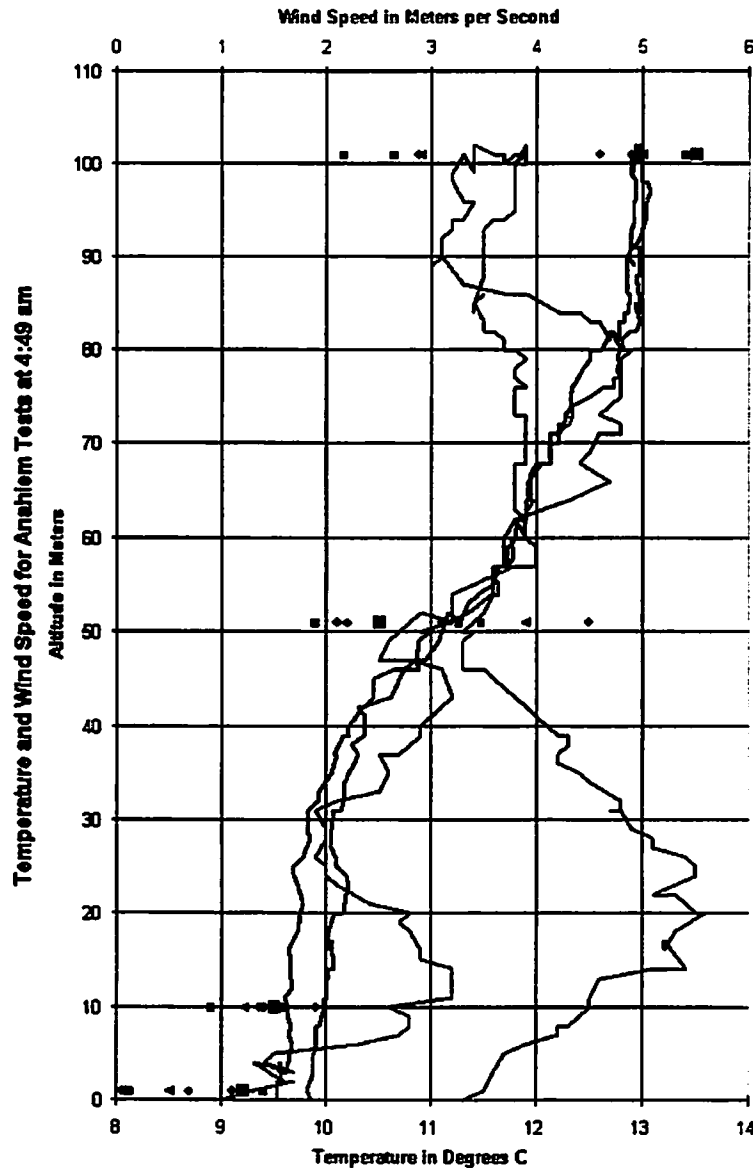


Figure 7: Meteorological Profiles Measured in Anaheim

Elevated ducting of sound explains much of the short term variability that is experienced in the measurements, but it can also be extended to any other type of measurement over long distances. Most notably, highway, rail, and aircraft noise measurements would be severely impacted by this type of propagation. In fact, we have all had experience with these types of phenomenon although it has not been well documented. Who has not had the experience of perceiving that suddenly a noise source, perhaps a train or a highway, seems to have moved closer or heard the sound of a passing jet airplane ebb and build far out of proportion with the airplanes path of flight.

This is not similar to the inclusion of a random variable disturbance in a PE computation, but rather, a specific, large scale, disturbance in the meteorology of the sound propagation medium. These disturbances are on a much smaller scale than those that affect long range sound propagation in the ocean, but their affects are pronounced. Extreme variations in level are possible, and in fact, have been experienced by many who have tried to document noise levels.

Ascending Sonde at 4:45 am in Anaheim

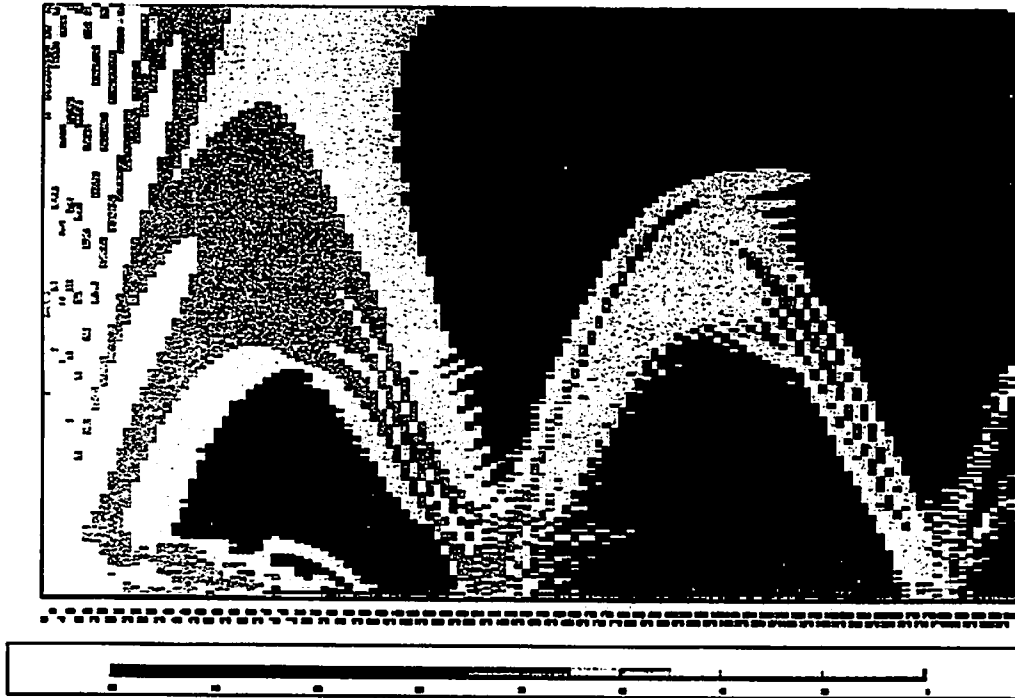


Figure 8: PE model results for Anaheim tests

4. CONCLUSIONS

The validation studies have shown good agreement between predictions and measurements for inversion conditions when modeling long term averages of wind and temperature and comparing the predictions to long term averages of received level. These predicted results now provide for a design which is not only functional in benign meteorological conditions, but one which functions in the more difficult inversion conditions. There are, however, short term fluctuations in these parameters which can lead to large increases in the received level. Complaints from the surrounding community are frequently a response, not to average levels which exist for most nights of the year and which may well conform to community noise regulations, but to seasonal peaks which clearly do exceed the regulations. The straw that broke the camels back so to speak. A noise containment design must surely deal with averaged parameters as well, but those special nights can now be predicted based on real conditions existing at the site on a regular basis.

The Gausbeam model has been developed to provide a more accurate tool for calculating sound propagation over distances of many kilometers based on actual meteorological conditions. It is an excellent design tool that allows the user to evaluate the effectiveness of barriers and reflectors all along the propagation path. The model can not deal with ducted propagation down wind because there is no provision for putting arbitrary sound speed profiles into it but that does not reduce the effectiveness or usefulness of the predictions. If a noise control design is successful in controlling emissions which could potentially be bent downwards by temperature or wind inversions, then that design will also avoid exciting potential ducting paths. Our experience has been that problems of noise intrusion into the community are normally related to either a clearly definable breach in the sound containment system or a specific, well defined, set of meteorological conditions. The trick will come in being able to accurately describe those conditions so that the model predicts the true impact of the sound source. This means that predictions need to be made based on meteorological

conditions which represent the typical worst case and not the yearly average. It also means that demonstrations of a sound containment system should be carried out under realistically difficult conditions as opposed to conditions where the atmosphere is either benign or even providing additional insertion loss. A direct result of this, of course, is that testing usually has to be carried out at night.

Sound propagation models may well eventually be based on three dimensional PE style computations where the PE and the Physical Space model are integrated together. Any model which ignores the actual wind and temperature profiles which are likely to exist is not likely to have much success in predicting the real sound pressure levels to which the community is responding with complaints. Current research is directed primarily at defining accurate models which are based on the physical laws that govern sound propagation. This represents just the first step in more accurate predictions. Results from the testing in Anaheim clearly show that meteorological models are of equal importance if one wishes to accurately predict the impact of a sound source on the surrounding community.

ON THE DEVELOPMENT OF APPROXIMATE MODELS FOR OUTDOOR SOUND PROPAGATION

Karsten Bo Rasmussen, Dept. of Acoustic Technology, Building 352
Technical University of Denmark, DK-2800 Lyngby, Denmark
Phone: +45 45 25 39 39 Fax: +45 45 88 05 77 Email: kbr@dat.dtu.dk

ABSTRACT

The suitable prediction model for outdoor sound propagation depends on the situation and the application. Computationally intensive methods such as Parabolic Equation methods, FFP methods and Boundary Element Methods all have advantages in certain situations. At present, none of these approaches are able to handle all the relevant aspects of propagation such as terrain features, atmospheric wind and temperature gradients and turbulence. How much wind can be tolerated when a model based upon a still homogeneous atmosphere is used? How does a terrain feature affect the sound propagation? An attempt is made to answer these questions and to obtain an increased understanding of the limits between which various approaches are applicable. This should help identifying the more promising approach for various applications.

INTRODUCTION

When outdoor acoustics are dealt with, a range of different calculation models are developed and used for various purposes including thermodynamic air absorption, prediction and analysis of outdoor sound fields with varying demands for accuracy and under different conditions. By nature, theoretical models deal with simplifications, and models predicting the interaction of the field from a point source with a surface having finite impedance are no exception. Computer models dealing with clear-cut cases such as propagation over a level ground surface with or without the presence of a screen and with or without the influence of wind and turbulence have been developed and will continue to be improved. Such models are usually tested in cases where the parameters investigated have a very significant influence of the result. The purpose of the present work is to investigate some limiting cases where the scenario falls between the simple categories. Two fundamental cases are looked into. The first case is an impedance surface which is almost but not quite level. The changes in level are not easily taken into account using analytical mathematical models except for Boundary Element Calculations which are time consuming. The second case is the limiting case of weak wind over an impedance surface. For short distances the influence of the wind speed is marginal and does not always behave according to conventional theory based upon effective sound speed profiles. The insertion loss of screens under the influence of wind is also commented on.

The purpose is to obtain some guidance as to how much measurements are influenced by such irregularities that will inevitably occur in practice. Such knowledge is useful in relation

to the applicability of existing calculation models as well as for the development of new models.

COMPLICATED TERRAIN GEOMETRY

The only well investigated case of complex geometry is the case of a simple screen. In this case various approximations can be used in order to obtain simulated results for the influence of the screen¹⁻². In this section we shall look into experimental data for a terrain where part of the surface is lowered slightly in comparison with the general level of the terrain (ditch-configuration). This case could be solved by means of Boundary Element calculations, but such an approach is impractical for longer distances or higher frequencies. An alternative approximate approach has been developed by Plovsing^{3,4} by means of Fresnel zone interpolation of different solutions for a simple plane ground, as previously developed by Hothersall and Harriott⁵ for the case of impedance variations.

The terrain geometry for which experiments have been performed is described in figure 1 and measured and calculated results are given in the time domain as well as in the frequency domain in the figures 2-6. The measurements have been carried out in a scale model based upon a 1:25 scaling ratio. The ditch is made of plywood and covered with fabric in order to obtain a suitable impedance ($\sigma=20 \text{ kNsm}^{-4}$ and $d_c=0.0167 \text{ m}$ in the 2PA model⁶). All distances and frequencies and impedances refer to full scale. Details about the scale model set-up may be found in Rasmussen².

Figure 2 shows time domain results for the ditch geometry. The measured data are from the scale model experiment, and the simulated data are based upon calculations for level terrain. The dashed curve is based upon calculations where the heights are taken from the bottom of the ditch instead of from the top. Obviously neither assumption is correct, and the first part of the measured response resembles the results for increased heights, whereas the latter part resembles the data for the original heights. This indicates that both terrain levels are at play and it actually turns out that the specular point of reflection is located on the terrain slope representing the transition between levels on the receiver side of the ditch.

The frequency domain results in figures 3 and 4, representing a 0.5 m receiver height, show that the measured data agree well with the Fresnel zone approach and that both terrain levels influence the results. For the 0.5 m receiver height the specular reflection point is located on the terrain slope, as mentioned above, whereas it is located in the bottom of the ditch for the cases of 1 m receiver height. Therefore the results for the greater receiver height (figures 5 and 6) should be well represented by the calculations for plane ground for increased heights (taking the bottom as reference) in the case of high frequencies, where the Fresnel zones are small. This is especially clear for the 15 m case, where the ditch occupies a larger proportion of the propagation path.

The overall picture is that a level change of 0.38 m leads to very significant changes in spectrum at the receiver point. The sound pressure level is affected from the low frequency dip and upwards in frequency. The results shown here, and additional results for a single change in level along the propagation path support the validity and usefulness of the Fresnel-zone calculation. As a more precise alternative to the Fresnel approach, Parabolic Equations could be used in combination with a field extrapolation technique⁷. This approach would be more

efficient for long distances than the choice of Boundary Elements⁸, but it would suffer from a potential source of inaccuracy because of the field extrapolation necessary when downslope propagation is involved⁷. Calculation methods based upon diffraction theory have been successful in many cases⁹ but are not well suited for taking small terrain features into account since they rely on obstacles having physical dimensions greater than one wavelength.

ON THE INFLUENCE OF WIND

The figures 7-11 demonstrate the influence of moderate wind. The measurements are carried out in model scale for a surface representing a full scale impedance of $\sigma=7 \text{ kNsm}^{-4}$ and $d_s=0.0160 \text{ m}$ in the 2PA model⁶. All parameters are referred to full scale conditions rather than model scale. The source height is 1.5 m. The wind speed was about 4 m/s, see figure 7. The measurement procedure is described in Rasmussen¹⁰. Simulations for no wind and measurements for no wind are included for comparison. Simulations using Crank- Nicolson PE-calculations^{7,11,12} are included for the logarithmic sound speed profile.

For the 15m distance the measured curves with and without wind follow each other closely until frequencies around 1kHz, whereas the deviations occur even for low frequencies for the 30 m distance. The influence of wind at lower frequencies is not predicted accurately by conventional state-of-the-art calculations, employing an effective sound speed gradient, as may be seen from the simulated data present in the figures for 30 metres. For the short distance of 15 metres, PE- type calculations suffer from near field problems at low frequencies. These deviations are moderate but in order to keep the focus on the influence of wind, the simulated data for no wind is also based upon PE-calculations. Hence, both simulated curves are subject to the same near field deviations and the wind is seen to have negligible effect. This means that theory predicts essentially no influence of this wind speed profile at low frequencies for 15 m as well as for 30 m, whereas measurements show that the wind does affect the levels at low frequencies for the 30 m distance.

The wind speed profile taken into account in these figures is given by,

$$v=v_0 \ln(z/z_0) \quad (1)$$

where $v_0=0.434 \text{ m/s}$ and $z_0=0.000108266$.

Figures 12 and 13 show measured data compared with PE-calculations. The measured data are from Rasmussen¹³ and were carried out in full scale over a grassy area. The same trend as for the above scale model results is seen in these full scale data for grass covered ground. The influence of wind at low frequencies is clearly more pronounced in measured data than in simulated data. These low frequency deviations occur regardless of the use of FFP type calculations¹⁴ or PE type calculations. The difference between measured and calculated data could be caused by the precise shape of the sound speed profile, but this is unlikely, since simulations show that low frequency data are insensitive to the exact shape of the profile¹⁵. The deviation is probably due to the limitations inherent in the effective sound speed profile approach. The primary reason for this deficiency in the state-of-the-art calculation methods is probably the symmetry around the source which is assumed in the models and which is not present under windy conditions. Further research into calculation methods taking wind into

account appears to be needed¹⁶.

The wind speed profile used in the simulations representing these full scale measurements was determined by $v_0 = 0.402$ m/s and $z_0 = 0.02$ for downwind and by $v_0 = -0.322$ m/s and $z_0 = 0.02$ for upwind.

The figures 14-16 provide a brief illustration of insertion loss of screens under windy conditions. The data originate from recent scale model experiments¹¹. It is seen that even very moderate wind speeds produce very significant changes in the insertion loss. These changes may be estimated by means of range dependent PE-calculations taking not only the wind speed profiles but also the estimated rate of change of these profiles as a function of range into account. Such results are shown in Figure 16. With some support from flow measurements the wind speed profiles have been assumed to be logarithmic even close to the screen. The wind speed function as a function of distance was found by means of interpolation between parameter values (v_0, z_0) obtained in positions before, over and after the screen. The interpolation took place in a zone beginning 5 m before the screen and ending 15 m after the screen. Turbulence has been ignored in these calculations. These results are described in detail in Rasmussen and Galindo¹¹.

CONCLUSION

When sound propagation in still air is considered, a change of height in the terrain may have a considerable influence even when the wavelength is as long as five times the change of height. A very useful first order approximation may be obtained by Fresnel-zone interpolation^{3,4}. More precise calculations must be based upon Boundary Element approaches or Parabolic Equation approaches.

When plane ground is considered, wind speeds of 2-4 m/s may influence the sound pressure level for distances as short as 20 m. This influence is stronger than predicted by the common effective sound speed profile interpretation of the wind and further research is needed.

When the insertion loss of screens is considered, even very moderate wind may have a 10 dB influence on the result. Any new screen design should therefore be tested for performance under the influence of wind.

REFERENCES

- ¹ D.C. Hothersall, S.N. Chandler-Wilde, M.N. Hajmirzae, "Efficiency of single noise barriers," *J. Sound Vib.* **146**, 303-322 (1991).
- ² K.B. Rasmussen, "Model experiments related to outdoor sound propagation over an earth berm," *J. Acoust. Soc. Am.* **96**, pp. 3617-3620 (1994).
- ³ B. Plovsing: "Outdoor sound propagation over a valley-shaped terrain," *Proc. Internoise 98*, 1998
- ⁴ B. Plovsing and J. Kragh: "Prediction of sound propagation in a homogeneous atmosphere over non-flat terrain," *DELTA Acoustics & Vibration Report No. AV 907/97*, 1997.
- ⁵ D.C. Hothersall, J.N.B. Harriott, "Approximate models for sound propagation above multi-impedance plane boundaries," *J. Acoust. Soc. Am.* **97**, 918-926 (1995)
- ⁶ Eq. 12 in K. Attenborough, "Ground parameter information for propagation modelling," *J. Acoust. Soc. Am.* **92**, 418-427 (1992)
- ⁷ Galindo Arranz The parabolic equation method for outdoor sound propagation, Department of Acoustic Technology, DTU, Report No. 68 (1996).
- ⁸ P. Jean, "A variational approach for the study of outdoor sound propagation and application to railway noise," *Journal of Sound and Vibration* **212**, 275-294, (1998).
- ⁹ K.B. Rasmussen "On the effect of terrain profile on sound propagation outdoors," *Journal of Sound and Vibration* **98**, 35-44 (1985).
- ¹⁰ K.B. Rasmussen, "Sound propagation over screened ground under upwind conditions," *J. Acoust. Soc. Am.* **100**, 3581-3586 (1996).
- ¹¹ Karsten B. Rasmussen, M. Galindo Arranz., "The insertion loss of screens under the influence of wind", Accepted for publication in *J. Acoust. Soc. Am.* (1998)
- ¹² Gilbert, K.E., White, M.J. "Application of the parabolic equation to sound propagation in a refracting atmosphere," *J. Acoust. Soc. Am.* **85**, 630-637 (1989).
- ¹³ K.B. Rasmussen, "The effect of wind and temperature gradients on sound propagation outdoors," Danish Acoustical Institute, Report 124 (1985)
- ¹⁴ K.B. Rasmussen, "Computer simulation of sound propagation over ground under the influence of atmospheric effects. Letter to the editor," *J. Sound Vib.* **141**, 347-354 (1990)
- ¹⁵ K.B. Rasmussen "Sound propagation over ground under the influence of a sound speed profile in the atmosphere" *J. Sound Vib.* **139**, 71-81 (1990)
- ¹⁶ K. Ming Li, Qiang Wang "Analytical solutions for outdoor sound propagation in the presence of wind," *J. Acoust. Soc. Am.* **102**, 2040-2049 (1997)

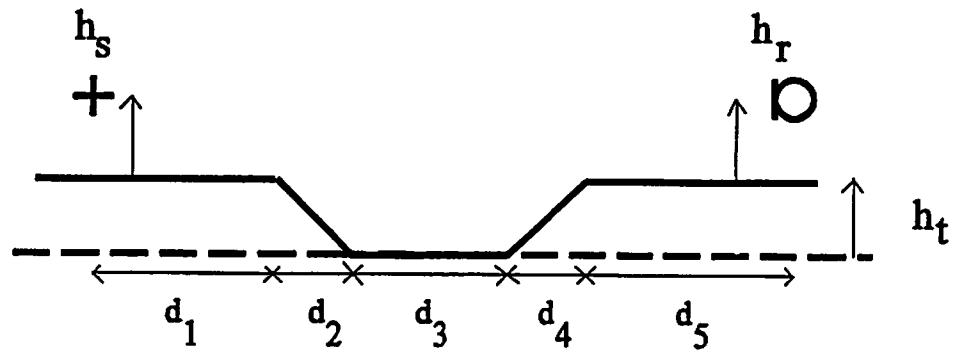


Figure 1. Terrain profile. $d_1=9.4\text{m}/1.9\text{m}$; $d_2=3.8\text{m}$; $d_3=3.8\text{m}$; $d_4=3.8\text{m}$; $d_5=9.4\text{m}/1.9\text{m}$; $d_t=0.38\text{m}$; $h_s=1.5\text{m}$. Impedance is given by $\sigma=20\text{kNsm}^{-4}$ and $d_e=0.0167\text{m}$ in 2PA model.

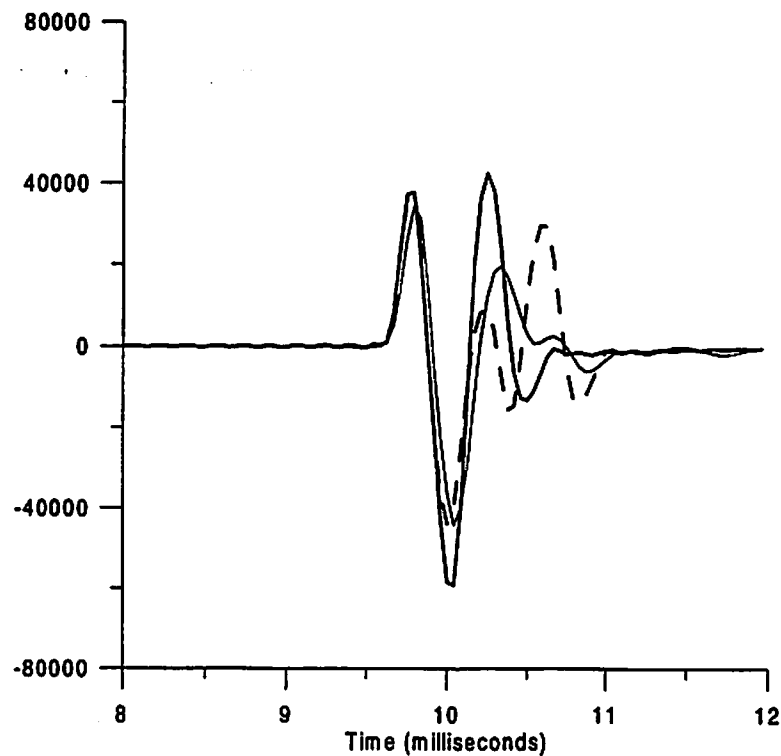


Figure 2 Time response for ditch for 15 m distance. Receiver at 0.5m Thin curve: Measured. Thick curve: Calculation for plane surface. Dashed curve: calculation for plane surface using increased heights.

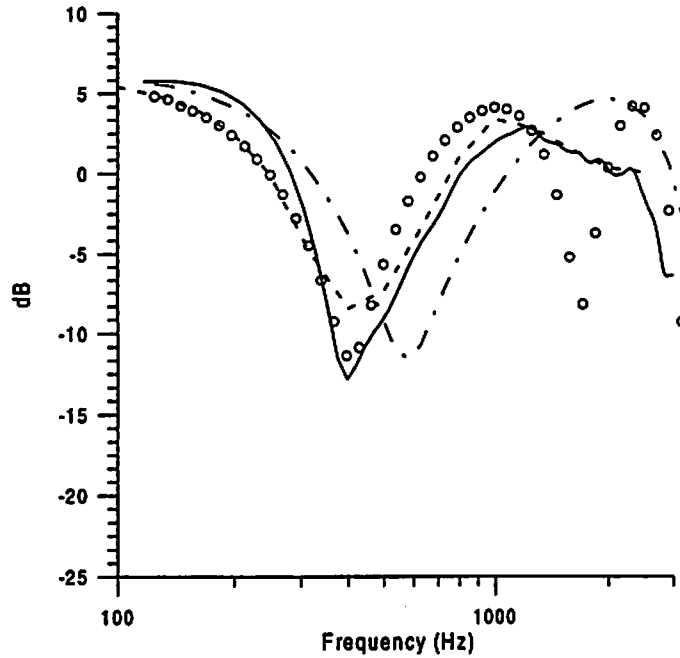


Figure 3 Ditch for 15m distance and 0.5m receiver height. Full curve, measured. Dashed curve, Fresnel zone calculations. Dashed-dot curve, Calculation for plane surface. \circ , calculation for plane surface using increased heights.

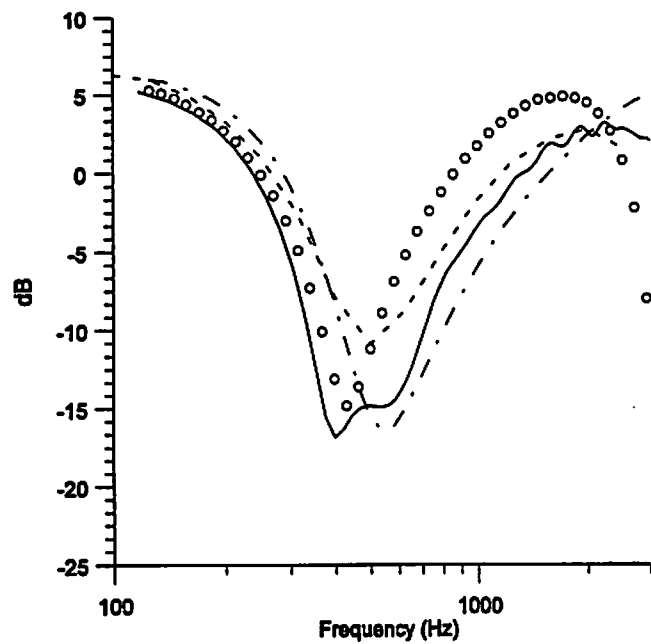


Figure 4 Ditch for 30m distance and 0.5m receiver height. Full curve, measured. Dashed curve, Fresnel zone calculations. Dashed-dot curve, Calculation for plane surface. \circ , calculation for plane surface using increased heights.

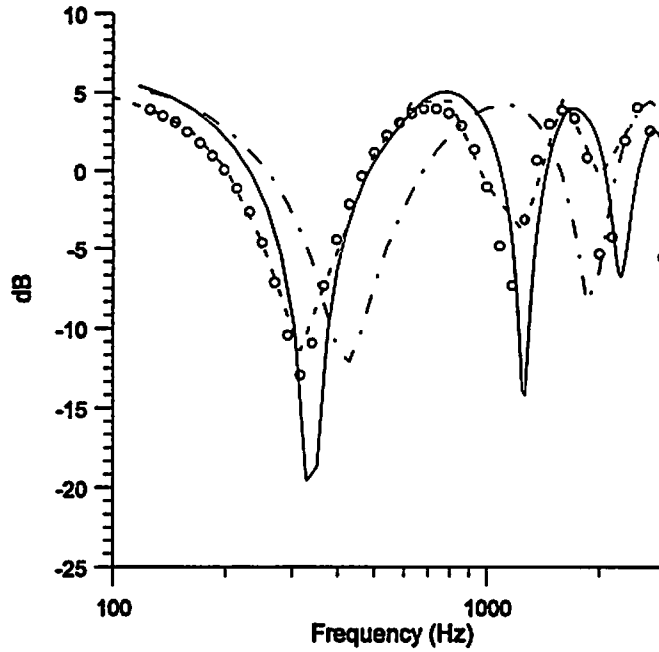


Figure 5 Ditch for 15m distance and 1m receiver height. Full curve, measured. Dashed curve, Fresnel zone calculations. Dashed-dot curve, Calculation for plane surface. \circ , calculation for plane surface using increased heights.

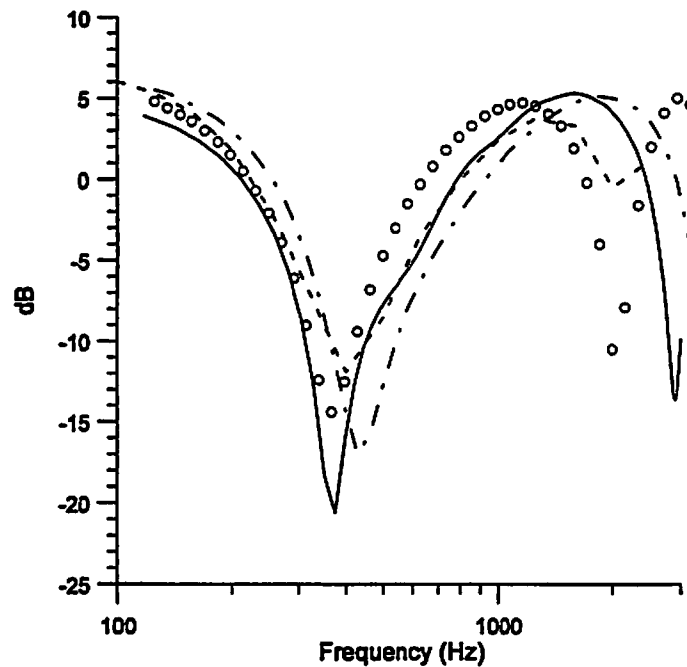


Figure 6 Ditch for 30m distance and 1m receiver height. Full curve, measured. Dashed curve, Fresnel zone calculations. Dashed-dot curve, Calculation for plane surface. \circ , calculation for plane surface using increased heights.

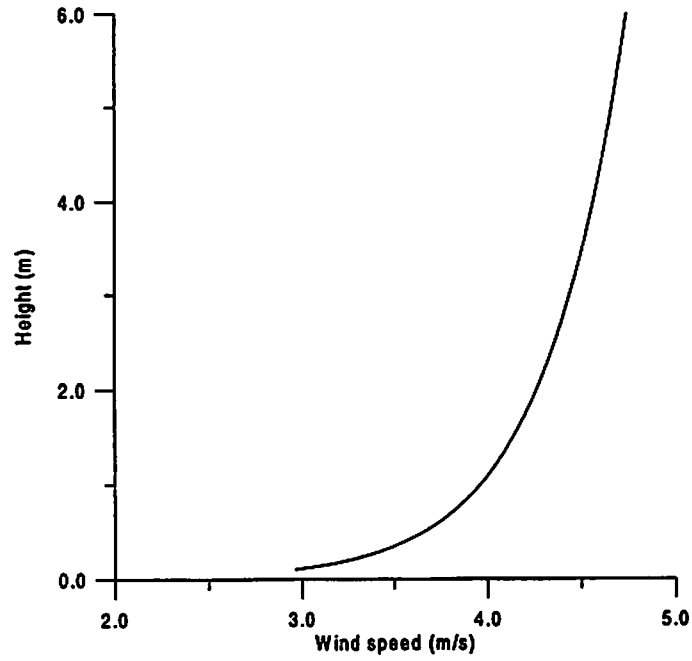


Figure 7 Analytical approximation to wind speed profile

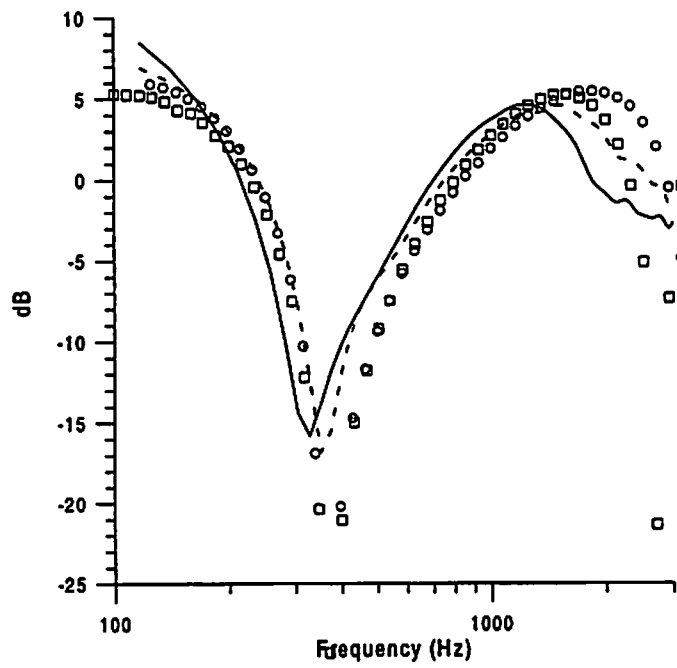


Figure 8 Distance 30m, Receiver height 1m. Full curve, measured for downwind, Dashed-dot curve, measured for no wind, \circ , calculated for no wind, \square , calculated for downwind

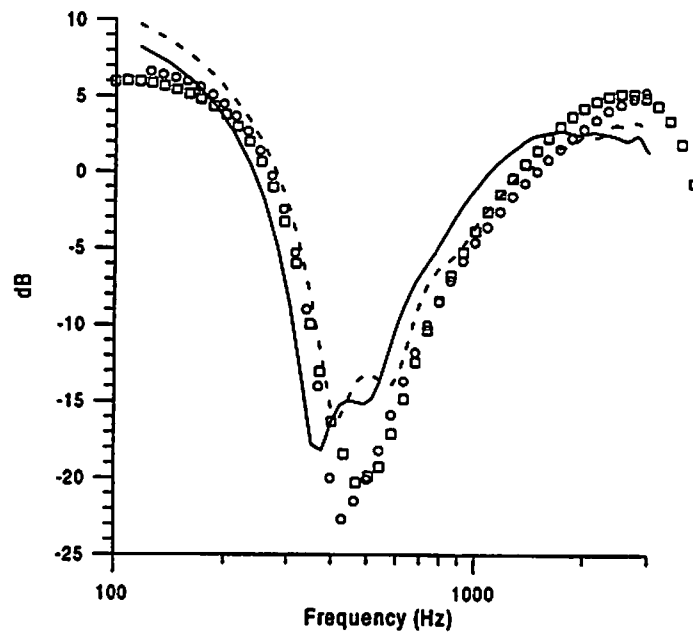


Figure 9 Distance 30m, Receiver height 0.5m. Full curve, measured for downwind, Dashed curve, measured for no wind, \circ , calculated for no wind, \square , calculated for downwind

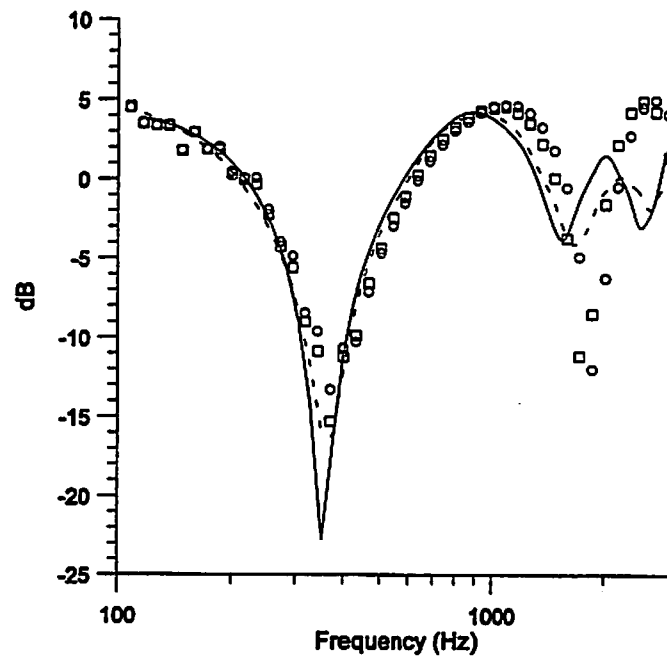


Figure 10 Distance 15m, Receiver height 1m. Full curve, measured for downwind, Dashed curve, measured for no wind, \circ , calculated for no wind, \square , calculated for downwind

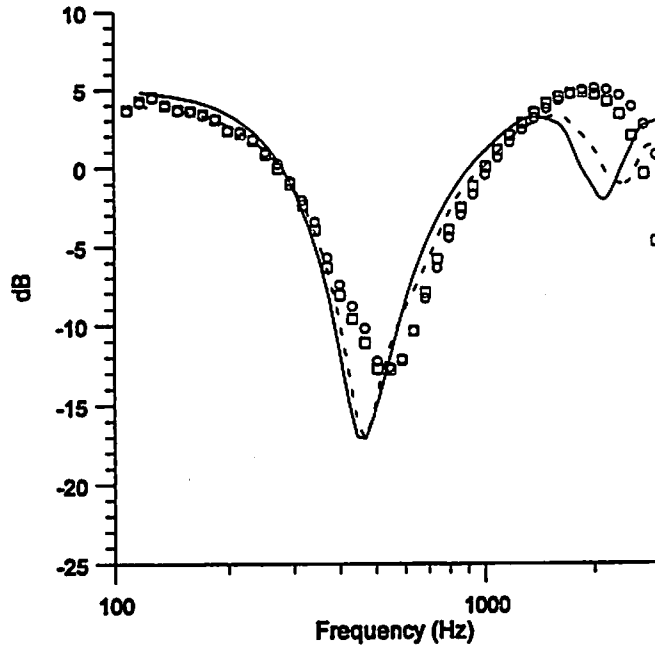


Figure 11 Distance 15m, Receiver height 0.5m. Full curve, measured for downwind, Dashed curve, measured for no wind, \circ , calculated for no wind. \square , calculated for downwind.

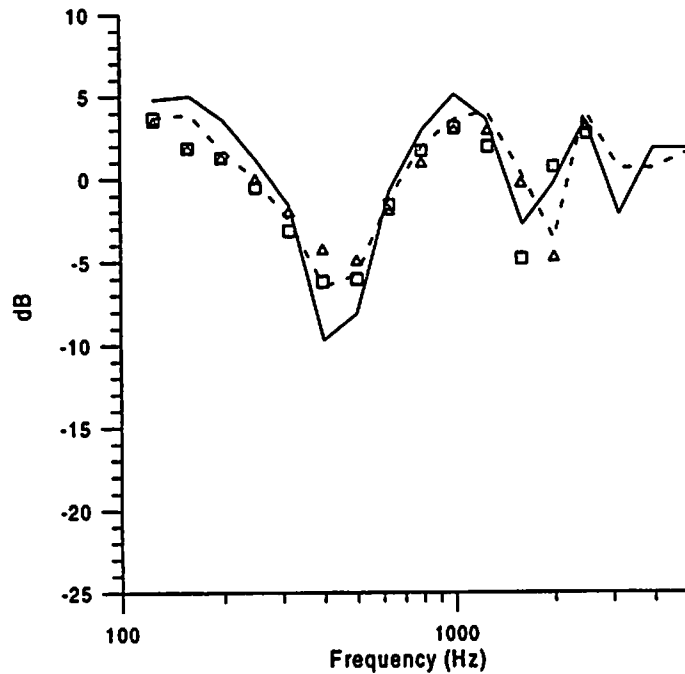


Figure 12 Distance 20m Source height 1.45 m, receiver height 1.5m. Full scale measurements. $\sigma = 200 \text{ kNsm}^{-4}$ in Delany-Bazley model. Wind speed +2.5 m/s and -2.0 m/s at 10m. Full curve, measured downwind. Interrupted curve, measured upwind. Logarithmic profile with roughness length 0.02 m. Square symbols, PE calculations downwind; Triangles, PE calculations upwind.

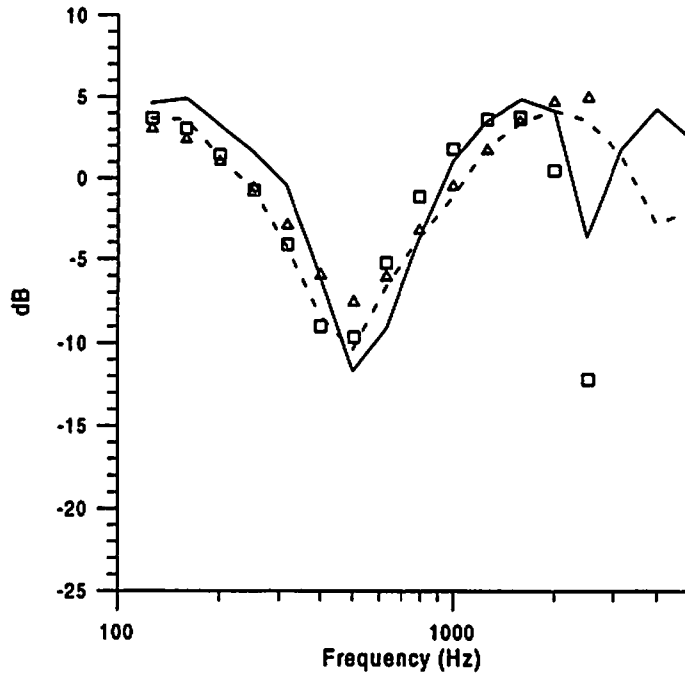


Figure 13. Measurements and PE-calculations for 40m. Key as in Fig.12.

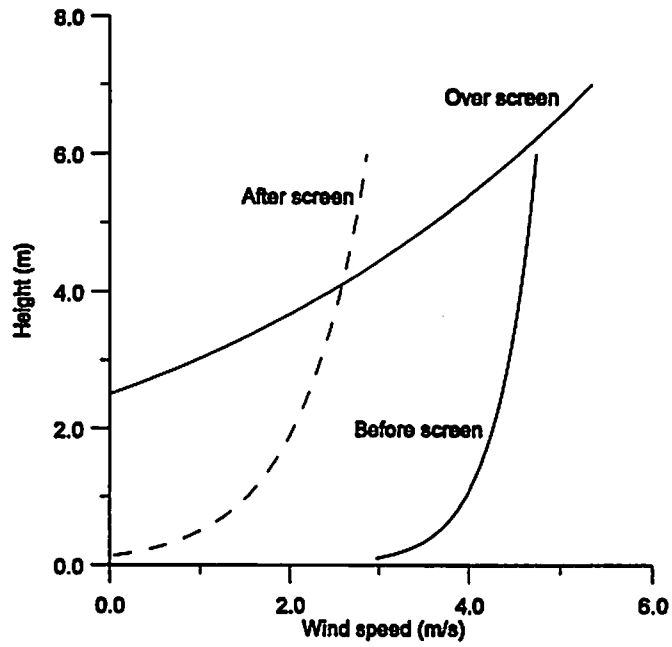


Figure 14. Wind speeds relevant for insertion loss of screen

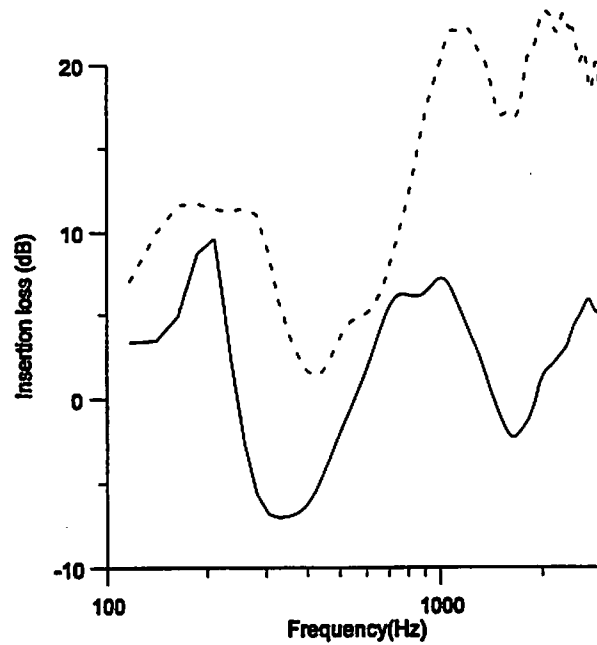


Figure 15. Measured insertion loss for screen on grass-covered ground. Full curve, downwind. Interrupted curve, upwind. Screen height 2.5m. Source height 1.5m. Receiver height 2.5m. Distance from source to screen 25m. Distance from screen to receiver 35m.

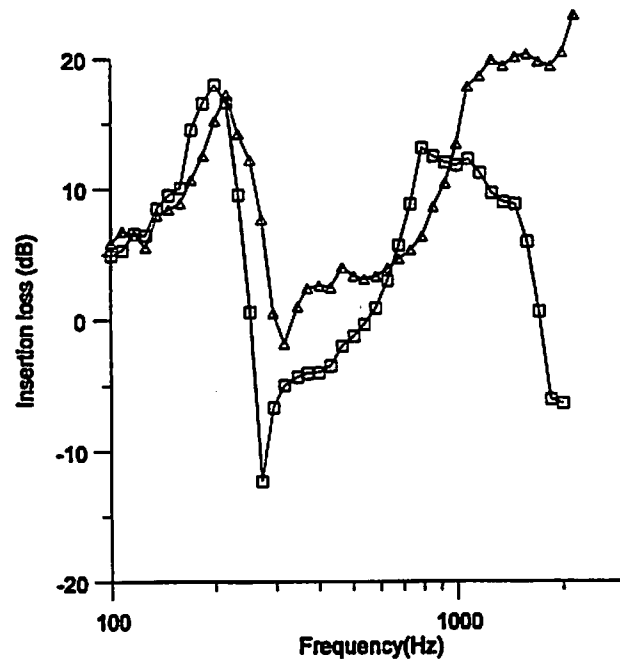


Figure 16. Calculated insertion loss for screen on grass-covered ground. Geometry and wind as in figure 15. Square symbols, downwind. Triangles, upwind. Impedance condition $\sigma = 7 \text{ kNsm}^{-4}$ and $d_c = 0.0160 \text{ m}$ in 2PA impedance model.

Modeling Outdoor Sound Propagation with Modeled Weather Data

Brian Magill and David Swanson

The Applied Research Laboratory
The Pennsylvania State College
P.O. Box 30, State College, PA 16804-0030

ABSTRACT

A method is described for obtaining the atmospheric and environmental data necessary for accurate outdoor sound propagation modeling from databases available on the World Wide Web. In order to achieve reasonable results, outdoor sound propagation modeling requires accurate wind and temperature profiles to a height equal to at least $1/10^{\text{th}}$ the propagation distance of interest. In past measurements, these profiles have been obtained from SODAR and RASS measurements. Under many circumstances, however, it may not be possible or even desirable to make these types of measurements on site. Currently, modeled weather data is being generated at the National Centers for Environmental Prediction on an hourly basis that contains atmospheric profiles for the Continental United States. The present research studies the feasibility of using these profiles, available on the Internet, for outdoor sound propagation.

One problem faced by researchers trying to predict how sound will propagate outdoors is access to upper atmospheric measurements. While it is quite easy to measure quantities such as temperature, wind speed and direction, and relative humidity at the surface and a few meters above the ground, it is can be quite expensive to use equipment such as radiosonde weather balloons, RASS (Radio-Acoustic Sounding System), and SODAR to determine meteorological quantities at higher distances in the atmosphere. There are some situations where it would be cumbersome to transport this additional equipment to a particular site as well. An alternative is to use modeled weather data. Currently modeled data are available for all of the Continental United States as well as part of Mexico and Canada. These models are on the mesoscale level so local weather variations have been averaged out. This could lead to lead to problems for situations where the site is along a lake or at the transition from a field to a forest. These variations have less effect as one goes higher in the atmosphere. This paper will discuss recent developments at the Advanced Sensors Group in the Applied Research Laboratory, Penn State in using modeled weather data to predict sound propagation.

Several types of weather data are currently being generated by the National Ocean and Atmospheric Administration (NOAA). Most, like the ETA, and NGM are for large-scale frontal systems. They have a grid spacing of 100 km or more and are generated at intervals of at least 6 hours. The Rapid Update Cycle (RUC) model⁽¹⁾, however, is generated on an hourly basis and a grid length ranging from 33km to 46km. RUC was developed by the Forecast Systems Laboratory and is run operationally by the National Centers for Environmental Prediction (NCEP). RUC uses a Lambert Conformal projection and has dimensions of 151 by 113 grid points. Vertically RUC data is available from the surface to 16 km. For isobaric levels it is available from 1000 down to 100 mbar. The 1000 mbar isobar is generally at a height from 100 to 200 m. RUC data is derived from radiosonde measurements, aircraft reports, wind profilers, surface observations, and satellite data. Data generated during the previous run is also fed back into the model. Every time the RUC program is run, an analysis of the United State's weather at the time the data was ingested is generated along with forecasts for the next 1 to the 12 hours. It takes roughly an hour to run the model. RUC files have a GRIB (Gridded Binary) format, which is an international standard, set up by the World Meteorological Organization (WMO). All records after the header record are self-contained. All grid points for particular type of data are stored together. The first section of any record describes the type of data stored, the type of levels (isobaric, isentropic, etc.), the level stored along with parameters such as station ID, date and time, forecast hour, and flags for the presence of mapping information. Since RUC data is mapped, each record contains a section with parameters describing how this mapping is set up. The RUC model calculates a considerable number of atmospheric quantities. The ones of interest in sound propagation are temperature, u and v wind speeds, and the relative humidity. (u and v winds are the components of the "east-west" and "north-south" winds, respectively) Certain quantities such as surface temperature might be useful for gross quality checks. Since the RUC data is calculated for fixed isobaric levels, height and isobaric information need to be stored as well. These data files are available to the public on NOAA's OSO server, which at the IP address 140.90.6.103 on the Internet. It generally takes a few hours for RUC data files to be transferred to the OSO Server. The server is generally down from around 1:00 to 3:00 AM in the morning. Over the past summer, data transfers from this server have been reliable at all other times, however. Typically RUC data is only kept for the past 24 hours.

Here, at the Advanced Sensors Group at the Applied Research Laboratory, RUC data files are downloaded automatically every hour from the OSO Server to a Pentium PC running Windows 95. The FTP session itself is controlled by a Perl script. If the process is successful, The script calls a C program which goes through file searching for records of isobaric data for height, temperature, wind speed and direction, and relative humidity. When a record of isobaric data is found, the program records the isobaric level and type

of data, and extracts the modeled data for the specified grid points. The data is then written to an ASCII text file and to an MS Access database.

MS Access is inexpensive, readily available and is to a certain extent a relational database. Relational databases have several advantages over hierarchical databases and text files. It enables database design with less redundant storage of information and chances that the database will be updated improperly. The technology is well established and has been used for a number of years in the business world. SQL, a language for manipulating and querying databases, is the standard for relational databases. It is easy to use, particularly for simple queries. Probably the most important feature is the ease in which data can be extracted from a relational database and displayed in many from many points of view. For example, a series of flat text file of RUC data could be written each which contain isobaric level, height, temperature, and wind information for a specific date. This is all the user needs if he wants to use upper atmospheric data for sound propagation calculations. It would be quite cumbersome to use these files to follow how the wind speed and direction evolve with time for a given isobaric level, however. One would have to write a program to scan each file, extract the specified isobaric level, order the information, and display it. Using a relational database, both queries could be done with a single SQL command. In a relational database, data are not stored with any preferred ordering or point of view. These features are controlled by the SQL statement at run time. SQL also can be used to find averages, standard deviations, and other aggregate quantities for a given attribute like temperature. This is also quite useful for examining spatial variations in the data of adjacent grid points. Finally, information from different sources, such as the ground sensors, can be stored in the same database as the RUC data in a clear, concise way. A single SQL statement can then be used to different views combining RUC these different sources of data.

Since the middle of June, RUC data has been stored for the grid point closest to State College, PA in preparation for field tests. Figure 1 shows the variations in height for the lowest two isobaric levels, 1000 and 975 mbars, for the month of July and August of 1998. The lowest level at 1000 mbar can vary from -50 m to 250 m. Local effects predominate as one approach the surface so any value beneath 100m is probably suspect. Any height less than 50m should definitely be discarded. Figure 2 shows the diurnal variations in temperature for three isobaric levels over the course of 4 days and figure 3 gives the corresponding variations in height. There is no correlation between heating and cooling of the isobaric layers and the height. Starting in mid-August the surrounding 4 grid points have been saved for 5 locations around the United States. The largest variation in temperature observed between surrounding grid points has been less than 3 Celsius. The variation in height has been between 35 to 40 m. This is still acceptable for sound propagation

measurements. Figures 4 and 5 give the temperature profiles, for August 30th, 1998 at 5:00 AM and 3:00 PM EDT, respectively.

RUC modeled weather data is a promising way to integrate upper atmospheric data with ground sensor data. The next step is to collect ground sensor data and interpolate intermediate values using surface similarity theory. This data can then be used to calculate the detection footprint using Parabolic Equation code.

References

- 1 Stanley G. Benjamin, John M. Brown, Kevin J. Brundage, Barry E. Schwartz, Tatiana G. Smirnova, and Tracy L. Smith, *RUC-2 Technical Procedures Bulletin – draft*, 1998

Height of Lowest Two Isobaric Levels for State College

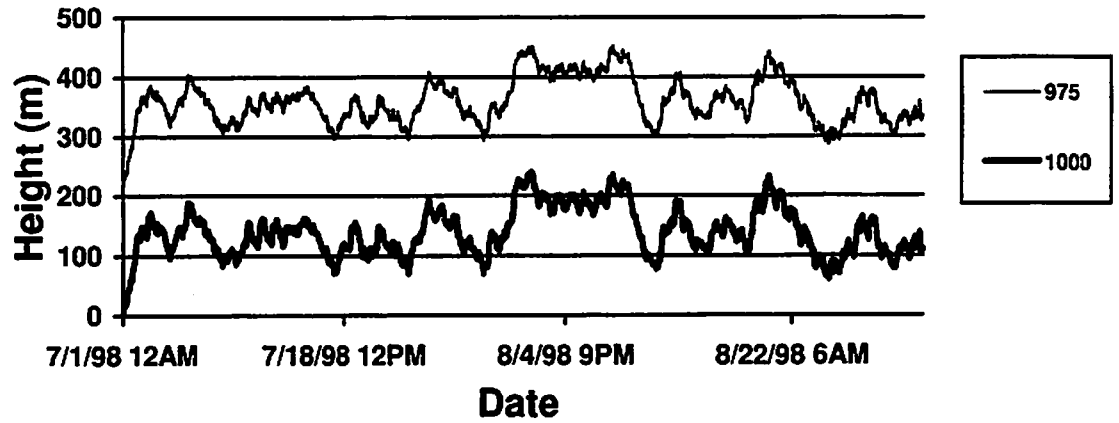


Figure 1

Variation in Temperature for 3 Isobaric Levels

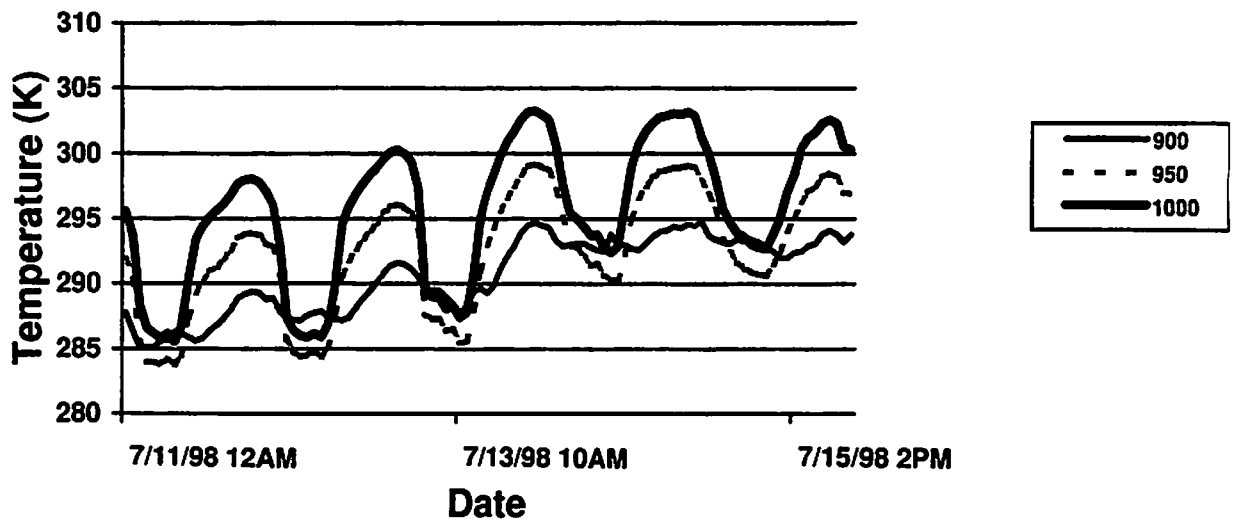


Figure 2

Corresponding Variation in Height for 3 Isobaric Levels

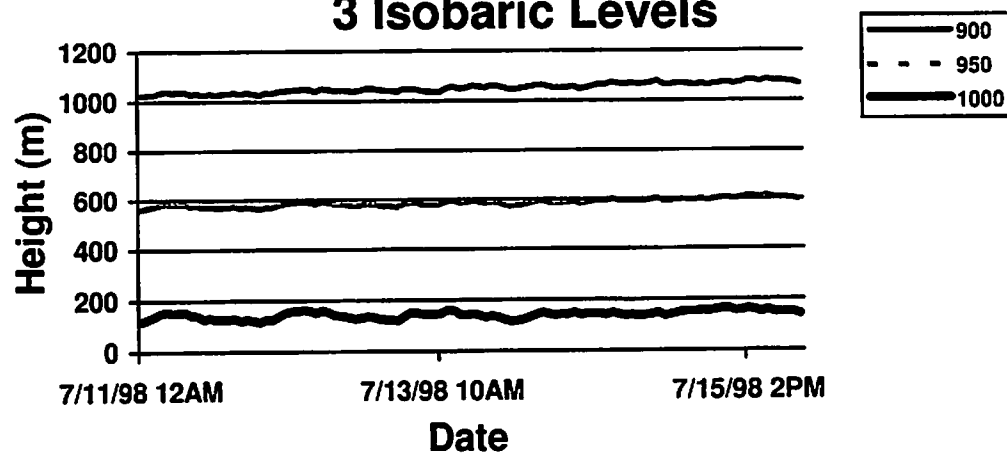


Figure 3

RUC Temperature Profile for State College 5:00 AM 8/30/98

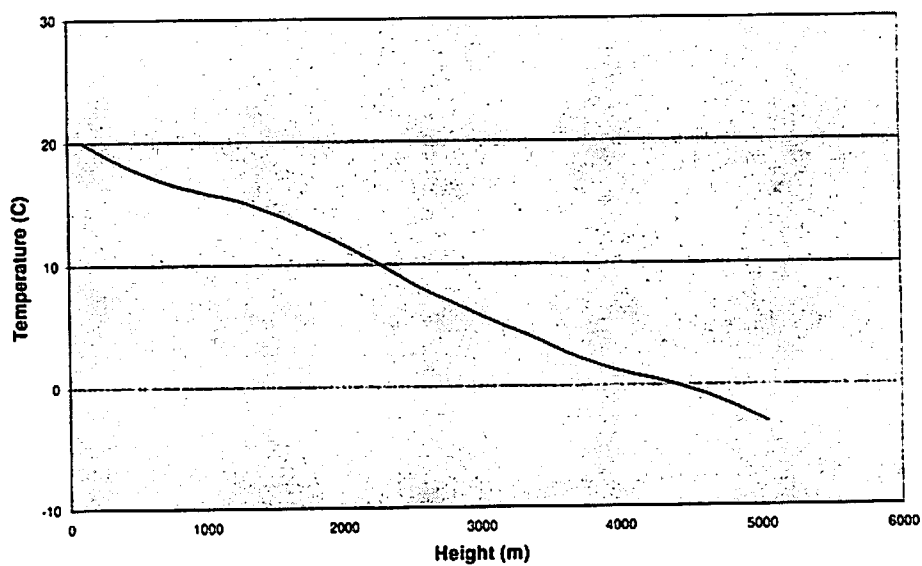


Figure 4

**RUC Temperature Profile for State College
3:00 PM 8/30/98**

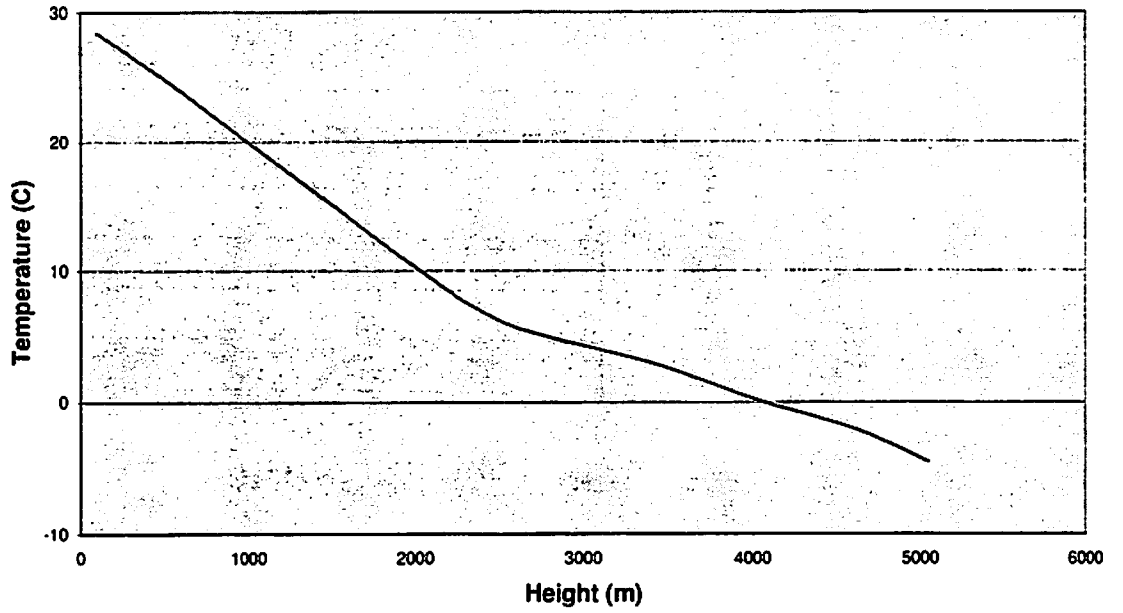


Figure 5

Description of Facilities for Propagation and Meteorological Measurements at Rock Springs, with Example Datasets

David E. Norris
GTE/BBN Technologies
1300 North 17th Street
Arlington, VA 22153

Phone: (703)284-4717, Fax: (703)284-4777, E-mail: dnorris@bbn.com

Dennis W. Thomson
Department of Meteorology
The Pennsylvania State University
State College, PA 16804

David C. Swanson
Applied Research Laboratory
The Pennsylvania State University
State College, PA 16804

Summary: A review of the meteorological and acoustic sensors available at the Rock Springs site is first made, followed by analyzed Rock Springs data from 1995 and 1996. Results for scattering of the acoustic intensity and fluctuations in the acoustic phase, both in the presence of atmospheric turbulence, are presented.

I. DESCRIPTION OF ROCK SPRINGS

The Rock Springs micrometeorological field site is located on flat farmland operated by Penn State's Larson Agricultural Research Center. The main test field is approximately half a kilometer wide and extends along the valley roughly one kilometer. Home to the field site are two permanent buildings and multiple meteorological and acoustic sensors.

A. Meteorological Sensors

A large variety of meteorological sensors are available for use at Rock Springs. Sonic anemometers are available for turbulence measurements, providing high resolution (20 Hz) sampling of surface-layer wind and temperature fields. Currently, seven ATI and two Gill sonic anemometers are configured in a horizontal array, where the ATI sonics are on loan from the U.S. Army Research Laboratory. Over the last year, this sonic array has been used in a Large Eddy Simulation (LES) modeling effort¹ as well as for the acoustic studies described in Sec. III

Hourly-averaged temperature and wind data are available from a system maintained by the U.S. Environmental Protection Agency. A monostatic acoustic sounder (SODAR), configured in a low-power mode, is in operation. In addition, a sensor suite comprising the Automated Surface Observing System (ASOS) is being tested. The system provides data on wind speed/direction, temperature, dewpoint, rainfall, visibility, cloud height, and lightning. Plans are underway to allow access to the ASOS data through a Web page.

Other sensors are in place at Rock Springs that are not mentioned here. The interested reader is referred to the second author for additional information.

B. Acoustic Sensors

Acoustic measurements at Rock Springs have become more and more sophisticated in recent years. In 1995, the standard configuration consisted of 2 B&K microphones recorded on a 2-channel DAT recorder. In 1996, 16 Sennheizer electret microphones were configured in a three-dimensional orthogonal array and recorded on a 16-channel DAT recorder. Figure 1 depicts the three-dimensional array in a logarithmic microphone spacing. In 1997, the acoustics group lead by David Swanson configured 32 Sennheizer microphones in a vertical planar array. Using a PC, the data were digitally sampled and stored real-time onto a hard-disk.

A picture of a portion of the Rock Springs site is given in Fig. 2. Visible from left to right are the 32-element planar array (without microphones), the three-dimensional orthogonal acoustic array, and the horizontal sonic anemometer array.

II. EXAMPLE: SCATTERING ANALYSIS

A. Review

Traditional scattering theory predicts that the signal intensity will have an exponential probability density function (pdf).² It neglects the fact that atmospheric turbulence is inherently inhomogeneous and intermittent. Periods of high activity are embedded in periods of relative calm. By considering intermittency, Wilson *et al.* successfully predicted the pdfs of fully-saturated, scattered signals measured within an acoustic shadow zone.³ The relation for the intensity pdf has one free parameter, the intermittency parameter σ , which characterized the strength of the intermittent effects. Figure 3 gives the intensity pdf for various values of σ . The local spatial and temporal changes in sound speed associated with intermittency increase the likelihood of measuring large values of scattered acoustic intensity.

B. Approach

Rice studied the statistics of a stable signal in the presence of noise and developed what is now called the Rice-Nagakami pdf.⁴ Following the same approach as Wilson *et al.*, but applying the Rice-Nagakami distribution instead of the Rayleigh distribution for the pressure, an intensity pdf has been derived for the case of incomplete saturation. The final expression

for intensity probability takes the form

$$P(I) = \frac{1}{\sqrt{2\pi}\sigma} \int_0^\infty \frac{1}{\bar{I}_0} \exp\left(-\frac{I + I_u}{\bar{I}_0}\right) I_0 \left(\frac{\sqrt{II_u}}{\bar{I}_0/2}\right) \exp\left(-\frac{(\log(\bar{I}_0/\langle I \rangle) - I_u) + \sigma^2/2)^2}{2\sigma^2}\right) \frac{d\bar{I}_0}{\bar{I}_0},$$

where $I_u = \langle I \rangle(1 - S)$. The two model parameters are the intermittency parameter, σ , and the saturation parameter, S . The saturation parameter ranges from 0 to 1 and characterizes the degree of saturation.

C. Experiment and Comparison

A field test was conducted at Rock Springs in 1995 over flat, hard ground at a range of 283 m, and at frequencies from 90 to 500 Hz. The meteorological conditions were sunny with a mean wind along the propagation path of 1.8 m/s. Downwind propagation data were collected over a 50 min period and normalized intensity distributions were calculated. The second and third intensity moments were used to find the intermittency and saturation parameters. The results are summarized in Table 1. Based upon σ , there is no intermittency

Table 1: Normalized intensity moments and theoretical parameters for field data.

Frequency (Hz)	Moments		Intermittency Parameter σ	Saturation Parameter S
	2 nd	3 rd		
90	0.10	0.0083	0.00	0.05
200	0.20	0.058	0.00	0.10
350	0.66	1.6	0.73	0.31
500	2.00	16	0.78	0.79

at 90 and 200 Hz, and significant intermittency at 350 and 500 Hz. Based upon S, the saturation increases with frequency, from almost unsaturated propagation at 90 Hz to nearly fully saturated propagation at 500 Hz.

The comparisons between the calculated and predicted intensity pdfs are shown in Fig. 4, where the intensity is normalized so that the mean is two. The agreement is excellent. The main features of the pdfs are the peak position and the tail magnitude. The peak position approached zero for nearly full saturation ($S \approx 1$), and approaches the mean for nearly no saturation ($S \approx 0$). The tail magnitude changes in response to the intermittency: the stronger the intermittency, the greater the probability of higher intensities.

III. EXAMPLE: PHASE FLUCTUATIONS

A. Review

Phase fluctuations and their relation to turbulence have been considered by others. In particular, Nobel *et al.* developed a model for phase fluctuations by simulating eddies using an elongated longitudinal vortex pair,⁵ and Wilson and Thomson developed an acoustic propagation model for signal variability that included the effects of large-scale, anisotropic turbulence.⁶ Both models were compared to field data, and a common conclusion was that the phase fluctuations were most influenced by large-scale atmospheric turbulence.

B. Approach

A field test was conducted at Rock Springs in 1996 over flat, hard ground during cloudy, windy conditions. A plane view of the setup is given in Fig. 5. The mean velocity was 6.4 m/s and the bearing offset between the wind and propagation direction was 12.3°. The receiver consisted of a three-dimensional microphone array mounted on a 6 m tower. Sources were positioned approximately upwind and downwind of the receiver at a distance D of 196 m. The source heights were 1 m, and they were configured to radiate continuous tones at eight discrete frequencies from 50 to 540 m. Concurrent with the acoustic measurements, wind data were recorded from a horizontal array of nine sonic anemometers positioned a distance $|Y|$ from the receiver ranging from 2 to 26 m.

The time delay of the incident acoustic wave as it passes from one microphone to another was calculated from the cross-correlation functions of the received acoustic magnitudes. From the time delays and the known microphone positions, angles of arrival were then estimated using a plane-wave assumption. The resulting angle-of-arrival estimates are shown in Figures 6 and 7.

Rays were traced through mean wind and temperature profiles derived from Monin-Obukhov similarity theory and mean meteorological measurements. Direct and ground-reflected eigenrays were found for downwind propagation. The predicted arrival angles agree well with the measurements at the higher frequencies (see Fig. 6). No eigenrays were found for upwind propagation, although the measurements suggest the presence of a direct, upward refracting ray.

Power spectral density estimates were computed over a 20 min test period using Welch's averaged periodogram method with a 2^{15} FFT, Hamming window, and 50% overlap. An example of the power spectral density for low winds is shown in Fig. 8. The dB scale in these plots is relative, where 0 dB roughly corresponds to the noise level at high frequencies and low winds. All source peaks are visible for low winds. However, for high winds, the overall difference between the peak and noise levels decreases, and the noise overcomes the peaks below 100 Hz.

The magnitude and phase fluctuations were recovered at the source frequencies by applying the Hilbert transform. The travel-time fluctuations were computed from the phase fluctuations by dividing out the source frequency. The results are given in Fig. 9. The travel-time fluctuations are observed to be highly correlated across the frequencies and have

time scales associated with large-scale atmospheric turbulence.

C. Theory and Comparison

From the turbulence data measured by the sonic anemometers, it was determined that the travel-time fluctuations were dominated by the velocity fluctuations along the propagation path. The maximum cross-correlation coefficient between these two signals was 0.7, as shown in Fig. 10.

In collaboration with Leif Kristensen and Jakob Mann of Risø National Laboratory, Denmark, travel-time fluctuations were predicted along the direct source-receiver ray by characterizing the velocity with an adaptation of the two-dimensional horizontal energy spectrum of Peltier *et al.*⁷ Predicted and measured correlations functions are found to agree well (see Fig. 10).

The variation in the point of maximum correlation was also characterized as a function of both sensor separation and wind direction. The interested reader is referred to Ref. 8 for more details on the 1996 experiment.

REFERENCES

1. C. Tong, J. C. Wyngaard, and J. Brasseur, "Experimental study of the subgrid-scale stresses in the atmospheric surface layer," *J. Atmos. Sci.*, in press (1998).
2. V. I. Tatarskii, *The Effects of the Turbulent Atmosphere on Wave Propagation*, Keter, Jerusalem, 1971.
3. D. K. Wilson, J. C. Wyngaard, and D. I. Havelock, "The effect of turbulent intermittency on scattering into an acoustic shadow zone," *J. Acoust. Soc. Am.* **99**, 3393-3400 (1996).
4. S. O. Rice, Mathematical analysis of random noise, in *Selected Papers on Noise and Stochastic Processes*, edited by N. Wax, pages 133-294, Dover Publications, New York, 1954.
5. J. M. Noble, H. E. Bass, and R. Raspet, "The effect of large-scale atmospheric inhomogeneities on acoustic propagation," *J. Acoust. Soc. Am.* **92**, 1040-1046 (1992).
6. D. K. Wilson and D. W. Thomson, "Acoustic propagation through anisotropic surface-layer turbulence," *J. Acoust. Soc. Am.* **96**, 1080-1095 (1994).
7. L. J. Peltier, J. C. Wyngaard, S. Khanna, and J. G. Brasseur, "Spectra in the unstable surface layer," *J. Atmos. Sci.* **53**, 49-61 (1996).
8. D. E. Norris, *Atmospheric Acoustic Propagation: Characterization of Magnitude and Phase Variability*, Ph.D. thesis, Graduate Program in Acoustics, The Pennsylvania State University (1998).

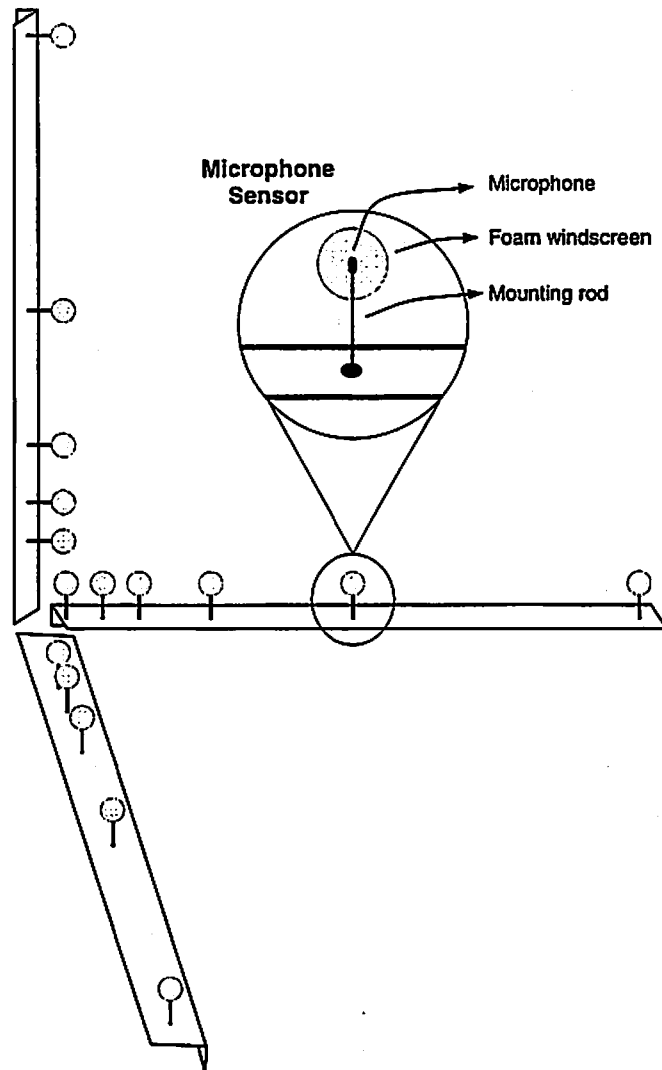


Figure 1: Microphone array structure and microphone sensors.

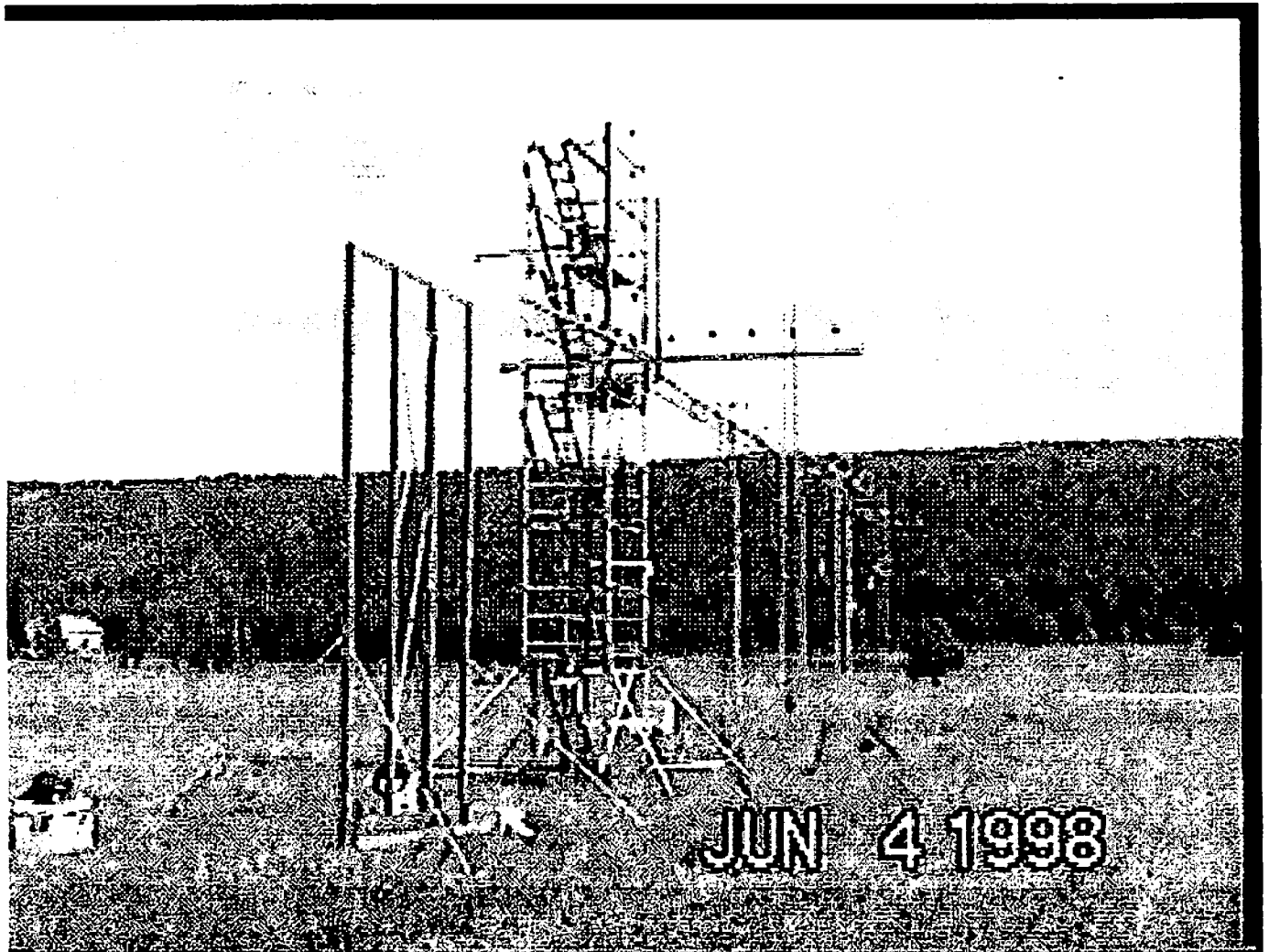


Figure 2: View at Rock Springs showing acoustic and sonic anemometer arrays.

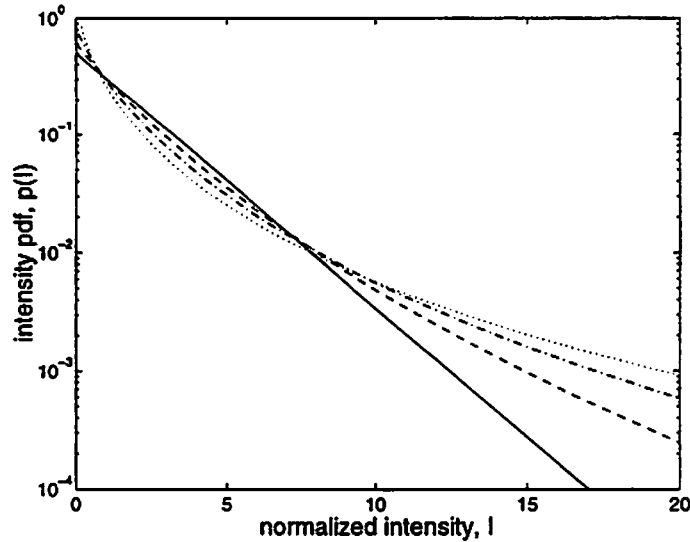


Figure 3: Intensity probability density function for no intermittency (solid line), intermittency parameter $\sigma = 0.2$ (dashed line), $\sigma = 0.5$ (dashed-dotted line), and $\sigma = 1.0$ (dotted line). (Reproduced from Wilson *et al.*, 1996)

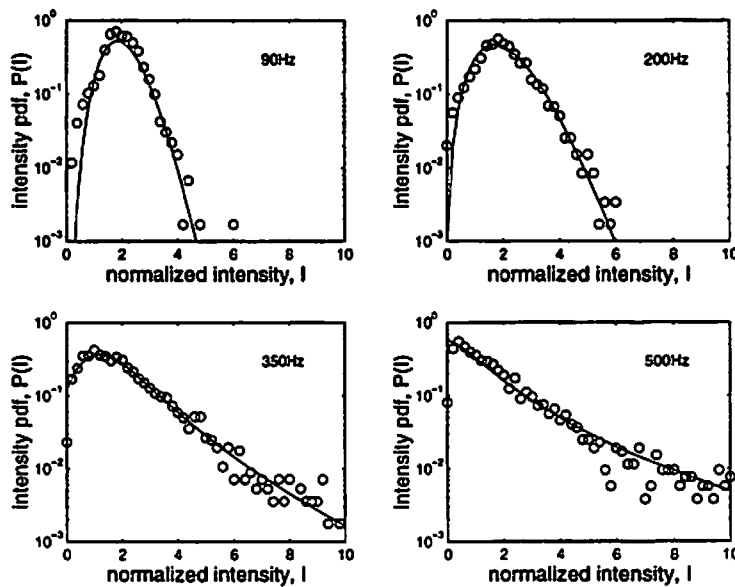


Figure 4: Experimentally determined intensity pdf (circles) and model prediction (solid line).

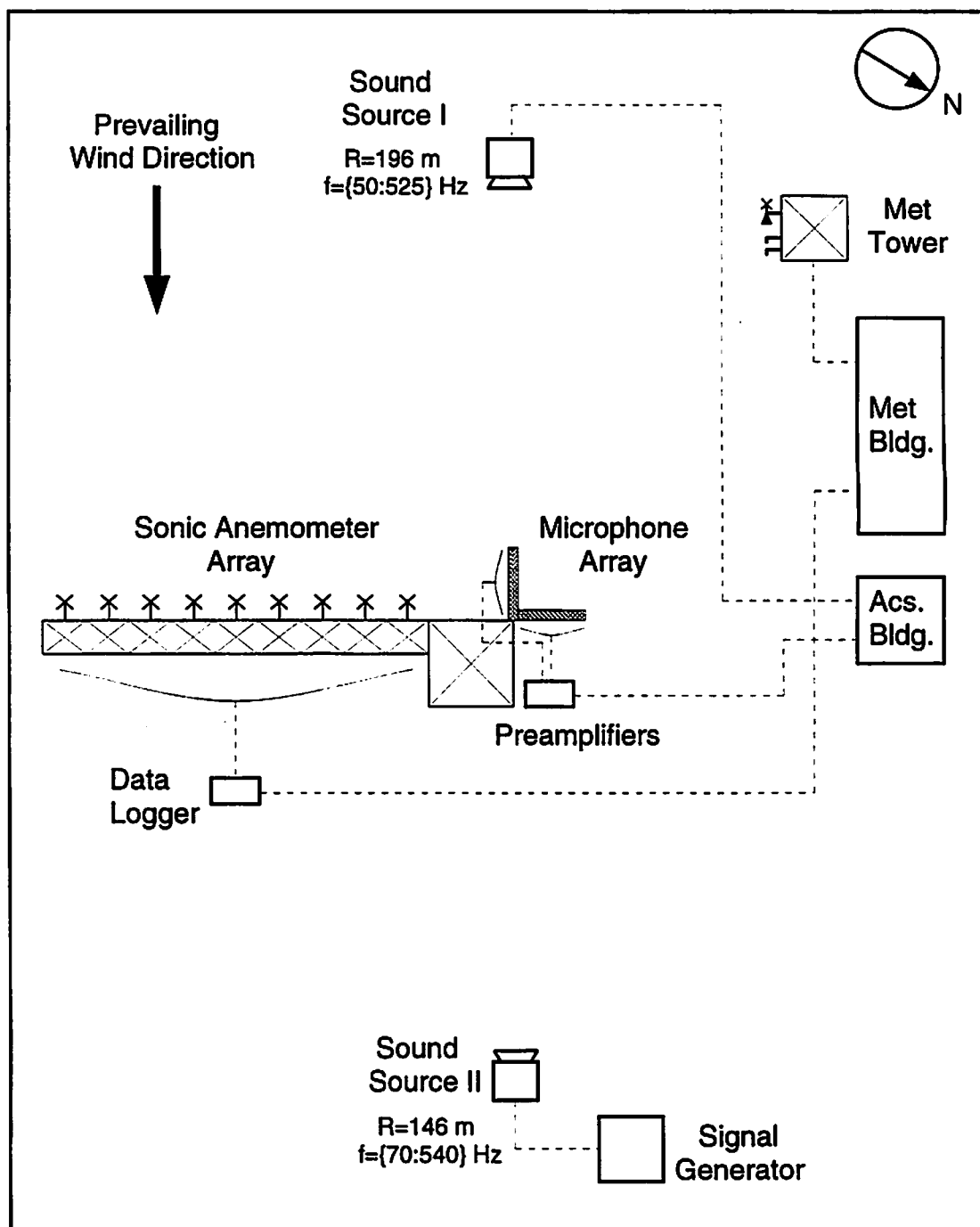


Figure 5: Plane view of the 1996 Rock Springs test setup (not to scale).

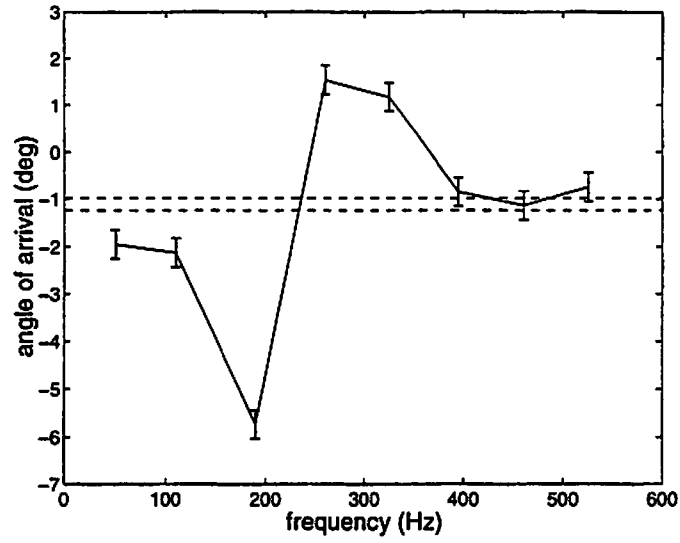


Figure 6: Angles of arrival for downwind propagation from measurements (solid) and predictions (dashed). Error bar indicates twice the calculated uncertainty.

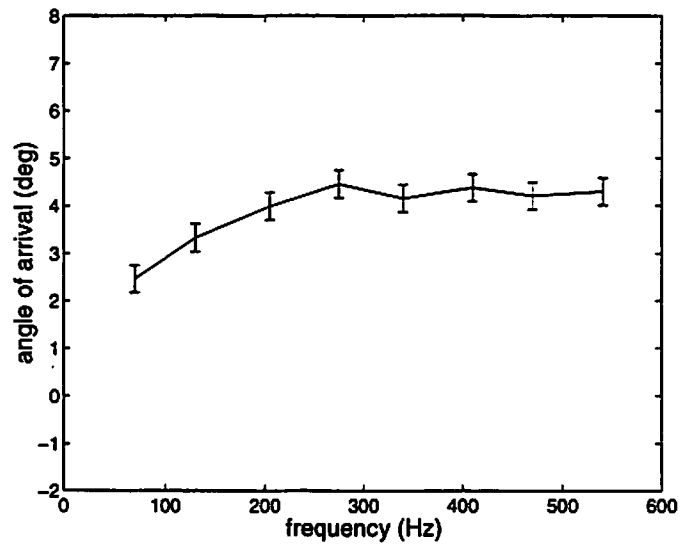


Figure 7: Angles of arrival for upwind propagation from measurements. Error bar indicates twice the calculated uncertainty.

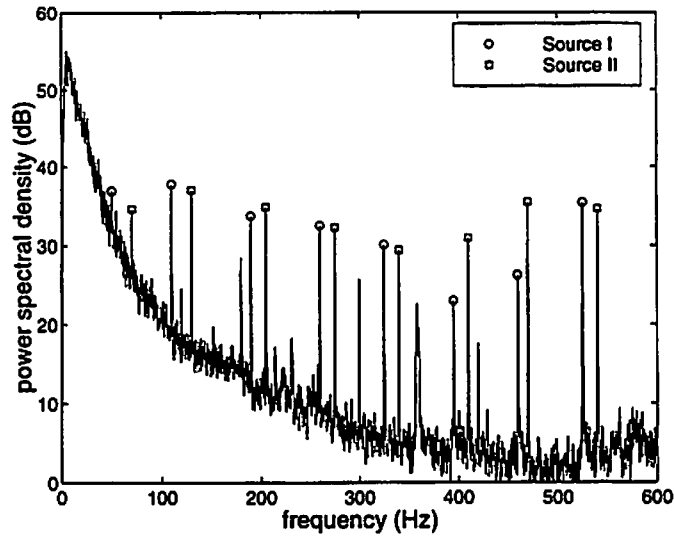


Figure 8: Power spectral density during low winds.

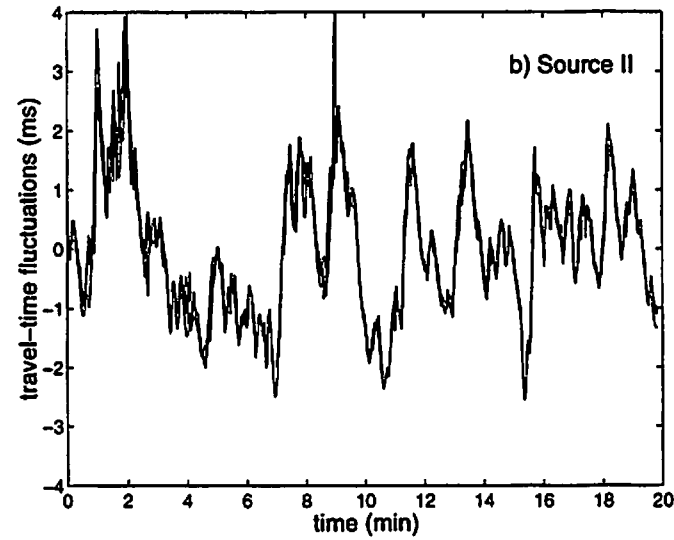


Figure 9: Overlaid travel-time fluctuations for upwind propagation at 130, 205, 275, and 410 Hz.

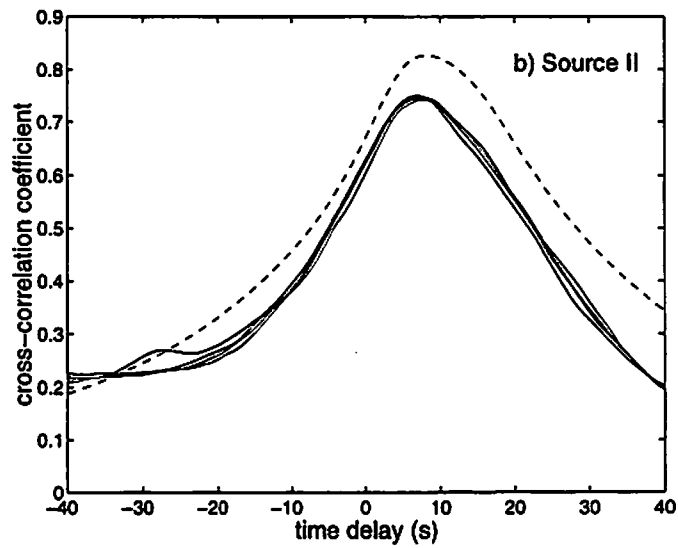


Figure 10: Cross-correlation between travel-time fluctuations and u-velocity fluctuations from measurements (solid lines) and model (dashed line).

Some Effects of Atmospheric Turbulence

ON THE APPLICATION OF TURBULENCE SPECTRAL/CORRELATION MODELS TO SOUND PROPAGATION IN THE ATMOSPHERE

D. Keith Wilson

U. S. Army Research Laboratory, ATTN: AMSRL-IS-EE,
2800 Powder Mill Rd., Adelphi, MD 20783-1197

Phone: (301) 394-2099; FAX: (301) 394-1155; E-mail: dkwilson@arl.mil

ABSTRACT

Calculations are made of the acoustical strength and diffraction parameters, and the mutual coherence function (MCF), using several models for atmospheric turbulence spectra and correlations. Among the models discussed are the basic isotropic Kolmogorov, Gaussian, and von Kármán models. Parameter selections for both shear and buoyantly generated turbulence are suggested. A new set of equations, which predict the turbulence length scales and the strength and diffraction parameters as a function of z/L_{mo} and z_i/L_{mo} (where z is the height from the ground, z_i the boundary-layer inversion height, and L_{mo} the Monin-Obukhov length), are derived for the Kolmogorov and von Kármán models. More sophisticated turbulence models are also discussed, incorporating anisotropy and inhomogeneity characteristic of atmospheric turbulence. These include Kristensen et al.'s spectral tensor, Mann's rapid-distortion model, and an equation for blocking of turbulent motions by the ground. The strength parameter and MCF are found to have very significant anisotropic behavior. The diffraction parameter, being based on a small-argument expansion of the correlation function, behaves isotropically. Ground blocking is found to have no effect on horizontal propagation.

1 INTRODUCTION

Many recent studies (Juvé et al., 1994; Ostashev, 1994; Wilson and Thomson, 1994; Boulanger et al., 1995; Stinson and Daigle, 1996; Ostashev et al., 1996; Gilbert et al., 1996) have discussed the importance of accurate representation of the turbulence spectrum in acoustical scattering calculations. Significant unresolved issues remain regarding selection of an appropriate spectral model, and appropriate values for model parameters. Several of the available models are described and compared in this paper, including the isotropic Gaussian, Kolmogorov, and von Kármán models, the anisotropic spectral tensor suggested by Kristensen et al. (1982), Mann's (1994) rapid-distortion theory, and a method for incorporating "blocking" of eddy motions by the ground. This paper emphasizes determination of model parameters, for both shear and buoyantly generated turbulence, as well as the characteristics of the different models when applied to scattering calculations. Only turbulent wind velocity spectra are considered, since the effect of velocity fluctuations is usually more important than temperature fluctuations, even when buoyant convection is the dominant mechanism for turbulence production (Wilson, 1996).

2 STATISTICS OF WAVES PROPAGATED THROUGH TURBULENCE

For simplicity, the emphasis of this paper is on line-of-sight propagation. Strength and diffraction parameters are used to characterize the propagation in response to turbulent fluctuations. The parameters quantify the propagation regime (i.e., weak/full saturation, and weak/strong scattering), and, once the regime has been deduced, can be used to calculate the amplitude and phase variances (Flatté et al., 1979). The paper also discusses the transverse mutual coherence function (MCF), which describes the coherence between a pair of sensors as a function of their separation normal to the direction of propagation.

The strength parameter Φ is simply the rms phase fluctuation calculated with geometrical acoustics. Assuming that the length X of the propagation path is much longer than the integral length scale \mathcal{L} parallel to the direction of propagation, the strength parameter is given by the equation (Flatté et al., 1979)

$$\Phi^2 = 2\sigma^2 k_0^2 X \mathcal{L}, \quad (1)$$

where*

$$\mathcal{L} = \frac{1}{\bar{\sigma}^2} \int_0^\infty \bar{R}(r\mathbf{e}_\parallel) dr, \quad (2)$$

$\bar{\sigma}^2$ is the variance and $\bar{R}(\cdot)$ the correlation function of the effective index-of-refraction fluctuations, and \mathbf{e}_\parallel is the unit vector in the direction of propagation. For calculation of the effects of wind velocity fluctuations on a forward-propagating acoustic wave, the correlation function in (2) is the autocorrelation of the velocity fluctuation component v parallel to the direction of propagation, normalized by a reference sound speed c_0 . [Only the along-path fluctuations are retained in the parabolic approximation to the wave equation (Ostashev, 1994); many of the results reviewed in this section were originally derived using the parabolic approximation.] I use overbars in this paper to indicate statistics of v/c_0 ; absence of an overbar implies statistics of v . Many of the equations, such as (2), are actually valid for either v/c_0 or v .

The diffraction parameter is proportional to the path-averaged ratio of the Fresnel zone radius to the correlation length L , the latter being defined by an expansion of the correlation function for small arguments perpendicular to the propagation direction (Flatté et al., 1979):†

$$R(r\mathbf{e}_\perp) = \sigma^2 \left(1 - \left| \frac{r}{L} \right|^{p-1} \right), \quad (3)$$

in which \mathbf{e}_\perp is the unit vector perpendicular to the propagation, and $p = 5/3$ for turbulence. The diffraction parameter is given by the equation‡ (Flatté et al., 1979)

$$\Lambda = \frac{X}{6L^2 k_0}. \quad (4)$$

The MCF is given by (Dashen, 1979; Ostashev et al., 1997; Wilson, 1998c)

$$\Gamma(\mathbf{r}_\perp) = \exp \left\{ -2\pi X k_0^2 [\bar{b}_\parallel(\mathbf{0}) - \bar{b}_\parallel(\mathbf{r}_\perp)] \right\}, \quad (5)$$

where X is the propagation distance (range), $k_0 = 2\pi f/c_0$ the acoustic wavenumber, f the frequency, and $b_\parallel(\mathbf{r}_\perp)$ the *two-dimensional (2D) correlation function* of the velocity fluctuations parallel to the direction of propagation. The 2D correlation equals a line integral of the usual 3D correlation function:

$$b_\parallel(\mathbf{r}_\perp) = \frac{1}{2\pi} \int_{-\infty}^{\infty} R(\mathbf{r}_\perp + u\mathbf{e}_\parallel) du. \quad (6)$$

It is convenient to define a *2D structure function* as

$$d_\parallel(\mathbf{r}_\perp) = 2 [b_\parallel(\mathbf{0}) - b_\parallel(\mathbf{r}_\perp)]. \quad (7)$$

The 2D structure function has a simple relationship to the phase structure function D_ϕ often encountered in scattering theory:

$$D_\phi(\mathbf{r}_\perp) = 2\pi k_0^2 X \bar{d}_\parallel(\mathbf{r}_\perp). \quad (8)$$

We see now that the main quantities of interest to be derived from the turbulence model (so that we can determine the strength and diffraction parameters, and the MCF) are the integral length scale \mathcal{L} , the correlation length L , and the 2D structure function.

3 SHEAR AND BUOYANTLY GENERATED TURBULENCE

In this section, I review some basic features of turbulence in the atmosphere, for the purpose of developing a basis for choosing parameters in the turbulence models.

*Some authors, including Flatté et al., define the integral length scale by integrating the correlation function from $-\infty$ to ∞ . The single-sided definition used in (2) is more customary in the turbulence literature.

†In Flatté et al.'s (1979) book, a distinction is made between horizontal and vertical correlation lengths. In turbulence, however, the correlation length is independent of direction for small separations. This is the *local isotropy* property of turbulence discussed by Tatarskii (1971).

‡This equation for the diffraction parameter holds so long as the Fresnel radius is small enough that the expansion of the correlation function (3) is valid; for turbulence r must lie within the inertial subrange ($r \ll L$).

3.1 Production and Dissipation

The two main production mechanisms for turbulence in the atmospheric boundary layer are shear and buoyancy. The rate of shear production of specific (per unit mass) turbulent kinetic energy (TKE) is $u_*^3/\kappa z$, where u_* is the friction velocity, $\kappa \simeq 0.40$ is von Kármán's constant, and z is height (Wyngaard, 1992). The rate of buoyant (convective) production is $(g/\theta)\langle w'\theta' \rangle$, where g is gravitational acceleration, θ' the fluctuation in potential temperature, and w' the vertical velocity fluctuation (Wyngaard, 1992). In clear daytime conditions, buoyant production typically dominates in the bulk of the boundary layer, although shear production dominates near the ground.

The level of the spectrum in the inertial subrange is determined by the TKE dissipation rate. For the 1D spectrum of the along-wind fluctuations, the inertial-subrange spectrum is (Kaimal et al., 1972)

$$F(k) = \frac{\alpha}{2} \epsilon^{2/3} k^{-5/3}, \quad (9)$$

where α is a constant, whose value is approximately 0.52 (Högström, 1996). A reasonable assumption for shear turbulence is that the average rate of TKE production is locally balanced by dissipation. This would imply a TKE dissipation rate of $\epsilon = u_*^3/\kappa z$ at altitudes dominated by shear production, hence determining the inertial subrange spectrum.

Since the temperature flux $\langle w'\theta' \rangle$ decreases linearly with height in a convective boundary layer, the average dissipation rate of turbulence in the boundary layer must be proportional to w_*^3/z_i , where $w_* = (gQ_s z_i/\theta_s)^{1/3}$ is the mixed-layer velocity scale, z_i is the inversion height, $Q_s = \langle w'\theta' \rangle_s$ is the surface temperature flux (equal to the surface heat flux divided by ρC_p), and θ_s is the surface temperature. Data analyzed by Caughey and Palmer (1979) suggest that $\epsilon = 0.8w_*^3/z_i$ in the mixed layer, but increases somewhat near the ground due to surface interactions.

3.2 Variances

Under conditions where shear production of turbulence dominates, the variances for the turbulent velocities are anisotropic. Based on spectral measurements by Kaimal et al. (1972), Kristensen et al. (1989) determine the variances

$$\sigma_1^2 = 4.77u_*^2, \quad \sigma_2^2 = 2.68u_*^2, \quad \text{and} \quad \sigma_3^2 = 1.46u_*^2, \quad (10)$$

where the subscript 1 indicates the along-wind direction, 2 the (horizontal) crosswind direction, and 3 the vertical. For an isotropic model, it is reasonable to set the variance equal to the average of the variances of the three velocity components. Hence, for shear turbulence, we have from (10)

$$\sigma^2 = 2.97u_*^2. \quad (11)$$

Under conditions where buoyant production of turbulence dominates the entire boundary layer, the velocity variances of the two horizontal components are equal, but the vertical velocity variance increases with height. More will be said regarding this behavior in Section 5.4. For now it is enough to state that far from the influence of the ground (typically 100 m or higher), the variance of all three velocity components is (Caughey & Palmer, 1979)

$$\sigma^2 \simeq 0.35w_*^2. \quad (12)$$

3.3 Højstrup's Hypothesis

When both shear and buoyancy production play significant roles in driving atmospheric turbulence (a common situation in the daytime boundary layer), a useful modeling assumption is that individual spectra representing the shear and buoyantly produced turbulence can simply be added together. This idea apparently originated with Højstrup (1982), who had good success applying it to 1D turbulence spectra. Peltier et al. (1996) subsequently applied the Højstrup's hypothesis to 2D TKE spectra. Here I assume [as was done previously by Wilson and Thomson (1994)] that the hypothesis is fully general, being valid for 3D correlations and spectra.

By setting the argument of the correlation function to zero, it follows that the variances are also additive. For example, the total variance from (11) and (12) is

$$\sigma^2 = 2.97u_*^2 + 0.35w_*^2 = u_*^2 \left[2.97 + 0.35 \left(-\frac{z_i}{\kappa L_{mo}} \right)^{2/3} \right] = w_*^2 \left[2.97 \left(-\frac{z_i}{\kappa L_{mo}} \right)^{-2/3} + 0.35 \right], \quad (13)$$

where $L_{mo} \equiv -T_s u_*^3 / \kappa g Q_s$ is the Monin-Obukhov length. [Note that $-z_i / \kappa L_{mo} = (w_* / u_*)^3$.]

By integrating the correlation function with respect to the propagation direction, it can be shown that the strength parameters and 2D structure functions are also additive. Integral length scales are variance-weighted sums:

$$\sigma^2 \mathcal{L} = \mathcal{L}_s \sigma_s^2 + \mathcal{L}_b \sigma_b^2, \quad (14)$$

where $\sigma^2 = \sigma_s^2 + \sigma_b^2$, and the subscript s is the shear contribution, and b the buoyancy contribution. As can be shown from (3), the correlation lengths combine in reciprocal fashion:

$$\frac{\sigma^2}{L^{p-1}} = \frac{\sigma_s^2}{L_s^{p-1}} + \frac{\sigma_b^2}{L_b^{p-1}}. \quad (15)$$

4 ISOTROPIC TURBULENCE MODELS

The term "isotropic turbulence" is actually an incongruous one, since turbulence by nature possesses an anisotropic energy subrange. Still, isotropy can often be a useful modeling assumption for several reasons. First, the energy subrange is nonuniversal and difficult to model. Therefore some simplifications are expedient and reasonable. Second, even when a model incorporating an anisotropic energy subrange is available, analytical derivation of scattering statistics such as the strength parameter is often impossible, and without such analytical results there may be little insight into the propagation physics. Finally, if the scattering comes primarily from the isotropic portion of the spectrum (the inertial and dissipation subranges), there is no motivation for accurately modeling the anisotropic portion of the spectrum.

4.1 General Relationships

A little background on correlations and spectra in isotropic, incompressible vector fields will be helpful in deriving equations for the turbulence models. As discussed by Batchelor (1953), the full autocorrelation function for an isotropic vector field is given by

$$R(\mathbf{r}) = \frac{r_{\parallel}^2}{r^2} R_{\parallel}(\mathbf{r}) + \frac{r_{\perp}^2}{r^2} R_{\perp}(\mathbf{r}), \quad (16)$$

where $\mathbf{r} = r_{\parallel} \mathbf{e}_{\parallel} + r_{\perp} \mathbf{e}_{\perp}$, $R_{\parallel}(\mathbf{r}) \equiv R(\mathbf{r} \mathbf{e}_{\parallel})$ is the correlation function for displacements parallel to the velocity fluctuations, and $R_{\perp}(\mathbf{r}) \equiv R(\mathbf{r} \mathbf{e}_{\perp})$ is the correlation for perpendicular displacements. If the flow field is incompressible,

$$R_{\perp}(\mathbf{r}) = R_{\parallel}(\mathbf{r}) + \frac{r}{2} \frac{dR_{\parallel}(\mathbf{r})}{dr}. \quad (17)$$

The integral length scale \mathcal{L} , needed for the strength parameter, is found by integrating $R_{\parallel}(\mathbf{r})$, and is independent of the direction of propagation for isotropic turbulence.

The 2D correlation function can be determined from the specific TKE spectrum $E(k)$ using the equation (Wilson, 1998c)

$$b_{\parallel}(r_{\perp}) = \frac{1}{2} \int_0^{\infty} \frac{E(k_{\perp})}{k_{\perp}} J_0(k_{\perp} r_{\perp}) dk_{\perp}, \quad (18)$$

where J_0 is the cylindrical Bessel function. Note that in isotropic turbulence, the 2D correlation function is independent of the direction of propagation, and depends only on the magnitude of r_{\perp} . The same statements apply to the MCF. Another relation for isotropic turbulence that we will find useful is (Batchelor, 1953)

$$E(k) = k^3 \frac{d}{dk} \left[\frac{1}{k} \frac{dF(k)}{dk} \right], \quad (19)$$

where $F(k)$, the 1D spectrum, is the Fourier transform of $R_{\parallel}(r)$. The 3D cross spectrum between fluctuations of the i th and j th velocity components is given by the equation (Batchelor, 1953)

$$\Phi_{ij}(k) = \frac{E(k)}{4\pi k^4} (\delta_{ij}k^2 - k_i k_j). \quad (20)$$

4.2 Kolmogorov Model

Kolmogorov's hypotheses (1941) imply that the structure function, defined by the equation $D_{\parallel}(r) = \langle [u(r\mathbf{e}_{\parallel}) - u(0)]^2 \rangle$, is proportional to $r^{2/3}$. Specifically, we write

$$D_{\parallel}(r) = C_V^2 r^{2/3}, \quad (21)$$

where C_V^2 is called the *structure-function parameter*. This relationship is valid in the inertial subrange. From (3) and (17) we find that the parallel correlation function has the small-argument expansion

$$R_{\parallel}(r) = \sigma^2 \left(1 - \frac{3}{4} \left| \frac{r}{L} \right|^{p-1} \right), \quad (22)$$

Since the definition of $D_{\parallel}(r)$ implies that $D_{\parallel}(r) = 2[R_{\parallel}(0) - R_{\parallel}(r)]$, we must have $p = 5/3$ in the correlation expansion with*

$$L = \left(\frac{3\sigma^2}{2C_V^2} \right)^{3/2}. \quad (23)$$

Hence the correlation length and diffraction parameter can be determined from the variance and C_V^2 . Values for the variance were given earlier, in Sec. 3.2.

Let us now consider the relationship between C_V^2 and the dissipation rate. Using the Fourier transform relationship between the correlation and spectral functions, it can be shown that

$$D_{\parallel}(r) = 4 \int_0^{\infty} (1 - \cos kr) F(k) dk. \quad (24)$$

Note that wavenumbers such that $kr \ll 1$ do not contribute to the integral, because of the filtering action of the $(1 - \cos kr)$ factor. Hence for small r , we may use (9) for the spectrum. The integration can then be performed, resulting in

$$D_{\parallel}(r) = \frac{3}{2} \Gamma\left(\frac{1}{3}\right) \alpha \epsilon^{2/3} r^{2/3}. \quad (25)$$

Comparing now with (21), we see†

$$C_V^2 = \frac{3}{2} \Gamma\left(\frac{1}{3}\right) \alpha \epsilon^{2/3} \simeq 2.1 \epsilon^{2/3}. \quad (26)$$

Hence, from (23),

$$L = 0.61 \frac{\sigma^3}{\epsilon}. \quad (27)$$

Assuming the validity of Højstrup's hypothesis, one can find the overall C_V^2 by adding together the contributions from shear and buoyancy turbulence. The result is

$$C_V^2 \simeq 2.1 \left(1.8 \frac{u_*^2}{z^{2/3}} + \frac{w_*^2}{z_i^{2/3}} \right). \quad (28)$$

*A similar equation appears in Tatarskii's (1971) book, except that a factor 2 replaces the 3/2, and C_N^2 replaces C_V^2 . The coefficient changes because the index-of-refraction field is scalar, whereas the velocity is vector. Ostashev (1994) has previously found similar modifications to scalar equations when they are adapted to vector fields.

†This relationship is analogous to one derived for the temperature structure-function parameter by Wyngaard, Izumi, and Collins (1971).

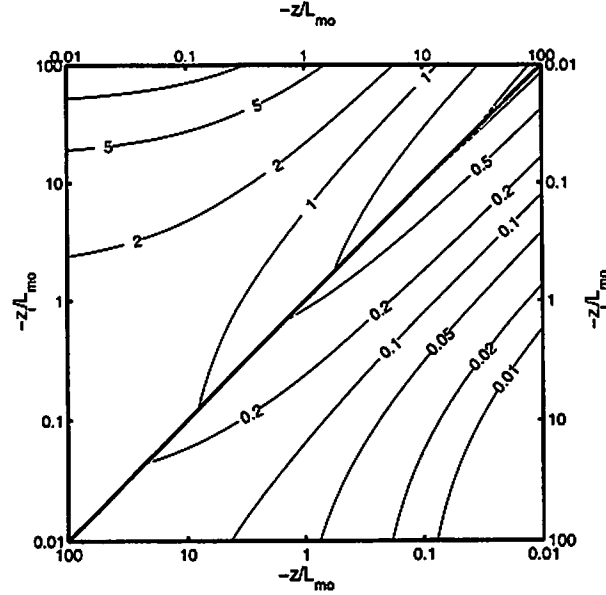


Figure 1: Normalized correlation length scale L as a function of $-z/L_{mo}$ and $-z_i/L_{mo}$, where z is height from the ground, z_i is the boundary-layer inversion height, and L_{mo} is the Monin-Obukhov length. The upper left corner shows L/z , and the lower right corner shows L/z_i .

Using this result for C_V^2 and σ^2 from (13), and substituting into (23), we have

$$L = 1.3z \left[\frac{1 + 0.12(-z_i/\kappa L_{mo})^{2/3}}{1 + 0.56(-z/\kappa L_{mo})^{2/3}} \right]^{3/2} = 0.12z_i \left[\frac{1 + 8.5(-z_i/\kappa L_{mo})^{-2/3}}{1 + 1.8(-z/\kappa L_{mo})^{-2/3}} \right]^{3/2}. \quad (29)$$

When the boundary layer is dominated by shear ($-z_i/L_{mo} \ll 1$) and the propagation height is within the shear layer ($-z/L_{mo} \ll 1$), we have the simple result $L = L_s \simeq 1.3z$. At the other extreme, when the boundary layer is dominated by buoyancy ($-z_i/L_{mo} \gg 1$) and the propagation height is above the shear layer ($-z/L_{mo} \gg 1$), we have $L = L_b \simeq 0.12z_i$. The full behavior of L/z and L/z_i is shown in Fig. 1. Figure 2 shows calculations of the diffraction parameter Λ , multiplied by the dimensionless groups $k_0 z^2/X$ and $k_0 z_i^2/X$.

Calculation of the strength parameter for the Kolmogorov model is more problematic. Eq. (22) is valid only for small r/L , and the integral length scale is nonconvergent when we attempt to use this small-argument expansion. In the turbulence literature (e.g., Tennekes and Lumley, 1972), the length scale $l = \sigma^3/\epsilon$ is often used to represent the large eddies, and assumed to be close in value to the integral length scale. From (27), we therefore have $\mathcal{L} \simeq l \simeq 1.6L$. Alternatively, we could simply assume that $R_{\parallel}(r)$ is given by (22) for $r < (4/3)^{3/2}L$, and zero otherwise. One then finds $\mathcal{L} = (2/5)(4/3)^{3/2}L \simeq 0.62L$. The corresponding result for scalars appears as (6.2.6) in Flatté et al. (1979). However, we have no assurance that either of these approximations for \mathcal{L} are, in general, good ones. In the following section, discussing the von Kármán model, we will see in fact that both approximations are generally poor.

The 2D structure function (and hence the MCF) can be determined by first substituting (9) into (19),* with the resulting energy spectrum

$$E(k) = \frac{55\alpha}{18} \epsilon^{2/3} k^{-5/3}. \quad (30)$$

From (7) and (18), we have

$$d_{\parallel}(\tau_{\perp}) = \int_0^{\infty} \frac{E(k_{\perp})}{k_{\perp}} [1 - J_0(k_{\perp} \tau_{\perp})] dk_{\perp}. \quad (31)$$

*Equation (19) only applies to isotropic turbulence. Even though large-scale turbulence is always anisotropic, it is reasonable to apply (19) to the smaller, inertial scales. (See, for example, Tennekes and Lumley (1972), p. 253.)

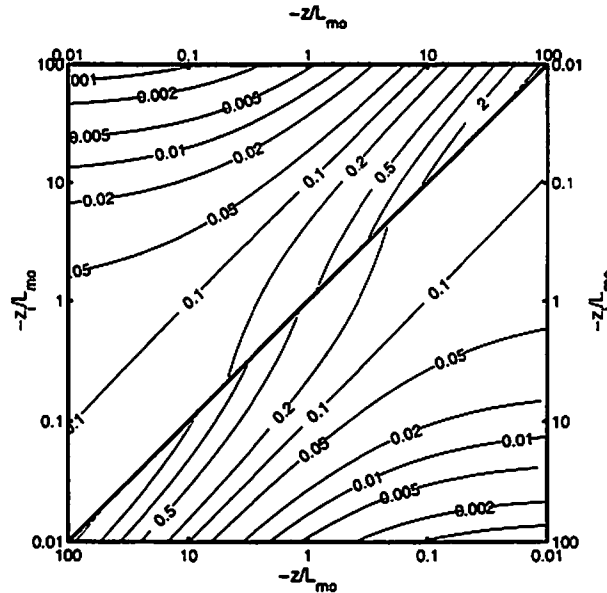


Figure 2: Upper left is the diffraction parameter Λ multiplied by $k_0 z^2/X$; lower right is $\Lambda k_0 z_i^2/X$.

The factor $[1 - J_0(k_\perp r_\perp)]$ filters out the effects of low-wavenumber turbulence on $d_\parallel(r_\perp)$, provided that r_\perp is within the inertial subrange. Hence (30) may be used in the integration. Making this substitution, and replacing the Bessel function with its integral representation, leads to

$$d_\parallel(r) = \frac{55\alpha}{18\pi} \epsilon^{2/3} \int_0^\infty \int_0^\pi [1 - \cos(kr \sin \theta)] k^{-5/3} d\theta dk.$$

Using the trigonometric identity $1 - \cos x = 2 \sin^2 x$, changing the order of integration, and then calculating the integrals using (3.823) and (3.621.1) in Gradshteyn and Ryzhik (1994), we have the result

$$d_\parallel(r) = \frac{11\sqrt{3}\Gamma(1/3)}{27^{2/3}\pi} B\left(\frac{1}{2}, \frac{4}{3}\right) \alpha \epsilon^{2/3} r^{5/3} = \frac{11\Gamma(1/6)}{30\sqrt{\pi}\Gamma(2/3)} C_V^2 r^{5/3} \simeq 0.85 C_V^2 r^{5/3}. \quad (32)$$

where $B(a, b) = \Gamma(a)\Gamma(b)/\Gamma(a+b)$ is the beta function. The second form follows from (26), and by performing further manipulations on the gamma functions. I derived this version of the 2D structure function previously (Wilson, 1998c) by taking the inertial-subrange limit of the von Kármán model. Here I have rederived the equation without making any assumptions regarding the energy-subrange structure of the turbulence.

4.3 Von Kármán Model

The von Kármán model is developed from the following equation for the specific energy spectrum:

$$E(k) = \frac{55}{9B(1/2, 1/3)} \frac{\sigma^2 k^4 \ell^5}{(1 + k^2 \ell^2)^{17/6}}, \quad (33)$$

where σ^2 is the variance parameter (the variance of a single velocity component), and ℓ is a length scale parameter.* The corresponding correlation function for separations *parallel* to the direction of the velocity components is (Wilson, 1998c)

$$R_\parallel(r) = \frac{2\sigma^2}{\Gamma(1/3)} \left(\frac{r}{2\ell}\right)^{1/3} K_{1/3}\left(\frac{r}{\ell}\right). \quad (34)$$

*Some previous authors (particularly those concerned with optical propagation) incorporate a spectral roll-off at high wavenumber, representing the dissipation subrange, in the von Kármán model. However, since the dissipation subrange has little effect on audible frequency sound waves, it is neglected here. This simplification allows us to analytically derive equations for the correlation and structure functions.

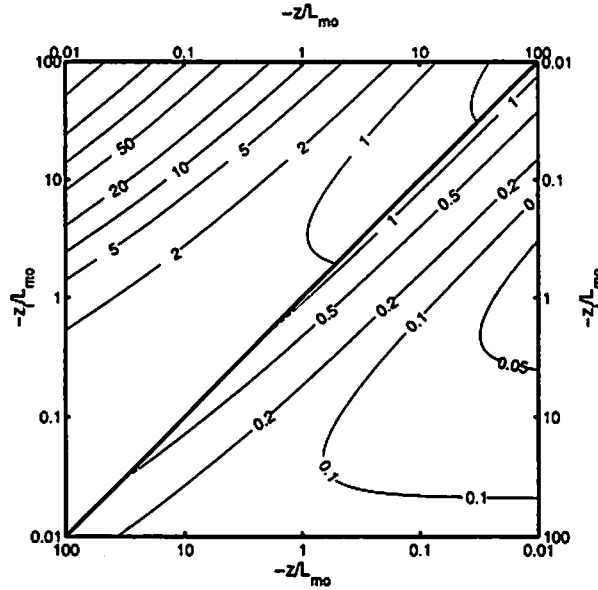


Figure 3: Normalized integral length scale \mathcal{L} (parallel to the velocity fluctuations) as a function of $-z/L_{m0}$ and $-z_i/L_{m0}$. Upper left is \mathcal{L}/z , lower right is \mathcal{L}/z_i .

The 1D longitudinal spectrum (the Fourier transform of the above correlation function) is

$$F(k) = \frac{1}{B(1/2, 1/3)} \frac{\sigma^2 \ell}{(1 + k^2 \ell^2)^{5/6}}. \quad (35)$$

A reasonable method for determining the parameters in the von Kármán model is to set the variance equal to the actual variance of the field, and then choose the length scale to match the Kolmogorov model in the inertial subrange. By taking the limit of (35) for large $k\ell$, and setting the result equal to the right side of (9), one finds

$$\ell = \left[\frac{2}{\alpha B(1/2, 1/3)} \right]^{3/2} \frac{\sigma^3}{\epsilon} \simeq 0.87 \frac{\sigma^3}{\epsilon}. \quad (36)$$

Applying this equation to shear and buoyancy turbulence yields $\ell = 1.8z$ and $\ell = 0.18z_i$, respectively.

Since the von Kármán and Kolmogorov models have the same inertial subrange, L and the diffraction parameter are the same for both models. Calculation of the strength parameter requires the integral length scale. A relationship between the integral length scale and ℓ can be found by integrating (34):

$$\mathcal{L} = \frac{\pi}{B(1/2, 1/3)} \ell \simeq 0.65 \frac{\sigma^3}{\epsilon}. \quad (37)$$

In the previous section it was argued, on the basis of the Kolmogorov model, that $\mathcal{L} \simeq 1.6L$. Comparison of equations (27) and (37) implies that $\mathcal{L} = 1.07L$ for the von Kármán model, a value reasonably close to the Kolmogorov estimate. The resulting values for shear and buoyancy turbulence are $\mathcal{L}_s = 1.3z$ and $\mathcal{L}_b = 0.13z_i$, respectively. According to (14), the general equation for \mathcal{L} involves weighting the length scales for each type of turbulence by the respective variances. The result can be written

$$\mathcal{L} \simeq 1.3z \frac{1 + 0.012(z_i/z)(-z_i/\kappa L_{m0})^{2/3}}{1 + 0.12(-z_i/\kappa L_{m0})^{2/3}} = 0.13z_i \frac{1 + 84(z/z_i)(-z_i/\kappa L_{m0})^{-2/3}}{1 + 8.5(-z_i/\kappa L_{m0})^{-2/3}}. \quad (38)$$

Contour plots of \mathcal{L}/z and \mathcal{L}/z_i are shown in Fig. 3. Calculations of the strength parameter Φ , multiplied by the dimensionless groups $c_0/(k_0 u_* \sqrt{Xz})$ and $c_0/(k_0 w_* \sqrt{Xz_i})$ (the shear and convective turbulence normalizations, respectively), are shown in Fig. 4.

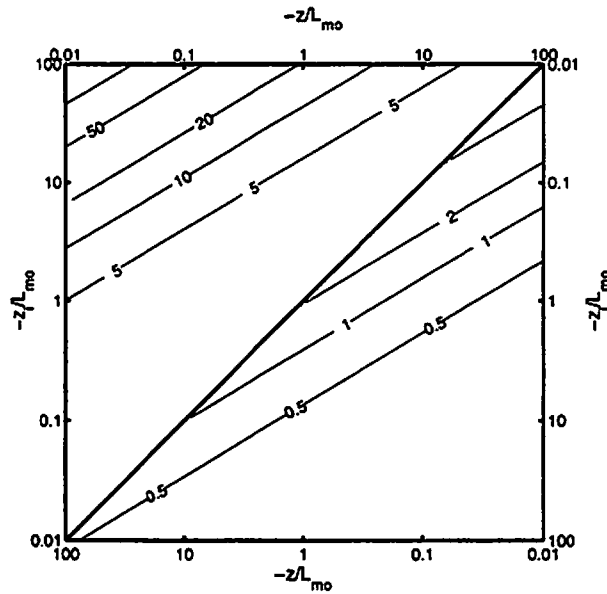


Figure 4: Upper left is the strength parameter Φ normalized by $c_0 / (k_0 u_* \sqrt{Xz})$; lower right is $\Phi c_0 / (k_0 w_* \sqrt{Xz_i})$.

Comparing Figs. 1 and 3, we observe no simple proportionality between \mathcal{L} and L over most of the range of $-z/L_{mo}$ and $-z_i/L_{mo}$, as we might have anticipated. On the contrary, there are very significant qualitative differences between \mathcal{L} and L : near the ground, \mathcal{L} usually is determined by the large, buoyancy driven eddies, whereas L is determined by smaller, shear-driven eddies. This holds true even for boundary layers with moderate surface heat fluxes. From a modeling standpoint, the different behaviors of \mathcal{L} and L result from using Højstrup's hypothesis. Physically, we can view the distinctive behavior of \mathcal{L} and L as resulting from the broad spectrum of spatial scales, spanning z to z_i , at which TKE is produced in the atmospheric boundary layer. \mathcal{L} and L are both "outer" scales in the sense that they characterize the energy-containing subrange; however, they respond to different parts of the production spectrum.

4.4 Gaussian Model

The Gaussian model is defined by the longitudinal correlation function

$$R_{||}(r) = \sigma^2 \exp\left(-\frac{r^2}{\ell_G^2}\right). \quad (39)$$

Fourier transformation yields the spectrum

$$F(k) = \frac{\sigma^2 \ell_G}{2\sqrt{\pi}} \exp\left(-\frac{k^2 \ell_G^2}{4}\right). \quad (40)$$

Because it does not realistically describe the inertial subrange, the Gaussian model is best suited to the energy-containing subrange. However, it has also been used successfully as an "applied filter" when scattering occurs from only a limited part of the turbulence spectrum (Wilson et al., 1998).

Selection of the Gaussian length scale parameter for scattering calculations is problematic (Wilson et al., 1998). If the Gaussian correlation function is expanded for small argument, and the result set equal to (3) with $p = 3$, then ℓ_G simply equals the correlation length L . In this case ℓ_G is also equal to a quantity known as the *Taylor microscale*, which falls within the inertial subrange (Wilson et al., 1998). In high Reynolds number turbulence, such as occurs in the atmospheric boundary layer, the Taylor microscale is much less than the integral length scale. Therefore choosing ℓ_G on the basis of the small-argument expansion leads to a very poor model for the large-eddy region of the turbulence spectrum.

A better procedure in most cases is to choose ℓ_G on the basis of the integral length scale of the turbulence. The integral length scale for the isotropic Gaussian model is $(\sqrt{\pi}/2)\ell_G$. If the values of \mathcal{L} in

the von Kármán and Gaussian models are equated, one has the relationship

$$\ell_G = \frac{2\Gamma(5/6)}{\Gamma(1/3)} \ell \simeq 0.73 \frac{\sigma^3}{\epsilon}. \quad (41)$$

This result implies $\ell_G = 1.5z$ for shear turbulence, and $\ell_G = 0.15z_i$ for buoyancy turbulence. These values are somewhat different from those suggested previously by Wilson and Thomson (1994), which were $1.0z$ and $0.4z_i$, respectively.

The Gaussian model has some utility in theoretical models of sound propagation through random media: it allows many results to be obtained in simple, analytical form, and makes clear the characteristics of the scattered signal statistics for wavelengths smaller than or larger than a single characteristic length scale for a random medium. However, because the Gaussian model is a very poor overall description of the spectrum of atmospheric turbulence, one cannot expect satisfactory results from it for a broad range of acoustic frequencies and atmospheric conditions.

4.5 G-Function Model

In Section 4.3, the length scale ℓ for the von Kármán model was chosen to obtain the proper spectral level within the inertial subrange. An unfortunate consequence of choosing ℓ in this manner is that the resulting spectral model may not agree well with the measured energy-subrange spectrum. As a result, the modeled integral length scale may not agree with the actual integral length scale. To overcome this difficulty, I have proposed (Wilson, 1998b) a generalized version of the von Kármán model, which allows the integral length scale to be specified independently. The energy spectrum is given by the equation

$$E(k) = \frac{4(5/6+b)(11/6+b)}{3B(1/2, 1/3+b)} \sigma^2 \ell (k^2 \ell^2)^{-5/6} B_{k^2 \ell^2 / (1+k^2 \ell^2)} \left(\frac{17}{6}, b \right), \quad (42)$$

where $B_x(a, b)$ is the incomplete beta function. Equivalently, the energy spectrum can be written

$$E(k) = \frac{4\sigma^2 \ell}{3\sqrt{\pi}\Gamma(1/3+b)} G_{22}^{12} \left(k^2 \ell^2 \left| \begin{matrix} 1/6, 1/6-b \\ 2, -5/6 \end{matrix} \right. \right), \quad (43)$$

where $G_{pq}^{mn}()$ is the Meijer's G -function (e.g., Erdélyi *et al.* 1953). When $b = 1$, (43) reduces to the von Kármán model. It can be shown (Wilson, 1998b) that the integral length scale corresponding to (43) is

$$\mathcal{L} = \frac{2\pi}{5B(1/2, 1/3+b)} \ell. \quad (44)$$

Values $b < 1$ result in integral length scales larger than the von Kármán model, and $b > 1$ results in smaller integral length scales. The 2D correlation function can also be determined analytically, with result

$$b(r) = \frac{\sigma^2 \ell}{3\sqrt{\pi}\Gamma(1/3+b)} \left[G_{13}^{30} \left(\frac{r^2}{4\ell^2} \left| \begin{matrix} 11/6 \\ 0, 5/6, b+5/6 \end{matrix} \right. \right) - G_{13}^{30} \left(\frac{r^2}{4\ell^2} \left| \begin{matrix} 11/6 \\ 1, 5/6, b+5/6 \end{matrix} \right. \right) \right]. \quad (45)$$

The G -functions in (45) can be computed using the commercial software package Mathematica. Figure 5 shows the 2D structure function for several ratios of the integral length scale to the von Kármán length scale. Although the appearance of the curves suggests that the inertial subrange asymptote in the G -function model depends on the integral length scale, in actuality the curves do converge very slowly as $r/\ell \rightarrow 0$. For large separations, increasing the integral length scale leads to larger values of the structure function.

5 ANISOTROPIC TURBULENCE MODELS

The main motivation for anisotropic modeling of turbulence is to improve realism within the energy-containing subrange. Because the turbulent production mechanisms (shear and buoyancy) act along preferred directions, energy-containing subrange turbulence is inherently anisotropic. Unfortunately modeling of the energy-containing subrange is a difficult topic, since (unlike the inertial subrange) no universal parameterizations are known.

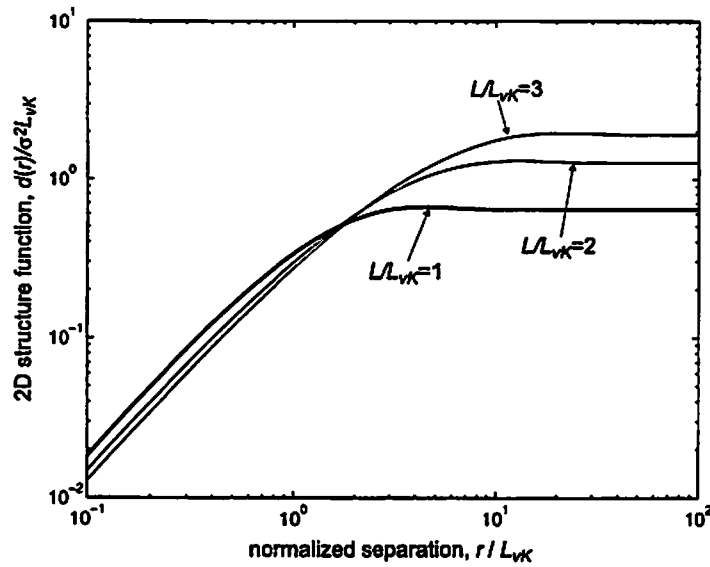


Figure 5: Two-dimensional structure function for the G -function model, for several values of the ratio L/L_{vK} , where L is the integral length scale in the G -function model, and L_{vK} is the von Kármán length scale.

5.1 Nonrigorous Gaussian Model

A simple anisotropic model can be constructed that uses a distinct length scale in each direction:

$$R(r_1, r_2, r_3) = \sigma^2 \exp\left(-\frac{r_1^2}{\ell_1^2} - \frac{r_2^2}{\ell_2^2} - \frac{r_3^2}{\ell_3^2}\right).$$

The model developed by Wilson and Thomson (1994) is based on sums of correlation functions having this form.* A useful feature of the nonrigorous anisotropic Gaussian model is that the length scales can be selected to equal the actual integral length scale \mathcal{L} in each direction. This results in good predictions for the strength parameter, and hence for the rms phase fluctuations. It also provides good predictions for the MCF when the separation between the sensors is somewhat larger than \mathcal{L} , since in this case $d(r) \simeq 2b(0) = \Phi^2 / (\pi k_0^2 X) = (2/\pi) \sigma^2 \mathcal{L}$.

Like the isotropic Gaussian model, determination of the length scales for the nonrigorous anisotropic Gaussian model can be problematic. If separate length scales are used for each velocity component, a total of nine length scale parameters are required. Wilson and Thomson (1994) devised a scheme based on directional dimensional analysis (DDA) to predict the length scales from z and z_i , but DDA is not well tested at present and likely provides only a rough, qualitative description of atmospheric turbulence structure.

The main disadvantage of the nonrigorous anisotropic Gaussian model is that it does not accurately describe the correlation function of the turbulence for small separations ($r_i \ll \ell_i$). The model does not necessarily obey local isotropy for small separations, and does not have a structure function consistent with Kolmogorov's scaling hypothesis. As a result predictions of the diffraction parameter, and of the MCF for sensor separations in the inertial subrange, are inherently poor. An additional problem with the nonrigorous anisotropic Gaussian model is that it does not satisfy incompressibility for arbitrary values of the length scale parameters. More rigorous approaches to modeling the 3D spectra/correlations of atmospheric turbulence are discussed in sections 5.2 to 5.4.

*There is an error in Eqs. (27) and (28) of Wilson and Thomson (1994): all occurrences of $1/\kappa^2$ should be replaced by κ^2 , and likewise for $1/\kappa_{fc}^2$. This mistake later resulted in an erroneous conclusion by Wilson (1998c), that the coherence was enhanced by propagation in the along-wind direction. The correct prediction is that coherence is degraded in the along-wind direction. Eq. (80) in Wilson (1998c) is correct, however.

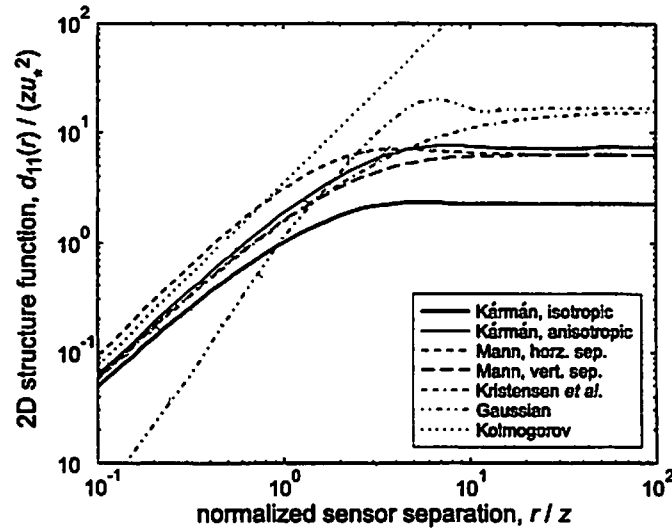


Figure 6: Two-dimensional structure functions for various turbulence models, for along-wind propagation.

5.2 Models Based on Kristensen et al.'s Spectral Tensor

Kristensen et al. (1989) suggested partitioning the energy spectrum for anisotropic turbulence into three independent scalar functions, $A_1(k)$, $A_2(k)$, and $A_3(k)$, where $E(k) = (4/3)\pi k^2 \sum_i A_i(k)$. By their hypothesis, the 3D spectral density tensor of the turbulent velocity fluctuations has the form

$$\Phi_{ij}(k) = \sum_{m=1}^3 A_m(k) \left(\delta_{mi} - \frac{k_m k_i}{k^2} \right) \left(\delta_{mj} - \frac{k_m k_j}{k^2} \right). \quad (46)$$

It is beyond the scope of this paper to discuss the mathematical details and implementation of Kristensen et al.'s spectral density tensor. Note that (46) does *not* provide a fully general description of anisotropic turbulence. The tensor assumes certain symmetry properties that may be unrealistic. Application of the tensor simply represents an initial (and practical) attempt at incorporating anisotropy into spectral models.

When Kristensen et al.'s spectral tensor is employed, it can be shown that the 2D correlation function for propagation in the x_1 -direction is determined from the equation (Wilson, 1998a)

$$b_{11}(r_2, r_3) = 2\pi \int_0^\infty A_1(k_\perp) J_0(k_\perp r_\perp) k_\perp dk_\perp, \quad (47)$$

and similarly for the x_2 - and x_3 -directions. Note that as a result of Kristensen et al.'s hypothesis, $b_{\parallel}(r_\perp)$ depends only on the magnitude of r_\perp , as it did for isotropic turbulence. However, $b_{\parallel}(r_\perp)$ *does* depend on the orientation of the propagation path.

The isotropic Gaussian and von Kármán models can be reformulated in an anisotropic form with Kristensen et al.'s spectral tensor (Wilson, 1998a). The procedure involves defining three independent functions A_i , each with its own variance and length scale. When the variances and length scales are equal, the isotropic energy spectrum for the corresponding model is recovered. The resulting anisotropic models are quite complicated, involving generalized hypergeometric functions for the Gaussian model, and Meijer's G -functions for the von Kármán model. A generalized form of the von Kármán model, devised by Kristensen et al., can also be used to construct the A_i 's. Two-dimensional structure functions based on the different models are shown in Fig. 6 for along-wind propagation, and in Fig. 7 for crosswind propagation. The structure functions predictions vary substantially from model to model; this implies, of course, that the MCF predictions are also quite different.

Generally speaking, the complexity of rigorous models based on Kristensen et al.'s spectral tensor, combined with their inherent (and perhaps unrealistic) symmetry properties, makes them unattractive at present for wave propagation calculations. However, it might be possible to beneficially exploit certain

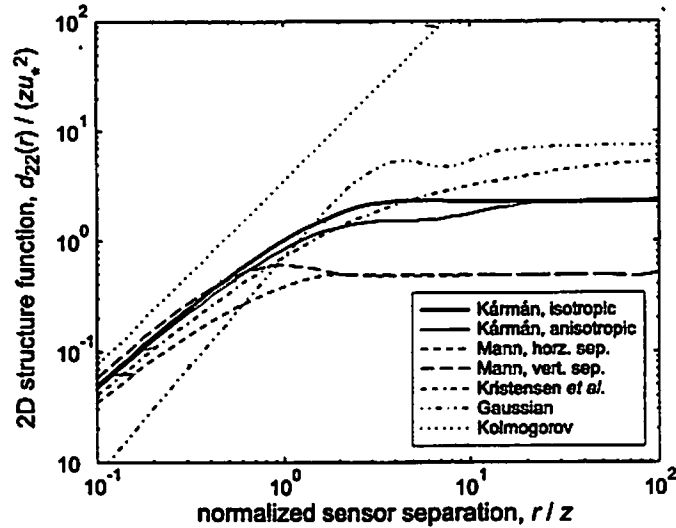


Figure 7: Two-dimensional structure functions for various turbulence models, for crosswind propagation.

properties of Kristensen *et al.*'s spectral tensor, such as the simple relationship between the 2D structure functions and the A_i 's, Eq. (47).

5.3 Mann's Rapid Distortion Theory Model

The Mann model (1994) is the result of a first-principle theoretical treatment of turbulence in a constant shear layer. The main hypothesis upon which Mann's model is based is called *rapid distortion theory*: In a turbulent shear layer, new eddies are perpetually being created, subjected to the forces of shear, and then eventually broken down into smaller eddies. Between the times when an eddy is created and when it is destroyed by shear forces, there exists an interval for which the eddy exists in a state that is "typical" for eddies having its same spatial dimensions. This interval is called the *eddy lifetime*.

A full discussion of rapid distortion theory and Mann's model is beyond the scope of this paper. However, the relevant equations are summarized here. Mann's equations for the 3D autospectra in a uniform (constant gradient) shear layer are

$$\Phi_{11}(\mathbf{k}) = \frac{E(k_0)}{4\pi k_0^4} [k_0^2 - k_1^2 - 2k_1 k_{30} \zeta_1 + (k_1^2 + k_2^2) \zeta_1^2], \quad (48)$$

$$\Phi_{22}(\mathbf{k}) = \frac{E(k_0)}{4\pi k_0^4} [k_0^2 - k_2^2 - 2k_2 k_{30} \zeta_2 + (k_1^2 + k_2^2) \zeta_2^2], \quad (49)$$

and

$$\Phi_{33}(\mathbf{k}) = \frac{E(k_0)}{4\pi k^4} (k_1^2 + k_2^2). \quad (50)$$

In the equations above, $E(k_0)$ is the *initial* (before the onset of shear distortion) energy spectrum. The isotropic von Kármán energy spectrum (33) is used. The initial wavenumber is $\mathbf{k}_0 = (k_1, k_2, k_{30})$, where $k_{30} = k_3 - \beta k_1$, and β is the nondimensional eddy lifetime, given by (Mann, 1994; Wilson, 1998a)

$$\beta = \frac{\sqrt{3}\Gamma}{kl} \left[B_{1/(1+k^2 l^2)} \left(\frac{1}{3}, \frac{5}{2} \right) \right]^{-1/2}. \quad (51)$$

where Γ is the eddy-lifetime parameter. The ζ_i follow from the equations $\zeta_1 = C_1 - (k_2/k_1) C_2$ and $\zeta_2 = (k_2/k_1) C_1 + C_2$, where

$$C_1 = \frac{\beta k_1^2 (k_0^2 - 2k_{30}^2 + \beta k_1 k_{30})}{k^2 (k_1^2 + k_2^2)}, \quad (52)$$

Model, Direction	σ^2/u_*^2	\mathcal{L}/z	$\Phi_{c0}/(k_0 u_* \sqrt{Xz})$
Mann model, along wind ($i = 1$)	4.77	1.49	3.77
Mann model, crosswind ($i = 2$)	2.56	0.212	1.04
Mann model, vertical ($i = 3$)	1.46	2.11	2.48
Isotropic von Kármán, all directions	2.97	1.34	2.82

Table 1: Normalized variances, integral length scales (velocity component parallel to the direction of integration), and strength parameters for the Mann turbulence model. The isotropic von Kármán model is shown for comparison.

and

$$C_2 = \frac{k_2 k_0^2}{(k_1^2 + k_2^2)^{3/2}} \arctan \left[\frac{\beta k_1 (k_1^2 + k_2^2)^{1/2}}{k_0^2 - \beta k_3 k_1} \right]. \quad (53)$$

A reasonable method for determining the parameter Γ is to match the ratio σ_1^2/σ_3^2 in the Mann model to the anisotropic variances given earlier in (10). This ratio should be $4.77/1.46 = 3.27$. The desired value of Γ , found by numerical integration, is $\Gamma = 3.58$ (Wilson, 1998a). To force σ_1^2 equal to $4.77u_*^2$ when $\Gamma = 3.58$, we then need to set (Wilson, 1998a)

$$\sigma^2 = 1.52u_*^2 \quad (54)$$

in the initial von Kármán spectrum. One can obtain the length scale by matching the dissipation rate of turbulent kinetic energy to $u_*^3/\kappa z$, with result (Wilson, 1998a)

$$\ell = 0.587z. \quad (55)$$

The diffraction parameter for the Mann model is the same as the shear-turbulence Kolmogorov model, since the dissipation rates in the two models are the same. Table 1 shows the variances, integral length scales, and strength parameters corresponding to the Mann model.

The 2D correlations for the Mann model must be determined, in general, by numerical evaluation of a 2D inverse Fourier transform of the 3D spectra. Figs. 6 and 7 show 2D structure functions resulting from such an evaluation, for along-wind and crosswind propagation, respectively.

5.4 Ground Blocking

In a previous paper (Wilson, 1997), I proposed an inhomogeneous, anisotropic spectral model for the buoyancy driven (convective) boundary layer that includes the effect of *blocking* by the ground. Blocking forces the vertical velocity variance to vanish at ground level. Continuity requires that the horizontal velocity variance also be modified. The basis of the ground-blocked spectral model is an equation that gives the observed turbulence spectrum in terms of an *a priori* homogeneous spectrum (i.e., the spectrum that would exist if the ground were not present). Derivation of this *blocking equation* is based on previous suggestions by Hunt and Graham (1978), with the assumptions of a no-slip lower boundary condition, and that the blocking does not itself generate vorticity. These assumptions allow the boundary effect to be modeled by potential flow theory. A straight forward derivation then leads to the equation

$$\begin{aligned} \phi_{ij}(k_1, k_2; z, z') &= \phi_{ij}^{(H)}(k_1, k_2; |z' - z|) \\ &+ e^{-k_h z'} m_j(k_1, k_2) \phi_{3i}^{(H)*}(k_1, k_2; z) \\ &+ e^{-k_h z} m_i^*(k_1, k_2) \phi_{3j}^{(H)}(k_1, k_2; z') \\ &+ e^{-k_h(z+z')} m_i^*(k_1, k_2) m_j(k_1, k_2) \phi_{33}^{(H)}(k_1, k_2; 0), \end{aligned} \quad (56)$$

where ϕ_{ij} (called the *2D cross spectrum*) is the Fourier transform of the correlation function $R_{ij}(r_1, r_2, z, z') \equiv \langle u_i(x, y, z) u_j(x + r_1, y + r_2, z') \rangle$ with respect to the two horizontal separations r_1 and r_2 , the superscripted “(H)” refers to the homogeneous spectrum, $m_1 = ik_1/k_h$, $m_2 = ik_2/k_h$, $m_3 = -1$, and $k_h^2 = k_1^2 + k_2^2$. In the

paper (Wilson, 1997), I used the von Kármán spectrum with parameters chosen for the convective conditions ($\sigma^2 = 0.35w_*^2$ and $\epsilon = 0.8w_*^3/z_i$), although the blocking equation can be applied to other homogeneous spectra.

The blocking equation predicts that the vertical velocity variance vanishes at the ground, and then increases with height in proportion to $z^{2/3}$ (Wilson, 1997). The horizontal variances at ground level equal 3/2 times their values away from the ground. These predictions are consistent with previous observations of convective boundary layers (Caughey & Palmer, 1979). Good agreement between predictions and measurements for other second-order convective-boundary-layer statistics, such as vertical cross correlations and horizontal spectra, is also obtained. One can construct a very satisfactory overall model for second-order boundary-layer statistics by using Højstrup's hypothesis, with Mann's model for the contribution from shear turbulence, and the ground-blocked model for the buoyancy turbulence.

Let us now consider the effect of ground blocking on horizontal acoustical propagation. The strength parameter is determined by the product of the variance and the integral length scale parallel to the velocity components. For horizontal propagation we can take the direction of propagation to be the x_1 -axis without loss of generality. Hence

$$\Phi^2 = k_0^2 X \int_{-\infty}^{\infty} R_{11}(r_1, 0, z, z) dr_1, \quad (57)$$

Using the Fourier transform relationship between R_{11} and ϕ_{11} , we can rewrite this equation as

$$\Phi^2 = 2\pi k_0^2 X \int_{-\infty}^{\infty} \phi_{11}(0, k_2, z, z) dk_2. \quad (58)$$

Since $m_1(0, k_2) = 0$, (56) implies that $\phi_{11}(0, k_2; z, z) = \phi_{11}^{(H)}(0, k_2; 0)$. Therefore the ground blocking has no effect on the strength parameter for horizontal propagation! A similar derivation, except with $r_2 \neq 0$ and $z \neq z'$, demonstrates that the 2D correlation function is unaffected by blocking. Hence the MCF is also unaffected. Finally, since blocking only affects the large eddies (compared to the height from the ground), local isotropy is preserved, and the correlation length used to calculate the diffraction parameter is unaffected by the blocking.

Considering the problem in Fourier space, the effect of the boundary is to cause the vertical velocity to deflect in the horizontal direction parallel to the wavenumber vector of a given mode. As a result, the velocity field near the ground essentially consists of the lower halves of roll-type vortices having randomized orientations.* The 2D spectrum used to calculate the strength parameter or structure function involves only the rolls having rotational axes parallel to the direction of propagation. Since these rolls have no velocity component aligned with the propagation, they do not affect the propagation.

6 CONCLUDING REMARKS

According to the formulation given in this paper, there are two basic length scales characterizing large-scale turbulence structure. One of these, the correlation length L , is associated with diffraction, and the other, the integral length scale \mathcal{L} , with geometric phase fluctuations (the "strength" of the turbulence). They could both be called "outer" scales in the sense that they characterize turbulence in the energy-containing subrange. However, L is determined by the total TKE dissipation rate, whereas \mathcal{L} is weighted toward the largest eddies. In an unstable atmospheric surface layer, total TKE production is usually dominated by shear-generated z -scale eddies, whereas the largest eddies are buoyantly generated and normally have sizes on the order of z_i . Hence L is often much smaller than \mathcal{L} . Physically, this discrepancy results from the fact that TKE is produced in the atmospheric boundary layer at a broad range of spatial scales. One might refer (tongue in cheek) to L as the "inner outer" scale, and to \mathcal{L} as the "outer outer" scale. However, such terminology would inevitably lead to confusion, since in nearly neutral conditions it is possible for the length scales to be nearly equal.

The strength parameter for acoustic wave propagation, being a function of the integral scale, is generally determined by the large, buoyantly driven eddies. The diffraction parameter, since it depends on the

*Roll vortex structures are often observed in the atmospheric boundary layer, with preferred alignment roughly in the direction of the mean wind. The "rolls" in the discussion here are not necessarily actual turbulence structures, but rather figments of the Fourier decomposition. They have random orientations in horizontally isotropic turbulence.

correlation length, is most affected by small, shear-driven eddies. This paper has provided some new parameterizations for the length scales L and \mathcal{L} , and for the strength and diffraction parameters, in terms of the turbulence scales z , z_i , u_* (the friction velocity), and Q_s (the surface heat flux). The mutual coherence function (MCF) was also modeled in terms of these turbulence scales.

The necessity of defining two separate length scales was discussed previously by Wilson and Thomson (1994). In that paper, the two length scales were referred to as the *parallel* length scale, L_{\parallel} , and the *perpendicular* length scale, L_{\perp} . These two scales are analogous to \mathcal{L} and L , respectively, in this paper. The main improvement in this paper is that equations for the two length scales were derived based on a von Kármán model, rather than a Gaussian model. The benefits of this approach are a more realistic turbulence model, and more rigorous equations for the model parameters.

When modifications to the turbulent flow caused by ground blocking of eddies were incorporated into the wave propagation calculations, the blocking was found to have no effect on the strength parameter and MCF for horizontal propagation, even though significant modifications to the flow field occur. This conclusion should not be construed as implying that the ground in general has no effect on acoustic wave propagation through turbulence. The blocking effect is just one aspect of this complicated problem. Other phenomena, such as flow modification by surface roughness and the role of ground-reflected acoustic waves (Daigle et al., 1978), are important and require further study.

ACKNOWLEDGMENTS

This paper is dedicated to John Wyngaard. Weaved throughout its fabric are some of the many things he taught me about turbulence during my tenure as a research associate at Penn State. Discussions with J. Brasseur, J. Mann, D. Norris, V. Ostashev, and D. Thomson also played an essential role in formulating the ideas presented here. I am indebted to these scientists and many others who have shared with me their expertise in the areas of turbulence and propagation.

REFERENCES

- Batchelor, G. K., 1953: *The Theory of Homogeneous Turbulence*. Cambridge Univ. Press, Cambridge, Great Britain.
- Boulanger, P., R. Raspet, and H. E. Bass, 1995: Sonic boom propagation through a realistic turbulent atmosphere. *J. Acoust. Soc. Am.*, **98**, 3412–3417.
- Caughey, S. J. and S. G. Palmer, 1979: Some aspects of turbulence structure through the depth of the convective boundary layer. *Q. J. R. Meteorol. Soc.*, **105**, 811–827.
- Daigle, G. A., J. E. Piercy, and T. F. W. Embleton, 1978: Effects of atmospheric turbulence on the interference of sound waves near a hard boundary. *J. Acoust. Soc. Am.*, **64**, 622–630.
- Dashen, R., 1979: Path integrals for waves in random media. *J. Math. Phys.*, **20**, 894–920.
- Erdélyi, A., W. Magnus, F. Oberhettinger, and F. G. Tricomi, 1953: *Higher Transcendental Functions*, volume 1. McGraw-Hill, New York.
- Flatté, S. M., R. Dashen, W. H. Munk, K. M. Watson, and F. Zachariassen, 1979: *Sound Transmission through a Fluctuating Ocean*. Cambridge University Press, Cambridge.
- Gilbert, K. E., X. Di, and R. R. Korte, 1996: Distorted-wave born approximation analysis of sound levels in a refractive shadow zone. In *Seventh International Symposium on Long Range Sound Propagation*, Ecole Centrale de Lyon, Lyon, France, 373–389.
- Gradshteyn, I. S. and I. M. Ryzhik, 1994: *Table of Integrals, Series, and Products*. Academic Press, San Diego.
- Högström, U., 1996: Review of some basic characteristics of the atmospheric surface layer. *Bound. Layer Meteorol.*, **78**, 215–246.
- Højstrup, J., 1982: Velocity spectra in the unstable planetary boundary layer. *J. Atmos. Sci.*, **39**, 2239–2248.
- Hunt, J. C. R. and J. M. R. Graham, 1978: Free-stream turbulence near plane boundaries. *J. Fluid Mech.*, **84**, 209–235.
- Juvé, D., P. Blanc-Benon, and P. Chevret, 1994: Sound propagation through a turbulent atmosphere: Influence of the turbulence model. In *Proceedings of the Sixth International Symposium on Long Range Sound Propagation*, Havelock, D. I. and Stinson, M. R., editors, NRC Canada, Ottawa, Canada, 270–282.

- Kaimal, J. C., J. C. Wyngaard, Y. Izumi, and O. R. Coté, 1972: Spectral characteristics of surface layer turbulence. *Q. J. R. Meteorol. Soc.*, **98**, 563-589.
- Kolmogorov, A. N., 1941: The local structure of turbulence in incompressible viscous fluid for very large Reynolds numbers. *C. R. Acad. Sci. URSS*, **30**, 301-305.
- Kristensen, L. and N. O. Jensen, 1982: Lateral coherence in isotropic turbulence and in natural wind. *Bound. Layer Meteorol.*, **17**, 353-373.
- Kristensen, L., D. H. Lenschow, P. Kirkegaard, and M. Courtney, 1989: The spectral velocity tensor for homogeneous boundary-layer turbulence. *Bound. Layer Meteorol.*, **47**, 149-193.
- Mann, J., 1994: The spatial structure of neutral atmospheric surface layer turbulence. *J. Fluid Mech.*, **273**, 141-168.
- Ostashev, V. E., 1994: Sound propagation and scattering in media with random inhomogeneities of sound speed, density and medium velocity. *Waves Rand. Med.*, **4**, 403-428.
- Ostashev, V. E., G. Goedecke, B. Brahler, V. Mellert, and H. Auvermann, 1996: Coherence functions of plane and spherical sound waves in the turbulent atmosphere with von karman spectra of temperature and wind velocity fluctuations. In *Proceedings of the Seventh International Symposium on Long Range Sound Propagation*, Ecole Centrale de Lyon, Lyon, France, 349-357.
- Ostashev, V. E., V. Mellert, R. Wandelt, and F. Gerdes, 1997: Propagation of sound in a turbulent medium. I. Plane waves. *J. Acoust. Soc. Am.*, **102**, 2561-2570.
- Peltier, L. J., J. C. Wyngaard, S. Khanna, and J. G. Brasseur, 1996: Spectra in the unstable surface layer. *J. Atmos. Sci.*, **53**, 49-61.
- Stinson, M. and G. Daigle, 1996: Meteorological measurements for use in sound propagation calculations. In *Proceedings of the Seventh International Symposium on Long Range Sound Propagation*, Ecole Centrale de Lyon, Lyon, France, 137-147.
- Tatarskii, V. I., 1971: *The Effects of the Turbulent Atmosphere on Wave Propagation*. Keter, Jerusalem.
- Tennekes, H. and J. L. Lumley, 1972: *A First Course in Turbulence*. MIT Press, Cambridge, Mass.
- Wilson, D. K., 1996: A brief tutorial on atmospheric boundary-layer turbulence for acousticians. In *Seventh International Symposium on Long Range Sound Propagation*, Ecole Centrale de Lyon, Lyon, France, 111-121.
- Wilson, D. K., 1997: A three-dimensional correlation/spectral model for turbulent velocities in a convective boundary layer. *Bound. Layer Meteorol.*, **85**, 35-52.
- Wilson, D. K., 1998a: Anisotropic turbulence models for acoustic propagation through the neutral atmospheric surface layer. Technical Report ARL-TR-1519, U.S. Army Research Laboratory, 2800 Powder Mill Road, Adelphi, MD 20783.
- Wilson, D. K., 1998b: A new model for turbulence spectra and correlations based on Meijer's *G*-functions. Technical Report ARL-TN-104, U.S. Army Research Laboratory, 2800 Powder Mill Road, Adelphi, MD 20783.
- Wilson, D. K., 1998c: Performance bounds for acoustic direction-of-arrival arrays operating in atmospheric turbulence. *J. Acoust. Soc. Am.*, **103**, 1306-1319.
- Wilson, D. K., J. G. Brasseur, and K. E. Gilbert, 1998: Acoustic scattering and the spectrum of atmospheric turbulence. Submitted to *J. Acoust. Soc. Am.*
- Wilson, D. K. and D. W. Thomson, 1994: Acoustic propagation through anisotropic, surface-layer turbulence. *J. Acoust. Soc. Am.*, **96**, 1080-1095.
- Wyngaard, J. C., 1992: Atmospheric turbulence. *Annu. Rev. Fluid Mech.*, **24**, 205-233.
- Wyngaard, J. C., Y. Izumi, and S. A. Collins, 1971: Behavior of the refractive-index-structure parameter near the ground. *J. Opt. Soc. Am.*, **61**, 1646-1650.

Interference of direct and ground reflected waves in a turbulent atmosphere

V.E. Ostashev and G.H. Goedecke
Dept. of Physics, Box 30001, New Mexico State University,
Las Cruces, NM 88003-8001

ABSTRACT

Predictions of interference of direct and ground reflected sound waves in a turbulent atmosphere are important for many concerns of atmospheric acoustics. The most advanced theory of this phenomenon has been developed by Clifford and Lataitis [1]. They present the analytical equation for the mean-square sound pressure $\langle |p|^2 \rangle$ due to a point source located above an impedance ground in a turbulent atmosphere with temperature fluctuations, and calculate $\langle |p|^2 \rangle$ for a Gaussian correlation function of these fluctuations. In the present paper, we generalize these results. We consider the interference of direct and ground reflected waves in a turbulent atmosphere with both temperature and wind velocity fluctuations, and calculate $\langle |p|^2 \rangle$ for Gaussian, Kolmogorov and von Karman spectra of these fluctuations. The temperature and wind velocity contributions to the mean-square pressure $\langle |p|^2 \rangle$ are compared as well as the values of $\langle |p|^2 \rangle$ for different spectra.

1 INTRODUCTION

The interference of the direct wave from the source S to the receiver R (both located above the impedance ground) and that reflected from the ground is one of the most important concerns in atmospheric acoustics, see Fig. 1. In most cases of practical interest, the resulting sound field is dramatically affected by atmospheric turbulence, which can result in increase of the mean-square sound pressure by several dozen dB. The most recent theory of this phenomenon has been developed by Clifford and Lataitis [1], who had generalized results of previous researchers. According to their theory, the sound pressure p at the receiver due to a point source is a sum the sound fields of the direct and ground reflected waves:

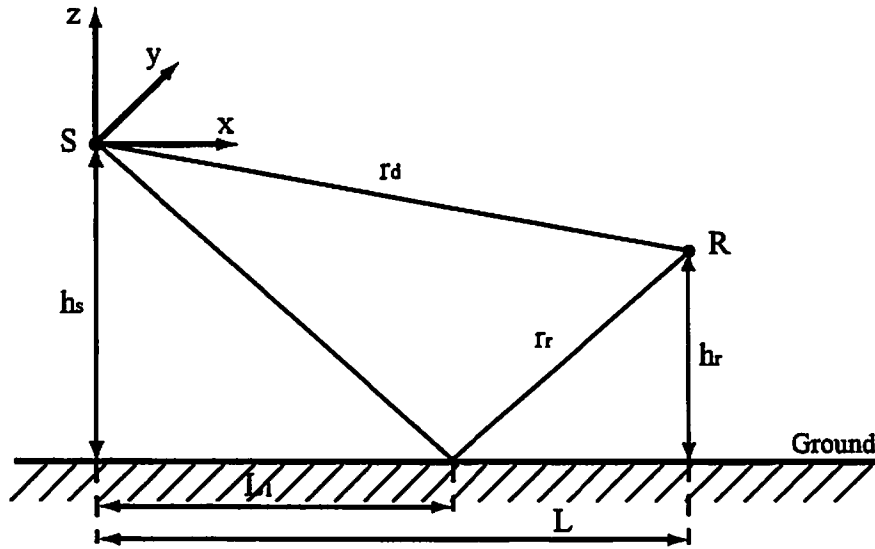


Figure 1: Geometry of the problem. S is the source located at the origin of the coordinate system (x,y,z) , and R is the receiver.

$$p = \frac{\exp(ikr_d + \psi_d)}{r_d} + Q \frac{\exp(ikr_r + \psi_r)}{r_r}. \quad (1)$$

Here, k is the sound wavenumber, $r_d = \sqrt{L^2 + (h_s - h_r)^2}$ and $r_r = \sqrt{L^2 + (h_s + h_r)^2}$ are the path length of the direct and ground reflected waves, h_s and h_r are the source and receiver heights, L is the horizontal distance between source and receiver, Q is the apparent strength of the image source, $\psi_d = iS_d + \chi_d$ are fluctuations in the complex phase of the direct wave, and $\psi_r = iS_r + \chi_r$ are those in the reflected wave (S and χ with the corresponding indexes are fluctuations in the phase and log-amplitude of the direct and reflected waves). Clifford and Lataitis used expressions for ψ_d and ψ_r , presented by Tatarskii [2], which are valid in the Rytov approximation. Strictly speaking, these expressions were obtained and are valid only for the case of sound scattering by temperature fluctuations. As has been shown in reference [3] and some other recent work, a generalization of equations for statistical moments of a sound field in an atmosphere with temperature fluctuations to the case of both temperature and wind velocity fluctuations is not trivial and has led to many mistakes in the literature.

Using the expressions for ψ_d and ψ_r , and after lengthy manipulations, Clifford and Lataitis came up with the final equation for the mean-square sound pressure in homogeneous and isotropic turbulence

$$\langle |p|^2 \rangle = \frac{1}{r_d^2} + \frac{|Q|^2}{r_r^2} + \frac{2|Q|T \cos[k(r_r - r_d) + \theta]}{r_d r_r}. \quad (2)$$

Here, Q has been represented in the form $Q = |Q|e^{i\theta}$, and the factor T is given by

$$T = \exp \left\{ -\alpha k^2 L \left[A(0) - \frac{1}{2h_r} \int_0^{2h_r L_1/L} A(z) dz + \frac{1}{2h_s} \int_0^{2h_s(1-L_1/L)} A(z) dz \right] \right\}, \quad (3)$$

where $L_1 = \frac{L}{h_r/h_s+1}$ (see Fig. 1), $\alpha = 1/2$ if $L_0 \ll \sqrt{L/k}$ where L_0 is the scale of random inhomogeneities in the medium, and $\alpha = 1$ if $L_0 \gg \sqrt{L/k}$, and $A(z)$ is given by

$$A(z) = \pi^2 \int_0^\infty dK K J_0(Kz) \Phi_T(K) / T_0^2. \quad (4)$$

Here, J_0 is the Bessel function, $\Phi_T(K)$ is the three-dimensional spectral density of temperature fluctuations, and T_0 is the mean value of the temperature.

The first term in Eq. (2) is proportional to the intensity of the direct wave, the second term is proportional to the intensity of the reflected wave, and the third term describes the interference of the direct and reflected waves. The factor T describes the reduction of this interference due to the presence of turbulence, so we call it the 'turbulence' factor. Clifford and Lataitis also calculated this factor for the Gaussian spectrum of temperature fluctuations.

It seems worthwhile to generalize Clifford and Lataitis' results in the following manner: (1) to rigorously derive an equation for $\langle |p|^2 \rangle$ not only for temperature but also for wind velocity fluctuations, since wind velocity contributions to the statistical moments of a sound field in an atmosphere usually dominate over temperature contributions; (2) to derive an equation for $\langle |p|^2 \rangle$ for anisotropic turbulence, since anisotropy can dramatically affect the statistical moments of a sound field; and (3) to calculate and compare $\langle |p|^2 \rangle$ for different spectra of temperature and wind velocity fluctuations used in the literature. These generalizations are presented below.

2 Mean-square sound pressure

We first generalize Eqs. (2)-(4) for the case of a turbulent atmosphere with anisotropic fluctuations in temperature and wind velocity. We start from parabolic equation (7.29) of reference [3] for the sound pressure p

$$2ik \frac{\partial p}{\partial x} + \left(\frac{\partial^2}{\partial y^2} + \frac{\partial^2}{\partial z^2} \right) p + 2k^2 \left(1 + \frac{\epsilon_{\text{mov}}}{2} \right) p = 0. \quad (5)$$

Here, (x, y, z) are the Cartesian coordinates (see Fig. 1), the source is located at the origin of the coordinate system, $\epsilon_{\text{mov}} = -\tilde{T}/T_0 - 2v_x/c_0$, where \tilde{T} are temperature fluctuations, v_x are fluctuations of the wind velocity component in the x -direction, and c_0 is the mean value of the sound speed.

The complex phase ψ_d of the direct wave can be obtained as the Rytov approximation to the solution of Eq. (5):

$$\begin{aligned} \psi_d &= \frac{k^2 L}{4\pi} \int_0^L dx \int_{-\infty}^{\infty} dy \int_{-h_s}^{\infty} dz \frac{\epsilon_{\text{mov}}(x, y, z)}{x(L-x)} \\ &\times \exp \left\{ \frac{ikL}{2x(L-x)} \left[\left(z + \frac{x}{L}(h_s - h_r) \right)^2 + y^2 \right] \right\}. \end{aligned} \quad (6)$$

It is worthwhile to express the complex phase ψ_r of the reflected wave as a sum of two terms: $\psi_r = \psi_1 + \psi_2$. These terms can also be obtained as the Rytov approximation to the solution of Eq. (5):

$$\begin{aligned} \psi_1 &= \frac{k^2 L}{4\pi} \int_0^{L_1} dx \int_{-\infty}^{\infty} dy \int_{-h_s}^{\infty} dz \frac{\epsilon_{\text{mov}}(x, y, z)}{x(L-x)} \\ &\times \exp \left\{ \frac{ikL}{2x(L-x)} \left[\left(z + \frac{x}{L}(h_s + h_r) \right)^2 + y^2 \right] \right\}, \end{aligned} \quad (7)$$

and

$$\begin{aligned} \psi_2 &= \frac{k^2 L}{4\pi} \int_{L_1}^L dx \int_{-\infty}^{\infty} dy \int_{-h_s}^{\infty} dz \frac{\epsilon_{\text{mov}}(x, y, z)}{x(L-x)} \\ &\times \exp \left\{ \frac{ikL}{2x(L-x)} \left[\left(z + 2h_s - \frac{x}{L}(h_s + h_r) \right)^2 + y^2 \right] \right\}. \end{aligned} \quad (8)$$

Using Eqs. (1), (6)-(8) and an approach analogous to that by Clifford and Lataitis, we obtain the equation for $\langle |p|^2 \rangle$. This equation coincides with Eq. (2), where the turbulence factor T is now given by

$$\begin{aligned} T &= \exp \left\{ -\alpha k^2 L \left[\tilde{A}(0, 0) - \frac{1}{2h_r} \int_0^{2h_r L_1/L} \tilde{A}(0, z) dz \right. \right. \\ &\left. \left. + \frac{1}{2h_s} \int_0^{2h_s(1-L_1/L)} \tilde{A}(0, z) dz \right] \right\}. \end{aligned} \quad (9)$$

Here, the function $\tilde{A}(y, z)$ is given by

$$\tilde{A}(y, z) = \frac{1}{4T_0^2} \int_{-\infty}^{\infty} B_T(x, y, z) dx + \frac{1}{c_0^2} \int_{-\infty}^{\infty} B_{xx}(x, y, z) dx, \quad (10)$$

where B_T is the correlation function of temperature fluctuations, and B_{xx} is the correlation function of fluctuations in the wind velocity component v_x . Eqs. (3) and (9) are similar but not identical. They differ by functions $A(z)$ and $\tilde{A}(0, z)$ which describe random inhomogeneities in an atmosphere.

Equation (9) can further be simplified by introducing the effective height $h = \frac{2h_s h_r}{h_s + h_r}$:

$$T = \exp \left\{ -\frac{\alpha k^2 L}{h} \int_0^h [\tilde{A}(0, 0) - \tilde{A}(0, z)] dz \right\}. \quad (11)$$

Eqs. (10) and (11) generalize Clifford and Lataitis' expression for the turbulence factor T for the cases of anisotropic turbulence and both temperature and wind velocity fluctuations.

3 Isotropic turbulence

In the rest of the paper we shall consider isotropic turbulence. In this case, substitution of Eq. (10) into Eq. (11) yields

$$T = \exp \left\{ -\alpha \pi^2 k^2 L \int_0^1 dt \int_0^\infty \left[\frac{\Phi_T(K)}{T_0^2} + \frac{4F(K)}{c_0^2} \right] [1 - J_0(hKt)] K dK \right\} \quad (12)$$

where $F(K)$ is the three-dimensional spectral density of wind velocity fluctuations.

Eq. (12) for the turbulence factor T looks similar to the equation for the coherence function Γ of the direct wave from source to receiver in a turbulent atmosphere (see Eq.(7.71) of [3]):

$$\Gamma(L, \rho) = \frac{\exp \left\{ -\pi^2 k^2 L \int_0^1 dt \int_0^\infty \left[\frac{\Phi_T(K)}{T_0^2} + \frac{4F(K)}{c_0^2} \right] [1 - J_0(K\rho t)] K dK \right\}}{(4\pi L)^2} \quad (13)$$

Here, ρ is the distance between two points of observation. The coherence function Γ of the direct wave is one of the most important statistical characteristics of a sound wave in a turbulent atmosphere and is presented in [3] for the Gaussian, Kolmogorov and von Karman spectra of temperature and wind velocity fluctuations, see Eqs.(7.87), (7.107) and (7.114) from [3].

Let us introduce the normalized coherence function $\tilde{\Gamma}(L, \rho) = (4\pi L)^2 \Gamma(L, \rho)$. Then, it follows from Eqs. (12) and (13), that the turbulence factor T can be expressed in terms of the normalized coherence function: $T = \tilde{\Gamma}^\alpha(L, h)$. This formula and Eqs.(7.87), (7.107) and (7.114) from [3] allow one to obtain the turbulence factor T for the Gaussian, Kolmogorov and von Karman spectra of temperature and wind velocity fluctuations.

3.1 Gaussian spectrum

For the Gaussian spectra of temperature and wind velocity fluctuations, the turbulence factor T is given by

$$T = \exp \left\{ -2\alpha\gamma_T^G L \left[1 - \frac{\sqrt{\pi}}{2D_G} \operatorname{erf}(D_G) \right] - 2\alpha\gamma_v^G L \left[1 - \frac{\sqrt{\pi}}{4D_G} \operatorname{erf}(D_G) - \frac{1}{2} e^{-D_G^2} \right] \right\}. \quad (14)$$

Here, $\gamma_T^G = \sqrt{\pi} k^2 \sigma_T^2 L_0 / (8T_0^2)$ is the extinction coefficient of the mean sound field due to temperature fluctuations with the Gaussian spectrum, $\gamma_v^G = \sqrt{\pi} k^2 \sigma_v^2 L_0 / (2c_0^2)$ is that due to wind velocity fluctuations, σ_T^2 and σ_v^2 are the variances of temperature and wind velocity fluctuations, $D_G = h/L_0$ is the wave parameter, and $\operatorname{erf}(D_G)$ is the error function.

3.2 Kolmogorov spectrum

For the Kolmogorov spectra of temperature and wind velocity fluctuations, the turbulence factor T is given by

$$T = \exp \left\{ -\alpha k^2 h^{5/3} L \frac{3BC_T^2}{8T_0^2} - \alpha k^2 h^{5/3} L \frac{11BC_v^2}{4c_0^2} \right\}. \quad (15)$$

Here, C_T^2 and C_v^2 are the structure parameters of temperature and wind velocity fluctuations, and the coefficient $B = 0.364$. The coefficient α in Eq. (15) is 1 since for the Kolmogorov spectrum the outer scale of turbulence L_0 tends to infinity.

3.3 von Karman spectrum

For the von Karman spectra of temperature and wind velocity fluctuations, the turbulence factor T is given by

$$T = \exp \left\{ -\frac{2\alpha L}{D_{vK}} \int_0^{D_{vK}} dt \left[\gamma_T^{vK} \left[1 - \frac{2^{1/6} t^{5/6}}{\Gamma(5/6)} K_{5/6}(t) \right] + \gamma_v^{vK} \left[1 - \frac{2^{1/6} t^{5/6}}{\Gamma(5/6)} \left(K_{5/6}(t) - \frac{t}{2} K_{1/6}(t) \right) \right] \right] \right\}. \quad (16)$$

Here, $K_\mu(t)$ is the modified Bessel function, $\gamma_T^{vK} = 3\pi^2 Ak^2 K_0^{-5/3} C_T^2 / (10T_0^2)$ is the extinction coefficient of the mean sound field due to temperature fluctuations with the von Karman spectrum, $\gamma_v^{vK} = 6\pi^2 Ak^2 K_0^{-5/3} 6C_v^2 / (5c_0^2)$ is that due to wind velocity fluctuations, the coefficient $A = 0.033$, K_0 is the wavenumber which appears in the von Karman spectrum and is inversely proportional to the outer scale of turbulence, and the wave parameter $D_{vK} = K_0 h$.

Equations (12), (14)-(16) are new results obtained in the paper. They clearly show that temperature contributions to the turbulence factor T and hence to the mean-square sound pressure $\langle |p|^2 \rangle$ are different from those due to wind velocity fluctuations.

4 Numerical results

In this section using Eqs. (2), (12) and (14)-(16), we numerically study the relative role of temperature and wind velocity contributions to the mean-square pressure $\langle |p|^2 \rangle$. We also compare $\langle |p|^2 \rangle$ for the Gaussian, Kolmogorov and von Karman spectra of turbulence.

4.1 Temperature and wind velocity contributions

We assume that the horizontal distance between source and receiver is $L = 100$ m, the source height is $h_s = 5$ m, the receiver height is $h_r = 3$ m, and that $Q = 1$, i.e. the ground is acoustically hard. Using Eqs. (2), (12) and (14)-(16) we calculate the relative sound pressure level W :

$$W = 10 \log \left(\langle |p|^2 \rangle / p_0^2 \right). \quad (17)$$

Here, $p_0 = 1/r_d$ is the amplitude of the sound pressure due to the source if there were no ground reflection.

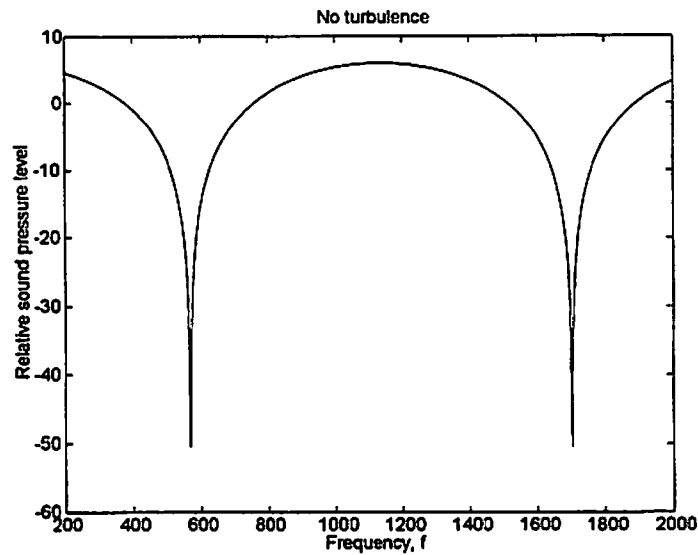


Figure 2: Relative sound pressure level due to interference of the direct and ground reflected waves in an atmosphere without turbulence.

The dependence of the relative sound pressure level W_0 on the sound frequency f in an atmosphere without turbulence is shown in Fig. 2. The frequency range is from 200 to 2000 Hz. The figure shows several maxima and minima in the dependence of W_0 on f due to interference of the direct and ground reflected waves.

The first minimum in W_0 is reproduced as a solid line in Fig. 3 in a more narrow frequency range from 550 to 590 Hz. Other parameters are the same as in Fig. 2. The dash-dotted line is the relative sound pressure level W_T^K calculated in a turbulent atmosphere having temperature fluctuations only, with the Kolmogorov spectrum. The structure parameter of temperature fluctuations, $C_T^2 = 4 \times 10^{-8} T_0^2 \text{ m}^{-2/3}$. It follows from Eq. (15) that the temperature fluctuations decrease the value of the turbulence factor T . This, according to Eq.(2), leads to partial destruction of the interference minimum in W . Therefore, the dash-dotted line in Fig. 3 lies significantly higher than the solid line.

The dashed line in Fig.3 is the relative sound pressure level W_v^K in a turbulent atmosphere having wind velocity fluctuations only, with the Kolmogorov spectrum. The structure parameter of wind velocity fluctuations, C_v^2 is chosen

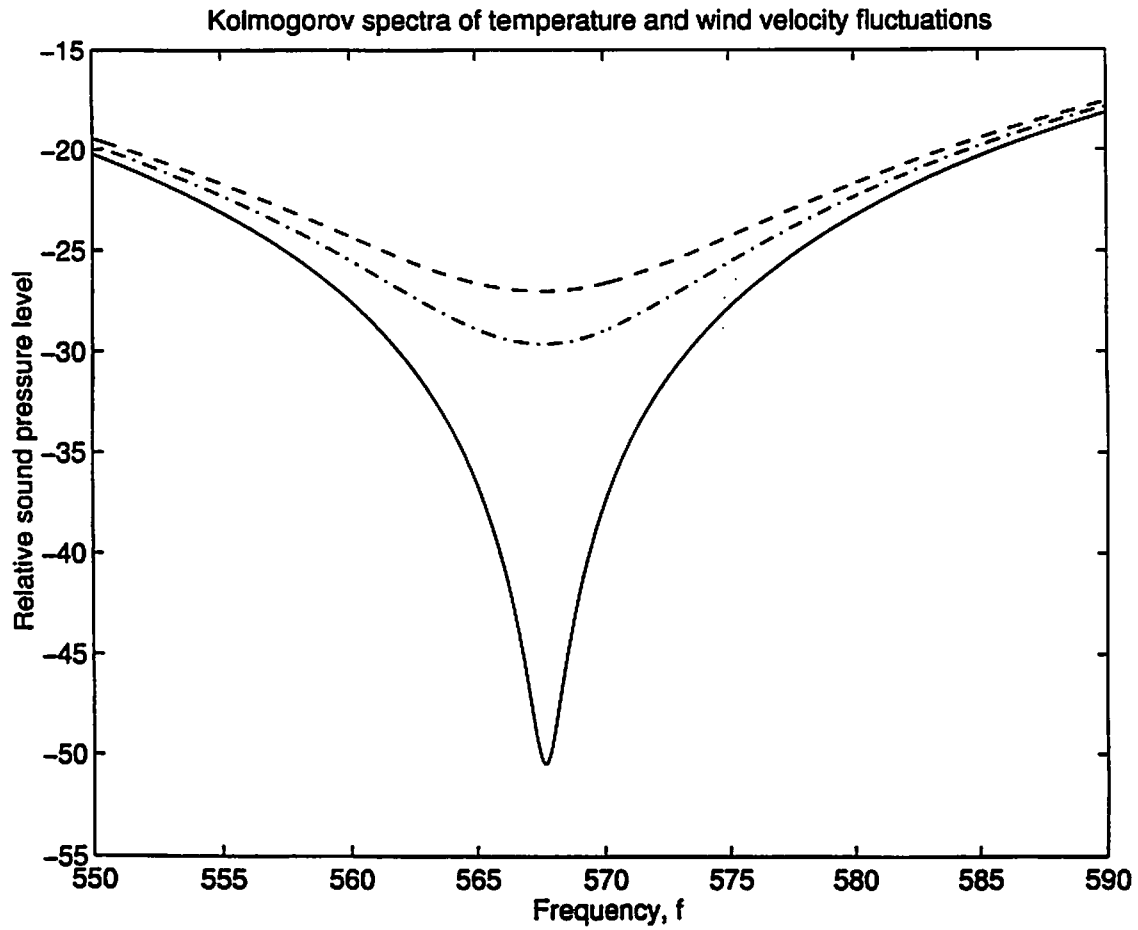


Figure 3: Relative sound pressure levels in an atmosphere with temperature fluctuations (the dash-dotted line), wind velocity fluctuations (the dashed line), and without turbulence (the solid line). The temperature and wind velocity fluctuations have the Kolmogorov spectrum.

to satisfy the relationship:

$$\frac{4C_v^2}{c_0^2} = \frac{C_T^2}{T_0^2}. \quad (18)$$

If this relationship were valid, the temperature and wind velocity contributions to the structure parameter of acoustic refractive index fluctuations would be the same. Eq.(18) is used in [3] and some other recent papers to compare the temperature and wind velocity contributions to the statistical moments of a sound field in a turbulent atmosphere. The maximum difference in W_T^K and W_v^K in Fig. 3 is a few dB. This difference is of the order of the maximum difference between W_T^K and W_v^K that we have numerically revealed so far for different geometries. Note that, for large enough L and k , the temperature contribution T_T to the turbulence factor T can exceed that due to the wind velocity contribution T_v by several dozen dB. However, in this case both T_T and T_v would be very small so $W_T^K \approx W_v^K$.

The temperature W_T and wind velocity W_v contributions to the relative sound pressure level W in an atmosphere with the Gaussian and von Karman spectra of turbulence have been studied. The frequency dependence of these contributions qualitatively coincide with those for the Kolmogorov spectrum, shown in Fig. 3.

4.2 Different spectra

Let W_v^K , W_v^G and W_v^{vK} be the wind velocity contributions to W for the Kolmogorov, Gaussian and von Karman spectra. These contributions are plotted in Fig. 4 by the dash-dotted, dotted and dashed lines, respectively. The solid line corresponds to W_0 and is the same as in Fig. 3. It is also assumed that $C_v^2 = 7.5 \times 10^{-8} c_0^2 \text{ m}^{-2/3}$, and $K_0 = [0.4(h_s + h_r)/2]^{-1}$. Other parameters are the same as in Figs. 2 and 3. In order to compare the relative sound pressure level for the von Karman spectrum with that for the Gaussian spectrum, a relationship between parameters of these spectra is needed. This relationship has been taken from [3] (see Eqs.(6.49) and (6.51)):

$$\sigma_v^2 = \frac{\Gamma^2(1/3)}{\pi^{24/3}\sqrt{3}} C_v^2 K_0^{-2/3}, \quad L_0 = 2\Gamma(5/6)/(\Gamma(1/3)K_0). \quad (19)$$

If Eq.(19) is valid, the variances of wind velocity fluctuations for the von Karman and Gaussian spectra are the same, and the integral lengths of these spectra are equal.

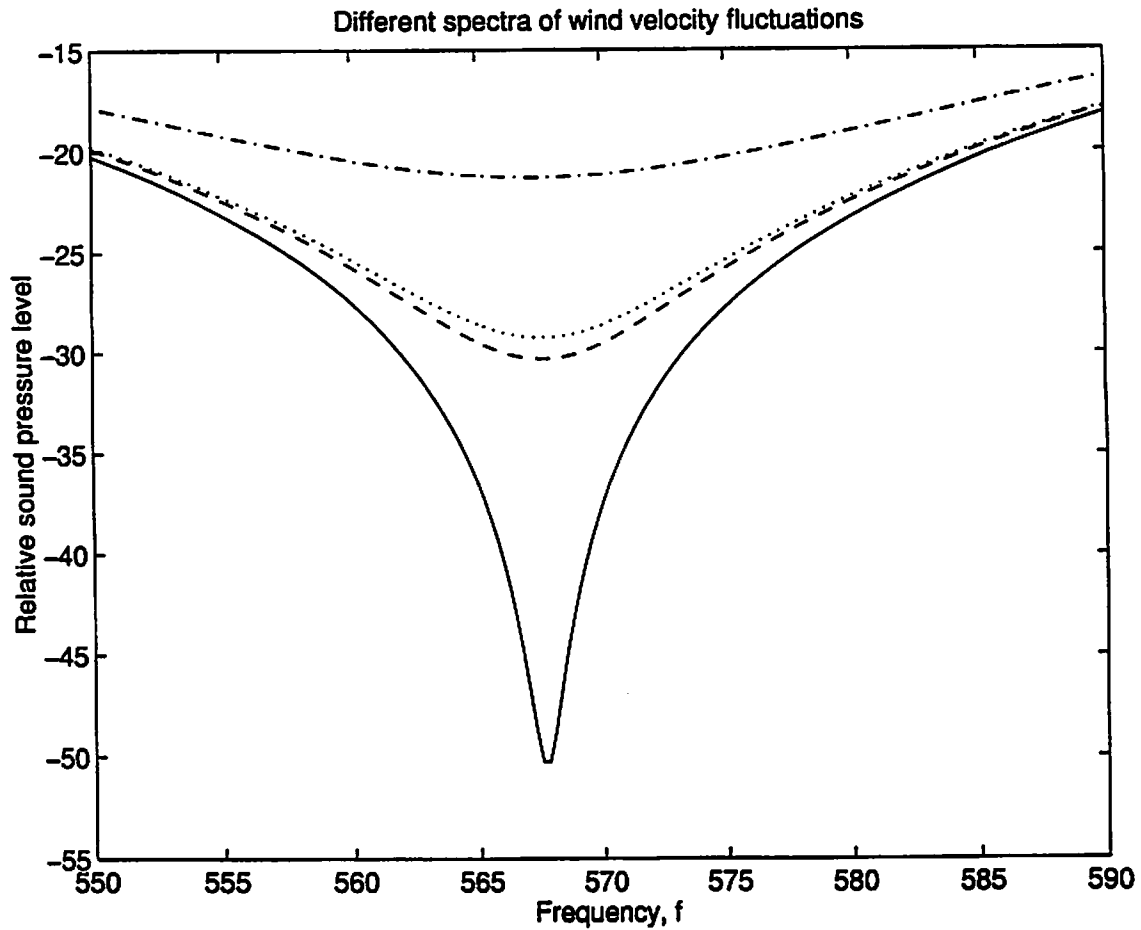


Figure 4: Relative sound pressure levels in an atmosphere with wind velocity fluctuations for the Kolmogorov (the dash-dotted line), Gaussian (the dotted line), and von Karman (the dashed line) spectra. The solid line corresponds to the relative sound pressure level in an atmosphere without turbulence.

It is seen from Fig. 4 that the interference minimum in the relative sound pressure level W is significantly suppressed in a turbulent atmosphere. Theoretical predictions based on the Gaussian and von Karman spectra are close to each other, while that based on the Kolmogorov spectrum differs from them. This is explained by the fact that for values of parameters which are used in figure, $\gamma_v^{vK}L = \gamma_v^G L \sim 0.7 \times 10^{-3}$. As follows from Fig. 7 (a) of reference [4] for such values of $\gamma_v^{vK}L = \gamma_v^G L$, the coherence functions for the Gaussian and von Karman spectra nearly coincide, while that for the Kolmogorov spectrum significantly differs from them. Since the turbulent parameter T can be expressed in terms of the coherence function ($T = \tilde{\Gamma}^\alpha(L, h)$), the relative sound pressure levels W for the Gaussian and von Karman spectra should be close to each other, while that for the Kolmogorov spectrum should differ from them.

For values of $\gamma_v^{vK}L = \gamma_v^G L \geq 100$ (see Fig. 7 (b) of [4]), the coherence function for the Kolmogorov spectrum nearly coincides with that for the von Karman spectrum, while the coherence function for the Gaussian spectrum significantly differs from them. In this case the turbulent parameters T for the Kolmogorov and von Karman spectra are very close to each other, while that for the Gaussian spectrum differs from them. Nevertheless, for such large values of $\gamma_v^{vK}L = \gamma_v^G L$, the values of W_v^K , W_v^G and W_v^{vK} are nearly the same since T is very small for all spectra so the third term in Eq.(2) can be omitted.

5 Conclusions

The equation for the mean-square sound pressure $\langle |p|^2 \rangle$ due to a point source located above the impedance ground in an atmosphere with temperature and wind velocity fluctuations has been derived. This equation is valid for anisotropic atmospheric turbulence. For a particular case of isotropic turbulence, the turbulence parameter T appearing in the equation for $\langle |p|^2 \rangle$ is expressed in terms of the coherence function of the direct wave from the source to the receiver. This important result has allowed us to obtain analytical formulas for T for the Kolmogorov, Gaussian and von Karman spectra of turbulence. Using these formulas, the relative contribution to $\langle |p|^2 \rangle$ due to temperature and wind velocity fluctuations has been studied numerically. Furthermore, the mean-square sound pressure $\langle |p|^2 \rangle$ for the Kolmogorov, Gaussian and von Karman spectra have been compared.

Acknowledgments This material is based upon work supported by the U.S. Army Research Office under contract number DAAH04-95-1-0593.

References

- [1] S.F. Clifford and R.J. Lataitis, "Turbulence effects on acoustic wave propagation," *J. Acoust. Soc. Am.* **73**, 1545-1550 (1983).
- [2] V.I. Tatarskii, *The effects of the turbulent atmosphere on wave propagation* (Israel Program for Scientific Translation, Jerusalem, 1971).
- [3] V.E. Ostashev, *Acoustics in Moving Inhomogeneous Media* (E & FN SPON, An Imprint of Thompson Professional, London, 1997).
- [4] V.E. Ostashev, B. Brähler, V. Mellert and G.H. Goedecke (1998) "Coherence functions of plane and spherical waves in a turbulent medium with the von Karman spectrum of medium inhomogeneities", *J. Acoust. Soc. Am.* V.104, (2), Pt. 1, 727-737.

The fluctuating field of a monopole source in a turbulent atmosphere above a ground surface. Time-averaged sound pressure level and statistical distributions.

Erik M. Salomons

TNO Institute of Applied Physics, P.O. Box 155, 2600 AD Delft, The Netherlands. salomons @ tpd.tno.nl

A theoretical description is presented of the propagation of spherical waves in a non-refracting, turbulent atmosphere above a ground surface. The time-averaged sound pressure level is expressed in terms of the coherence factor Γ , which is related to the mutual coherence function. Two approaches are described to the computation of the coherence factor, a heuristic approach and a new, rigorous approach. The rigorous approach is based on Rytov's integral solution of the wave equation for a turbulent medium, evaluated for the half-space above the ground surface. The rigorous approach is an improvement with respect to the approach of Clifford and Lataitis [J. Acoust. Soc. Am. 73, 1545-1550 (1983)], by the fact that the ground reflection of scattered waves is taken into account. The heuristic approach is based on a well-known expression for the coherence factor $\Gamma(\rho)$ for an unbounded system, using $\rho = h$ where h is the maximum transverse separation between the two sound rays between the source and the receiver (the direct ray and the ray reflected by the ground). Daigle *et al.* found better agreement with experimental data by using $\rho = \frac{1}{2} h$ [J. Acoust. Soc. Am. 64, 622-630 (1978)]. Here it is shown, however, that $\rho = h$ gives the best agreement of the heuristic approach with the rigorous approach, and also with results of numerical computations with the parabolic equation method. The fluctuations of the sound pressure level are also studied in this paper. Three different methods are developed for computing statistical distributions of the sound pressure level. The first method assumes Gaussian distributions for the log-amplitude and phase fluctuations of the two spherical waves that arrive at a receiver, the direct wave and the wave reflected by the ground. This method is similar to the method developed by Hidaka *et al.* [J. Acoust. Soc. Jpn. (E) 6, 247-256 (1985)]. The other two methods are based on a Monte Carlo evaluation of the above mentioned heuristic and rigorous Rytov solutions, respectively. The accuracy of the three methods is investigated numerically for some situations, by comparison with results of computations with the parabolic equation method. Further, evidence is provided for the saturation of the log-amplitude fluctuations, for large distance and/or high frequency.

INTRODUCTION

A remarkable phenomenon in outdoor sound propagation near the ground is the occurrence of large fluctuations of the transmission loss. This means that large fluctuations occur in the sound received from a constant source. These fluctuations originate from atmospheric turbulence. Theoretical studies of wave propagation in unbounded turbulent media have been presented by Tatarskii,^{1,2} Chernov³ and Ishimaru.⁴ Ingard and Maling⁵ have indicated that the fluctuations are considerably larger when the source or the receiver is near a ground surface. This is a consequence of the interference between the direct waves and the waves reflected by the ground. Small phase fluctuations in the direct and reflected waves may cause large fluctuations in the total field, in particular near interference minima.

Daigle *et al.*⁶⁻⁸ have reported several experimental and theoretical studies of sound propagation through atmospheric turbulence near the ground. These studies have focused in particular on the time-averaged sound pressure level, which is the quantity that is commonly used for outdoor noise control. The theoretical approach of Daigle *et al.* for computing the time-averaged sound pressure level is based on the transverse or mutual coherence function $\Gamma(\rho)$, where ρ is the transverse separation between two distant receivers in an unbounded turbulent system with a monopole source.

For the system with a ground surface and a single receiver, Daigle *et al.* use for ρ the maximum transverse separation between the two sound rays between the source and the receiver (the direct ray and the ray reflected by the ground), multiplied by an empirical factor $\frac{1}{2}$. The empirical factor $\frac{1}{2}$ was introduced to obtain agreement with experimental data. The heuristic approach of Daigle *et al.* was generalised by L'Espérance *et al.*⁹ to downward refracting, turbulent atmospheres, with more than two (curved) sound rays between the source and the receiver.

Inspired by the work of Daigle *et al.*, Clifford and Lataitis¹⁰ presented a rigorous approach to the computation of the time-averaged sound pressure level, and obtained a result that is energy conserving. A problem with the approach of Clifford and Lataitis is the fact that the ground reflection of scattered waves is ignored. This causes inaccuracies when the source or the receiver is close to the ground surface.

This paper presents a rigorous approach to the computation of the time-averaged sound pressure level in a system with a monopole source in a turbulent atmosphere above a ground surface. The approach presented here is more direct than the approach of Clifford and Lataitis, and moreover does not ignore the ground reflection of scattered waves. Another advantage of the present approach is the fact that it is based on a stochastic Fourier-Stieltjes expansion of the fluctuating field of the acoustic index of refraction in the turbulent atmosphere. This stochastic expansion allows an extension of the present approach to the computation of statistical distributions of the sound pressure level, as will be shown in the second part of this paper (see below).

One of the reasons for developing the rigorous approach was to study the accuracy of the heuristic approach of Daigle *et al.* In particular, it will be shown by comparison with computational results of the rigorous approach that there is no theoretical justification for the empirical factor $\frac{1}{2}$. This implies also that the empirical factor $\frac{1}{2}$ should not be used in the generalised approach for a downward refracting atmosphere.⁹

The second part of the paper is devoted to the fluctuations of the sound pressure level in a system with a monopole source in a turbulent atmosphere above a ground surface. Numerous experimental studies of outdoor sound propagation near the ground have focused on the fluctuations of the transmission loss.^{5-8,11-17} These studies indicate that the fluctuations are usually considerably larger than 10 dB, for propagation distances of a few hundred meters or more. The measurements of Parkin and Scholes^{12,13} show standard deviations up to 10 dB. Daigle *et al.*⁸ have provided experimental evidence for a saturation of the log-amplitude fluctuations, while the phase fluctuations increase with distance without limit.

In this paper, three methods are developed for computing statistical distributions of the sound pressure level in a system with a monopole source in a turbulent atmosphere above a ground surface. The first method is similar to the method developed by Hidaka *et al.*¹⁸ This method assumes Gaussian distributions for the phase and log-amplitude fluctuations of the direct and reflected waves. The other two methods are extensions of the two methods for computing the time-averaged sound pressure level, which are presented in the first part of this paper.

It is assumed that the time-averaged atmosphere is non-refracting. Therefore, the validity of the results is limited to relatively short propagation distances and/or weakly refracting atmospheres (this limitation does not apply to the above mentioned conclusion about the use of the empirical factor $\frac{1}{2}$). This work should be considered as a basis for future work for refracting atmospheres.

I. SYSTEM

A system is considered with a harmonic monopole source and a receiver above a ground surface, in a turbulent atmosphere (see Fig. 1). It is assumed that the ground surface is reflecting (*i.e.*, rigid), but the extension to a finite-impedance ground surface will also be discussed. A rectangular xyz co-ordinate system is used, with the source at position $(0,0,z_s)$ and the receiver at position $(L,0,z_r)$. The ground surface is at $z = 0$. We assume $L \gg z_s, z_r$.

The turbulent atmosphere is modelled as a non-moving medium, with an (effective) sound speed that represents both wind speed and temperature fluctuations. It is assumed that the time-averaged atmosphere is non-refracting, so that the acoustic index of refraction $n = c_0/c$ (c is the sound speed and c_0 the average sound speed) can be written as $n(x,y,z) = 1 + \mu(x,y,z)$, where the fluctuation μ has zero time average, $\langle \mu \rangle = 0$. Averaging over the time will be performed by ensemble-averaging over different random realisations of the turbulent atmosphere. It is assumed further that the turbulent atmosphere is homogeneous and isotropic, either in three dimensions or in two dimensions (see below).

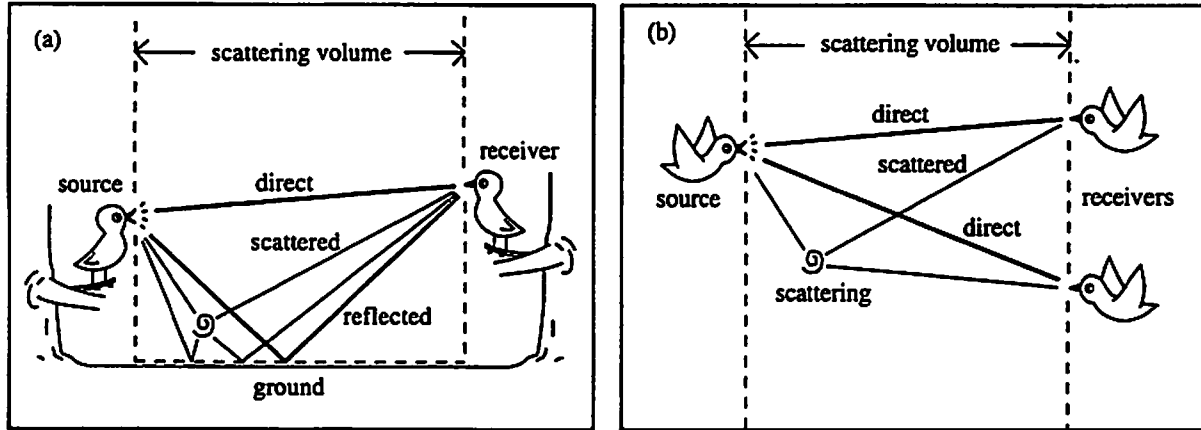


FIG. 1. Illustration of the rigorous (a) and heuristic (b) approaches to the computation of sound propagation from a source to a receiver in a turbulent atmosphere above a ground surface. Thick solid lines represent the sound rays corresponding with the direct and reflected waves. Thin solid lines represent waves that reach the receiver by scattering at turbulent inhomogeneities in the atmosphere.

II. GENERAL EXPRESSIONS

The fluctuating sound pressure field at the receiver is written as the sum of the direct field and the field reflected by the ground surface:

$$p = p_1 + p_2 \quad (1)$$

with

$$p_j = p_0 \frac{\exp(i[kr_j - \omega t] + \psi_j)}{r_j / r_0} \quad \text{for } j = 1, 2 \quad (2)$$

where

$$\psi_j \equiv \chi_j + iS_j = \ln(p_j / p_{j,0}) \quad (3)$$

with χ_j the log-amplitude fluctuation and S_j the phase fluctuation, and $p_{j,0}$ the value of p_j in a non-turbulent atmosphere ($\psi_j = 0$). Here p_0 is a constant pressure, ω the angular frequency, $k = \omega / c_0$ the wave number, $r_0 = 1$ m, $r_1 = \sqrt{L^2 + (z_s - z_r)^2}$ and $r_2 = \sqrt{L^2 + (z_s + z_r)^2}$. The amplitude and phase fluctuations originate from sound speed fluctuations, i.e., atmospheric turbulence. The phase fluctuations have zero time average, $\langle S_j \rangle = 0$, but the time average of the log-amplitude fluctuations is different from zero (see below).

Following Clifford and Lataitis,¹⁰ we assume $T \ll \tau_t$, where $T = 2\pi/\omega$ is the period of the harmonic waves and τ_t is a characteristic period of the turbulence. In other words, we assume that the relevant turbulent fluctuations are slow compared with the harmonic variations of the acoustic waves.

The sound pressure $p(t)$ is equal to the real part of the complex sound pressure p given by Eq. (1). The (fluctuating) short-time average of the squared sound pressure is $\overline{p^2(t)} = \frac{1}{2} pp^*$, an average over time τ_r , with $T \ll \tau_r \ll \tau_c$. The corresponding (fluctuating) relative sound pressure level (*i.e.*, sound pressure level relative to free field) is $\Delta L = 10 \lg \left(\frac{\overline{p^2(t)}}{\overline{p_{1,0}^2(t)}} \right)$, with $\overline{p_{1,0}^2(t)} = \frac{1}{2} p_0^2 r_0^2 / r_1^2$. The long-time average is $\langle \overline{p^2(t)} \rangle = \langle \frac{1}{2} pp^* \rangle$, an average over time τ_c , with $\tau_c \gg \tau_r$. The corresponding (time-averaged) relative sound pressure level is $\langle \Delta L \rangle = 10 \lg \left(\frac{\langle \overline{p^2(t)} \rangle}{\langle \overline{p_{1,0}^2(t)} \rangle} \right)$.

From Eqs. (1) to (3) one finds the relation¹⁸

$$\Delta L = 10 \lg \left(\exp(2\chi_1) + \frac{r_1^2}{r_2^2} \exp(2\chi_2) + 2 \frac{r_1}{r_2} \exp(\chi_1 + \chi_2) \cos(kr_1 - kr_2 + \Delta S) \right) \quad (4)$$

with $\Delta S = S_1 - S_2$. For the generalisation of Eq. (4) to a finite-impedance ground surface, see Hidaka *et al.*¹⁸ For the long-time average $\langle \Delta L \rangle$, we find from Eqs. (1) to (3):

$$\begin{aligned} \langle \Delta L \rangle = 10 \lg \{ & \langle \exp(2\chi_1) \rangle + \frac{r_1^2}{r_2^2} \langle \exp(2\chi_2) \rangle + \\ & + \frac{r_1}{r_2} [\exp(i[kr_1 - kr_2]) \langle \exp(\psi_1 + \psi_2^*) \rangle + \exp(-i[kr_1 - kr_2]) \langle \exp(\psi_1^* + \psi_2) \rangle] \} \end{aligned} \quad (5)$$

To evaluate this expression, we assume that χ_j and S_j are random variables with Gaussian distributions, and use the relation^{2,10}

$$\langle \exp(ay) \rangle = \exp\left(\frac{1}{2} a^2 \sigma_y^2 + a \langle y \rangle\right),$$

for a Gaussian random variable y , with $\sigma_y^2 = \langle (y - \langle y \rangle)^2 \rangle$ and a a constant. For the evaluation of the first two terms in Eq. (5), we find

$$\langle \exp(2\chi_j) \rangle = \exp(2\sigma_{\chi_j}^2 + 2\langle \chi_j \rangle),$$

with $\sigma_{\chi_j}^2 = \langle (\chi_j - \langle \chi_j \rangle)^2 \rangle$ the variance of the log-amplitude fluctuations. Conservation of energy implies $\langle \exp(2\chi_j) \rangle = 1$, and we find the relation $\langle \chi_j \rangle = -\sigma_{\chi_j}^2$ (see Clifford and Lataitis,¹⁰ or Tatarskii² section 70). The other two terms in Eq. (5) can be evaluated in a similar way. This gives:

$$\langle \Delta L \rangle = 10 \lg \left(1 + \frac{r_1^2}{r_2^2} + 2 \frac{r_1}{r_2} \Gamma_0 \right) \quad (6)$$

with

$$\begin{aligned} \Gamma_0 = \exp(\langle \chi_1 \chi_2 \rangle - \frac{1}{2} \sigma_{\chi_1}^2 - \frac{1}{2} \sigma_{\chi_2}^2 - \langle \chi_1 \chi_2 \rangle + \langle S_1 S_2 \rangle - \frac{1}{2} \sigma_{S_1}^2 - \frac{1}{2} \sigma_{S_2}^2) \\ \times \cos(kr_2 - kr_1 + \langle \chi_1 S_2 \rangle - \langle \chi_2 S_1 \rangle + \langle \chi_2 S_2 \rangle - \langle \chi_1 S_1 \rangle) \end{aligned} \quad (7)$$

where

$$\begin{aligned} \sigma_{\chi_j}^2 &= -\frac{1}{2} + \sqrt{\frac{1}{4} + \langle \chi_j^2 \rangle} \\ \sigma_{S_j}^2 &= \langle S_j^2 \rangle \end{aligned} \quad (8)$$

The expression for $\sigma_{\chi_j}^2$ follows from the relations $\sigma_{\chi_j}^2 = \langle (\chi_j - \langle \chi_j \rangle)^2 \rangle$ and $\langle \chi_j \rangle = -\sigma_{\chi_j}^2$. For weak turbulence with $\langle \chi_j^2 \rangle \ll \frac{1}{4}$ we have $\sigma_{\chi_j}^2 = \langle \chi_j^2 \rangle$. Using $\langle \chi_j \rangle = -\sigma_{\chi_j}^2$ we find that

for $\langle \chi_j^2 \rangle \ll \frac{1}{4}$ the term $\langle \chi_1 \chi_2 \rangle$ in the exponent in Eq. (7) can be neglected (this term is missing in the article of Clifford and Lataitis¹⁰). Finally, the terms $\langle \chi_j S_k \rangle$ in the argument of the cosine in Eq. (7) may be neglected for weak turbulence¹⁰ (see Section III.D). This gives:

$$\langle \Delta L \rangle = 10 \lg \left(1 + \frac{r_1^2}{r_2^2} + 2 \frac{r_1}{r_2} \cos(kr_1 - kr_2) \Gamma \right) \quad (9)$$

with the coherence factor Γ given by:

$$\Gamma = \exp(\langle \chi_1 \chi_2 \rangle - \frac{1}{2} \langle \chi_1^2 \rangle - \frac{1}{2} \langle \chi_2^2 \rangle + \langle S_1 S_2 \rangle - \frac{1}{2} \langle S_1^2 \rangle - \frac{1}{2} \langle S_2^2 \rangle) \quad (10)$$

The problem of computing $\langle \Delta L \rangle$ is reduced to the problem of computing Γ for a system with a ground surface. This will be the subject of Section III.

It follows from Eqs. (1), (2) and (9) that the coherence factor can also be defined as:

$$\Gamma = \frac{\langle p_1 p_2^* \rangle + \langle p_1^* p_2 \rangle}{\langle p_1 p_2^* \rangle_0 + \langle p_1^* p_2 \rangle_0} \quad (11)$$

where index 0 is used for a non-turbulent atmosphere. The quantity $\langle p_1 p_2^* \rangle$ is usually referred to as the mutual coherence function (MCF). Thus, the coherence factor Γ is equal to the real part of the MCF, normalised to unity for a non-turbulent atmosphere.

In Refs. 2 and 4 an expression is derived for the MCF, for the field of a monopole source in an unbounded turbulent atmosphere (*i.e.* a system without a ground surface) (see Eqs. 20-64 and 20-69 in Ref. 4, or section 70 in Ref. 2). In this case, p_1 and p_2 are the complex sound pressures at two distant receivers in the unbounded atmosphere. The derivation is based on the parabolic equation approximation. Insertion of the expression for the MCF in Eq. (11) yields exactly the result (10) for the coherence factor Γ , which was derived from the assumption of Gaussian distributions for χ_j and S_j . This agreement may be considered as an indirect confirmation of the Gaussian distributions (this confirmation is valid only for weak turbulence, as we assumed that the turbulence is weak in the derivation of Eq. 9).

III. TIME-AVERAGED SOUND PRESSURE LEVEL

In this section, we develop expressions for the coherence factor Γ for a system with a ground surface. In Section III.A, we first develop an expression for Γ for an unbounded system. In Section III.B, an approximate method is described to use this expression for a system with a ground surface. In Section III.C, a rigorous derivation is presented for a system with a ground surface. In Section III.D, some numerical examples are presented.

III.A. Coherence factor for an unbounded system

In this section we give expressions for the coherence factor Γ for an unbounded system with isotropic or axisymmetric turbulence. The expression for isotropic turbulence follows directly from previous work.^{2,4} The expression for axisymmetric turbulence is useful for comparison with numerical results of computational methods such as the parabolic equation (PE) method.^{19,20}

A.1. Isotropic and axisymmetric turbulence

In this paper we consider turbulent atmospheres that are homogeneous and isotropic either in three dimensions or in two dimensions. Turbulent atmospheres that are homogeneous and isotropic in two dimensions are of interest for comparison with results of computational methods based on the axisymmetric approximation (such as the PE method). The axisymmetric approximation implies that the system has rotational symmetry around the vertical axis through the source, and the computations are performed in a vertical plane, say, the xz plane. For PE computations for a turbulent atmosphere,^{19,20} it is assumed that the turbulent field is homogeneous and isotropic in the xz plane and

independent of the y co-ordinate. This type of turbulence will be referred to as axisymmetric turbulence, in the following. Three dimensional homogeneous and isotropic turbulence will be referred to simply as isotropic turbulence.

A.2. General expression for the coherence factor

We consider an unbounded turbulent atmosphere with a monopole source at position $\bar{r}_s = (0, 0, z_s)$ and two distant receivers at positions $\bar{r}_1 = (L, y_1, z_1)$ and $\bar{r}_2 = (L, y_2, z_2)$ (with $L \gg y_1, z_1, y_2, z_2, z_s$). In general, the covariances $\langle \chi_1 \chi_2 \rangle$ and $\langle S_1 S_2 \rangle$ depend on both \bar{r}_1 and \bar{r}_2 . In the case of homogeneous turbulence, the covariances depend only on the vector $\bar{r}_1 - \bar{r}_2$. In the case of (homogeneous and) isotropic turbulence, the covariances depend only on the distance $\rho = |\bar{r}_1 - \bar{r}_2|$. In the case of axisymmetric turbulence, we consider only systems with $y_1 = y_2 = 0$ and again the covariances depend only on $\rho = |\bar{r}_1 - \bar{r}_2|$. The covariances are denoted as $B_x(\rho) = \langle \chi_1 \chi_2 \rangle$ and $B_s(\rho) = \langle S_1 S_2 \rangle$. The coherence factor (10) becomes:

$$\Gamma(\rho) = \exp[B_x(\rho) - B_x(0) + B_s(\rho) - B_s(0)] \quad (12)$$

for an unbounded system.

A.3. Rytov's first-order solution

Before we give the expressions for the covariances $B_x(\rho)$ and $B_s(\rho)$ in the next section, we briefly describe Rytov's first-order solution⁴ and other basic steps in the derivation of these expressions.

We consider an unbounded system, with a monopole source at position $\bar{r}_s = (0, 0, z_s)$ and a receiver at position $\bar{r} = (L, y, z)$. The turbulent atmosphere is represented by the fluctuating acoustic index of refraction $\mu(x, y, z)$. The corresponding fluctuating sound pressure field is represented by the quantity $\psi = \ln p/p_0$, where p_0 is the undisturbed sound pressure. Application of Rytov's perturbation method to the constant-frequency wave equation for a non-moving atmosphere (for a moving atmosphere see Ostashev *et al.*²¹) yields the following first-order solution for ψ :

$$\psi(\bar{r}) = \int_{V'} h(\bar{r}, \bar{r}') \mu(\bar{r}') d\bar{r}' \quad (13)$$

where the integral is over the scattering volume V' between the source and the receiver: $\bar{r}' = (x', y', z')$ with $0 \leq x' \leq L$ (backscattering is neglected). The function $h(\bar{r}, \bar{r}')$ is given by:

$$h(\bar{r}, \bar{r}') = \frac{k^2}{2\pi(x'/L)(L-x')} \exp\left[i \frac{k}{2} \frac{|\bar{\rho}' - \bar{\rho}_s| - (x'/L)(\bar{\rho} - \bar{\rho}_s)|^2}{(x'/L)(L-x')}\right] \quad (14)$$

with $\bar{\rho} = (y, z)$, $\bar{\rho}' = (y', z')$ and $\bar{\rho}_s = (0, z_s)$. The fluctuating field $\mu(\bar{r}')$ is represented by the following stochastic Fourier-Stieltjes integral:

$$\mu(\bar{r}') = \int \exp(i\bar{\kappa} \cdot \bar{\rho}') dv(x', \bar{\kappa}) \quad (15)$$

with $\bar{\kappa} = (\kappa_y, \kappa_z)$ and random amplitudes dv that satisfy the relation

$$\langle dv(x', \bar{\kappa}) dv^*(x'', \bar{\kappa}') \rangle = F_\mu(x' - x'', \bar{\kappa}) \delta(\bar{\kappa} - \bar{\kappa}') d\bar{\kappa} d\bar{\kappa}' \quad (16)$$

where $\delta(\bar{\kappa} - \bar{\kappa}')$ is the Dirac delta function and the function $F_\mu(x, \bar{\kappa})$ is related to the three-dimensional spectral density $\Phi_\mu(\bar{\kappa})$ of the function $\mu(\bar{r})$ by:

$$\int_{-\infty}^{\infty} F_\mu(x, \bar{\kappa}) dx = 2\pi \Phi_\mu(\bar{\kappa}) \quad (17)$$

The functions F_μ and Φ_μ for isotropic and axisymmetric turbulence are described in Appendix A.

From Eqs. (13)-(17), expressions for the covariances $B_x(\rho)$ and $B_s(\rho)$ have been derived (see e.g. Ref. 4). In the next section, these expressions are evaluated for isotropic and axisymmetric turbulence.

A.4. Evaluation for isotropic and axisymmetric turbulence

In this section, we use the notation $B_1 \equiv B_x$ and $B_2 \equiv B_s$. Rytov's method yields the following general expression for B_j ($j = 1, 2$) for homogeneous turbulence:⁴

$$B_j(\bar{\rho}) = 2\pi L \int_0^1 dt \int \int \exp(i\bar{\kappa} \cdot \bar{\rho} t) H_j^2[Lt(1-t), \kappa] \Phi_\mu(\bar{\kappa}) d\kappa_y d\kappa_z \quad (18)$$

with $\kappa = \sqrt{\kappa_y^2 + \kappa_z^2}$, $H_1(x, \kappa) = k \sin(\frac{1}{2}x\kappa^2 / k)$ and $H_2(x, \kappa) = k \cos(\frac{1}{2}x\kappa^2 / k)$. In the following, Eq. (18) is evaluated for isotropic turbulence and axisymmetric turbulence.

A.4.a. Isotropic turbulence

For the case of isotropic turbulence, a transformation to polar co-ordinates κ, θ_κ is applied in Eq. (18). This gives:

$$B_j(\rho) = 4\pi^2 L \int_0^1 dt \int_0^\infty J_0(\kappa\rho t) H_j^2[Lt(1-t), \kappa] \Phi_\mu(\kappa) \kappa d\kappa \quad (19)$$

with Bessel function J_0 . The coherence factor given by Eq. (12) becomes:

$$\Gamma(\rho) = \exp\left(4\pi^2 L k^2 \int_0^1 dt \int_0^\infty [J_0(\kappa\rho t) - 1] \Phi_\mu(\kappa) \kappa d\kappa\right) \quad (20)$$

For a Gaussian correlation function of the fluctuating index of refraction:

$$B_\mu(r) = \mu_0^2 \exp\left(-\frac{r^2}{a^2}\right) \quad (21)$$

with μ_0 the standard deviation of μ and a the correlation length, we have:

$$\Phi_\mu(\kappa) = \mu_0^2 \frac{a^3}{8\pi^{3/2}} \exp\left(-\frac{\kappa^2 a^2}{4}\right) \quad (22)$$

and we obtain:

$$B_j(\rho) = \frac{1}{4} \pi^{1/2} L k^2 \mu_0^2 a^3 \int_0^1 \left[F(\rho t, 0, \frac{1}{4} a^2) + (-1)^j F(\rho t, Lt(1-t)/k, \frac{1}{4} a^2) \right] dt \quad (23)$$

with the function $F(\alpha, \beta, \gamma)$ defined and evaluated in Appendix B. Using the relation

$F(\rho t, 0, \frac{1}{4} a^2) - F(0, 0, \frac{1}{4} a^2) = 2a^{-2} [\exp(-\rho^2 t^2 / a^2) - 1]$, the following expression is obtained for the coherence factor:

$$\Gamma(\rho) = \exp\left(-\pi^{1/2} L k^2 \mu_0^2 a \left[1 - \frac{1}{2} \pi^{1/2} \frac{\text{erf}(\rho/a)}{(\rho/a)} \right]\right) \quad (24)$$

where $\text{erf}(x) = 2\pi^{-1/2} \int_0^x \exp(-t^2) dt$ is the error function.

A.4.b. Axisymmetric turbulence

For axisymmetric turbulence, we set $B_\mu(\bar{r}) = B_\mu(\sqrt{x^2 + z^2})$ so that $B_\mu(\bar{r}) = 1$ for vectors \bar{r} perpendicular to the propagation plane $y = 0$. This implies (see Appendix A):

$$\Phi_\mu(\bar{K}) = F_\mu(\sqrt{\kappa_x^2 + \kappa_z^2}) \delta(\kappa_y) \quad (25)$$

with $\vec{\kappa} = (\kappa_x, \kappa_y, \kappa_z)$, F_μ the two-dimensional spectral density of the fluctuating index of refraction, and δ the Dirac delta function. Equation (18) becomes (denoting κ_z as κ):

$$B_j(\rho) = 4\pi L \int_0^1 dt \int_0^\infty \cos(\kappa \rho t) H_j^2[Lt(1-t), \kappa] F_\mu(\kappa) d\kappa \quad (26)$$

The coherence factor given by Eq. (12) becomes:

$$\Gamma(\rho) = \exp \left(4\pi L k^2 \int_0^1 dt \int_0^\infty [\cos(\kappa \rho t) - 1] F_\mu(\kappa) d\kappa \right) \quad (27)$$

For the Gaussian correlation function (21), we have:

$$F_\mu(\kappa) = \mu_0^2 \frac{a^2}{4\pi} \exp\left(-\frac{\kappa^2 a^2}{4}\right) \quad (28)$$

and we obtain:

$$B_j(\rho) = \frac{1}{2} L k^2 \mu_0^2 a^2 \int_0^1 \left[I(\rho t, 0, \frac{1}{4} a^2) + (-1)^j I(\rho t, Lt(1-t)/k, \frac{1}{4} a^2) \right] dt \quad (29)$$

with the function $I(\alpha, \beta, \gamma)$ defined and evaluated in Appendix B. Using the relation $I(\rho t, 0, \frac{1}{4} a^2) - I(0, 0, \frac{1}{4} a^2) = \pi^{1/2} a^{-1} [\exp(-\rho^2 t^2 / a^2) - 1]$, the expression (24) is obtained for the coherence factor. Thus, the coherence factor for axisymmetric turbulence is identical with the coherence factor for isotropic turbulence, in the case of the Gaussian correlation function (21).

III.B. Heuristic approach for a system with a ground surface

The unbounded system studied in the previous section is geometrically equivalent to a system with a ground surface, by using the ground surface as a symmetry plane. The two receivers in the unbounded system correspond with the receiver and the image receiver in the system with the ground surface. This suggests that the expressions derived in the previous section for the covariances $B_j(\rho)$ and the coherence factor $\Gamma(\rho)$ may be used also for the system with the ground surface. The only problem is the fact that the turbulent atmosphere in the unbounded system is completely random whereas the turbulent atmosphere in the system with the ground surface has the ground surface as a symmetry plane. The image atmosphere below the ground surface is an exact copy of the atmosphere above the ground surface. As a consequence, for the argument ρ of the functions $B_j(\rho)$ and $\Gamma(\rho)$ one should not use the separation $2z_r$ between the receiver and the image receiver. A better choice for ρ is the maximum vertical separation $h = 2z_s z_r / (z_s + z_r)$ between the two sound rays between source and receiver, the direct ray and the ray reflected by the ground surface (see Fig. 1a). The mean vertical separation between the two rays in the unbounded system (see Fig. 1b) is then equal to $z_s z_r / (z_s + z_r)$, which is identical with the mean vertical separation between the two rays in the bounded system. Thus, Eq. (9) becomes:

$$\langle \Delta L \rangle = 10 \lg \left(1 + \frac{r_1^2}{r_2^2} + 2 \frac{r_1}{r_2} \cos(kr_1 - kr_2) \Gamma(\rho) \right) \quad (30)$$

with $\Gamma(\rho)$ given by Eq. (12) with $\rho = h$. It should be noted that Daigle *et al.*⁶ found best agreement with experimental data by setting $\rho = \frac{1}{2} h$. The generalisation of Eq. (30) for a finite-impedance ground surface is given in Refs. 7 and 10.

III.C. Rigorous approach for a system with a ground surface

C.1. Derivation

In this section we present a rigorous derivation of expressions for the covariances in Eq. (7) and in the coherence factor (10), for a system with a ground surface. The received field is the sum of the direct field and the field reflected by the ground (see Fig. 1). The fluctuating direct and reflected fields can be computed with Rytov's solution (13) evaluated at the receiver position $\bar{r} = (L, y, z)$ and the image receiver position $\bar{r}_i = (L, y, -z)$, respectively. This means that we replace the half-space system with ground surface by a full-space system without ground surface. As the atmosphere for $z < 0$ must be a mirror image of the atmosphere for $z > 0$, we use the field $\mu(x', y', |z'|)$ instead of $\mu(x', y', z')$ in Eq. (13). Using Eq. (15), Eq. (13) becomes:

$$\psi(L, y, z) = \int_0^L \int_{-\infty}^{\infty} \int_{-\infty}^{\infty} dx' dy' dz' \int \exp(i\kappa_y y' + i\kappa_z |z'|) h(\bar{r}, \bar{r}') dv(x', \kappa_y, \kappa_z) \quad (31)$$

with

$$h(\bar{r}, \bar{r}') = \frac{k^2}{2\pi(x'/L)(L-x')} \exp\left[i \frac{k}{2} \frac{[y' - (x'/L)y]^2}{(x'/L)(L-x')}\right] \exp\left[i \frac{k}{2} \frac{[z' - z_1]^2}{(x'/L)(L-x')}\right] \quad (32)$$

where $z_1 \equiv (x'/L)z + (1 - x'/L)z_0$. The integral over y' in Eq. (31) can be evaluated (using the relations given in appendix C):

$$\int_{-\infty}^{\infty} \exp(i\kappa_y y') \exp\left(ik \frac{[y' - (x'/L)y]^2}{2(x'/L)(L-x')}\right) dy' = \exp(i\kappa_y y x'/L) \sqrt{\frac{\pi x'}{k L} (L-x') (1+i)} \exp\left(-i \frac{(x'/L)(L-x')}{2k} \kappa_y^2\right) \quad (33)$$

The integral over z' is written as:

$$\int_{-\infty}^{\infty} \exp(i\kappa_z |z'|) \exp\left(ik \frac{(z' - z_1)^2}{2(x'/L)(L-x')}\right) dz' = I_1 + I_2 \quad (34)$$

with

$$I_1 = \int_0^{\infty} \exp(i\kappa_z z') \exp\left(ik \frac{(z' - z_1)^2}{2(x'/L)(L-x')}\right) dz' \quad (35)$$

$$I_2 = \int_{-\infty}^0 \exp(-i\kappa_z z') \exp\left(ik \frac{(z' - z_1)^2}{2(x'/L)(L-x')}\right) dz' \quad (36)$$

These integrals can be evaluated (using the relations given in Appendix C):

$$I_1 = \exp(i\kappa_z z_1) \sqrt{\frac{\pi x'}{k L} (L-x') (1+i)} \exp\left(-i \frac{(x'/L)(L-x')}{2k} \kappa_z^2\right) \frac{1}{2} [1 - (1-i)F_f(v_1)] \quad (37)$$

$$I_2 = \exp(-i\kappa_z z_1) \sqrt{\frac{\pi x'}{k L} (L-x') (1+i)} \exp\left(-i \frac{(x'/L)(L-x')}{2k} \kappa_z^2\right) \frac{1}{2} [1 - (1-i)F_f(v_2)] \quad (38)$$

with $v_1 = -z_1 \sqrt{a} + \frac{1}{2} \kappa_z / \sqrt{a}$, $v_2 = z_1 \sqrt{a} + \frac{1}{2} \kappa_z / \sqrt{a}$, where $a = k / [2(x'/L)(L-x')]$, and

$F_f(x) = C(x\sqrt{2/\pi}) + iS(x\sqrt{2/\pi})$ where C and S are the Fresnel integrals. Equation (31) becomes:

$$\psi(L, y, z) = \int_0^L dx' \int T(x', \kappa_y, \kappa_z, y, z) dv(x', \kappa_y, \kappa_z) \quad (39)$$

with

$$T(x', \kappa_y, \kappa_z, y, z) = ik \exp\left(-i \frac{(x'/L)(L-x')}{2k} \kappa^2\right) \exp(i\kappa_y y x'/L) \left\{ \exp(i\kappa_z z_1) \frac{1}{2} [1 - (1-i)F_f(v_1)] + \right. \\ \left. \exp(-i\kappa_z z_1) \frac{1}{2} [1 - (1-i)F_f(v_2)] \right\} \quad (40)$$

The log-amplitude fluctuation χ and the phase fluctuation S are obtained from ψ by the relations $\chi = (\psi + \psi^*)/2$ and $S = (\psi - \psi^*)/(2i)$. Since μ is real, we have $d\nu^*(x', -\bar{\kappa}) = d\nu(x', \bar{\kappa})$, so that Eq. (39) gives (with the substitution $\bar{\kappa} \rightarrow -\bar{\kappa}$):

$$\psi^*(L, y, z) = \int_0^L dx' \int T^*(x', -\kappa_y, -\kappa_z, y, z) d\nu(x', \kappa_y, \kappa_z) \quad (41)$$

We obtain

$$\chi(L, y, z) = \int_0^L dx' \int T_r(x', \kappa_y, \kappa_z, y, z) d\nu(x', \kappa_y, \kappa_z) \quad (42)$$

$$S(L, y, z) = \int_0^L dx' \int T_i(x', \kappa_y, \kappa_z, y, z) d\nu(x', \kappa_y, \kappa_z) \quad (43)$$

with

$$T_r(x', \kappa_y, \kappa_z, y, z) = \frac{1}{2} [T(x', \kappa_y, \kappa_z, y, z) + T^*(x', -\kappa_y, -\kappa_z, y, z)] \quad (44)$$

$$T_i(x', \kappa_y, \kappa_z, y, z) = \frac{1}{2i} [T(x', \kappa_y, \kappa_z, y, z) - T^*(x', -\kappa_y, -\kappa_z, y, z)] \quad (45)$$

This gives, using Eqs. (16) and (17) (for details, see the corresponding derivation for an unbounded system⁴):

$$\langle \chi(L, y, z_{r1}) \chi(L, y, z_{r2}) \rangle = 2\pi \int_0^L d\eta \int_{-\infty}^{\infty} \int_{-\infty}^{\infty} T_r(\eta, \kappa_y, \kappa_z, y, z_{r1}) T_r^*(\eta, \kappa_y, \kappa_z, y, z_{r2}) \Phi_\mu(\bar{\kappa}) d\kappa_y d\kappa_z \quad (46)$$

$$\langle S(L, y, z_{r1}) S(L, y, z_{r2}) \rangle = 2\pi \int_0^L d\eta \int_{-\infty}^{\infty} \int_{-\infty}^{\infty} T_i(\eta, \kappa_y, \kappa_z, y, z_{r1}) T_i^*(\eta, \kappa_y, \kappa_z, y, z_{r2}) \Phi_\mu(\bar{\kappa}) d\kappa_y d\kappa_z \quad (47)$$

$$\langle \chi(L, y, z_{r1}) S(L, y, z_{r2}) \rangle = 2\pi \int_0^L d\eta \int_{-\infty}^{\infty} \int_{-\infty}^{\infty} T_r(\eta, \kappa_y, \kappa_z, y, z_{r1}) T_i^*(\eta, \kappa_y, \kappa_z, y, z_{r2}) \Phi_\mu(\bar{\kappa}) d\kappa_y d\kappa_z \quad (48)$$

where $T_r^* = T_r$ and $T_i^* = T_i$. For convenience, the variable η running from 0 to L may be replaced by the scaled variable $t = \eta/L$ running from 0 to 1. With the expressions (46) to (48), the covariances in Eqs. (7) and (10) can be computed. The covariances $\langle \chi_1 \chi_2 \rangle$, $\langle S_1 S_2 \rangle$ and $\langle \chi_1 S_2 \rangle$ are obtained by setting $z_{r1} = z$ and $z_{r2} = -z$ (z is the height of the receiver, $-z$ the height of the image receiver). The covariances $\langle \chi_1 \chi_1 \rangle$, $\langle S_1 S_1 \rangle$ and $\langle \chi_1 S_1 \rangle$ are obtained by setting $z_{r1} = z$ and $z_{r2} = z$. The covariances $\langle \chi_2 \chi_2 \rangle$, $\langle S_2 S_2 \rangle$ and $\langle \chi_2 S_2 \rangle$ are obtained by setting $z_{r1} = -z$ and $z_{r2} = -z$. With these expressions for the covariances, the time-averaged relative sound pressure level (9) can be computed. One may also use the more rigorous Eqs. (6) and (7), if necessary.

As indicated before, we consider the two cases of isotropic turbulence and axisymmetric turbulence in this paper. For isotropic turbulence we have $\Phi_\mu(\bar{\kappa}) = \Phi_\mu(\kappa)$. For axisymmetric

turbulence, we have (see Appendix A) $\Phi_\mu(\bar{\kappa}) = F_\mu(\sqrt{\kappa_x^2 + \kappa_z^2}) \delta(\kappa_y)$, and after substitution in Eqs. (46) to (48) (with $\kappa_x = 0$) the integral over κ_y can be performed analytically.

The rigorous computational approach presented above is an improvement with respect to the approach of Clifford and Lataitis.¹⁰ Their approach ignores the ground reflection of scattered waves, or equivalently, the scattering from the image atmosphere below the ground (see Eqs. 7 and 8 in the

article of Clifford and Lataitis). This causes inaccuracies when the source or the receiver is close to the ground surface.

C.2. Interpretation

Instead of using the concept of the image atmosphere below the ground, one can also derive Eq. (31) by using the half-space Green's function

$$G(\bar{r} - \bar{r}') = \exp(ik|\bar{r} - \bar{r}'|) / 4\pi|\bar{r} - \bar{r}'| + \exp(ik|\bar{r} - \bar{r}_i'|) / 4\pi|\bar{r} - \bar{r}_i'|,$$

with $\bar{r}' = (x', y', z')$ and $\bar{r}_i' = (x', y', -z')$, instead of the full-space Green's function

$$G(\bar{r} - \bar{r}') = \exp(ik|\bar{r} - \bar{r}'|) / 4\pi|\bar{r} - \bar{r}'|$$

in the derivation of Rytov's solution (13). The second term in the half-space Green's function represents the ground reflection of scattered waves. This term corresponds with the integration $\int_{-\infty}^0 dz'$ in Eq. (31), *i.e.*, scattering from the image atmosphere below the ground. The physical scattering volume is of course limited to $z' > 0$.

For a possible generalisation of the rigorous approach to a finite-impedance ground surface, one might include a spherical-wave reflection coefficient in the second term of the half-space Green's function. The problem is that this reflection coefficient is a complex function of \bar{r}' , so the derivation given in the previous section becomes very complicated for a finite-impedance ground surface. For lack of a solution to this problem, one may neglect the effects of ground absorption on the coherence factor. This seems a reasonable approximation.

III.D. Numerical examples

For the numerical examples presented here, the Gaussian correlation function (21) of the fluctuating index of refraction was used, with $a = 1.1$ m and $\mu_0^2 = 10^{-5}$ (unless indicated otherwise). The values of a and μ_0^2 are based on the work of Daigle *et al.*^{6,8}

Figure 2 shows an example of the observation that the heuristic approach for the coherence factor is in reasonable agreement with the rigorous approach. The figure shows the coherence factor Γ and the covariances $\langle \chi_i \chi_k \rangle$ and $\langle S_j S_k \rangle$ as a function of the receiver height z_r , for isotropic turbulence, $z_s = 2$ m, $L = 40$ m and $f = 1000$ Hz. For receiver height $z_r = 0$ we have $\Gamma = 1$, as the receiver and the image receiver coincide in this case. Symbols in the figure represent the heuristic approach for $\rho = h$, $\rho = \frac{1}{2}h$ and $\rho = 2h$ (see Section III.A.4.a), lines represent the rigorous approach (Eqs. 46 and 47). The agreement between the heuristic approach and the rigorous approach is best for $\rho = h$. The agreement for $\rho = h$ is better for the coherence factor Γ than for the covariances. Apparently, some cancellation of deviations occurs in the summation in Eq. (10). The agreement for $\rho = h$ confirms that $\rho = h$ is a good choice for the argument of the coherence factor in the heuristic approach.

A similar agreement between the two approaches was observed for the following situations: $(z_s, L, f, \mu_0^2) = (2, 40, 250, 10^{-5})$, $(2, 40, 1000, 3 \times 10^{-6})$, $(2, 10, 1000, 10^{-5})$, $(2, 200, 1000, 10^{-5})$, and $(5, 40, 1000, 10^{-5})$ (with z_s and L in meters, f in Hz). The largest deviations for Γ were observed for the situation with $L = 200$ m: *e.g.* for $z_r = 1$ m the heuristic approach with $\rho = h$ gives $\Gamma = 0.65$ while the rigorous approach gives $\Gamma = 0.57$.

For the six situations indicated above, we also determined the magnitude of the sum $\delta S \equiv \langle \chi_1 S_2 \rangle - \langle \chi_2 S_1 \rangle + \langle \chi_2 S_2 \rangle - \langle \chi_1 S_1 \rangle$ in the argument of the cosine function in Eq. (7), for $0 \leq z_r \leq 4$ m. The sum δS was neglected in the derivation of Eq. (9). For the five situations with $L \leq 40$ m we found $|\delta S| < 0.03$, for the situation with $L = 200$ m we found $|\delta S| < 0.18$.

Figure 3 shows the time-averaged relative sound pressure level $\langle \Delta L \rangle$ for four situations: $(f, z_s) = (250, 3)$, $(500, 2.4)$, $(1000, 1.5)$ and $(2000, 0.9)$ (with f in Hz and z_s in m). We used equal source height and receiver height, *i.e.*, $z_s = z_r$. The lines represent the heuristic approach for $\rho = h$,

$\rho = \frac{1}{2}h$ and $\rho = 2h$, the symbols represent results of computations performed with the Crank-Nicholson parabolic equation (PE) method.^{19,20} The agreement between the heuristic approach and the PE results is best for $\rho = h$. The relative sound pressure level is too low for $\rho = \frac{1}{2}h$ and too high for $\rho = 2h$. For comparison, we also included results for a non-turbulent atmosphere. As expected, turbulence causes a reduction of the depth of the ground interference dip. For the PE computations we used a grid spacing of 0.1λ (λ is the wavelength) and a system height of 2000 grid spacings, including an absorbing top layer of 1000 grid spacings to eliminate spurious reflections from the top surface. The PE results were obtained by averaging over 500 random realisations of the turbulent atmosphere. Since the PE method assumes that the system has axial symmetry around the vertical axis through the source, the turbulent field is axisymmetric in this case. Therefore the lines were also computed for axisymmetric turbulence. The difference between the levels for axisymmetric turbulence and isotropic turbulence, however, vanishes in these cases, with a Gaussian correlation function of the fluctuating index of refraction.

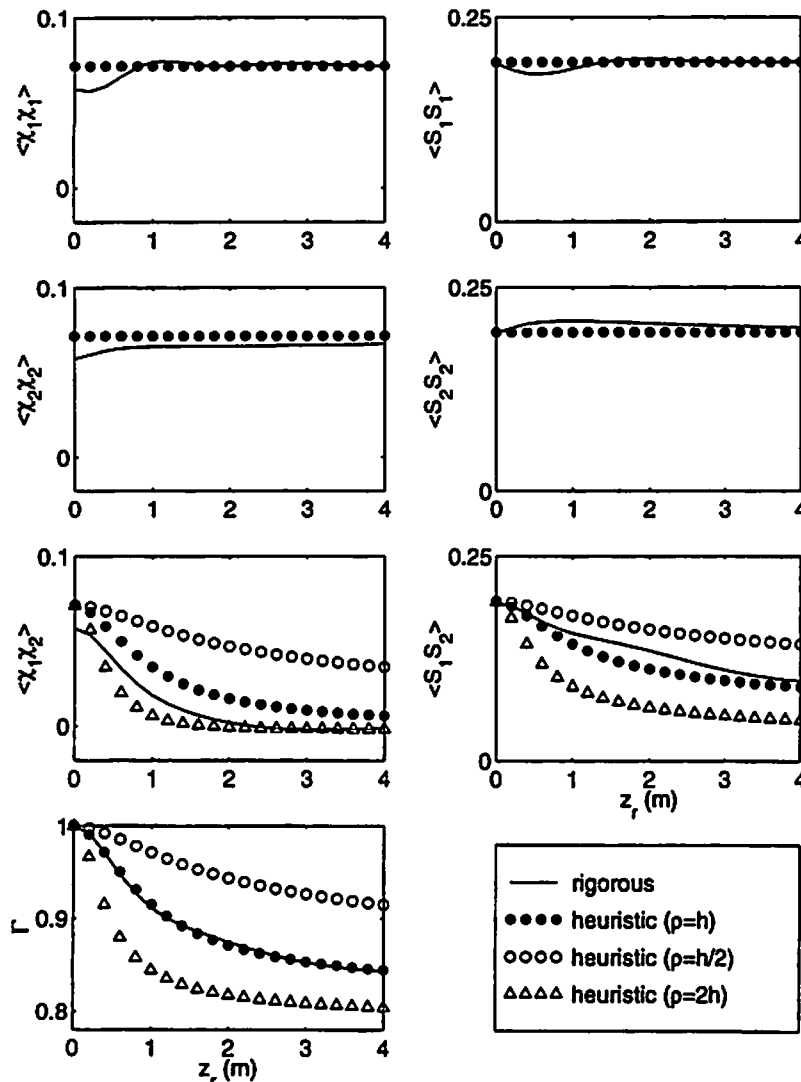


FIG. 2. The covariances $\langle \chi_i \chi_i \rangle$ and $\langle S_i S_i \rangle$ and the coherence factor Γ as a function of the receiver height z_r , for a system with source height $z_s = 2$ m, source-receiver distance $L = 40$ m and frequency 1000 Hz.

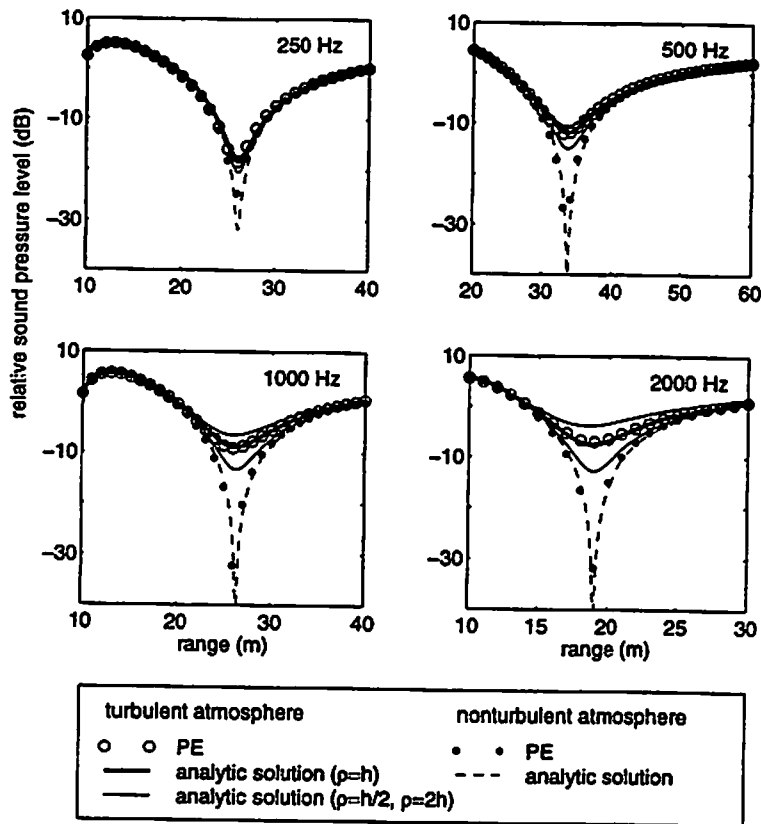


FIG. 3. The time-averaged relative sound pressure level $\langle \Delta L \rangle$ as a function of range L , for four frequencies. The lines represent analytic solutions computed with the heuristic approach, symbols represent computations with the PE method.

III.E. Concluding remarks

The rigorous approach for computing the time-averaged sound pressure level, which was presented in this section, requires the evaluation of triple integrals. With current computers this is a numerical problem that is easily solved. The heuristic approach for computing the time-averaged sound pressure level, however, requires considerably less numerical effort, and appears sufficiently accurate for most practical applications. We have shown that $\rho = h$ is the best choice for the argument of the coherence factor in the heuristic approach, where h is the maximum transverse separation between the two sound rays between the source and the receiver. In contrast, Daigle *et al.*⁶ found better agreement of the heuristic approach with experimental data by setting $\rho = \frac{1}{2}h$. The reason for this is not clear; inaccuracy in the description of the turbulent atmosphere may have played a role.

Further, we have shown that for a comparison between PE results and analytic results, a distinction should be made between axisymmetric and isotropic turbulence, except for the case of a Gaussian correlation function of the fluctuating index of refraction.

IV. STATISTICAL DISTRIBUTIONS OF THE SOUND PRESSURE LEVEL

Using Eq. (4), statistical distributions of the fluctuating relative sound pressure level can be computed from statistical distributions of the fluctuating variables χ_1 , χ_2 and ΔS . In this section, three methods are described for computing these distributions.

IV.A. Computational method 1: Gaussian distributions of χ_1 , χ_2 and ΔS

In this section, the first computational method is described for constructing a statistical distribution of the fluctuating relative sound pressure level. The method is based on the assumption of Gaussian distributions for χ_1 , χ_2 and ΔS , and is similar to the method developed by Hidaka *et al.*¹⁸ Two different approaches are described to the numerical implementation of the method. The first approach is straightforward, but numerically rather inefficient. The second approach is more efficient.

A.1. Straightforward approach

The random variables ΔS and χ_j ($j = 1, 2$) are discretized as follows:

$$\Delta S_k = k \delta S, \quad \text{with } k = -K, -K+1, \dots, K$$

$$\chi_{1,m} = m \delta \chi, \quad \text{with } m = -M, -M+1, \dots, M$$

$$\chi_{2,n} = n \delta \chi, \quad \text{with } n = -N, -N+1, \dots, N.$$

Here K , M and N are large integers, and δS and $\delta \chi$ are small discretization intervals. We introduce the probability distributions w_k , v_m and v_n :

w_k is the statistical probability that ΔS lies in the interval between $\Delta S_k - \frac{1}{2} \delta S$ and $\Delta S_k + \frac{1}{2} \delta S$,

v_m is the statistical probability that χ_1 lies in the interval between $\chi_{1,m} - \frac{1}{2} \delta \chi$ and $\chi_{1,m} + \frac{1}{2} \delta \chi$,

v_n is the statistical probability that χ_2 lies in the interval between $\chi_{2,n} - \frac{1}{2} \delta \chi$ and $\chi_{2,n} + \frac{1}{2} \delta \chi$.

Following Refs. [18,22], we assume that ΔS , χ_1 and χ_2 are independent Gaussian random variables, with probability distributions:

$$w_k = \frac{1}{\sigma_{\Delta S} \sqrt{2\pi}} \exp\left(-\frac{\Delta S_k^2}{2\sigma_{\Delta S}^2}\right) \delta S \quad (49)$$

$$v_m = \frac{1}{\sigma_{\chi} \sqrt{2\pi}} \exp\left(-\frac{(\chi_{1,m} - \langle \chi_1 \rangle)^2}{2\sigma_{\chi}^2}\right) \delta \chi \quad (50)$$

and analogously for v_n . We have used here $\sigma_{\chi_1} = \sigma_{\chi_2} = \sigma_{\chi}$, as we assumed $L \gg z_s, z_r$. We use the relation $\langle \chi_j \rangle = -\sigma_{\chi}^2$ in Eq. (50) (see Section II). The variances $\sigma_{\Delta S}^2$ and σ_{χ}^2 are given by:

$$\sigma_{\Delta S}^2 \equiv \langle (\Delta S)^2 \rangle \equiv \langle (S_2 - S_1)^2 \rangle \quad (51)$$

and

$$\sigma_{\chi}^2 = -\frac{1}{2} + \sqrt{\frac{1}{4} + \langle \chi_j^2 \rangle} \quad (52)$$

For weak turbulence with $\langle \chi_j^2 \rangle \ll \frac{1}{4}$, Eq. (52) gives $\sigma_{\chi}^2 \approx \langle \chi_j^2 \rangle$. Following Refs. [22, 8], we express $\sigma_{\Delta S}^2$ in terms of the correlation function $B_S(\rho) = \langle S(\mathbf{r}) S(\mathbf{r}+\rho) \rangle$:

$$\sigma_{\Delta S}^2 = 2B_S(0) - 2B_S(\rho) \quad (53)$$

and similarly for σ_{χ}^2 :

$$\sigma_{\chi}^2 = -\frac{1}{2} + \sqrt{\frac{1}{4} + B_{\chi}(0)} \quad (54)$$

For the correlation functions $B_S(\rho)$ and $B_{\chi}(\rho)$ we use free-field expressions, derived in Refs. [2,4] for an unbounded system with a monopole source in a turbulent atmosphere and two distant receivers separated by a distance ρ (see also Sections III.A,B). In this case we consider a system with a ground

surface and a single receiver, and we use for the distance ρ the maximum vertical separation $h = 2z_s z_r / (z_s + z_r)$ of the two sound rays between the source and the receiver, the direct ray and the ray reflected by the ground surface.

Using Eqs. (4) and (49) to (54), we construct a statistical distribution for the fluctuating relative sound pressure level. It consists of discrete values ΔL_{kmn} of the relative sound pressure level, with statistical weights $w_k v_m v_n$. The long-time average of the relative sound pressure level is:

$$\langle \Delta L \rangle = 10 \lg \left(\sum_{k,m,n} w_k v_m v_n 10^{\Delta L_{kmn}/10} \right) \quad (55)$$

We define separate variances for the positive and negative deviations of the relative sound pressure level from its long-time average value (55):

$$\sigma_+^2 = \sum_{k,m,n}^+ w_k v_m v_n (\Delta L_{kmn} - \langle \Delta L \rangle)^2 / \sum_{k,m,n}^+ w_k v_m v_n \quad (56)$$

where the sum is over indices k, m, n with $\Delta L_{kmn} > \langle \Delta L \rangle$, and

$$\sigma_-^2 = \sum_{k,m,n}^- w_k v_m v_n (\Delta L_{kmn} - \langle \Delta L \rangle)^2 / \sum_{k,m,n}^- w_k v_m v_n \quad (57)$$

where the sum is over indices k, m, n with $\Delta L_{kmn} < \langle \Delta L \rangle$. The positive deviations from the long-time average are represented by the level $\Delta L_+ \equiv \langle \Delta L \rangle + \sigma_+$, the negative deviations by the level $\Delta L_- \equiv \langle \Delta L \rangle - \sigma_-$.

A.2. Alternate approach

A more efficient approach makes use of random numbers with Gaussian distributions. Various algorithms exist for generating a set of random numbers with a Gaussian distribution.²³ The approach is as follows. We generate a set of random values of ΔS with distribution (49), a set of random values of χ_1 with distribution (50), and a set of random values of χ_2 with a distribution given by the analogue of Eq. (50). The three sets have equal lengths N_{random} (e.g. $N_{\text{random}} = 50\,000$). Substitution in Eq. (4) yields a set of values of the relative sound pressure level, which has automatically the correct statistical distribution. This means that Eqs. (55), (56) and (57) hold with all w_k, v_m and v_n equal to unity.

IV.B. Computational method 2: Monte Carlo evaluation of Rytov solution for unbounded system

Following the heuristic approach presented in Section III.B, the fluctuating variables ψ_1 and ψ_2 in Eq. (2) can be computed for an unbounded system with a turbulent atmosphere and two receivers 1 and 2 at $x = L$, at heights $z_1 = z_r$ and $z_2 = z_r - h$, respectively. The vertical separation of the receivers is $h = 2z_s z_r / (z_s + z_r)$, the maximum vertical separation of the two sound rays between the source and the receiver (see Fig. 1). In this section, a computational method is described for computing random realisations of the fluctuating variable ψ (i.e. ψ_1 or ψ_2) in an unbounded system. The method is based on the first-order Rytov solution for weak turbulence, and makes use of random realisations of the fluctuating field μ . This approach may be considered as Monte Carlo sampling of Rytov's solution.

B.1. Rytov's first-order solution

We consider an unbounded system, with a monopole source at position $\vec{r}_s = (0,0,0)$ and a receiver at position $\vec{r} = (L, y, z) = (L, \vec{\rho})$, with $\vec{\rho} = (y, z)$. The fluctuating sound pressure field at the receiver is p , the undisturbed field is p_0 . Rytov's first-order solution for the function $\psi \equiv \ln p/p_0$ is given by Eqs. (13) and (14) in Section III.A. The fluctuating index of refraction μ was written as a Fourier-Stieltjes integral:

$$\mu(\vec{r}') = \int \exp(i\vec{k} \cdot \vec{\rho}') dv(x', \vec{k}) \quad (58)$$

with $\vec{k} = (\kappa_y, \kappa_z)$ and random amplitudes dv . Using Eqs. (14) and (58), Eq. (13) yields:⁴

$$\psi(L, \vec{\rho}) = \int_0^L dx' \int \exp(i\vec{k} \cdot \vec{\rho} x'/L) H[(x'/L)(L-x'), \vec{k}] dv(x', \vec{k}) \quad (59)$$

with

$$H[(x'/L)(L-x'), \vec{k}] = ik \exp\left[-i \frac{(x'/L)(L-x')}{2k} \kappa^2\right] \quad (60)$$

with $\kappa^2 = \kappa_y^2 + \kappa_z^2$. Equations (58) and (59) will be used for the computations of random realisations of the fluctuating fields μ and ψ . From the realisations of ψ , we obtain statistical distributions of the phase and the amplitude of spherical waves in a turbulent atmosphere.

This approach can also be applied to axisymmetric systems. These systems have axial symmetry around the vertical z axis through the source, and are described in the xz plane. In this case we have $\vec{r} = (L, z)$, $\vec{\rho} = z$, $\vec{k} = \kappa_z$ in Eqs. (58) to (60), and $\kappa^2 = \kappa_z^2$ in Eq. (60). Computations for axisymmetric systems are useful for comparison with results of numerical simulations with the axisymmetric PE method. These simulations are based on the same random realisations of the field μ as Eq. (59) is, *i.e.* the simulations are based on Eq. (58).

B.2. Construction of realisations of the fluctuating fields μ and ψ

The discrete approximation of Eq. (58) for the field μ is:

$$\mu(\vec{r}) = \sum_{n=1}^N \exp(i\vec{k}_n \cdot \vec{\rho}) dv(x, \vec{k}_n) \quad (61)$$

The discrete approximation of Eq. (59) for the field ψ is given by an analogous expression. Using a random number generator, sets of \vec{k}_n and $dv(x, \vec{k}_n)$ can be generated that yield realisations of the field μ that satisfy two conditions: *i*) μ must be real, and *ii*) the correlation function $\langle \mu(\vec{r} + \vec{s}) \mu(\vec{r}) \rangle$ must be equal to a given function $B_\mu(s)$. The first condition is satisfied by replacing each pair $\vec{k}_n, dv(x, \vec{k}_n)$ by two pairs: $\vec{k}_n, \frac{1}{2} dv(x, \vec{k}_n)$ and $-\vec{k}_n, \frac{1}{2} dv^*(x, -\vec{k}_n)$. The second condition requires a distinction between three-dimensional fields and two-dimensional fields (two-dimensional fields are used for axisymmetric systems; see above).

B.2.a. Three-dimensional fields

Three-dimensional fields $\mu(x, y, z)$ are obtained with the following expressions:

$$\vec{K}_n \equiv (\kappa_{nx}, \kappa_{ny}, \kappa_{nz}) = (\kappa_n \cos\phi_n \sin\theta_n, \kappa_n \sin\phi_n \sin\theta_n, \kappa_n \cos\theta_n) \quad (62)$$

$$dv(x, \vec{k}_n) = \sqrt{8\pi \Delta\kappa} \sqrt{\Phi_\mu(\kappa_n)} \kappa_n \exp(i\kappa_{nx}x + i\alpha_n) \quad (63)$$

where $\kappa_n \equiv |\vec{K}_n| = n \Delta\kappa$, ϕ_n and α_n are random angles between 0 and 2π , $\cos\theta_n$ a random number between 1 and -1, and $\Phi_\mu(\kappa)$ the three-dimensional spectral density of μ . We have $\vec{k}_n = (\kappa_{ny}, \kappa_{nz})$ in Eq. (61), so that $\vec{k}_n \cdot \vec{\rho} = \kappa_{ny}y + \kappa_{nz}z$. The numerical examples presented in Section IV.D are for a Gaussian correlation function $B_\mu(s) = \mu_0^2 \exp(-s^2/a^2)$, corresponding with a Gaussian spectral density $\Phi_\mu(\kappa) = \mu_0^2 a^3 \exp(-\kappa^2 a^2/4) / 8\pi^{3/2}$. For this case, we use $\Delta\kappa = 0.1/a$ and $N = 80$.

To prove that this yields the correct correlation function $B_\mu(s)$, we write the spectral decomposition of $B_\mu(s)$ as follows (valid for homogeneous, isotropic random fields μ):

$$B_{\mu}(s) = \overline{\int \int \int \cos(\bar{K} \cdot \bar{s}) \Phi_{\mu}(\kappa) d\bar{K}} = \int_0^{\pi} \int_0^{2\pi} \int_0^{\infty} \cos(\bar{K} \cdot \bar{s}) \Phi_{\mu}(\kappa) \kappa^2 d\kappa \sin \theta d\theta d\phi = \langle 4\pi \int_0^{\infty} \cos(\bar{K} \cdot \bar{s}) \Phi_{\mu}(\kappa) \kappa^2 d\kappa \rangle \quad (64)$$

where angular brackets denote averaging over the angles θ and ϕ . The integral is approximated by a finite sum:

$$B_{\mu}(s) = \langle 4\pi \Delta\kappa \sum_n \cos(\bar{K}_n \cdot \bar{s}) \Phi_{\mu}(\kappa_n) \kappa_n^2 \rangle \quad (65)$$

The same result is obtained from Eqs. (61) and (63):

$$\langle \mu(\bar{r} + \bar{s}) \mu(\bar{r}) \rangle = \langle 8\pi \Delta\kappa \sum_n \sqrt{\Phi_{\mu}(\kappa_n)} \kappa_n \cos(\bar{K}_n \cdot \bar{r} + \alpha_n + \bar{K}_n \cdot \bar{s}) \sum_m \sqrt{\Phi_{\mu}(\kappa_m)} \kappa_m \cos(\bar{K}_m \cdot \bar{r} + \alpha_m) \rangle \quad (66)$$

Here we have used the condition that μ must be real. Now the averaged products $\cos(\bar{K}_n \cdot \bar{r} + \alpha_n + \bar{K}_n \cdot \bar{s}) \cos(\bar{K}_m \cdot \bar{r} + \alpha_m)$ vanish unless $n = m$. We have, using the goniometric relations $\cos^2 x = \frac{1}{2} + \frac{1}{2} \cos 2x$ and $\sin x \cos x = \frac{1}{2} \sin 2x$:

$$\begin{aligned} & \langle \cos(\bar{K}_n \cdot \bar{r} + \alpha_n + \bar{K}_n \cdot \bar{s}) \cos(\bar{K}_n \cdot \bar{r} + \alpha_n) \rangle = \\ & \langle \cos^2(\bar{K}_n \cdot \bar{r} + \alpha_n) \cos(\bar{K}_n \cdot \bar{s}) \rangle - \langle \sin(\bar{K}_n \cdot \bar{r} + \alpha_n) \cos(\bar{K}_n \cdot \bar{r} + \alpha_n) \cos(\bar{K}_n \cdot \bar{s}) \rangle = \frac{1}{2} \cos(\bar{K}_n \cdot \bar{s}) \end{aligned} \quad (67)$$

This gives Eq. (65), which completes the proof.

B.2.b. Two-dimensional fields

Two-dimensional fields $\mu(x, z)$ can be deduced from three-dimensional fields $\mu(x, y, z)$, but are obtained more efficiently with the following expressions:

$$\bar{K}_n \equiv (\kappa_{nx}, \kappa_{nz}) = (\kappa_n \cos \phi_n, \kappa_n \sin \phi_n) \quad (68)$$

$$dv(x, \bar{k}_n) = \sqrt{4\pi \Delta\kappa} \sqrt{F_{\mu}(\kappa_n) \kappa_n} \exp(i\kappa_{nx} x + i\alpha_n) \quad (69)$$

where $\kappa_n \equiv |\bar{K}_n| = n \Delta\kappa$, ϕ_n and α_n are random angles between 0 and 2π , and $F_{\mu}(\kappa)$ is the two-dimensional spectral density of μ . We have $\bar{k}_n = \kappa_{nz}$ in Eq. (61), so that $\bar{k}_n \cdot \bar{\rho} = \kappa_{nz} z$. For a Gaussian correlation function $B_{\mu}(s) = \mu_0^2 \exp(-s^2 / a^2)$, corresponding with a Gaussian spectral density $F_{\mu}(\kappa) = \mu_0^2 a^2 \exp(-\kappa^2 a^2 / 4) / 4\pi$, we use $\Delta\kappa = 0.1/a$ and $N = 60$.

The proof that this yields the correct correlation function $B_{\mu}(s)$, is analogous to the three-dimensional case. We approximate the spectral decomposition of $B_{\mu}(s)$ as follows:

$$B_{\mu}(s) = \overline{\int \int \cos(\bar{K} \cdot \bar{s}) F_{\mu}(\kappa) d\bar{K}} = \langle 2\pi \Delta\kappa \sum_n \cos(\bar{K}_n \cdot \bar{s}) F_{\mu}(\kappa_n) \kappa_n \rangle \quad (70)$$

where angular brackets denote averaging over the angle ϕ . The same result is obtained from Eqs. (61) and (69).

IV.C. Computational method 3: Monte Carlo evaluation of Rytov solution for system with ground surface

Rytov's solution (59) for an unbounded system is of the same form as the solution (39) in Section III.C for a system with a ground surface. Therefore, the approach described in the previous section can also be applied to the rigorous solution (39). The fluctuating variables ψ_1 and ψ_2 in Eq. (2) now correspond with the receiver at height $z_1 = z_r$ and the image receiver at height $z_2 = -z_r$, respectively. The solution (39) takes into account the symmetry of the turbulent atmosphere with respect to the ground surface at $z = 0$.

IV.D. Numerical examples

In this section, results are presented of computations performed with the methods described in the foregoing. All results are for a Gaussian correlation function of the fluctuating index of refraction $B_\mu(s) = \mu_0^2 \exp(-s^2 / a^2)$, with $a = 1.1$ m and $\mu_0^2 = 10^5$ (see Refs. 6, 8). Before presenting examples for systems with a ground surface (Section D.2), we first investigate the accuracy of the assumption of Gaussian distributions in computational method 1 (Section D.1).

D.1. Distributions of χ and S for an unbounded system

Computational method 1 is based on the assumption of Gaussian distributions for the phase and log-amplitude fluctuations of spherical waves in a turbulent atmosphere. We can use computational method 2 to investigate the accuracy of this assumption. Therefore we consider an unbounded system, and compute Monte Carlo realisations of the fluctuating variable ψ at a single receiver (instead of two receivers for a system with a ground surface). From the values of ψ we obtain values of the phase S and the log-amplitude χ . A number of 2000 Monte Carlo realisations was used for each computation.

First we consider the variances $\langle S^2 \rangle$ and $\langle \chi^2 \rangle$. Figure 4 shows the variances as a function of range L for axisymmetric turbulence, for the frequencies 125, 250, 500 and 1000 Hz. The lines represent the analytic solutions which are used in method 1, the circles represent method 2. We also included results of the parabolic equation (PE) method, both the Crank-Nicholson PE (CNPE) method^{19,20} and the Green's function PE (GFPE) method.^{24,25} Details of the PE computations are given below. Figure 5 is as Fig. 4, but for isotropic turbulence. The agreement between the different computational methods is good, although for frequency 125 Hz the PE results in Fig. 4 deviate slightly from the analytic results. The maximum range in the figures is $L = 40$ m, and the largest variances occur for frequency 1000 Hz, $\langle S^2 \rangle \approx 0.2$ and $\langle \chi^2 \rangle \approx 0.05$. This means that the turbulence may be considered as weak.

Figure 6 shows the probability density distributions of the phase fluctuation S and the log-amplitude fluctuation χ for range $L = 40$ m, for axisymmetric turbulence. We also included PE results. Figure 7 is as Fig. 6, but for isotropic turbulence. The circles represent computational method 2, the lines represent corresponding Gaussian distributions (with standard deviations computed from the variances). Figures 6 and 7 show that the distribution of the phase fluctuations is Gaussian in good approximation, while the distribution of the log-amplitude fluctuations deviates from a Gaussian at high frequency.

We now give details of the PE computations. For the CNPE computations we used a grid spacing of 0.1λ (λ is the wavelength) and system heights of 2000, 2500, 4000 and 8000 grid spacings for the four frequencies, respectively, including an absorbing top layer of 500 grid spacings to eliminate spurious reflections from the top surface. We used a CNPE code for systems with a ground surface, but we used a source height of 125 m and a receiver height of 125 m, so that the ground effect was negligible for propagation over a distance of 40 m. For the GFPE computations we used a vertical grid spacing of 0.1λ and a horizontal range step of 1 m. The system heights were $N = 2048, 4096, 8192$ and 8192 grid spacings for the four frequencies, respectively. We used a GFPE code for systems without a ground surface; the periodicity of the FFT algorithm implies that the system is in fact an infinite vertical sequence of periodic images of height N . The values of N are large enough to ensure that the effect of periodic images of the source is negligible for propagation over a distance of 40 m. Each CNPE or GFPE result was obtained from a set of 500 propagation runs for different random realisations of the turbulent atmosphere.

D.2. Distributions of the relative sound pressure level for a system with a ground surface

Next we present examples of fluctuations of the relative sound pressure level, for a system with a ground surface.

Figure 8 shows the quantities $\langle \Delta L \rangle$, ΔL_+ and ΔL_- (see Section IV.A) as a function of range L for axisymmetric turbulence, for four situations: $(f, z_s) = (250, 3)$, $(500, 2.4)$, $(1000, 1.5)$ and $(2000, 0.9)$, where f is the frequency (in Hz) and z_s is the source height (in m). We used equal source height and receiver height, *i.e.*, $z_s = z_r$. The curves represent computational method 1 (using $N_{\text{random}} = 50\,000$, see Section IV.A.2), the symbols represent CNPE results. For comparison, we also computed the curves for isotropic turbulence; we found that the deviations from the curves for axisymmetric turbulence shown in Fig. 8 are very small. For the CNPE computations we used a grid spacing of 0.1λ and a system height of 2000 grid spacings, including an absorbing top layer of 1000 grid spacings to eliminate spurious reflections from the top surface. The CNPE results were obtained by averaging over 500 random realisations of the turbulent atmosphere.

Figure 9 shows the probability density distribution of the relative sound pressure level at frequency 1000 Hz and range $L = 40$ m (for $z_s = 1.5$ m and $z_r = 1.5$ m), for axisymmetric turbulence. Figure 10 is as Fig. 9, but for isotropic turbulence (except for the PE results, which are always for axisymmetric turbulence). These two figures contain results of four computational methods: CNPE and computational methods 1, 2 and 3. Values of $\langle \Delta L \rangle$, σ_+ and σ_- are given in the legends. Method 3 gives a smaller value for σ_- than the methods 1 and 2 do. The smaller value from method 3 is confirmed by the PE result.

Figure 11 provides evidence for the saturation of log-amplitude fluctuations.^{8,26} The figure shows the quantities $\langle \Delta L \rangle$, ΔL_+ and ΔL_- as a function of range L , for axisymmetric turbulence, $f = 2000$ Hz, $z_s = 10$ m and $z_r = 10$ m. The symbols represent CNPE results (based on 350 random realisations of the turbulent atmosphere; a grid spacing of 0.02 m was used and a system height of 80 m). The lines represent computational method 1 (using $N_{\text{random}} = 50\,000$) including a saturation $\sigma_\chi \leq \sigma_{\chi, \text{max}}$ (*i.e.*, when $\sigma_\chi > \sigma_{\chi, \text{max}}$, σ_χ is set equal to $\sigma_{\chi, \text{max}}$). The five graphs in Fig. 11 are for five different values of $\sigma_{\chi, \text{max}}$. The agreement with the PE results is best for $\sigma_{\chi, \text{max}} = 0.5$, or $\sigma_{\chi, \text{max}}^2 = 0.25$. This value is of the same order as the upper limit of the weak-turbulence region $\sigma_{\chi, \text{max}}^2 = 0.2 - 0.5$ given in Refs. [2,4]. Brownlee²⁶ predicted saturation at $\sigma_{\chi, \text{max}}^2 = 0.27$.

It should be noted that our estimate of the saturation value $\sigma_{\chi, \text{max}}^2 = 0.25$ might be affected by the fact that computational method 1 overestimates the fluctuations of the relative sound pressure level, at least for weak turbulence (see Fig. 9). It should be noted further that the most direct PE approach to observe the saturation would be to simulate propagation in an unbounded system, by using a system with source and receiver well above the ground surface (as in Section D.1, but for larger range and/or higher frequency). The numerical effort for this approach was too large.

IV.E. Concluding remarks

Method 1 for computing statistical distributions of the sound pressure level appears sufficiently accurate for most practical applications. If a higher accuracy is required, method 2 or preferably method 3 may be used, but these methods require a larger numerical effort. All three methods are limited to weak turbulence, but the range of validity may be extended simply by limiting the variance $\langle \chi^2 \rangle$ to a saturation value of about 0.25 (note that this limitation should also be applied in the coherence factor described in Section III). Further, all three methods are restricted to non-refracting atmospheres. An extension of this work to downward refracting atmospheres will be the subject of future work.

- ¹ V.I. Tatarski, *Wave Propagation in a Turbulent Medium* (McGraw-Hill, New York, 1961) p. 3-26, 122-156, 173-188.
- ² V.I. Tatarskii, *The Effects of the Turbulent Atmosphere on Wave Propagation* (Israel Program for Scientific Translations, Jerusalem, 1971) p. 1-33, 218-258, 414-423.
- ³ L.A. Chernov, *Wave Propagation in a Random Medium* (McGraw-Hill, New York, 1960) p. 5-11, 58-83.
- ⁴ A. Ishimaru, *Wave Propagation and Scattering in Random Media* (Academic, New York, 1978) p. 347-387, 407-422, 513-519.
- ⁵ U. Ingard and G.C. Maling, Jr., "On the effect of atmospheric turbulence on sound propagated over ground", *J. Acoust. Soc. Am.* **35**, 1056-1058 (1963)
- ⁶ G.A. Daigle, J.E. Piercy and T.F.W. Embleton, "Effects of atmospheric turbulence on the interference of sound waves near a hard boundary", *J. Acoust. Soc. Am.* **64**, 622-630 (1978)
- ⁷ G.A. Daigle, "Effects of atmospheric turbulence on the interference of sound waves above a finite impedance boundary", *J. Acoust. Soc. Am.* **65**, 45-49 (1979)
- ⁸ G.A. Daigle, J.E. Piercy and T.F.W. Embleton, "Line-of-sight propagation through atmospheric turbulence near the ground", *J. Acoust. Soc. Am.* **74**, 1505-1513 (1983)
- ⁹ A. L'Espérance, P. Herzog, G.A. Daigle and J.R. Nicolas, "Heuristic model for outdoor sound propagation based on an extension of the geometrical ray theory in the case of a linear sound speed profile", *Applied Acoustics* **37**, 111-139 (1992)
- ¹⁰ S.F. Clifford and R.J. Lataitis, "Turbulence effects on acoustic wave propagation over a smooth surface", *J. Acoust. Soc. Am.* **73**, 1545-1550 (1983)
- ¹¹ U. Ingard, "A review of the influence of meteorological conditions on sound propagation", *J. Acoust. Soc. Am.* **25**, 405-411 (1953)
- ¹² P.H. Parkin and W.E. Scholes, "The horizontal propagation of sound from a jet engine close to the ground, at Radlett", *J. Sound Vib.* **1**, 1-13 (1964)
- ¹³ P.H. Parkin and W.E. Scholes, "The horizontal propagation of sound from a jet engine close to the ground, at Hatfield", *J. Sound Vib.* **2**, 353-374 (1965)
- ¹⁴ M. Delany, "Sound propagation in the atmosphere: a historical review", *Acustica* **38**, 201-223 (1977)
- ¹⁵ J.E. Piercy, T.F.W. Embleton and L.C. Sutherland, "Review of noise propagation in the atmosphere", *J. Acoust. Soc. Am.* **61**, 1403-1418 (1977)
- ¹⁶ S. Canard-Caruana, S. Lewy, J. Vermorel and G. Parmentier, "Long range sound propagation near the ground", *Noise Control Eng. J.* **34**, 111-119 (1990)
- ¹⁷ T.F.W. Embleton, "Tutorial on sound propagation outdoors", *J. Acoust. Soc. Am.* **100**, 31-48 (1996)
- ¹⁸ T. Hidaka, K. Kageyama and S. Masuda, "Fluctuation of spherical wave propagating over a ground through atmospheric turbulence", *J. Acoust. Soc. Jpn. (E)* **6**, 247-256 (1985)
- ¹⁹ K.E. Gilbert, R. Raspet, and X. Di, "Calculation of turbulence effects in an upward-refracting atmosphere", *J. Acoust. Soc. Am.* **87**, 2428-2437 (1990).
- ²⁰ P. Chevret, Ph. Blanc-Benon and D. Juve, "A numerical model for sound propagation through a turbulent atmosphere near the ground", *J. Acoust. Soc. Am.* **100** 3587-3599 (1996)
- ²¹ V.E. Ostashev, V. Mellert, R. Wandelt and F. Gerdes, "Propagation of sound in a turbulent medium. I. Planes waves", *J. Acoust. Soc. Am.* **102**, 2561-2570 (1997).
V.E. Ostashev, F. Gerdes, V. Mellert, and R. Wandelt, "Propagation of sound in a turbulent medium. II. Spherical waves", *J. Acoust. Soc. Am.* **102**, 2571-2578 (1997).
(Note: the e.m. convention $\epsilon = 2\mu$ is used for the refractive index fluctuation in these two papers, which introduces a difference of a factor of 4 in the variances).
- ²² V.I. Tatarskii, "Review of scintillation phenomena", In: *Wave propagation in random media (scintillation)*, Ed. V.I. Tatarskii, A. Ishimaru and V.U. Zavorotny (I.O.P. Publishing and SPIE, Washington, 1993) p. 2-15
- ²³ S.E. Koonin, "Computational Physics" (Adison-Wesley, Redwood City, 1986) p. 191-195
- ²⁴ K.E. Gilbert and X. Di, "A fast Green's function method for one-way sound propagation in the atmosphere", *J. Acoust. Soc. Am.* **94**, 2343-2352 (1993)
- ²⁵ X. Di and K.E. Gilbert, "The effect of turbulence and irregular terrain on outdoor sound propagation", *Proc. Sixth Symp. on Long-Range Sound Prop.*, Ottawa Canada (1994) p. 315-333
- ²⁶ L.R. Brownlee, "Rytov's method and large fluctuations", *J. Acoust. Soc. Am.* **53**, 156-161 (1973)

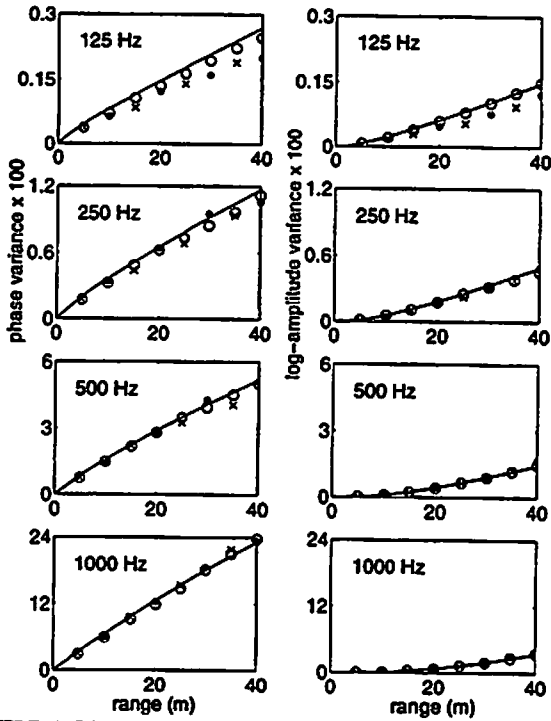


FIG 4. Phase and log-amplitude variances as a function of range, for an unbounded axisymmetric system: analytic solutions used in method 1 (lines), method 2 (o), CNPE(•), and GFPE (x).

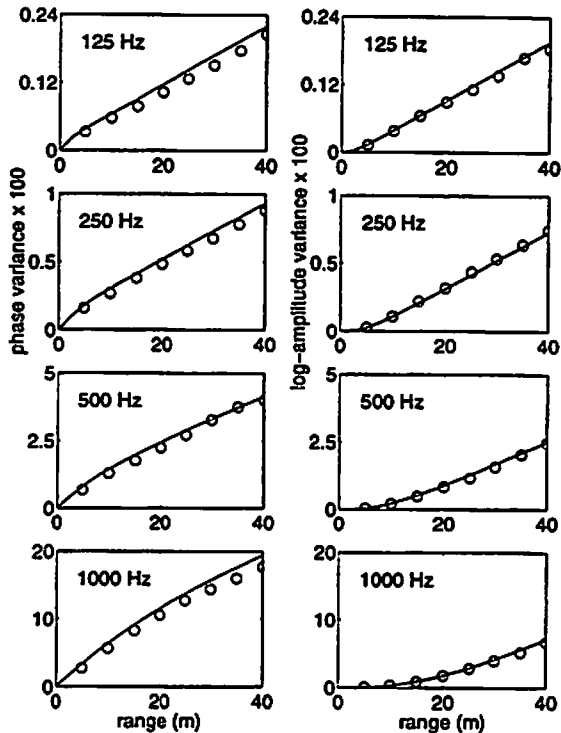


FIG. 5. As Figure 4, for an isotropic system.

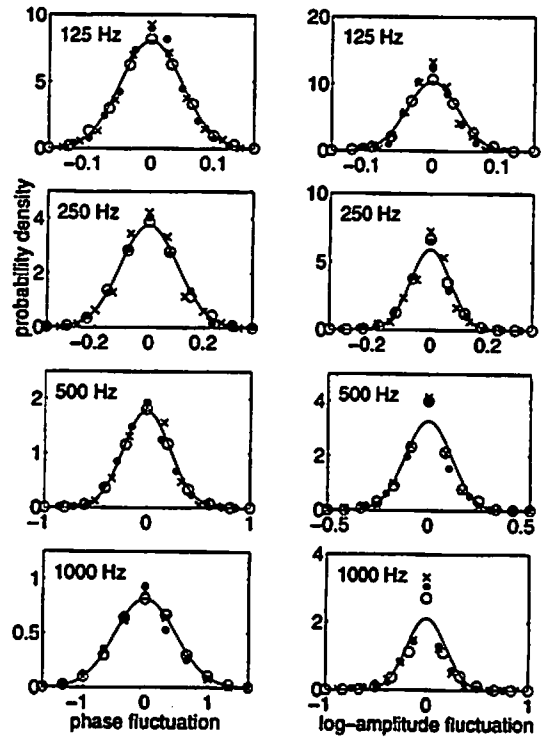


FIG. 6. Probability density distributions of S and χ at range $L = 40$ m, for an unbounded axisymmetric system: method 2 (o) and corresponding Gaussians (lines), CNPE (•), and GFPE (x).

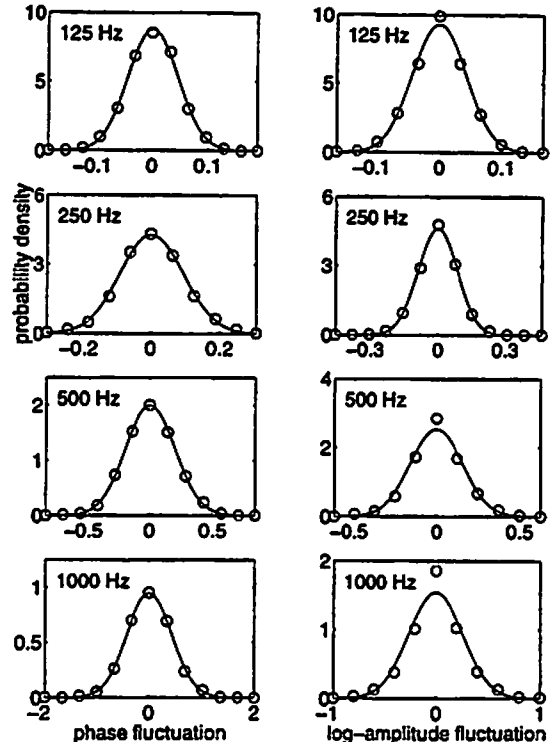


FIG. 7. As Figure 6, for an isotropic system.

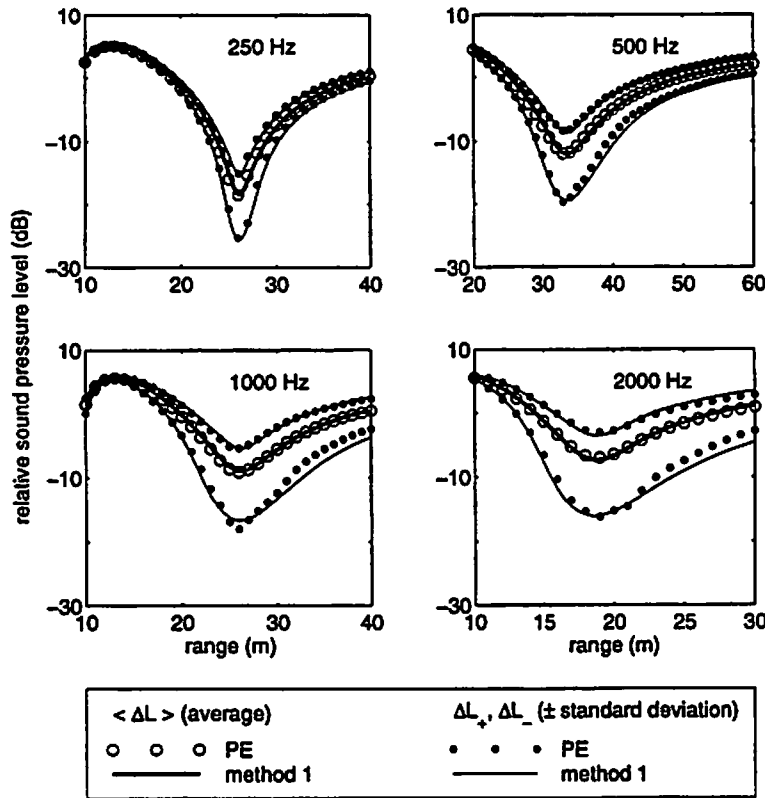


FIG. 8. $\langle \Delta L \rangle$, ΔL_{+} , and ΔL_{-} as a function of range, for axisymmetric turbulence, and $f = 250, 500, 1000$ and 2000 Hz, respectively with $z_r = 3, 2.4, 1.5$ and 0.9 m, and $z_s = z_r$.

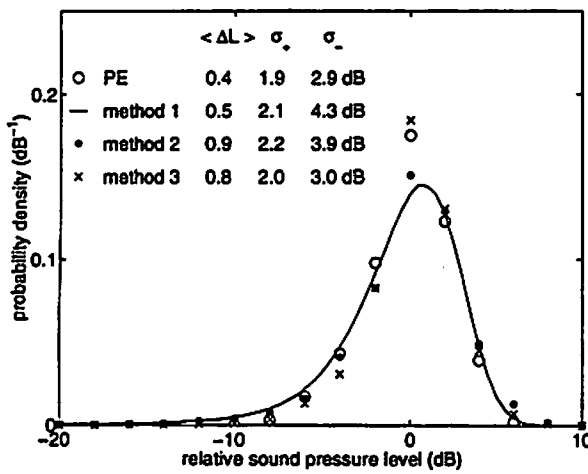


FIG. 9. Probability density distribution of the relative sound pressure level for axisymmetric turbulence, for $f = 1000$ Hz, $L = 40$ m, $z_s = 1.5$ m and $z_r = 1.5$ m.

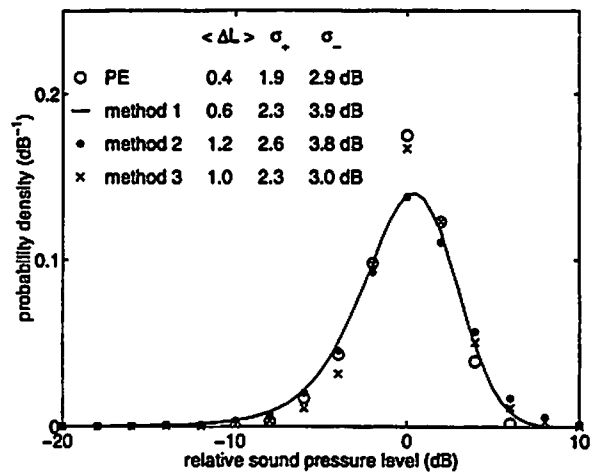


FIG. 10. As Figure 9, for isotropic turbulence (except PE).

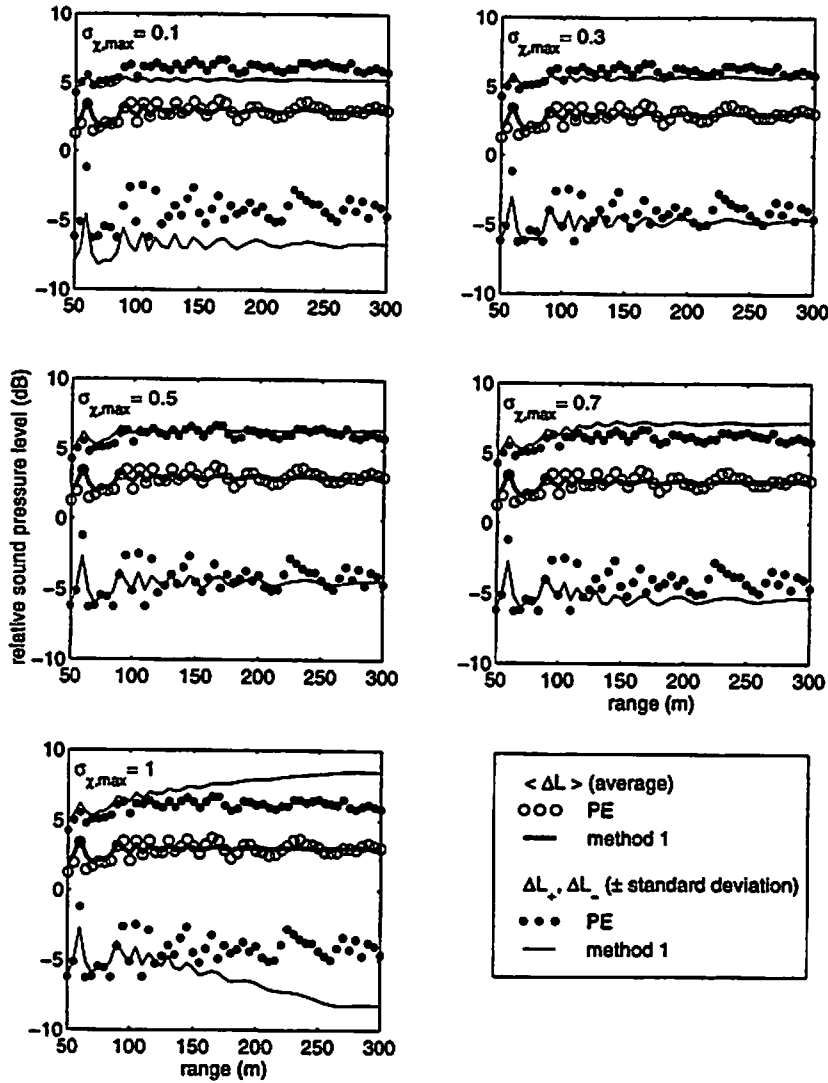


FIG. 11. $\langle \Delta L \rangle$, ΔL_{+} , and ΔL_{-} as a function of range, for axisymmetric turbulence, $f = 2000$ Hz, $z_r = 10$ m and $z_s = 10$ m, and five values of the saturation limit $\sigma_{\chi, \max}$.

APPENDIX A. Isotropic and axisymmetric turbulence

The fluctuating field $\mu(\vec{r})$ is represented by the following stochastic Fourier-Stieltjes integral:^{1,2,4}

$$\mu(\vec{r}) = \int \exp(i\vec{K} \cdot \vec{r}) dv(\vec{K}) \tag{A1}$$

with $\vec{K} = (\kappa_x, \kappa_y, \kappa_z)$ and random amplitudes dv that satisfy the relations

$$\langle dv(\vec{K}) \rangle = 0, \quad \langle dv(\vec{K}) dv^*(\vec{K}') \rangle = \Phi_{\mu}(\vec{K}) \delta(\vec{K} - \vec{K}') d\vec{K} d\vec{K}' \tag{A2}$$

where δ is the Dirac delta function and the function $\Phi_{\mu}(\vec{K})$ is the three-dimensional spectral density of the function $\mu(\vec{r})$. The correlation function of $\mu(\vec{r})$ is:

$$B_{\mu}(\vec{r}) \equiv \langle \mu(\vec{r}_1) \mu^*(\vec{r}_2) \rangle = \int \Phi_{\mu}(\vec{K}) e^{i\vec{K} \cdot \vec{r}} d\vec{K} \tag{A3}$$

with $\vec{r} = \vec{r}_1 - \vec{r}_2$. The inverse Fourier transform is:

$$\Phi_{\mu}(\bar{K}) = (2\pi)^{-3} \int B_{\mu}(\bar{r}) e^{-i\bar{K}\cdot\bar{r}} d\bar{r} \quad (\text{A4})$$

An example is the Gaussian correlation function

$$B_{\mu}(r) = \mu_0^2 \exp\left(-\frac{r^2}{a^2}\right) \quad (\text{A5})$$

with μ_0 the standard deviation of μ and a the correlation length, with Gaussian spectral density:

$$\Phi_{\mu}(\kappa) = \mu_0^2 \frac{a^3}{8\pi^{3/2}} \exp\left(-\frac{\kappa^2 a^2}{4}\right) \quad (\text{A6})$$

where $\kappa = |\bar{K}|$.

The fluctuating field $\mu(\bar{r})$ can also be represented by a two-dimensional stochastic Fourier-Stieltjes integral:

$$\mu(\bar{r}) = \int \exp(i\bar{\kappa}\cdot\bar{\rho}) dv(x, \bar{\kappa}) \quad (\text{A7})$$

with $\bar{\rho} = (y, z)$ and random amplitudes dv that satisfy the relations

$$\langle dv(x, \bar{\kappa}) \rangle = 0, \quad \langle dv(x', \bar{\kappa}') dv^*(x'', \bar{\kappa}'') \rangle = F_{\mu}(x, \bar{\kappa}) \delta(\bar{\kappa} - \bar{\kappa}') d\bar{\kappa} d\bar{\kappa}' \quad (\text{A8})$$

where $x = x' - x''$, $\bar{\kappa} = (\kappa_y, \kappa_z)$ and $F_{\mu}(x, \bar{\kappa})$ is the two-dimensional spectral density of the function $\mu(\bar{r})$. The correlation function becomes:

$$B_{\mu}(x, \bar{\rho}) = \int F_{\mu}(x, \bar{\kappa}) e^{i\bar{\kappa}\cdot\bar{\rho}} d\bar{\kappa} \quad (\text{A9})$$

The inverse Fourier transform is:

$$F_{\mu}(x, \bar{\kappa}) = (2\pi)^{-2} \int B_{\mu}(x, \bar{\rho}) e^{-i\bar{\kappa}\cdot\bar{\rho}} d\bar{\rho} \quad (\text{A10})$$

An example is the Gaussian correlation function

$$B_{\mu}(x, \rho) = \mu_0^2 \exp\left(-\frac{x^2}{a^2}\right) \exp\left(-\frac{\rho^2}{a^2}\right) \quad (\text{A11})$$

with spectral density:

$$F_{\mu}(x, \kappa) = \mu_0^2 \frac{a^2}{4\pi} \exp\left(-\frac{x^2}{a^2}\right) \exp\left(-\frac{\kappa^2 a^2}{4}\right) \quad (\text{A12})$$

Equations (A4) and (A10) give the following two relations:

$$F_{\mu}(x, \bar{\kappa}) = \int_{-\infty}^{\infty} \Phi_{\mu}(\bar{K}) \exp(i\kappa_x x) d\kappa_x \quad (\text{A13})$$

$$\Phi_{\mu}(\bar{K}) = (2\pi)^{-1} \int_{-\infty}^{\infty} F_{\mu}(x, \bar{\kappa}) \exp(-i\kappa_x x) dx \quad (\text{A14})$$

Choosing $\kappa_x = 0$ we obtain the relation:

$$\Phi_{\mu}(\bar{K}) = (2\pi)^{-1} \int_{-\infty}^{\infty} F_{\mu}(x, \bar{\kappa}) dx \quad (\text{A15})$$

which is used in the derivation of the phase and log-amplitude correlation functions.

1. 3d-isotropic field μ

If $\mu(\bar{r})$ is homogeneous and isotropic in three dimensions, Eq. (A4) implies

$\Phi_{\mu}(\bar{K}) = \Phi_{\mu}(|\bar{K}|)$ and Eq. (A10) implies $F_{\mu}(x, \bar{\kappa}) = F_{\mu}(|x|, |\bar{\kappa}|)$.

2. 2d-isotropic field μ

If $\mu(\vec{r})$ is independent of y and homogeneous and isotropic in the xz plane, then

$B_\mu = B_\mu(\sqrt{x^2 + z^2})$. This type of turbulent fields are used in computational methods (such as the PE method) based on the axisymmetric approximation. In this case Eq. (A4) gives:

$$\Phi_\mu(\vec{K}) = (2\pi)^{-2} \iint B_\mu(\sqrt{x^2 + z^2}) \exp(-i[\kappa_x x + \kappa_z z]) dx dz (2\pi)^{-1} \int \exp(-i\kappa_y y) dy \quad (\text{A16})$$

which can be written as:

$$\Phi_\mu(\vec{K}) = F_\mu(\sqrt{\kappa_x^2 + \kappa_z^2}) \delta(\kappa_y) \quad (\text{A17})$$

with $F_\mu(\kappa) \equiv F_\mu(x=0, \kappa)$. Equation (A10) gives:

$$F_\mu(x, \vec{K}) = (2\pi)^{-1} \int B_\mu(\sqrt{x^2 + z^2}) \exp(-i\kappa_z z) dz (2\pi)^{-1} \int \exp(-i\kappa_y y) dy \quad (\text{A18})$$

Comparison of Eqs. (A16) and (A18) yields Eq. (A14).

APPENDIX B. The functions $F(\alpha, \beta, \gamma)$ and $I(\alpha, \beta, \gamma)$

We define the function $F(\alpha, \beta, \gamma)$ as follows:

$$\begin{aligned} F(\alpha, \beta, \gamma) &= \int_0^\infty J_0(\alpha\kappa) \cos(\beta\kappa^2) \exp(-\gamma\kappa^2) \kappa d\kappa \\ &= \text{Re} \int_0^\infty J_0(\alpha\kappa) \exp(-\gamma\kappa^2 + i\beta\kappa^2) \kappa d\kappa \end{aligned} \quad (\text{B1})$$

Using the relation $J_0(\alpha\kappa) = (2\pi)^{-1} \int_0^{2\pi} \exp(i\kappa\alpha \cos\theta) d\theta$, we obtain:

$$\begin{aligned} F(\alpha, \beta, \gamma) &= \frac{1}{2\pi} \text{Re} \int_0^\infty \int_0^{2\pi} \exp(i\alpha\kappa \cos\theta) \exp(-\gamma\kappa^2 + i\beta\kappa^2) \kappa d\kappa d\theta \\ &= \frac{1}{2\pi} \text{Re} \int \int \exp(i\alpha\kappa_y) \exp(-\gamma\kappa_y^2 + i\beta\kappa_y^2) \exp(-\gamma\kappa_z^2 + i\beta\kappa_z^2) d\kappa_y d\kappa_z \end{aligned} \quad (\text{B2})$$

where a transformation $(\kappa, \theta) \rightarrow (\kappa_y, \kappa_z)$ has been applied. The integral over κ_z yields a factor $\sqrt{\pi} / \sqrt{\gamma - i\beta}$, and with the notation $\kappa \equiv \kappa_y$, we obtain:

$$F(\alpha, \beta, \gamma) = \frac{1}{\sqrt{\pi}} \int_0^\infty \cos(\alpha\kappa) \exp(-\gamma\kappa^2) \text{Re} \frac{\exp(i\beta\kappa^2)}{\sqrt{\gamma - i\beta}} d\kappa \quad (\text{B3})$$

Using $(\gamma - i\beta)^{-1/2} = (\gamma^2 + \beta^2)^{-1/4} \exp[\frac{1}{2}i \arctan(\beta / \gamma)]$, we obtain:

$$F(\alpha, \beta, \gamma) = \frac{1}{\sqrt{\pi}(\gamma^2 + \beta^2)^{1/4}} \int_0^\infty \cos(\alpha\kappa) \exp(-\gamma\kappa^2) \cos(\frac{1}{2} \arctan \frac{\beta}{\gamma} + \beta\kappa^2) d\kappa \quad (\text{B4})$$

We define the function $G(\alpha, \beta, \gamma, \delta)$ as follows:

$$\begin{aligned} G(\alpha, \beta, \gamma, \delta) &= \int_0^\infty \cos(\alpha\kappa) \cos(\beta\kappa^2 + \delta) \exp(-\gamma\kappa^2) d\kappa \\ &= \frac{1}{2} \text{Re} \int \exp[-(\gamma - i\beta)\kappa^2 + i\alpha\kappa + i\delta] d\kappa \end{aligned} \quad (\text{B5})$$

With the substitution $z = \kappa\sqrt{\gamma - i\beta}$ we obtain:

$$G(\alpha, \beta, \gamma, \delta) = \frac{\sqrt{\pi}}{2\sqrt{\gamma^2 + \beta^2}} \operatorname{Re} \left(\exp \left[-\frac{\alpha^2}{4(\gamma^2 + \beta^2)} (\gamma + i\beta) + i\delta \right] \sqrt{\gamma + i\beta} \right) \quad (\text{B6})$$

Using $(\gamma + i\beta)^{1/2} = (\gamma^2 + \beta^2)^{1/4} \exp[\frac{1}{2}i \arctan(\beta/\gamma)]$, we obtain:

$$G(\alpha, \beta, \gamma, \delta) = \frac{\sqrt{\pi}}{2(\gamma^2 + \beta^2)^{1/4}} \exp \left(-\frac{\alpha^2 \gamma}{4(\gamma^2 + \beta^2)} \right) \cos \left(\frac{1}{2} \arctan \frac{\beta}{\gamma} - \frac{\alpha^2 \beta}{4(\gamma^2 + \beta^2)} + \delta \right) \quad (\text{B7})$$

Equations (B4) and (B5) give the relation:

$$F(\alpha, \beta, \gamma) = \frac{1}{\sqrt{\pi}(\gamma^2 + \beta^2)^{1/4}} G(\alpha, \beta, \gamma, \delta = \frac{1}{2} \arctan \frac{\beta}{\gamma}) \quad (\text{B8})$$

which yields, with the notation $D \equiv \gamma^2 + \beta^2$:

$$F(\alpha, \beta, \gamma) = \frac{1}{2D} \exp \left(-\frac{\alpha^2 \gamma}{4D} \right) \left(\gamma \cos \frac{\alpha^2 \beta}{4D} + \beta \sin \frac{\alpha^2 \beta}{4D} \right) \quad (\text{B9})$$

where the relations $\cos(\arctan \beta/\gamma) = \gamma/\sqrt{\gamma^2 + \beta^2}$ and $\sin(\arctan \beta/\gamma) = \beta/\sqrt{\gamma^2 + \beta^2}$ have been used. We define the function $I(\alpha, \beta, \gamma) \equiv G(\alpha, \beta, \gamma, \delta=0)$. Using the relations $\cos \frac{1}{2} \phi = \sqrt{\frac{1}{2} + \frac{1}{2} \cos \phi}$ and $\sin \frac{1}{2} \phi = \sqrt{\frac{1}{2} - \frac{1}{2} \cos \phi}$, we obtain:

$$I(\alpha, \beta, \gamma) = \frac{\sqrt{\pi}}{2^{3/2} D^{1/4}} \exp \left(-\frac{\alpha^2 \gamma}{4D} \right) \left(\sqrt{1 + \frac{\gamma}{\sqrt{D}}} \cos \frac{\alpha^2 \beta}{4D} + \sqrt{1 - \frac{\gamma}{\sqrt{D}}} \sin \frac{\alpha^2 \beta}{4D} \right) \quad (\text{B10})$$

APPENDIX C. The Fresnel integrals and related integrals

The Fresnel integrals are $C(z) = \int_0^z \cos(\frac{\pi}{2} t^2) dt$ and $S(z) = \int_0^z \sin(\frac{\pi}{2} t^2) dt$. We have

$C(\infty) = S(\infty) = \frac{1}{2}$ and $C(-z) = -C(z)$ and $S(-z) = -S(z)$. The following relation is easily obtained:

$$\int_0^z \exp(iw^2) dw = \sqrt{\frac{\pi}{2}} \left[C \left(z \sqrt{\frac{2}{\pi}} \right) + iS \left(z \sqrt{\frac{2}{\pi}} \right) \right] \quad (\text{C1})$$

from which the following relation is obtained:

$$\int_z^{\infty} \exp(iw^2) dw = \sqrt{\frac{\pi}{2}} (1+i)^{1/2} \left\{ 1 - (1-i) \left[C \left(z \sqrt{\frac{2}{\pi}} \right) + iS \left(z \sqrt{\frac{2}{\pi}} \right) \right] \right\} \quad (\text{C2})$$

Using the algebraic equation:

$$aw^2 + bw = \left(\sqrt{a}w + \frac{b}{2\sqrt{a}} \right)^2 - \frac{b^2}{4a} \quad (\text{C3})$$

the following relations are easily derived:

$$\int_{-\infty}^{\infty} \exp(i[aw^2 + bw]) dw = \sqrt{\frac{\pi}{2a}} (1+i) \exp \left(-i \frac{b^2}{4a} \right) \quad (\text{C4})$$

$$\int_u^{\infty} \exp(i[aw^2 + bw]) dw = \sqrt{\frac{\pi}{2a}} (1+i) \exp \left(-i \frac{b^2}{4a} \right)^{1/2} \left\{ 1 - (1-i) \left[C \left(v \sqrt{\frac{2}{\pi}} \right) + iS \left(v \sqrt{\frac{2}{\pi}} \right) \right] \right\} \quad (\text{C5})$$

with $v = u\sqrt{a} + \frac{1}{2}b/\sqrt{a}$.

Influence of Atmospheric Turbulence on Sound Reduction by a Thin, Hard Screen: A Parameter Study Using the Sound Scattering Cross-section

Jens Forssén

Dept. of Applied Acoustics, Chalmers University of Technology, Göteborg, S-41296, Sweden. Tel +46 31 7722196. Fax +46 31 7722212. E-mail jf@ta.chalmers.se

Summary

A prediction scheme is presented that uses a small number of pre-calculated data to predict the energy scattered by the turbulence and the diffracted energy for a large variety of situations with a thin, hard screen in the absence of a ground surface. This is done by applying transformations for variations in frequency and in geometrical scale, for both the scattered and the diffracted energies.

The influence of the turbulence scattering on the sound reduction by a screen is shown to grow when the geometry is increased in scale or when the frequency is increased. Moreover, the influence of the scattering grows when the screen-receiver distance is increased, and the weak scattering at angles near 90° leads to a dip in the influence of the scattering when the screen height is increased.

An example calculated for one geometry and with a typical traffic noise spectrum as input shows that taking into account atmospheric turbulence can significantly reduce the performance of a noise barrier, not only at high frequencies, but also when measured in dB(A).

A three-dimensional integration of the scattered energy is shown to be simplified by an analytical integration in one dimension, which makes the numerical solution far quicker.

1. Introduction

To correctly predict the sound reduction by a noise barrier in an outdoor environment, the fact that the atmosphere is never homogeneous cannot be ignored. Wind and temperature gradients cause curved ray paths and the atmospheric turbulence causes scattering and decorrelation of the sound waves. The scattering has been shown to cause an increased sound energy in the acoustic shadow formed by upward refraction (e.g. [1]). In a similar way the scattering reduces the performance of a noise barrier [2, 3]. Especially for high frequencies and large scale geometries, the turbulence scattering will significantly influence

the sound reduction by a noise barrier. A situation of interest with a large scale geometry is when using large buildings as road traffic noise barriers.

For predicting the effects of a turbulent atmosphere on sound reduction by a thin, hard screen, a model developed by Daigle [2] is used. In the model the energy scattered by the turbulence is calculated using the sound scattering cross-section by Tatarskii [4] and then added to the diffracted energy in the shadow of the screen. With this model Daigle investigated five different geometries and the predictions were compared with measured data [2]. The comparison showed a fairly good agreement between predictions and measurements, and that neglecting the turbulence scattering would yield a poor prediction, especially at higher frequencies.

To determine when the atmospheric turbulence significantly influences the sound reduction by a screen, a large set of situations need to be investigated, i.e. many parameters need to be varied. The model used does allow the results predicted for one situation to be straight forwardly transformed to other situations and thereby the number of parameters used in the calculations can be reduced. Using the physically based Kolmogorov spectrum for the representation of the turbulence allows a straight forward transformation of the results for one frequency to other frequencies. In this study no ground effects are taken into account, leading to a straight forward frequency dependence of the diffraction as well. Moreover, the results when enlarging or diminishing the geometry in scale can also be predicted using straight forward transformations, both for the scattering and the diffraction. Considering all these transformation properties of the model, the predictions of the scattering and the diffraction for all situations of interest can be compactly presented as a small amount of data, as shown in the following.

When omitting the ground surface in the predictions the barrier insertion loss will in general be overestimated. For instance, if the receiver is placed on a hard ground, the overestimation will be 6 dB (the scattered level relative to the diffracted field will, however, be the same). If the receiver is placed above the ground, the insertion loss will be more difficult to predict since it will be determined by the interference between direct and ground reflected waves. For high enough frequencies, however, the direct and ground reflected waves, from both diffraction and scattering, will add energy wise, since the waves will be uncorrelated due to the randomness of the medium as well as of the ground surface. Then, the insertion loss will be overestimated by about 3 dB for an elevated receiver, and the scattered level relative to the diffracted field will be the same as without ground.

For future work a model similar to the one used here can be developed to take into account a finite impedance ground surface, thick barriers of finite length, a

non-constant sound speed profile, and locally homogeneous turbulence. Moreover, it should be possible to include the decorrelation between a direct and a ground reflected wave that is due to the atmospheric turbulence.

2. Theory

The acoustic energy scattered into the shadow of the screen is calculated using the sound scattering cross-section by Tatarskii [4]. The diffracted energy is calculated separately and then added to the scattered energy, according to the model developed by Daigle [2].

2.1 Diffraction

The diffraction is calculated for a thin, hard screen using uniform theory of diffraction [5, 6]. When no ground is present the diffracted energy is inversely proportional to the frequency. Analogously, if the geometry is increased in scale, by some scaling factor, the diffracted energy relative to free field is inversely proportional to the scaling factor.

The main restriction of the uniform theory of diffraction is that it is only applicable when the source and receiver are located more than a quarter of a wavelength away from the screen [7]. For a more extensive description of the uniform theory of diffraction, see e.g. [5].

2.2 Sound scattering cross-section

The sound scattering cross-section is a single scattering approximation where the field incident on a scattering object is assumed to be well approximated by the field calculated for a non-turbulent atmosphere. The energy scattered from each object will be added to the total field and thus the model is not energy conserving. This means that it is restricted to small perturbations of the sound field, which implicates that the propagation distance cannot be too large. Also the fluctuations of the medium have to be small, so that the acoustic field inside a scattering object can be approximated by the incident field, i.e. the Born approximation.

The atmospheric turbulence is approximated as homogeneous and isotropic, which means that it is described by the same statistics in all points and in all directions.

Furthermore a far field condition has to be fulfilled,

$$\rho \gg l^2/\lambda, \quad (1)$$

where l is the correlation length of the turbulence (about 1 m), λ the acoustic wavelength, and ρ the distance from a scattering elementary volume to the receiver (see Figure 1). Condition (1) justifies an uncorrelated summation of the

contribution from different elementary scattering volumes and the total received scattered energy can be written as [2]

$$E_s = \int_V p_0^2 \frac{\sigma(\theta)}{\rho^2} dV, \quad (2)$$

where p_0 is the amplitude of the incident pressure, $\sigma(\theta)$ the scattering cross-section, and θ the scattering angle. The volume of integration V consists of all points in line of sight from both source and receiver (i.e. the striped area in Figure 1).

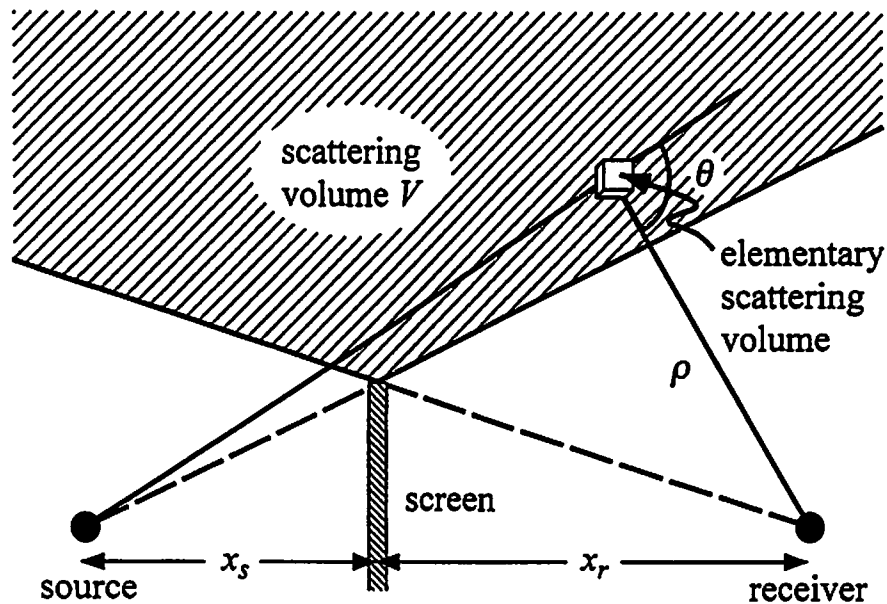


Figure 1. Geometry for the sound scattering cross-section.

Following Tatarskii [4, p. 160] the scattering cross-section is written

$$\sigma(\theta) = \frac{\pi k^4}{2} \cos^2 \theta \left[\frac{\Phi(\kappa)}{T_0^2} + \frac{4F(\kappa)}{c_0^2} \cos^2 \frac{\theta}{2} \right], \quad (3)$$

where $\Phi(\kappa)$ and $F(\kappa)$ are the spectral densities of the temperature and the wind velocity fluctuations respectively, T_0 the mean temperature, c_0 the mean sound velocity, and κ the wave number of the turbulence, fulfilling the Bragg condition

$$\kappa = 2k \sin \frac{\theta}{2}. \quad (4)$$

It can be noted in equation (3) that for right angles $\cos^2 \theta = 0$, and the scattering cross-section will be zero.

The incident pressure p_0 in equation (2) is calculated without taking into account the field diffracted by the screen. This will lead to an overestimation of the scattered energy since the strongest scattering will come from parts of the

scattering volume that are near the shadow boundary, where the incident pressure is weakened by diffraction. A more accurate prediction of the scattered energy can be obtained by considering the diffracted field in the entire scattering volume.

Equation (2) describes the time average of the energy scattered by the turbulence. The turbulence can be seen as a composition of Bragg planes with separation distance $2\pi/\kappa$ causing scattering of energy proportional to the spectral density at κ .

According to this model the scattered energy will, relative to free field, change with the same factor as the geometry is scaled. To see this let the height of the screen, as well as its distance from source and receiver, be doubled. Substituting for these new variables in the integral (2) will cause an increase by a factor eight in dV and a factor four in ρ^2 , whereas p_0^2 will stay constant relative to free field. As a result the scattered energy will be doubled, i.e. increased by 3 dB, relative to free field. This dependence of the scattered energy on the scaling of the geometry is, due to the single scattering approximation, restricted to short ranges, as stated above. It is, however, assumed here that, for frequencies of interest for road traffic noise situations, the single scattering approximation is realistic up to at least a few hundred meters in range. Measurements or further theoretical work is needed to confirm the validity of this assumption.

Both $\Phi(\kappa)$ and $F(\kappa)$ in equation (3) are assumed to be described by the Kolmogorov spectrum (see Figure 2), with amplitudes C_7^2 and C_7^2 respectively.

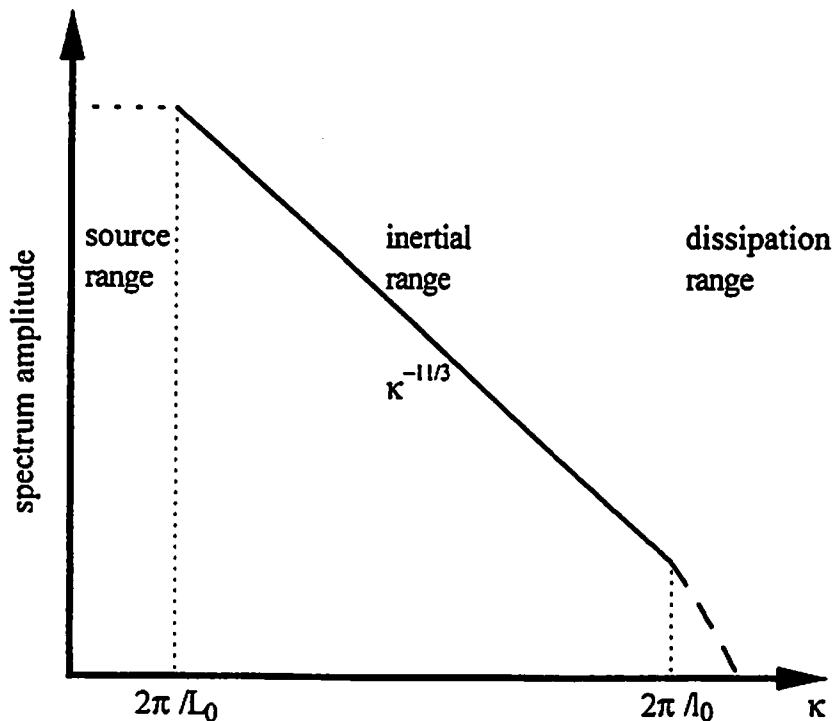


Figure 2. Kolmogorov spectrum of the turbulence.

In the inertial range, where the spectrum amplitude is proportional to $\kappa^{-1/3}$, the scattering cross-section can be written as

$$\sigma(\theta) = 0.38k^{1/3} \frac{\cos^2 \theta}{(2 \sin(\theta/2))^{1/3}} \left[0.13 \frac{C_T^2}{T_0^2} + \frac{C_v^2}{c_0^2} \cos^2 \frac{\theta}{2} \right]. \quad (5)$$

In equation (5) it can be seen that the scattered energy changes with frequency as $f^{1/3}$.

The strength of the turbulence in the source range, i.e. for $\kappa < 2\pi/L_0$, will depend on the large structures of the terrain and is not easily determined. In this study the spectrum amplitude in the source range is assumed to be constant, at a value equal to the amplitude at $\kappa = 2\pi/L_0$ for the inertial range. When calculating the integral (2) the constant value of the spectrum in the source range has to be considered if the scattering angle theta is small or if the frequency is low, according to the Bragg condition (4). This leads to that only in the situations when a negligible part of the scattered energy comes from the source range can the straight forward frequency scaling according to equation (5) be applied.

The value of l_0 is as small as 1-2 mm and therefore the dissipation range will not be of importance in the audio range.

2.3 Implementation

When calculating the integral (2) numerically, the volume of integration V is increased until further contribution to the scattered energy is negligible. For flat geometries, i.e. when the source and receiver are located far away from a low screen, a sufficient volume of integration is from the source to the receiver about L high and $2L$ wide, where L is the distance between the source and receiver. However, for less flat geometries there will be significant back scattering, i.e. scattering at angles greater than 90° , and then the volume of integration has to be increased.

The integral (2) can be solved analytically in one dimension by taking advantage of the angle dependence of the integrand, as shown in Appendix 1. This makes the numerical solution far quicker.

3. Results

In the calculations the values of the parameters for the strength of the turbulence are chosen with guidance from Daigle's measurements [2] so as to represent a strong but not unrealistically strong turbulence: $C_v^2 = 1$, $C_T^2 = 10$, and $L_0 = 1.1$ m.

In the first subsection the general results are presented and in the second subsection the influence on a typical road traffic noise spectrum is calculated for one geometry.

3.1 General results

The results are presented in two sets of tables. The variables are the screen height H and the screen-receiver distance x_r , in meters. Each set of tables consists of one table with the diffracted level relative to free field L_{D0} and one table with the scattered level relative to the diffracted field ΔL_{S0} . The results are presented for the frequency $f_0 = 2000$ Hz, and for a distance $x_{s0} = 40$ m from the source to the screen. The first set of tables (Tables 1 and 2) describes the situation where the receiver is on the same height as the source (see Figure 3). The second set of tables (Tables 3 and 4) describes the situation where the receiver is half the screen height above the source (see Figure 4).

The results can be transformed for another value of the frequency f or of the source-screen distance x_s . If x_s is changed, the tabulated results at the screen height $H \cdot x_{s0}/x_s$ and at the screen-receiver distance $x_r \cdot x_{s0}/x_s$ should be used. Then, to the results for the scattering $10 \cdot \log(x_s/x_{s0})$ is added, and to the results for the diffraction $10 \cdot \log(x_s/x_{s0})$ is subtracted. For a change in frequency $10/3 \cdot \log(f/f_0)$ is added to the scattered level and $10 \cdot \log(f/f_0)$ is subtracted from the diffracted level. Hence, the scattered level relative to the diffracted field will increase by 6 dB if the geometry is enlarged in scale by a factor two. For a doubling of frequency the increase will be 4 dB. The resulting levels using the above transformations can also be formulated as

$$\Delta L_S = \Delta L_{S0} + 10 \cdot \log(x_s/x_{s0}) + 10/3 \cdot \log(f/f_0) \quad (6)$$

and

$$L_D = L_{D0} - 10 \cdot \log(x_s/x_{s0}) - 10 \cdot \log(f/f_0), \quad (7)$$

where ΔL_S is the scattered level relative to the diffracted field and L_D the diffracted level relative to free field. The total level L_{D+S} can then be written

$$L_{D+S} = 10 \cdot \log\left(10^{L_D/10} + 10^{(L_D + \Delta L_S)/10}\right). \quad (8)$$

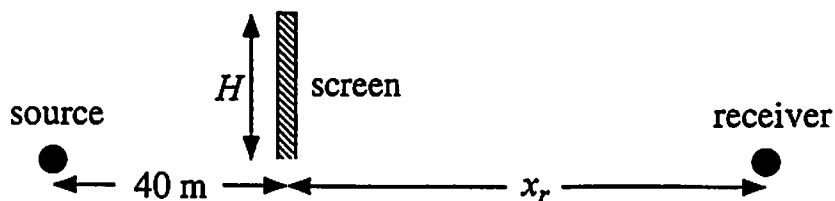


Figure 3. Geometry with the receiver at the same height as the source.

	$x_r=10$	20	30	40	50	60	70	80	90	100
$H=5$	-26.4	-25.0	-24.2	-23.7	-23.3	-23.0	-22.8	-22.6	-22.5	-22.4
10	-31.1	-30.0	-29.3	-28.9	-28.6	-28.3	-28.1	-28.0	-27.9	-27.8
15	-33.9	-32.9	-32.3	-31.8	-31.5	-31.3	-31.1	-31.0	-30.8	-30.7
20	-36.1	-35.1	-34.4	-33.9	-33.6	-33.4	-33.2	-33.0	-32.9	-32.8
25	-38.0	-36.9	-36.1	-35.6	-35.3	-35.0	-34.8	-34.6	-34.5	-34.3
30	-39.6	-38.5	-37.6	-37.1	-36.7	-36.4	-36.1	-35.9	-35.8	-35.6
35	-41.1	-39.9	-39.0	-38.4	-37.9	-37.6	-37.3	-37.1	-36.9	-36.7
40	-42.5	-41.2	-40.2	-39.5	-39.0	-38.6	-38.3	-38.1	-37.9	-37.7

Table 1. Diffracted level relative to free field, L_{D0} (dB), at the same height as the source.

	$x_r=10$	20	30	40	50	60	70	80	90	100
$H=5$	-7.1	-3.0	-0.6	1.0	2.2	3.1	3.9	4.5	5.1	5.6
10	-6.3	-4.4	-2.5	-0.9	0.4	1.4	2.3	3.0	3.7	4.2
15	-5.0	-3.8	-2.6	-1.5	-0.5	0.4	1.2	1.9	2.6	3.1
20	-4.1	-2.9	-2.0	-1.1	-0.4	0.3	1.0	1.6	2.1	2.6
25	-3.4	-2.1	-1.2	-0.5	0.1	0.7	1.3	1.8	2.3	2.7
30	-2.9	-1.6	-0.6	0.1	0.7	1.3	1.8	2.2	2.7	3.1
35	-2.5	-1.2	-0.2	0.6	1.2	1.8	2.3	2.7	3.1	3.5
40	-2.2	-0.8	0.2	1.0	1.7	2.2	2.7	3.1	3.5	3.9

Table 2. Scattered level relative to the diffracted field, ΔL_{S0} (dB), at the same height as the source.

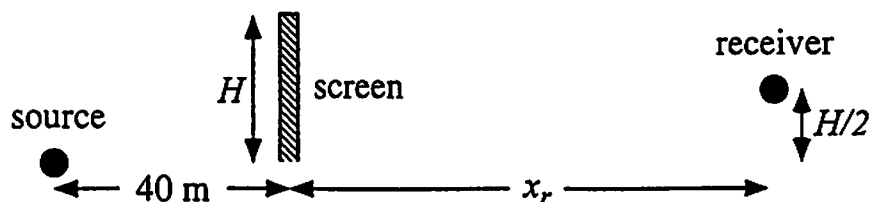


Figure 4. Geometry with the receiver half the screen height above the source.

	$x_r=10$	20	30	40	50	60	70	80	90	100
$H=5$	-22.7	-21.9	-21.6	-21.4	-21.3	-21.2	-21.2	-21.2	-21.2	-21.1
10	-27.7	-27.1	-26.9	-26.7	-26.7	-26.6	-26.6	-26.6	-26.6	-26.6
15	-30.5	-30.0	-29.8	-29.7	-29.6	-29.6	-29.6	-29.6	-29.6	-29.6
20	-32.5	-32.1	-31.9	-31.8	-31.7	-31.7	-31.6	-31.6	-31.6	-31.6
25	-34.2	-33.7	-33.5	-33.3	-33.3	-33.2	-33.2	-33.2	-33.1	-33.1
30	-35.6	-35.1	-34.8	-34.6	-34.5	-34.5	-34.4	-34.4	-34.4	-34.4
35	-36.9	-36.3	-35.9	-35.7	-35.6	-35.6	-35.5	-35.5	-35.4	-35.4
40	-38.0	-37.3	-37.0	-36.7	-36.6	-36.5	-36.4	-36.4	-36.3	-36.3

Table 3. Diffracted level relative to free field, L_{D0} (dB), at half the screen height above the source.

	$x_r=10$	20	30	40	50	60	70	80	90	100
$H=5$	-6.0	-2.0	0.1	1.5	2.6	3.4	4.1	4.7	5.3	5.7
10	-7.3	-3.8	-1.6	-0.0	1.2	2.1	2.9	3.6	4.1	4.7
15	-6.6	-4.5	-2.6	-1.1	0.0	1.0	1.8	2.5	3.1	3.6
20	-5.7	-4.1	-2.7	-1.5	-0.4	0.4	1.2	1.8	2.4	2.9
25	-4.9	-3.4	-2.3	-1.3	-0.4	0.4	1.1	1.7	2.2	2.7
30	-4.3	-2.8	-1.7	-0.8	-0.0	0.7	1.3	1.9	2.4	2.8
35	-3.8	-2.3	-1.2	-0.3	0.4	1.1	1.6	2.2	2.7	3.1
40	-3.4	-1.9	-0.8	0.1	0.8	1.5	2.0	2.5	3.0	3.4

Table 4. Scattered level relative to the diffracted field, ΔL_{S0} (dB), at half the screen height above the source.

From the tabulated results it can be seen that the influence of the scattering grows when the distance from the screen to the receiver x_r is increased. When the screen height H is increased, it can be seen that the influence of the scattering first decreases and then increases, which is due to the weak scattering near 90° . Hence, when the screen height is large, the dominating scattering is at angles larger than 90° . When the screen height is further increased, also the influence of the scattering will increase. This dependence would be different for other spectral densities of the turbulence. For instance, a Gaussian spectral density would lead to a faster decrease of the scattered energy relative to free field when the height of a high screen is further increased.

As already discussed above, the transformation of the scattered level when changing the frequency is only valid within the inertial range of the turbulence spectrum. To get a rough estimate of when this transformation is valid one can use the Bragg condition (4) for the smallest scattering angle (i.e. at the screen edge) and thereby find a lower frequency limit. For example, if the receiver is half the screen height above the source (see Figure 4) and if $H = 10$ m and $x_r = 100$ m, the smallest scattering angle is about 17° . Inserting $\theta = 17^\circ$, $\kappa = 2\pi/L_0$, and $k = 2\pi f/c$ in the Bragg condition (4) leads to a lower frequency limit $f = c/(2L_0 \sin \frac{\theta}{2}) = 1050$ Hz, with $c = 340$ m/s. For even lower frequencies the scattering will be overestimated

using this prediction scheme. For many situations, however, the dominating scattering will be produced at higher frequencies, and the contribution at low frequencies can be omitted.

3.2 Influence on road traffic noise

The geometry in the example above, with $H = 10$ m, $x_s = 100$ m, $x_r = 40$ m, and with the receiver half the screen height above the source, can be seen as a model for a building along the road side (see Figure 4). The tabulated results, for this geometry and the frequency $f_0 = 2000$ Hz, are $L_{D0} = -26.6$ dB and $\Delta L_{S0} = 4.7$ dB. By applying the formulas (6-8) for transformation of the results to other frequencies, the influence on a traffic noise spectrum can be estimated for the geometry. For this example a reference traffic noise spectrum according to ISO 717-1:1986(E) is used (see Figure 5). The spectrum is for a car speed of 90 km/h and has been normalised to 0 dB(A). Not to overestimate the scattering at low frequencies, the scattered energy is assumed to be zero up to the third octave band 800 Hz.

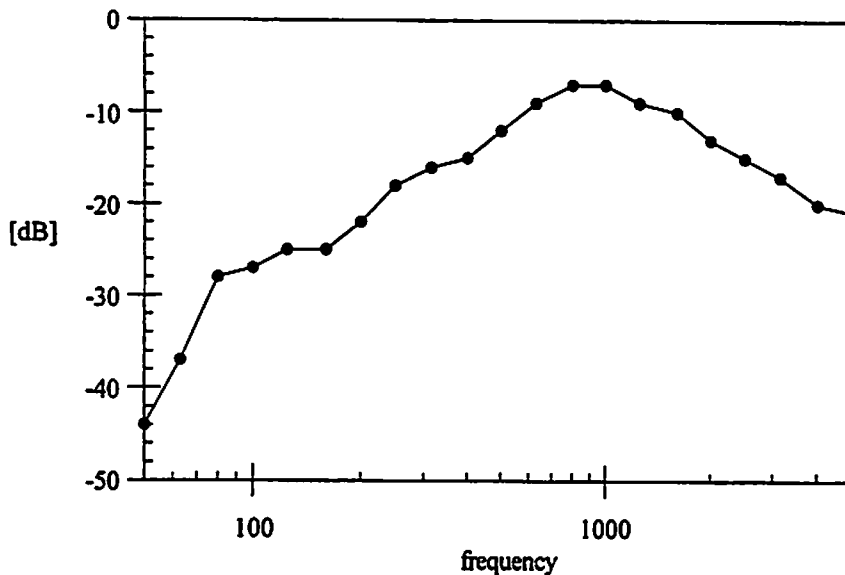


Figure 5. A-weighted reference traffic noise spectrum in third octave bands, normalised to 0 dB(A).

The resulting spectra for the diffraction L_D and for the total level, including the scattering by the turbulence, L_{D+S} are shown in Figure 6. The diffracted level is about -22 dB(A), and it can also be seen that the screen causes an increased influence of the low frequency components of the traffic noise. (It can be noted again that, for a hard ground surface directly beneath the receiver, the sound reduction by the barrier would decrease by 6 dB, i.e. from -22 dB(A) to -16 dB(A).) The difference between the total level L_{D+S} and the diffracted level L_D show, at the

The effects of temperature and wind velocity
stratification on sound scattering
cross-section in a turbulent atmosphere

V.E. Ostashev, G.H. Goedecke, and R.C. Wood

Department of Physics,

New Mexico State University, Las Cruces, NM 88003-8001

H. Auvermann

US Army Research Laboratory,

2800 Powder Mill Road, Adelphi MD 20783-1155

S.F. Clifford

NOAA/ERL/ETL,

325 Broadway, Boulder, Colorado 80303

Abstract

The equation for the sound scattering cross-section, σ , in a turbulent atmosphere is well known in the literature for the case when the mean temperature is constant and the mean wind velocity is zero. This equation is a theoretical basis for acoustic remote sensing of the atmosphere, and has other important applications, for example, in studying sound scattering into refractive shadow zones and in noise reduction by barriers. In this paper, the equation for σ is generalized for the case of sound scattering in a realistic stratified moving atmosphere with vertical profiles of temperature and wind velocity. It is shown that the differences in temperature and wind velocity between the height of the scattering and the source-receiver height can significantly affect σ for the scattering angles close to 90° and 180° . The derived equation for σ is compared with those obtained by Clifford and Brown [1] and by Ye [2] for a model of a stratified moving

atmosphere as two homogeneous layers in relative motion. It is also explained why the equation for σ derived by Clifford and Brown is different from that derived by Ye.

1 Introduction

The sound scattering cross-section per unit volume, σ , is one of the most important statistical characteristics of a sound wave scattered by atmospheric turbulence. Suppose that a sound wave propagating in the direction of the unit vector \mathbf{n}_0 is incident on a volume V containing random inhomogeneities (Fig. 1). Then σ is proportional to the mean intensity $\langle I_s \rangle$ of the wave scattered in the direction of the unit vector \mathbf{n}_s : $\sigma(\mathbf{n}_s - \mathbf{n}_0) = \langle I_s \rangle R^2 / (I_0 V)$. Here, I_0 is the intensity of the incident wave, and R is the distance from the scattering volume to the point of observation. The angle Θ between the vectors \mathbf{n}_s and \mathbf{n}_0 is called the scattering angle. The equation for σ is a theoretical basis for acoustic sounding of the atmosphere by sodars, and is also important for many other problems, e.g. sound scattering into a shadow zone.

An equation for σ was derived in 1961 by Monin [3] for the case of the Kolmogorov spectrum of temperature and wind velocity fluctuations:

$$\sigma(\Theta) = 4.08 \times 10^{-3} \frac{k_0^{1/3} \cos^2 \Theta}{(\sin(\Theta/2))^{11/3}} \left[\frac{C_T^2}{T_0^2} + \frac{22 \cos^2(\Theta/2) C_v^2}{3 c_0^2} \right]. \quad (1)$$

Here, k_0 is the sound wavenumber, C_T^2 and C_v^2 are the structure parameters of temperature and wind velocity fluctuations respectively, T_0 is the mean temperature, and c_0 is the mean value of the adiabatic sound speed. The cross-section σ can be represented as a sum of two terms, $\sigma(\Theta) = \sigma_T(\Theta) + \sigma_v(\Theta)$, where σ_T and σ_v are the contributions to σ due to sound scattering by temperature and wind velocity fluctuations, respectively. The temperature contribution to the sound scattering cross-section, $\sigma_T(\Theta)$, normalized to $1.45 \times 10^{-2} k_0^{1/3} C_T^2 / T_0^2$, and the wind velocity contribution, $\sigma_v(\Theta)$, normalized to $5.33 \times 10^{-2} k_0^{1/3} C_v^2 / c_0^2$, are plotted in Fig. 2 versus the scattering angle Θ . σ_T and σ_v have different dependences on Θ . In particular, for the important case of backscattering ($\Theta = 180^\circ$), $\sigma_v = 0$, while σ_T reaches a finite nonzero value, proportional to C_T^2 . From Eq. (1),

$$\sigma(180^\circ) = 4.08 \times 10^{-3} k_0^{1/3} C_T^2 / T_0^2. \quad (2)$$

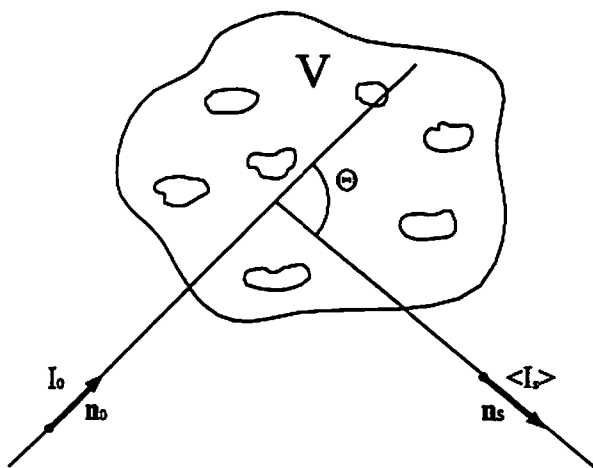


Figure 1: Sound scattering in a turbulent atmosphere. The unit vector \mathbf{n}_0 is in the direction of the wave incident on the scattering volume V , and \mathbf{n}_s is in the direction of the scattered wave.

This formula has been widely used for remote sensing of vertical profiles of $C_T^2(z)$ by sodars, where z is the height above the ground. Indeed, a monostatic sodar allows one to remotely measure the intensity of a sound impulse scattered at the height z , and hence the sound scattering cross-section σ at this height. Then, using Eq. (2), one can restore the dependence of C_T^2 on z .

The dependence of σ_T and σ_v on Θ in Monin's equation, and hence the considered technique for remote sensing of C_T^2 , are valid only if the mean value of wind velocity \mathbf{v} is zero, and the mean value of the adiabatic sound speed c is constant. However, this never happens in the real atmosphere. Therefore, it is an interesting and important problem to derive an equation for the sound scattering cross-section σ for the case when the wind velocity vector $\mathbf{v}(z)$ is not zero and depends on z , and when the sound speed $c(z)$ also depends on z .

This problem has been addressed in two papers; the first one was by Clifford and Brown [1], and the second by Ye [2]. Clifford and Brown's results have also been reproduced in many subsequent papers and reviews. Clifford and Brown [2] argued that it is very difficult to derive an equation for σ for the case of arbitrary profiles of $\mathbf{v}(z)$ and $c(z)$ in an atmosphere. Therefore, they assumed that $c = \text{const}$ and that the wind stratification can

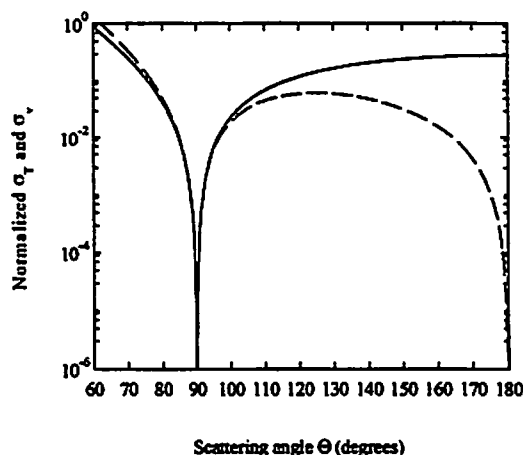


Figure 2: Temperature, σ_T , and wind velocity, σ_v , contributions to the sound scattering cross-section versus the scattering angle Θ . Dashed line corresponds to σ_v , solid line corresponds to σ_T .

be approximately replaced by two homogeneous layers. In the lower layer, v is zero, and in the upper layer v is constant and equal to the value of v near the scattering volume. They also gave qualitative arguments that σ , calculated for this model of an atmosphere as two homogeneous layers in relative motion, should probably be the same as for a realistic profile of $v(z)$ to the order v/c , which is always small in the atmosphere.

In a recent paper [2], Ye used an approach different from that of Clifford and Brown, and came up with an equation for σ for the same model of an atmosphere as two homogeneous layers in relative motion. Ye's equation is somewhat different from that found by Clifford and Brown, but in his paper, Ye did not explain this disagreement.

In this paper, we report on what we have done in the considered problem. First, we have derived an equation for σ for the model of an atmosphere as two homogeneous layers in relative motion by a rigorous approach. The equation obtained is different from both Clifford and Brown's equation and Ye's equation. Then we have explained why our results differ from both, and also why theirs disagree with each other. Finally, and maybe most importantly, we have derived an equation for σ for the case of arbitrary vertical profiles of $v(z)$ and $c(z)$. Here, it seems appropriate to present these results in reverse order.

2 A stratified moving atmosphere

Before deriving an equation for σ for arbitrary profiles of $c(z)$ and $\mathbf{v}(z)$, we shall review some results from acoustics in moving media, which can be found, for example, in the book *Acoustics in Moving Inhomogeneous Media* [4]. Let us consider a sound wave propagating in an atmosphere where the wind velocity vector is \mathbf{v} . The surface of constant phase (i.e., the wavefront) of this wave is denoted by $\Psi(\mathbf{R})$, $\mathbf{R} = (x, y, z)$ being the Cartesian coordinates. The unit vector normal to the wavefront is denoted by \mathbf{n} ; it coincides with the direction of the wave vector of this wave, $\mathbf{k} = n\mathbf{k}$. There are two velocities associated with the considered wave. The phase velocity \mathbf{u}_{ph} , which is the velocity of propagation of the wavefront, is given by $\mathbf{u}_{ph} = (c + \mathbf{n} \cdot \mathbf{v})\mathbf{n}$ and is in the same direction as the unit vector \mathbf{n} . The group velocity, $\mathbf{u}_{gr} = c\mathbf{n} + \mathbf{v} = s\mathbf{u}_{gr}$, is the velocity of acoustic energy propagation of this wave. If $\mathbf{v} \neq \mathbf{0}$, the group velocity differs from the phase velocity. In particular, the unit vector \mathbf{s} in the direction of the group velocity does not coincide with the unit vector \mathbf{n} normal to the wavefront. When calculating the trajectory of a sound wave, we should use the group velocity \mathbf{u}_{gr} and the unit vector \mathbf{s} , since \mathbf{s} is tangential to the trajectory, while the unit vector \mathbf{n} is not. Finally, consider this wave in the coordinate system comoving with the wind velocity \mathbf{v} . It can be shown that in the comoving coordinate system, the vectors \mathbf{k} and \mathbf{n} remain the same, while \mathbf{s} is changed. In other words, \mathbf{k} and \mathbf{n} are invariant under Galilean transformations, while \mathbf{s} is not.

Let us now calculate the sound scattering cross-section in a stratified moving atmosphere. A schematic diagram of the problem is shown in Fig. 3. The source S emits a sound wave which is scattered by random inhomogeneities in the scattering volume V . One of the scattered waves is received by the receiver R . The unit vectors \mathbf{s}_0 and \mathbf{s} are in the direction of propagation of the emitted wave near the source and the scattering volume. The unit vectors \mathbf{n}_0 and \mathbf{n} , normal to the wavefront of the emitted wave near the source and scattering volume, do not coincide with \mathbf{s}_0 and \mathbf{s} , if the wind velocity is not zero. Analogously, \mathbf{s}_s and $\mathbf{s}_{0,s}$ are the unit vectors in the direction of propagation of the scattered wave near the scattering volume and receiver, while \mathbf{n}_s and $\mathbf{n}_{0,s}$ are the unit vectors normal to the wavefront in these regions. Let D be a small region which includes the scattering volume and where the wind velocity \mathbf{v} and the sound speed c are almost constant. We will derive an expression for σ in the coordinate system moving with the same velocity \mathbf{v} as the wind velocity in this region D . In this comoving

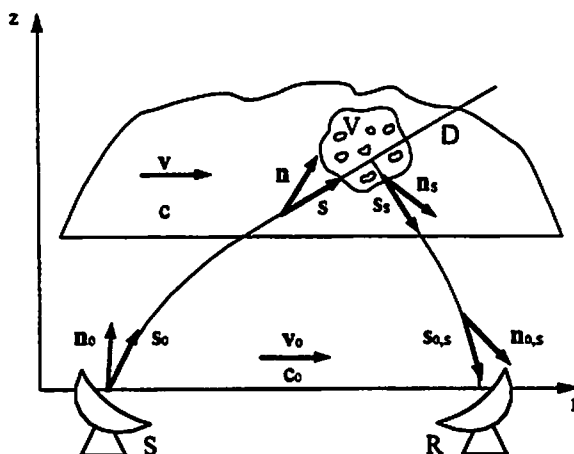


Figure 3: Sound scattering in a stratified moving atmosphere. S is the source, R is the receiver, and V is the scattering volume.

coordinate system, and in the region D , there is no wind, and the vectors \mathbf{n} and \mathbf{s} coincide, as do the vectors \mathbf{n}_s and \mathbf{s}_s , and the equation for the sound scattering cross-section σ coincides with that derived by Monin, as expressed in Eq. (1). Noting that $\cos \Theta = \mathbf{n} \cdot \mathbf{n}_s$, Eq. (1) can be expressed in the equivalent form

$$\sigma = 1.45 \times 10^{-2} \frac{k^{1/3} (\mathbf{n} \cdot \mathbf{n}_s)^2}{(1 - \mathbf{n} \cdot \mathbf{n}_s)^{11/6}} \left[\frac{C_T^2}{T_0^2} + \frac{11C_v^2 (1 + \mathbf{n} \cdot \mathbf{n}_s)}{3c_0^2} \right]. \quad (3)$$

Here, k is the wavenumber of the emitted wave in the region D . This equation is valid in the comoving coordinate system. It has the same form in the ground-fixed coordinate system because k , \mathbf{n} , and \mathbf{n}_s are invariant under the Galilean transformations. The next step in deriving the desired equation for σ is to express k and $\mathbf{n} \cdot \mathbf{n}_s$ in terms of the unit vectors \mathbf{n}_0 and $\mathbf{n}_{0,s}$. This can be done by using the refraction law for the normal to the wavefront in a stratified moving atmosphere (see Eq. (3.48) of reference [4]), which is valid in the geometric acoustic approximation. As a result,

$$k = k_0 \frac{c_0 + \mathbf{e}_0 \cdot \mathbf{v}_{0,\perp} \cos \theta}{c + \mathbf{e}_0 \cdot \mathbf{v}_\perp \cos \theta + v_z \sin \theta}. \quad (4)$$

Here, \mathbf{v}_\perp and v_z are the horizontal and vertical components, respectively, of the wind velocity vector \mathbf{v} in the region D ; θ is the grazing angle of the unit

vector \mathbf{n} , so that $\mathbf{n} = (\mathbf{e} \cos \theta, \sin \theta)$, where \mathbf{e} is the two-dimensional unit vector in the direction of the horizontal projection of \mathbf{n} . Quantities with the subscript 0 are evaluated at the source-receiver height. We also assume that $v_{0,z} = 0$. Furthermore, in Eq. (4)

$$\cos \theta = \frac{\cos \theta_0}{N} \frac{1 - M_{\perp} + NM_z \sqrt{(1 - M_{\perp})^2 - \cos^2 \theta_0 (N^{-2} - M_z^2)}}{(1 - M_{\perp})^2 + M_z^2 \cos^2 \theta_0}, \quad (5)$$

where $N = c_0/c$ is the refractive index in a motionless atmosphere, $M_{\perp} = \cos \theta_0 \mathbf{e}_0 \cdot (\mathbf{v}_{\perp} - \mathbf{v}_{0,\perp})/c_0$, and $M_z = v_z/c_0$.

The unit vector \mathbf{n}_s of the scattered wave can be expressed in the form $\mathbf{n}_s = (\mathbf{e}_s \cos \theta_s, \sin \theta_s)$, where θ_s is the grazing angle and \mathbf{e}_s is the unit vector in the horizontal direction. Then, $\mathbf{n} \cdot \mathbf{n}_s = \mathbf{e} \cdot \mathbf{e}_s \cos \theta \cos \theta_s - \sin \theta \sin \theta_s$. It follows from section 3.4.2 of reference [4], that $\mathbf{e} = \mathbf{e}_0$, and $\mathbf{e}_s = \mathbf{e}_{0,s}$. Therefore,

$$\mathbf{n} \cdot \mathbf{n}_s = \mathbf{e}_0 \cdot \mathbf{e}_{0,s} \cos \theta \cos \theta_s - \sin \theta \sin \theta_s. \quad (6)$$

The grazing angle θ_s of the scattered wave in the region D can be expressed in terms of the grazing angle $\theta_{0,s}$ at the receiver height by the formula similar to Eq. (5):

$$\cos \theta_s = \frac{\cos \theta_{0,s}}{N} \frac{1 - M_{\perp,s} - NM_z \sqrt{(1 - M_{\perp,s})^2 - \cos^2 \theta_{0,s} (N^{-2} - M_z^2)}}{(1 - M_{\perp,s})^2 + M_z^2 \cos^2 \theta_{0,s}}, \quad (7)$$

where $M_{\perp,s} = \cos \theta_{0,s} \mathbf{e}_{0,s} \cdot (\mathbf{v}_{\perp} - \mathbf{v}_{0,\perp})/c_0$.

Eqs. (4)-(7) express k and $\mathbf{n} \cdot \mathbf{n}_s$ in Eq. (3) in terms of the unit vectors $\mathbf{n}_0 = (\mathbf{e}_0 \cos \theta_0, \sin \theta_0)$ and $\mathbf{n}_{0,s} = (\mathbf{e}_{0,s} \cos \theta_{0,s}, \sin \theta_{0,s})$. The apparent scattering angle Θ_0 is the angle between directions of the emitted and received waves (i.e., the angle between the vectors \mathbf{s}_s and $\mathbf{s}_{0,s}$), which can be measured experimentally. Using the relationship between the vectors \mathbf{n} and \mathbf{s} (see Eq. (3.33) from reference [4]), one obtains

$$\cos \Theta_0 = \mathbf{s}_0 \cdot \mathbf{s}_{0,s} = \frac{\mathbf{n}_0 \cdot \mathbf{n}_{0,s} + (\mathbf{e}_0 \cos \theta_0 + \mathbf{e}_{0,s} \cos \theta_{0,s}) \cdot \mathbf{v}_{0,\perp}/c_0 + v_{0,\perp}^2/c_0^2}{[AB]^{1/2}} \quad (8)$$

where $\mathbf{n}_0 \cdot \mathbf{n}_{0,s} = \mathbf{e}_0 \cdot \mathbf{e}_{0,s} \cos \theta_0 \cos \theta_{0,s} - \sin \theta_0 \sin \theta_{0,s}$, $A = 1 + 2 \cos \theta_0 \mathbf{e}_0 \cdot \mathbf{v}_{0,\perp}/c_0 + v_{0,\perp}^2/c_0^2$, and $B = 1 + 2 \cos \theta_{0,s} \mathbf{e}_{0,s} \cdot \mathbf{v}_{0,\perp}/c_0 + v_{0,\perp}^2/c_0^2$.

The sound scattering cross-section $\sigma(\Theta_0)$ for arbitrary profiles of $c(z)$ and $\mathbf{v}(z)$ can then be calculated by using Eqs. (3)-(8). For given values of \mathbf{e}_0 , θ_0 ,

$e_{0,s}$, $\theta_{0,s}$, the values of Θ_0 , k , and $\mathbf{n} \cdot \mathbf{n}_s$, are calculated by using Eqs. (8), (4), and (5)-(7), respectively. Substitution of the obtained values of k and $\mathbf{n} \cdot \mathbf{n}_s$ into Eq. (3) yields the sound scattering cross-section. This approach allows one to calculate σ as a function of Θ_0 . It can be shown from Eqs. (3)-(8) that $\sigma(\Theta_0)$ depends on the values of the wind velocity and sound speed only at the height of the scattering volume (\mathbf{v} and c), and the source-receiver height (\mathbf{v}_0 and c_0), and does not depend on the vertical profiles of the wind velocity and sound speed between these heights. This is an important new result. The vertical profiles of the wind velocity $\mathbf{v}(z)$ and sound speed $c(z)$ affect the ray path of the emitted and scattered waves, and hence the position of the scattering volume. Finding this position is probably an involved problem, but we do not need to solve this problem when calculating σ . This result has probably not been understood previously.

3 Numerical results

Using Eqs. (3)-(8), let us study the dependence of the temperature and the wind velocity contributions to the sound scattering cross-section σ_T and σ_v on the scattering angle Θ_0 . For simplicity, we assume that $\mathbf{v}_{0,\perp} = 0$, $v_z = 0$, and that all vectors in Fig. 3 are located in a vertical plane. We use $c_0 = 340$ m/s. Fig. 4 shows a plot of $\sigma_T(\Theta_0)$, normalized to $1.45 \times 10^{-2} k_0^{1/3} C_T^2 / T_0^2$, for $\theta_0 = 25^\circ$, and $\mathbf{v}_\perp = 0$. A solid line corresponds to the case of $\Delta c = c - c_0 = 10$ m/s, and a dashed line corresponds to $\Delta c = 0$. Due to a difference of $\Delta c = 10$ m/s in sound speed between the height of the scattering volume and the source-receiver height, the position of the minimum of σ_T for $\Delta c = 0$ is shifted from 90° . Furthermore, the finite value of Δc does not affect the value of σ_T for backscattering, i.e., for $\Theta_0 = 180^\circ$.

Figure 5 shows a plot of $\sigma_v(\Theta_0)$, normalized to $5.33 \times 10^{-2} k_0^{1/3} C_v^2 / c_0^2$, for $\theta_0 = 25^\circ$, and $\mathbf{v}_\perp = 0$. Again, a solid line corresponds to the case of $\Delta c = 10$ m/s, and a dashed line corresponds to $\Delta c = 0$. As in Fig. 4, the finite value of Δc causes a shift in the position of the minimum for σ_v , but does not change σ_v for backscattering.

The effects of the wind velocity shift between the height of the scattering volume and the source-receiver height on $\sigma_T(\Theta_0)$ and $\sigma_v(\Theta_0)$ are shown in Figs. 6 and 7 for $\theta_0 = 25^\circ$ and $\Delta c = 0$. A solid line corresponds to $v_\perp = -18$ m/s, and a dashed line corresponds to $v_\perp = 0$. A difference in wind velocities between the height of the scattering volume and the source-receiver height

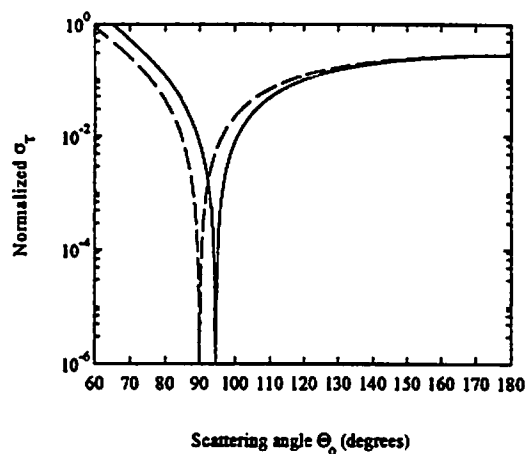


Figure 4: Temperature contribution σ_T to the sound scattering cross-section versus the scattering angle Θ_0 for $v_{\perp} = 0$ and $\theta_0 = 25^\circ$. Dashed line corresponds to the case $\Delta c = 0$, solid line corresponds to $\Delta c = 10$ m/s.

causes a shift in positions of the minima of σ_T and σ_v from 90° . Furthermore, σ_T is not affected by this difference for backscattering, while σ_v is affected significantly. The latter result is very important. According to this result, both temperature and wind velocity fluctuations contribute to the sound backscattering cross-section $\sigma(180^\circ) = \sigma_T(180^\circ) + \sigma_v(180^\circ)$, if there is a difference in wind velocities between the height of the scattering volume and the source-receiver height. In this case, measurements of $\sigma(180^\circ)$ by a monostatic sodar do not allow one to retrieve C_T^2 unambiguously, because Eq. (2) does not hold anymore. The contribution from C_v^2 may introduce significant errors in such a technique for remote sensing of C_T^2 , which are often revealed in practice, and can even make it impossible in some cases.

4 Two homogeneous layers in relative motion

We have shown that the sound scattering cross-section σ depends only on wind velocities and sound speeds at the height of the scattering volume and the source-receiver height. This suggests a conclusion that σ in a stratified moving atmosphere is equal to that for a model of an atmosphere as two homogeneous layers in relative motion with the corresponding difference in

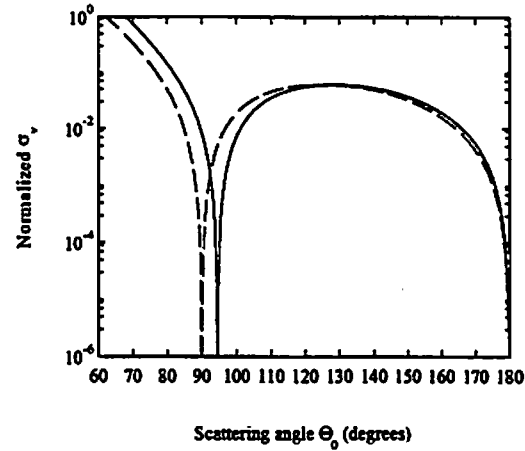


Figure 5: Wind velocity contribution σ_v to the sound scattering cross-section versus the sound scattering angle Θ_0 for $v_{\perp} = 0$ and $\theta_0 = 25^\circ$. Dashed line corresponds to the case $\Delta c = 0$, solid line corresponds to $\Delta c = 10$ m/s.

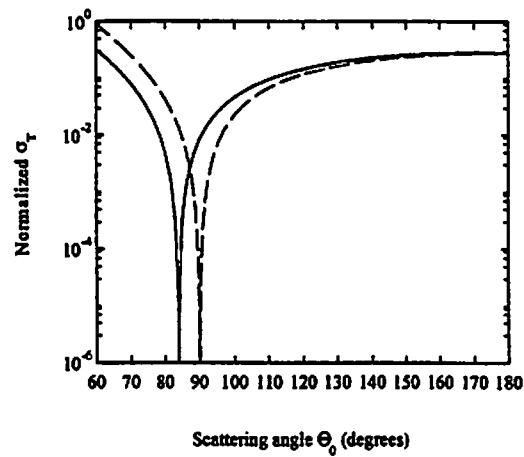


Figure 6: Temperature contribution σ_T to the sound scattering cross-section versus the scattering angle Θ_0 for $\Delta c = 0$ and $\theta_0 = 25^\circ$. Dashed line corresponds to the case $v_{\perp} = 0$, solid line corresponds to $v_{\perp} = -18$ m/s.

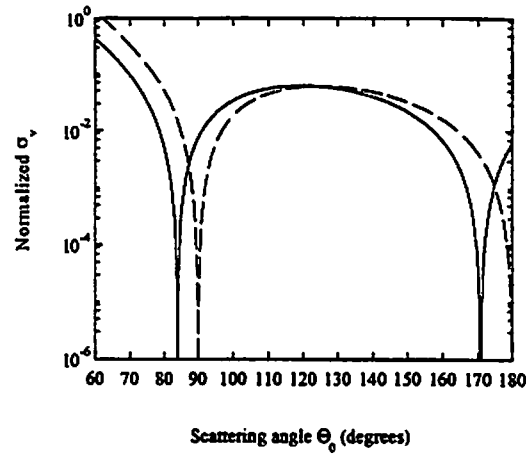


Figure 7: Wind velocity contribution σ_v to the sound scattering cross-section versus the scattering angle Θ_0 for $\Delta c = 0$ and $\theta_0 = 25^\circ$. Dashed line corresponds to the case $v_{\perp} = 0$, solid line corresponds to $v_{\perp} = -18$ m/s.

v and c between the layers. This conclusion is proved rigorously below for the particular case of $c = c_0 = \text{const}$, and $v_0 = 0$. Sound scattering in an atmosphere as two homogeneous layers in relative motion is schematically shown in Fig. 8.

The derivation of the equation for σ for the model in Fig. 8 is similar, but not identical, to that for the model of a stratified moving atmosphere. For the former model, we need to find a relationship between the vectors \mathbf{n} and \mathbf{n}_0 , and the vectors \mathbf{n}_s and $\mathbf{n}_{0,s}$ at the interface $z = z_0$ of two layers, which is at rest. To find this relationship, we equate sound pressure of the emitted wave at both sides of the interface, and equate sound pressure of the scattered wave at both sides of the interface. As a result, we get the refraction law for the normal to the wavefront at the interface:

$$\frac{c_0}{\cos \theta} + \mathbf{e} \cdot \mathbf{v}_{\perp} + v_z \tan \theta = \frac{c_0}{\cos \theta_0}, \quad \mathbf{e} = \mathbf{e}_0, \quad (9)$$

and

$$\frac{c_0}{\cos \theta_s} + \mathbf{e}_s \cdot \mathbf{v}_{\perp} - v_z \tan \theta_s = \frac{c_0}{\cos \theta_{0,s}}, \quad \mathbf{e}_s = \mathbf{e}_{0,s}. \quad (10)$$

Using Eqs. (3)-(10), it can be rigorously shown that σ for a stratified moving medium is given by the same equation as that for two homogeneous layers

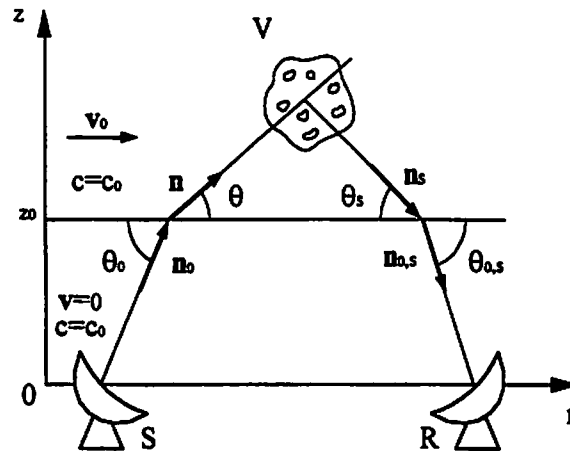


Figure 8: Sound scattering in an atmosphere as two homogeneous layers in relative motion. S is the source, R is the receiver, and V is the scattering volume.

in relative motion, if in these two models, the wind velocities at the height of the scattering volume are the same.

The derived equation for σ for two homogeneous layers in relative motion also allows us to understand equations for σ for the same model derived by Clifford and Brown [1], and by Ye [2]. We have shown that the equation for σ derived by Clifford and Brown is correct to order v/c to which all calculations were done by these authors. If $v_z = 0$, the equation for σ derived by Ye is correct to any order of v/c . However, if $v_z \neq 0$, Ye's equation is not correct if the interface is at rest, i.e., if it is at some fixed height z_0 . As has been shown above, the interface must be at rest if we want to obtain the same equation for σ for a stratified moving atmosphere and for two homogeneous layers in relative motion. In reference [2], it was assumed that frequencies of the emitted and scattered waves are changed at the interface. However, this is correct only if the interface is moving vertically with the velocity v_z and is not correct if it is at rest. (Note that there is no direct statement in reference [2] about whether the interface is at rest or is moving.)

5 Conclusions

We have derived the equation for the sound scattering cross-section σ in a stratified moving atmosphere with the vertical profiles $c(z)$ and $v(z)$. We have shown that σ depends only on the values of c and v at the height of the scattering volume and at the source-receiver height and does not depend on the behavior of $c(z)$ and $v(z)$ between these heights. The effects of c and v on σ have been studied graphically. We have shown that in the presence of a wind, the sound backscattering can be significantly affected by wind velocity fluctuations. This can significantly complicate remote sensing of C_T^2 using monostatic sodars. Finally, we have derived the equation for σ for the model of an atmosphere as two homogeneous layers in relative motion and explained why the predictions by Clifford and Brown [1] are different from those by Ye [2].

Acknowledgments:

This material is based upon work supported by the U.S. Army Research Office under contract numbers DAAH04-95-1-0593 and DAAG55-97-1-0178, and by the U.S. Army Research Laboratory.

References

- [1] S.F. Clifford and E.H. Brown, "Acoustic scattering from a moving turbulent medium," *J. Acoust. Soc. Am.* **55**, 929-933 (1974).
- [2] Z. Ye, "Sound scattering from a moving turbulent medium," *J. Acoust. Soc. Am.* **102**, 752-758 (1997).
- [3] A.S. Monin, "Characteristics of the scattering of sound," *Sov. Phys. Acoustics* **7**, No.4, 370-373 (1961).
- [4] V.E. Ostashev, *Acoustics in Moving Inhomogeneous media* (E & FN SPON, An Imprint of Thompson Professional, London, 1997).

Influence of the Doppler Effect on the Bandwidth of Acoustical Signals Scattered from Atmospheric Turbulence

by

Harry J. Auvermann
Information Science and Technology Directorate
U. S. Army Research Laboratory
Adelphi, Maryland 20783
Phone: 301/394-2088 FAX: 301/394-4797
e-mail: hauverma@arl.mil

and

George H. Goedecke
Department of Physics
New Mexico State University
Las Cruces, New Mexico 88003
Phone: 505/646-1926 FAX: 505/646-1934
e-mail: ggoedeck@nmsu.edu

Abstract

As was shown in a seventh symposium proceedings paper, acoustic scattering from a collection of turbules moving with the average wind could account for the amplitude variations observed in a shadow zone signal. That analysis assumed the frequency of the detected signal contribution from each turbule was a constant value, either the same as the source frequency or slightly deviated from it. The bandwidth so determined from relative changes of scattering geometry among the distribution of turbules was significantly smaller than had been measured. In this paper, the change in received frequency is accounted for as the scattering geometry varies with turbule position relative to source and detector locations. The results presented are obtained by calculation of time delays experienced as a signal travels from source to scatterer to detector in the moving medium. The Born approximation far field scattering amplitude for the turbule is evaluated for the scattering angle and frequency in existence when the signal reaches the scatterer location to relate the scattered signal magnitude to the incident signal magnitude. The bandwidth of the received signal varies with turbule size. The signal spectrum from several scatterers of mixed sizes is compared to that observed in a recent experiment.

1. Introduction

The conclusion of the paper published in the proceedings of the previous symposium [1] was that the bandwidth of a shadow zone signal modeled by scattering from turbules moving with the average wind but having no relative motion with respect to each other would not be wide enough to represent experimental findings. In the analysis of that paper, the signal received by the

detector was assumed to be the same form as that generated by the source. Only the magnitude change caused by the scattering process was accounted for. In this paper the effect of motion on the phase of the scattered signal is taken into account. The analysis presented below has been simplified from that necessary to account for ground reflections and wind speed gradients. Thus, the picture is that of a source and detector isolated from the ground maintained in unchanging relative positions, but at the same time subject to a uniform constant wind field. The scatterers making up the turbulence model are considered swept along by the wind field. In simplest terms, the characterization of the detector signal in terms of the source signal would be the same as if the scatterers were airborne objects like balloons rather than turbules. In our case here, rather than use the scattering amplitude for a balloon, that for a temperature turbule is used. The scattering properties of temperature turbules are somewhat less complex than those for velocity turbules, which were employed in the previous paper. In this picture, ground reflection effects and the direct signal will not be treated.

2. Doppler frequency shift in the experiment geometry

Proceeding from the picture depicted in the introduction, a coordinate system is imposed in the following fashion. Suppose a coordinate system is attached to the geometry of a real world experiment involving a wind induced shadow zone. In this precursor coordinate system, the wind velocity is directed generally towards the source from the detector, the source and detector positions are a few meters away from the x-axis and the source - detector separation is a few hundred meters. To simplify the mathematical description and minimize the number of geometric parameters, move the origin to the source, rotate the axes until the x-axis is parallel to the wind velocity vector, and then rotate the y - z axes about the x-axis until the detector is in the new x - z plane. In the new coordinate system, the path of a single scatterer is a line parallel to the x-axis with it's x coordinate the only one changing with time. The source coordinates are all zero, and the y-coordinate of the detector is zero. This coordinate system applicable to a constant and uniform wind field picture allows a general placement of the scatterer path identified by the y - z coordinates of the path intersection with the y - z plane.

At the beginning of our investigation it was not clear that such simplifications of the problem as described above would produce significant results. The first clue that a reasonably good approximation to the true answer could be obtained from a simple geometry resulted from calculation of the Doppler shift for an even simpler geometry, namely one wherein the scatterer path is in the x - z plane. A plot of the frequency shift generated by a scatterer located in the x - z plane is presented in figure 1 for typical experimental conditions. Data for this graph was calculated from the relation [2] given in equation (1) . In the equation, ε is the ratio of the

$$\varepsilon = \bar{\beta} \cdot (\hat{k} - \hat{r}) \quad (1)$$

Doppler shift frequency to the wave frequency, $\bar{\beta}$ is the wind velocity vector divided by the acoustic wave speed, \hat{k} is the unit vector in the direction of the incident wave, and \hat{r} is the unit vector in the direction of the scattered wave to the point of interest, typically the detector location. The large center dot (\cdot) indicates the vector inner product. In the figure, the detector

location vector is $\vec{d} = 325 \hat{x} - 10 \hat{z}$ and $\vec{u} = -0.01 \hat{x}$. In figure 1, the quantity 500ϵ is plotted as a function of the x-position for a for three different z positions. The scale is set to show the asymptotic tendency of the shift frequency. Thus, on the down-wind side of the detector, the frequency shift approaches +10 hertz, while on the up-wind side of the source, the frequency shift approaches -10 hertz. The z axis scale is expanded in figure 2 to show more

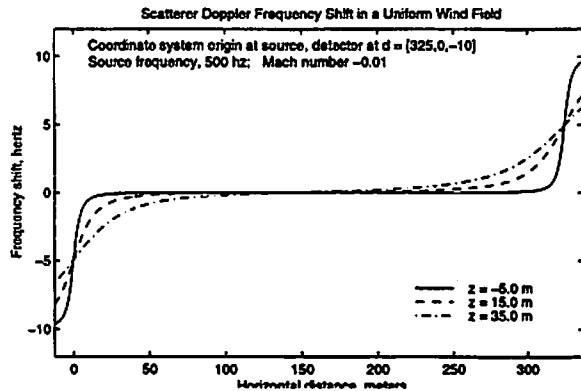


Figure 1. Doppler frequency shift

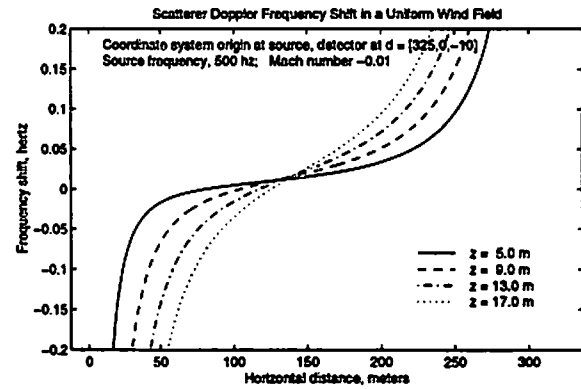


Figure 2. Expanded scale Doppler frequency shift

clearly the nature of the frequency shift variation in the region between source and detector. The frequency shift for a scatterer whose elevation is between 13 and 17 meters is observed to be 0.1 hz at about 220 m and -0.1 hz at about 70 m. The conclusion is the frequency shift resulting from the Doppler effect is sufficiently large to approximate bandwidth measurements encountered in shadow zone turbulence scattering experiments.

3. Geometry for the shadow zone signal calculation

Returning to the geometry described in the first paragraph of Section 2, a general identification of the numerous vectors involved is presented in figure 3. In this figure, vectors for three time instants are defined. The first instant labeled t_s is the time an arbitrary impulse is imparted to the medium by the source. The thinking here is that although the source supplies energy to the medium in a continuous fashion with respect to time, we are isolating for consideration a vanishingly short portion of the signal. The second time instant labeled t_p is the instant at which the signal impulse reaches the scatterer. The third time instant labeled t_d is the time at which the signal impulse manufactured by the scatterer at time t_p reaches the detector. In the calculation, t_d will be considered the independent variable which means that a progression of detector times will be selected for which the signal characteristics at the source will be determined. These source signal characteristics after propagation will constitute the detector signal and will be determined based upon what happened at the source at t_s and at the scatterer at t_p . The scatterer position vector is presumed known by the expression in equation (2). In equation (2), $\vec{p}(t)$ is the

$$\vec{p}(t) = \vec{p}_0 + \vec{v} t \quad (2)$$

position vector at time t , \bar{p}_0 is the position vector at time zero, and \bar{v} is the velocity vector. The vectors necessary or auxiliary to the calculation are defined mathematically in equation (3).

$$\begin{aligned}
 \bar{v} &= v_x \hat{x} = c \mu \hat{x}; & m &= \sqrt{\mu^2} \\
 \bar{p}_0 &= p_x \hat{x} + p_y \hat{y} + p_z \hat{z}; & \bar{d} &= d_x \hat{x} + d_z \hat{z} \\
 \bar{p}_d &= \bar{p}(t_d); & \bar{p}_p &= \bar{p}(t_p); & \bar{p}_s &= \bar{p}(t_s) \\
 \bar{r}_{d0} &= -p_y \hat{y} - (p_z - d_z) \hat{z}; & \bar{r}_{s0} &= p_y \hat{y} + p_z \hat{z} \\
 \bar{r}_{d1} &= \bar{d} - \bar{p}_d; & \bar{r}_{d2} &= \bar{d} - \bar{p}_p \\
 \bar{r}_{s1} &= \bar{p}_s; & \bar{r}_{s2} &= \bar{p}_p
 \end{aligned}
 \tag{3}$$

These relations are given to show the sign convention of the vector components. The quantities and locations labeled in figure (3) are described in the following sentences. S is the scatterer

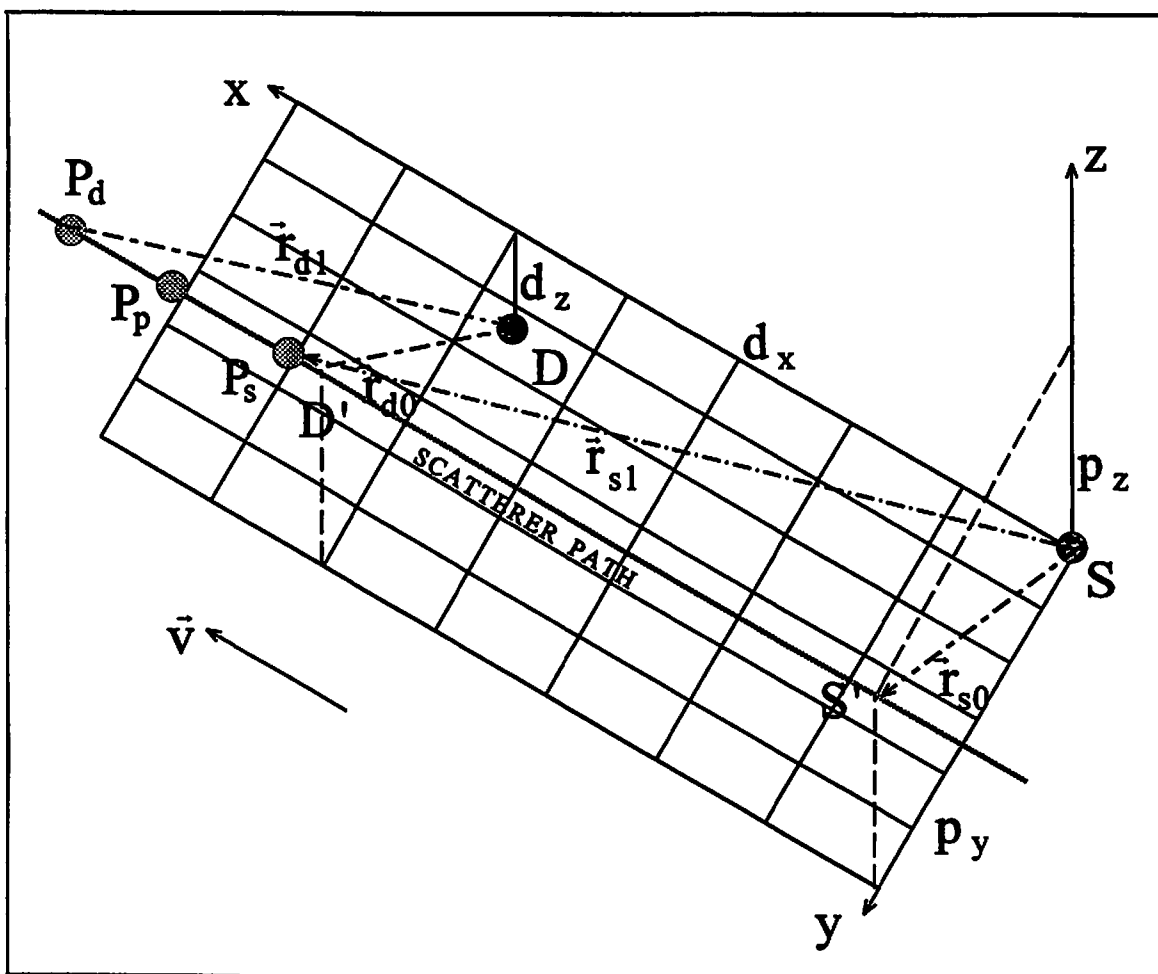


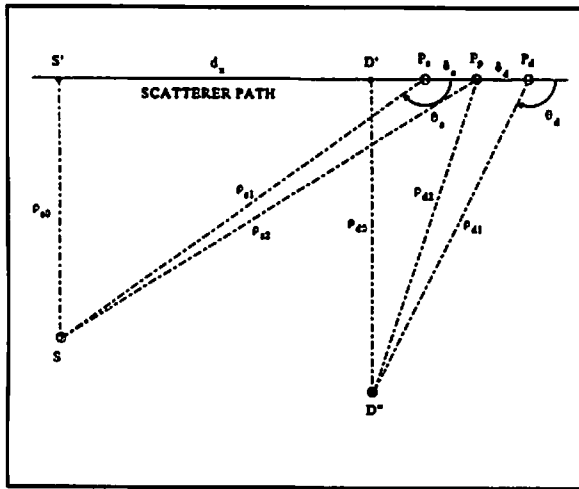
Figure 3. Calculation geometry and coordinate system.

location; D is the detector location, P_s is the scatterer location at time t_s, P_p is the scatterer location at time t_p, and P_d is the location of the scatterer at time t_d. The perpendicular vector from the scatterer path (at D') to the detector is \vec{r}_{d0} whereas the perpendicular vector from the source to the scatterer path (at S') is \vec{r}_{s0} . The \vec{r}_{d1} vector is from P_d to the detector. The \vec{r}_{s1} vector is from the source to P_s. The \vec{r}_{d2} vector is from P_p to the detector. The \vec{r}_{s2} vector is from the source to P_p. The latter two vectors are not shown on the figure. The vector \vec{v} is shown directed as if all it's components are positive. The quantity μ might be termed a signed Mach number. The quantity m is the magnitude of μ .

The relations in equation (3), being vector relations, are general and will give correct answers regardless of the value of the time at which equation (3) is evaluated or the orientation of \vec{v} . The answers are thus correct in the different regimes associated with the scatterer motion. The different regimes are ten in number: 1) all scatterer locations beyond D', 2) . . . , 5) P_s and P_p are between S' and D' with P_d beyond D', 6) . . . , and, 10) P_s and P_p short of S' with P_d between S' and D'. In the following, attention must be paid to the concerns connected with translation of vector length calculations back into the appropriate vector expressions.

In figure 3 observe that in general the vectors (\vec{r}_{d0} , \vec{r}_{d1} , \vec{r}_{d2}) are in a single plane and the vectors (\vec{r}_{s0} , \vec{r}_{s1} , \vec{r}_{s2}) are in another plane. The common feature of these two planes is the scatterer path.

Since the entire problem before us is resolved if the times (t_p, t_s) are calculated knowing t_d, and since time is a scalar quantity, it is appropriate to make the calculations using scalar relations. To accommodate this idea, the various r-vectors are represented by ρ symbols with the same subscripts where the various ρ's are the vector magnitudes. Accordingly, the detector vector plane may be revolved around the scatterer path into the source vector plane and be represented as shown in figure 4. The symbols in figure 4 that have not been defined before are: D' is the



location of the detector after rotation of the detector vector plane; δ_s is the distance from P_s to P_p; δ_d is the distance from P_p to P_d; θ_s is the angle between the more positive end of the scatterer path and the ray path ρ_{s1} at P_s; and, θ_d is the angle between the more positive end of the scatterer path and the ray path ρ_{d1} . This picture and these definitions make the physics of the problem easier to describe. After the impulse is transferred to the medium by the source, everything happens in the moving medium. The impulse travels along the ray ρ_{s1} which appears to be attached to the scatterer. It arrives at the time t_p when the scatterer is at P_p. The scatterer

Figure 4. Geometry of scalar quantities

emits a spherical wave front. Since this spherical wave front is also traveling along in the moving medium, the ray which intersects the detector location at t_d is ρ_{d1} . The scatterer moves the distance δ_s in the time taken by the impulse to travel from the source to the scatterer. Likewise,

the scatterer moves the distance δ_d in the time taken by the impulse to travel from the scatterer to the detector. Equation (5) expresses these relationships. In equation (6), the x position of the

$$\delta_s = \mu \rho_{s1}; \quad \delta_d = \mu \rho_{d1} \quad (5)$$

scatterer x_p is determined in two ways, from source related quantities and from detector related

$$\begin{aligned} -\rho_{s1} \cos(\theta_s) &= x_p - \mu \rho_{s1} \\ -\rho_{d1} \cos(\theta_d) &= x_p - d_x - \mu \rho_{d1} \end{aligned} \quad (6)$$

quantities. By identifying the symbols S_{gns} and S_{gnd} as the sign of the respective cosine functions above, the relations of equation (6) may be represented as in equation (7). Subtracting the two relations in equation (7), an expression is obtained relating ρ_{s1} to ρ_{d1} and constant

$$\begin{aligned} -S_{gns} (\rho_{s1}^2 - \rho_{s0}^2)^{1/2} &= x_p - \mu \rho_{s1} \\ -S_{gnd} (\rho_{d1}^2 - \rho_{d0}^2)^{1/2} &= x_p - d_x - \mu \rho_{d1} \end{aligned} \quad (7)$$

geometric quantities. Two suitable squaring operations will produce a quartic relation between these two variables which may be useful in an analytical investigation. For a numerical investigation, the situation is much simpler. The relations for the calculation of the time t_p are in equation (8) where x_d is the x position of the scatterer at time t_d . Squaring the first

$$\begin{aligned} \rho_{d1} &= [(d_x - x_d)^2 + p_y^2 + (d_z - p_z)^2]^{1/2} \\ t_p &= t_d - \rho_{d1} / c; \quad \bar{r}_{s2} = \bar{p}(t_p) \\ x_p &= \hat{x} \cdot \bar{r}_{s2} \end{aligned} \quad (8)$$

expression in equation (7) and solving for ρ_{s1} results in equation (9). In equation (9), the radical

$$\rho_{s1} = \left(\frac{1}{1 - \mu^2} \right) \left[\pm \sqrt{\rho_{s2}^2 - \mu^2 \rho_{s0}^2} - \mu x_p \right] \quad (9)$$

term is dominant with both x_p and μ sign sensitive. For ρ_{s1} to be positive, the sign of the radical must be positive. Finally, calculate t_s and determine \bar{r}_{s1} as in equation (10). In the

$$\begin{aligned} t_s &= t_p - \rho_{s1} / c; \quad \bar{r}_{s1} = \bar{p}(t_s) \\ \hat{k} &= \bar{r}_{s1} / \rho_{s1}; \quad \hat{r} = \bar{r}_{d1} / \rho_{d1} \end{aligned} \quad (10)$$

equation, and in accord with usual scattering practice, the incident wave direction and the scattered wave direction have been defined by the unit vectors \hat{k} and \hat{r} respectively.

4. Born approximation scattering for a plane wave

Scattering theory for plane waves begins with the inhomogeneous wave equation given in generic form in equation (11) for the pressure variation $\eta(\vec{r}) e^{-i\omega t}$ ($k = \omega/c = 2\pi f_0$).

$$(\nabla^2 + k^2)\eta(\vec{r}) = -4\pi S(\vec{r}) \eta(\vec{r}) \quad (11)$$

The function $S(\vec{r})$ is a localized stationary operator that depends in general on the temperature and/or velocity variations in the medium. Given an incident plane wave $\eta_{in}(\vec{r}) = e^{i\vec{k}\cdot\vec{r}}$, the implicit solution to equation (11) is shown in equation (12). In equation (12), $\eta_s(\vec{r})$ is the

$$\begin{aligned} \eta(\vec{r}) &= \eta_{in}(\vec{r}) + \eta_s(\vec{r}) \\ \eta_s(\vec{r}) &= \int d^3r_1 e^{i\vec{k}\cdot\vec{r}_1} S(\vec{r}_1) \eta(\vec{r}_1) / r_{12} \end{aligned} \quad (12)$$

scattered field, and $r_{12} = |\vec{r} - \vec{r}_1|$ is the distance from a point local to the media variation to the observation point \vec{r} . The integration symbol above indicates a volume integral over all space. In the far field, the scattered wave has the form shown in equation (13). In this

$$\eta_s(\vec{r}) = e^{i\vec{k}\cdot\vec{r}} f(\hat{r}) / r \quad (13)$$

expression, $f(\hat{r})$ is known as the scattering amplitude and has the dimensions of length. The specific form of the integral for the scattering amplitude is shown in equation (14). The

$$f(\hat{r}) = \int_{V_s} d^3r_1 e^{-i\vec{k}\cdot\vec{r}_1} S(\vec{r}_1) \eta(\vec{r}_1) \quad (14)$$

integration need only be over the scattering volume V_s associated with the detector located in the direction \hat{r} and assumed to be in the far field. In the First Born Approximation, the incident field is substituted for the field interior to the scattering volume. This substitution is reflected in equation (15). The new scattering volume V_s is determined by the intersection of the volume

$$f(\hat{r}) = \int_{V_s} d^3r_1 e^{-i\vec{k}\cdot\vec{r}_1} S(\vec{r}_1) e^{i\vec{k}\cdot\vec{r}_1} \quad (15)$$

illuminated by the source and the volume observed by the detector. Since the object in this paper is to treat turbulence as a superposition of turbules the scattering amplitude for a single turbule is the goal of this derivation. The scattering volume need only be over the space for which $S(\vec{r}_1)$ is essentially different from zero. With these assumptions in mind and specializing to temperature turbules, the expression in equation (16) results after an integration by parts and supposing the

$$f_T(\hat{r}) = (k^2 / 4\pi T_\infty) \hat{k} \cdot \hat{r} \int_{V_s} d^3r_1 \Delta T_0(\vec{r}_1) e^{-i\vec{K}\cdot\vec{r}_1}; \quad \vec{K} = k(\hat{r} - \hat{k}) \quad (16)$$

accompanying surface integrals to be zero. The construct $\Delta T_0(\vec{r}_1) / T_\infty$ is the relative temperature field with T_∞ the asymptotic constant temperature far from the turbule. This relation has been given previously [3] where the integral is a Fourier transform for the variable \vec{K} which is denoted by the symbol $\Delta \vec{T}_0(\vec{K})$. The dot product before the integral sign in the notation of this paper is $\cos(\psi)$ where ψ is the scattering angle.

In connection with the above development, notice that the time dependence has been suppressed but that it can be reintroduced by simply multiplying by it. Therefore, the theory presented in this section, applicable to propagation and scattering in a medium with time invariant conditions, shows that the source signal time history is reproduced exactly if the source is sinusoidal. Since the approximations are first order, superposition holds which means that a source signal with a finite range of frequency components would be accurately reproduced by the scattering process. The conclusion is that our method of inferring the source state that caused a particular detector state outlined in Section 3 is accurate to within the assumptions of far field First Born Approximation scattering theory for an invariant medium. Application of this theory to the case of a moving medium is the subject of the next section.

5. Application of scattering theory

The intent in this section is to present the specific form of the detected signal for a temperature turbule with a Gaussian envelop function $\vec{B}_T(y)$. From equations (19), (22) and (34) of the reference [3], the definitions in equation (17) are extracted. In equation (17), δT is a

$$\begin{aligned} \vec{T}(\vec{K} a) &= \pi^{3/2} (\delta T) \vec{B}_T(K a) \\ \vec{B}_T(y) &= e^{-y^2/4} \end{aligned} \quad (17)$$

temperature variation amplitude and a is the characteristic size of the turbule. The form of the corresponding scattering amplitude is shown in equation (18). The detector signal is assumed to

$$\begin{aligned} f_T(\hat{r}) &= \pi^{3/2} k^2 a^3 (\delta T / 4 \pi T_\infty) \cos(\psi) e^{-\vec{K}^2 a^2/4} \\ \vec{K}^2 &= k^2 (\hat{r} - \hat{k}) \cdot (\hat{r} - \hat{k}) = 2k^2(1 - \cos(\psi)) \end{aligned} \quad (18)$$

be proportional to the sound pressure amplitude P_d at the detector location. This quantity is related to the reference sound pressure amplitude P_R at a distance R from the source in general by the expression in equation (19) where r_s is the source - scatterer distance and r_d is the

$$P_d = P_R f(\hat{r}) \left(\frac{R}{r_s r_d} \right) \quad (19)$$

scatterer - detector distance. The assumption is made in equation (19) that the incident wave at the scatterer is a plane wave whose exitance (watts/meter²) is that of a spherical wave originating

at the source location. It is now possible to write down the detector signal amplitude $s_d(t_d)$ which is done in equation (20). The last ingredient is the form of the source signal $s_s(t_s)$.

$$s_d(t_d) = \pi^{3/2} k^2 a^3 \left(\frac{\delta T}{4 \pi T_\infty} \right) \left(\frac{\cos(\psi)}{\rho_{s1} \rho_{d1}} \right) \exp(-(k a)^2 (1 - \cos(\psi)/2)) s_s(t_s) \quad (20)$$

This is given in equation (21). The factor S_s is a constant related to $P_R R$ in equation (19). The

$$\begin{aligned} s_s(t) &= S_s \sin(2 \pi f_0 t) \\ k &= k(t_p); \quad \cos(\psi) = \cos(\psi(t_p)) \end{aligned} \quad (21)$$

symbol f_0 is the constant frequency of the source. Implied in the formulation of equation (21) is that the source is an isotropic radiator. Also indicated in equation (21) are the evaluation times for the symbols (k, ψ) . The assumption is made here that these two quantities should be evaluated at the scatterer location. The symbol k involves the frequency and a geometric argument easily gives the ratio of the frequency at the scatterer f_p to the source frequency as shown in equation (22). The cosine factor may be determined from the dot product of two unit

$$\begin{aligned} f_p / f_0 &= 1 - \vec{\beta} \cdot \hat{k} = 1 - \vec{\beta} \cdot \hat{r}_{s1} \\ k(t_p) &= k_0 (1 - \vec{\beta} \cdot \hat{r}_{s1}); \quad k_0 = 2 \pi f_0 / c \end{aligned} \quad (22)$$

vectors as shown in equation (23). A partially expanded version of the signal equation is shown

$$\cos(\psi(t_p)) = \hat{r}_{s1} \cdot \hat{r}_{d1} = \vec{r}_{s1} \cdot \vec{r}_{d1} / (\rho_{s1} \rho_{d1}) \quad (23)$$

in equation (24). Equation (24) is the basis for the calculations and results reported in this paper.

$$\begin{aligned} s_d(t_d) &= C (1 - \vec{\beta} \cdot \hat{r}_{s1})^2 \left(\frac{\vec{r}_{s1} \cdot \vec{r}_{d1}}{(\rho_{s1} \rho_{d1})^2} \right) \sin(k_0 c t_s) \\ &\quad \exp \left\{ -(\chi_0^2 / 2) (1 - \vec{\beta} \cdot \hat{r}_{s1})^2 \left[1 - \left(\frac{\vec{r}_{s1} \cdot \vec{r}_{d1}}{\rho_{s1} \rho_{d1}} \right) \right] \right\} \\ C &= \pi^{3/2} \chi_0^2 a \left(\frac{\delta T}{4 \pi T_\infty} \right) S_s \\ \chi_0 &= k_0 a \end{aligned} \quad (24)$$

The next section details how the calculations were carried out.

6. Model computational strategy

The experiment from which the data of interest comes is similar to one that has been described elsewhere [4]. The detector disposition and the data processing in the reference were the same as

that for later experiments in 1996. The available data was taken between 17 September and 29 October. The source in these experiments was a 24" horn placed adjacent to detector 14 at the 325 meter mark. It was at the top of the 10 meter tower used for four temperature sensors. The tower was 10 meters to the side of the detector 14 on the north side of the runway. The source was excited by six tones combined on a tape that was played into the amplifier driving the horn. The data set of direct interest is the one identified with the number GA3006. This data was recorded between 2:27:00 and 2:41:60 P.M (for a total of 900 seconds) on 29 October. Of the six tones used at this time the one at 500 hz is of immediate concern. Temperature, wind velocity, and wind direction data was also recorded. A tripod mounting a cup anemometer and a wind direction sensor was located at about 590 meters from detector 0 slightly to the north of the runway center line. The source was directed towards detector 9 at the 200 meter mark and was pointed down at an angle estimated here to be 12.5 degrees. Primarily, the data from detector 26 at the 650 meter location will be that addressed. The prior analysis that was performed on the original data resulting in the present data set is described in the Journal article [4]. In brief, the process was as follows using procedures written for use in MATLAB [5]. The original data, which was sampled at 8000 hz consisted of 7,200,000 points. This data set was then addressed in 4096 point increments. A Fourier Transform (FT) was applied to each increment. This spectrum was then frequency shifted approximately 400 hz lower and filtered. The exact frequency shift was such that a 500 hz component would appear at 101.5625 hz. An Inverse Fourier Transform (IFT) was performed and the resulting increment was decimated 20:1. Data from all increments were assembled in a new data file for each frequency at each detector site; thus each data set contains 360,000 data points with the interesting signal at approximately 100 hz with sampling at 400 hz.

The model computational strategy mimicked the above data reduction scheme for the most part. The source frequency was set to be $f_0 = 500$ hz and t_d was incremented at 1/8000 second intervals starting at zero for successive slices containing 4096 points. The detected signal at each time in the slice was computed using equation (23). In the only change from the data reduction scheme, the resulting time series were accumulated for ten slices (a group) before frequency shifting and decimation was applied. No filtering was applied because we are dealing here with a noiseless theoretical data set. The number of ten-slice groups calculated was 20 covering 102.4 seconds. It was found for all three turbule sizes that this time period was sufficiently long to allow the turbule to travel completely through the scattering volume. The calculated data sets were padded with zeros so that the resulting real number data array contained 360,000 elements.

7. Presentation of results

Additional information concerning the experimental measurements identified by the designation GA3006 are relevant to the results to be presented. The orientation of the detector array was 315 degrees magnetic north. The average wind direction during the data taking period was 307 degrees. Cup anemometer data taken at a height of two meters indicate an average wind velocity of 2.662 meters/second. The average temperature at a height of 0.49 meters was 10.204 Celsius. The average temperature at a height of 1.12 meters was 9.8327 Celsius. Using a grass height of 0.05 meter, the computed wind speed and sound speed profiles are shown in fig. 5. These profiles are for components along the detector array axis. They show that the wind and sound

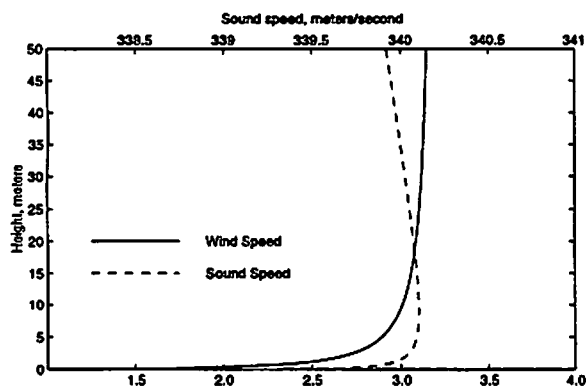


Figure 5. Wind and sound speed profiles

speed profiles have the majority of their variation below 10 meters. Our assumption of uniform wind and sound speed should give a good approximation to the true state of affairs. There will be some ray bending that will not be accounted for. Curve data for a height of 25.0848 meters shows the wind speed to be 3.1052 meters/second and the sound speed to be 340.0489 meters/second. These are the values to be used in the model. Translating to the model coordinate system, the chosen starting parameters for the calculation are recorded in equation (25).

The position of the turbule path was chosen somewhat arbitrarily. The main consideration was to have the turbule initially outside of the

$$\begin{aligned}
 p_x &= 350; & p_y &= 10.0; & p_z &= 15.0948 \\
 d_x &= 325; & d_z &= -10.0 \\
 \bar{v} &= -3.1052 \hat{x}; & c &= 340.0489; & \mu &= -0.091 \\
 f_0 &= 500; & \lambda_0 &= 0.6801 \\
 \chi_m &= 2\pi a_m / \lambda_0 = 16.667; & a_m &= 1.804
 \end{aligned} \tag{25}$$

scattering volume. The nominal wavelength λ_0 is specified above and is the wavelength of a 500 hz wave in the moving medium. The largest turbule size a_m was somewhat arbitrarily chosen on the basis of previous work [1]. The time history of the signal amplitude as this turbule passed through the scattering volume is shown in fig. 6 for 102.4 seconds of the model calculation.

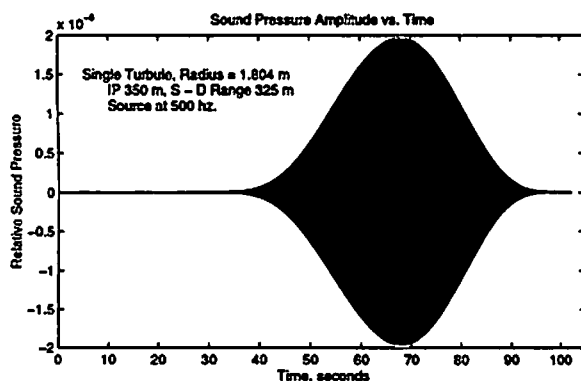


Figure 6. Single turbule scattered signal time history

Another turbule of the same size on the same scatterer axis path will produce a scattered signal similar to the one shown. The only difference will be that it will be displaced in time. The difference in the calculation algorithm will be that p_x will change. In the FT regime for a 900 second data interval, the harmonics are spaced 1/900 hz apart. To delay the first harmonic a time Δt seconds would require a phase delay of $2\pi \Delta t / 900$ radians. To delay the second harmonic this same time interval would require a phase delay of $4\pi \Delta t / 900$ radians. The phase delay for harmonic n would be $2\pi n \Delta t / 900$ radians. To delay the entire

turbule, then, requires only that each spectra component n be multiplied by the factor $\exp(-2\pi n i \Delta t / 900)$. The corresponding displacement of the starting position would be $\Delta p_x = -v_x \Delta t$. This scheme was used to generate the signal for four additional identical turbules; the signal magnitude result for all five turbules is

shown in fig. 7. The spectra for the single turbule and for the multi-turbule signals are shown in fig. 8. In fig. 9, the spectrum for a single turbule is superimposed upon the measured spectrum. In the latter, the amplitude of the model spectrum has been multiplied by 1,500,000 to more clearly show the resemblance. In addition, the spectra from single turbules whose sizes were 1.4937 m and 1.2368 m are included in fig. 9 to show the variation of the bandwidth with turbule size. The three half amplitude bandwidths were approximately 0.084, 0.108, and 0.127 hz in descending order of turbule radius.

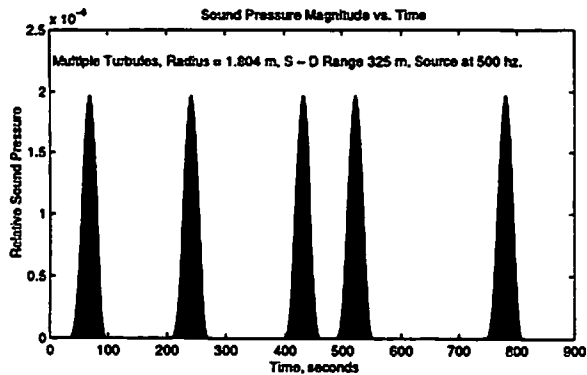


Figure 7. Multi-turbule scattered signal time history

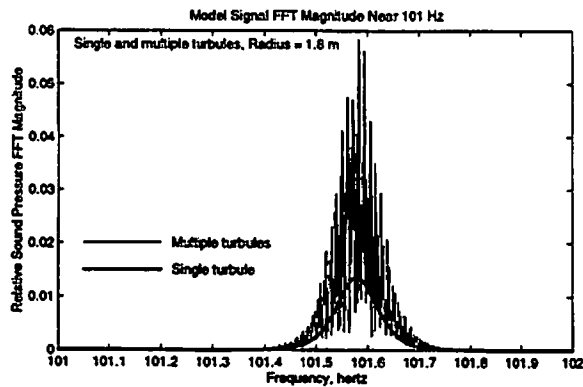


Figure 8. Model spectra for a single turbule and five turbules

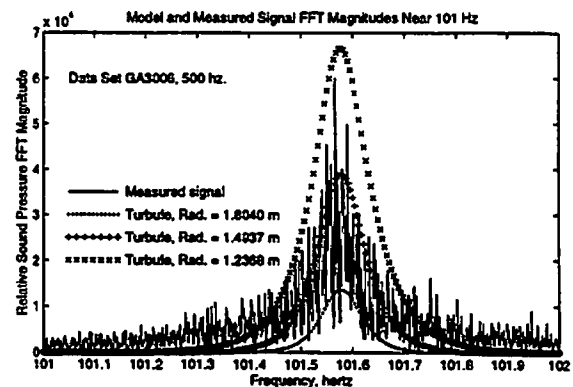


Figure 9. Model single turbule spectrum and measured spectrum

2. Summary of results and conclusions

Subject to the assumptions made in the development of the theory presented in section 3, the close agreement between the measured and model bandwidth exhibited in fig. 9 suggests that the difference in Doppler frequency shift with scatterer position is the primary cause of, or a major contributor to, the bandwidth of wind induced shadow zone signals. An interesting facet of our results is the universal nature of the frequency shift function. Universal as used here refers to the fact that any scatterer of any type or size will produce the same phase shift function, the integral of the frequency shift function, as it moves along a given path provided the Frozen Turbulence Hypothesis holds to a reasonably good approximation. A second facet of this work that is of significance is the realization that turbules of the same size class manifest themselves in the frequency domain as components of the signal differing by a known phase function. The spectrum of the signal has a noise like appearance when many turbules are hidden in it. Obviously, these many can be resolved by a simple Inverse Fourier Transform operation in theory using our noiseless model. How many turbules can be resolved in actual experimental

data with a non-zero signal to noise ratio? A curious feature of the signal is that, in the case of the data set examined in this paper, just a few components (two or three hundred) in the frequency domain carry all the turbulence distribution information contained in 360,000 data points in the time domain. The many turbule spectrum of figure 8 and the measured spectrum of figure 9 were not smoothed so that their resemblance (subjective appraisal) can be appreciated.

It is important here to comment on the results presented in another paper in the proceedings of the last symposium [7]. These authors examine the coherence time for an experiment similar to the one cited in this paper. For upwind propagation at 500 hz and 325 m distance, a value of $\tau = 0.4$ seconds is given in their figure 4. If $2\pi \Delta f \tau = 1$, then $\Delta f = 0.4$ hz would be the corresponding bandwidth. For data set GA3006, the radiation pattern in the backward direction is not known. Reasoning from an assumption of a piston in a sphere [8] for $\mu \cong 3$, the backward intensity pattern has a narrow peak with a maximum intensity of one-tenth of that in the forward direction and has other structure. Rather than this, our theory above assumed an isotropic radiator. Our result was about 0.1 hz. This value was for a few large temperature turbules, however. In figure 9, the central peak of the measured spectrum is surrounded by a region that falls off more slowly than the peak region. This portion of the spectrum probably results from scattering of large numbers of smaller turbules. Our figure 1 shows that a small isotropic scatterer moving through an extended experimental region would produce a frequency change of 20 hz given sufficient source power. Thus, the possibility exists that the bandwidth given by Galindo and Havelock [7] can also result from the "locally frozen" [9] turbulence assumption. It seems clear that some combination of horizontal and vertical Doppler shifts are the primary cause of shadow zone signal bandwidth spreading. The horizontal component will disappear if the scattering volume is completely in the far field. It is also clear that proper differentiation of the influence of different turbule size classes is essential for the theory of this paper to represent the entire scattered signal spectrum. Can the data be decomposed into turbule size class components rather than frequency components? Perhaps some form of analysis using wavelet theory will prove that the answer to this question is yes.

The authors wish to express their appreciation to Dr. David I. Havelock of National Research Council of Canada for supplying the experimental data used in this paper, for advise concerning data processing, and for several suggestions on the paper itself. We also wish to thank Dr. Keith Wilson for providing the code used to calculate the sound speed and wind speed profiles.

References

- (1.) Auvermann, H. J., 1996, "Comparison of coherent summation to incoherent summation of acoustic signals scattered from turbulence," Proceedings of the Seventh International Symposium on Long Range Sound Propagation, Ecully, France, 24 -26 July, 1996, pp 161-173.
- (2.) Ostashev, V. E., 1997, "Acoustics in Moving Inhomogeneous Media," E & FN Spon, Thomson Professional, London, (adapted from equation 5.47, ch. 5, sect. 5.4.4.)
- (3.) Goedecke, G. H. and H. J. Auvermann, "Acoustic scattering by atmospheric turbules," J. Acoust. Soc. Am. 102 (2), Pt. 1, August, 1997, (eqs. 2 and 3).

(4.) Havelock, D. I., D. Xiao, G. A. Daigle and M. R. Stinson, "Spatial coherence of a sound field in a refractive shadow: Comparison of simulation and experiment," *J. Acoust. Soc. Am.* 98(4), October, 1995.

(5.) MATLAB Reference Guide, The Math Works, Inc., Natick, MA 01760, 1992

(6.) Goedecke, G. H., 1992, "Scattering of Acoustical Waves by a Spinning Atmospheric Turbulence," CR-92-0001-2, U. S. Army Research Laboratory, White Sands Missile Range, NM 88002-5501.

(7.) Galindo, M. and D. I. Havelock, 1996, "Temporal coherence of a soundfield in the turbulent atmosphere near the ground," *Proceedings of the Seventh International Symposium on Long Range Sound Propagation*, Ecully, France, 24 -26 July, 1996, pp 149-159.

(8.) Morse, P. M., 1948, "Vibration and Sound," McGraw-Hill, New York, pp. 324.

(9.) Tatarskii, V. I., 1971, "The Effects of the Turbulent Atmosphere on Wave Propagation," TT-6850464, National Technical Information Service, U. S. Department of Commerce, Springfield, VA 22161.